



University
of Glasgow

Hughes, Gareth Wynn (2005) A realistic, parametric compilation of optimised heliocentric solar sail trajectories. PhD thesis.

<http://theses.gla.ac.uk/5007/>

Copyright and moral rights for this thesis are retained by the author

A copy can be downloaded for personal non-commercial research or study, without prior permission or charge

This thesis cannot be reproduced or quoted extensively from without first obtaining permission in writing from the Author

The content must not be changed in any way or sold commercially in any format or medium without the formal permission of the Author

When referring to this work, full bibliographic details including the author, title, awarding institution and date of the thesis must be given.

A Realistic, Parametric Compilation of Optimised Heliocentric Solar Sail Trajectories

Gareth Wynn Hughes, B.Sc.(Hons)

Thesis submitted to the Faculty of Engineering,
University of Glasgow, for the Degree of Doctor of Philosophy

University of Glasgow
Department of Aerospace Engineering

June 2005

© 2005 Gareth W. Hughes

Acknowledgements

I would like to thank Prof. Colin R. McInnes of the University of Strathclyde (formerly of the University of Glasgow) for his supervision and for suggesting avenues of research for this thesis. His efforts in negotiating research contracts and short consultancy projects are greatly appreciated, both in terms of the results I was able to use in this thesis, and also from a financial aspect. I am grateful for his encouragement throughout my research.

A large proportion of the results in this thesis were produced while working under European Space Agency ESA/ESTEC contract 16534/02/NL/NR – Technical Assistance in the Study of Science Payloads Transported through Solar Sailing. Useful feedback on the trajectory analyses was received from Alessandro Atzei and Dr. Peter Falkner at ESA/ESTEC.

I would also like to thank Dr. David L. Carroll of the University of Illinois, Urbana-Champaign, Illinois, USA, for the use of the Fortran77 Genetic Algorithm that he developed, which was utilised in this thesis.

Finally, I would like to thank my family for their understanding during my period of research, and would like to dedicate this thesis to the memory of my half-sister, Amy.

Abstract

In this thesis, a selection of numerical optimisation methods were developed for application to realistic solar sail heliocentric trajectory optimisation problems. A Non-Linear Programming method based on Sequential Quadratic Programming was developed, with the sail controls parameterised in time. This method was hybridised with Genetic Algorithms or locally-optimal analytical control laws to generate an initial guess, where required. The goal of this thesis is to create a detailed catalogue of trajectories to a broad range of heliocentric targets, subject to realistic constraints on trip-time, sail performance, and thermal-limited solar approach. This thesis illustrates the wide range of targets in the solar system that can be reached with solar sailing. In addition, the trajectory problems for which solar sailing is not attractive are also identified.

Trajectory analysis of sample return missions to the terrestrial planets, Mars, Venus and Mercury, has been conducted. Extensive departure date scans were performed, where it was found that there are minima and maxima in trip-time, separated by discontinuities, providing effective launch windows. Roundtrip optimal launch dates were identified, after combining outbound and return departure date scans. For Mercury rendezvous, the application of positive launch excess velocity and a Venus gravity assist was investigated, where a small trip-time saving can be made.

Trajectories to rendezvous with the Short Period Comet Wirtanen have been optimised, where it was found that a significant reduction in trip time and launch mass could have been realised, relative to a conventional mission. An investigation of using higher performance sails to flyby Long Period Comets has also been conducted, to demonstrate that solar sailing could be used to reach newly discovered comets soon after first discovery, such as the previous Hale-Bopp apparition. It is also shown that solar sailing could be used, instead of solar electric propulsion, to rendezvous with two Main-Belt asteroids, with a reduction in launch mass. The

open ended nature of solar sailing was used to show that rendezvous with two further asteroids is also possible. It is also shown that a three-phase trajectory concept, utilising an inclination cranking manoeuvre, could be used to return a sample from a high inclination Near-Earth Asteroid, that would be essentially impossible to reach using conventional propulsion.

It is demonstrated that flyby missions to the outer planets, such as Pluto are feasible in reasonable timescales using a solar photonic assist concept. However, due to the faint solar radiation pressure at Jupiter, only flyby missions are practical to the Jovian system with solar sails. An extensive trade-off between launch hyperbolic excess energy, Jupiter arrival velocity, trip-time, and the number of photonic assist loops has been conducted. By contrast, solar sailing appears to be the only feasible option for missions to the Heliopause at 200 AU. Heliopause trajectory analysis included investigation of the number of loops, and the effect of thermally-constrained closest solar approach on escape velocity and trip-time. It was found that, in order to reach the Heliopause in 25 years, a solar sail of characteristic acceleration of order 1.5 mm s^{-2} would be required, executing a thermally constrained solar photonic assist at 0.25 AU. Investigation of the effect of positive launch energy is also conducted for Heliopause trajectories.

A key near-term mission application for solar sails is a Solar Polar Orbiter. Trajectory analysis has revealed that a solar sail transfer to a true solar polar orbit, Earth resonant at 0.48 AU, in 5 years would require a characteristic acceleration of 0.42 mm s^{-2} . In the course of the parametric analysis, two-phase and three-phase scenarios were investigated, with an assessment of the effect of spiralling down to a close cranking orbit radius from positive launch excess energy.

Finally, new transfers to exotic, displaced Non-Keplerian Orbits have been optimised for a range of final orbit dimensions among one family of these unique orbits. For lower performance sails, transfers to artificial Lagrange points have been optimised, in the context of the Geostorm and Polar Observer missions.

Nomenclature

The following list shows the key symbols in use in this thesis. All symbols, including those not listed here, are defined where they are used in the text.

a	Semi-major axis
A	Total solar sail area
a_c	Characteristic acceleration
c	Speed of light
\mathbf{c}, c_R, c_T	Blended control law required vector, radial, transverse components
C_3	Hyperbolic excess launch energy
e	Eccentricity
\mathbf{f}	Sail thrust vector
f	True anomaly
G_a, G_e	Blended control law weighting function coefficients
H	Hamiltonian function of optimal control theory
i	Inclination
M	Total solar sail spacecraft mass
m_p	Sail payload mass
m_s	Sail assembly mass
\mathbf{n}	Sail normal vector
p	Semi-latus rectum
P, P_{AU}	Solar radiation pressure, at 1 AU

\mathbf{q}	Required force vector
\mathbf{r}, r	Sun-spacecraft vector, radial distance from the Sun
\tilde{r}	Sail reflectivity
S	Radial sail thrust component
T_s	Sail film temperature
T	Transverse sail thrust component
t, t_f	Time, terminal time
v_∞	Hyperbolic excess velocity (at flyby)
v_r, v_θ, v_ϕ	Spherical polar velocity components
W	Normal sail thrust component
W, W_E	Solar flux, at Earth distance
z	Non-Keplerian Orbit vertical displacement
$\alpha, \tilde{\alpha}, \alpha^*$	Sail cone angle, required cone angle, and optimal cone angle
β	Sail lightness number
$\delta, \tilde{\delta}, \delta^*$	Sail clock angle, required clock angle, and optimal clock angle
Δv	Velocity increment
$\varepsilon, \varepsilon_f, \varepsilon_b$	Emissivity, front surface, back surface
η	Sail reflective efficiency factor
θ	Azimuth angle
κ_a, κ_e	Blended control law weighting factors
λ	Primer vector
μ	Gravitational parameter
ρ	Non-Keplerian Orbit horizontal displacement
σ	Total sail loading

σ_s	Sail assembly loading
$\tilde{\sigma}$	Stefan-Boltzmann constant
ϕ	Elevation angle
ω	Argument of perihelion
Ω	Right ascension of ascending node

Glossary of Terms

The following list shows the acronyms and terms in use in this thesis. All these terms are defined where they are first used in the text.

AU	Astronomical unit(s)
CFRP	Carbon Fibre Reinforced Plastic
DLR	German Aerospace Centre
ESA	European Space Agency
ESTEC	European Space Technology Centre
GA	Genetic Algorithm, or Gravity Assist
IHP	Interstellar Heliopause Probe
ISP	Interstellar Precursor
JAXA	Japan Aerospace Exploration Agency
JPL	Jet Propulsion Laboratory
LPC	Long Period Comet
NASA	National Aeronautics and Space Administration
NEA	Near-Earth Asteroid
NKO	Non-Keplerian Orbit
RTN	Radial-Transverse-Normal spacecraft rotating frame
SPC	Short Period Comet
SQP	Sequential Quadratic Programming
SRP	Solar Radiation Pressure

Contents

Acknowledgements	ii
Abstract	iii
Nomenclature	v
Glossary of Terms.....	viii
1 Introduction	1
1.1 Solar Sailing.....	2
1.2 Historical and Physical Principles.....	2
1.3 Sail Design Configurations	4
1.3.1 3-axis Stabilised	4
1.3.2 Spin-Stabilised	7
1.3.3 Compound Sail.....	8
1.4 Performance Metrics	9
1.5 Non-Ideal Effects	11
1.6 Solar Sail Orbital Dynamics.....	12
1.7 Locally Optimal Control Laws.....	15
1.8 Thesis Goals and Objectives	23
2 Trajectory Optimisation Methods	27
2.1 Indirect Methods	28
2.2 Direct Methods.....	32
2.2.1 Global Search Methods.....	33

Branch and Bound Methods.....	33
Genetic Algorithms	34
Simulated Annealing.....	35
2.2.2 Local Search Methods.....	36
2.3 Heliocentric Trajectory Optimisation Method	37
2.3.1 Solar Sail Dynamical Model	38
2.3.2 Control Representation	38
2.3.3 Non-Linear Programming Optimisation Method.....	40
2.3.4 Initial Control Estimates and Genetic Algorithms	41
3 Inner Solar System Trajectories	43
3.1 Mars Trajectories	44
3.1.1 Departure Date Scans	46
3.1.2 Earth–Mars Phase	46
3.1.3 Mars – Earth Phase	53
3.2 Venus Trajectories	57
3.2.1 Earth–Venus Phase	59
3.2.2 Venus – Earth Phase	63
3.3 Mercury Trajectories	69
3.3.1 Departure Date Scans	71
3.3.2 Earth–Mercury Phase	72
3.3.3 Mercury–Earth Phase	75
3.3.4 Selected Optimal Earth – Mercury Trajectory	76
3.3.5 Selected Optimal Mercury – Earth Trajectory	79
3.3.6 Effect of Non-Zero C_3 at Earth Departure	83
3.3.7 Venus Gravity Assist	85

3.4 Summary and Discussion	89
4 Small-Body Trajectories	92
4.1 Small-Body Encounters	93
4.1.1 Short Period Comet Rendezvous (Wirtanen).....	95
4.1.2 Long Period Comet Flybys	99
4.1.3 Hale-Bopp Perihelion Flyby	99
4.1.4 Hale-Bopp Descending Node Flyby	102
4.1.5 Dual Comet Flyby	105
4.1.6 Hale-Bopp Opportunity Mission Analysis.....	106
4.1.7 Main-Belt Asteroid Survey	108
4.2 High Energy Asteroid Sample Return.....	112
4.2.1 Trajectory Structure	112
4.2.2 Earth-to-Cranking Orbit.....	113
4.2.3 Inclination Cranking	115
4.2.4 Cranking Orbit to/from Ellipse	117
4.2.5 Earth – Asteroid Phases	122
4.2.6 Asteroid – Earth Phases	128
4.3 Summary and Discussion	134
5 Outer Solar System Trajectories.....	136
5.1 Jupiter Trajectories.....	137
5.1.1 Earth – Jupiter Circular-Coplanar Transfer	137
5.1.2 Jupiter Fast Flyby.....	140
5.1.3 Minimised Relative Velocity Flyby	145
5.1.4 Effect of Positive C_3 on Minimised Arrival Velocity for Lower Characteristic Accelerations	149

5.2 Pluto Trajectories	158
5.2.1 Single Photonic Assist Fast Flyby	161
5.2.2 Triple Photonic Assist – Slow Flyby	167
5.3 Summary and Discussion.....	170
6 Interstellar Heliopause Probe Trajectories.....	172
6.1 Fast IHP Mission (single loop)	175
6.2 Slow IHP Mission (multiple loops).....	182
6.3 Jupiter Gravity Assist on Escape Trajectory	196
6.4 Effect of Excess C_3 at Launch.....	201
6.5 Summary and Discussion.....	205
7 Solar Polar Orbiter Trajectories.....	207
7.1 Solar Polar Orbit Transfer.....	208
7.2 Approximate Trip-Times	209
7.3 Inward Spirals to Low Inclinations at 0.48 AU	213
7.4 Excess Launch Energy ($C_3 > 0$)	214
7.5 Reference Trajectory.....	216
7.6 Fast Mission to 0.48 AU Polar Orbit	224
7.7 Summary and Discussion.....	225
8 Non-Keplerian Orbit Transfers	226
8.1 Two-Body Non-Keplerian Orbits	226
8.2 Three-Body Non-Keplerian Orbits	233
8.2.1 Transfer to Geostorm Orbit.....	236
8.2.2 Transfers to Polar Observer Orbit.....	240
8.3 Summary and Discussion.....	247
9 Conclusions and Discussion.....	248

9.1 Inner Solar System trajectories	248
9.2 Small-Body Trajectories	249
9.3 Outer Solar System Trajectories	250
9.4 Interstellar Heliopause Probe Trajectories	250
9.5 Solar Polar Orbiter Trajectories	251
9.6 Non-Keplerian Orbit Transfers	252
9.7 Further Work.....	252
9.8 Key Thesis Contributions.....	253
References.....	255

List of Tables

4.1	5.0 mm s ⁻² Wirtanen rendezvous times	96
4.2	Wirtanen rendezvous times against characteristic acceleration	97
4.3	Sailcraft sizing for 1.0 mm s ⁻² Wirtanen rendezvous mission with Rosetta payload	98
4.4	Hale-Bopp perihelion flyby times	100
4.5	2.0 mm s ⁻² Hale-Bopp, minimised relative velocity, perihelion flyby times ...	100
4.6	Hale-Bopp descending node flyby times	103
4.7	Example Long Period Comet nodal flyby times	105
4.8	Sailcraft sizing for 0.362 mm s ⁻² Hale-Bopp nodal flyby	108
4.9	Sailcraft sizing for 1.0 mm s ⁻² asteroid rendezvous mission with Dawn payload	110
4.10	Sailcraft sizing for 1.0 mm s ⁻² asteroid rendezvous mission with reduced payload	110
4.11	Asteroid Sample Return mission timeline	134
6.1	Representative effect of JGA on 200 AU trip time (0.85 mm s ⁻²)	198
8.1	Geostorm transfer initial conditions at Earth escape.....	236
8.2	Polar Observer hover-point transfer initial heliocentric conditions	240

List of Figures

1.1	ATK 20 x 20 m sail deployment test in vacuum chamber [NASA/ATK]	6
1.2	ESA/DLR 20 x 20 m sail ground deployment test in 1999 [DLR]	6
1.3	1993 Znamya-2 spinning reflector experiment [SRC Energia]	7
1.4	Compound sail mirror configuration [McInnes, 2000a]	8
1.5	Control angle definition	14
1.6	Required force vector for locally optimal trajectories	17
1.7	Maximising the rate of change of the semi-major axis	18
1.8	Maximising the rate of change of the eccentricity	19
1.9	Blending control laws for elliptical orbit transfer	22
1.10	Cranking orbit using inclination control law	23
2.2	Two methods of discretised control representation	39
3.1	Circular coplanar trip-times from 1 AU to 1.525 AU, against characteristic acceleration	45
3.2	Earth–Mars departure date scan	48
3.3	Departure date optimal Earth–Mars rendezvous trajectory (0.5 mm s^{-2})	49
3.4	Sub-optimal departure date Earth–Mars rendezvous (0.5 mm s^{-2})	49
3.5	Earth–Mars rendezvous control profile	50
3.6	Earth–Mars rendezvous orbital element evolution	50
3.7	Earth–Mars heliocentric distance and sail film temperature	52
3.8	Earth – Mars telecommunications angles	53
3.9	Mars – Earth Departure Date Scan	55

3.10 Mars – Earth rendezvous trajectory (0.86 mm s^{-2}).....	55
3.11 Mars-Earth rendezvous control profile	56
3.12 Mars-Earth rendezvous orbital element evolution	56
3.13 Mars–Earth heliocentric distance and sail film temperature.....	57
3.14 Circular coplanar trip-times from 1 AU to 0.723 AU, against characteristic acceleration	58
3.15 Earth–Venus departure date scan (0.2 mm s^{-2})	59
3.16 Departure date optimal Earth–Venus rendezvous (0.2 mm s^{-2})	61
3.17 Sub-optimal departure date Earth–Venus rendezvous (0.2 mm s^{-2})	61
3.18 Earth–Venus rendezvous control profile.....	62
3.19 Earth–Venus rendezvous orbital element evolution	62
3.20 Earth–Venus heliocentric distance and sail film temperature.....	63
3.21 Venus–Earth departure date scan (0.48 mm s^{-2})	64
3.22 Venus Sample Return departure date mapping	65
3.23 Total mission duration dependence on Earth departure date	65
3.24 Venus – Earth rendezvous trajectory (0.48 mm s^{-2}).....	67
3.25 Venus – Earth rendezvous control profile.....	68
3.26 Venus – Earth rendezvous orbital element evolution	68
3.27 Venus – Earth heliocentric distance and sail film temperature.....	69
3.28 Circular coplanar trip-times from 1 AU to 0.387 AU, against characteristic acceleration	71
3.29 Earth–Mercury departure date scan (0.25 mm s^{-2}).....	73
3.30 Example Earth–Mercury trajectory (2013 opportunity)	74
3.31 Earth–Mercury control profile (2013 opportunity).....	74
3.32 Total mission duration as a function of Earth departure date	76
3.33 Selected 2014 opportunity 0.25 mm s^{-2} Earth–Mercury trajectory.....	77
3.34 Selected 2014 opportunity Earth–Mercury control profiles.....	78

3.35 Earth – Mercury orbital element evolution	78
3.36 Earth – Mercury heliocentric distance and sail film temperature	79
3.37 Mercury – Earth trip time variation about selected departure date	80
3.38 0.7839 mm s^{-2} Mercury – Earth return trajectory	81
3.39 Mercury – Earth control profile	81
3.40 Mercury – Earth orbital element evolution	82
3.41 Mercury – Earth heliocentric distance and sail film temperature	82
3.42 Effect of hyperbolic excess energy at launch for Earth-Mars transfers	83
3.43 Effect of hyperbolic excess energy at launch (with 2353 kg Mercury sample return payload taken from McInnes <i>et al</i> [2003c])	85
3.44 Earth-Mercury transfer with Venus gravity assist	87
3.45 Venus gravity assist cone angle profile.....	88
3.46 Time history of semi-major axis and eccentricity.....	88
4.1 1.0 mm s^{-2} Wirtanen rendezvous trajectory	96
4.2 Wirtanen rendezvous orbital element evolution	97
4.3 5.0 mm s^{-2} Hale-Bopp perihelion flyby.....	101
4.4 2.0 mm s^{-2} Hale-Bopp minimised relative velocity flyby.....	101
4.5 5.0 mm s^{-2} Hale-Bopp descending node flyby.....	104
4.6 2.0 mm s^{-2} Hale-Bopp flyby and return trajectory.....	104
4.7 Earth – Hale-Bopp – Mueller dual comet nodal flyby.....	106
4.8 Launch date contingency against characteristic acceleration for Hale-Bopp nodal encounter	107
4.9 Earth – Vesta – Ceres rendezvous.....	111
4.10 Ceres – Lucina – Lutetia rendezvous.....	111
4.11 Earth to 0.3 AU cranking orbit transfer time ($C_3=0$)	114
4.12 0.5 mm s^{-2} positive C_3 Earth to 0.3 AU cranking orbit transfer time.....	115
4.13 Cranking time against inclination change.....	116

4.14 Crank time against characteristic acceleration and inclination change.....	116
4.15 Departure date optimal total one-way transfer time to 2001 QP153	120
4.16 0.5 mm s^{-2} Asteroid-0.3 AU departure true anomaly scan.....	121
4.17 0.64 mm s^{-2} Asteroid-0.3 AU departure true anomaly scan.....	121
4.18 0.5 mm s^{-2} Earth-cranking orbit spiral with $C_3=37 \text{ km}^2 \text{ s}^{-2}$	122
4.19 Earth-cranking orbit cone angle profile	123
4.20 Earth-cranking orbit orbital element evolution	123
4.21 Earth-cranking orbit heliocentric distance and sail film temperature	124
4.22 0.5 mm s^{-2} inclination crank-up trajectory	125
4.23 Crank-up control angle profiles and inclination change	125
4.24 0.5 mm s^{-2} cranking orbit-asteroid rendezvous	126
4.25 Cranking orbit-asteroid rendezvous cone angle profile	126
4.26 Cranking orbit-asteroid rendezvous orbital element evolution.....	127
4.27 Cranking orbit-asteroid heliocentric distance and sail film temperature	127
4.28 0.64 mm s^{-2} asteroid-cranking orbit transfer	128
4.29 Asteroid-cranking orbit transfer cone angle profile	129
4.30 Asteroid-cranking orbit transfer orbital element evolution.....	129
4.31 Asteroid-cranking orbit transfer heliocentric distance and sail film temperature	130
4.32 0.64 mm s^{-2} inclination crank-down trajectory	130
4.33 Crank-down control angles profiles and inclination change.....	131
4.34 0.64 mm s^{-2} cranking orbit-Earth spiral	132
4.35 Cranking orbit-Earth control angle profiles	132
4.36 Cranking orbit-Earth orbital element evolution	133
4.37 Cranking orbit-Earth heliocentric distance and sail film temperature	133
5.1 Earth – Jupiter circular-coplanar transfer time for flat and compound sails....	138

5.2	5.7 year Earth – Jupiter transfer (3.0 mm s^{-2}).....	139
5.3	Perihelion constrained 10 year trajectory to 100 AU [Sauer, 1999]	140
5.4	Fast Jupiter coplanar flyby times using solar photonic assist	141
5.5	1.0 mm s^{-2} Jupiter fast coplanar flyby (2.1 years).....	142
5.6	1.0 mm s^{-2} Jupiter fast coplanar flyby control angle profile	143
5.7	0.65 mm s^{-2} Jupiter fast coplanar flyby.....	143
5.8	0.5 mm s^{-2} dual photonic assist Jupiter flyby trajectory.....	144
5.9	0.5 mm s^{-2} dual photonic assist control profile	145
5.10	Minimised relative velocity, single photonic assist flyby, curves for 0.65, 0.75, and 1.0 mm s^{-2}	147
5.11	0.5 mm s^{-2} Earth–Jupiter, 5.39 year, dual photonic assist flyby, with minimised arrival excess velocity	147
5.12	0.5 mm s^{-2} Earth–Jupiter, 5.39 year, dual photonic assist flyby control profile	148
5.13	0.5 mm s^{-2} Earth–Jupiter, 5.39 year, orbital element evolution	148
5.14	0.5 mm s^{-2} Earth–Jupiter, 5.39 year, distance and sail film temperature	149
5.15	Minimum trip time against characteristic acceleration for a dual photonic assist Earth-Jupiter transfer ($C_3=0$).....	151
5.16	0.5 mm s^{-2} Earth-Jupiter trajectory: effect of increasing C_3 to reduce number of heliocentric revolutions, thereby reducing arrival velocity.....	151
5.17	Minimised arrival velocity against trip time for 0.50 mm s^{-2} (C_3 in units of $\text{km}^2 \text{ s}^{-2}$)	152
5.18	Minimised arrival velocity against trip time for 0.45 mm s^{-2} (C_3 in units of $\text{km}^2 \text{ s}^{-2}$)	152
5.19	Minimised arrival velocity against trip time for 0.43 mm s^{-2} (C_3 in units of $\text{km}^2 \text{ s}^{-2}$)	153
5.20	Minimised arrival velocity against trip time for 0.40 mm s^{-2} (C_3 in units of $\text{km}^2 \text{ s}^{-2}$)	153

5.21	0.5 mm s ⁻² , C ₃ =10 km ² s ⁻² single loop, Earth-Jupiter trajectory, with ‘overshoot’ and coast segment outside of 5.2 AU (2300 days).....	155
5.22	Earth-Jupiter, 6 year, 0.37 mm s ⁻² trajectory with minimised arrival velocity	156
5.23	0.37 mm s ⁻² trajectory control angle profile.....	156
5.24	0.37 mm s ⁻² trajectory orbital element evolution	157
5.25	0.37 mm s ⁻² trajectory heliocentric distance and sail film temperature	157
5.26	Trip times to 30 AU against characteristic acceleration [Sweetser and Sauer, 2001]	160
5.27	Pluto flyby single photonic assist trip times (departure Feb. 5, 2014).....	162
5.28	Pluto single photonic assist flyby velocity (departure Feb. 5, 2014).....	162
5.29	Launch date scan for 1.0 mm s ⁻²	164
5.30	3.0 mm s ⁻² fully optimised single photonic assist Pluto flyby	164
5.31	Magnified image of initial 3.0 mm s ⁻² single photonic assist	165
5.32	3.0 mm s ⁻² single photonic assist Pluto flyby cone and clock angle profile	165
5.33	3.0 mm s ⁻² single photonic assist Pluto flyby orbital elements	166
5.34	3.0 mm s ⁻² single photonic assist Pluto flyby heliocentric distance and sail film temperature.....	166
5.35	0.5 mm s ⁻² triple photonic assist Pluto flyby.....	167
5.36	Magnified image of initial 0.5 mm s ⁻² Pluto flyby.....	168
5.37	0.5 mm s ⁻² triple photonic assist Pluto flyby control angle profile	169
5.38	0.5 mm s ⁻² triple photonic assist Pluto flyby orbital elements	169
5.39	0.5 mm s ⁻² triple photonic assist Pluto flyby heliocentric distance and sail film temperature.....	170
6.1	NASA Interstellar Probe, 0.25 AU solar pass [Wallace <i>et al</i> , 2000]	174
6.2	0.75 mm s ⁻² , 21 year trajectory, 0.1 AU solar pass [Leipold <i>et al</i> , 2003]	174
6.3	Constrained perihelion contours of velocity at 5 AU.....	176
6.4	Constrained perihelion contours of trip time to 200 AU.....	176

6.5	Unconstrained 20 year trajectory to 250 AU (0.1 AU solar approach) [Sauer, 1999]	177
6.6	15 year 3.0 mm s^{-2} single photonic assist IHP trajectory ($r_p = 0.25 \text{ AU}$)	178
6.7	25 year 1.5 mm s^{-2} single photonic assist IHP trajectory ($r_p = 0.25 \text{ AU}$)	178
6.8	Variation of trip time about optimal launch date to Heliopause nose for 3.0 mm s^{-2}	179
6.9	15 year 3.0 mm s^{-2} trajectory to Heliosphere nose at 200 AU	180
6.10	15 year mission X-Z out-of-ecliptic projection (escape asymptote is not in X-Z plane – final elevation 7.5°)	180
6.11	15 year mission control angle profile.....	181
6.12	15 year mission orbital element temporal evolution.....	181
6.13	15 year mission heliocentric radius and sail film temperature.....	182
6.14	46 year 0.5 mm s^{-2} triple photonic assist IHP trajectory ($r_p = 0.27 \text{ AU}$)	183
6.15	36 year 0.75 mm s^{-2} dual photonic assist IHP trajectory ($r_p = 0.26 \text{ AU}$).....	183
6.16	26 year 0.85 mm s^{-2} dual photonic assist IHP trajectory ($r_p = 0.16 \text{ AU}$).....	184
6.17	Perihelion radius contours showing sensitivity of perihelion velocity to aphelion radius for closed orbits	186
6.18	Half-arc trajectory velocity at 5 AU with closest approach contours	186
6.19	Reflectivity contours for closest approach with 520 K thermal limit	188
6.20	Reflectivity contours for closest approach with 623 K thermal limit	188
6.21	Reflectivity contours for closest approach with 800 K thermal limit	189
6.22	Reflectivity contours for closest approach with 1000 K thermal limit	189
6.23	Variation of trip time about optimal launch date to Heliopause nose for 1.5 mm s^{-2}	191
6.24	24 year 1.5 mm s^{-2} trajectory to Heliosphere nose at 200 AU	191
6.25	24 year mission X-Z out-of-ecliptic projection (escape asymptote is not in X-Z plane – final elevation 7.5°)	192

6.26	24 year mission control angle profile.....	192
6.27	24 year mission orbital element temporal evolution.....	193
6.28	24 year mission heliocentric radius and sail film temperature.....	193
6.29	29 year 1.0 mm s ⁻² dual photonic assist IHP trajectory ($r_p = 0.25$ AU).....	195
6.30	26.5 year 1.0 mm s ⁻² dual photonic assist IHP trajectory ($r_p = 0.20$ AU).....	195
6.31	Approximate Jupiter gravity assist Δv	197
6.32	25 year 0.85 mm s ⁻² trajectory with Jupiter gravity assist	199
6.33	25 year 0.85 mm s ⁻² , pre-JGA control angle profile	199
6.34	25 year 0.85 mm s ⁻² , pre-JGA orbital element temporal evolution.....	200
6.35	25 year 0.85 mm s ⁻² , pre-JGA heliocentric radius and sail film temperature ..	200
6.36	Effect of positive C_3 with and against Earth velocity for 0.85 mm s ⁻²	202
6.37	$C_3 = 20$ km ² s ⁻² 3.0 mm s ⁻² IHP trajectory	203
6.38	$C_3 = 20$ km ² s ⁻² 1.5 mm s ⁻² IHP trajectory	204
6.39	$C_3 = 20$ km ² s ⁻² 0.85 mm s ⁻² IHP trajectory ($r_p = 0.16$ AU).....	204
6.40	29 year $C_3 = 30$ km ² s ⁻² 0.75 mm s ⁻² IHP trajectory ($r_p = 0.20$ AU).....	205
7.1	Cranking times from zero to 82.75°, against cranking orbit radius and solar sail characteristic acceleration	210
7.2	Two-phase trip times to polar orbit, by cranking at resonances	210
7.3	Three-phase, total trip times to 1 AU ($N=1$) solar polar orbit.....	211
7.4	Three-phase total trip times to 0.63 AU ($N=2$) solar polar orbit.....	212
7.5	Three-phase total trip times to 0.48 AU ($N=3$) solar polar orbit.....	212
7.6	Effect of optimised spiral to low inclinations on total trip time to 0.48 AU polar orbit	214
7.7	Spiral-in time to cranking orbit radii of 0.30, 0.40 and 0.48 AU for characteristic accelerations of 0.3, 0.4 and 0.5 mm s ⁻² , against launch C_3	215
7.8	0.42 mm s ⁻² Solar Polar Orbit transfer trajectory	217
7.9	0.42 mm s ⁻² Solar Polar Orbiter mission X-Z projection	218

7.10	0.42 mm s ⁻² Solar Polar Orbiter mission optimised phase	218
7.11	0.42 mm s ⁻² trajectory optimised phase control angle profile	219
7.12	0.42 mm s ⁻² trajectory optimised phase orbital elements	219
7.13	Optimised phase heliocentric distance and sail film temperature	220
7.14	0.42 mm s ⁻² cranking phase trajectory	221
7.15	0.42 mm s ⁻² cranking phase control profile	221
7.16	0.42 mm s ⁻² cranking phase orbital elements	222
7.17	0.42 mm s ⁻² cranking phase heliocentric distance and sail film temperature...222	
7.18	Solar polar orbit propagation telecommunications angles	223
7.19	Solar polar orbit propagation Earth–spacecraft distance	223
7.20	0.5 mm s ⁻² , Fast 3.1 year trajectory to 0.48 AU polar orbit	224
8.1	Sun-centred Non-Keplerian Orbit (inertial frame) [adapted from McInnes, 1999]	227
8.2	Contours of lightness number against displaced NKO dimension	229
8.3	Transfer times to 1 year displaced Non-Keplerian Orbits	230
8.4	Minimum-time transfer to Earth synchronous 0.5 x 0.5 AU, 1 year NKO.....	231
8.5	Control profile for transfer to Earth synchronous 0.5 × 0.5 AU NKO	232
8.6	Minimum-time transfer to three different NKOs	232
8.7	Solar sail in a restricted three-body system.....	233
8.8	Contours of (ideal) sail loading for families of artificial equilibria [C. R. McInnes]	234
8.9	Geostorm Sub-L ₁ point orbit geometry in ecliptic plane (not to scale)	237
8.10	Optimal 0.3223 mm s ⁻² transfer, from Earth escape to Geostorm orbit.....	238
8.11	Magnified image of final Geostorm Sub-L ₁ point approach.....	239
8.12	Geostorm transfer Earth-relative trajectory (Sun-Earth along positive x-axis)239	
8.13	Polar Observer hover-point geometry in vertical plane (not to scale)	241

8.14 Transfer time to Polar Observer hover-point, dependence on characteristic acceleration	242
8.15 Optimal 0.3227 mm s^{-2} transfer to 45° 400 Earth radii hover-point	243
8.16 Polar observer transfer control profile	244
8.17 Polar observer transfer Earth-relative trajectory (with sphere of influence depicted).....	244
8.18 Polar observer transfer Earth – Sail distance along trajectory	245
8.19 Ecliptic projection and X-Z projection of positive control angle bias trajectory dispersion (Earth-centred Sun-line relative axes)	246
8.20 Positive control angle bias trajectory dispersion (Earth centred Sun-line relative axes)	246

Chapter 1

Introduction

In this Chapter, a brief introduction to the history and principles of solar sailing will be provided. After a short discussion of the various solar sail design configurations and required materials technologies, the key performance metrics used in this thesis will be outlined. The effect of a non-ideal sail is also pointed out. An introduction to the solar sail orbital dynamics and sail orbits is provided, which leads to the definition of the optimal sail force vector, used in generating a set of locally optimal control laws. These control laws are important because they will be used at various points in this thesis, to generate initial guesses for optimisation.

It is noted that in this thesis there will be no specific literature review section. Due to the broad and diverse range of different trajectory problems addressed in different chapters, it would seem excessively complex to include a review of all the literature in one place. Instead, for each aspect of this thesis, the previous research in the literature is discussed in the initial pages of each chapter. Previous literature is also referenced as appropriate throughout the thesis. A discussion of the conference and journal papers published by the Author, either as the main or co-author, is provided at the end of this Chapter. Throughout the course of this thesis, many of the results have been published in international journals and conference proceedings, and have thus been subjected to peer review.

Lastly, the final section of this Chapter outlines the main thesis goals and the outstanding questions which will be addressed, providing a clear discussion of what is new. In addition, in each subsequent chapter, the chapter-specific goals will be outlined, and then a chapter-specific conclusion is provided.

1.1 Solar Sailing

Solar sailing is an elegant form of propulsion that does not rely on reaction mass for motive force. Instead, the continuous source of solar photons impinging on a large, thin, gossamer reflector imparts momentum, giving the solar sail a very small, but continuous acceleration. This small acceleration can yield a considerable Δv for long duration interplanetary missions, at essentially no propellant expense. Solar sailing can eliminate the need for gravity assists, particularly when spiralling to targets such as Mercury, deep within the solar gravity well. Since propellant mass is not an issue, the trajectory aspects of sample return missions become significantly simpler, not requiring the transportation of any propellant for the return journey to the target body. High-energy targets such as high-energy comets and asteroids can be reached without resorting to gravity assists and large launch vehicles, or are even truly enabled by solar sailing. Outer solar system missions become easier via a close solar pass, where the increased solar radiation pressure can yield the high velocities necessary to reach Jupiter, Pluto and beyond, without resorting to gravity assists. Solar sailing enables transfers to true polar orbits about the Sun, and also to exciting displaced Non-Keplerian Orbits, enabling new and exotic vantage points which are not possible with conventional propulsion systems. However, development of lightweight structures, very thin reflecting films, highly reliable deployment mechanisms, and miniaturised payloads must take place to enable acceptable trip times for solar sails. It is also important that efficient, optimal thrust steering profiles are found for each mission, so that the solar sail can reach its destination in the minimum time, while satisfying realistic operational constraints.

1.2 Historical and Physical Principles

The principle of solar radiation pressure has been known since the 17th Century when, in 1619, Johannes Kepler proposed that the tail of a comet is pushed away from the Sun by some radial repulsive force. This was consistent with the corpuscular theory of light, which prevailed at the time [Koblik, 2003, p.3]. Interplanetary dust is also affected by light pressure in a process known as the Poynting-Robertson effect [McInnes, 1999, p.32]. The concept of light pressure was demonstrated theoretically by James Clerk Maxwell in 1873, in addition to his

groundbreaking work on Electricity and Magnetism. Russian physicist Peter Lebedew measured photon pressure experimentally in 1900 [McInnes, 1999]. The use of this concept to propel a spacecraft was first envisaged by the Russian pioneers of astronautics, Konstantin Tsiolkovsky in 1921, and Fridrickh Tsander in 1924. After a period, solar sailing was re-invented in the 1950s, notably by Carl Wiley in 1951, and Richard Garwin, who first conceived the term 'solar sailing' in a technical publication in 1958 [Garwin, 1958]. There was great optimism for the promise of solar sailing in the 1950s, however, the difficult problems of constructing and deploying a large gossamer structure were not realised. After preliminary work at NASA, Jerome Wright discovered a solar sail rendezvous trajectory to Halley's Comet. Subsequently, work was conducted for a Halley rendezvous mission, during the late 1970s at NASA/JPL, both in hardware and trajectory design. Numerous design concepts were analysed, which included characterisation of structural dynamics and control, as well as manufacture of potential sail film materials. However, solar electric propulsion (SEP) was at a more advanced development stage, and the solar sail option was dropped in 1977. Ultimately, the SEP costs increased and the rendezvous mission was cancelled. Since then numerous design activities have been conducted by the World Space Foundation after its formation in 1979, and also the Union pour la Promotion de la Propulsion Photonique (U3P) in 1981. In the 1990s, progress in hardware concepts was made with the deployment of large structures in space, such as the 1993 Znamya reflector, and the 14 m Inflatable Antenna Experiment, deployed from Space Shuttle STS-77 in 1996. The 1990s saw a large increase in the number of technical papers on solar sailing, as hardware development accelerated. The 1999 publication of a book by McInnes provided a complete review of solar sail research up to then, in addition to the discovery of novel new orbits and mission applications, and probably supplied the stimulus for the rapid research activities taking place today [McInnes, 1999].

Solar sails are propelled by the momentum imparted by the photons incident on the sail film, emanating from the Sun. For a perfect reflector, this force is doubled, due to Newton's third law, as the reflected photons impart a reaction force. The consequence of this is that the thrust produced by an ideal solar sail is directed normal to the, ideally flat, reflecting surface. The effect of Solar Radiation Pressure (SRP) impinging on a surface can be described by the Quantum description,

pioneered by Max Planck, where photons transport momentum and energy, and by the Wave description, due to Maxwell, whereby an electromagnetic wave generates a Lorentz force [McInnes, 1999, pp. 34-38]. The results of these two theories are equivalent, consistent with wave-particle duality, and the resulting solar radiation pressure is given by, $P = W/c$, where W is the solar flux and c is the speed of light in vacuo. At 1 AU, the solar radiation pressure is $4.56 \times 10^{-6} \text{ N m}^{-2}$. Since the solar flux has an inverse square variation with heliocentric distance, the SRP and hence sail thrust also varies as an inverse square law. Naturally, the thrust produced by the solar sail cannot be directed towards the Sun. The solar sail can spiral outwards from the Sun by directing a component of the thrust along the velocity vector, increasing its orbital angular momentum. Inward spiralling is accomplished by directing a component of the thrust against the velocity vector, decreasing the orbital angular momentum. This may seem inefficient compared with ion propulsion, which is free to thrust in any direction, but solar sails have the key advantage of not requiring propellant.

1.3 Sail Design Configurations

1.3.1 3-axis Stabilised

The traditional solar sail design is the 3-axis stabilised concept. The configuration is usually a square. Several substrate segments are thinly coated with highly reflective and emissive materials, and these segments are then bonded to form four triangular sail quadrants, attached to four deployable booms cantilevered from a central load bearing hub, which also initially serves as a deployment module. Upon successful sail deployment, the deployment module and associated motors and drives can then be jettisoned, to reduce the mass of the sail assembly. The four booms must be sized according to the increased bending loads imposed as sail area increases. The main driver in solar sail development is to reduce the boom linear density, without sacrificing buckling strength, in addition to reducing the sail film areal density. The booms must also be sized to provide adequate tension to the sail film, to keep it flat and remove wrinkles. Ideally, attitude control could be achieved using small segments of sail material known as tip-vanes, mounted on the boom tips, to translate the centre of light pressure with respect to the centre of mass, generating control

torques. Conversely, the spacecraft subsystems and payload could be mounted on a deployable mast gimbaled at the central hub. This would translate the centre of mass with respect to the centre of light pressure, thereby generating a control torque. Detailed attitude control models have recently been devised [Wie, 2001].

Significant progress has been made in recent years within NASA, both in terms of booms and sail film technology, but also in recent ground deployment tests. L'Garde have developed space rigidised, inflatable booms for NASA, with a linear density as low as 14 g m^{-1} , and are using commercially available $0.9 \mu\text{m}$ Mylar as the sail film, which has been successfully aluminised. In 2004, L'Garde built a 10 m square sail model and have successfully deployed it in the 30 m NASA Glenn Research Center vacuum chamber. The other main contractor for NASA is Alliant Techsystems (ATK, formerly ABLE Engineering), who have designed graphite coilable booms with a low linear density of order 40 g m^{-1} . Extrapolated boom data is available to fabricate sails up to $300 \times 300 \text{ m}$ [Murphy *et al*, 2002]. These booms have a long proven flight heritage, with the most recent application being 32 m booms for the International Space Station solar arrays. The ATK sail design uses these booms and $2 \mu\text{m}$ CPI polyimide film, manufactured by SRS Technologies. In 2005, ATK also conducted a ground deployment test of a 20 m square sail, in the 30 m vacuum chamber at NASA Glenn Research Center, shown in Figure 1.1. In addition, candidate films and materials have been exposed to electron radiation and simulated space environment effects. Such tests are very important to determine the suitability of sail films for future deep-space missions. Long-life films must be developed that can withstand high thermal loads and thermal cycling in some missions.

European activities in solar sail hardware design have focused on the development of composite booms by the German Aerospace Centre, DLR, which are made of Carbon Fibre Reinforced Plastic (CFRP) of linear density 100 g m^{-1} . A successful ground deployment test of a $20 \times 20 \text{ m}$ solar sail was accomplished in 1999, using the DLR booms and commercially available $7.6 \mu\text{m}$ Kapton film, shown in Figure 1.2. This film gauge is only suitable for technology demonstrator missions and does not meet the thickness requirements for operational solar sail missions. The DLR booms will be used for the ESA/DLR in-orbit demonstration mission planned for launch in early 2006.

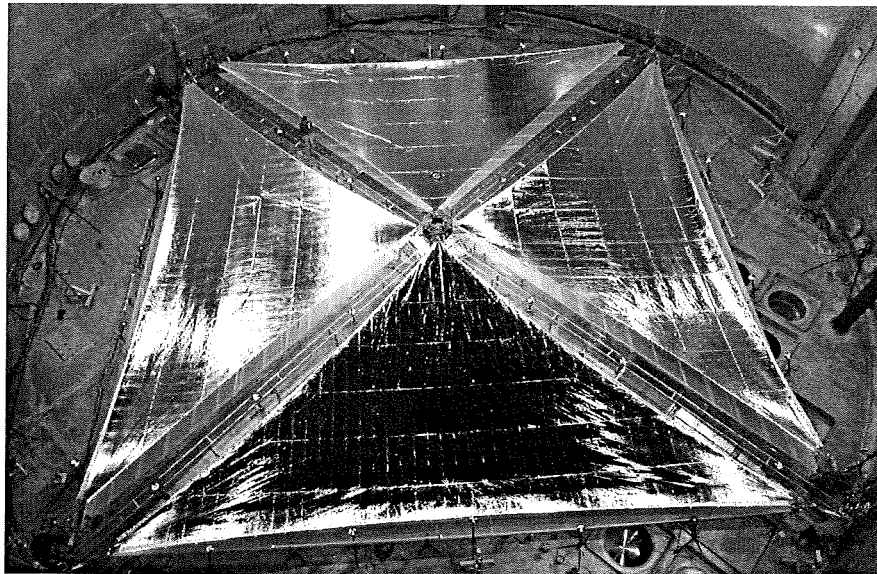


Figure 1.1: ATK 20 x 20 m sail deployment test in vacuum chamber [NASA/ATK]

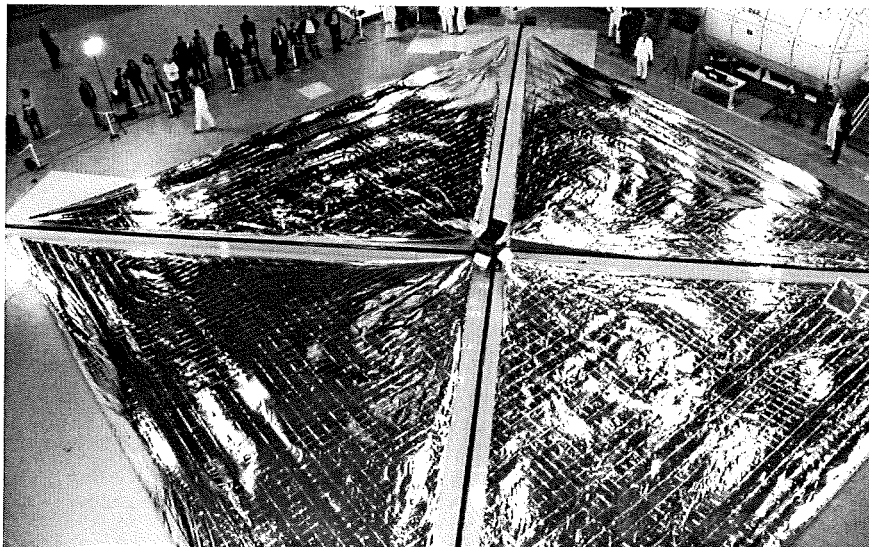


Figure 1.2: ESA/DLR 20 x 20 m sail ground deployment test in 1999 [DLR]

There are also a number of private ventures involved in solar sail design. Cosmos-1 was launched in June 2005, but upper stage separation failed. This is a 600 m², 3-axis stabilised sail weighing 40 kg, divided into 8 rigid blades, each of length 15 m with an independent gimbal. The blades are deployed by inflatable booms and the sail film is made of 5 μ m aluminised, reinforced Mylar. The ‘windmill’ design will enable attitude control by cyclic or collective pitching of the blades, similar to helicopter rotors. An important development has taken place in Japan during August 2004, when the Japan Aerospace Exploration Agency (JAXA) deployed two 10 m ‘clover-leaf’ sail structures in space at sub-orbital altitudes of 122 and 169 km, from an S-310 sounding rocket.

1.3.2 Spin-Stabilised

Considerable mass savings can be achieved by reducing or eliminating the bulky booms in 3-axis stabilised designs, which need to be strong in compression to withstand bending loads, and so become heavier, for larger sails. This can be achieved by using spin-induced deployment and tensioning. This concept was successfully demonstrated in Russia by the Space Regatta Consortium (SRC) and Energia in 1993, where a spinning 20 m reflector called Znamya-2 was deployed from a Progress supply vehicle (Figure 1.3), using an on-board electric motor. The goal of this experiment was to investigate methods of reflecting sunlight onto the polar regions of northern Russia during the long, dark arctic winters.

The solar sail proposed for the NASA Interstellar Probe Mission (ISP) is a spin-stabilised concept, 410 m in diameter, with an areal density of 1 g m^{-2} , composed of six segments which unfurl from six gores that form a hexagon [Wallace *et al*, 2000, Garner *et al*, 2000, Salama *et al*, 2003]. A laboratory experiment of the spinning disk sail deployment was achieved using $2.5 \mu\text{m}$ Mylar to a diameter of 80 cm [Salama *et al*, 2003]. The sail film material for the ISP mission will use a carbon microtruss fabric, developed by Energy Science Laboratories Inc. One other design that employs spin-induced tension is the Heliogyro [MacNeal, 1967]. This concept comprises several long (of order a few km) reflective blades emanating radially from a central hub. Deployment is achieved by simply unwinding the blades from lateral rolls on the hub. Attitude control can be accomplished by twisting the blades at the hub to perform cyclic or collective pitching manoeuvres. However, issues are raised concerning the dynamics of extremely high aspect ratio sail blades.

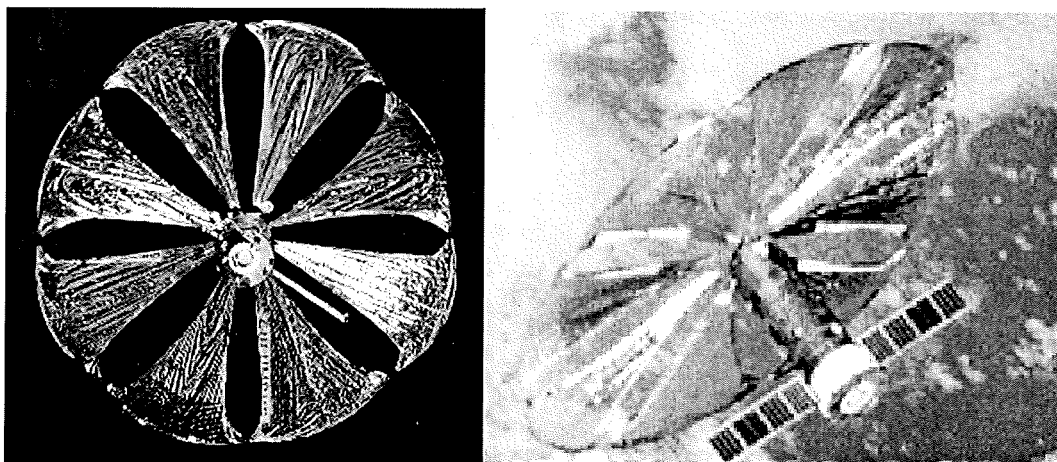


Figure 1.3: 1993 Znamya-2 spinning reflector experiment [SRC Energia]

1.3.3 Compound Sail

The concept of the compound sail was first envisaged by Soviet researchers in the 1970s [Malanin and Repyakh, 1974], and has been also been re-invented as the solar photon thruster [Forward, 1990]. This concept is also known as the Cassegrain sail, discovered independently by C. Uphoff [Uphoff, 1994]. The compound sail works by separating the function of *collecting* solar photons from that of *reflecting* the photons [Forward, 1990]. The compound sail consists of a large Sun-pointing spherical reflector of comparable dimension to equivalent flat solar sails, which concentrates incoming solar radiation onto a small collimating mirror. The collimated light can then be reflected onto a third reflector (focal point also along the Sun-line axis), which can be articulated to provide sail thrust. The mirrors on the sail structure must be arranged such that the resultant thrust is directed through the system's centre of mass, to prevent undesired torques [McInnes, 2000a]. The compound sail mirror arrangement is shown schematically in Figure 1.4, where the main reflector is parabolic to focus light onto the collimator. This focusing of the sunlight could also be used for power generation, since the photon flux on the collimator is greatly magnified.

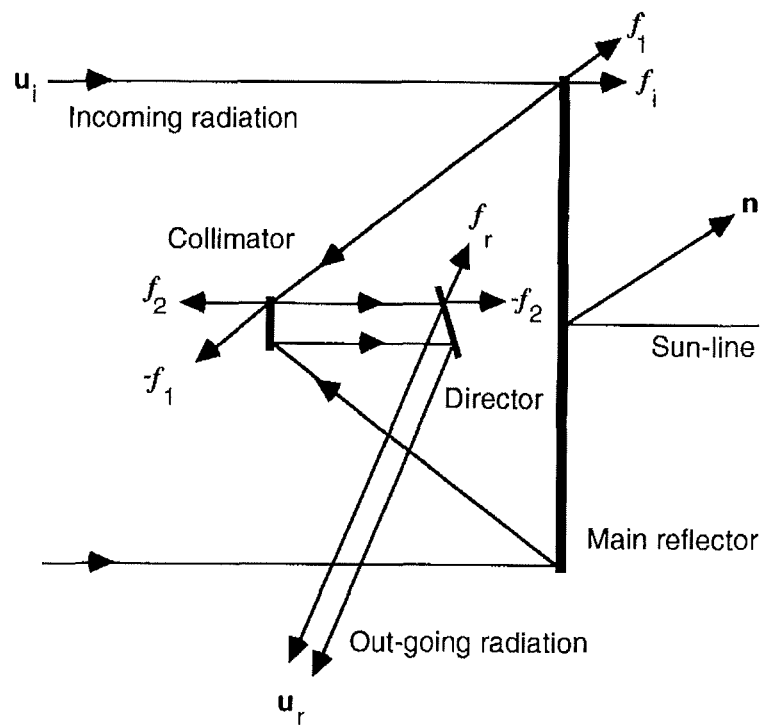


Figure 1.4: Compound sail mirror configuration [McInnes, 2000a]

A conventional, flat solar sail has a thrust that varies as the *cosine squared* of the cone angle between the sail normal and the Sun-line. Even for an ideal, perfectly reflecting sail, a loss of efficiency is evident as the sail is pitched at larger angles from the Sun-line. When the compound sail design is utilised, the thrust magnitude varies only with the *cosine* of the angle between the thrust vector and the Sun-line (this is shown in Forward [1990] and McInnes [2000a]). This results in an increased thrust magnitude advantage over the flat sail as the sail is pitched away from the Sun-line, particularly at large incidence angles. For an ideal compound sail, a pitch angle of 45° from the Sun-line results in a thrust magnitude increase of 41% over an ideal flat sail.

The beneficial effect on minimum-time trajectories of using a compound sail has been analysed by McInnes [2000a] for Earth-Mars transfers, and will be briefly extended to Jupiter transfers in Chapter 5 of this thesis. Similarly, it is noted that for a fixed trip time, the payload mass fraction can be greater for a compound solar sail. The compound sail remains a theoretical concept and no studies have been conducted into the practicality of constructing the triple-mirror arrangement discussed above. It may be that considerable extra mass is required to align and articulate the mirrors, over the conventional single sail concept. There are also issues associated with deployment and attitude control of a curved collector.

1.4 Performance Metrics

Throughout this thesis, the parameter defining the solar sail performance is known as the Characteristic Acceleration, a_c , the solar radiation pressure induced acceleration at 1 AU with the sail normal orientated along the sun-spacecraft line. This performance parameter is thus dependent on both the area of the sail and the total mass of the sail structure and spacecraft. Therefore, it is independent of whether a high performance sail and heavy payload, or low performance sail and miniaturised payload, is used. For this reason it is a useful performance metric for the trajectory analysis in this thesis. The characteristic acceleration is related to the local photon pressure at 1 AU, P_{AU} ($4.56 \times 10^{-6} \text{ N m}^{-2}$), the sail film reflective surface area, A , and total spacecraft mass, M , by Eq. 1.1. The overall reflective efficiency factor, η , can be incorporated to take account of non-perfect reflectivity. For an ideal sail this

factor is unity. Since the characteristic acceleration is that at 1 AU, it is independent of orbit radius. The actual acceleration varies as the inverse squared of the heliocentric orbit radius, and is thus significantly higher close to the Sun.

$$a_c = \frac{2\eta P_{AU} A}{M} \quad [1.1]$$

An equivalent performance parameter, used when analysing families of Non-Keplerian Orbits in Chapter 8, is the Sail Lightness Number, β . This is a dimensionless number, defined as the ratio of the local solar radiation pressure acceleration, with the sail facing the Sun, to the local solar gravitational acceleration. The lightness number is thus also independent of orbit radius. It can be shown that a characteristic acceleration of 1.0 mm s^{-2} corresponds to a dimensionless sail lightness number of 0.168, or a unit lightness number corresponds to a characteristic acceleration of 5.93 mm s^{-2} .

To separate the performance of the solar sail structure from the mass of the payload, the sail assembly loading, σ_s , is defined. This is defined as the areal density of the solar sail assembly, which is the total sail assembly mass, including tensioning and supporting structures and mechanisms, divided by the useful reflecting area, shown in Eq. 1.2. The total spacecraft mass is made up of the sail assembly mass, m_s , and the sail payload mass, m_p , as in Eq. 1.3.

$$\sigma_s = \frac{m_s}{A} \quad [1.2]$$

$$M = m_s + m_p = \sigma_s A + m_p \quad [1.3]$$

If the total solar sail mass is obtained from Eq. 1.1 as in Eq. 1.4, then the solar sail payload mass fraction, κ , can be obtained, defined in Eq. 1.5. This then relates the characteristic acceleration used in parametric trajectory analysis, and the solar sail technology level, to the solar sail payload that can be transported.

$$M = \frac{2\eta P_{AU} A}{a_c} \quad [1.4]$$

$$\kappa = \frac{m_p}{M} = 1 - \frac{a_c \sigma_s}{2\eta P_{AU}} \quad [1.5]$$

Similarly, Eq. 1.6 is used to determine the sail area for a given assembly loading, payload mass, and characteristic acceleration. It is important to stress here that the solar sail payload is the spacecraft cruise stage and subsystems, and if necessary, any probes or landers required, attached to the sail assembly. In this thesis, the solar sail payload is not the scientific payload of conventional spacecraft.

$$A = \frac{a_c m_p}{2\eta P_{AU} - a_c \sigma_s} \quad [1.6]$$

1.5 Non-Ideal Effects

In this thesis, the solar sail is usually assumed to be a perfect, flat reflector for trajectory optimisation purposes. In reality, a fraction of the incident radiation will be absorbed due to non-perfect reflectivity (aluminium has a reflectivity of 85-95%). To reduce thermal loading, a proportion of this energy must be re-radiated from the back surface of the sail using a highly emissive coating such as chromium (emissivity of 64%). A real sail will also have wrinkles, causing non-specular reflective effects. The photon pressure will cause the sail to billow, however well designed the supporting structure may be. These factors have the effect of reducing the available thrust produced on a particular sail area and cause the thrust orientation to become offset from the sail normal – the centre-line effect. This becomes particularly important at high incidence angles, when the sail normal is pitched at large angles from the Sun-line. The imperfect effects mentioned will not be considered in the trajectory analysis in this thesis, except for mass sizing purposes, to relate sail assembly loading to characteristic acceleration. McInnes [1999, pp. 43-53] shows the optical and parametric force models, which have also been investigated by Cichan and Melton [2001]. Optical coefficients and parametric force coefficients were originally calculated during design work for the NASA/JPL comet Halley rendezvous mission [Wright, 1992]. In this thesis, the optical and billowing models were applied to a 356 day Earth-Mars rendezvous trajectory, originally discovered by Sauer [1976] with an ideal characteristic acceleration of 1.0 mm s^{-2} . Using the trajectory optimisation methods in Chapter 2, it was found that the non-ideal sail force model prolonged the trip time by 47 days (13%). The effect on trip time of a non-ideal sail is not insignificant, but it will be minimal for trajectories that

do not involve large pitch angles. The ideal sail trajectories shown in this thesis should be regarded as the best case, and are perhaps appropriate for future sail designs that will be less affected by billowing and will have highly reflective coatings. It may be necessary to constrain the sail pitch angle to some maximum angle to minimise the effects of a non-ideal sail. This was not investigated in this thesis.

1.6 Solar Sail Orbital Dynamics

The vector equation of motion of a solar sail spacecraft moving in a heliocentric orbit is defined by Eq. 1.7, where \mathbf{r} is the position vector of the spacecraft with respect to the Sun, at time t . The gravitational parameter of the Sun is defined by μ . For an ideal sail, the thrust vector is aligned along the sail normal direction, \mathbf{n} , with the pitch or cone angle, α , defined as the angle between the sail normal and the radial vector.

$$\frac{d^2\mathbf{r}}{dt^2} + \frac{\mu}{r^2}\hat{\mathbf{r}} = \beta \frac{\mu}{r^2}(\hat{\mathbf{r}}\cdot\mathbf{n})^2\mathbf{n} \quad [1.7]$$

When the sail pitch angle is fixed, with the sail thrust vector aligned along the Sun-line, families of conic section orbits can be produced. These are not Keplerian orbits in the strictest sense, since the solar gravity is effectively reduced by the solar radiation pressure force acting on the spacecraft in a directly opposing direction. They are effectively conic section orbits with a modified gravitational parameter, $\tilde{\mu} = \mu(1 - \beta)$ [McInnes, 1999, p.121], since solar gravity and solar radiation pressure both vary as the inverse square of the solar distance. For a lightness number of zero, so with no solar sail, the orbit is defined as circular and Keplerian. When the solar sail is deployed and pitched to a Sun facing attitude, then the modified orbit is elliptical for lightness numbers between zero and 0.5, with an increasing eccentricity for higher sail performance. With a lightness number of exactly 0.5 then there is a transition from an elliptical orbit to a parabolic orbit, which defined the lightness number necessary for direct escape. When the lightness number increases to between 0.5 and unity, a hyperbolic orbit results, which can similarly be defined using the equations for hyperbolic Keplerian orbits, but with the modified gravitational parameter, $\tilde{\mu}$. When the lightness number is exactly unity, then there

is the interesting situation where the solar gravity is completely cancelled out. This could enable rectilinear orbits or solar levitators, providing the anti-Sunward pointing sail thrust is maintained, via zero pitch control. With extremely high performance sails exhibiting lightness numbers of greater than unity, the Sun now becomes placed at the opposite focus of the conic section. In this regard, there is the exotic situation whereby solar radiation pressure now becomes the primary force, with the solar gravity acting as a perturbation.

When the solar sail thrust is orientated at a fixed, non-zero pitch angle to the Sun-line, with a low sail performance, the motion follows a logarithmic spiral trajectory [Bacon, 1957, Tsu, 1959, London, 1960]. The radial component of the sail thrust reduces the effective gravitational force on the sail as for zero pitch, however the component of thrust in the transverse direction acts to increase (or decrease) the orbital angular momentum of the sail. For a logarithmic spiral, the local solar sail speed is always less than the local circular orbit speed [McInnes, 1999, p.131]. This means that coplanar transfer by logarithmic spiral, between two circular orbits, cannot be achieved without a hyperbolic excess at launch to place the solar sail onto the logarithmic spiral, and then circularising the orbit on arrival at the final circular orbit. These discontinuities in the boundary conditions pose problems in the practical application of logarithmic spirals to orbit transfers. However, the logarithmic spiral often provides a good first guess for an optimisation method that can deal with this two-point boundary value problem. From an implicit relationship between the sail pitch angle and spiral angle, it is observed that there is an optimum sail pitch angle that maximises the spiral angle for each sail lightness number, always close to 35° [McInnes, 1999, p.132].

The solar sail thrust vector direction, \mathbf{n} , is defined by two angles to completely cover the outward hemisphere of allowable orientations, as shown in Figure 1.5, in the Radial-Transverse-Normal (RTN) frame. These are, the cone angle, $\alpha \in [-\pi/2, \pi/2]$, between the sail normal, \mathbf{n} , and the Sun-sail vector, \mathbf{r} , and the clock angle, $\delta \in [0, \pi]$, between the projection of the sail normal and some reference direction, \mathbf{p} , onto a plane normal to the Sun-line [McInnes, 1999, p.115]. The thrust vector (ideal sail normal) is defined by Eq. 1.8. In order to find a set of optimal sail control angles, a required direction, \mathbf{q} is defined, along which the component of the

sail thrust is to be maximised, shown in Eq. 1.9, where the tilde notation specifies the cone and clock angles of the required thrust direction.

$$\mathbf{n} = \cos \alpha \hat{\mathbf{r}} + \sin \alpha \cos \delta \hat{\mathbf{p}} + \sin \alpha \sin \delta \hat{\mathbf{p}} \times \hat{\mathbf{r}} \quad [1.8]$$

$$\mathbf{q} = \cos \tilde{\alpha} \hat{\mathbf{r}} + \sin \tilde{\alpha} \cos \tilde{\delta} \hat{\mathbf{p}} + \sin \tilde{\alpha} \sin \tilde{\delta} \hat{\mathbf{p}} \times \hat{\mathbf{r}} \quad [1.9]$$

The force in this required direction is given by Eq. 1.9 and 1.10. It is noted that setting $\delta = \tilde{\delta}$ maximises the force component in direction \mathbf{q} . By differentiating Eq. 1.10 with respect to the cone angle and finding the turning points, $\partial f_q / \partial \alpha = 0$, then the optimal sail cone angle, α^* , is obtained, which maximises the force in the required direction, shown in Eq. 1.11 [McInnes, 1999, p.116].

$$f_q = 2PA(\mathbf{n} \cdot \hat{\mathbf{r}})^2 (\mathbf{n} \cdot \mathbf{q}) \quad [1.9]$$

$$f_q = 2PA \cos^2 \alpha \left[\cos \alpha \cos \tilde{\alpha} + \sin \alpha \sin \tilde{\alpha} \cos(\delta - \tilde{\delta}) \right] \quad [1.10]$$

$$\tan \alpha^* = \frac{-3 + \sqrt{9 + 8 \tan^2 \tilde{\alpha}}}{4 \tan \tilde{\alpha}} \quad [1.11]$$

Thus, the sail cone angle which maximises the force in the transverse direction, so that $\tilde{\alpha} = 90^\circ$, is given by $\tan \alpha^* = 1/\sqrt{2}$. This optimal angle is 35.26° , which enables the maximum rate of increase in orbital angular momentum. It is noted that the pitch angle which maximises the logarithmic spiral angle, for low sail lightness numbers, is also close to this optimal angle.

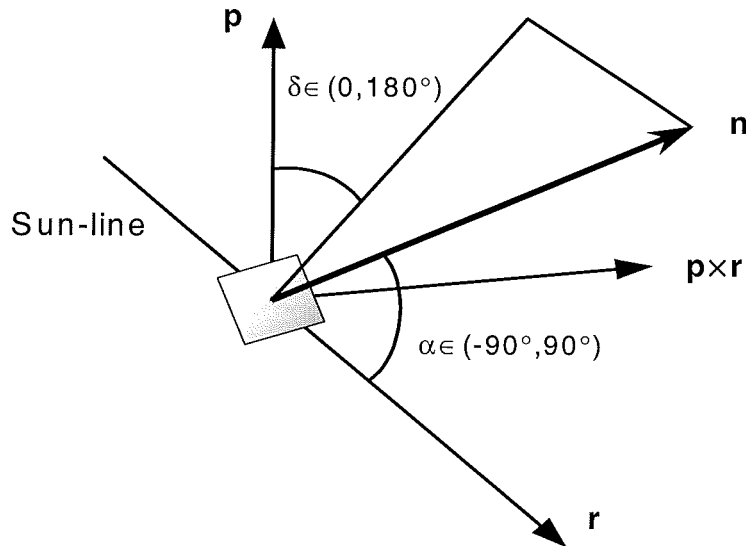


Figure 1.5: Control angle definition

Hence, a simple optimal strategy of increasing (or decreasing, using a negative cone angle) the orbital angular momentum and orbit energy has been described. This description of the optimal sail force vector is the key to formulating a set of locally optimal control laws that can maximise the rate of change of a particular orbital element. These analytical control laws will be described in the next section, where the optimal control angles are derived to maximise the thrust in a direction defined by the variational equation of the orbital element concerned.

1.7 Locally Optimal Control Laws

A set of analytical control laws can be derived to maximise the rate of change of a particular orbital element. These control laws can sometimes be used to create initial guesses for the optimisation methods discussed in Chapter 2. Firstly, the equations of motion can alternatively be represented in terms of the Lagrange variational equations, shown in Eqs. 1.12-17, where p is the semi-latus rectum, n is the orbital mean motion, and the other symbols have their usual meanings [McInnes, 1999, p.120]. These equations are particularly useful to analyse the rate of change of a particular orbital element, while leaving the other time-averaged elements unchanged.

$$\frac{da}{df} = \frac{2pr^2}{\mu(1-e^2)^2} \left[Se \sin f + T \frac{p}{r} \right] \quad [1.12]$$

$$\frac{de}{df} = \frac{r^2}{\mu} \left[S \sin f + T \left(1 + \frac{r}{p} \right) \cos f + T \frac{r}{p} e \right] \quad [1.13]$$

$$\frac{di}{df} = \frac{r^3}{\mu p} \cos(f + \omega) W \quad [1.14]$$

$$\frac{d\Omega}{df} = \frac{r^3}{\mu p \sin i} \sin(f + \omega) W \quad [1.15]$$

$$\frac{d\omega}{df} = -\frac{d\Omega}{df} \cos i + \frac{r^2}{\mu e} \left[-R \cos f + T \left(1 + \frac{r}{p} \right) \sin f \right] \quad [1.16]$$

$$\frac{dt}{df} = \frac{r^2}{\sqrt{\mu p}} \left[1 - \frac{r^2}{\mu e} \left[S \cos f - T \left(1 + \frac{r}{p} \right) \sin f \right] \right] \quad [1.17]$$

In the definition of the rotating RTN frame, the radial (S), transverse (T), and normal (W) components of the solar sail thrust are defined by Eqs. 1.18, 1.19, and 1.20.

$$S = \beta \frac{\mu}{r^2} \cos \alpha^3 \quad [1.18]$$

$$T = \beta \frac{\mu}{r^2} \cos \alpha^2 \sin \alpha \sin \delta \quad [1.19]$$

$$W = \beta \frac{\mu}{r^2} \cos \alpha^2 \sin \alpha \cos \delta \quad [1.20]$$

The variational equations can be used to formulate a set of control laws that maximise the rate of change of a particular orbital element. These control laws cannot enable true optimality, since they only optimise the local force vector, and they are often called closed loop methods [Otten and McInnes, 1999]. Global optimality requires the use of numerical methods, and even then, the true optimum solution is hard to attain (see Chapter 2). Following the description by McInnes [1999, pp. 136-141] and Otten and McInnes [1999], a general formulation of the Lagrange variational equations is given by Eq. 1.21, where $\mathbf{f} = (S, T, W)$ is the solar radiation pressure thrust exhibited by the sail, and $\boldsymbol{\lambda} = (\lambda_1, \lambda_2, \lambda_3)$ is a vector of functions of the solar sail orbital elements, Z . In optimal control theory, this required force vector is often called the primer vector, and is illustrated in Figure 1.6.

$$\frac{dZ}{df} = \boldsymbol{\lambda}(Z) \cdot \mathbf{f} \quad [1.21]$$

Similar to the definition of the optimal force vector in the previous section, the force component along the primer vector is given by Eq. 1.22. With reference to Figure 1.6, for two-dimensional planar trajectories where $W = 0$ and $\lambda_3 = 0$, Eq. 1.23 is obtained. By maximising the thrust in the required direction, $\partial f_\lambda / \partial \alpha = 0$, then Eq. 1.11 again results, to determine the optimal cone angle that maximises the rate of change of the particular orbital element, Z . The components of the primer vector can be obtained by taking the variational equation of interest and, ignoring common scaling factors, using the dot product.

$$f_\lambda = 2PA(\mathbf{n} \cdot \hat{\mathbf{r}})^2 \mathbf{n} \cdot \boldsymbol{\lambda} \quad [1.22]$$

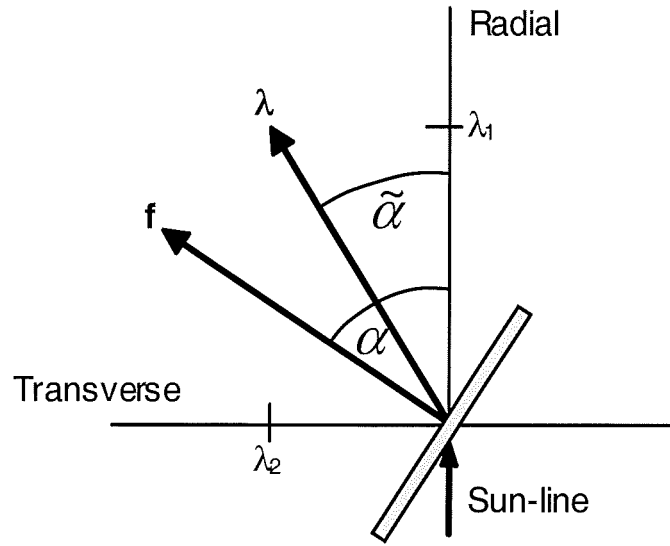


Figure 1.6: Required force vector for locally optimal trajectories

$$\tan \tilde{\alpha} = \left[\frac{\lambda_2}{\lambda_1} \right] \quad \tilde{\delta} = \frac{\pi}{2} \quad [1.23]$$

Therefore, the primer vector components that maximise the first variational equation for the rate of change of semi-major axis are shown in Eq. 1.24 and 1.25. The required cone angle is then given by Eq. 1.26, through substitution of the orbit equation for r . The optimum cone angle is then found via Eq. 1.11.

$$\lambda_1 = e \sin f \quad [1.24]$$

$$\lambda_2 = p/r \quad [1.25]$$

$$\tan \tilde{\alpha} = \frac{1 + e \cos f}{e \sin f} \quad [1.26]$$

To maximise the rate of change of the orbit eccentricity, the components of the primer vector are found to be Eqs. 1.27 and 1.28, which gives a required cone angle shown in Eq. 1.29. Equivalent control laws can be derived for the other planar orbital elements, such as argument of periaapsis, and radius of periaapsis and apoapsis.

$$\lambda_1 = \sin f \quad [1.27]$$

$$\lambda_2 = \left[1 + \frac{r}{p} \right] \cos f + e \frac{r}{p} \quad [1.28]$$

$$\tan \tilde{\alpha} = \frac{2 + e \cos f}{1 + e \cos f} \cot f + \frac{e \operatorname{cosec} f}{1 + e \cos f} \quad [1.29]$$

The effect of these control laws, which will be used for generating initial guesses in Chapters 4, 5, and 6, will be illustrated. The equations of motion are integrated using a fourth-order Runge-Kutta loop, with a step-size of 0.58 days, over three complete revolutions of the Sun. The initial orbit was elliptical, with a semi-major axis of 1.25 AU and eccentricity of 0.2, and the characteristic acceleration used was 0.5 mm s^{-2} . These parameters were also used by McInnes [1999, p.139], since they illustrate the effect of the control laws clearly. The effect of the control law that maximises the rate of change of semi-major axis is shown in Figure 1.7.

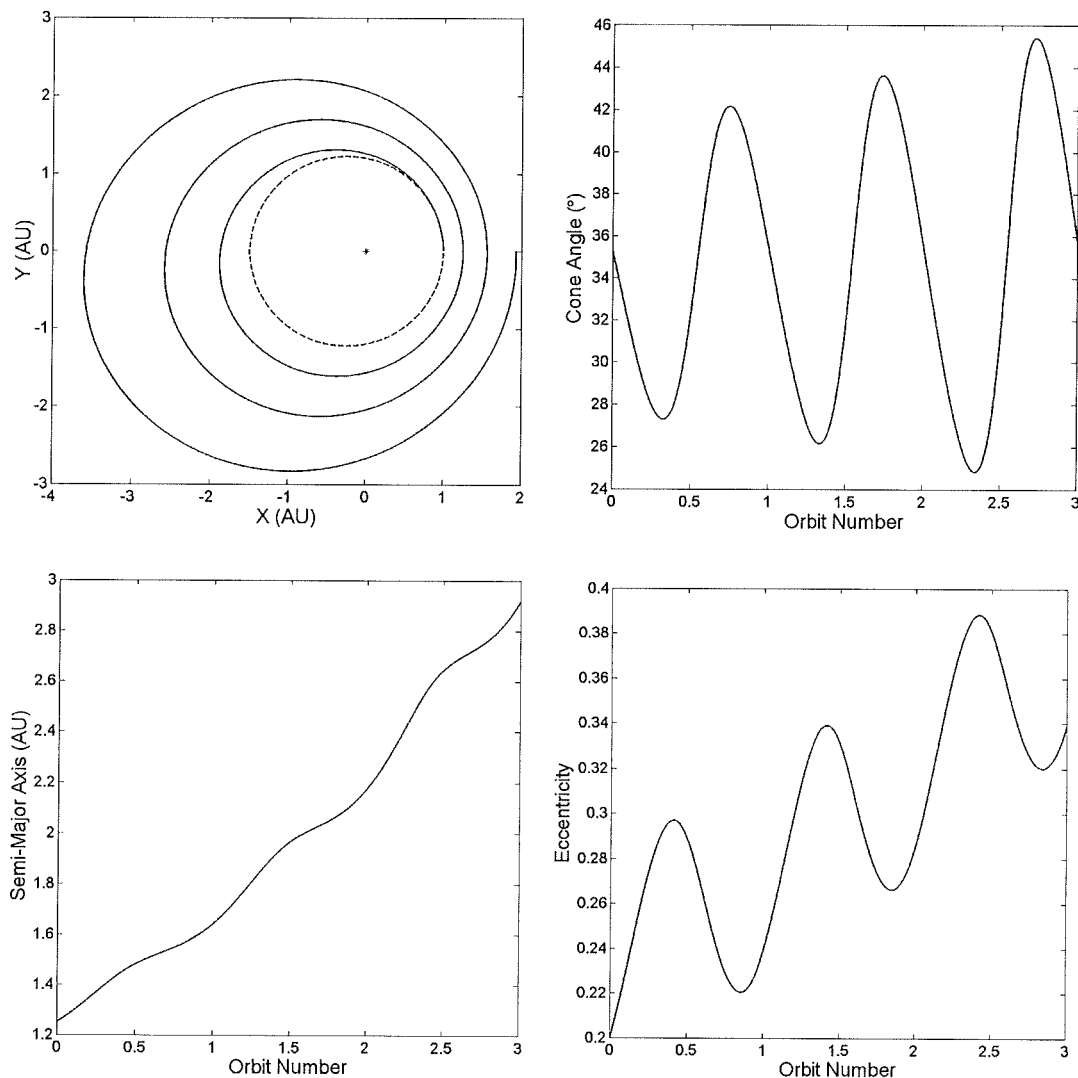


Figure 1.7: Maximising the rate of change of the semi-major axis

In this case, there is no constraint imposed on the maximum cone angle, as was used by McInnes [1999], and similar features are noted to those described in McInnes [1999, pp. 140-141]. The semi-major axis control law was not used alone in this thesis, but it was blended with the eccentricity control law, for generating initial guesses for Near-Earth Asteroid rendezvous in Chapter 4. This blending process is described in the following pages, for simultaneous changes in the semi-major axis and eccentricity. Firstly, the control law that maximises the rate of change of the orbit eccentricity is illustrated in Figure 1.8. It is observed that this control law can be used to rapidly attain low perihelia. This is particularly useful for producing optimisation initial guesses for executing the ‘solar photonic assist’ manoeuvre, used in Chapters 5 and 6, for reaching the outer solar system. However, it is noted that rapid slews are required just before perihelion, which may be problematic if discretising the control profile for optimisation, and for attitude control.

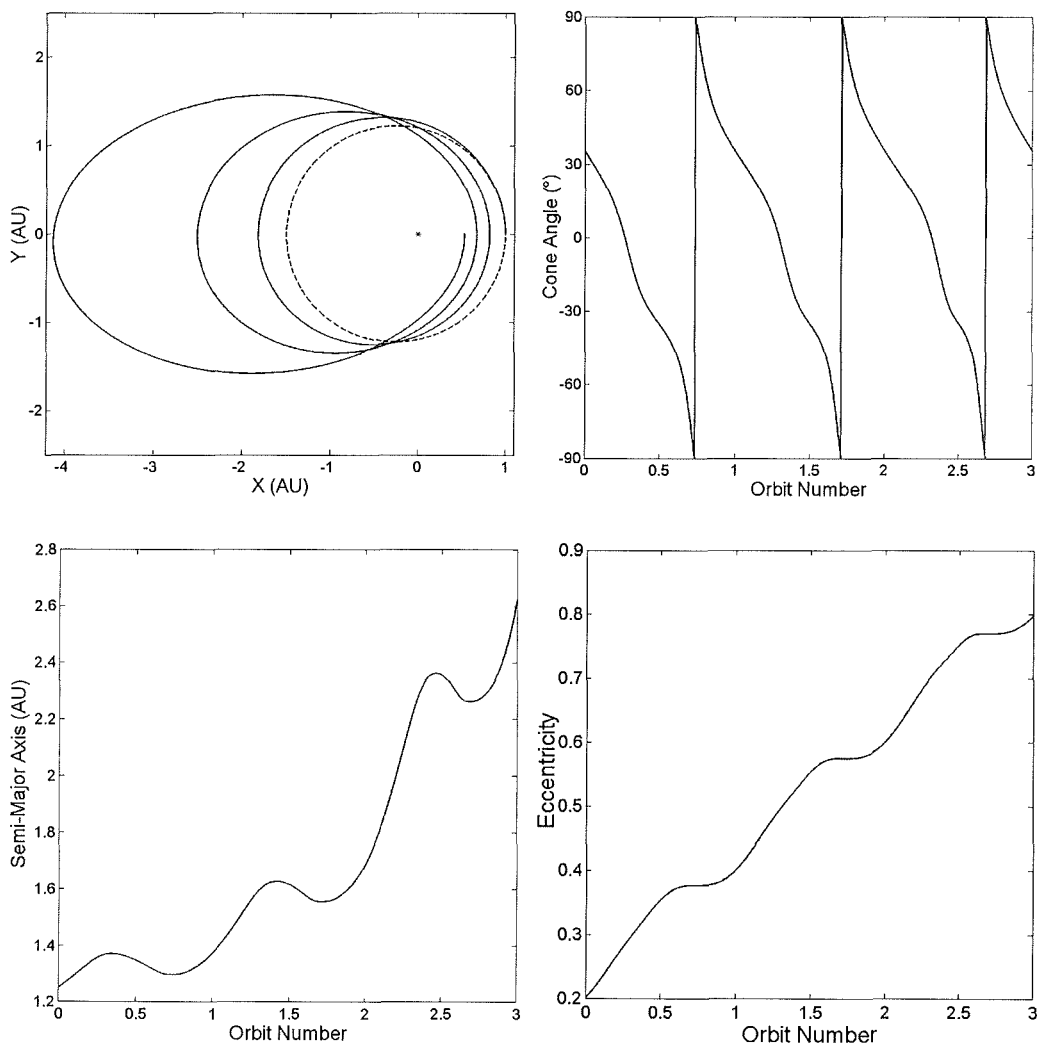


Figure 1.8: Maximising the rate of change of the eccentricity

To blend the in-plane steering laws for semi-major axis and eccentricity, the method follows that shown by Kluever [1998] and Otten and McInnes [1999]. Blending has also been extensively developed for planet-centred solar sail trajectories by Macdonald and McInnes [2001]. The required angles from each control law, $\tilde{\alpha}_a$ and $\tilde{\alpha}_e$, are blended by forming the required in-plane vector, \mathbf{c} , which is the resultant vector formed by adding the two vectors, λ_a and λ_e , from each control law. The radial (R) and transverse (T) components of this vector are shown in Eq. 1.30 and Eq. 1.31, respectively, where each control law term has been weighted by an appropriate weighting factor, κ_a and κ_e . These weighting factors are function of the instantaneous, initial (o), and desired final (f) orbital elements, as shown in Eq. 1.32 and Eq. 1.33. In this way, as one of the spacecraft instantaneous orbital elements approaches the target orbital element, then the weighting of the particular control law is reduced, to place more emphasis on the other orbital elements that may be further from the desired target value. The constant weighting coefficients, G_a and G_e , can be manually selected to enable a desired transfer between different orbits. This blending process is particularly useful for finding preliminary control profiles for transfer to and from highly elliptical orbits, where the control profile required is not obvious.

$$c_R = \kappa_a \cos \tilde{\alpha}_a + \kappa_e \cos \tilde{\alpha}_e \quad [1.30]$$

$$c_T = \kappa_a \sin \tilde{\alpha}_a + \kappa_e \sin \tilde{\alpha}_e \quad [1.31]$$

$$\kappa_a = G_a \frac{(a_o - a)}{|a_f - a_o|} \quad [1.32]$$

$$\kappa_e = G_e (e_f - e) \quad [1.33]$$

Then, the overall required cone angle, $\tilde{\alpha}$, can be obtained from Eq. 1.34, similar to Eq. 1.23, with reference to Figure 1.6. To avoid singularities in calculating the optimal cone angle from the required cone angle, the cosine form of Eq. 1.11 is used here, and was also used in generating Figures 1.7 and 1.8. This is shown in Eq. 1.35. With the sine and cosine of the required cone angle obtained from c_R and c_T , via trigonometry, Eq. 1.35 can equivalently be represented by Eq. 1.36.

$$\tan \tilde{\alpha} = \left[\frac{c_T}{c_R} \right] \quad [1.34]$$

$$\tan \alpha^* = \frac{-3 \cos \tilde{\alpha} + \sqrt{9 \cos^2 \tilde{\alpha} + 8 \sin^2 \tilde{\alpha}}}{4 \sin \tilde{\alpha}} \quad [1.35]$$

$$\tan \alpha^* = \frac{-3c_R + \sqrt{9c_R^2 + 8c_T^2}}{4c_T} \quad [1.36]$$

Blending locally-optimal control laws can produce preliminary transfers to highly elliptical orbits, such as comets. For low characteristic accelerations, many revolutions are required, and so the optimal control profile is not obvious, but blended control laws can produce approximate initial solutions. In Chapter 4, optimised transfers to comet Wirtanen will be presented. In a simple analysis, blending control laws for semi-major axis and eccentricity, a 0.5 mm s^{-2} spiral from a 1 AU orbit to an eccentric orbit, of semi-major axis 3.094 AU and eccentricity 0.658, can be quickly produced, with a transfer time of 2005 days (5.49 years). The inclination, right ascension of ascending node, argument of periapsis, and ephemeris of each body is ignored. The optimal relative weighting coefficients of, $G_a=0.51$ and $G_e=1$, were selected by trial-and-error. The trajectory, cone angle profile, semi-major axis and eccentricity profile, shown in Figure 1.9, are only approximate, since the integration step-size was 0.58 days and the final orbital elements were satisfied to a tolerance of 10^{-3} . Blended control laws were only used occasionally in this thesis, when simple initial guesses (see Chapter 2) were not adequate for the optimisation algorithm. In future work, it may be prudent to increase the hybridisation of analytical control laws with optimisation methods. Recently, Macdonald [2005] has had some success using blended control laws for heliocentric trajectories.

Changes in the out-of-plane orbital elements, such as inclination and right ascension of the ascending node, can be effected by the use of simple switching functions. For the maximum rate of change of inclination, the solar sail thrust can be directed alternately above and below the orbit plane every half-orbit, as defined by Eq. 1.37, where W is the force along the RTN normal direction. Here, $sign$ represents +1 or -1, depending on the sign of the function in square brackets.

$$sign W = sign[\cos(f + \omega)] \quad [1.37]$$

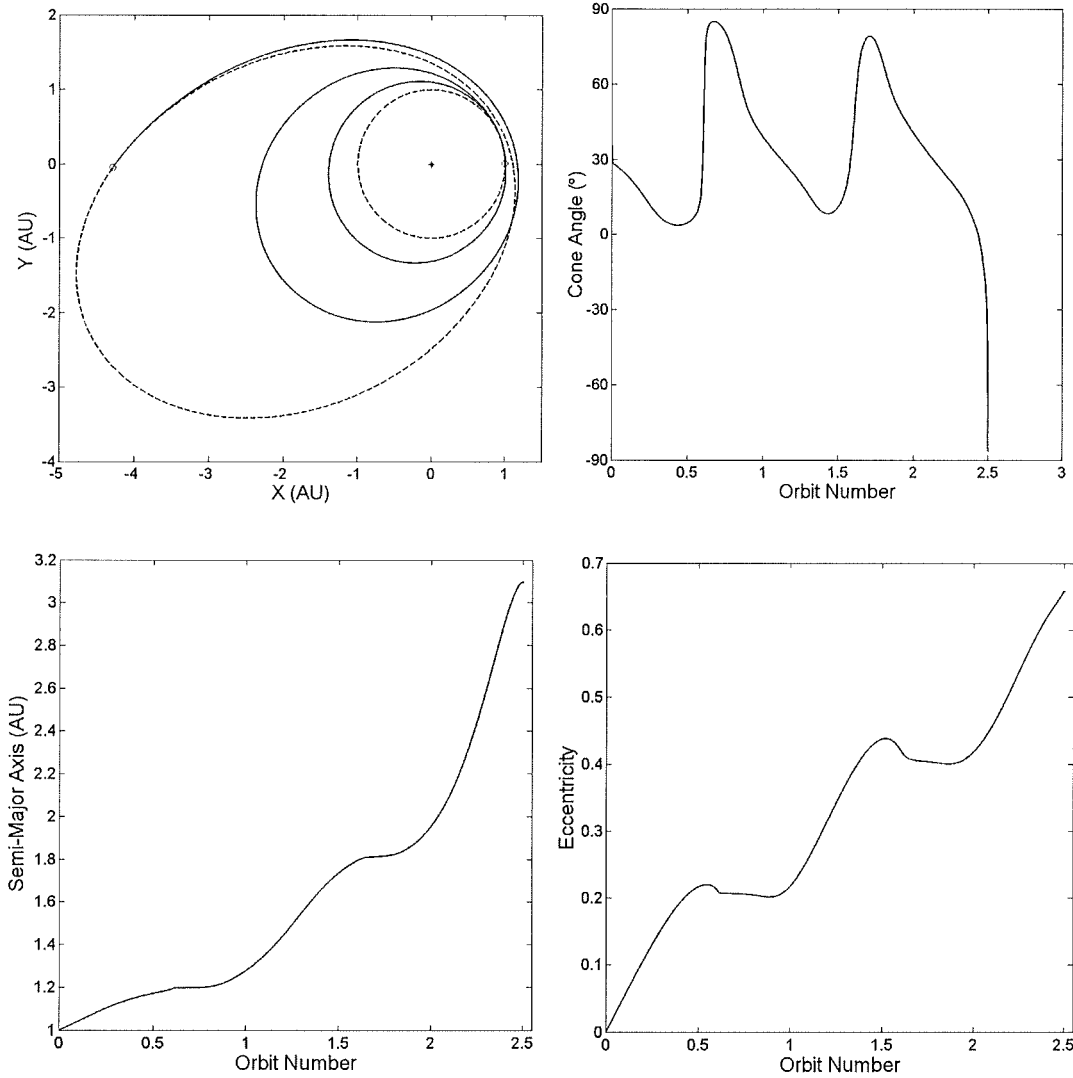


Figure 1.9: Blending control laws for elliptical orbit transfer

The optimal sail cone angle that maximises the out-of-plane sail thrust is 35.26° , given by Eq. 1.38, for the sail clock angle control law in Eq. 1.39. The effect of this control law is to generate a ‘cranking’ orbital manoeuvre, as depicted in Figure 1.10, starting from a 0.3 AU circular orbit, with a characteristic acceleration of 0.5 mm s^{-2} . This orbital ‘cranking’ manoeuvre takes 584 days (1.6 years) to reach a 90° polar orbit. This orbital cranking control law will be used in parametric studies in Chapters 4 and 7, for reaching high inclinations.

$$\alpha^* = \tan^{-1} \left[\frac{1}{\sqrt{2}} \right] \quad [1.38]$$

$$\delta^* = \frac{\pi}{2} (1 - \text{sign}[\cos(f + \omega)]) \quad [1.39]$$

McInnes [1999, pp. 143-146] has shown that, by substituting the control law into the inclination variational equation, Eq. 1.14, and integrating over one orbit, the change in inclination per orbit is independent of orbit radius and only depends on the sail lightness number, as $\Delta i = 88.2\beta$ degrees per orbit. However, closer orbits to the Sun have shorter orbit periods, and so the time to achieve an overall inclination change is shorter. In addition, the constant radial force component means that the orbit period will increase slightly during cranking [McInnes, 1999].

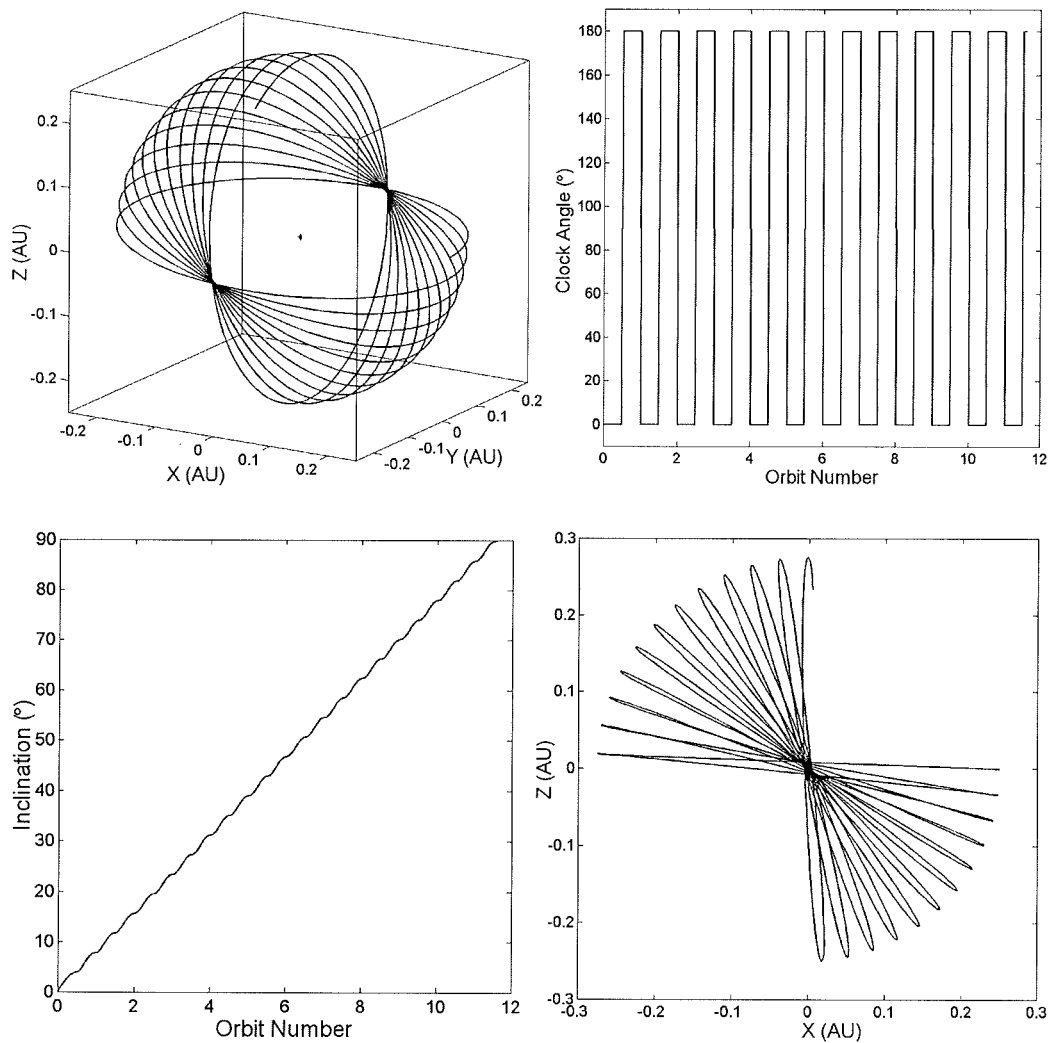


Figure 1.10: Cranking orbit using inclination control law

1.8 Thesis Goals and Objectives

In this section, the thesis goals will be outlined. The primary thrust of this thesis is to produce optimised, minimum-time solar sail trajectories to a representative wide

range of bodies in the solar system, from a realistic understanding of trajectory constraints, such as thermal issues and launch windows. This will serve as a reference catalogue of trajectories for future work, which is more extensive than those produced by Leipold [2000], for example, and includes broad parametric investigations such as departure date scans. In addition, the thesis provides a critical evaluation of the utility of solar sailing and, importantly, identifies missions which are not suitable for solar sails. The results generated in this thesis have been presented at numerous international conferences, listed below. The underscore indicates whether the author has been the main or co-author of the paper. A great deal of the material on sample return missions originated in Technical Notes 1 to 4 of a research contract for ESA/ESTEC, in which the author conducted detailed parametric trajectory analyses, and generated Technology Reference trajectories [McInnes *et al*, 2003a, 2003b, 2003c, 2003d].

- [1] Hughes, G. W., Macdonald, M., McInnes, C. R., Atzei, A., and Falkner, P., "Analysis of a Solar Sail Mercury Sample Return Mission," 55th International Astronautical Congress, Vancouver, Canada, October 4-8, 2004.
- [2] Hughes, G. W., Macdonald, M., McInnes, C. R., Atzei, A., and Falkner, P., "Terrestrial Planet Sample Return Missions Using Solar Sail Propulsion," 5th IAA International Conference on Low-Cost Planetary Missions, ESA/ESTEC, The Netherlands, September 24-26, 2003.
- [3] Hughes, G. W., and McInnes, C. R., "Small-Body Encounters Using Solar Sail Propulsion," IAC-02-S.6.07, 53rd International Astronautical Congress, The World Space Congress – 2002, Houston, Texas, October 10-19, 2002.
- [4] Hughes, G. W., and McInnes C. R., "Mercury Sample Return Missions Using Solar Sail Propulsion," IAC-02-W.2.08, 53rd International Astronautical Congress, The World Space Congress – 2002, Houston, Texas, October 10-19, 2002.
- [5] Hughes, G. W., and McInnes, C. R., "Solar Sail Hybrid Trajectory Optimisation," AAS/AIAA Astrodynamics Specialists Conference, Quebec City, Canada, July 30 – August 2, 2001.

Some of the results have also been published in international journals, such as the *AIAA Journal of Spacecraft and Rockets*. Therefore, they have been subjected to peer review, demonstrating their originality and quality. In three of the of the six articles listed below, the author has been the main-author of the paper. Publications 1 and 2 are still undergoing peer review, but it is anticipated that they will also be published in due course.

- [1] Hughes G. W., Macdonald, M., McInnes C. R., Atzei, A., and Falkner, P., “Sample Return from Mercury and other Terrestrial Planets Using Solar Sail Propulsion,” submitted to *Journal of Spacecraft and Rockets*, February, 2005.
- [2] Macdonald, M., Hughes G. W., McInnes C. R., Lyngvi, A., and Falkner, P., “Solar Polar Orbiter Mission,” submitted to *Journal of Spacecraft and Rockets*, February, 2005.
- [3] Hughes, G. W., and McInnes, C. R., “Small-Body Encounters Using Solar Sail Propulsion,” *Journal of Spacecraft and Rockets*, Vol. 41, No.1, January-February, 2004, pp. 140-150.
- [4] McInnes, C. R., Hughes, G. W., and Macdonald, M., “Payload Mass Fraction Optimisation for Solar Sail Cargo Missions,” *Journal of Spacecraft and Rockets*, Vol. 39, No. 6, November-December 2002, pp. 933-935.
- [5] McInnes, C. R., Hughes, G. W., and Macdonald, M., “Low-Cost Mercury Orbiter and Sample Return Missions Using Solar Sail Propulsion,” *The Aeronautical Journal*, Paper No. 2790, August, 2003, pp. 469-478.
- [6] Hughes, G. W., and McInnes, C. R., “Solar Sail Hybrid Trajectory Optimization for Non-Keplerian Orbit Transfers,” *Journal of Guidance, Control and Dynamics*, Vol. 25, No. 3, May-June 2002, pp. 602-604.

During the course of this work, the problem of optimisation of heliocentric trajectories was addressed for a large and varied range of deep-space scenarios. After an introduction to solar sailing in Chapter 1, it was shown that analytical knowledge of orbital dynamics can be used to generate locally-optimal trajectories for preliminary understanding of heliocentric manoeuvres. This leads on to Chapter 2, which describes the plethora of numerical trajectory optimisation procedures available, and shows how the chosen method was adapted and applied for the

heliocentric optimisation problems. Chapter 3 presents the results of a detailed study into sample return missions from the terrestrial planets, which includes extensive launch date scans and launch window identification. Chapter 4 shows trajectories to small bodies, high energy asteroids and comets in particular. Chapter 5 details trajectories to the outer planets, Jupiter and Pluto, and how the far reaches of the Heliopause can be attained in Chapter 6. Chapter 7 shows trajectories to a true solar polar orbit. Finally, Chapter 8 shows new transfers to unique displaced orbits and artificial Lagrange points. The primary thesis objectives to be addressed in these chapters have evolved as the research period progressed, and are summarised in the list below.

- To conduct a brief survey of the optimisation methods available for low-thrust trajectory optimisation, and subsequently develop a suitable method for optimising heliocentric solar sail trajectories.
- Undertake parametric optimisation of outbound and return rendezvous trajectories to Mars, Venus and Mercury, including investigation of optimal departure windows and launch opportunities.
- Investigation of solar sail trajectories to small-bodies, including rendezvous and flyby of comets, main-belt asteroid rendezvous, and the possibility of sample return from a high-energy small-body.
- To perform parametric analyses of trajectories to Jupiter, including a trade-off of using multiple close solar loops with minimised relative velocity at flyby and the use of positive hyperbolic excess energy. In addition, to investigate the possibility of reaching Pluto using solar sails.
- Conduct a detailed study of trajectories to the Heliopause, with a parametric investigation of using multiple loops and positive hyperbolic excess energy. The thermal aspects of closest solar approach before escape, will be considered concurrently.
- To generate trajectories to a true solar polar orbit, with parametric analysis of the effect of inclination cranking orbit radius and positive C_3 on transfer time.
- Generation of new transfers to displaced Non-Keplerian Orbits, and artificial Lagrange points, requiring three-body dynamics.

Chapter 2

Trajectory Optimisation Methods

In this Chapter, a brief survey of the numerical optimisation methods available in the literature for low-thrust trajectories is conducted. The Indirect method of optimal control theory is also described, which is the method traditionally used for low-thrust trajectory optimisation. Numerous Direct methods are described, using both global search and local search algorithms. During the initial stages of this thesis, many different algorithms were applied to the problem of solar sail trajectory optimisation. The most successful method in its application is described in the third section of this Chapter, along with a description of the solar sail dynamical model, control representation, and the approach to generating initial guesses. This method was used for generating the results in the remainder of this thesis. However, it is stressed here that the objective of this thesis was not to create or apply the best, most robust optimisation algorithm, but to generate a broad range of trajectories to a number of diverse targets. This was accomplished using a method which was fast to implement, and produced results close to the global optimum.

Optimisation is a process of selecting parameters such that a function of these parameters achieves an extremal value. This may also be subject to a number of equality or inequality constraints that depend on the parameters and, possibly, the objective function itself, which can also be an optimisation variable. When the problem is subject to constraints then it is naturally termed a 'constrained optimisation problem'. Optimisation methods are required in almost all branches of engineering and many branches of applied science, especially in economics. It is essential that in a world with limited resources, that the most is made of what is available, in order to achieve maximum benefit out of a commodity, whether that be time, money, fuel, energy, or spacecraft propellant. Generally, optimal control problems are classed as problems of the Mayer form if the controls appear linearly in

the equations of motion [Seywald and Kumar, 1995]. Unless the control parameters are in terms of the unit vectors in the inertial frame, then this is not usually the case for low-thrust trajectory optimisation problems. More often, the controls are characterised by non-dimensional angles such as pitch and yaw. This means that, in order to transform the controls to the frame in which the equations of motion are evaluated, non-linear trigonometric terms appear. Problems in which the controls appear non-linearly in the equations of motion are classified as problems of the Bolza form [Seywald and Kumar, 1995]. The problem of solar sail trajectory optimisation in this thesis is thus of the Bolza form. Low thrust trajectory optimisation can be divided into two main categories, the Indirect and the Direct method. These two methods are distinguished by the fact that the Direct method directly optimises the controls in question, relying on the final constraint evaluation (the function evaluation is a 'black-box'), whereas the Indirect method formulates the problem in terms of adjoint variables or co-states, with the equations of motion implicitly linked to the optimisation method.

2.1 Indirect Methods

This method is typically embodied by the branch of optimal control theory known as the Calculus of Variations (CoV) [Bryson and Ho, 1975]. This method has the primary advantage that it can produce truly optimal results, since there is no discretisation of the variables. The basic premise is that the controls themselves are not explicitly optimised, but rather, they are represented by a set of co-state or adjoint variables which form the Lagrange multiplier function of the objective function and constraints. This method has been employed for general fixed or variable thrust reaction propulsion systems for many years, specifically for Solar Electric Propulsion (SEP) [Melbourne and Sauer, 1961, Melbourne and Sauer, 1963, Breakwell and Rauch, 1966, Bruschi and Vincent, 1971, Bauer *et al*, 1982, Bauer *et al*, 1983, Schlinghoff, 1987, Bartholomew-Biggs *et al*, 1987, Cochran and Lee, 1991, Thorne and Hall, 1996, Teofilato and De Pasquale, 1998]. This method is widely used as it has been incorporated into NASA/JPL's low-thrust mission design tools, SEPTOP and VARITOP. Classically, the method has also been used for generating minimum-time solar sail trajectories [Zhukov and Lebedev, 1964, Sauer,

1976, Jayaraman, 1980, Wood, 1982, Simon and Zakharov, 1995, Powers *et al*, 1999, Colasurdo and Casalino, 2001]. Indeed, Sauer has used this method to produce an large range of solar sail trajectories, which serves as a benchmark for validating new results [Sauer, 1976]. The CoV method is implemented by forming the Hamiltonian function which incorporates the equations of motion. Each term in the function is weighted by a Lagrange multiplier, the co-state of the state variable defined by that term. The minimised performance index of the solar sail problem is defined by $J = t_f$, the transfer duration, but for other propulsion systems this could be the inverse of the final spacecraft mass so as to minimise propellant consumption. A mass co-state is not required with solar sails, since no propellant is used.

To further explain the Indirect method, the following illustration is for the case of two-dimensional, co-planar transfer (open final azimuth) between two circular orbits. The vector equation of motion can be resolved into two-dimensional polar co-ordinates (radius, r , azimuth angle, θ , radial velocity, v_r , and tangential velocity, v_θ) by the equations of motion given in Eqs. 2.1 – 2.4.

$$\dot{r} = v_r \quad [2.1]$$

$$\dot{\theta} = \frac{v_\theta}{r} \quad [2.2]$$

$$\dot{v}_r = \frac{v_\theta^2}{r} - \frac{\mu}{r^2} + \beta \frac{\mu}{r^2} \cos^2 \alpha \cos \alpha \quad [2.3]$$

$$\dot{v}_\theta = -\frac{v_r v_\theta}{r} + \beta \frac{\mu}{r^2} \cos^2 \alpha \sin \alpha \quad [2.4]$$

Since the variation of θ is not relevant in this simplified analysis, then Eq. 2.2 is not required. A co-state vector, $(\lambda_1, \lambda_2, \lambda_3)$, is assigned to the variables (r, v_r, v_θ) for which variation is considered. For the general problem, the velocity co-state is often called the primer vector in optimal control theory. A variational function called the Hamiltonian, H , is constructed from the equations of motion, as in Eq. 2.5. The rate of change of the co-state vector can be obtained by partial differentiation of the Hamiltonian function, with respect to each variable.

$$H = \lambda_1 v_r + \lambda_2 \left[\frac{v_\theta^2}{r} - \frac{\mu}{r^2} + \beta \frac{\mu}{r^2} \cos^2 \alpha \cos \alpha \right] + \lambda_3 \left[-\frac{v_r v_\theta}{r} + \beta \frac{\mu}{r^2} \cos^2 \alpha \sin \alpha \right] \quad [2.5]$$

For a solar sail, minimisation of the transfer time is accomplished by maximising the Hamiltonian at all points in the trajectory, through an appropriate choice of the sail cone and clock angles. To maximise the Hamiltonian, the sail clock angle must be the same as the clock angle of the primer vector (not relevant for the 2D case), and the optimal sail cone angle such that the component of the sail force along the primer vector is maximised, as in Section 1.6 for the optimal sail force vector. The Hamiltonian can be extremised with respect to the control angle, α , by equating the partial derivative to zero, $\partial H/\partial\alpha = 0$. By partial differentiation, and then cancelling common scaling factors, $\beta\mu\cos\alpha/r^2$, gives Eq. 2.6.

$$\frac{\partial H}{\partial\alpha} = 0 = -3\lambda_2 \cos\alpha \sin\alpha + \lambda_3 \cos^2\alpha - 2\lambda_3 \sin^2\alpha \quad [2.6]$$

Converting the sine terms to tangent form, leaves a quadratic equation in $\tan\alpha$, shown in Eq. 2.7.

$$-2\lambda_3 \tan^2\alpha - 3\lambda_2 \tan\alpha + \lambda_3 = 0 \quad [2.7]$$

The optimum control angle can be obtained by solving this quadratic equation. There are of course two solutions for α corresponding to a maximum and minimum of the Hamiltonian. By differentiating a second time and checking for the sign of $\partial^2 H/\partial\alpha^2$, it is found that the root which produces the maximum value of H is given by Eq. 2.8, which is similar in form to the equation for the optimal cone angle in Section 1.6.

$$\tan\alpha = \frac{-3\lambda_2 - \sqrt{9\lambda_2^2 + 8\lambda_3^2}}{4\lambda_3} \quad [2.8]$$

The co-state equations must also be found as a function of time, which is achieved by numerical integration. Their time derivatives are obtained by the partial differentiation of the Hamiltonian with respect to each of the state variables, $\dot{\lambda}_i = -\partial H/\partial x_i$, as shown in Eqs. 2.9 – 2.11 for the simple 2D case. The negative sign comes from the satisfaction of the transversality condition, $H(t_f)_{+1} = 0$, that ensures the final transfer time is minimised (not maximised).

$$\dot{\lambda}_1 = \frac{\lambda_2 v_\theta^2}{r^2} - \frac{2\lambda_2 \mu}{r^3} + \frac{2\lambda_2 \beta \mu}{r^3} \cos^3\alpha - \frac{\lambda_3 v_r v_\theta}{r^2} + \frac{2\lambda_3 \beta \mu}{r^3} \cos^2\alpha \sin\alpha \quad [2.9]$$

$$\dot{\lambda}_2 = -\lambda_1 + \frac{\lambda_3 v_\theta}{r} \quad [2.10]$$

$$\dot{\lambda}_3 = -\frac{2\lambda_2 v_\theta}{r} + \frac{\lambda_3 v_r}{r} \quad [2.11]$$

The equations of motion and the co-state variation equations are then numerically integrated to propagate the trajectory. However, even though the state boundary conditions are specified by the orbit transfer problem, the co-state boundary conditions are not known. An iterative numerical method must be implemented, such as Newton's method or a multiple-shooting algorithm, so that the boundary conditions and transversality condition are satisfied, and the true-minimum transfer time can be converged upon. An initial guess for the co-states must be supplied to ensure convergence to the optimal solution. However, these co-states are not intuitive and the problem is often highly sensitive to them, and only from experienced engineering judgement and an intensive process of trial-and-error can feasible starting co-states be obtained. In addition, small changes in the control profile can have a very small effect on the transfer time, such that convergence to the true-minimum time solution is often difficult. Moreover, a continuous variation of the sail pitch angle could be problematic to accomplish from an engineering standpoint. The Calculus of Variations is often called an Indirect method, and forms the basis of the NASA/JPL VARITOP low-thrust trajectory optimisation tool, which has been used very successfully, but only by users who have many years of experience of using the method, which is something of a 'black-art'. Nevertheless, the Indirect method can produce true-minimum time trajectories, has an elegant mathematical basis, and does not usually require any expensive commercial optimisation packages – which is why it is widely used throughout the literature on low-thrust trajectory design problems. The Indirect method was not used for generating the results in this thesis, due to the problems highlighted above and because it is not flexible enough to be applied to a diverse range of problems. It is also difficult to incorporate constraints into the method.

2.2 Direct Methods

While the Indirect method of optimal control theory can provide true-minimum time trajectories for solar sails, it is often easier to parameterise the trajectory in an open-loop fashion. Then, gradient-based, deterministic, Non-Linear Programming methods are often used to solve the two-point boundary value problem by iteratively selecting a discretised control angle profile, that satisfies the boundary conditions and orbit constraints, whilst minimising the transfer time. As will be discussed in section 2.3, the cone and clock angles can be characterised by interpolation between a set of discrete points along the trajectory. As the number of optimised parameters is increased, then the control profile increasingly approximates the true-optimal, continuous control profile of the Indirect method of optimal control theory. Direct methods of trajectory optimisation are termed such because the control variables themselves are directly optimised to achieve the desired minimum time solution and satisfy the boundary constraints and any internal constraints imposed on the particular problem. The control variables are explicitly optimised so that, due to finite computational power, they must be discretised and as such can attain only near-minimum/maximum solutions. In solar sail trajectory optimisation, it has been found that penalties in the objective function are negligible with only moderate numbers of control variables [Hughes and McInnes, 2001], but more complex trajectories will require more control variables. If the number of control variables could hypothetically be increased to infinity then this would produce true-optimum solutions, and continuous control profiles, equivalent to using the Indirect CoV method. During trajectory propagation, the instantaneous control angles can be characterised by numerical interpolation between them to further approximate a continuous control profile. This can be achieved through constant values between nodes, linear interpolation, cubic splines or hermite interpolants.

Some of the algorithms that can solve the direct optimisation problem will now be described. While most optimisation algorithms are deterministic, gradient-based methods, there exist a few stochastic, probabilistic methods. True global optimisation is also something of a 'black art', since substantial computing power is necessary and the many problem specific parameters affect the ability of an algorithm to converge to a global optimum. Most trajectory optimisation problems have an extremely complex search space topography. Although there is usually only

one true global extremum, there are multiple extrema and saddle-points, which would entrap an optimisation algorithm at each of their local optimum values. Almost all deterministic methods are local optimisers because they use gradient information to search from an initial point along the direction of steepest search space gradient. Ultimately it is the choice of this initial starting region which dictates whether a local or the global minimum is obtained. Stochastic methods can sometimes find global optima because they use random variations in the variables to effectively sample and visualise a broad swathe of the search space domain. Numerous algorithms are now available which claim to be able to find global solutions using deterministic methods, although a stochastic element is almost always necessary. A truly global optimiser, which requires no engineering insight into the problem at hand and can produce optimal solutions without an appropriate selection of optimisation parameters, is the ultimate goal of the optimisation community. Often, the most robust optimisers involve hybridisation of global and local search methods.

2.2.1 Global Search Methods

Global search methods can be divided into two classes, deterministic-like methods such as branch and bound methods which can find solutions with high accuracy, and heuristic algorithms such as stochastic methods which implement random approaches to avoid local extrema, based on probabilistic theory. In reality, all global search methods rely on some stochastic element, although it is more subtly applied in some algorithms.

Branch and Bound Methods

Having their origins in combinatorial optimisation, Branch and Bound methods entail recursive splitting of the search space into successively smaller parts. Some parts are, however, biased with respect to others. The parts that are preferenced are selected according to bounds on the objective function to eliminate large parts of the search space fairly early, reducing the computational burden. The disadvantage is that branch and bound methods will only work if analytical knowledge of the objective function is held. A promising concept called Multilevel Coordinate Search has also been developed, which combines the advantages of

branch and bound methods with the generality of the heuristic methods [Huyer and Neumaier, 1999]. These methods appeared to be unsuitable for solar sail trajectory optimisation.

Genetic Algorithms

Stochastic in nature, Genetic Algorithms (GAs) are based on the Darwinian concept of natural selection and survival of the fittest [Goldberg, 1989]. They differ from conventional optimisation algorithms in that they search from a population of points, or individuals, and hence a global picture of the search space can be determined. Genetic Algorithms utilise stochastic processes, unlike deterministic calculus-based methods, so they are more able to avoid local minima. The parameter set of control angles is encoded in a binary ‘chromosome’, the length of which can be adjusted according to the precision required in the solution. This mapping between a binary number and a real valued parameter is given by Eq. 2.12 [Fowler *et al*, 1999], where U_{max} and U_{min} represent the maximum and minimum values the variable can take, and l is the number of binary bits used to represent the variable in the chromosome.

$$\Pi_{map} = \frac{U_{max} - U_{min}}{2^l - 1} \quad [2.12]$$

The Genetic Algorithm will attempt to *maximise* the objective function and so the fitness function must be set negative or inverted, for the minimum time requirement usually specified for solar sail trajectory optimisation. In addition, it is problematic to incorporate constraints in a single valued fitness function, so they are added as penalty terms with appropriate weighting coefficients. The penalty function method is adopted in this thesis, although other authors have used the concept of Pareto-fronts with some success [Hartmann *et al*, 1998]. Therefore, the goal of the GA is to maximise this fitness by evolving the population (sets of control angles) over a number of generations to determine the optimum parameter set. A number of genetic operators are executed as evolution proceeds through reproduction. There are many of these, and only the main ones used in this thesis will be described here. *Tournament Selection* compares two individuals at random and lets the one with the highest fitness go on to reproduce. This process is repeated with the remaining individuals until the whole population is covered. *Single-point Crossover* facilitates information exchange between the selected parents and randomly interchanges

sections of the parents' genomes, the so-called characteristic parameter set. *Mutation* helps maintain genetic diversity in the population by randomly 'flipping' a bit in the chromosome [Rauwolf and Friedlander, 1999]. One special operator used is *Elitism*, which copies the fittest individual from one generation to the next to prevent it inadvertently being lost. These operators are consistent with previous authors [Goldberg, 1989, Fowler *et al*, 1999].

Genetic Algorithm parameters, population size, maximum number of generations, crossover probability and mutation probability are selected according to problem difficulty. Clearly, the larger the population size and maximum number of generations, the chance of finding the global optimum is increased, but the computing time must be kept reasonable and finite. Genetic Algorithms have been applied successfully to electric propulsion trajectory optimisation by a number of authors [Trottemant and Biesbroeck, 2000, Coverstone-Carroll *et al*, 2000, Hartmann *et al*, 1998, Rauwolf and Coverstone-Carroll, 1996, Coverstone-Carroll, 1996], as well as to chemical propulsion [Crain *et al*, 1999]. GAs have also been recently applied to solar sail trajectory design [Rauwolf and Friedlander, 1999, Hughes and McInnes, 2002b]. There are many variants on the evolutionary optimisation theme, and recently Dachwald has had much success using a method of Evolutionary Neurocontrol, based on Artificial Neural Networks [Dachwald and Seboldt, 2002] However, this method does not perhaps satisfy the trajectory boundary conditions adequately enough.

Simulated Annealing

While Genetic Algorithms take their impetus from the biological world, Simulated Annealing is a stochastic optimisation method that models a process in the physical realm. The process by which atoms in molten metals cool into their crystalline solid state is modelled. It is termed 'annealing' by analogy with the process of heating and cooling that is used to harden materials in metallurgy [Hartmann, 1999]. In simulated annealing, the atoms are the parameters and the crystalline structure is the parameter set. The cost-function of the function evaluation is analogous to the energy of the atomic configuration. Optimisation proceeds by adjusting the temperature of the system until thermal equilibrium is reached. The Metropolis algorithm is the underlying, governing principle of this method, and represents the probability of a certain structure realigning. This

probability is related to the energy change between these different states, ΔE , the (simulated) temperature, T , and Boltzmann's constant, k , by Eq. 2.13.

$$P = e^{\frac{-\Delta E}{kT}} \quad [2.13]$$

Simulated Annealing has traditionally been applied to econometric problems with some success [Goffe *et al*, 1994]. Previous authors have obtained better results by hybridising simulated annealing with a local optimiser and applying it to simple benchmark problems [Desai and Patil, 1996]. For the solar sail trajectory optimisation problems in this thesis, simulated annealing did not appear suitable, but further research into using this method may prove fruitful.

2.2.2 Local Search Methods

A plethora of Direct, open-loop numerical methods exist for trajectory optimisation, many of which are summarised in Betts [1998]. Multiple Shooting methods have been used to good effect for low-thrust optimisation and are accomplished by the propagation of adjacent trajectory segments backwards and forwards in time in an iterative process in an attempt to get the segment boundary states to match up in an optimal way. A successful application of Multiple Shooting has been achieved by Kemble [2001, 2002]. In Direct Transcription, or Collocation methods, [Betts, 1994, Eagle, 2000, Scheel and Conway, 1994, Conway, 1997, Conway, 1995, Tang and Conway, 1995, Enright and Conway, 1991, Enright and Conway, 1992] the state vectors at multiple points along the trajectory also become constrained parameters, in addition to the control profile. This method was first described by Hargraves and Paris [1987], where the trajectory is represented by piecewise cubic polynomials. The state and control vectors at the discrete nodes and the collocation point at the segment centre define the unique polynomials for each segment [Cichan and Melton, 2001]. The derivative of the cubic is then compared with the derivative of the equations of motion to obtain the defect, the difference between the two. A Non-Linear Programming solver is then used to select the optimal controls and segment boundary states that drive this defect to zero, to enable the optimal solution. Many authors have had success with this algorithm for low-thrust trajectory optimisation using electric propulsion in two and three dimensions, and Cichan and Melton

[2001] have had success for two-dimensional solar sail trajectory optimisation. However, in this thesis feasible solutions were difficult to obtain, when optimising three-dimensional solar sail transfers and so the method was not used any further. For problems with a large number of variables, Differential Inclusion concepts have been studied, which remove explicit control dependence from the problem statement [Coverstone-Carroll and Williams, 1994]. This has the effect of reducing the dimension of the parameter space and requires fewer nonlinear constraints in the resulting Non-Linear Programming problem. Differential Inclusion was not studied further in this thesis, for solar sailing. The method adopted in this thesis optimises the control parameters alone using a method based on Sequential Quadratic Programming (SQP), which is described in the following section.

2.3 Heliocentric Trajectory Optimisation Method

In the early stages of this thesis, the different available optimisation methods were applied to solar sail benchmark test problems, such as the problem of coplanar transfer between the Earth and Mars. The main focus was not to use or develop the best optimisation algorithm, but to use an optimisation algorithm which was, in general, fast to implement and performed effectively for the majority of trajectory problems in this thesis. After a preliminary assessment, it seemed that an optimisation method based on a Sequential Quadratic Programming (SQP) algorithm produced reliable results, with an appropriate initial guess of the control angle parameters. In fact, very limited results were achieved with the other direct methods discussed above. It may be that there are better algorithms than the SQP method, but much further work would be required to develop such methods. The SQP algorithm performed well, and so no further investigation of the other available algorithms was conducted. The method used in this thesis may not be state-of-the-art, but the focus was on generating results, rather than developing algorithms. In this section, a description of the SQP-based, heliocentric solar sail optimisation method is provided, after definition of the mathematical model and of how the control angles can be represented.

2.3.1 Solar Sail Dynamical Model

The solar sail has been assumed to be a flat, perfectly reflecting surface for optimisation purposes, with no resulting centre-line effect. However, for sail-film temperature calculations, imperfect reflectivity and absorption have been taken into account. The variational equations of the modified equinoctial orbital elements [Walker *et al*, 1985] are explicitly integrated, using an adaptive step-size, variable order, Adams-Moulton-Bashforth method. Relative and absolute integration error tolerances were set at 10^{-12} . Generally, two-body dynamics were modelled with the primary body, the Sun, considered to be a point mass and a point source of radiation. The sole perturbation considered was that due to solar photon pressure, with the solar wind negligible in comparison. The spacecraft was often assumed to have zero hyperbolic excess velocity ($C_3=0$) at the Earth's sphere of influence and at arrival at the target body. In cases where excess launcher capacity was available, then positive hyperbolic excess launch energy was utilised. The cartesian state vectors of the Earth and other planets were obtained using an analytical approximation to the J2000 ephemeris [Eagle, 1999]. Small body ephemeris was approximated using the most recent orbital elements and time of periapsis passage. For interplanetary trajectories, the sphere of influence of each planet or small-body was assumed to be a point, defined by the ephemeris.

2.3.2 Control Representation

As also discussed in Chapter 1, the solar sail thrust vector direction, \mathbf{n} has been defined by two angles to completely cover the outward hemisphere of allowable orientations. These are, the cone angle, $\alpha \in [-\pi/2, \pi/2]$, between the sail normal, \mathbf{n} , and the Sun-sail vector, \mathbf{r} , and the clock angle, $\delta \in [0, \pi]$, between the projection of the sail normal and some reference direction onto a plane normal to the Sun-line [McInnes, 1999]. Other authors [Sauer, 1976] often define the cone angle as $\alpha \in [0, \pi/2]$, and the clock angle as $\delta \in [0, 2\pi]$, which is equally valid in covering the hemisphere of outward thrust for a solar sail. A direct, parameter optimisation scheme was implemented with the trajectory divided into segments, equally spaced in time between zero and the terminal time. The control variables (cone and clock angles) to be optimised are then the discrete nodes at the segment boundaries. The

instantaneous controls are then characterised by linear interpolation between the nodes across each segment. It would also be possible to use Hermite or Cubic polynomials, but if the nodal resolution is high enough then linear interpolation more than adequately approximates a continuous profile. A simpler control representation would be to have the cone and clock angles fixed relative to the Sun-line in each segment, which may be more easily accomplished in practice through passive means. These different control representations are illustrated in Figure 2.1. Using linear interpolation, as the number of nodes was increased then a close approximation to a continuous profile was achieved. Problems requiring more revolutions, or more rapid control variation (usually for lower accelerations) clearly needed more segments. 50 segments (51 nodes) were usually sufficiently accurate, but problems requiring rapid slews needed 200 or more segments (201 nodes).

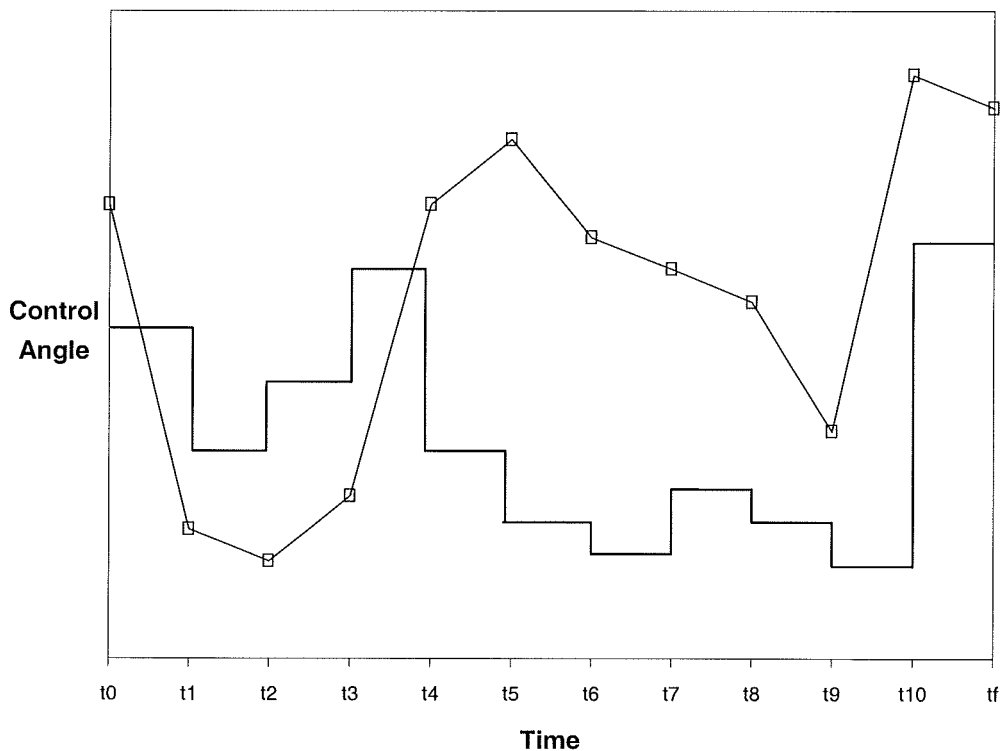


Figure 2.2: Two methods of discretised control representation

2.3.3 Non-Linear Programming Optimisation Method

The optimisation problem for the trajectories in the following chapters was, to select the variables which minimised the transfer time (the objective function), or minimised or maximised the velocity at a point, whilst satisfying the end-point boundary conditions and any mid-course constraints. There are six end-point cartesian state vector constraints for rendezvous, and three for flyby, in addition to any problem specific constraints, such as minimum orbit radius. Therefore, the objective function, J , must be minimised, subject to the equality constraints, $c_i = 0$, for $i = 1$ to n , where n is the total number of constraints. This can be formulated as a general optimal control problem, where the objective function, J has the form shown in Eq. 2.14 and where, \mathbf{x} is the state vector of 6 elements, \mathbf{u} is the control vector, and t_f is the terminal time.

$$J(\mathbf{x}(t_f), \mathbf{u}, t_f) = f(\mathbf{x}(t_f), \mathbf{u}, t_f) + \int_0^{t_f} g(\mathbf{x}(t), \mathbf{u}, t) dt \quad [2.14]$$

This was transcribed to a Non-Linear Programming (NLP) problem, solved using NPSOL 5.0 (or NPOPT 6.2 within SNOPT), a Fortran77 package based on Sequential Quadratic Programming (SQP), developed at Stanford University. A Matlab version was also available, but was found to be too slow, due to the large numbers of function evaluations necessary in various loops. SQP is a deterministic gradient-based method that employs a quasi-Newton approximation to the Karush-Kuhn Tucker, first-order conditions of optimality, resulting in a sub-problem of minimising a quadratic approximation to the function of Lagrange multipliers incorporating the objective and constraints. NPSOL incorporates an augmented Lagrangian merit function, and a BFGS quasi-Newton approximation to the Hessian matrix of the Lagrangian function. The SQP method involves major and minor iterations, with the minor iteration of the Quadratic Program sub-problem determining the search direction [Gill *et al*, 1998]. Gradient evaluation was approximated by finite differences, which increases computing time, but does not require any deeper knowledge of the search space. The internal details of the SQP algorithm are not important, but it has been widely used for low-thrust trajectory optimisation [Kluever, 1997]. The optimality termination tolerance was usually set to be 10^{-3} , with the constraint feasibility tolerance usually set at 6.685×10^{-6} . This

ensured that final boundary conditions were satisfied to within 1000 km for each position element and to within 0.2 m s^{-1} for each velocity element, without performing excessive iterations. Where problems could not be solved, then the tolerances were relaxed to enable a feasible solution. This less accurate solution was sometimes re-optimised with tighter tolerances to obtain the desired accuracy and optimality.

2.3.4 Initial Control Estimates and Genetic Algorithms

Although NPSOL is fairly robust compared with other methods of solving two-point boundary value problems such as those in this thesis, it nevertheless employs gradient-based, deterministic, local search procedures. It therefore requires an initial guess for the cone and clock angle profiles, and transfer time, that is within proximity of the actual solution, to ensure a feasible solution is obtained. This poses a number of problems when optimising interplanetary transfers at differing characteristic accelerations and departure dates. For the majority of trajectories, successive forward integrations were performed and trajectories visualised until an estimated control profile produced a spacecraft end-point state vector that was close enough to the target end-point state vector to allow NPSOL to find an optimal solution. In a number of cases where engineering insight could not be used, the global search properties of a Genetic Algorithm (GA) were employed to generate the initial guess. For the GA parameters, the population size selected was usually 2000 with a maximum number of generations of 300, and a crossover probability of 0.6, and mutation probability of 0.0015. These were the same as those used by Rauwolf and Friedlander [1999]. The single-valued fitness function (which is maximised) is a measure of the performance of an individual (binary ‘chromosome’ of the optimisation variables) within the population and incorporates the transfer time and the end-point boundary constraints (which are minimised). The fitness function was similar to that used by Bader [2002]. The constraints were incorporated into the fitness function as penalty terms in Eq. 2.15, where, c_t is the weighting coefficient of the transfer time (10^{-11}), and c_{state} is the weighting coefficient of each state constraint (10^3 for all constraints). y_i is the state vector element for the spacecraft (s/c) and the target (tgt), for $i = 1$ to n , where n is the total number of end-point state constraints (for example, there are six constraints for rendezvous, and three for flyby).

$$fitness_{GA} = \frac{1}{J_{GA}} = \frac{1}{c_f t_f^2 + \sum_{i=1}^n c_{state} (y_i^{s/c} - y_i^{tgt})^2} \quad [2.15]$$

Genetic Algorithms or the locally-optimal analytical control laws, described in Section 1.7, were often used to generate first solutions, before homotopy (incremental feedback) was used for subsequent parametric analyses. An explanation of the incremental feedback method is provided Chapter 3, where it is first used.

Chapter 3

Inner Solar System Trajectories

In this Chapter, an extensive study of solar sail transfers to the other three terrestrial planets is conducted, in the context of planetary sample return missions. Usually, other authors concentrate on one-way missions. Solar sailing often excels for a one-way journey, but here it will be demonstrated that propellant-free solar sails have a considerable capability for round-trip planetary sample return missions. Although solar sails are not restricted to launch windows, planetary phasing ensures that different departure dates result in different trip times - the aspects of this will be investigated in some detail in this chapter. The questions which will be addressed are as follows.

- For outbound trajectories to Mars, Venus and Mercury, what is the variation of transfer time with characteristic acceleration, and what is the behaviour of the problem at higher characteristic accelerations?
- What are the optimal Earth departure windows in a 10 year timeframe? How is the trip time affected by departure date, and where are the trip time maxima and minima located? What is the overall shape of the departure date scan, and are the changes abrupt or more gradual?
- After sample acquisition, what is the effect of the return journey departure date scan on total mission duration? What is the overall minimum total mission duration when outbound and return departure scans are combined? The optimal outbound departure date may not be the same as the overall optimal date when the planet centred phases and return trajectory are accounted for.
- What is the effect of heliocentric distance on sail film temperature along such trajectories?

- What is the effect of using positive launcher hyperbolic excess velocity on outbound trip time? Can the trip time to Mercury be reduced by using a Venus gravity assist en-route?

3.1 Mars Trajectories

The Earth–Mars low thrust trajectory optimisation problem has long been the standard benchmark test case applied to solar sail, and more frequently Solar Electric Propulsion (SEP), trajectory optimisation techniques. Classically, the branch of optimal control theory known as the Calculus of Variations has been adopted to formulate the optimal controls [Sauer, 1976]. The majority of solar sail studies assume the idealised case of transfer between circular, coplanar orbits of 1 and 1.525 AU, with open final azimuthal position, to which the Pontryagin Maximum Principle has been applied [Zhukov and Lebedev, 1964, Colasurdo and Casalino, 2001]. Indeed, Sauer has been instrumental in generating optimal heliocentric solar sail and SEP trajectories using the SEPTOP, and the more general VARITOP low-thrust optimisation tools developed at the NASA Jet Propulsion Laboratory. However, departure date optimality for realistic missions is badly documented in the literature, since single departure date trajectory optimisation is often a highly complicated process in itself. Many authors concentrate on rather small deviations about a particular date, and do not investigate the long-term variation [Simon and Zakharov, 1995]. Long-term variation has been investigated, to some extent, by Frisbee, but details of the departure date scan process are not apparent and appear ad-hoc at best [Frisbee and Brophy, 1997, Frisbee, 2001]. During this section, current knowledge is greatly expanded for the optimal departure date opportunities open to solar sails in the 2010-2020 time-frame, for Earth-Mars transfers, in the context of a Mars sample return mission.

In the first instance, the variation of Earth-Mars circle-to-circle coplanar trip time was investigated as a function of characteristic acceleration, using the NPSOL optimisation method discussed in Chapter 2, with 50 control segments (51 nodes). This provides the minimum time for a solar sail to transfer from a 1 AU circular orbit to a 1.525 AU circular orbit, with open azimuthal position on each orbit. Transfer times for up to 1.0 mm s^{-2} are shown in Figure 3.1. This analysis was carried out,

using incremental feedback, up to 10.0 mm s^{-2} , where the trip time levels off at 213 days. These circular coplanar Earth-Mars transfers provide some validation of the parameterised optimisation algorithm, since the trip-time for 1.0 mm s^{-2} is very close to the true optimal solution, obtained through the use of the Calculus of Variations [Zhukov and Lebedev, 1964, Sauer, 1976]. For further analysis of Earth-Mars trajectories, a characteristic acceleration of 0.5 mm s^{-2} was chosen, to enable a single revolution Earth-Mars spiral, and maintain a reasonable mission duration and sail size, when Mars capture time was taken into account for a possible Mars sample return mission [McInnes *et al*, 2003a].

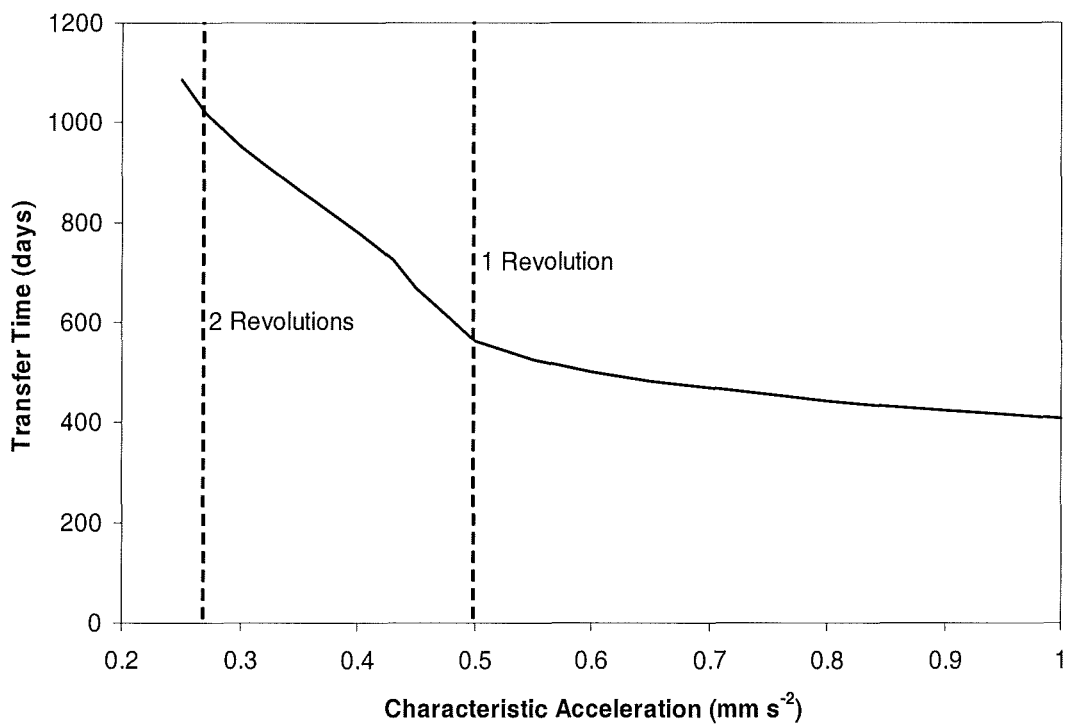


Figure 3.1: Circular coplanar trip-times from 1 AU to 1.525 AU, against characteristic acceleration

3.1.1 Departure Date Scans

Often, the Genetic Algorithm (GA) was used to generate a starting guess for one or two departure dates in the time frame considered (2010-2020). Only 10 control segments (11 nodes) were used for this problem, to reduce the extreme computational burden imposed when using a GA. If a suitable initial guess, interpolated to 51 nodes, could produce a satisfactory solution, then the solution at that departure date was used as the initial guess for other departure dates (adjusted in small increments). It was evident that some trajectories required an extra revolution, because it appeared that the sail had just missed its target – therefore the initial control profile was infeasible since it was out-of-phase with the target. Some transfer times for optimal trajectories separated by just a few days in departure date could be vastly different because of inclination changes and extra revolutions, so many of the transfer time estimates were also infeasible. This problem could often be surmounted by making the increment in departure date successively smaller until a feasible solution could be found. This technique was applied in conducting departure date scans. An automated loop was set up with an initial, standard departure date increment specified. The number of runs of NPSOL to execute was specified at the outset as the maximum loop index. Each time an optimal, feasible solution was obtained, at the next step in the loop, the departure date was incremented by the standard increment (1 or 7 days). If a feasible solution was not obtained, then the current departure date increment was reduced by a factor of 2 until the next feasible, optimal solution was found. This process could be accomplished forwards and backwards in time by specifying a positive or negative standard departure date increment. Occasionally, departure date scans became blocked by a discontinuity in the departure date–trip time space, due to an extra revolution being required, and the control profile and trip time being radically different. In such cases it was necessary to generate a new initial guess beyond this discontinuity and then carry on the departure scan further, or work back to the discontinuity.

3.1.2 Earth–Mars Phase

Multiple departure date scans were executed from two different starting dates, with departure date increments both backwards and forwards in time. Some departure

date scans tended towards local optimality, due the starting guesses being locally optimal and the subsequent amplification of these non-optimal errors. In the course of this process, it was observed that independently initiated departure date scans often tended to overlap one another, and it could clearly be seen that certain slopes were composed of trajectories that were more optimal than others. Departure dates scans that were sub-optimal were discarded and scans giving lower trip times were assumed to be the new globally optimal trajectories. Most scans were not smooth, but the general trend was clear. Anomalous spikes in the departure date scans corresponding to locally optimal minima could be removed by re-optimising across that range of dates. It was found to be excessively time consuming to keep traversing back and forth through the departure date range (2010 to 2020), so when the final departure date scans were deemed to be near-globally optimal, they were patched together into a continuous departure date profile. This final departure date profile had clear mid to long-term characteristics, but lacked fine, short-term continuity. Thus, the departure date scan was sampled to obtain the general trend curve shown in Figure 3.2. It can be seen that there are 4 minima in the range January 1, 2010 to May 13, 2018 (the initial starting trajectories), which occur of order 780 days apart, corresponding to the Earth-Mars synodic period. These departure opportunities occur on October 6, 2011 (578 days), November 5, 2013 (587 days), November 13, 2015 (682 days) and November 21, 2017 (706 days). It should be noted, however, that these minima are not of the same trip time, due to the inclination and eccentricity of the Martian orbit. The minima gradually rise over the epoch considered, and will probably repeat across a longer-term timescale.

For an example mission, the minimum time trajectory closest to the year 2010 (the desired departure epoch) occurs when the spacecraft departs on October 6, 2011, arriving at Mars sphere of influence 578 days (1.58 years) later on May 5, 2013. The trajectory is shown in Figure 3.3 with Mars arrival achieved after just over 1 heliocentric revolution, 62.3° beyond perihelion. For comparison, a trip time maxima of 1164 days occurs if departure is postponed by 91 days to January 5, 2012. Figure 3.4 shows the trajectory, where it can be seen that an extra revolution around the Sun is required due to the spacecraft just missing Mars on its first pass. The spacecraft then has to wait for the next rendezvous opportunity by incorporating coast phases and an inner loop within the Earth's orbit. This extra revolution, due to

the unfavourable planetary alignment at departure, would only incur a temporal penalty, since propellant mass is not an issue for a solar sail. Solar sails are not restricted to departure date windows as stringently as SEP or chemical propulsion, but clearly it is of benefit to mission performance to choose a departure date that would provide the minimum mission duration. In addition, it can be seen that relatively modest departure delays can incur quite severe penalties in mission duration.

The 2011 opportunity departure date optimal trajectory is selected for the base-line sample return mission definition. It can be seen in Figure 3.5 that the cone and clock angle controls have a smooth form and an oscillatory nature. This is an indication that the trajectory is near-globally optimal. The cone angle varies by only 24° , from 24.7° to 48.7° , while the clock angle varies by 46° , from 61.9° to 108.0° and so no sub-optimal coast phases are present. In addition, this means that there is a modest Sun aspect angle on the cruise stage during the Earth-Mars trajectory. The non-specularly reflective, centre-line effect, on thrust magnitude and orientation is much larger as the cone angle approaches $\pm 90^\circ$. Therefore, the ideal sail considered for trajectory analysis purposes is seen as a valid assumption. The temporal evolution of the spacecraft's instantaneous orbital elements is shown in Figure 3.6. The maximum rate of change of inclination to accomplish orbit inclination increase occurs during the first 120 days of flight when the solar photon flux is higher.

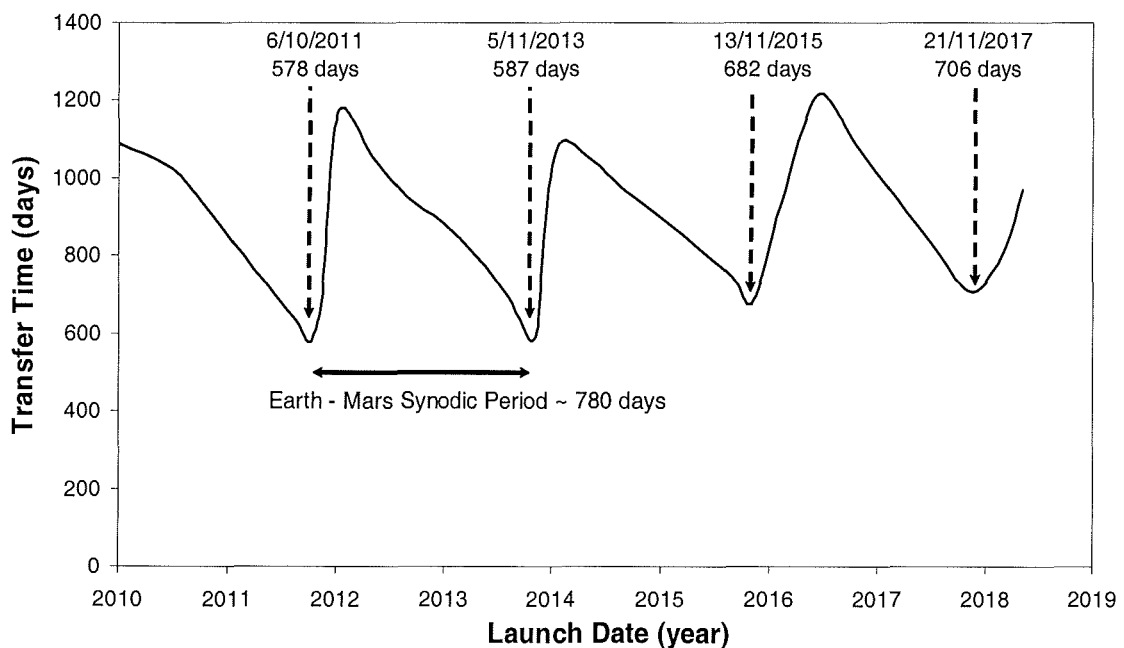


Figure 3.2: Earth-Mars departure date scan

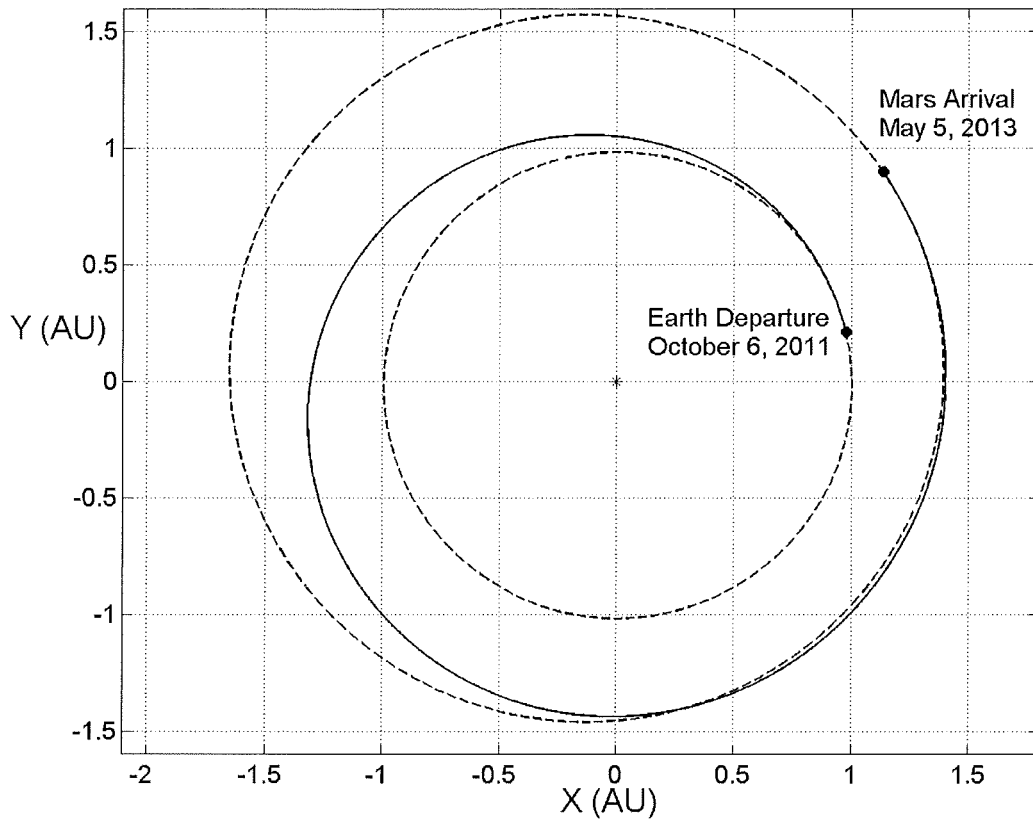


Figure 3.3: Departure date optimal Earth-Mars rendezvous trajectory (0.5 mm s^{-2})

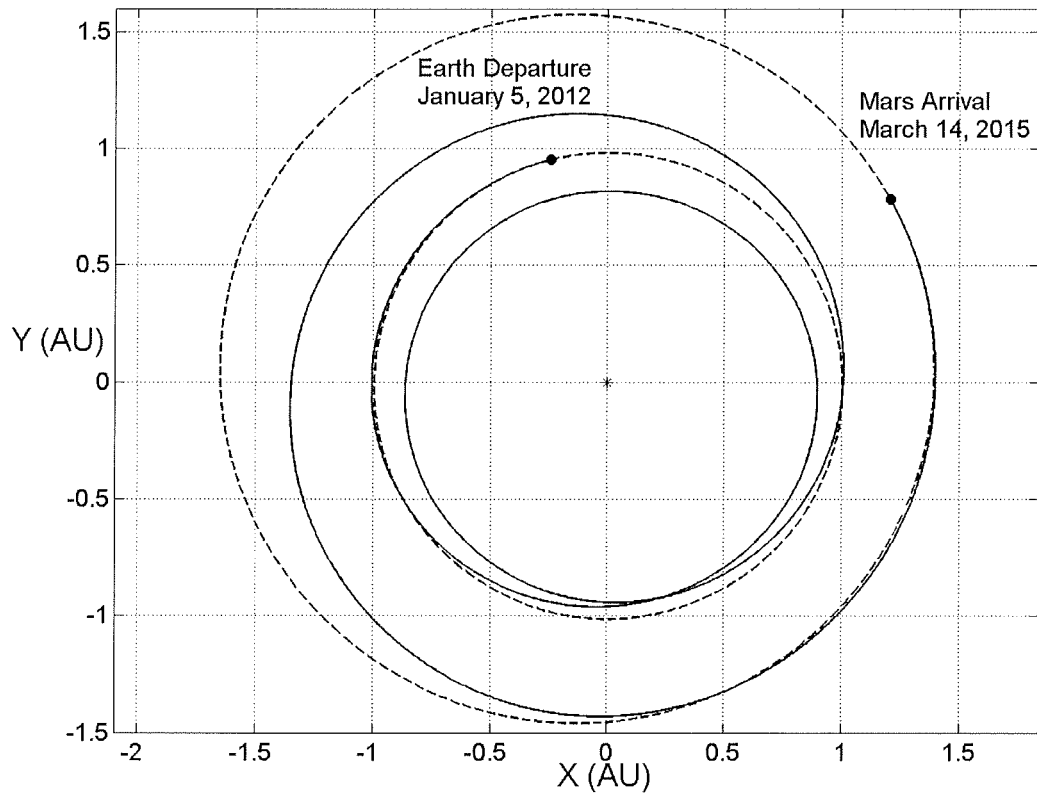


Figure 3.4: Sub-optimal departure date Earth-Mars rendezvous (0.5 mm s^{-2})

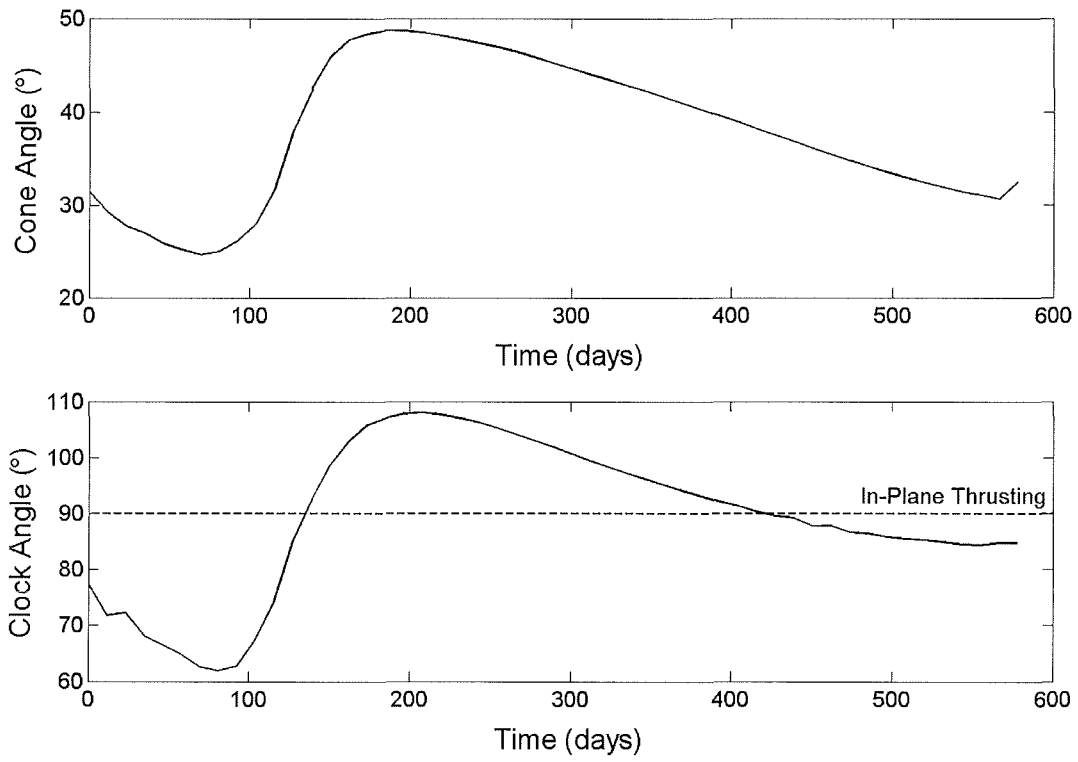


Figure 3.5: Earth-Mars rendezvous control profile

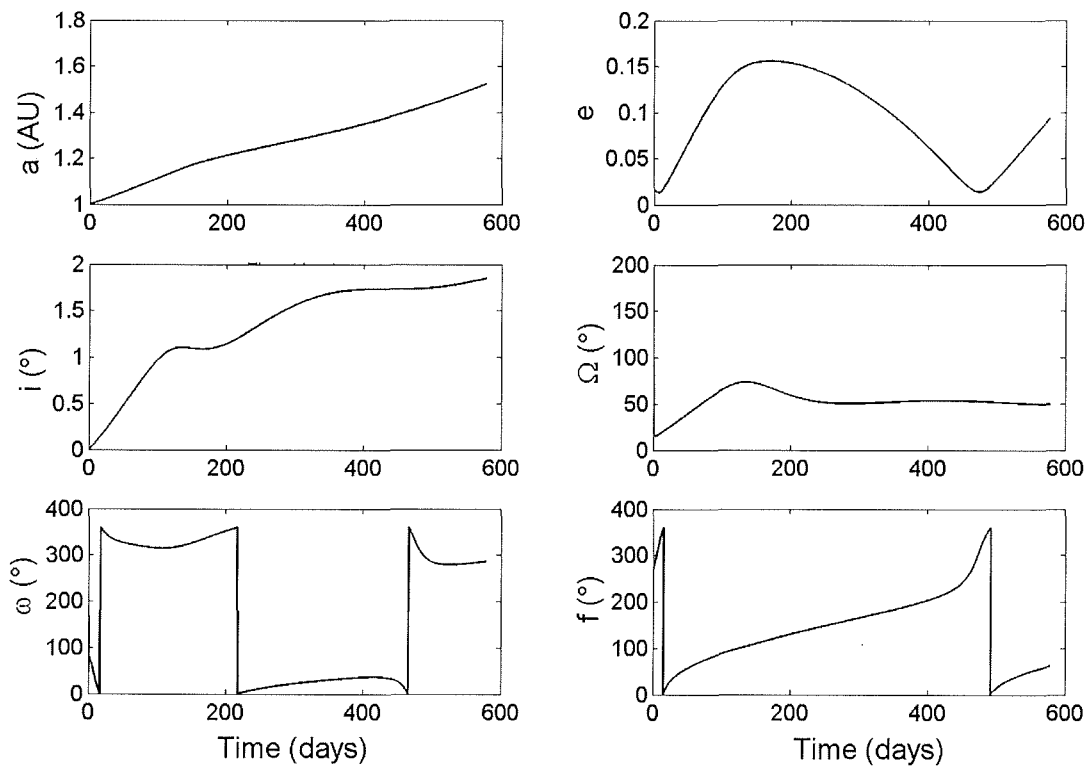


Figure 3.6: Earth-Mars rendezvous orbital element evolution

A critical parameter to be considered in the design and subsequent orbital manoeuvres of a solar sail is the sail film temperature T_s . The real sail reflectivity, \tilde{r} will be somewhat less than unity. For temperature calculation purposes, it will be assumed that the sail aluminium coating has a conservative reflectivity of 0.85 and so there will be some degree of energy absorption. Since the sail film is extremely thin it has almost no thermal capacity, and temperature changes are therefore essentially instantaneous [McInnes, 1999]. It is assumed that there is no emission from the front (aluminised) surface (front emissivity, $\varepsilon_f = 0$) and that a highly emissive coating such as Chromium is applied to the back surface, with an emissivity, ε_b , of 0.64. A high polyimide substrate temperature (>520 K) could cause serious degradation of the sail film substrate, coatings and adhesives, which would reduce or inhibit sail performance. Temperature control is of particular importance close to the Sun, but is of lower significance for Earth-Mars trajectories. From black-body thermodynamics, the power emitted from unit area of the sail, of emissivity ε , at temperature T_s , is $\varepsilon\tilde{\sigma}T_s^4$ where $\tilde{\sigma}$ is the Stefan-Boltzmann constant ($5.67 \times 10^{-8} \text{ J s}^{-1} \text{ m}^{-2} \text{ K}^{-4}$). The sail equilibrium temperature is then obtained from the thermal balance between the input and output power, $(\varepsilon_f + \varepsilon_b)\tilde{\sigma}T_s^4$ and $(1 - \tilde{r})W \cos \alpha$ respectively, where W is the incident solar flux. W can be scaled by the Earth-Sun distance, r_E , by Eq. 3.1, where W_E is the solar energy flux at 1 AU ($1368 \text{ J s}^{-1} \text{ m}^{-2}$). The sail film equilibrium temperature is therefore obtained as a function of the heliocentric distance r , and the incidence (cone) angle α by Eq. 3.2.

$$W = W_E \left(\frac{r_E}{r} \right)^2 \quad [3.1]$$

$$T_s = \left[\frac{1 - \tilde{r}}{\varepsilon_f + \varepsilon_b} \frac{W_E}{\tilde{\sigma}} \left(\frac{r_E}{r} \right)^2 \cos \alpha \right]^{1/4} \quad [3.2]$$

For the selected 2011 Earth-Mars trajectory, the variation of sail film temperature is shown in Figure 3.7 along with the heliocentric distance on the trajectory. The maximum film temperature is 266 K (-7 °C) obtained 27 days into the spiral, well below the likely upper limit for polyimide films of order 520 K.

In order to assess the impact of the trajectory on the mission telecommunications link, the three angles that define the triangle between the Earth,

Sun and Sail have been calculated using the scalar products of their constituent vectors. The sum of these angles is always 180° . The Earth-Sun-Sail, Sun-Sail-Earth and Sun-Earth-Sail angles are shown in Figure 3.8. It can be seen that the Earth-Sun-Sail angle approaches 180° at 560 days, 17.8 days before Mars arrival. At this point, this angle does not quite reach 180° due to the non-coplanar nature of the trajectory and planetary orbital inclination. However, due to the finite size of the solar disc and considerable extent of the solar corona, the alignment is taken to be a solar conjunction. At solar conjunction, all Earth-spacecraft telemetry is lost for a period. Loss of good line-of-sight close to a critical phase of the mission at rendezvous is a clear disadvantage of this trajectory. The other geometry that may become problematic is when the Earth-Sun-Sail angle is close to zero. The Sun-Sail-Earth angle is at a minima of 7° , and the Sun-Earth-Sail angle is at a maximum of 172° at 40 days. During this geometry, the Sun and Sail are in opposition with respect to the Earth and are diametrically opposite or antipodal from the point of view of the Earth. When viewed from the solar sail, the Earth and Sun will be in almost the same position in the sky, and so telecommunications will not be possible while the Earth is within the solar radio disk. It is also of importance to note that Mars arrival occurs when the Earth and Mars are 173.1° out of phase, which leads to a long path length for telecommunications, again at a critical mission phase. It is the author's view that this arrival Earth-Mars phasing is thought to be a characteristic of departure date optimal trajectories, although further investigation is required.

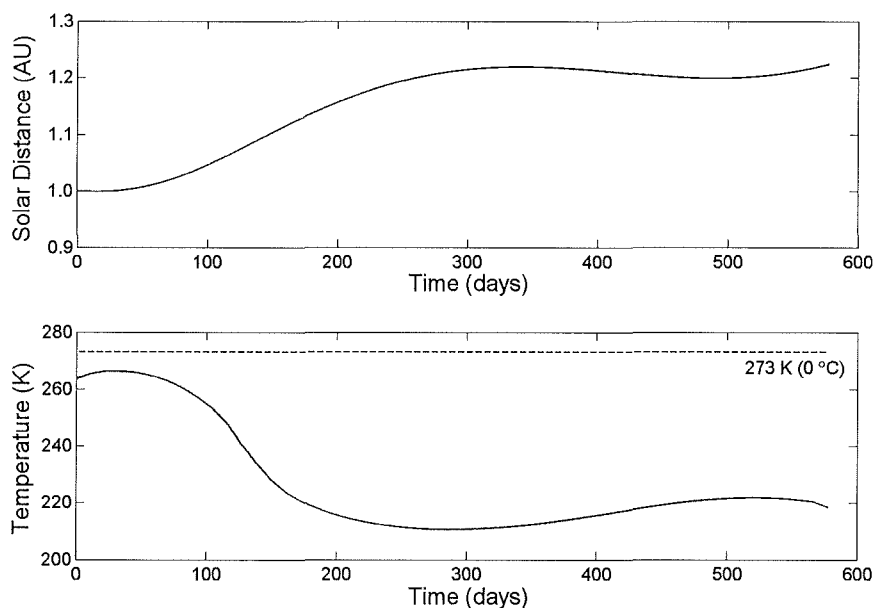


Figure 3.7: Earth-Mars heliocentric distance and sail film temperature

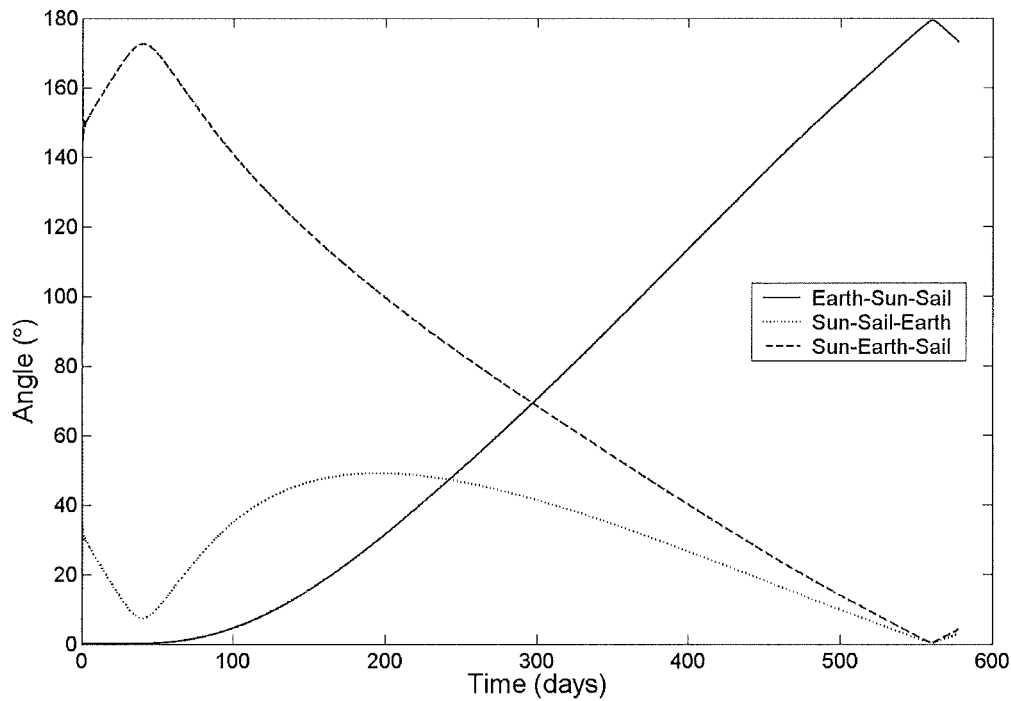


Figure 3.8: Earth – Mars telecommunications angles

3.1.3 Mars – Earth Phase

In the Mars sample return context [McInnes *et al*, 2003a], Mars Sphere of Influence arrival occurs on May 5, 2013 from where the Mars centred capture spiral is initiated. After the lander descends to the surface, the ascent vehicle returns the sample to dock with the orbiting solar sail. It is envisaged that the lander and ascent vehicle are left at Mars, so the solar sail only has to transport the reduced mass of the sample canister back to the Earth. Since the return payload mass is reduced, then for a fixed sail area, the return characteristic acceleration increases from 0.5 mm s^{-2} to 0.862 mms^{-2} . The Mars orbit escape time is affected by the parking orbit departure date, because of Mars' eccentricity and subsequent solar radiation pressure variation along its orbit. The lander stay-time thus defines the parking orbit departure date and escape spiral duration [McInnes *et al*, 2003a]. The stay-time is ultimately constrained by interplanetary launch opportunities and so must be selected (with equal regard to consequential variance in escape duration) to ensure a departure date optimal Mars – Earth return trajectory.

A narrow departure date scan was conducted around the expected Mars' sphere of influence departure date (from approximate Mars escape data [McInnes *et*

al, 2003a]), from March 28, 2015 to July 31, 2015 using the Genetic Algorithm to generate the initial guess. Unfortunately, further forwards departure date propagation was barred by the presence of a discontinuity on May 25, 2015, suggesting the solar sail had just missed the Earth and an extra revolution was necessary. The Genetic Algorithm was again used to obtain an initial control guess beyond this step in the departure date profile. Then a departure date scan was conducted backwards in time to meet the discontinuity. The final patched departure date scan is shown in Figure 3.9. It was discovered that there was a departure date minimum of 467 days on May 17, 2015. A Mars departure date beyond the discontinuity would allow for an extended surface stay-time, but would degrade mission performance due to the extra 100 days necessary for the return spiral. It would be highly attractive to leave Mars close to the departure date minimum, so a Mars' sphere of influence departure date of May 23, 2015 was selected, when the Mars centred phase was accounted for.

The optimal solution found for Mars departure on May 23, 2015 was for a trip-time of 471 days, arriving back at the Earth's sphere of influence on September 5, 2016, after less than a single revolution about the Sun. Again, since the lander and ascent vehicle have been discarded the solar sail characteristic acceleration for the Earth return trajectory has increased from 0.5 mm s^{-2} , to 0.862 mm s^{-2} , resulting in a fast return spiral. The resulting optimum trajectory is shown in Figure 3.10. It can be seen from Figure 3.11 that the sail cone angle profile is smooth and varies by 45° , from -23.5° to -68.8° , while the clock angle is less smooth, probably due to the exact departure date minimum not being selected as the departure date. Figure 3.12 shows the temporal evolution of the instantaneous orbital elements along the trajectory. The maximum rate of change of inclination occurs towards the end of the trajectory, as expected. The heliocentric distance variation as a function elapsed time is shown in Figure 3.13, along with the corresponding variation of the sail film temperature with distance and cone angle. The maximum sail temperature is again well below the upper limit (of order 520 K) at 259 K (-14°C), 432 days into the trajectory.

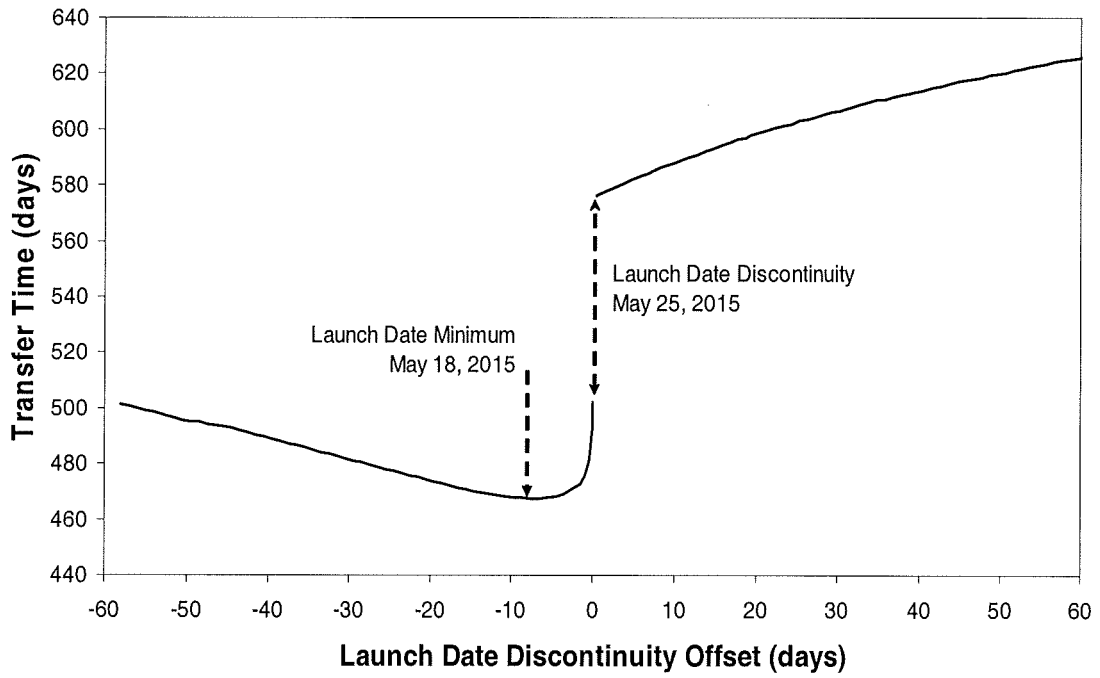


Figure 3.9: Mars – Earth Departure Date Scan

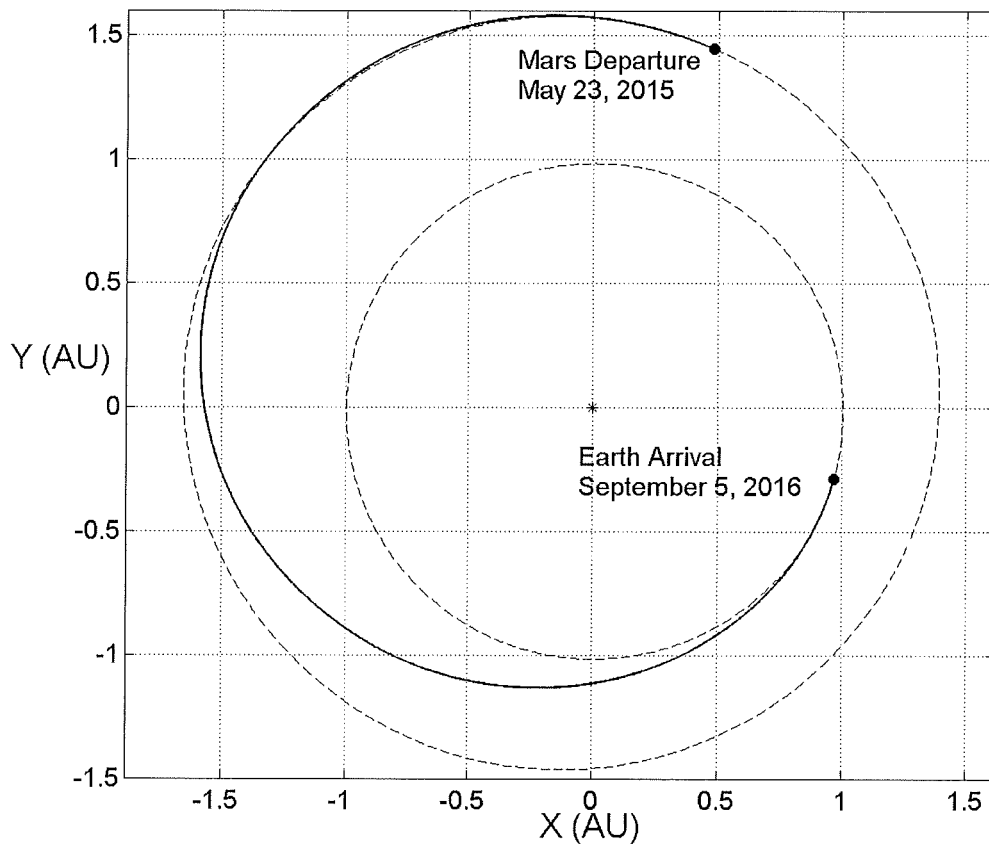


Figure 3.10: Mars – Earth rendezvous trajectory (0.86 mm s^{-2})

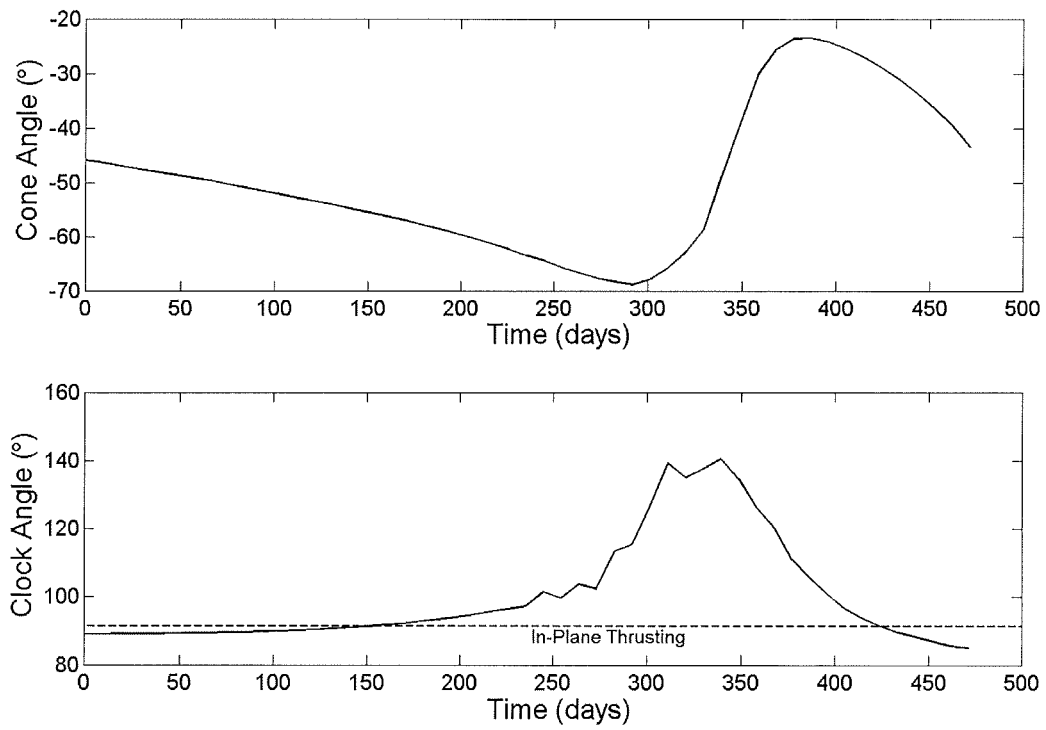


Figure 3.11: Mars-Earth rendezvous control profile

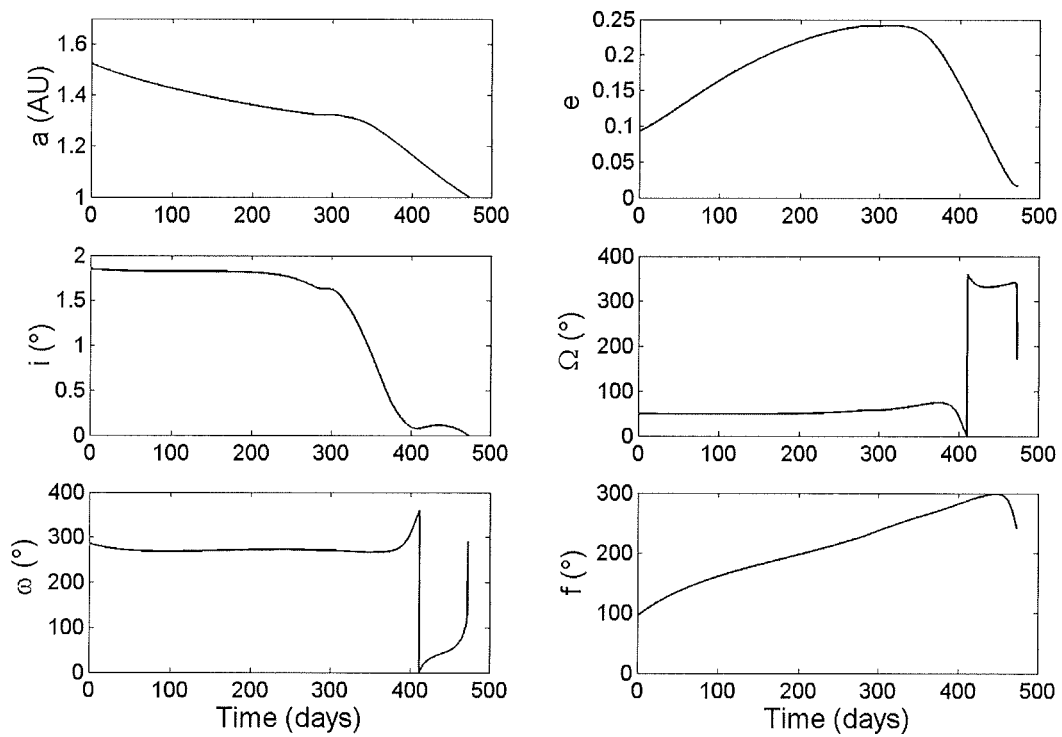


Figure 3.12: Mars-Earth rendezvous orbital element evolution

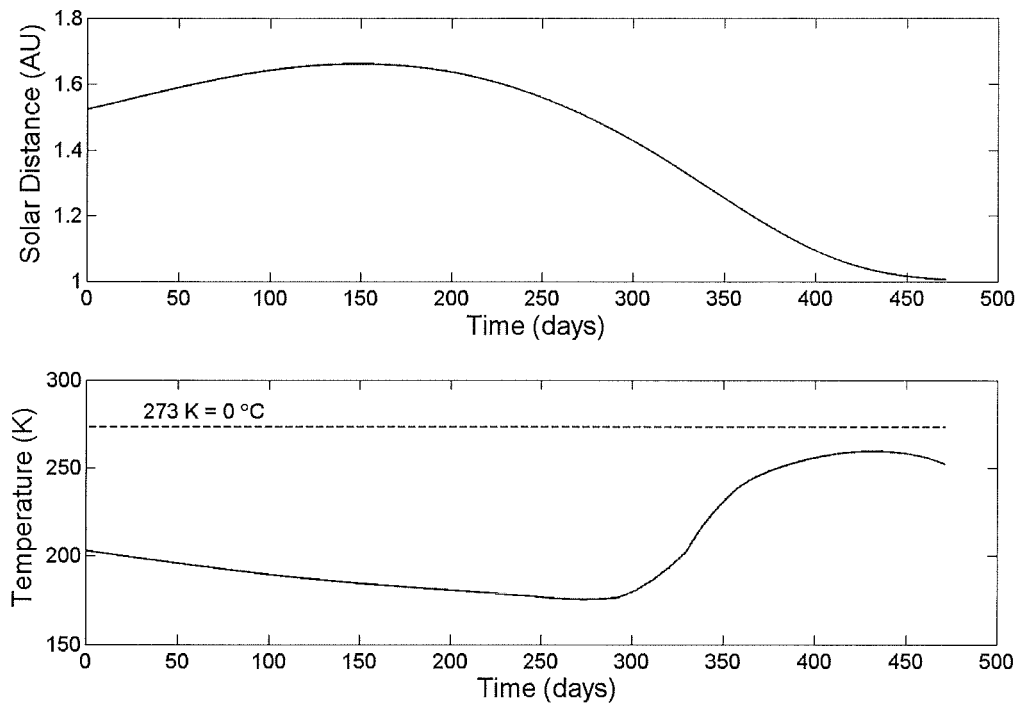


Figure 3.13: Mars–Earth heliocentric distance and sail film temperature

3.2 Venus Trajectories

Transfers from Earth to Venus have not been investigated and documented in as much detail as those to Mars in the literature. Again, the Calculus of Variations has been adopted to formulate the optimal controls. The majority of solar sail studies assume the idealised case of transfer between circular, coplanar orbits of 1 AU and 0.723 AU, with open final azimuthal position, to which the Pontryagin Maximum principle has been applied [Zhukov and Lebedev, 1964]. Rendezvous trajectories, using real ephemeris data, are extremely limited, but have been investigated to some extent using the VARITOP low-thrust optimisation tool developed at the NASA Jet Propulsion Laboratory [Sauer, 1976]. Sauer has investigated Venus rendezvous trajectories for a characteristic acceleration of 1.0 mm s^{-2} for two different departure opportunities, one of which was the departure date optimal trajectory in the year 1981. Details of the method used for generating the initial guess are unclear and appear to be the result of extensive trial and error and much experience. During this section, current knowledge is greatly expanded on what are the optimal departure date opportunities open to solar sails in the 2010-2020 time-frame, since there is very

limited work in the literature. This may be due to the fact that Venus is relatively close to the Earth, and so it seems superfluous to use solar sailing to get there when chemical propulsion can easily reach Venus in short trip times. However, due to the thick atmosphere and high surface gravity of Venus, the lander for a sample return mission will be very large, so solar sailing may offer some advantages in terms of increased payload mass fraction.

Firstly, as for Mars, the variation of Earth-Venus circle-to-circle coplanar trip time was investigated as a function of characteristic acceleration, with 50 control segments (51 nodes). Transfer times from 0.1 mm s^{-2} up to 1.0 mm s^{-2} are shown in Figure 3.14, where the curve appears to level off above 0.5 mm s^{-2} . Again, rounded steps in the curve indicate a complete number of heliocentric revolutions. For further analysis of roundtrip Earth-Venus trajectories, a characteristic acceleration of 0.2 mm s^{-2} was chosen with 2 revolutions, to minimise the sail size in the context of a Venus sample return mission, with the necessary large lander [McInnes *et al*, 2003b].

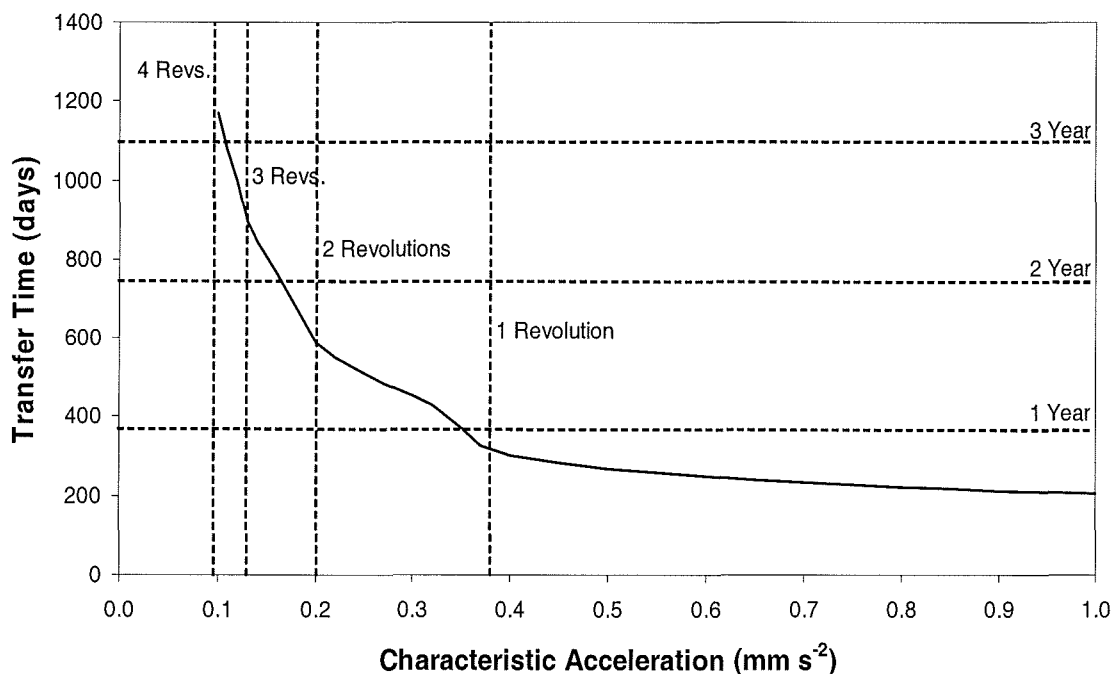


Figure 3.14: Circular coplanar trip-times from 1 AU to 0.723 AU, against characteristic acceleration

3.2.1 Earth–Venus Phase

Multiple departure date scans were executed from two different starting dates for the outbound characteristic acceleration of 0.2 mm s^{-2} , with departure date increments both backwards and forwards in time, as for the Mars departure date scanning. Similar features and problems were observed, as in sections 3.1.1 and 3.1.2. Similarly, the departure date scan was sampled to obtain the general trend curve shown in Figure 3.15. It can be seen that there are 6 minima in the range February 14, 2008 to September 20, 2017, which occur of order 584 days apart, corresponding to the Earth-Venus synodic period. These departure opportunities occur on September 1, 2009 (669 days), March 31, 2011 (677 days), November 4, 2012 (661 days), May 14, 2014 (688 days), January 11, 2016 (689 days), and September 2, 2017 (670 days). It should be noted, however, that these minima are not of the same trip time, due to the slight inclination and eccentricity of the Venesian orbit. The minima gradually rise over the epoch considered, and repeat approximately every 5 Venus synodic periods.

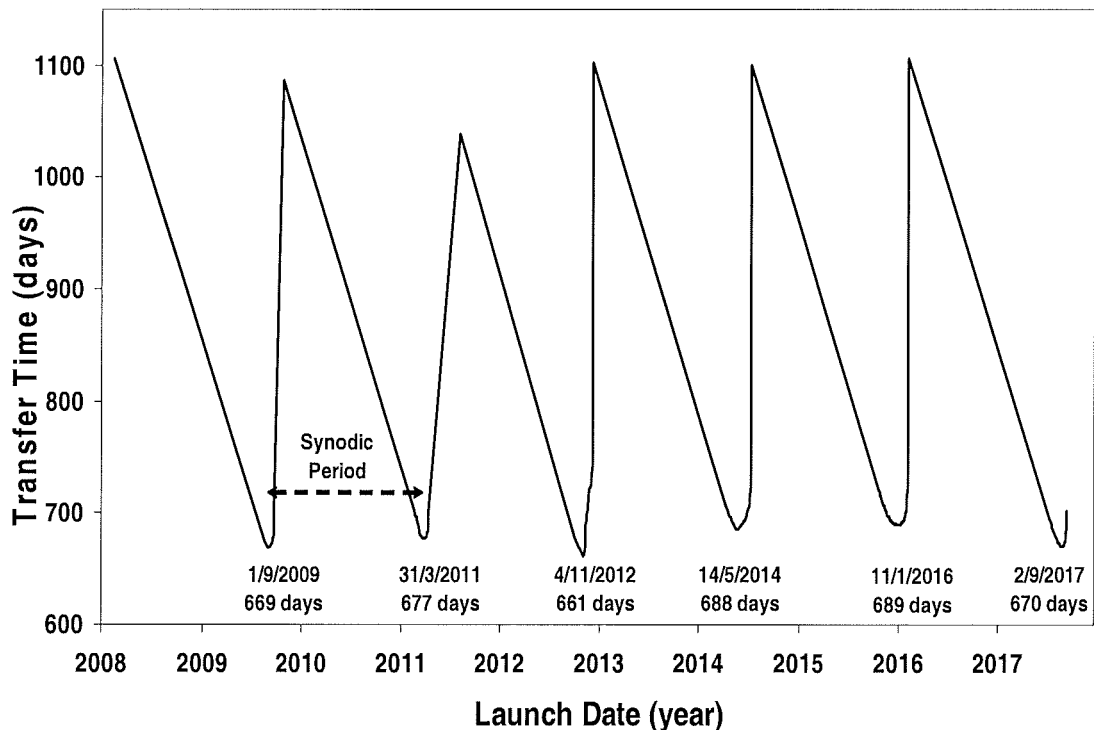


Figure 3.15: Earth–Venus departure date scan (0.2 mm s^{-2})

The first minimum time trajectory after January 1, 2010 (the desired departure epoch for an example mission) occurs when the spacecraft is launched on March 31, 2011, arriving at the Venusian sphere of influence 676 days (1.85 years) later on February 4, 2013. The trajectory is shown in Figure 3.16 with Venus arrival achieved after $2\frac{1}{4}$ heliocentric revolutions, 25.5° before aphelion. For comparison, a trip time maxima of 1038 days occurs if departure is postponed by 128 days to August 6, 2011. Figure 3.17 shows the sub-optimal-date trajectory, where it can be seen that an extra revolution around the Sun is required due to the spacecraft just missing Venus on its first pass. The spacecraft then has to wait for the next rendezvous opportunity by incorporating coast phases and an inner loop within Venus' orbit. This extra revolution, due to the unfavourable planetary alignment at departure, would again only incur a temporal penalty, since propellant mass is not an issue for a solar sail.

The 2011 opportunity departure date optimal trajectory is selected for the roundtrip mission definition in the first instance. It can be seen in Figure 3.18 that the cone and clock angle controls have a smooth form and an oscillatory nature. This is an indication that the trajectory is near-globally optimal. The cone angle varies by only 16° , from -44.9° to -28.6° , while the clock angle varies by 93° , from 23.1° to 115.7° and so no sub-optimal coast phases are present. The temporal evolution of the spacecraft's instantaneous orbital elements is shown in Figure 3.19. Semi-major axis reduction and inclination increase occurs continuously along the trajectory since the available thrust is low.

Temperature control is of particular importance closer to the Sun, and is of moderate significance in the Earth-Venus region. For the selected 2011 Earth-Venus trajectory, the variation of sail film temperature is shown in Figure 3.20 along with the heliocentric distance on the trajectory. The maximum film temperature is 306 K (33°C), at Venus arrival, well below the upper limit for polyimide films of order 520 K. The worst case sail film temperature in orbit at Venus is 324 K (zero cone angle and at perihelion).

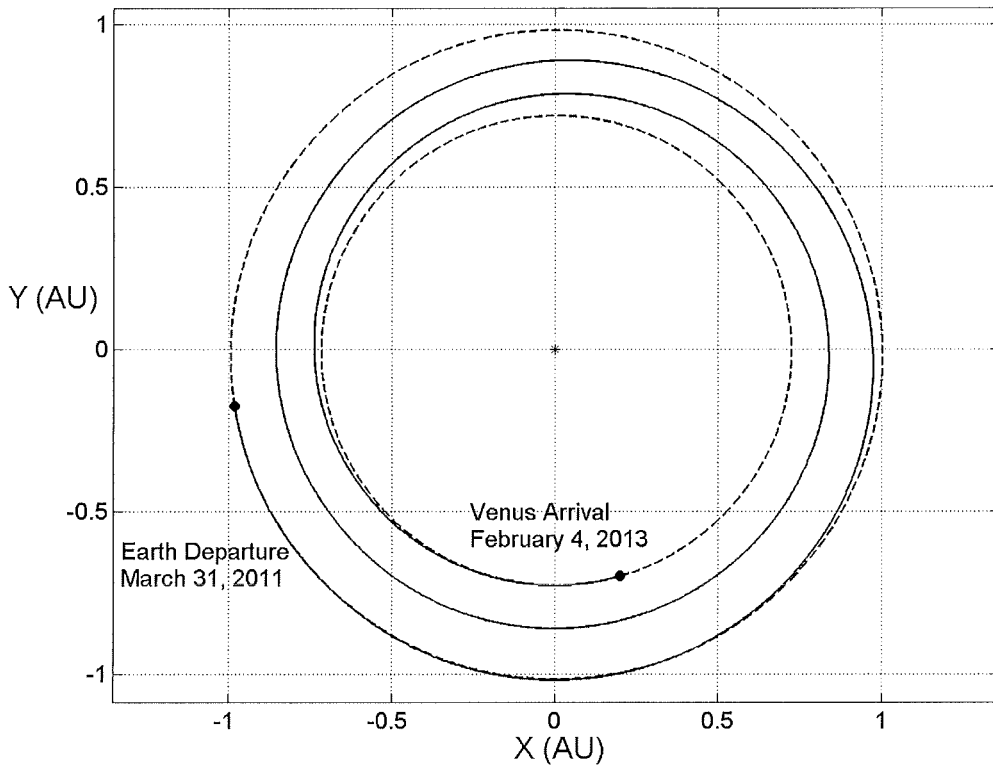


Figure 3.16: Departure date optimal Earth–Venus rendezvous (0.2 mm s^{-2})

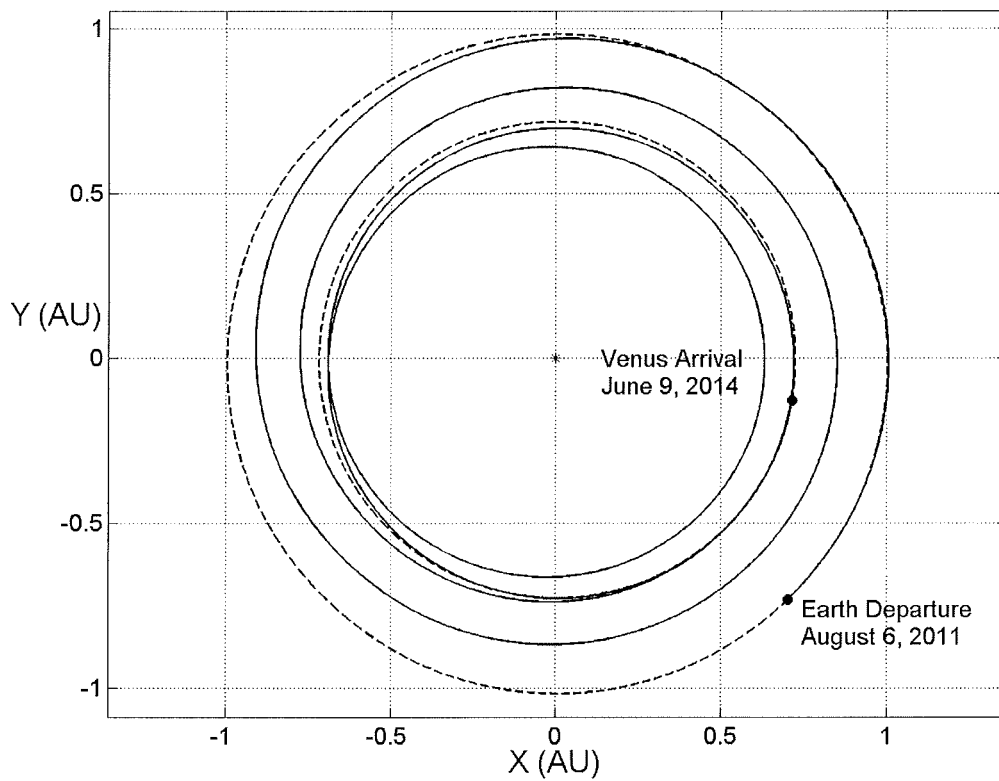


Figure 3.17: Sub-optimal departure date Earth–Venus rendezvous (0.2 mm s^{-2})

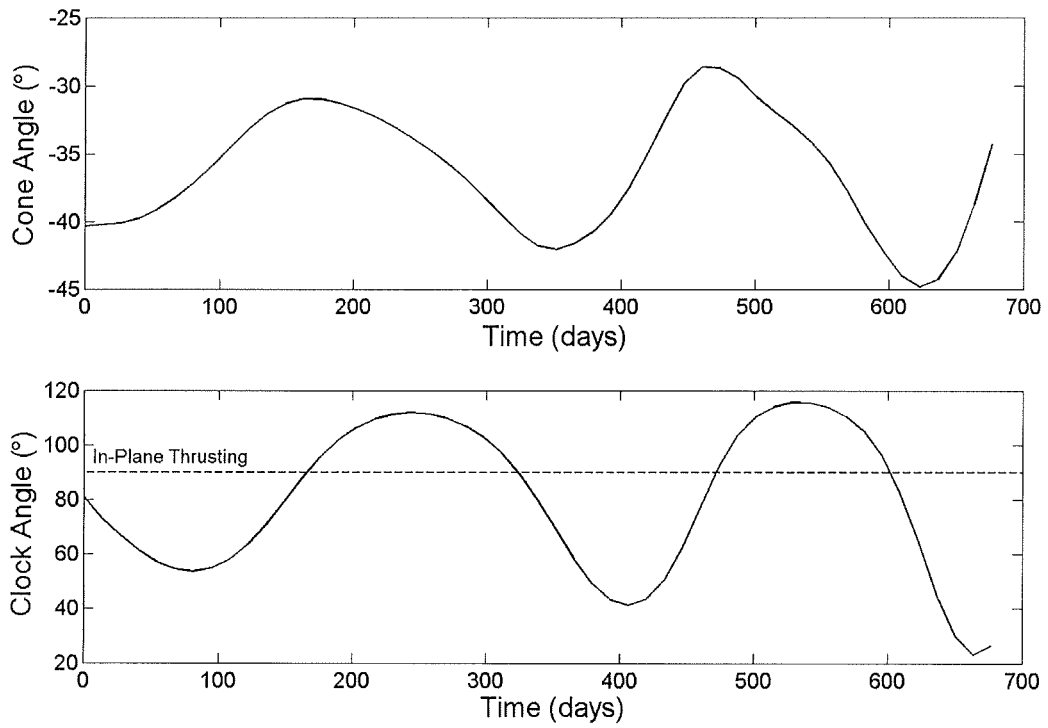


Figure 3.18: Earth-Venus rendezvous control profile

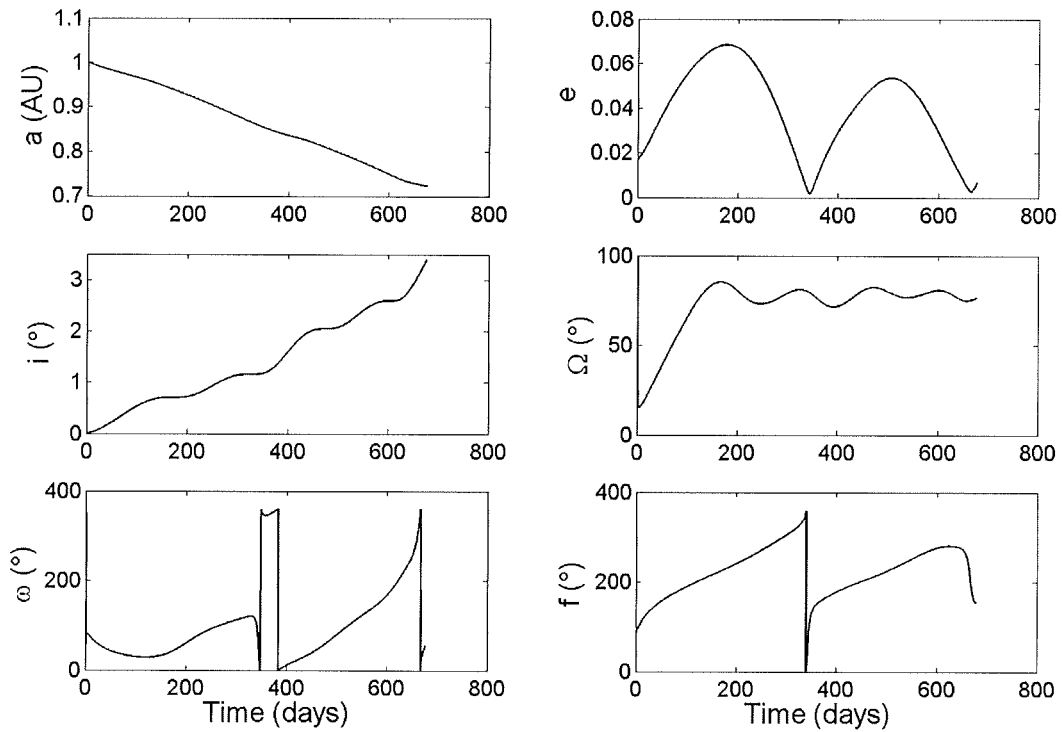


Figure 3.19: Earth-Venus rendezvous orbital element evolution

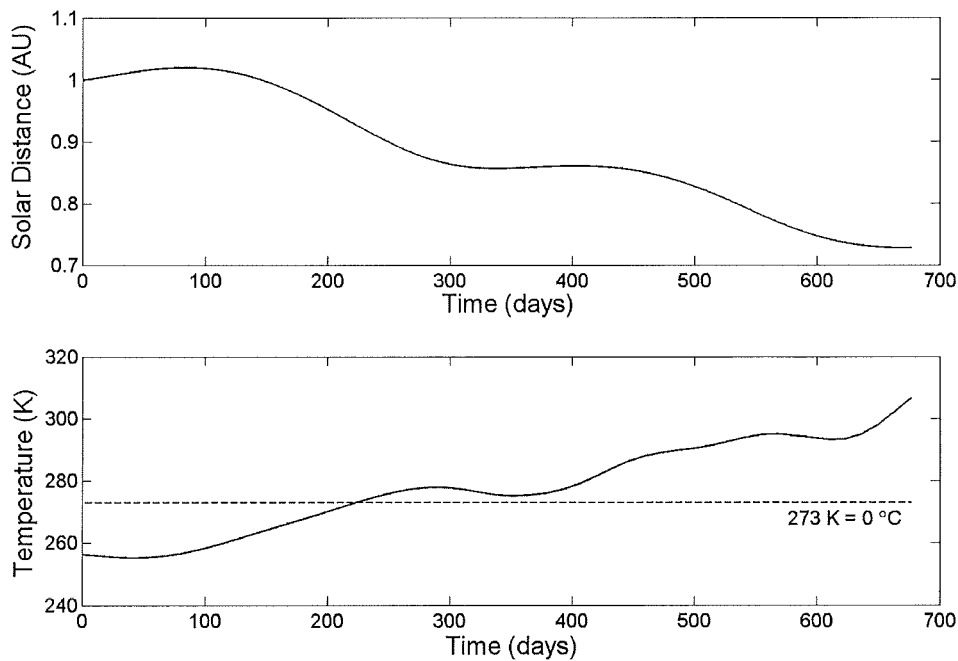


Figure 3.20: Earth–Venus heliocentric distance and sail film temperature

3.2.2 Venus – Earth Phase

Departure date scans were conducted forwards and backwards (for comparison) in time to identify a return opportunity and any sub-optimal penalty that may be necessary. This return departure date scan is shown in Figure 3.21 for the return characteristic acceleration of 0.48 mm s^{-2} . The acceleration has increased due to the jettison of the sizeable lander at Venus [McInnes *et al*, 2003b]. For a fixed lander stay-time, together with planet centred spiralling, the initial Venus sphere of influence departure date was August 13, 2014 in McInnes *et al* [2003b]. This is not a departure date optimal departure date and lies nearer to a maximum than a minimum, at 521 days. Payload constraints may mean it may not be possible to allow for any in-orbit science operations, so waiting in the parking orbit for the minimum trip time departure opportunity is rather pointless and would unnecessarily prolong the total mission duration. Therefore, it may be possible to perform a trade-off by selecting a sub-optimal Earth departure date in order that the Venus departure date might become more optimal, ultimately so that the overall mission duration is minimised. The approach taken here is similar to the procedure employed for a small body sample return mission [Sauer, 1976], but the range of the departure date scans is much broader.

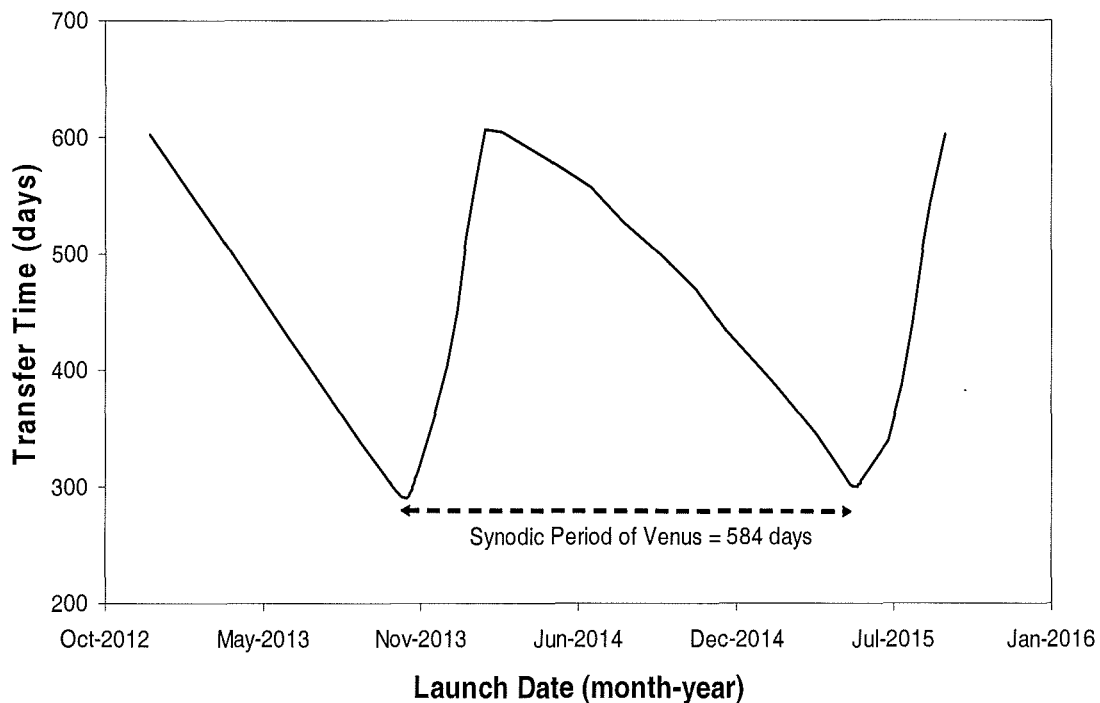


Figure 3.21: Venus–Earth departure date scan (0.48 mm s^{-2})

The Earth-Venus departure date scan, in the region of the 2011 minimum, was expressed as a function of Venus sphere of influence arrival date and plotted on the same axes as the Venus-Earth trip time as a function of Venus sphere of influence departure date. It was then possible to use the extent of the Venus capture, sample acquisition, and escape duration, taken from McInnes *et al* [2003b], to combine pairs of points on these curves that can be mapped together to obtain the total round-trip mission duration as a function of Earth departure date. This was accomplished by adding the Venus-centred time to the Venus arrival date and matching up the resulting date with Venus departure dates on the Venus-Earth departure date scan. This can be performed automatically with an interpolation algorithm. In order to obtain a match, the resolution of each departure date scan had to be comparably fine, accomplished by linear interpolation. Figure 3.22 shows the intermediate step of mapping pairs of points from the two scans, and the departure range over which the Earth departure date can be optimised. Figure 3.23 shows the effect of combining the pairs of points into the total mission duration as a function of Earth departure date.

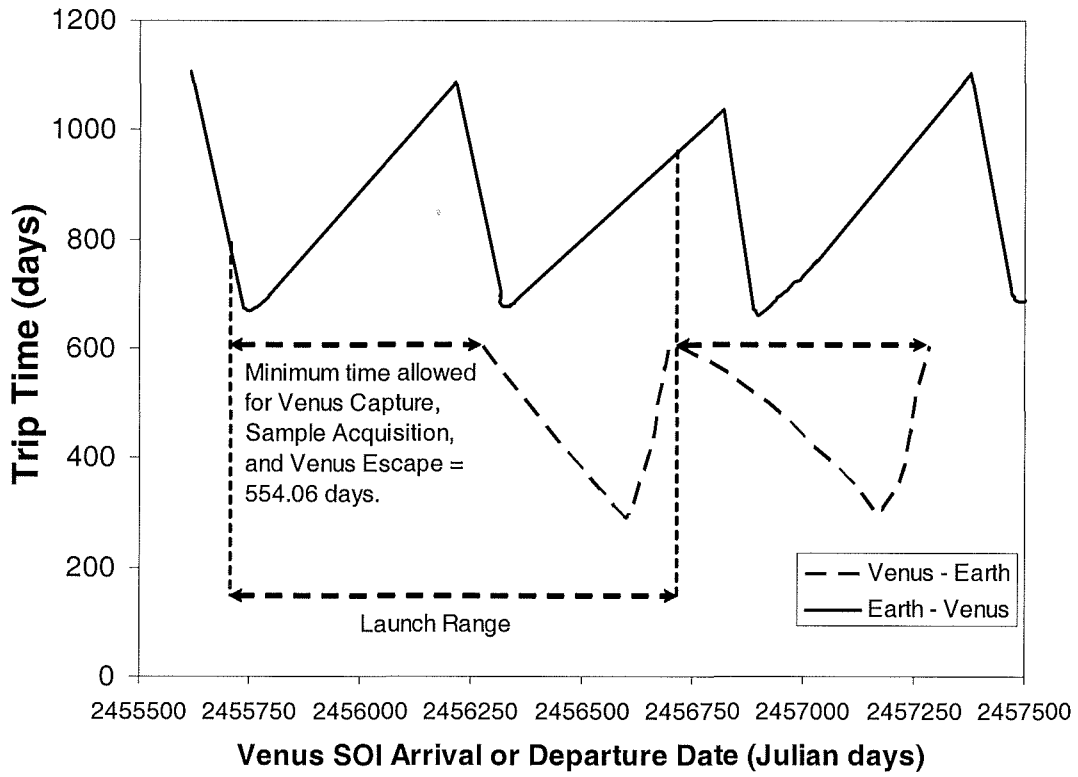


Figure 3.22: Venus Sample Return departure date mapping

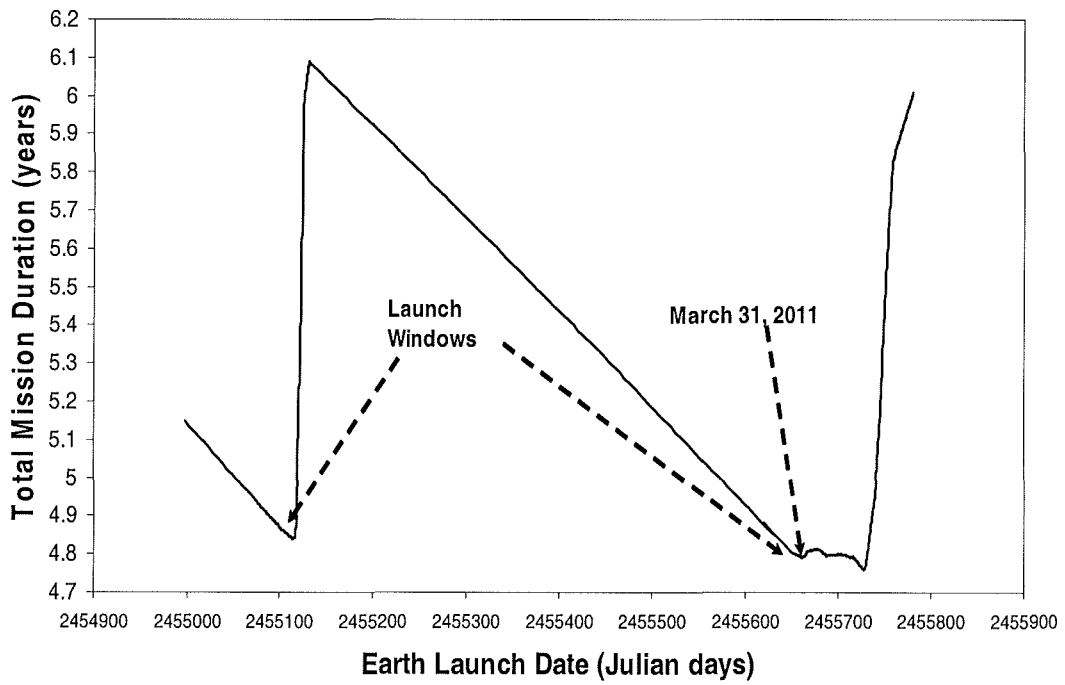


Figure 3.23: Total mission duration dependence on Earth departure date

It can be seen that there are two launch windows in the region of interest with a minimum mission duration launch window in 2011. It is noted that the optimal departure date for the Earth-Venus phase of March 31, 2011, detailed in Section 3.2.1, also lies at the beginning of a total trip time launch window, even though the return Venus-Earth phase is sub-optimal with respect to Venus departure date. This suggests that the total mission duration is affected more strongly by the outbound trip time, since these times are longer, because of the lower sail acceleration, and so make up a larger fraction of the total mission duration. Therefore, the Earth departure date will remain in this case as March 31, 2011. By setting an upper limit on the mission duration of 5 years, it can be seen that there are two windows, the first starting August 9, 2009 which is 65 days (2 months) long and the second (which is selected for example), starting January 13, 2011 which is 166 days (5.5 months) long, as can be seen in Figure 3.23.

The optimal solution for Venus departure on August 13, 2014 was for a trip-time of 521 days (as stated previously), arriving back at the Earth's sphere of influence on January 17, 2016, after just over two revolutions about the Sun. Again, since the lander and ascent vehicle have been discarded, the solar sail characteristic acceleration for the Earth return trajectory has increased from 0.2 mm s^{-2} , to 0.48 mm s^{-2} , resulting in a relatively fast return spiral. The resulting optimum trajectory is shown in Figure 3.24. It can be seen from Figure 3.25 that the sail cone and clock angle profiles are irregular because of the departure date sub-optimality. The trajectory is still considered to be time-optimal, but the sub-optimal Venus departure date means that the solar sail would just miss the Earth for a uniform outward spiral (reverse of Figure 3.16), and has to spiral inside the orbit of Venus during the first revolution. This portion of the trajectory has an increased orbital velocity, and so has the effect of allowing the solar sail to 'catch-up' with the Earth. The optimisation algorithm must enforce these unfavourable boundary conditions, and so has chosen a cone angle profile that strays away from the optimal 35° value, but is optimal overall. Small irregularities in the control profiles are an artefact of the numerical algorithm only, and reflect the fact that the trip-time is relatively insensitive to small fluctuations in the control angles (although this becomes more significant closer to the Sun). The cone angle varies by 169.7° , from -87.7° to -82.0° . The clock angle varies by 179.7° , from 0.2° to 179.9° . Figure 3.26 shows

the temporal evolution of the instantaneous orbital elements along the trajectory. The maximum reduction of inclination occurs between 100 and 200 days where the solar flux is higher, due to the inner loop closer to the Sun (see distance variation in Figure 3.27) inside the orbit of Venus. Semi-major axis boost then predominates for the remainder of the trajectory. The heliocentric distance variation as a function elapsed time is shown in Figure 3.27, along with the corresponding variation of the sail film temperature with distance and cone angle. The temperature profile is again slightly irregular because of fluctuations in the sail orientation. The maximum sail temperature is again well below the upper limit (of order 520 K) at 341 K (68 °C), 161 days into the trajectory.

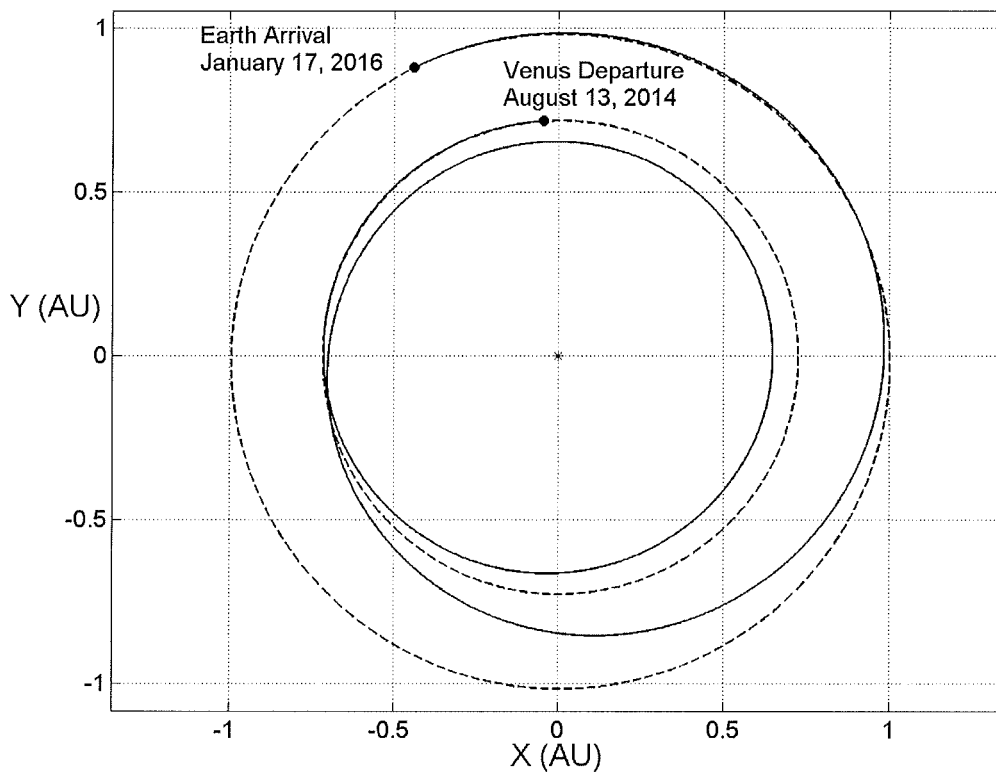


Figure 3.24: Venus – Earth rendezvous trajectory (0.48 mm s^{-2})

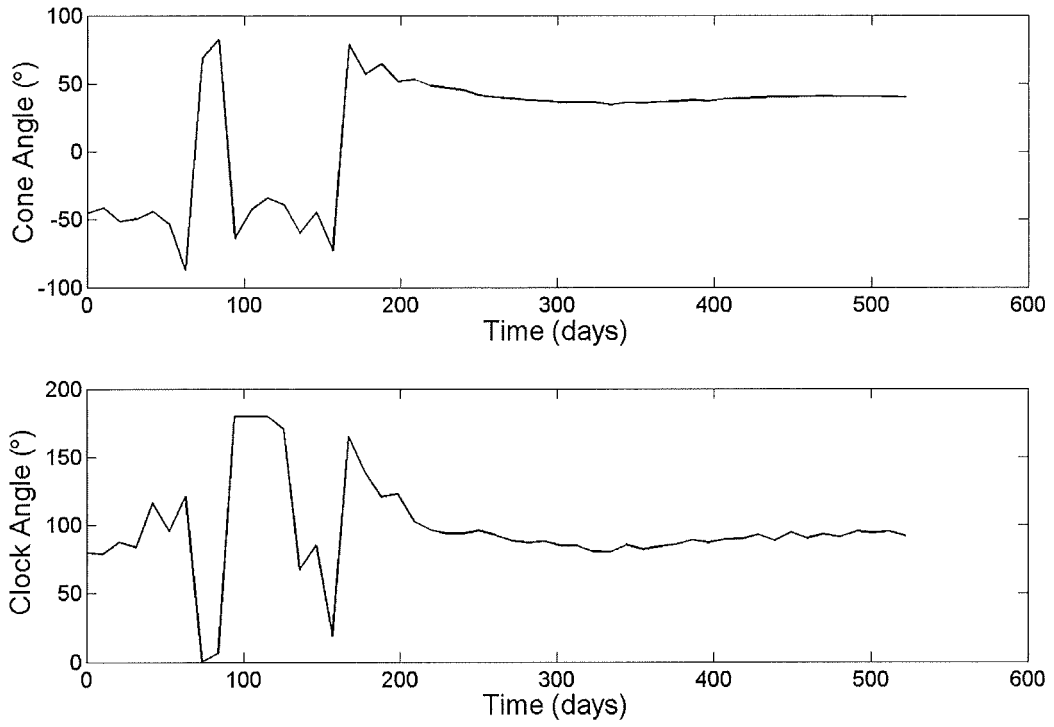


Figure 3.25: Venus – Earth rendezvous control profile

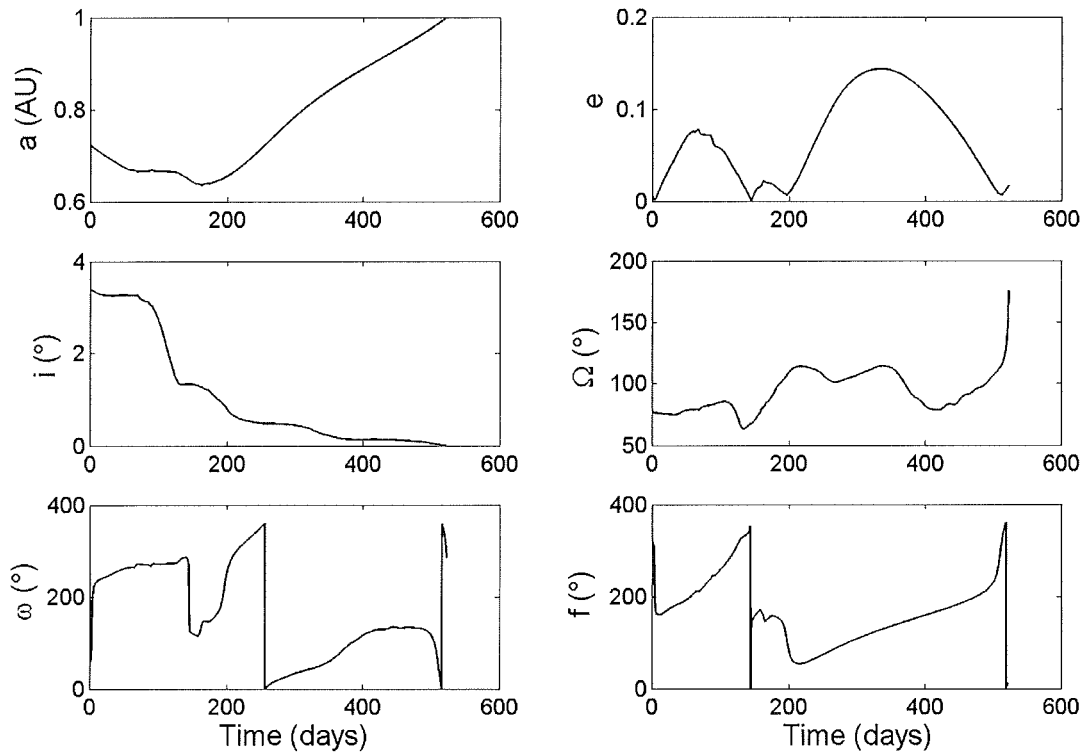


Figure 3.26: Venus – Earth rendezvous orbital element evolution

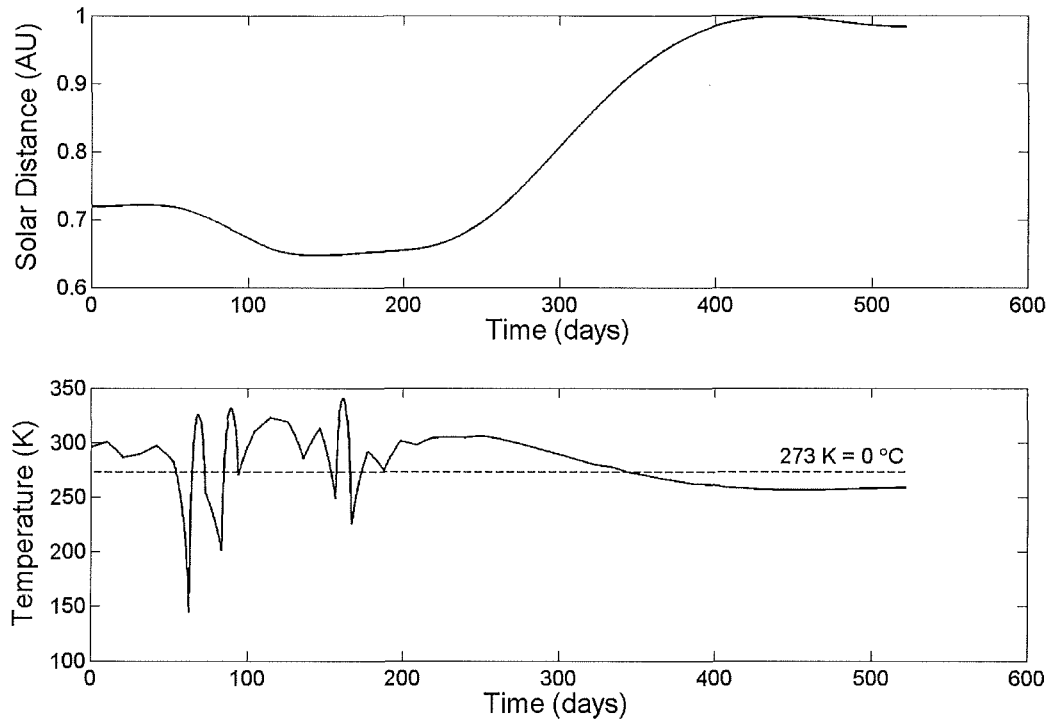


Figure 3.27: Venus – Earth heliocentric distance and sail film temperature

3.3 Mercury Trajectories

From a trajectory standpoint, it has long been acknowledged that Mercury represents the most difficult terrestrial planet to reach. The Δv required for a direct ballistic transfer from Earth parking orbit to a low Mercury parking orbit is of order 13 km s^{-1} [McInnes *et al*, 2003]. Mercury's location deep within the solar gravity well means that it is only feasible to reach the planet using chemical propulsion, via a long and complex sequence of gravity assists to reduce propellant mass requirements [Yen, 1985]. The higher specific impulse exhibited by Solar Electric Propulsion (SEP) can reduce the number of gravity assists needed and reduce propellant requirements, and hence launch mass, but the mission duration and launch mass is still sizeable. The ESA cornerstone BepiColombo mission will use SEP combined with 2 Venus and 2 Mercury gravity assists to reduce propellant requirements, but nevertheless a dual Soyuz-Fregat split-launch in 2009 is envisaged, with Mercury arrival after 3.5 years [Anselmi and Scoon, 2001, Scoon *et al*, 2000]. NASA has launched a smaller ballistic mission to Mercury, MESSENGER, aboard a Delta II 7925H in 2004, which also employs 2 Venus and 2 Mercury gravity assists,

reaching Mercury after 5 years [Santo *et al*, 2001]. It should be stressed that these missions are orbiter/lander missions, and not sample returns. The return to Earth of a sample from Mercury, deep within the solar gravity well, is one of the most energetically demanding solar system mission concepts imaginable. However, solar sail propulsion is extremely well suited to this class of mission, since propellant mass is not an issue, and the solar radiation pressure at Mercury is greatly enhanced over that at 1 AU.

The potential of solar electric and solar sail propulsion has long been acknowledged as a viable means of reaching Mercury due to the inverse square relationship between thrust and radial distance from the Sun. An overwhelming proportion of the low-thrust optimisation literature concentrates on using SEP [Kluever and Abu-Saymeh, 1998, Tahan and Guelman, 2000, Vasile and Bernelli-Zazzera, 2001, Kemble, 2001], although a large volume of trajectory data does exist for Mercury transfers using solar sail propulsion, since many authors have recognised the benefits for this target [Sauer, 1976, French and Wright, 1986, Leipold *et al*, 1995, Rauwolf and Friedlander, 1999, Colasurdo and Casalino, 2001, Hughes and McInnes, 2002a]. The most comprehensive trajectory data in the open literature has been published by Sauer, and by Leipold, which includes rendezvous trajectories [Sauer, 1976, Leipold, 2000]. However, this thesis provides new data sets by considering both launch windows, and return trajectories.

As for Mars and Venus, the variation of Earth-Mercury, 1 AU to 0.387 AU, coplanar trip time was investigated as a function of characteristic acceleration, now with 50 control segments (51 nodes). Optimisations were also conducted with up to 200 segments, but there was negligible penalty in using a lower resolution parameterisation, despite the rapidly varying nature of the control profiles. Transfer times from 0.1 mm s^{-2} up to 1.0 mm s^{-2} are shown in Figure 3.28, where the curve appears to level off at about 0.6 mm s^{-2} . The points where there is an integer number of revolutions have been labelled, where it is clear that multiple revolutions are required. There is no clear break-point here, and for further analysis of roundtrip Earth-Mercury trajectories, a characteristic acceleration of 0.25 mm s^{-2} was chosen, to minimise sail size whilst maintaining a reasonable mission duration, in the context of a sample return mission [McInnes *et al*, 2003c].

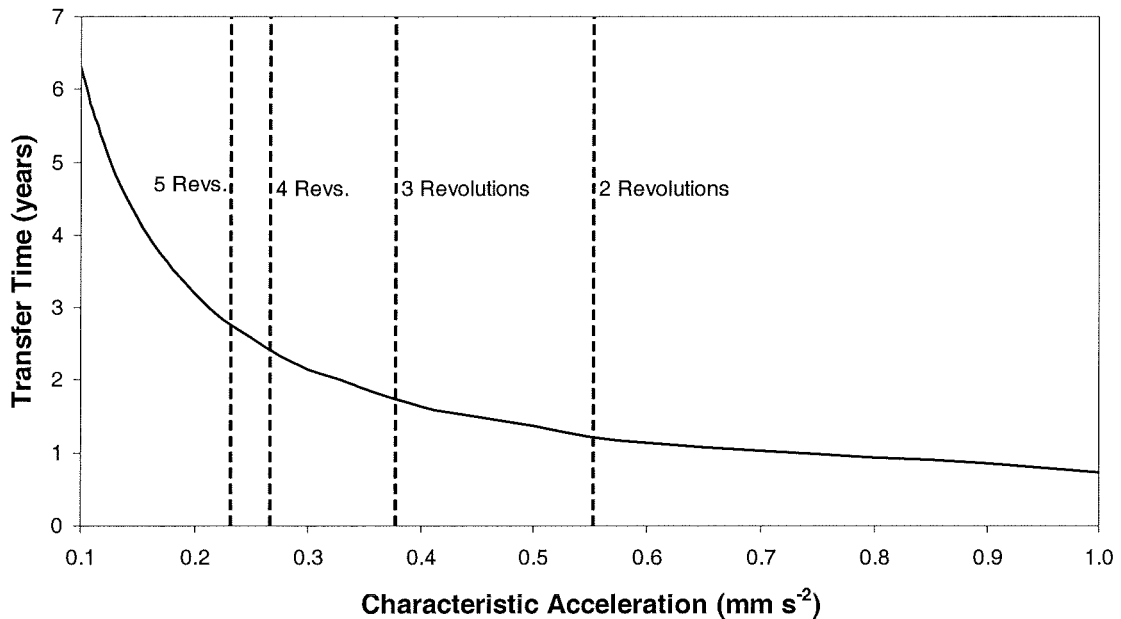


Figure 3.28: Circular coplanar trip-times from 1 AU to 0.387 AU, against characteristic acceleration

3.3.1 Departure Date Scans

Formulating an initial guess for Mercury trajectories with solar sails exhibiting low characteristic acceleration is a vastly more complex task than for Mars or Venus. This is because the low target semi-major axis leads to a large number of heliocentric revolutions being required, in addition to matching the quite significant target body eccentricity. Mercury's inclination of 7° also means that a non-intuitive initial estimate of the out-of-plane thrusting component is required, so that the spacecraft and target state vectors are comparable. Due to the large number of heliocentric revolutions required, the optimal control profiles were discovered to be oscillatory in form, with the 'frequency' determined by the number of heliocentric revolutions. When one of these solutions was used as the initial guess for different departure dates, the control profile could be 'out-of-phase', or the trajectory may need an extra revolution.

Extensive trial-and-error analysis has been conducted by using constant-plane, patched logarithmic spirals and circular coplanar solutions to find a feasible guess. Adjustment of the departure date was also conducted to ensure the estimated control profile produced a spacecraft end-point state vector that was close enough to

the target end-point state vector in the visualised trajectory, so that NPSOL could then converge. The Genetic Algorithm, as used occasionally for Mars and Venus trajectories, was ineffective in generating direct, low-acceleration initial guesses, since the number of revolutions dictated that the control profiles have a rapid fluctuation. The nature of Genetic Algorithms means that only a small number of control nodes can be used, to keep computation time reasonable, which cannot accurately represent the actual control profile required. The departure date scanning process was the same as that used for Mars and Venus, with the departure date increment adjusted accordingly.

3.3.2 Earth–Mercury Phase

Multiple departure date scans were executed from different starting dates for the selected outbound characteristic acceleration of 0.25 mm s^{-2} , with departure date increments both backwards and forwards in time. Some departure date scans tended towards local optimality due the starting guesses being locally optimal and the subsequent amplification of these non-optimal errors. In the course of this process it was observed that independently initiated departure date scans often tended to overlap one another, and it could clearly be seen that certain slopes were composed of trajectories that were more optimal than others. Departure date scans that were sub-optimal were discarded and scans giving lower trip times were assumed to be the new globally optimal trajectories. The range of the final departure date scan taken is somewhat narrower than for Mars or Venus trajectories, because of time-consuming problems with departure date propagation during certain launch epochs. The departure date scan was sampled to obtain the general trend curve shown in Figure 3.29, which although only across 3 years, clearly shows the sawtooth nature of the scan. It can be seen that there are 3 minima in the range May 12, 2012 to April 13, 2015, which occur approximately 355 days apart, corresponding to 4 Mercury orbits or 3 Earth-Mercury Synodic periods of just less than one Earth year. These launch opportunities occur on April 30, 2013 (1048 days), April 19, 2014 (1041 days), and April 10, 2015 (1036 days). It should be noted, however, that these minima are not of the same trip time, due to the inclination and eccentricity of the Hermian orbit. The minima gradually decrease over the epoch considered, but it is expected that the

minima will repeat over a seven-year cycle, when an approximate integer number of Mercury orbits (29) occur in 7 Earth years.

As an example, the first minimum-time trajectory in this launch epoch occurs when the spacecraft is launched on April 30, 2013, arriving at the Hermian sphere of influence 1048 days (2.87 years) later on March 14, 2016. The trajectory is shown in Figure 3.30 with Mercury arrival achieved after $5 \frac{1}{4}$ heliocentric revolutions, 64.6° after aphelion. It is thought that post aphelion arrivals at Mercury are characteristic of Earth-Mercury spirals, due to Mercury's orbital eccentricity. The smooth and oscillatory control profiles are shown in Figure 3.31. The cone angle varies by 31.5° , from -48.1° to -16.6° , while the clock angle varies by 105.5° , from 65.3° to 170.8° .

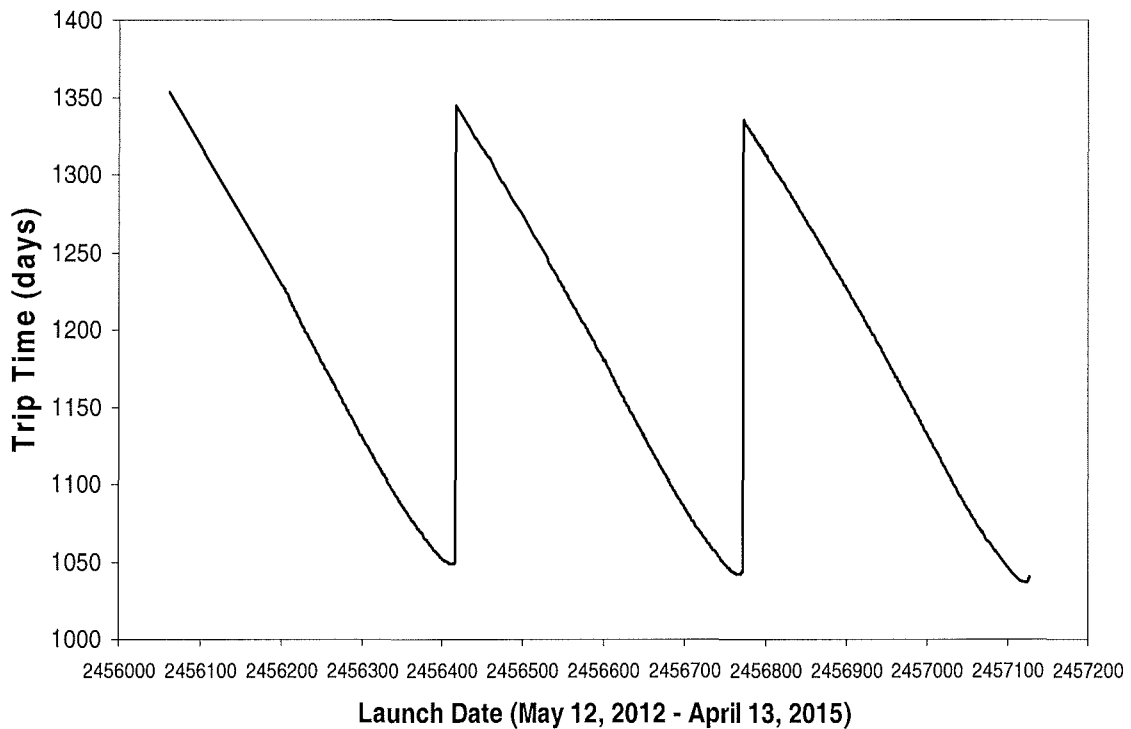


Figure 3.29: Earth-Mercury departure date scan (0.25 mm s^{-2})

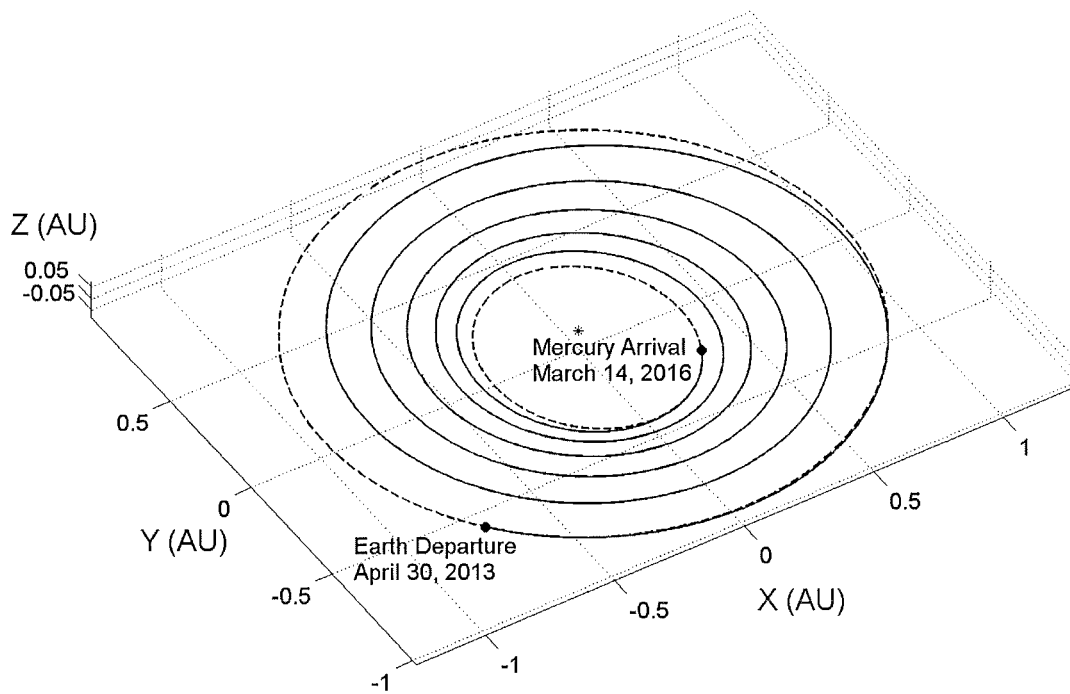


Figure 3.30: Example Earth–Mercury trajectory (2013 opportunity)

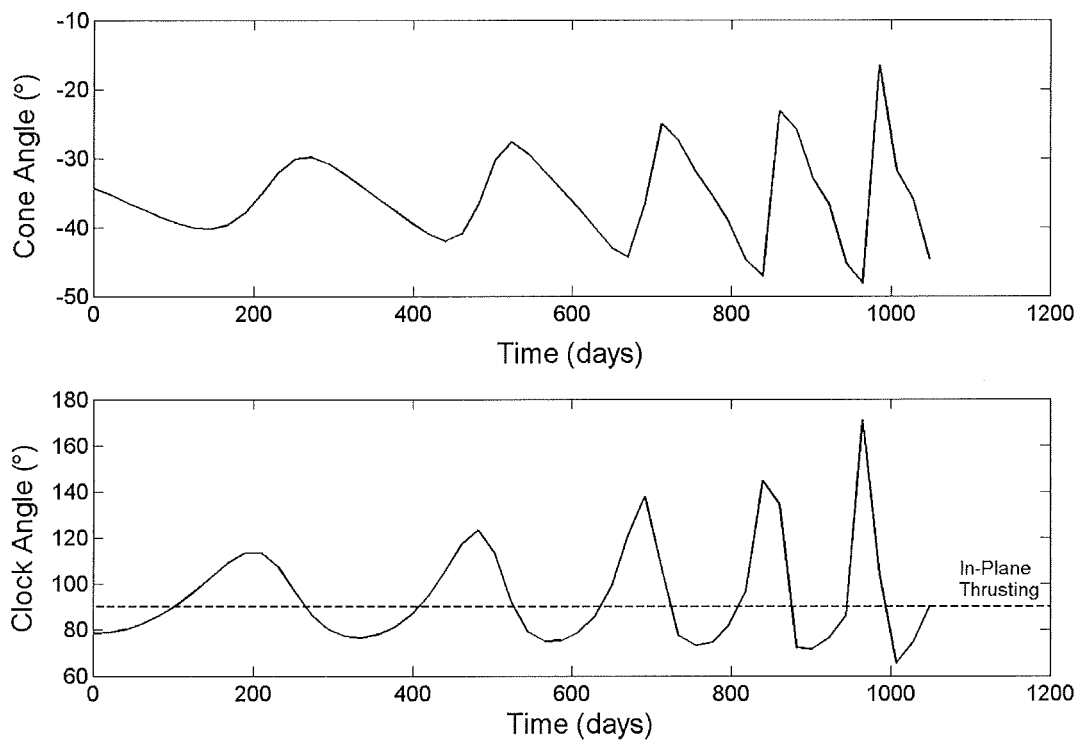


Figure 3.31: Earth–Mercury control profile (2013 opportunity)

3.3.3 Mercury–Earth Phase

The range of dates over which to conduct the return departure date scan was first identified. The capture and escape spiral durations, calculated by M. Macdonald for all arrival dates in the period of interest, were added to a prescribed stay-time initially set at 40 days to be conservative [McInnes *et al*, 2003c]. The earliest and latest Mercury sphere of influence departure dates were therefore obtained. The return departure date scan was then only required from June 3, 2016 to May 26, 2018. The return trajectories were calculated using a characteristic acceleration of 0.7839 mm s^{-2} , since the lander has been jettisoned [McInnes *et al*, 2003c]. A feasible initial starting guess was obtained through trial-and-error, somewhat beyond the region of interest, but the departure date scan was then conducted backwards to cover the required date range.

It is possible to map the Earth-Mercury and Mercury-Earth departure date scans, together with the corresponding capture and escape times to a circular parking orbit and stay-time, to obtain the total mission duration as a function of Earth departure date. This can be done via a similar method to that for Venus in Section 3.2. In this manner, optimal Earth departure date windows can be established, within the time-frame considered. These departure date windows are strongly influenced by the positions of the outbound spiral minima, since the outbound trip times are the longest component of the total mission duration, due to the lower outbound characteristic acceleration. The total trip time scan is shown in Figure 3.32, where it can be seen that the total departure date scan bears a strong resemblance to the Earth – Mercury scan. It can clearly be seen that the total minimum trip time windows correspond to the outbound trip time minima. However, in reality, the selected launch opportunity will be dictated by the Mercury parking orbit arrival thermal constraints, and the need to wait in a forced Sun-synchronous orbit for a feasible landing opportunity, again due to thermal constraints. These quite complex issues have been discussed in detail in McInnes *et al* [2003c].

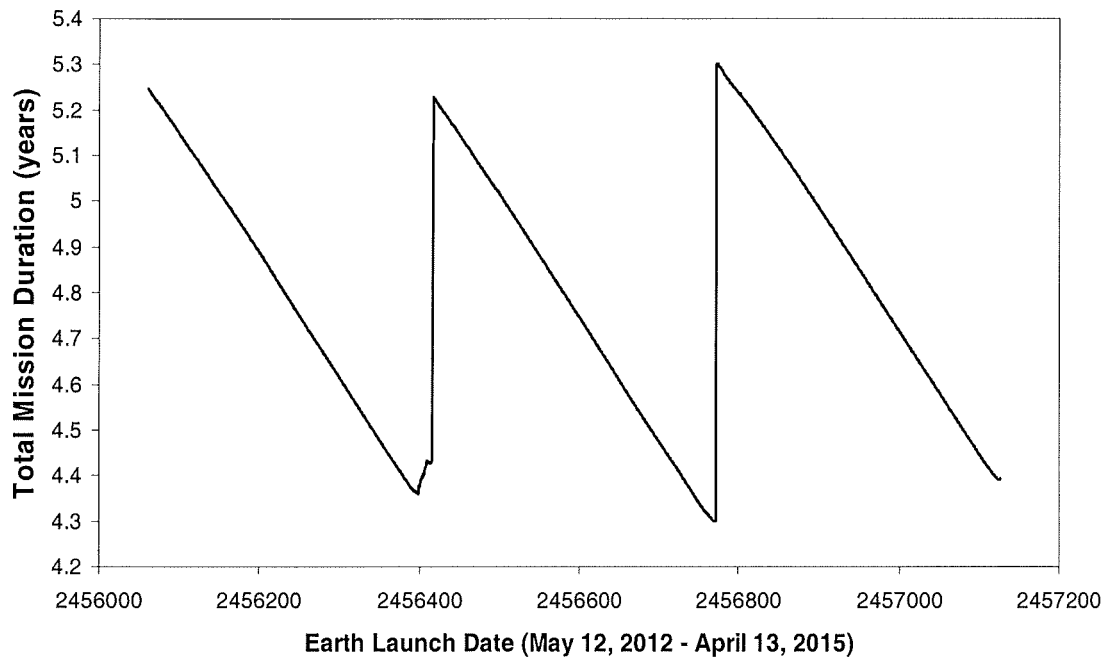


Figure 3.32: Total mission duration as a function of Earth departure date

3.3.4 Selected Optimal Earth – Mercury Trajectory

Constraints on arrival date at Mercury, due to thermal constraints on the lander dictate that the combined total mission duration departure date scan is perhaps not the best approach to take, as has been noted in McInnes *et al* [2003c]. Analysis of the arrival true anomaly at Mercury along with capture times has revealed that it would be necessary, for certain arrival dates, to wait in a forced Sun-synchronous orbit for a favourable planetary position to reduce thermal loads when lander descent commences [McInnes *et al*, 2003c]. At the outset though, the outbound trajectory departing on April 19, 2014 was selected (2014 opportunity), with a resulting Earth-Mercury spiral lasting 1041 days (2.85 years). Mercury sphere of influence arrival occurs on February 24, 2017 after $5 \frac{1}{4}$ heliocentric revolutions, 48.6° beyond aphelion, as shown below in Figure 3.33. In Figure 3.34 it can be seen that the control angle profiles are smooth (as smooth as possible when using 50 control segments with such rapid variation) and are oscillatory in form. The cone angle varies by 34.9° , from -53.9° to -19.0° , while the clock angle varies by 95.1° , from 59.4° to 154.5° .

The temporal evolution of the instantaneous orbital elements of the spacecraft is shown in Figure 3.35, where it can be seen that the maximum rate of change of orbital inclination occurs during the latter portion of the trajectory, where the solar radiation pressure is greatly increased. Figure 3.36 shows the variation of heliocentric distance together with the variation of the sail film equilibrium temperature with time. The sail film temperature has again been modelled using a black-body analogy. With the sail using an aluminium front coating of 85% reflectivity and zero emissivity, and chromium back coating of 64% emissivity, the maximum sail film temperature reached is 443.7 K (170.7 °C). This is still below the predicted upper limit for such thin films of 520 K. The maximum possible sail film temperature using this model, would be when the sail is facing the Sun (zero cone angle) at Mercury perihelion (0.3075 AU). The film temperature in that case would still be less than the upper constraint at 494.5 K, although constraints may have to be imposed on the sail cone angle close to perihelion to provide a suitable margin on the sail film temperature.

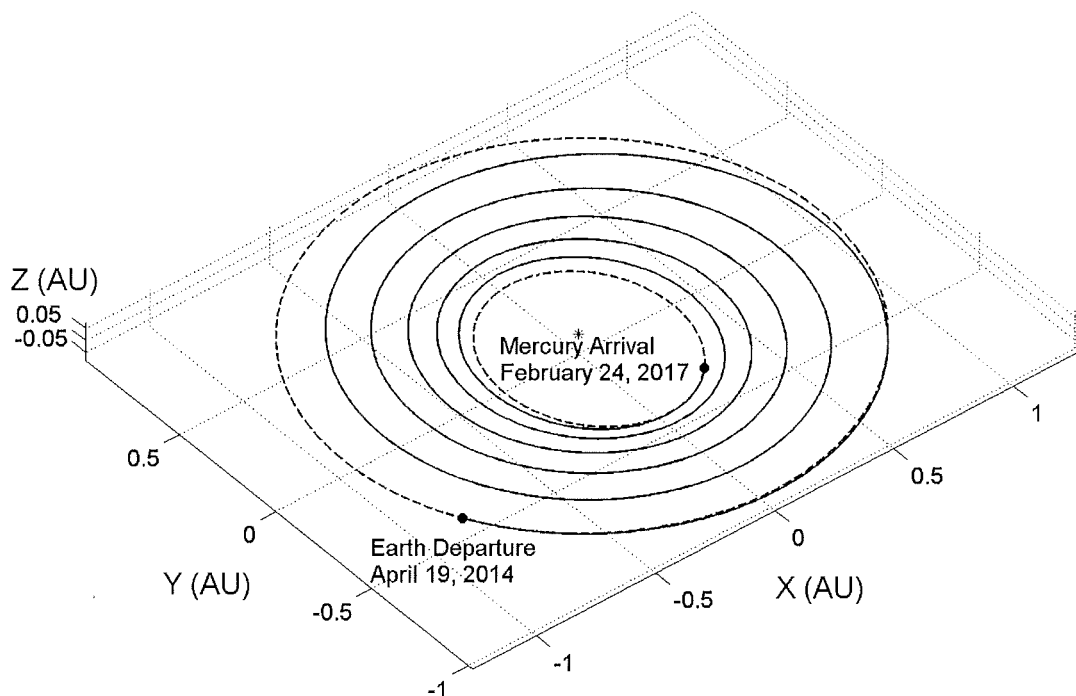


Figure 3.33: Selected 2014 opportunity 0.25 mm s^{-2} Earth–Mercury trajectory

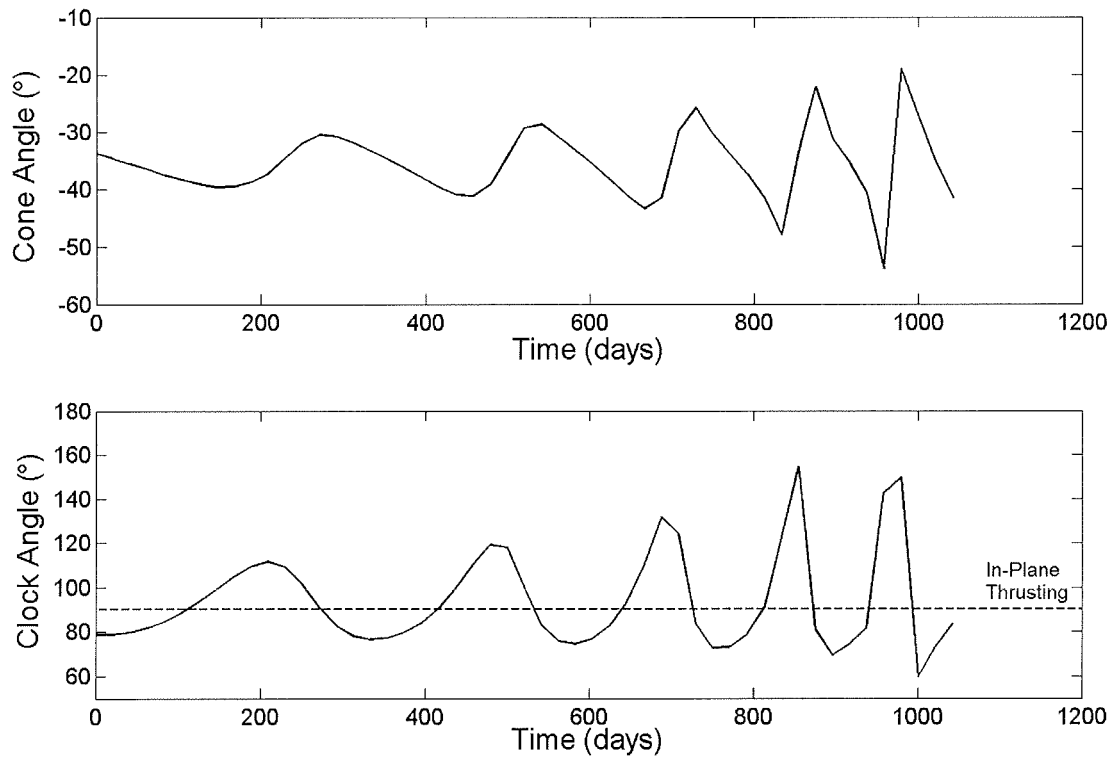


Figure 3.34: Selected 2014 opportunity Earth–Mercury control profiles

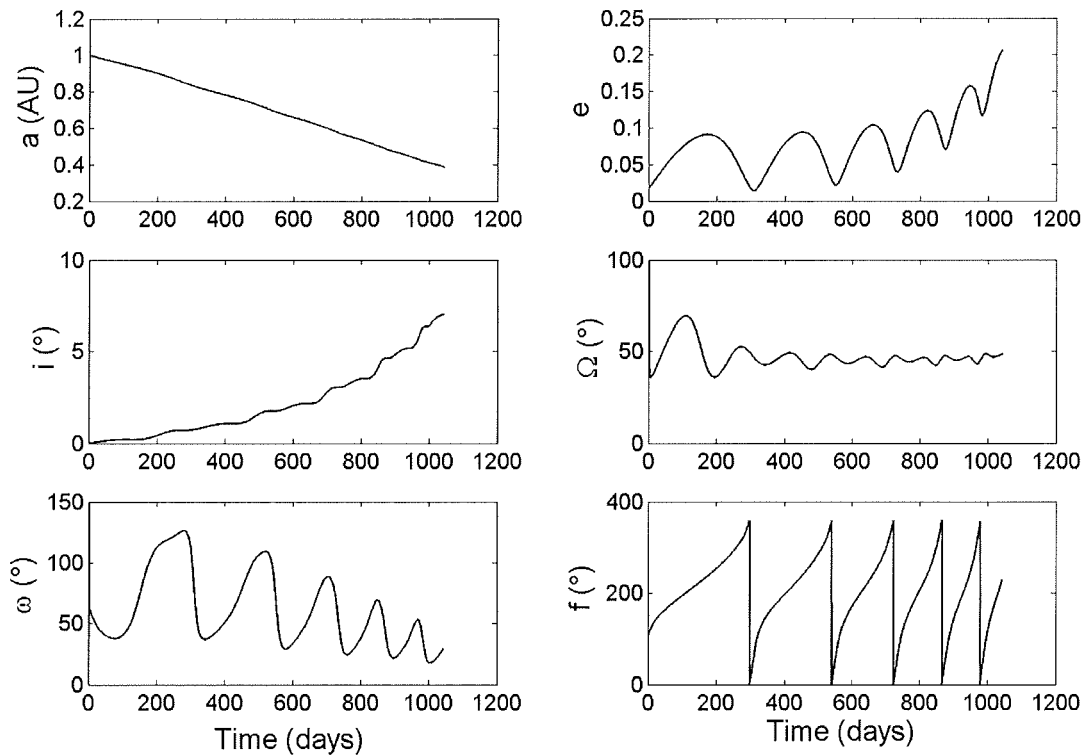


Figure 3.35: Earth – Mercury orbital element evolution

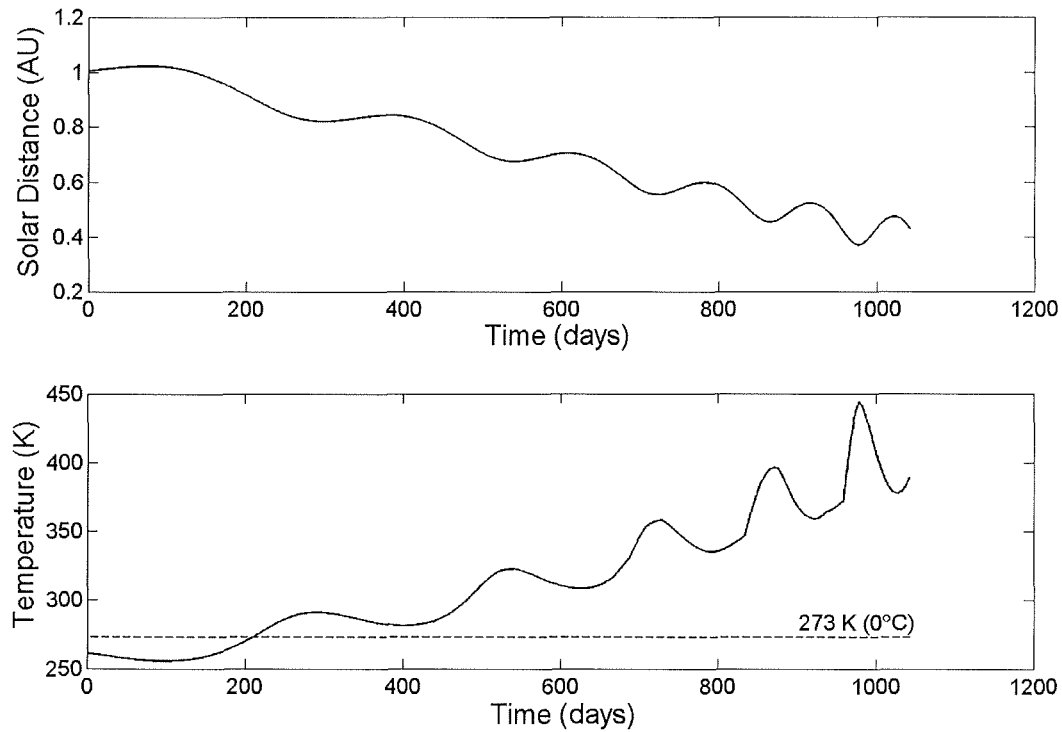


Figure 3.36: Earth – Mercury heliocentric distance and sail film temperature

3.3.5 Selected Optimal Mercury – Earth Trajectory

After Mercury capture, sample acquisition and escape, the specific escape date from the Mercury sphere of influence when heliocentric spiralling commences, is September 3, 2017 [McInnes *et al*, 2003c]. A short time-scale departure date scan about this point is shown in Figure 3.37, with the Mercury – Earth trip time shown against offset from the selected departure date. It can be seen that the selected departure date lies 30 days before the minimum in the return trip time. However, the trip-time penalty is relatively small and so the Mercury – Earth trip time is 369 days (1.01 years), arriving back at the Earth on September 8, 2018. The trajectory executes almost 2 revolutions about the Sun, with Mercury departure 69.2° prior to perihelion. This is not the most optimal point to depart Mercury’s orbit, but the constraints from the planet-centred phase of the mission dictate such a departure point [McInnes *et al*, 2003c]. The return trajectory is shown in Figure 3.38. In Figure 3.39 it can be seen that the control angle profiles are not entirely smooth since the trajectory is not departure date optimal, but the oscillatory nature is evident. The cone angle varies by 51.5° , from 35.4° to 86.9° , and briefly approaches 90° because

some coasting is necessary so that the sail can wait for a favourable alignment for Earth rendezvous, again because of some departure date sub-optimality. The clock angle varies by 144.8° , from 35.2° to 180° . The maximum out-of-plane thrusting occurs in the first 20 days, to reduce the orbital inclination when enhanced solar radiation pressure is available.

The temporal evolution of the instantaneous orbital elements of the solar sail are shown in Figure 3.40, where it can be seen that the maximum rate of change of orbital inclination occurs during the initial phase of the trajectory, where the solar radiation pressure is greatly increased. Figure 3.41 shows the variation of heliocentric distance together with the variation of the equilibrium sail film temperature with time. Minimum degradation of the sail reflectivity and emissivity has been assumed with the front reflectivity remaining at 0.85 and zero emissivity. The back emissivity is also 0.64, as previously assumed. The maximum sail film temperature reached is 453.8 K (180.8°C). This is again below the predicted upper limit for thin films, of order 520 K.

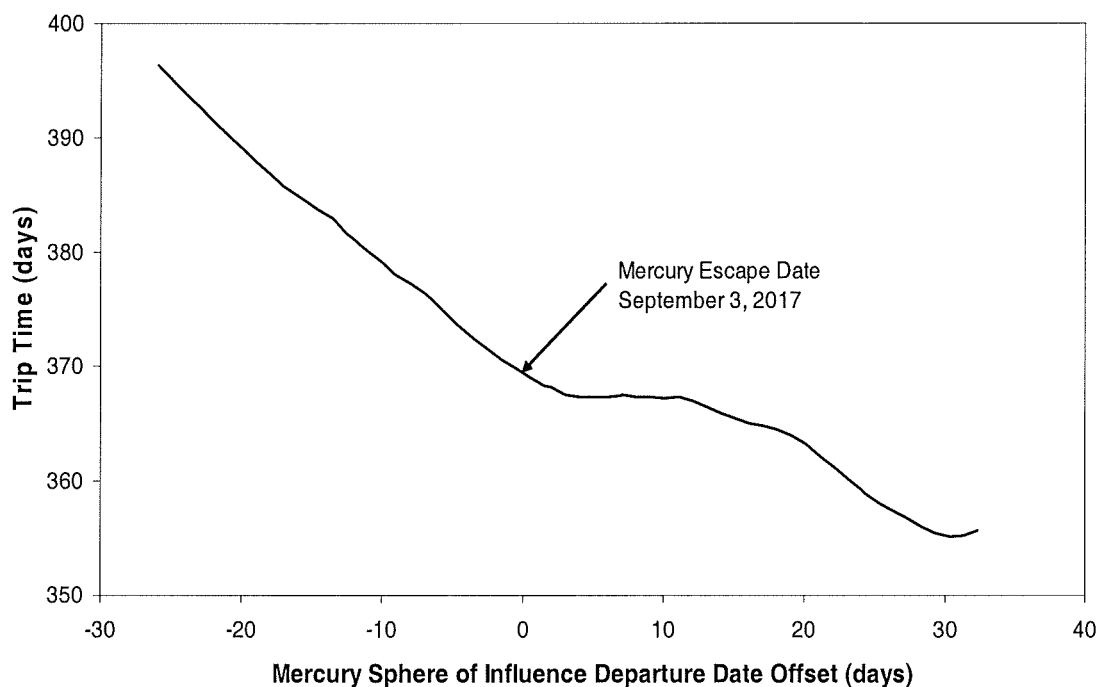


Figure 3.37: Mercury – Earth trip time variation about selected departure date

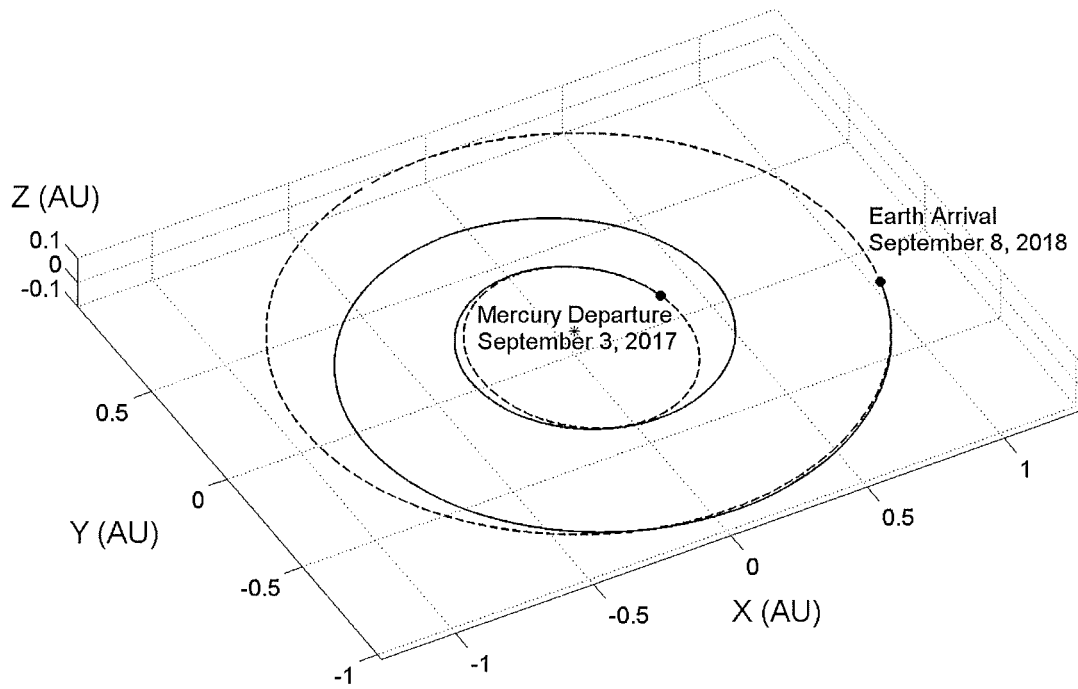


Figure 3.38: 0.7839 mm s^{-2} Mercury – Earth return trajectory

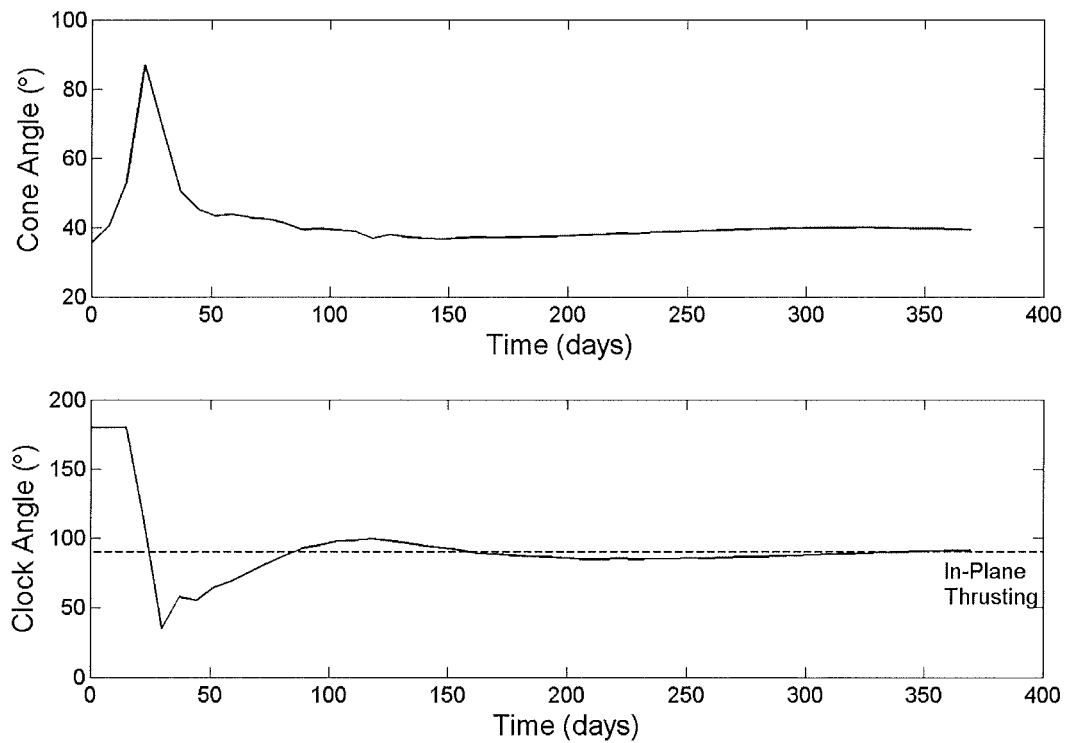


Figure 3.39: Mercury – Earth control profile

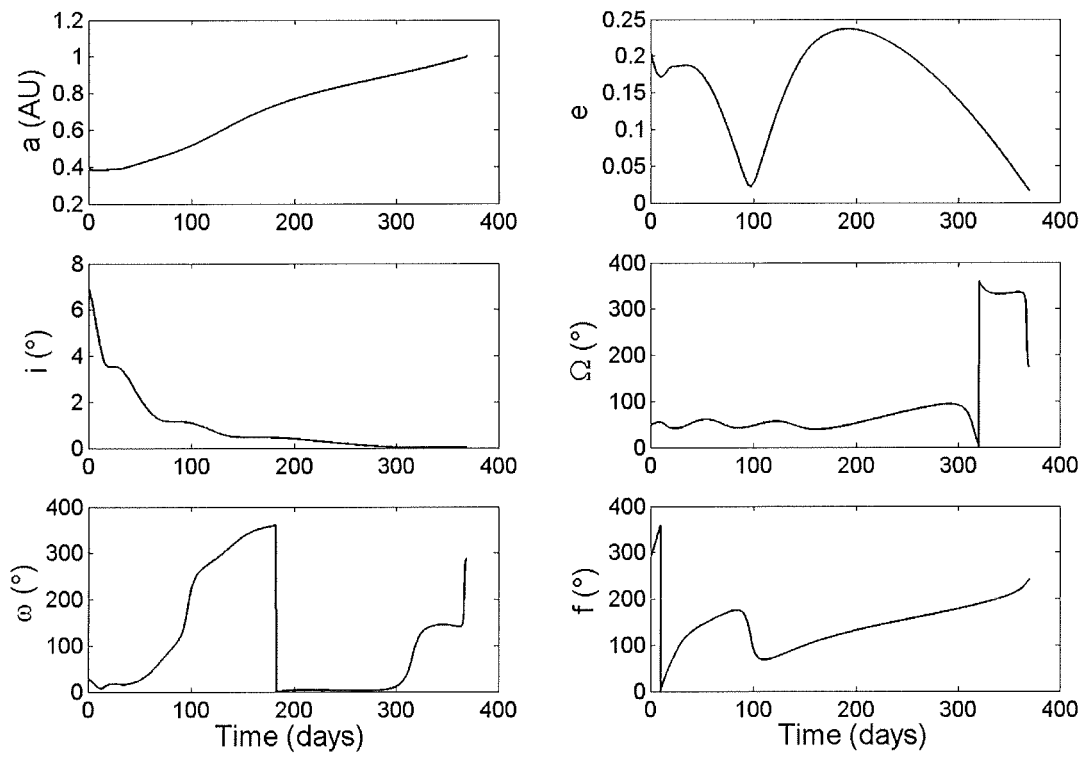


Figure 3.40: Mercury – Earth orbital element evolution

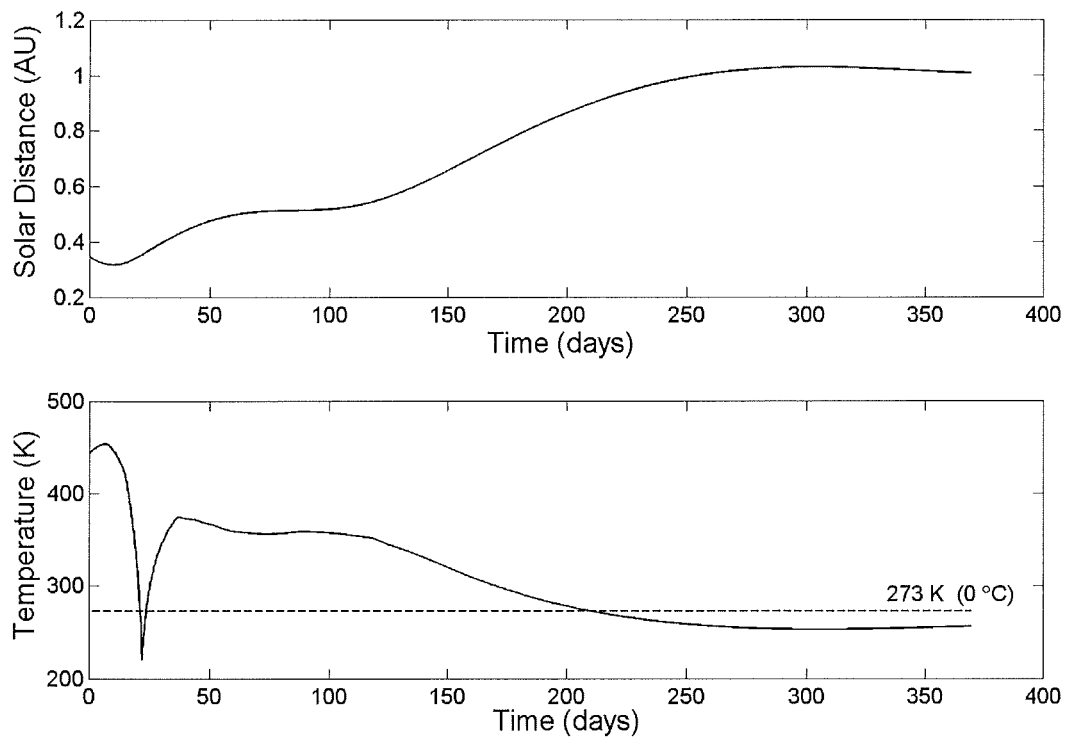


Figure 3.41: Mercury – Earth heliocentric distance and sail film temperature

3.3.6 Effect of Non-Zero C_3 at Earth Departure

The excess payload capacity available from a larger launch vehicle could be used to increase the excess departure energy at the Earth's sphere of influence, and so reduce trip time for a Mercury mission. In preliminary work, it was discovered that increasing the C_3 for outward spirals to near-circular orbits, such as to Mars, poses little benefit to trip time, as can be seen in Figure 3.42 (produced using the same method as for Mercury below). The effect is only slightly more pronounced at lower accelerations, since the trip times are longer. The small effect is because of the weak solar radiation pressure available at Mars distance, to circularise the high initial eccentricity delivered by the launch vehicle. Interestingly, increasing the launch excess further becomes even detrimental for the 0.25 mm s^{-2} curve, further suggesting that the low performance sail cannot remove the initial eccentricity without prolonging trip time. In addition, Mars and Venus are close enough to the Earth that increasing the C_3 for a solar sail trajectory seems unnecessary, since the C_3 when using chemical propulsion to Mars is fairly low, of order $10 \text{ km}^2 \text{ s}^{-2}$. However, excess launch energy would be of benefit for transfers to highly elliptical orbits such as that of Eros, which have perihelia close to the Earth [Leipold, 2000]. For inward spirals to Mercury, it has been found that significant advantages exist, due to the greatly enhanced solar radiation pressure available to reduce the initial orbit eccentricity delivered by the launch vehicle.

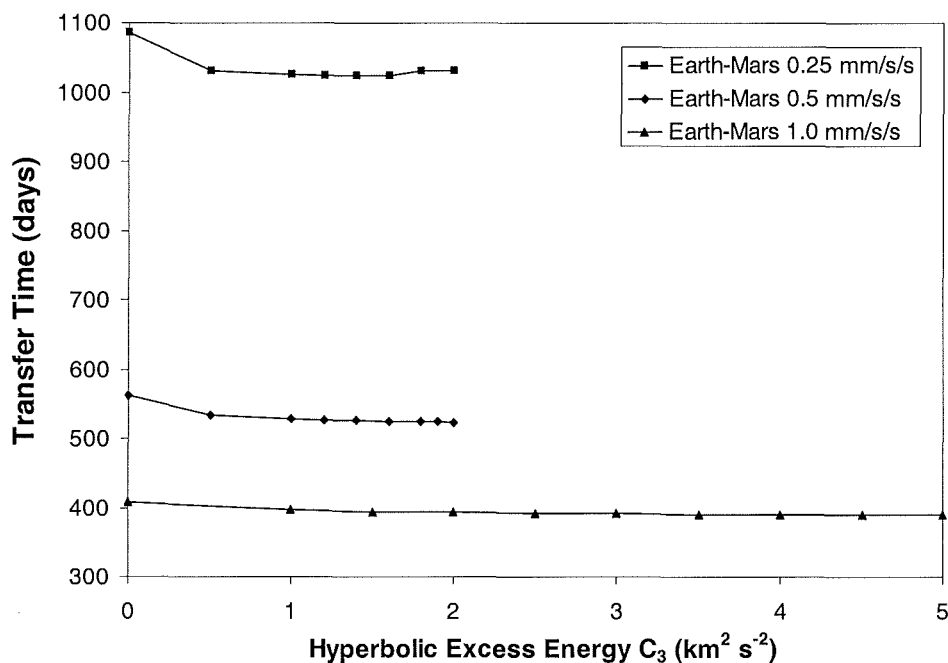


Figure 3.42: Effect of hyperbolic excess energy at launch for Earth-Mars transfers

To demonstrate these advantages, circular co-planar transfers to 0.387 AU were considered with open final azimuth. The positive C_3 supplied by the launch vehicle was tangential to the Earth's orbital velocity, with zero declination. Because an inward spiral is considered, the excess velocity was applied in the opposite direction to the Earth's orbital velocity, to reduce the orbital angular momentum, thereby lowering the perihelion. To define an upper limit on the excess velocity, the orbital elements of a Mercury-crossing initial orbit are defined by an aphelion, $r_a = 1$ AU, perihelion, $r_p = 0.387$ AU, inclination, $i = 0$, argument of perihelion, $\omega = \pi$, right ascension of ascending node, $\Omega = 0$, and initial true anomaly = π . Therefore, the resulting semi-major axis to reach a Mercury crossing orbit directly is 0.6935 AU, with an eccentricity of 0.44196. When converted to a Cartesian state vector, this results in an initial heliocentric circular velocity of 22.25 km s^{-1} , meaning that the launch hyperbolic excess velocity opposite to the Earth's motion is 7.56 km s^{-1} , and so the launch C_3 is $56.78 \text{ km}^2 \text{ s}^{-2}$. This is rather high, and indeed is beyond the practical capacity of most existing launchers (with a Mercury lander payload), demonstrating the difficulty in reaching Mercury by purely ballistic means. The upper limit taken here will be that for an 0.5 mm s^{-2} solar sail with a maximum C_3 of $25 \text{ km}^2 \text{ s}^{-2}$ [Sauer, 1976].

The initial guesses used for optimisation purposes were for the $C_3=0$ circular co-planar transfers to Mercury already generated for characteristic accelerations of 0.5 and 0.25 mm s^{-2} . The launch excess energy was increased (opposite to Earth's orbital velocity) using an incremental feedback method. The results are shown in Figure 3.43, where it can be seen that there is a significant advantage in using launcher excess performance in reducing trip times to inner planets such as Mercury. The optimisation process became difficult beyond $19 \text{ km}^2 \text{ s}^{-2}$ for a characteristic acceleration of 0.25 mm s^{-2} and beyond $25 \text{ km}^2 \text{ s}^{-2}$ for 0.5 mm s^{-2} . The curves appear to level off, so that the optimal solution cannot be improved upon and so NPSOL could not converge. It is of interest to note that the curve levels off at a lower C_3 for 0.25 mm s^{-2} . Because of this lower characteristic acceleration, it is harder to damp out the large initial eccentricity with a lower performance solar sail. The effect of increasing the launch excess energy is greater for the lower acceleration due to the inherently longer trip times, but the upper limit on C_3 is lower because of the reduced damping ability. In McInnes *et al* [2003c], the total Mercury Sample Return mission

launch mass of 2353 kg allows for an excess launch energy of $8 \text{ km}^2 \text{ s}^{-2}$ on a Zenit 3-SL launch vehicle. When a hyperbolic excess of $8 \text{ km}^2 \text{ s}^{-2}$ is applied at launch, the trip time can potentially be reduced by up to 28 % over the zero hyperbolic excess trip time. The true ephemeris rendezvous with excess launch energy will of course be affected by departure date and planetary phasing and would require a new departure date scan, but the advantage is clear.

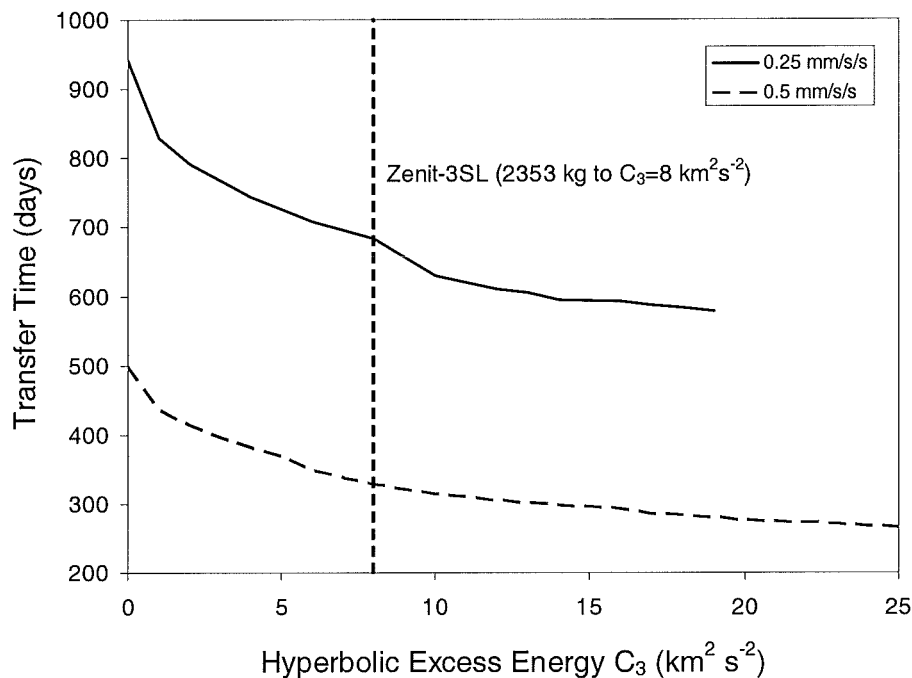


Figure 3.43: Effect of hyperbolic excess energy at launch (with 2353 kg Mercury sample return payload taken from McInnes *et al* [2003c])

3.3.7 Venus Gravity Assist

As was noted previously, gravity assists play an essential role in any chemical or SEP mission to Mercury. In many cases, multiple gravity assists are implemented to reduce propellant requirements at the expense of mission duration and launch window width. Gravity assists are not necessary when using solar sail propulsion, but could in principle lead to reductions in transfer times. To the author's knowledge, no other studies exist detailing the use of gravity assists with solar sail propulsion for optimised trajectories to Mercury. However, Koblik has used locally-optimal control laws with multiple gravity assists at the terrestrial planets, for reaching elliptical near-Sun orbits (0.167 AU) or solar impactor trajectories [Koblik,

2003]. In a simplified and idealised analysis, the use of a Venus gravity assist has been investigated for the simple case of a 2D circular, co-planar transfer from Earth orbit to Mercury orbit with open final azimuth angle. The gravity assist is modelled as an impulsive Δv in one plane only. The characteristic acceleration was assumed to be 0.25 mms^{-2} , consistent with the other analyses in this section.

To begin with, the transfer time for the direct transfer (without gravity assist) was obtained for comparison. The initial conditions correspond to Earth escape with $C_3=0$, while the final conditions are for open final azimuth, and a final circular orbit at 0.387 AU. The direct spiral transfer time was 942 days, as was shown in Figure 3.28. Next, an optimisation (using 51 nodes) was performed for a Venus flyby with the same initial conditions. The final conditions were constrained to be the Venus circular orbit radius of 0.723 AU. The actual azimuthal position of the planet was ignored for this simplified analysis, although it can be assumed that the flyby could be achieved by selecting the correct Earth departure date. The trip time to Venus flyby was found to be 496 days. A 2D gravity assist was then effected at Venus orbit using a simple patched conic approximation. The incoming Venus relative velocity can be written as Eq. 3.3, where \mathbf{v}_1 is the initial heliocentric velocity, and \mathbf{v}_p is the instantaneous velocity of Venus. Therefore, the relative velocity between spacecraft and planet is, $\Delta v = |\mathbf{v}_\infty^-|$. The rotation angle of the planet-centred hyperbolic asymptote is then given by Eq. 3.4, where r_{peri} is the radius of closest approach to Venus, and μ_p is the gravitational parameter of Venus.

$$\mathbf{v}_\infty^- = \mathbf{v}_1 - \mathbf{v}_p \quad [3.3]$$

$$\beta = 2 \sin^{-1} \left[\left(1 + \frac{\Delta v^2 r_{peri}}{\mu_p} \right)^{-1} \right] \quad [3.4]$$

In two dimensions, the rotation matrix from the incoming to the outgoing relative hyperbolic excess velocity is given by Eq. 3.5, which is then transformed to the modified heliocentric velocity using Eq. 3.6, where \mathbf{v}_2 is the final heliocentric velocity.

$$\mathbf{v}_\infty^+ = \begin{bmatrix} \cos \beta & -\sin \beta \\ \sin \beta & \cos \beta \end{bmatrix} \mathbf{v}_\infty^- \quad [3.5]$$

$$\mathbf{v}_2 = \mathbf{v}_p + \mathbf{v}_\infty^+ \quad [3.6]$$

A range of pericentre flyby altitudes were investigated, initially for 600 km, and the initial conditions for the post-Venus flyby to Mercury rendezvous phase were determined. The trajectory was then optimised using 51 control nodes. The two phases were then incorporated into a single function to optimise the flyby geometry and pericentre altitude. The total trip time was found to be 800 days with an optimal flyby altitude of 2292 km above the surface of Venus. This corresponded to a trip time saving of 142 days over the direct transfer, but of course launch windows would be severely compromised if planetary ephemerides were to be taken into account. The trajectory is shown in Figure 3.44, where the first-phase inward-spiral trajectory has been targeted to pass just inside the orbit of Venus. The planet removes some orbital energy from the spacecraft, so that the instantaneous eccentricity increases and the solar sail spiral becomes steeper, dropping into a lower orbit more quickly. The control angles are shown in Figure 3.45, and the temporal evolution of the instantaneous semi-major axis and eccentricity is shown in Figure 3.46. The step change in the orbital elements due to the impulsive gravity assist can clearly be seen in Figure 3.46.

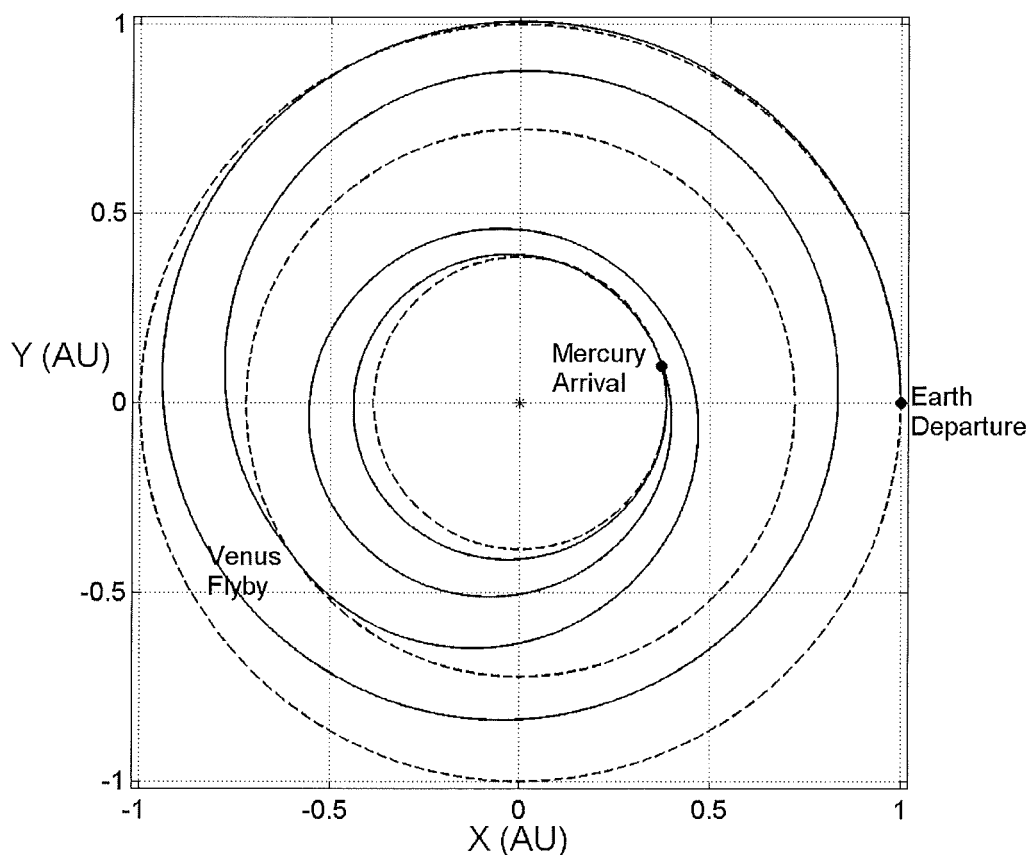


Figure 3.44: Earth-Mercury transfer with Venus gravity assist

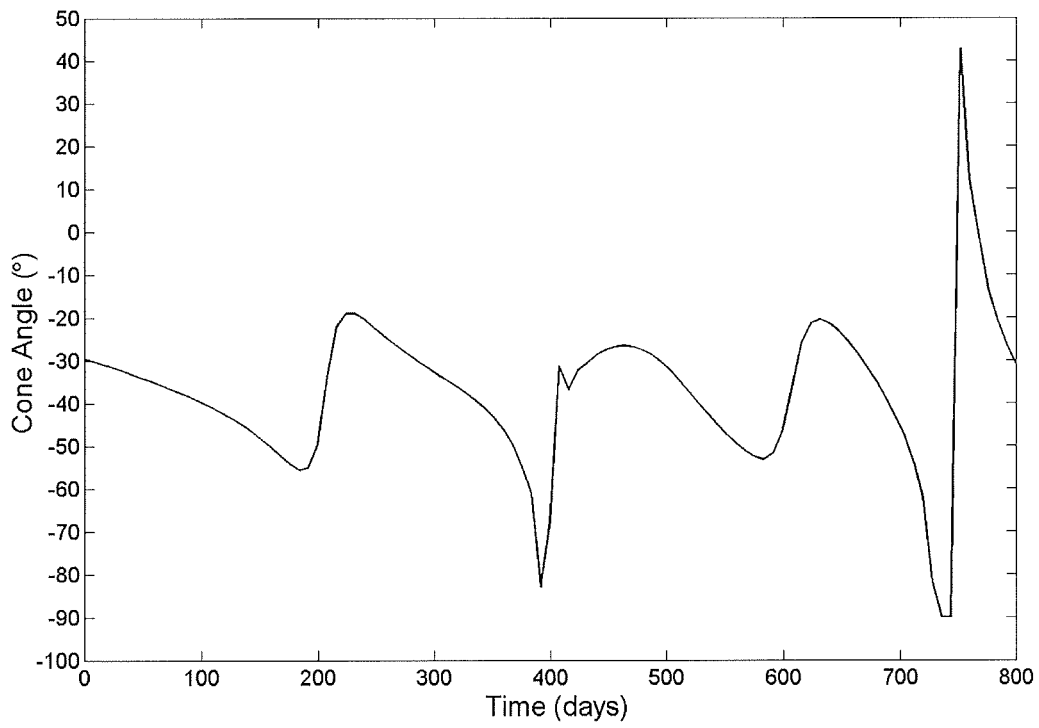


Figure 3.45: Venus gravity assist cone angle profile

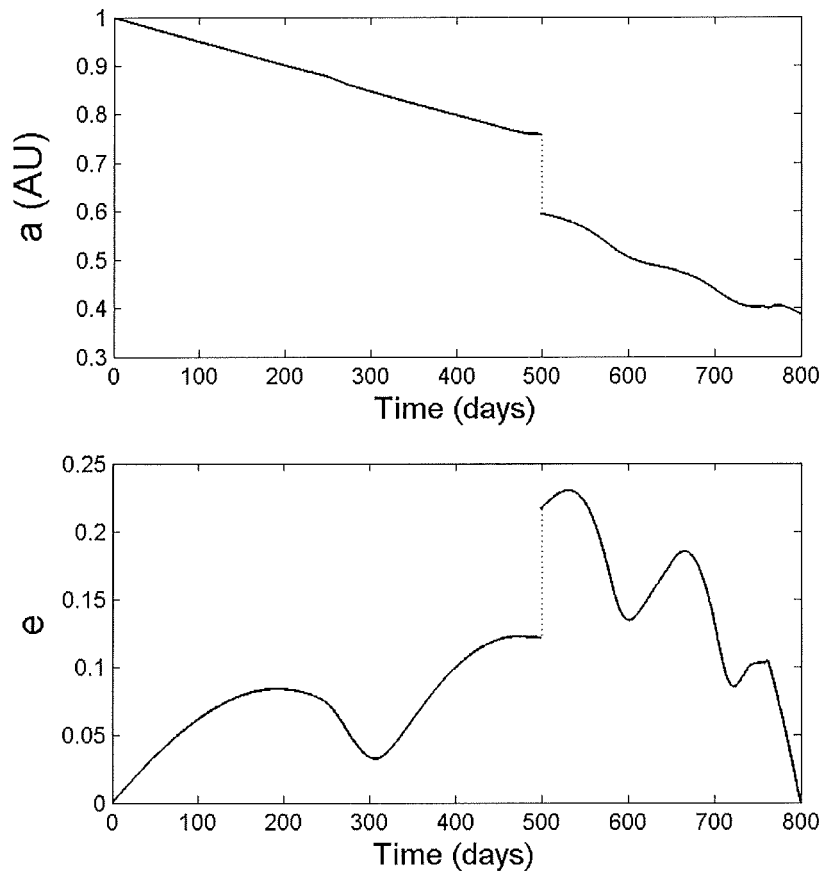


Figure 3.46: Time history of semi-major axis and eccentricity

3.4 Summary and Discussion

In this Chapter, outbound and return trajectories to the three other terrestrial planets, Mars, Venus and Mercury were analysed in some detail, and new data sets and extensive departure date scans were produced for the round-trip journeys. For Mars rendezvous, the variation of outbound trip time with characteristic acceleration was analysed and it was found that the curve seems to level off above 0.6 mm s^{-2} . A characteristic acceleration of 0.5 mm s^{-2} was chosen for further analysis, which corresponds to one revolution and enables an outbound trip time of under 600 days. For Venus rendezvous, the curve levelled off above 0.5 mm s^{-2} , and a characteristic acceleration of 0.2 mm s^{-2} , corresponding to 2 revolutions, was selected for further analysis, to minimise sail size, since any Venus lander is likely to be very large. For Mercury rendezvous, the curve levelled off above 0.6 mm s^{-2} , and a characteristic acceleration of 0.25 mm s^{-2} was chosen to keep the round-trip mission duration under 5 years. The results of this preliminary analysis were also validated against values in the literature.

For the three planets, departure date scans were generated using incremental feedback of the departure date. It was found that there are minimum time departure windows for planetary rendezvous, which are generally 'sawtooth' in shape, with discontinuities just beyond the trip-time minima. Just beyond these discontinuities lie maxima in trip-time, from where the trip-time gradually decreases again towards the following minima, as departure date is progressed. The presence of discontinuities in the departure date scans is due to the solar sail just missing the target planet and having to execute another revolution for rendezvous. For Mars and Venus rendezvous the trip-time minima are separated by one Earth-Mars or Earth-Venus Synodic period, respectively. Due to the much quicker orbit period of Mercury and higher number of trajectory revolutions, the Mercury rendezvous trip-time minima are separated by 4 Mercury orbit periods or 3 Earth-Mercury Synodic periods. The minima (and maxima) are not quite of the same trip-time due to the eccentricities and inclinations of the planets, but the sequence repeats over several years. From a trajectory optimisation standpoint, the initial starting solution in the departure date scan curve affected the optimality and trend of the resulting curve,

when using an incremental feedback method of stepping the departure date in increments while feeding back the solution as the next initial guess. If the initial point was sub-optimal, then this sub-optimality was propagated through the resulting departure date scan curve. This problem was solved by re-optimisation at different departure dates, and by scanning both backwards and forwards in time across the departure date range and discarding locally optimal curves in favour of more optimal departure date scans. In general, the gradient of all scans was similar for each planet.

Return journey departure date scans have also been generated using the same method. Since the characteristic acceleration is markedly increased, due to lander jettison after sample acquisition, the return trip-times were lower than the outbound trip-times, which dominate the overall sample return mission duration. Nevertheless, return scans were generated and combined with the outbound scans and planet-centred durations, using an interpolation and table-lookup method. Again, optimal Earth departure opportunities were identified, which corresponded approximately to the outbound departure windows. With appropriate launch opportunities selected for Earth escape ($C_3=0$), for Mars sample return the mission duration is just under 5 years, for Venus sample return it is also under 5 years. These mission durations are unattractive, since conventional propulsion could return a sample from these planets in much less time. However, solar sail Mercury sample return is possible in 4.4 years, with doubtless a much reduced launch mass. Conventional propulsion would require many time consuming gravity assists and a much greater mission duration and launch mass.

For all selected example trajectories, the sail film temperature was modelled using a black-body approximation. The temperature is related to the sail pitch angle and heliocentric distance, where it was found that it did not exceed the accepted limit for aluminium/chromium coated polyimide films of 520 K, although the effect of extended exposure at Mercury orbit was not investigated.

Since Mars and Venus are quite close to the Earth and relatively easy to reach using positive launcher excess and chemical propulsion, it was not necessary to investigate using solar sailing with positive launch excess energy for these planets. However, preliminary analysis revealed that using positive launch excess energy to reach Mars with a solar sail does not reduce trip-time by much, since the sail must be used to circularise the trajectory on approach to Mars' orbit, and it can even have a

detrimental effect. For Mercury rendezvous, however, the use of positive launch excess energy can be highly beneficial, since the solar sail thrust is greatly increased on approach to Mercury's orbit and the sail can easily circularise the trajectory. It was found that the outbound trip-time can be reduced by up to 28% in a particular case. Finally, a brief investigation showed that, although not necessary for solar sailing, a Venus gravity assist en-route to Mercury could reduce outbound trip-time by of order 140 days for $C_3=0$.

Chapter 4

Small-Body Trajectories

In this Chapter, solar sail trajectories to various small bodies will be investigated, covering Short and Long Period Comets, Main-Belt Asteroids, and Near Earth Asteroids. Since the range of possible targets is extremely large and diverse, a few representative targets have been selected as examples of high-energy bodies that could be reached using solar sailing. The first section, Small-Body Encounters, has been published in the *Journal of Spacecraft and Rockets* [Hughes and McInnes, 2004]. Problems to be addressed include solar sail rendezvous of the Short Period Comet Wirtanen, which was the original target of the Rosetta mission. The variation of trip-time against characteristic acceleration will briefly be investigated, and then the launch mass and sail size will be calculated, against sail assembly loading, based on the Rosetta cruise stage.

The next part of section 4.1 concerns the use of a solar sail to flyby a newly discovered Long Period Comet shortly after its first discovery, either at perihelion or the closest orbit node. By definition, previous examples of Long Period Comets are selected to demonstrate this, such as Hale-Bopp and others. The variation of trip-time against characteristic acceleration and relative flyby velocity will be investigated. The open-ended nature of solar sailing will be used to show how a second comet could also be reached, or how the solar sail could return to Earth. Brief mission analysis will be performed to investigate the variation of launch date contingency after first discovery against characteristic acceleration, and how the sail size is affected by sail assembly loading.

The final part of section 4.1 will show how a solar sail could be used to replace the solar electric propulsion component of the NASA Dawn mission to accomplish a dual rendezvous of Main-Belt asteroids Vesta and Ceres. This is

complemented by a brief analysis using the Dawn cruise stage, and an investigation of launch mass and sail size against sail assembly loading and cruise stage mass. The open-ended nature of solar sailing will be used to show how the mission objectives could be extended to two further asteroids.

The second section in this Chapter will demonstrate how a solar sail could be used to return a sample from a high-energy, high-inclination Near-Earth Asteroid. A triple phase trajectory using an inclination cranking manoeuvre will be applied. This will involve a parametric analysis of crank time against inclination change and characteristic acceleration, to determine the total trip time against characteristic acceleration.

4.1 Small-Body Encounters

Large databases exist, of comets whose orbital elements have been more accurately determined via successive observations, such as those of the Bureau des Longitudes in Paris. The material structure of these relics from the early solar system is only beginning to be understood. The comet nucleus is thought to be composed of dust and rock with a significant fraction of ice binding it together. Comets have undertaken a long evolutionary path and many are thus pristine examples of matter from the early solar system, condensing from the ancient solar nebula at the same time as when the outer planets and their satellites were in their infancy [Sims, 2000]. It is now known that many comets form in the Oort Cloud on the edge of interstellar space at 50,000 AU from the Sun. Shorter period comets can originate from the Edgeworth-Kuiper Belt, which starts just beyond Neptune's orbit. There may also be a further repository, the so-called Inner Oort Cloud, which tells us that the source region can be closer to the planetary domain [Perozzi and Fabiani, 1998]. Comets are divided, somewhat arbitrarily, into two categories depending on their orbital characteristics. Short Period Comets (SPCs), which have periods of less than 200 years originating in the Kuiper Belt, and those of greater than 200 years: the Long Period Comets (LPCs) born in the Oort Cloud.

The most famous Short Period Comet, 1P/Halley, in common with all comets, has a highly inclined and eccentric orbit, but is unusual in that it has a retrograde orbit. In 1976, the NASA Jet Propulsion Laboratory (JPL) conducted a

detailed mission study for a planned solar sail rendezvous with Halley on its 1986 inner solar system passage [Wright, 1992, pp. 42-44]. The solar sail element was subsequently replaced with solar electric propulsion, but ultimately the mission was cancelled. The European Space Agency (ESA) spacecraft Giotto encountered Halley in 1986 at a large relative velocity of 68 km s^{-1} , but nonetheless valuable information and low-resolution images were acquired. The ESA Rosetta spacecraft missed a January 2003 opportunity to Comet Wirtanen, and has since been retargeted to Comet 67P/Churyumov-Gerasimenko, launched in February 2004. Numerous studies have been conducted into Short Period Comet rendezvous missions enabled by solar electric propulsion [Sims, 2000, Kluever, 2000].

The apparition of bodies classified as Long Period Comets has generated much enthusiasm within the science community. Their eccentricities approach unity and a few have previously been observed to be extra-solar in origin. Although, recent research suggests that almost all LPCs do in fact have elliptical orbits, once their orbits are properly computed via modern methods of estimating the uncertainties. The non-gravitational effects due to sublimation of CO and H₂O are responsible for small adjustments in the orbital elements to make previously 'hyperbolic' comets become 'elliptical' [Królikowska, 2001]. LPCs have undergone a limited number of passages, if any, though the inner solar system. Because of this, they are regarded to be the best preserved bodies in the solar system since they have had limited solar interaction and consequential cometary activity [Perozzi *et al*, 1996]. Rendezvous with a newly discovered LPC would be highly impractical, so research conducted so far has involved using ballistic means to flyby at one of the orbit nodes of a new LPC shortly after first discovery [Perozzi and Fabiani, 1998, Perozzi *et al*, 1996]. The ill-fated CONTOUR mission was launched, by NASA, on July 3, 2002 and was to use successive Earth gravity assists to perform slow flybys of the Short Period Comets Encke then Schwassmann-Wachmann 3, and then allow for retargeting to a newly discovered LPC should that exciting opportunity have arisen. In this section, the possibility of using solar sails to reach comets and asteroids is investigated. Solar sailing is attractive for reaching these, often high energy, bodies, by virtue of the elimination of reliance on propellant mass.

4.1.1 Short Period Comet Rendezvous (Wirtanen)

The ESA spacecraft, Rosetta is a European Space Agency Horizon (2000) 'cornerstone' mission. The original objective of this mission was to rendezvous with the short period comet 46P/Wirtanen. This opportunity has been missed and a new target of 67P/Churyumov-Gerasimenko has been identified, but the original target Wirtanen mission was investigated with solar sailing for comparison purposes. It should be noted again here that solar sails are not restricted by launch windows, which allows for more flexibility in target selection. This ballistic mission was to have a total trip time of almost 9 years, and was to use one Mars and two Earth gravity assists to reduce chemical propellant mass requirements. This extremely long trip time would have also been offset by conducting science observation during en-route flybys of the mainbelt asteroids, Otawara and Siwa. Departure was scheduled for January 12, 2003 from the Kourou spaceport aboard an Ariane 5 launch vehicle, which was to provide $11.6 \text{ km}^2 \text{ s}^{-2}$ of hyperbolic excess energy. The maximum (wet) launch mass was 2.95 tonnes. The subsystems, lander and scientific payload account for 878.3 kg, in addition to 2.07 tonnes of propellant, engine and tanks. This enormous quantity of propellant is necessary for a chemical mission to a high energy target with such a large spacecraft. To replace the primary propulsion system with a solar sail could in principle reduce the launch mass and enable a lower cost launch vehicle to be used. Solar sail trajectory and mission analysis was therefore conducted for this baseline mission.

Rendezvous with a comet in a highly eccentric orbit is difficult to achieve, so the formulation of the initial guess is easier with a low number of heliocentric revolutions, enabled by high acceleration capability. Initially, the characteristic acceleration was set at 5.0 mm s^{-2} . This acceleration is representative of very high performance sails, such as those considered by NASA/JPL for Heliopause missions [Garner *et al*, 2000]. In the first instance, the launch date was fixed at October 1, 2007. The transfer times are shown in Table 4.1 for increasing control node resolution. These solutions were then used as the initial control estimate for the launch date variable optimisations. For 50 control segments (51 nodes), the solution found was 205.0 days for an optimal launch date of October 17.3, 2007. The characteristic acceleration was then decreased by incremental solution feedback along with the launch date variable. Appropriate bounds were selected for the

launch date to ensure that the solution did not stray too close to the boundaries, which caused algorithm convergence problems. The results are shown in Table 4.2. The trajectory with a characteristic acceleration of 1.0 mm s^{-2} is shown in Figure 4.1, where the trip time of 2.86 years is a 68 % reduction over the 8.9 year, ballistic trip time. The temporal evolution of the semi-major axis and inclination is shown in Figure 4.2. It can be seen that maximum rate of change of inclination occurred during the first 300 days of flight where the solar photon flux was higher. After this initial ‘cranking’, semi-major axis boost occurs and Wirtanen is reached shortly before its aphelion.

No. of control segments	Number of control nodes	Transfer time (days)
5	6	231.0
10	11	228.4
20	21	211.9
50	51	208.1

Table 4.1: 5.0 mm s^{-2} Wirtanen rendezvous times

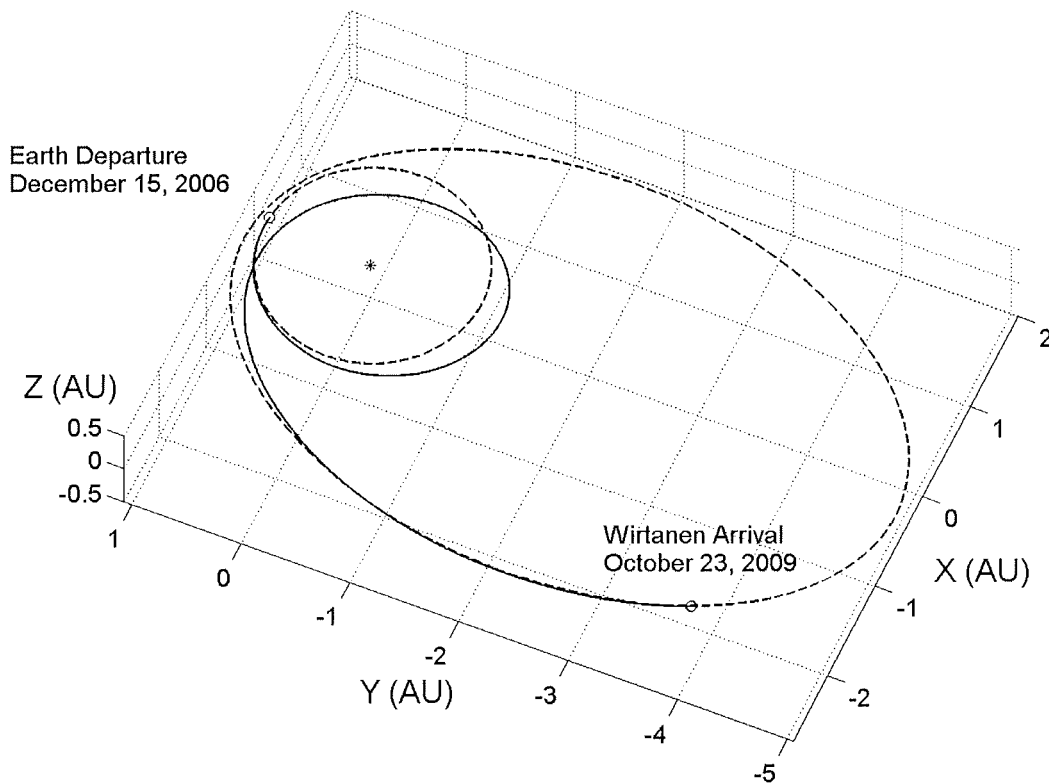


Figure 4.1: 1.0 mm s^{-2} Wirtanen rendezvous trajectory

Characteristic acceleration (mm s ⁻²)	Optimal launch date (day/month/year)	Transfer time (days)
5.0	19/10/2007	208
4.0	14/10/2007	237
3.0	1/9/2007	279
2.0	3/10/2007	490
1.0	15/12/2006	1043

Table 4.2: Wirtanen rendezvous times against characteristic acceleration

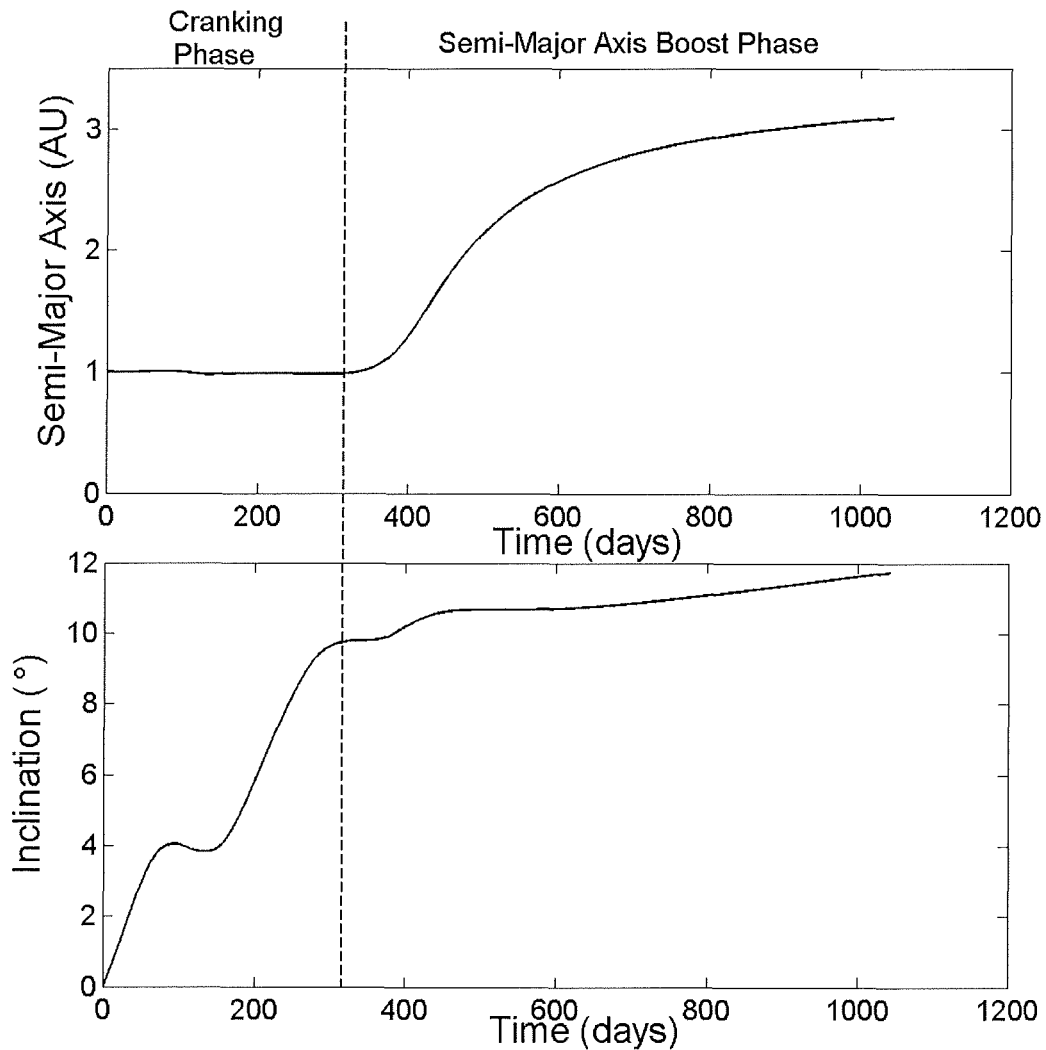


Figure 4.2: Wirtanen rendezvous orbital element evolution

Using the Rosetta spacecraft mass (minus the propellant and propulsion components) of 878.3 kg, some analysis was conducted into the required sail dimensions to enable this trajectory. Once total spacecraft mass (including sail structure) was determined, then a launch vehicle could be selected. The solar sail technology level is defined by the sail assembly loading. A L'Garde sail concept was to use 0.9 μm film of 85% propulsive reflectivity, with linear boom densities as low as 14.1 g m^{-1} , which could perhaps have enabled a highly attractive sail assembly loading of 3.4 g m^{-1} [Cohen *et al*, 2002]. Although, due to some growth in boom mass, recent calculations suggested this would have increased to 3.56 g m^{-2} .

Table 4.3 shows the variation of launch mass with sail assembly loading, with the resulting square sail side length. If a sail were fabricated with the same performance of the L'Garde sail ($\sigma_s = 3.56 \text{ g m}^{-2}$) then the 458 m by 458 m sailcraft would weigh 1624 kg. This is an extremely large sail, but represents a 44% reduction in launch mass ($C_3=0$) over the original Rosetta mission ($C_3= 11.6 \text{ km}^2 \text{ s}^{-2}$) and would mean that a smaller, cheaper launch vehicle could be used, such as a Soyuz ST-Fregat or Delta II 7925-10. The solar sail could also be used to escape from Geosynchronous Transfer Orbit (GTO), and then reach Wirtanen in 2.86 years, much less than the original Rosetta 8.9 year trip time.

Sail Assembly Loading, σ_s (g m^{-2})	Payload Mass Fraction, κ	Launch Mass (kg)	Square Sail Side Length (m)
2	0.742	1183.7	390.8
3	0.613	1432.8	430.0
3.56	0.541	1623.4	457.5
4	0.484	1814.7	483.8
5	0.355	2474.1	564.9
6	0.226	3886.3	708.1
7	0.097	9054.6	1080.8

Table 4.3: Sailcraft sizing for 1.0 mm s^{-2} Wirtanen rendezvous mission with Rosetta payload

4.1.2 Long Period Comet Flybys

An analysis using high-performance sails was conducted to permit fast flyby intercepts of newly discovered Long Period Comets. Because of the nature of this problem, previous comet apparitions were adopted to demonstrate the feasibility of a late launch to quickly intercept a new LPC using a solar sail. Since the time between discovery of a new LPC such as Hale-Bopp and perihelion passage was less than 2 years, this then leaves a very short time-span for spacecraft preparation, orbit planning and launch/operational phases. Therefore, for future new LPC apparitions, it is envisaged that the stowed sail would hibernate in GTO or Geostationary Orbit (GEO) with a small science payload. When a target is sighted, the sail would deploy and the spacecraft could rapidly escape from Earth orbit to reach the new LPC.

4.1.3 Hale-Bopp Perihelion Flyby

As an example of the type of new LPC that could appear, the case of the 1995 apparition of the Comet C/1995 O1/Hale-Bopp was considered. Because of the inclination and orbit geometry, the perihelion is displaced quite far above the ecliptic plane. Therefore, initially, a high performance sail was utilised with a characteristic acceleration of 5.0 mm s^{-2} . The optimisation problem was then to minimise the transfer time such that the launch date was the time of perihelion passage minus the transfer time. The final solution established by NPSOL was 208.8 days, resulting in a launch date of September 4.4, 1996. The trajectory is shown in Figure 4.3. The characteristic acceleration was then decreased by the incremental feedback method. The number of linear interpolation nodes was increased to 21 nodes, with 20 trajectory segments. These results are shown in Table 4.4. It was then attempted to minimise the transfer time *and* the relative velocity at flyby. NPSOL only permits for one objective function so the relative velocity at flyby was encoded as an extra inequality constraint. The upper limit on this inequality was specified so that NPSOL would force the additional variable to be below the limit. This upper limit was decreased in increments while passing the solution back each time as the next initial guess. This was performed for a characteristic acceleration of 2.0 mm s^{-2} , with the unconstrained relative velocity being 58.6 km s^{-1} . The results are shown in Table 4.5. The final relative velocity was always equal to the upper bound set for

each transfer. The trajectory for the 36 km s^{-1} flyby is shown in Fig. 4.4. It can be seen that the vertical component of the spacecraft and comet velocity is closely matched.

Characteristic acceleration (mm s^{-2})	Transfer time (days)
5.0	208.7
4.0	251.7
3.0	387.8
2.0	537.1
1.64	665.2

Table 4.4: Hale-Bopp perihelion flyby times

Minimised relative velocity at flyby (km s^{-1})	Transfer time (days)
55	540.3
50	556.9
45	585.3
40	629.7
37	652.1
36	661.3

Table 4.5: 2.0 mm s^{-2} Hale-Bopp, minimised relative velocity, perihelion flyby times

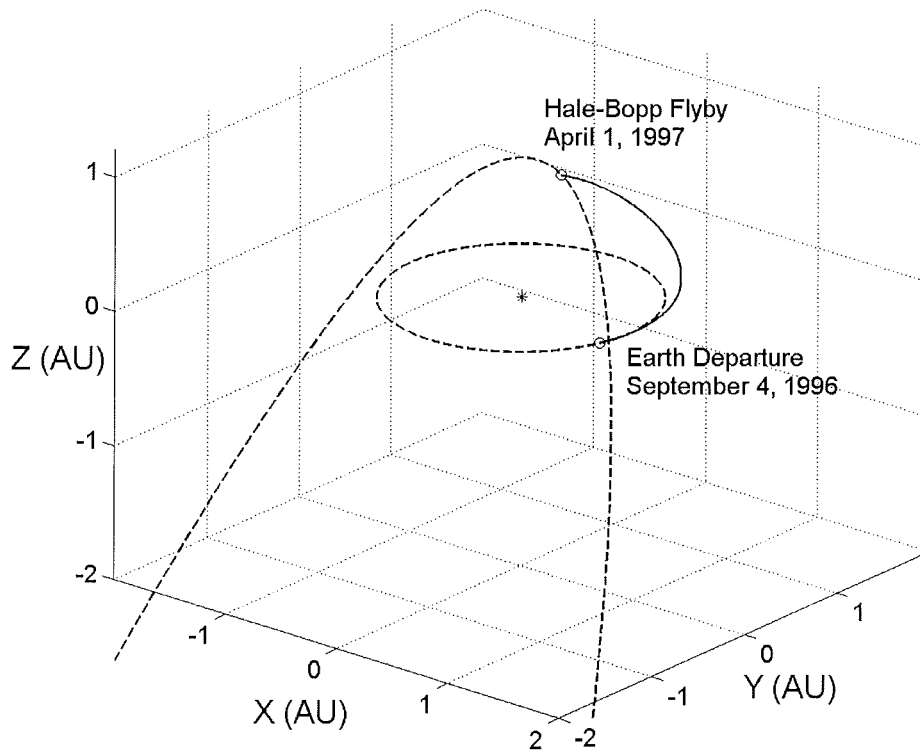


Figure 4.3: 5.0 mm s^{-2} Hale-Bopp perihelion flyby

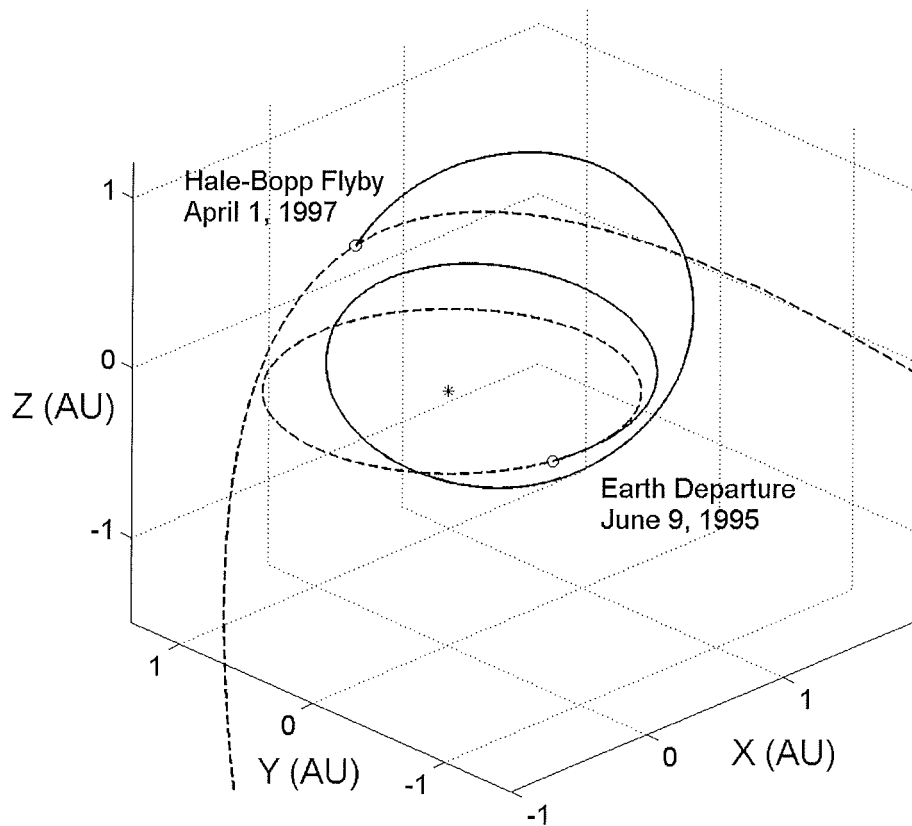


Figure 4.4: 2.0 mm s^{-2} Hale-Bopp minimised relative velocity flyby

4.1.4 Hale-Bopp Descending Node Flyby

High performance sails are required to enable the high accelerations necessary to intercept many comets at perihelion. It would be easier to intercept a comet at one of its orbit nodes since the transfer trajectory can remain within the ecliptic plane – inclination changes are not necessary. The spacecraft can also be more readily returned to the Earth if required. Other new comets, subsequently discovered, could then also be intercepted at one of their nodes – the inclination of the heliocentric parking orbit plane is thus standardised whilst waiting for the next new comet.

The perihelion flyby optimisation algorithm was adjusted to perform flyby at a user-specified node (the nearest node to Earth orbit was always taken). The Descending Node of Hale-Bopp was the easiest node to reach, as it was the closest to the Earth's orbit, so it was selected for flyby. The characteristic acceleration was initially set at 5.0 mm s^{-2} and the number of control nodes set at 21 (20 segments). The optimal solution was 201.5 days, departing October 17.1, 1996. The relative flyby velocity was less than for the perihelion flyby case at 46.6 km s^{-1} , as expected, and the trajectory is shown in Figure 4.5. The trajectory has an inward 'kink', just before flyby, because of the excessive acceleration capability available, the outward thrust constraint, and the comet nodal passage phasing with the Earth ephemeris. The final semi-major axis of the spacecraft was 0.6156 AU and the eccentricity was 0.9951. If the spacecraft remained in this orbit then the perihelion distance would be 449,000 km, which is less than the Sun's radius (695,000 km), and solar surface impact would occur. To avoid this, the sail should be steered towards the next new comet, or into a safer parking orbit, or could be returned to Earth for potential dust sample return or telemetry download. It should be noted here that the post-flyby options available are broad, since the solar sail has a near infinite Δv capability.

The Earth return trajectory was optimised since it had the most easily defined criteria. No minimisation of flyby relative velocity was implemented so, in general, the higher the characteristic acceleration, the higher the instantaneous flyby velocity. Unfortunately, once the solar sail was on a hyperbolic orbit, the optimiser could not generate a feasible solution to allow re-capture into a closed orbit. Therefore, it was considered to be easier to use a lower acceleration for flyby and Earth return, since the flyby eccentricity would be lower. The characteristic acceleration was therefore

decreased with the resulting flyby times shown in Table 4.6. A characteristic acceleration of 2.0 mm s^{-2} was selected for the flyby and return trajectory. The relative velocity at flyby in this case was 50.4 km s^{-1} . The perihelion distance of the instantaneous spacecraft flyby trajectory was 34 million km or 48.9 solar radii, so if the sail was jettisoned the spacecraft would not, in principle, impact the Sun. For the return trajectory the optimal solution was of 261.4 days, starting from the flyby initial conditions and returning to Earth sphere of influence with zero hyperbolic excess velocity. The arrival date back at the Earth was January 22.9, 1998 and the total trip time for flyby and return was 531.7 days (1.46 years). The total trip time is therefore the minimum turn-around time for each new comet intercept with Earth return for this characteristic acceleration. The entire round-trip trajectory is shown in Figure 4.6. A catalogue of additional comet nodal flyby trajectories has been generated to numerous comets as presented in Table 4.7.

Characteristic acceleration (mm s^{-2})	Transfer time (days)
5.0	201.5
4.0	217.6
3.0	239.2
2.0	270.3
1.0	328.7 ^a
0.5	404.7 ^a
0.2	664.4 ^a

^aUsed 51 control nodes instead of 21.

Table 4.6: Hale-Bopp descending node flyby times

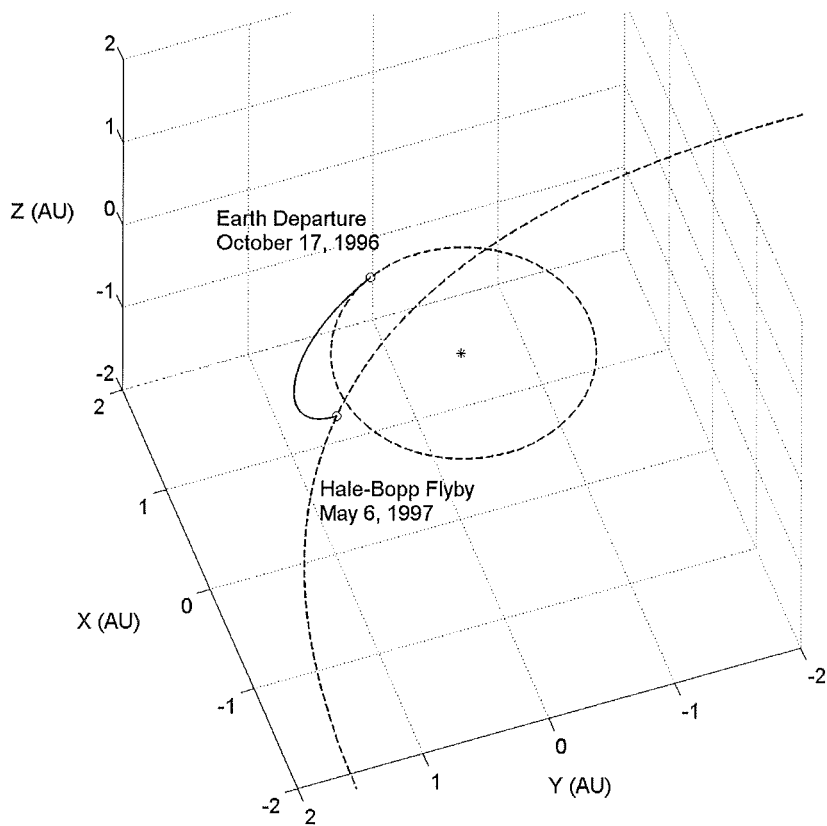


Figure 4.5: 5.0 mm s^{-2} Hale-Bopp descending node flyby

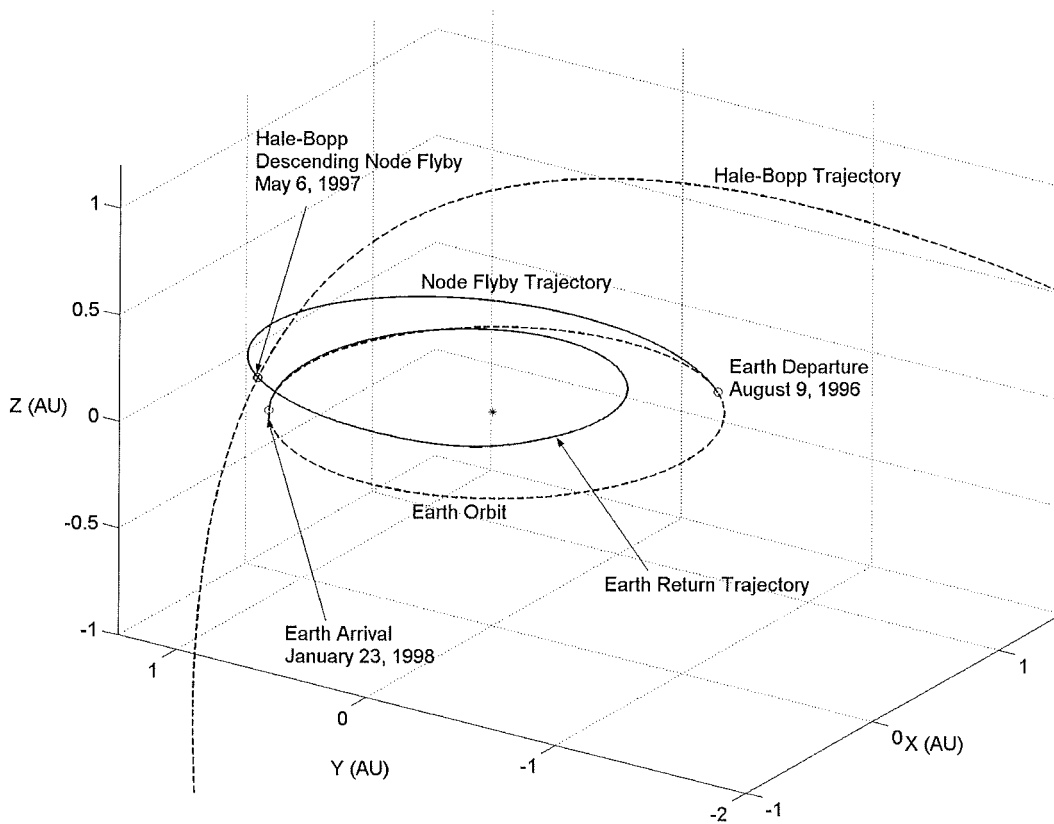


Figure 4.6: 2.0 mm s^{-2} Hale-Bopp flyby and return trajectory

Comet	a_c (mm s ⁻²)	Node ^a	Transfer Time (days)	Earth Return Time (days) ^b
C/1995 O1 Hale-Bopp	2.0	D	270.3	261.4
C/1995 Y1 Hyakutake	2.0	A	240.0	H
C/1999 T1 McNaught-Hartley	2.0	A	237.8	H
C/1999 F1 Catalina	5.0	D	589.2	H
C/1999 N2 Lynn	2.0	A	192.8	283.9
C/1999 H1 Lee	2.0	A	268.9	244.5

^aD = Descending, A= Ascending.

^bH = Hyperbolic Escape at Flyby

Table 4.7: Example Long Period Comet nodal flyby times

4.1.5 Dual Comet Flyby

An alternative extension of the Hale-Bopp Nodal flyby mission could have been to continue on to flyby another LPC at one of its nodes. In principle, the near infinite Δv capability could enable several new Long Period Comets to be intercepted. The comet C/1997 D1/Mueller was discovered on February 17, 1997. The discovery date is less than three months before the Hale-Bopp encounter occurred, with the sail en-route to flyby. In this analysis, Mueller was intercepted at its descending node using the same characteristic acceleration of 2.0 mm s⁻², as before. The transfer time was constant since it was just the difference in the date between Hale-Bopp and Mueller nodal descent. Therefore, Mueller nodal flyby occurred 146.1 days after Hale-Bopp nodal flyby, on September 29, 1997. The trajectory is shown in Figure 4.7. The relative velocity at Hale-Bopp was 50.4 km s⁻¹ and was 57.6 km s⁻¹ at Mueller. At Mueller flyby the spacecraft reached a hyperbolic escape trajectory due to the close solar photonic assist at 28.3 Solar radii. This close approach to the Sun would pose serious thermal loading problems on the sail structure, although high emissivity rear coatings could perhaps control sail film temperature.

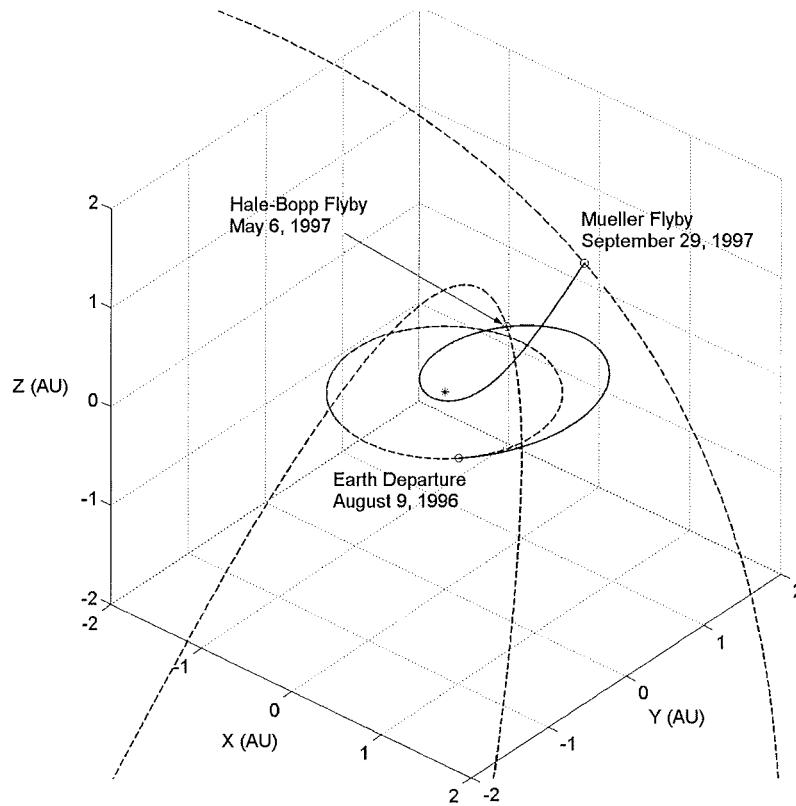


Figure 4.7: Earth – Hale-Bopp – Mueller dual comet nodal flyby

The heliocentric velocity was 45 km s^{-1} , which is considerably greater than the 28.1 km s^{-1} solar system escape velocity, at Mueller Flyby. It is of interest to note that the Heliopause (at 100 AU) could then be reached in 12 years with the outer Heliopause boundary (200 AU), the edge of interstellar space, attained in 24 years. Heliopause trajectories will be investigated in greater detail in Chapter 6, along with a thermal analysis. Multiple flybys and the potential for solar system escape, shows the great versatility of solar sail propulsion.

4.1.6 Hale-Bopp Opportunity Mission Analysis

More extensive analysis was conducted into the previous Hale-Bopp nodal flyby case, initially for a characteristic acceleration of 2.0 mm s^{-2} . The solar sail escape phase from the Earth's Sphere of Influence was modelled by M. Macdonald [2005] using analytical control laws, taking into account geopotential perturbations, lunar and solar gravity, and Earth and lunar shadow with umbra and penumbra effects [Macdonald and McInnes, 2001]. After hibernation of the stowed sail in GTO, the sail was deployed on June 8th, the escape spiral duration was 59 days, reaching

escape conditions ($C_3=0$) on August 6th. The interception phase was then initiated on August 9, 1996. The discovery date of Hale-Bopp was July 23, 1995 so this would have left 321 days of contingency (difference between discovery and sail deployment). It is envisaged that the spacecraft and sail could hibernate in GTO or GEO until required by the appearance of a new LPC. Conversely, the escape times from GEO, for the range of characteristic accelerations used in the interception phase, were obtained and added to the heliocentric transfer times. First discovery, launch date contingency time against characteristic acceleration is plotted in Figure 4.8. Zero contingency occurred for a characteristic acceleration of 0.362 mm s^{-2} . A mass and area sizing investigation was conducted for a sail exhibiting this acceleration magnitude. Although a perfect sail was assumed for optimisation purposes, an imperfect sail reflective efficiency of 85 % was chosen for the mass sizing exercise. Square sail side length, as a function of sail assembly loading and payload mass is shown in Table 4.8. A payload mass of 100 kg is representative of small science missions and for a payload mass of 20 kg micro-satellite technology is envisaged with a small camera and 'stripped-down' payload. The sail/spacecraft composite with a conservative assembly loading of 15 gm^{-2} could have delivered a payload of 50 kg using square sail dimensions of less than $90 \times 90 \text{ m}$ and with a total mass of 167 kg. This total mass is within the GEO auxiliary payload capability of a Delta IV class launcher, although a dedicated launch would probably be required.

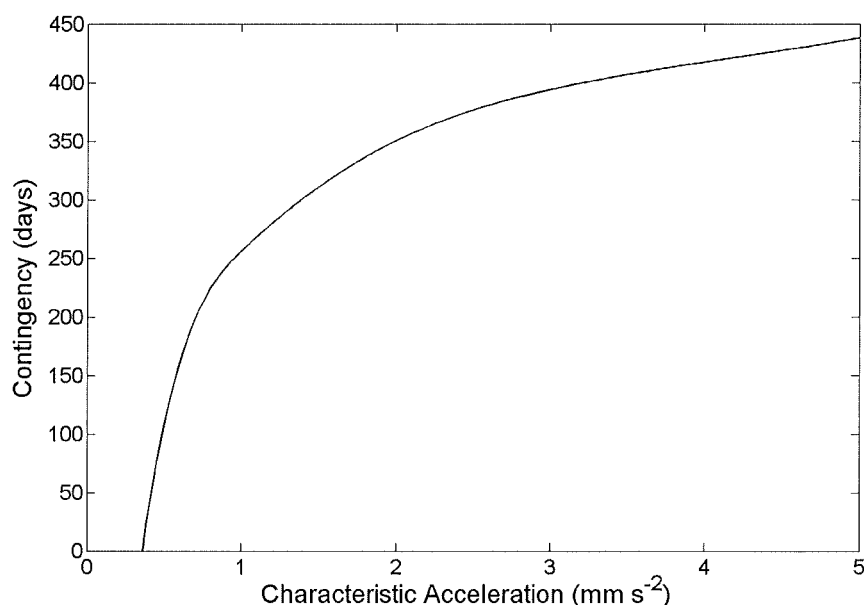


Figure 4.8: Launch date contingency against characteristic acceleration for Hale-Bopp nodal encounter

Sail Assembly Loading, σ_s (g m ⁻²)	Payload Mass Fraction, κ	Sail Side Length (m) for Payload Masses of		
		20 kg	50 kg	100 kg
5	0.767	34.9	55.2	78.1
10	0.533	41.9	66.2	93.6
15	0.300	55.8	88.3	124.9

Table 4.8: Sailcraft sizing for 0.362 mm s^{-2} Hale-Bopp nodal flyby

4.1.7 Main-Belt Asteroid Survey

A plethora of planetesimals exist in the solar system. The gravitational forces of Mars and Jupiter prevented planetary accretion of Main-belt asteroids, so they can provide evidence of how the solar system formed. A high density of Near-Earth Objects (NEOs) also abound, which include some of the shorter period comets. Expanding knowledge of these objects is vital to catalogue the possible threats to Earth, along with obvious scientific considerations. The NEAR-Shoemaker mission to 433 Eros was a major breakthrough in the understanding of Near-Earth Asteroids (NEAs). Solar sail rendezvous trajectories have been previously analysed in the literature using solar sails by Leipold [2000], and also using solar electric propulsion by Colasurdo and Casalino [2002]. Yen also compares solar sail and solar electric propulsion for dual asteroid rendezvous missions [Yen, 2001]. This section builds on Yen's previous work, and includes mass sizing analysis and extension of the target asteroids to two further asteroids. Yen states that for more than two rendezvous, solar sail propulsion is expected to be superior to solar electric propulsion. Integral to any small-body rendezvous mission is if a solar sail can maintain itself in orbit around the weak gravitational field of an asteroid or comet. This has been treated in the literature where it was found that certain stable orbits and unstable hover points exist [Morrow *et al*, 2001, Morrow, 2002].

Multiple Asteroid rendezvous missions have immense Δv requirements. Missions to rendezvous with more than two or three target objects make chemical or even solar electric propulsion much less viable as candidate transfer methods [Yen,

2001]. The structural and material endurances are the only limiting factors dictating the number and range of asteroids with which the solar-sail propelled spacecraft can encounter throughout its lifetime. Solar electric propulsion has been adopted as the primary propulsion system for NASA's Discovery Class mission, Dawn. Dawn is a dual asteroid rendezvous mission scheduled for launch on May 27, 2006 aboard a Delta II 7925H (2925H). The objective of this mission is to rendezvous with inner main-belt asteroids, Vesta and Ceres. Dawn takes 4.2 years to reach Vesta from Earth and, following 11 months in orbit about Vesta, reaches Ceres in 3.1 years. Solar electric propulsion is used, with the 3 NSTAR Xenon engines processing 400 kg of propellant via a 7.5 kW GaAs solar array. The total wet launch mass is 1108 kg. Therefore, the dry mass (including propulsion) is 708 kg. Approximate propulsion system sizing is taken from Kluever [2000] and assumes that 2 Power Processing Units (PPUs), a Digital Control Unit, 3 Engine Gimbals, and Xenon tank/feedlines, amount to 360 kg with the solar array included. The mass of the spacecraft, without propulsion, is of order 348 kg. To adapt this spacecraft to other propulsion methods, a small solar array must be added for electrical power. For example, NEAR-Shoemaker solar array mass was 46.1 kg, so it is assumed that a 'propulsion non-specific' Dawn spacecraft weighs of order 400 kg. However, it is noted that Main-belt asteroid missions are likely to require large solar arrays for operation at 2 AU. The Dawn mission has been reconfigured to utilise solar sail propulsion, for the same Earth launch date of May 27, 2006 and 11 month orbiter stay-times at each asteroid. The trajectories are shown in Figure 4.9 for a sail characteristic acceleration of 1.0 mm s^{-2} . The Earth-Vesta phase was 3.2 years long and the Vesta-Ceres phase lasted 3.7 years. Using a more modest characteristic acceleration of 0.52 mm s^{-2} , the sail would take 4.9 years to reach Vesta, but the inter-asteroid phases would be prolonged due to the diminished solar photon pressure out at the Main-belt distance from the Sun. Sail sizing was conducted for a 1.0 mm s^{-2} sail with the Dawn payload and is shown in Table 4.9. It was found that if a sail assembly loading of 3.56 g m^{-2} were utilised, the launch mass could be reduced by 33 % to around 740 kg. The solar sail component would be of mass 340 kg and of square side length 309 m. If a high performance sail such as this could not be fabricated, or the sail dimensions were problematically large, perhaps some payload and bus miniaturisation could be accomplished. Table 4.10 shows the launch masses and sail side lengths for lower performance sails with reduced

payload masses. The mission objectives have also been extended from Vesta and Ceres to two further asteroids, Lucina and Lutetia, to further demonstrate the viability of using a solar sail in a Main-belt asteroid survey scenario. The trajectories from Ceres to Lucina to Lutetia are shown in Figure 4.10 for 1.0 mm s^{-2} , again with 11 month stay-times at each asteroid. This again shows the open-ended nature of solar sailing, but the total four asteroid rendezvous mission duration is very long at over 20 years. It is envisaged that highly autonomous solar sails could survey many asteroids over long timescales.

Sail Assembly Loading, σ_s (g m^{-2})	Payload Mass Fraction, κ	Launch Mass (kg)	Side Length (m)
1	0.871	459.2	243
2	0.742	539.1	264
3	0.613	652.5	290
3.56	0.541	739.4	309
4	0.484	826.4	327
5	0.355	1126.8	381

Table 4.9: Sailcraft sizing for 1.0 mm s^{-2} asteroid rendezvous mission with Dawn payload

Sail Assembly Loading, σ_s (g m^{-2})	Payload Mass Fraction, κ	Launch Mass (kg); Sail Side Length (m) for Payload Masses of		
		100 kg	200 kg	300 kg
5	0.355	282; 191	563; 270	845; 330
6	0.226	442; 239	885; 338	1327; 414
7	0.097	1031; 365	2062; 516	3093; 632

Table 4.10: Sailcraft sizing for 1.0 mm s^{-2} asteroid rendezvous mission with reduced payload

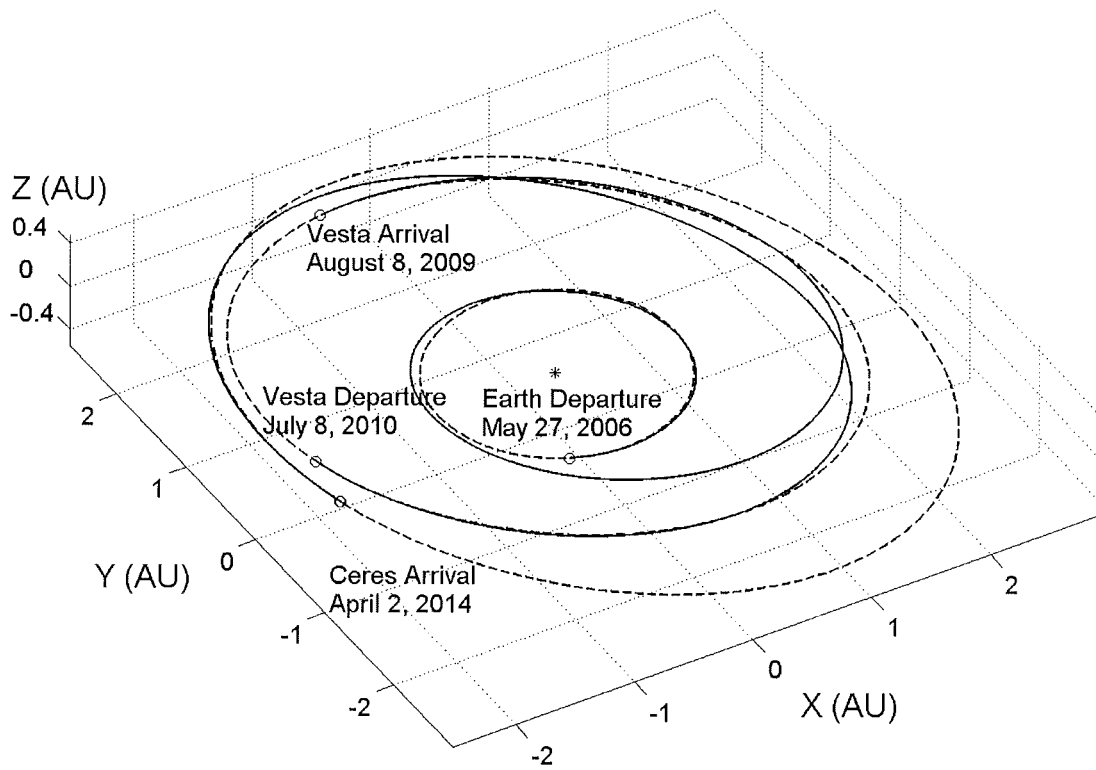


Figure 4.9: Earth – Vesta – Ceres rendezvous

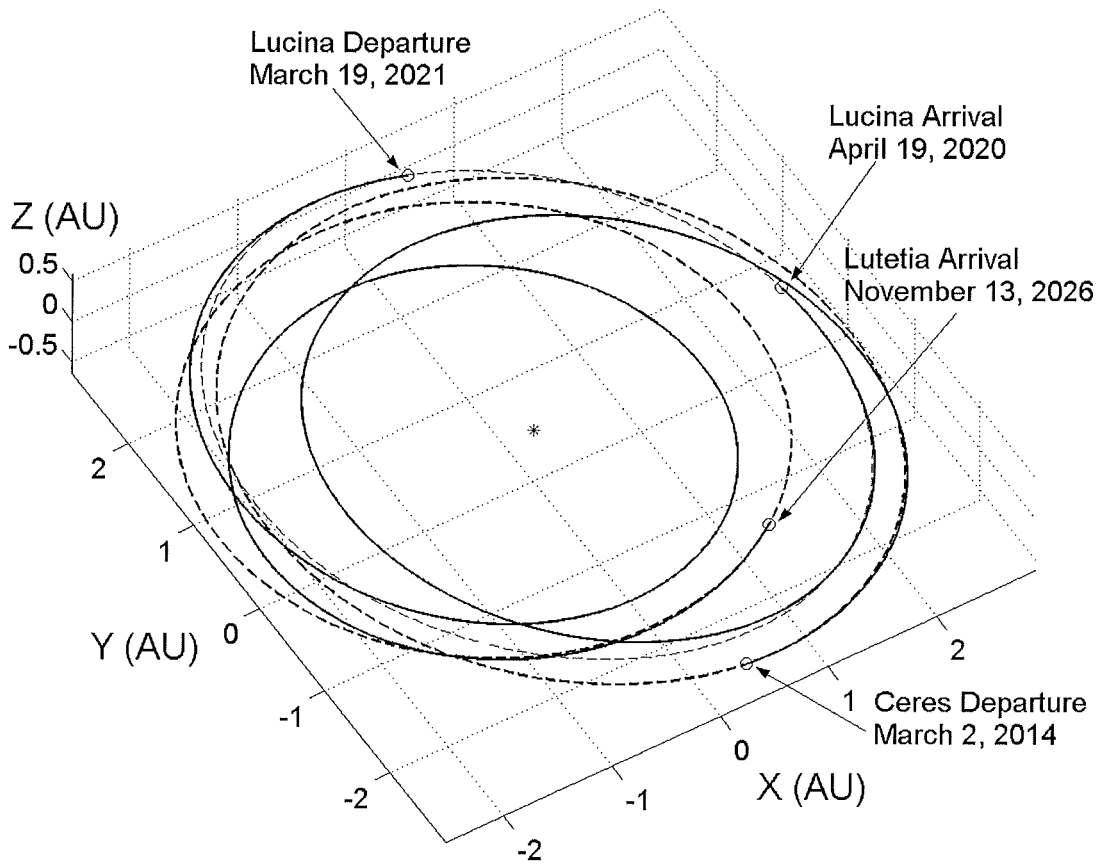


Figure 4.10: Ceres – Lucina – Lutetia rendezvous

4.2 High Energy Asteroid Sample Return

To further demonstrate the enabling advantages of solar sailing in reaching high energy small bodies, this section will show the exotic trajectory analysis of returning a sample from a high-inclination Near Earth Asteroid (NEA), that would be near-impossible to accomplish using chemical and solar electric propulsion. The target selected was 2001 QP 153, which has a high inclination of 50.2° relative to the ecliptic. The selection criteria applied, to narrow down the list of possible targets, included a lower perihelion limit of 0.3 AU and an upper aphelion limit of 1.3 AU, for spacecraft thermal and power system reasons. The resulting list was narrowed down to five candidate NEAs by selecting only those with inclinations above 45° . NEA 2001 QP 153 was chosen from these five, since it has an Earth close approach in 2017, which is perhaps beneficial for telecommunications. Subsystems analysis and sail sizing has been conducted elsewhere for a sample return mission to this target [McInnes *et al.*, 2003d].

4.2.1 Trajectory Structure

A three-phase approach has been adopted to break the extremely complex trajectory optimisation problem into manageable mission phases. The approach used centres on the key concept of the *cranking orbit* to reach high orbit inclinations. This method was employed by NASA/JPL during a detailed study of a comet Halley rendezvous mission in the mid-1970s. Since, comet Halley orbits in a retrograde manner, the orbit angular momentum vector of the spacecraft had to be inverted, to point below the ecliptic plane. The strategy adopted was to spiral to a very low, circular heliocentric orbit at 0.25 AU (due to the film thermal limits, at a sail cone angle of greater than 35°). The sail is then pitched to an optimum cone angle of 35.26° , but with a simple switching control law employed for the clock angle, which results in a 180° sail rotation every half orbit when the out-of-plane force is directed alternately above and below the ecliptic plane [McInnes, 1999]. Because propellant mass is not an issue for solar sails, essentially any orbit inclination can be reached, even for a low-performance sail, with a multiple revolution, cranking spiral. Once the desired orbit inclination is reached, the spiral from the circular orbit to the eccentric small-body orbit can be accomplished through an in-plane transfer, with

little further out-of-plane adjustment necessary. The complete mission profile for this mission scenario therefore consists of 3 phases for the outbound trajectory, a target characterisation and sample acquisition phase, and 3 phases for the return trajectory. These phases will now be discussed in more detail in the following subsections.

4.2.2 Earth-to-Cranking Orbit

Using an inclination cranking control law (explained in Chapter 1 and again in section 4.2.3 below), McInnes [1999, pp.144-145] shows that, although inclination change per orbit is independent of the solar sail orbit radius, the total time required to achieve a given change in inclination is not. Since the orbit period diminishes with orbit radius, the quickest inclination changes are achieved using close heliocentric orbits [McInnes, 1999]. Therefore, the lowest possible circular cranking orbit radius is desired to achieve the quickest change in inclination. Aside from the obvious thermal considerations, there will be a trade-off between the decrease in cranking time, and the increased time required to reach a close heliocentric orbit, and the subsequent time to spiral outwards again. This is a complex problem which is addressed in more detail in Chapter 7 for a Solar Polar Orbiter, but in this analysis the cranking orbit radius will be defined predominantly by the maximum allowable sail film temperature. As in previous chapters, an aluminium front coating of 0.85 reflectivity and chromium back coating of 0.64 emissivity will be assumed, along with the predicted upper limit on thin films of 520 K. A black-body approximation has again been implemented. The NASA/JPL comet Halley study used a 0.25 AU cranking orbit, but this is only thermally possible if the sail cone angle is always above 35°. To allow for some flexibility in the sail attitude, a slightly larger cranking orbit radius was selected at 0.3 AU, allowing a maximum worst case temperature of 501 K with the sail facing the Sun. A circular 0.3 AU orbit also has a short period of just 60 days, meaning that the waiting period to match the right ascension of ascending node and argument of perihelion (once at the desired inclination of the target), is a maximum of 30 days for each. This short period essentially means that the Earth/asteroid phasing with the cranking orbit is removed from the problem, and so the position of the spacecraft on the 0.3 AU cranking orbit is not critical. Preliminary analysis was conducted using circular-coplanar transfer

spirals to the 0.3 AU circular cranking orbit. The characteristic acceleration of the solar sail was varied from 0.25 to 1.5 mm s⁻² and the resulting transfer times are shown in Figure 4.11.

The effect of increasing the launch excess energy (C_3) was investigated to reduce the spiral-down time to 0.3 AU, since any small savings on the substantial trip-time to Asteroid 2001 QP153 would clearly be of benefit. A characteristic acceleration of 0.5 mm s⁻² has been selected for the outbound trajectory (see Section 4.2.4). The effect of increasing the launch C_3 was investigated for this characteristic acceleration and is shown in Figure 4.12. The effect of varying characteristic acceleration on positive C_3 inward transfers was investigated in Chapter 3 for transfer to Mercury, and the results here were expected to be comparable. The single acceleration chosen will be representative of what savings can be achieved using excess launcher performance. A Soyuz-Fregat launcher was baselined, which can deliver a 485 kg solar sail spacecraft [Hughes *et al*, 2003, McInnes *et al*, 2003d] to a positive hyperbolic excess energy of $C_3 \sim 37 \text{ km}^2 \text{ s}^{-2}$. The approximate transfer time to the initial cranking orbit when using this launcher is thus 288 days, a saving of 46% over the zero hyperbolic excess transfer time.

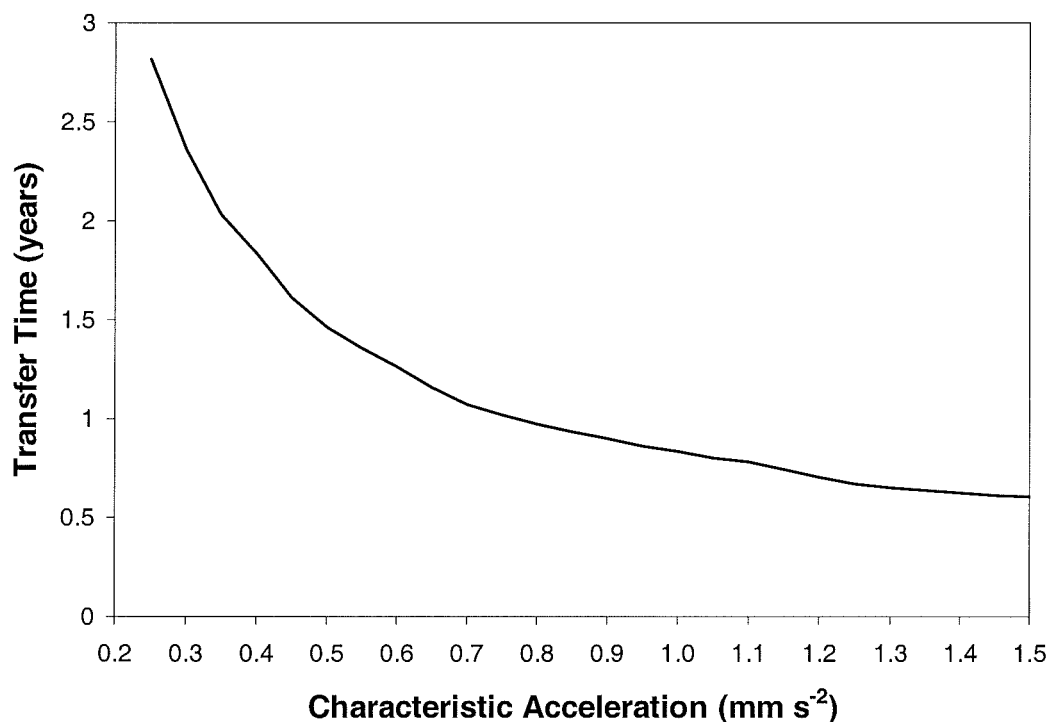


Figure 4.11: Earth to 0.3 AU cranking orbit transfer time ($C_3=0$)

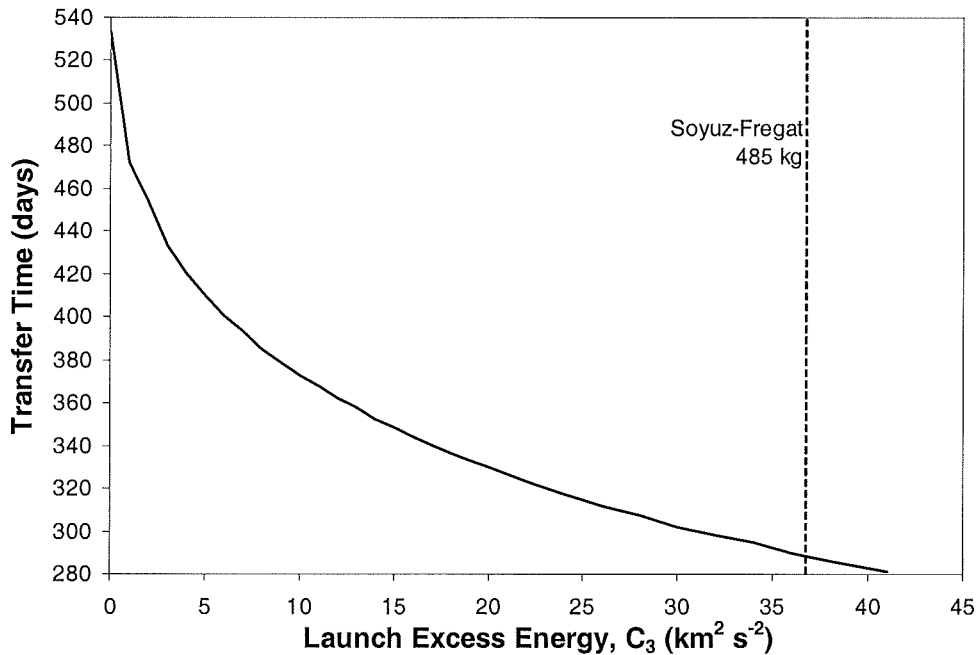


Figure 4.12: 0.5 mm s^{-2} positive C_3 Earth to 0.3 AU cranking orbit transfer time

4.2.3 Inclination Cranking

The approach used to raise the orbit inclination is based on an analytical control law that maximises the rate of change of inclination by switching the clock angle by 180° every half orbit. This technique has been employed by McInnes [1999] and also in combination with other control laws, to considerable advantage, by Otten and McInnes [1999]. The cone angle is fixed at an optimum angle of 35.26° , to provide maximum out-of-plane thrust, although this of course results in a radial force component. However, the final cranked orbit has a shape fairly close to the initial orbit. The control laws are shown mathematically in Eq. 4.1 and 4.2, and were incorporated into a program that integrated the variational equations of motion using a 4th order Runge-Kutta method with an inclination termination tolerance set at 10^{-3} . It should be noted here that the opposite mode of cranking down from an inclined orbit to the ecliptic plane is possible by reversing the sign of the clock angle control law, as required for the return phase of the mission. For a given inclination change, the time required to effect that change is the same for cranking up or down. In Eq. 4.2, *sign* is defined as plus or minus one, depending on the sign of the cosine term.

$$\text{Cone Angle: } \alpha = \tan^{-1}\left(\frac{1}{\sqrt{2}}\right) \quad [4.1]$$

$$\text{Clock Angle: } \delta = (\pi/2)\{1 - \text{sign}[\cos(\omega + f)]\} \quad [4.2]$$

The effect of the sail characteristic acceleration and final cranked orbit inclination on cranking time was investigated using the control laws defined above. This was a useful tool to determine the approximate trip times to a range of asteroids, before selection of 2001 QP 153 [McInnes, *et al*, 2003d], since analytical cranking spirals could be generated quickly and easily. The trip time dependence is shown graphically in Figure 4.13, and alternatively in Figure 4.14.

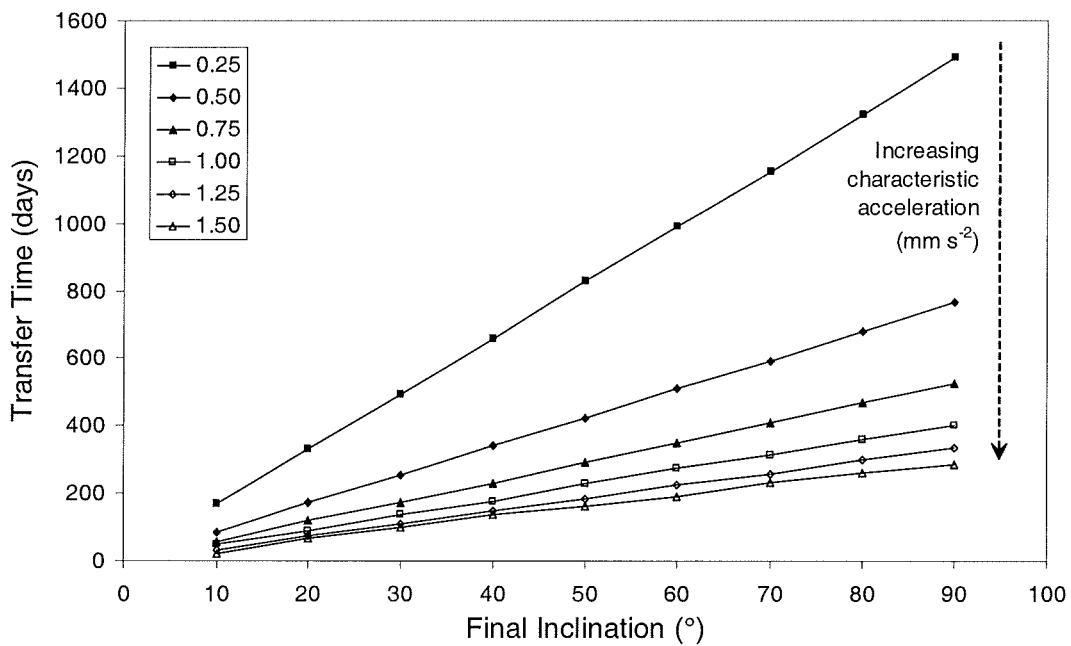


Figure 4.13: Cranking time against inclination change

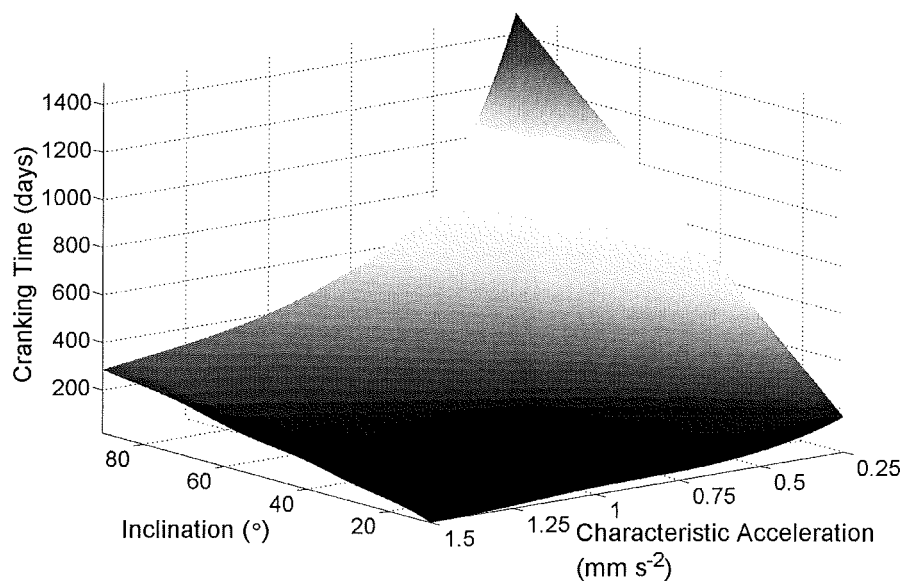


Figure 4.14: Crank time against characteristic acceleration and inclination change

4.2.4 Cranking Orbit to/from Ellipse

Once in the 0.3 AU orbit, cranked up to the same inclination as the target asteroid, the sail can perform a minimum-time spiral to the asteroid. Once the asteroid characterisation and science survey is complete, and a landing site selected, sample acquisition can be accomplished. After the sample canister is re-attached to the carrier, the sail can then the spiral back from the elliptical asteroid orbit to the inclined cranking orbit, to begin the crank-down. For simplicity, this is accomplished in the same plane. In addition, to satisfy thermal constraints, a lower limit of 0.3 AU was specified as an inequality constraint for the in-plane optimisation. NPSOL was used, but now the final boundary constraints were formulated as a combination of the final orbital element errors. Only the semi-major axis, eccentricity, and inclination (constant) need be constrained.

A critical concept which was discovered was that the optimal outbound and inbound trajectories were *symmetric*, as has been observed previously for circle-to-circle transfers. Once a solution was found for an outbound spiral, the cone angle profile could be reversed and inverted to propagate the trajectory in the opposite sense. The final position on the asteroid orbit in relation to the line of apsides also had to be taken into account, with the trajectory in the return direction having an initial departure position symmetric about the line of apsides of the asteroid orbit. For example, if arrival at the asteroid orbit occurred a certain angular distance prior to perihelion (or aphelion), then the symmetrical return trajectory with the same transfer-time and reverse-negative cone angle profile, would need to depart that *same* angular distance *beyond* perihelion (or aphelion). The 2001 QP153 arrival and departure dates were defined to be fixed relative to an Asteroid-Earth close-approach on August 8, 2017 [McInnes *et al*, 2003d], so in this way a true anomaly scan can be conducted based on the return trajectory, from 0 to 360° about the asteroid's orbit for both the outbound characteristic acceleration of 0.5 mm s^{-2} and return acceleration of 0.64 mm s^{-2} . It is noted that the characteristic acceleration increases for the return journey, since the lander has been jettisoned [McInnes *et al*, 2003d].

Low performance solar sail transfers from circular orbits to elliptical orbits typically have several revolutions and simple logarithmic spiral or manually-visualised initial guesses generally do not suffice. The larger number of control nodes also means that the problem does not lend itself well to a Genetic Algorithm

solution, which was unsuccessful in this application. Therefore, an alternative approach was necessary. Blended analytical control laws have been applied to planet-centred manoeuvres for solar sails to good effect, due to the extremely large number of revolutions involved [Macdonald and McInnes, 2001, Macdonald, 2005]. Similar control laws have been developed and applied to heliocentric trajectories, and although locally-(sub)optimal results are produced, they can be used for generating very robust initial guesses for non-linear programming based optimisers such as NPSOL [Otten and McInnes, 1999]. For this thesis, initial guesses were generated by blending the semi-major axis and eccentricity control laws, while the final argument of perihelion could be matched by selecting the correct departure true anomaly. The blending of the semi-major axis control law and eccentricity control law is accomplished by weighting the control laws depending on the errors between the instantaneous and desired orbital elements. In addition, these control law weighting functions had extra weighting coefficients applied according to the particular transfer problem. In this case, the semi-major axis weighting function coefficient was 0.7 with the eccentricity weighting function coefficient set at 1.0. For more details on the heliocentric blended control laws and weighting functions used, refer to Section 1.7 and Otten and McInnes [1999].

In the first instance, an initial guess was generated for a transfer from 0.3 AU to the asteroid orbit, with open final argument of perihelion. This trajectory was then sampled, and discretised, at 51 nodes and passed to NPSOL, which was executed with an appropriate adjustment of the transfer time bounds, to obtain the best minimum possible. Since the transfer was to an open final true anomaly and argument of perihelion, this was the departure date optimal trajectory. The method has been used to generate trajectories to a number of different asteroids for approximate trip time assessment, to enable selection of this target asteroid [McInnes *et al*, 2003d]. The departure date optimal optimisation from the 0.3 AU circular orbit to the selected asteroid 2001 QP153 has been performed for a range of characteristic accelerations to help in selecting the required sail performance to enable an acceptable transfer time. By approximate analysis of the feasible range of accelerations, along with the selected payload mass and sail assembly loading, the performance range was taken to be 0.3 mm s^{-2} to 0.7 mm s^{-2} [McInnes *et al*, 2003d]. It is also recalled that the outbound and return transfer times are equivalent, with the

appropriate initial true anomaly. The variation of the total 3-phase outbound approximate trip time is shown in Figure 4.15. This includes the crank up times from Section 4.2.3 and also the circular coplanar spirals between the Earth and 0.3 AU, from Section 4.2.2. With the outbound acceleration selected, the return acceleration can be calculated from a given payload mass, upon jettison of the lander and sample acquisition system [McInnes *et al*, 2003d]. If the outbound acceleration and the respective return value is then selected from the curve in Figure 4.15, an approximate, total mission duration can be obtained. It can be seen that specifying a characteristic acceleration of 0.5 mm s^{-2} for the outbound leg and 0.64 mm s^{-2} for the return (for the mission considered in McInnes *et al* [2003d]), yields an approximate total mission duration of order 6.63 years. This will of course be prolonged by any waiting necessary in the 0.3 AU orbit for the correct ascending node and/or argument of perihelion alignment. However, since the 0.3 AU orbit period is only 60 days, this waiting period is negligible. The use of the Soyuz ST-Fregat to $C_3 > 0$ can potentially reduce these trip times further.

The optimal inclined 0.3 AU to asteroid transfer was optimised using the blending/NPSOL method (with just a and e constrained) yielding a solution of 387.9 days. The initial true anomaly was adjusted by trial and error until the final argument of perihelion was matched with the asteroid. The correct initial true anomaly on the inclined 0.3 AU orbit was found to be 191.2° , with a final true anomaly on the asteroid orbit of 112.9° . For a return trajectory with the cone angles reversed and inverted, the correct initial true anomaly on the asteroid orbit would therefore be 112.9° *before* perihelion (i.e. symmetric about the line of apsides), at an asteroid true anomaly of 247.1° . Since problems arise in selecting the correct true anomaly for argument of perihelion satisfaction, it was deemed necessary to perform return departure date scans by varying the initial true anomaly on the asteroid orbit from zero to 360° . The final argument of perihelion on the 0.3 AU orbit is undefined, since the eccentricity is zero. This means that a database of trajectories can be generated for rendezvous with, or departure from, any asteroid position. The departure/arrival date scan only needs to be conducted over one period of 2001 QP153 since the intermediate, short-period, 0.3 AU cranking orbit essentially removes the sensitivity to phasing with the Earth. Return trip scans were conducted for both the outbound characteristic acceleration of 0.5 mm s^{-2} and the return

acceleration of 0.64 mm s^{-2} , bearing in mind the symmetry of the trajectories. The return trip scans are shown in Figure 4.16 and 4.17, with the desired 2001 QP153 arrival and departure dates noted as the corresponding angular positions in the epoch of the close approach. The desired arrival date is February 8, 2017, six months prior to an Earth close approach on August 8, 2017, at an asteroid true anomaly of 224.4° . The close approach is a key mission milestone since it may be possible to have near real-time commanding of the lander during sample acquisition. Arrival is 44.4° after asteroid aphelion. In order for a reversed and inverted, ellipse-circle cone angle profile to produce a circle-ellipse trajectory that arrives at the asteroid at the correct true anomaly, the initial guess used must be the ellipse-circle trajectory that departs the asteroid orbit at a true anomaly of 135.6° , as shown in Figure 4.16. The desired circle-ellipse solution is therefore the mirror image about the asteroid line of apsides. The ellipse-circle trajectory would arrive on the 0.3 AU orbit at an angle of 224.4° from the ascending node (common to both circle and ellipse). If this angle is reflected about the asteroid line of apsides, the initial 0.3 AU orbit circle-ellipse true anomaly is then 243.2° from the ascending node. This reversed-inverted cone angle profile departs the 0.3 AU circular orbit 243.2° after the ascending node passage on November 24, 2015 and arrives 442 days later, six months prior to the Earth close approach. For the actual 0.64 mm s^{-2} return scan in Figure 4.17 it can be seen that the desired departure date (2 weeks after close approach) is near to a maximum in trip time, but this is not too severe a penalty, since it is only 33 days from the departure date minimum of 318 days.

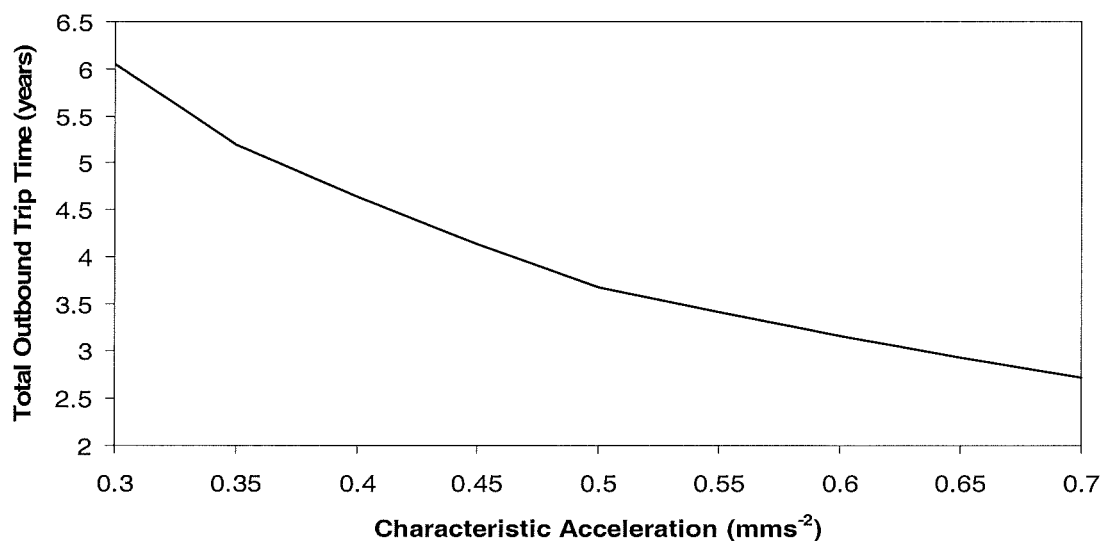


Figure 4.15: Departure date optimal total one-way transfer time to 2001 QP153

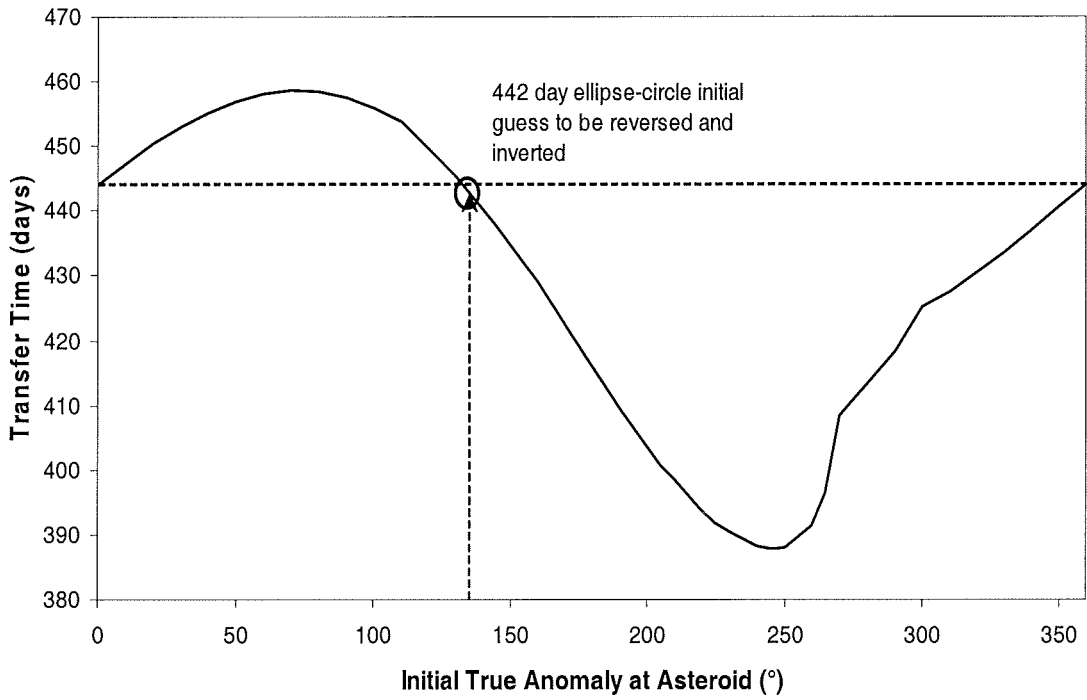


Figure 4.16: 0.5 mm s^{-2} Asteroid-0.3 AU departure true anomaly scan

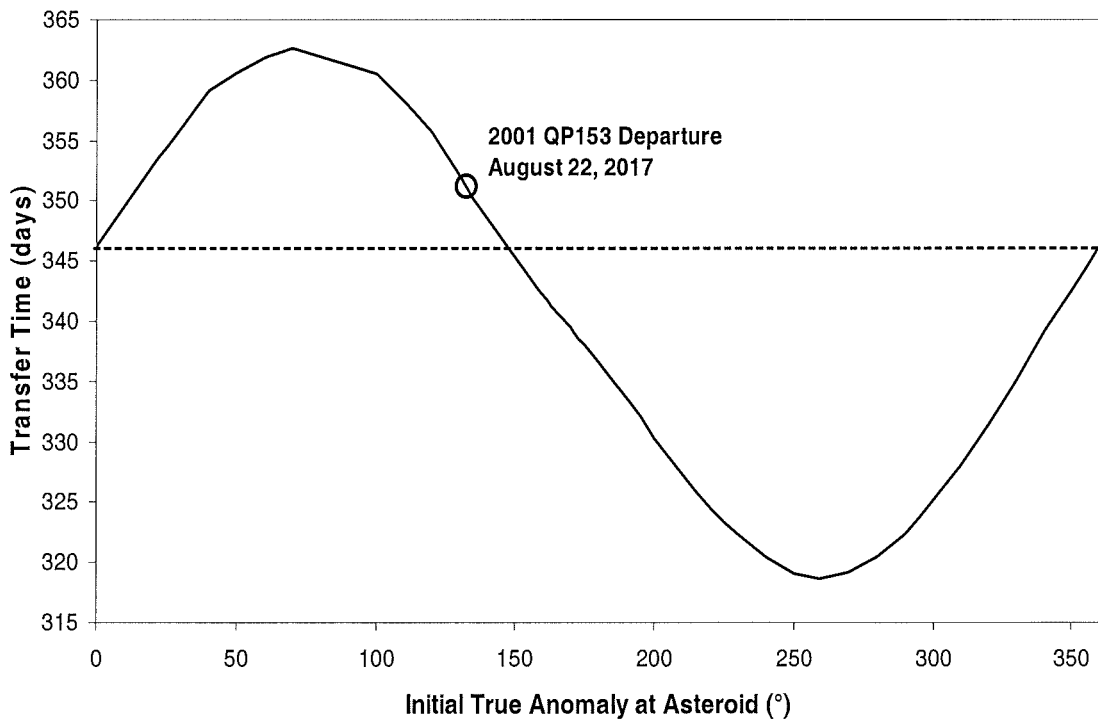


Figure 4.17: 0.64 mm s^{-2} Asteroid-0.3 AU departure true anomaly scan

4.2.5 Earth – Asteroid Phases

Since both the spiral to and from 0.3 AU and the cranking phases are dependent on the departure and arrival date on the cranked 0.3 AU orbit, all dates have been obtained by working back from the asteroid-0.3 AU spirals.

The comparatively inexpensive Soyuz ST–Fregat launch vehicle has been selected not only because of its cost, but because it can enable a 0.7 year reduction in transfer time [McInnes *et al*, 2003d]. After working back from the asteroid arrival date, an Earth launch date of December 14, 2013 to a hyperbolic excess energy of $C_3=37 \text{ km}^2 \text{ s}^{-2}$ is found. The large positive C_3 means that the solar sail can spiral down to a 0.3 AU circular orbit in just 286 days. Arrival at the cranking orbit is on September 26, 2014. The trajectory is shown in Figure 4.18 for a much reduced 2.3 revolution trajectory. Figure 4.19 shows the oscillatory cone angle profile and, since this a coplanar transfer, the clock angle is 90° (entirely in-plane thrusting). Figure 4.20 shows the temporal evolution of the orbital elements, where the inclination varies by a negligible amount due to numerical errors, but is included for completeness. In Figure 4.21 it can be seen that the sail film temperature does not exceed 500 K (theoretical maximum at 0.3 AU).

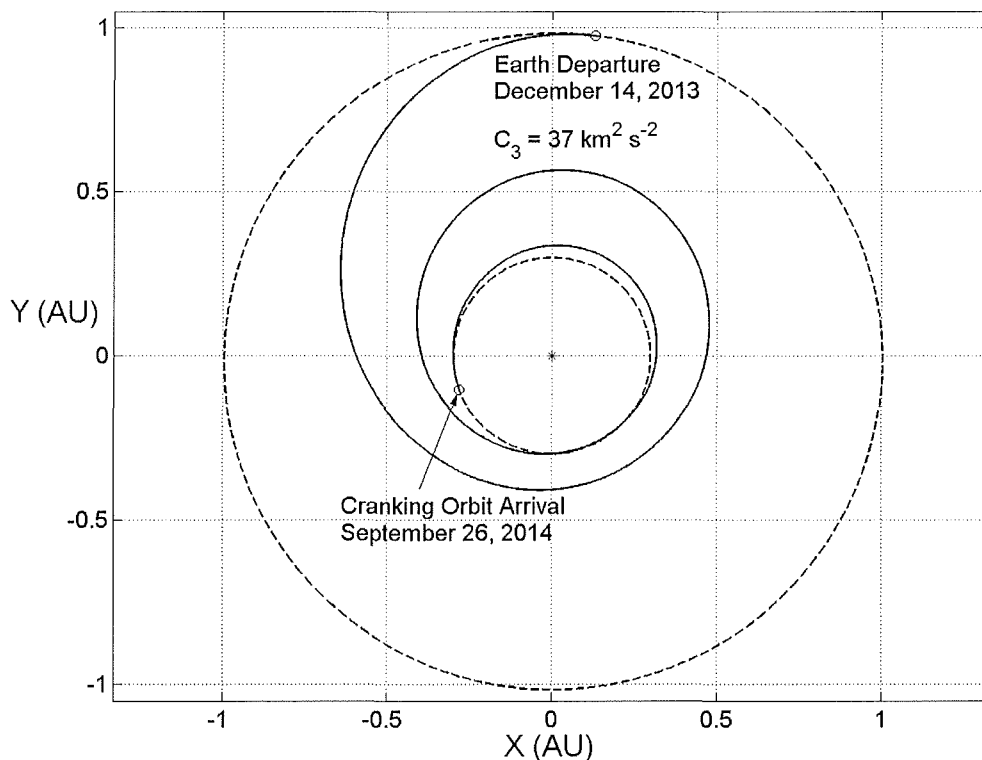


Figure 4.18: 0.5 mm s^{-2} Earth-cranking orbit spiral with $C_3=37 \text{ km}^2 \text{ s}^{-2}$

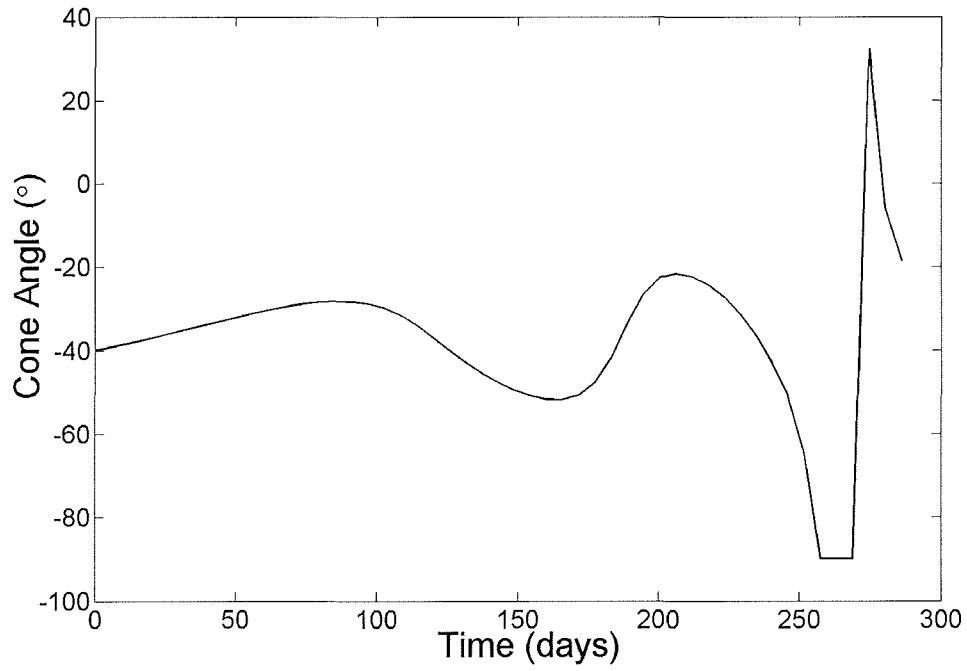


Figure 4.19: Earth-cranking orbit cone angle profile

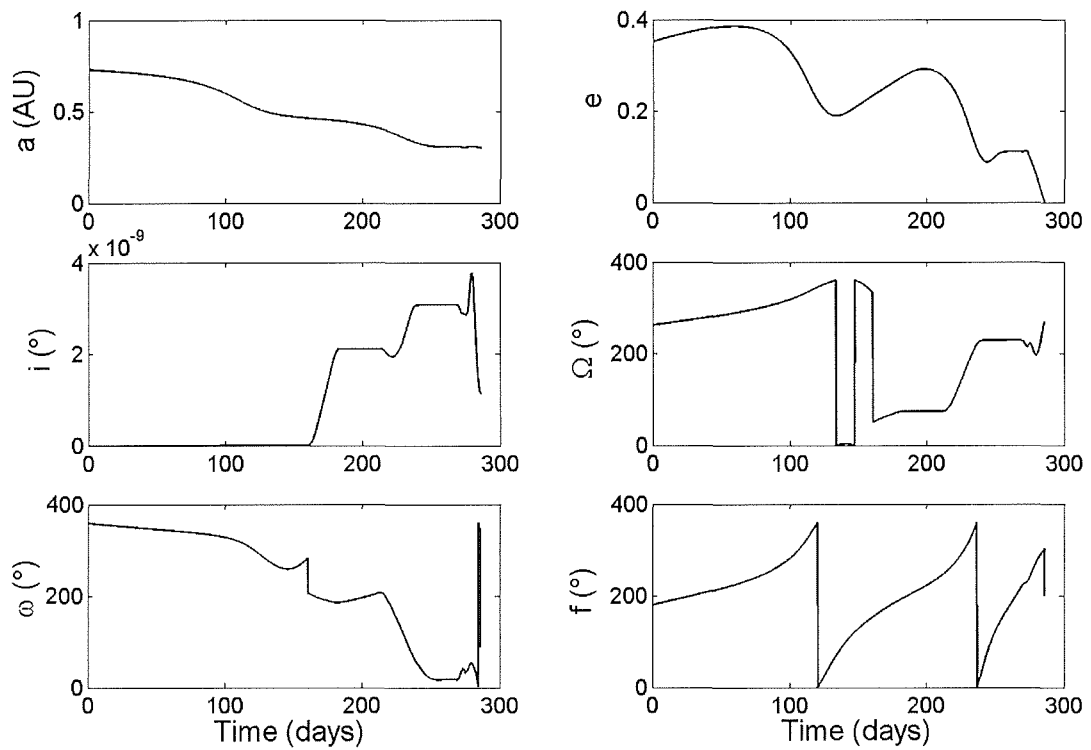


Figure 4.20: Earth-cranking orbit orbital element evolution

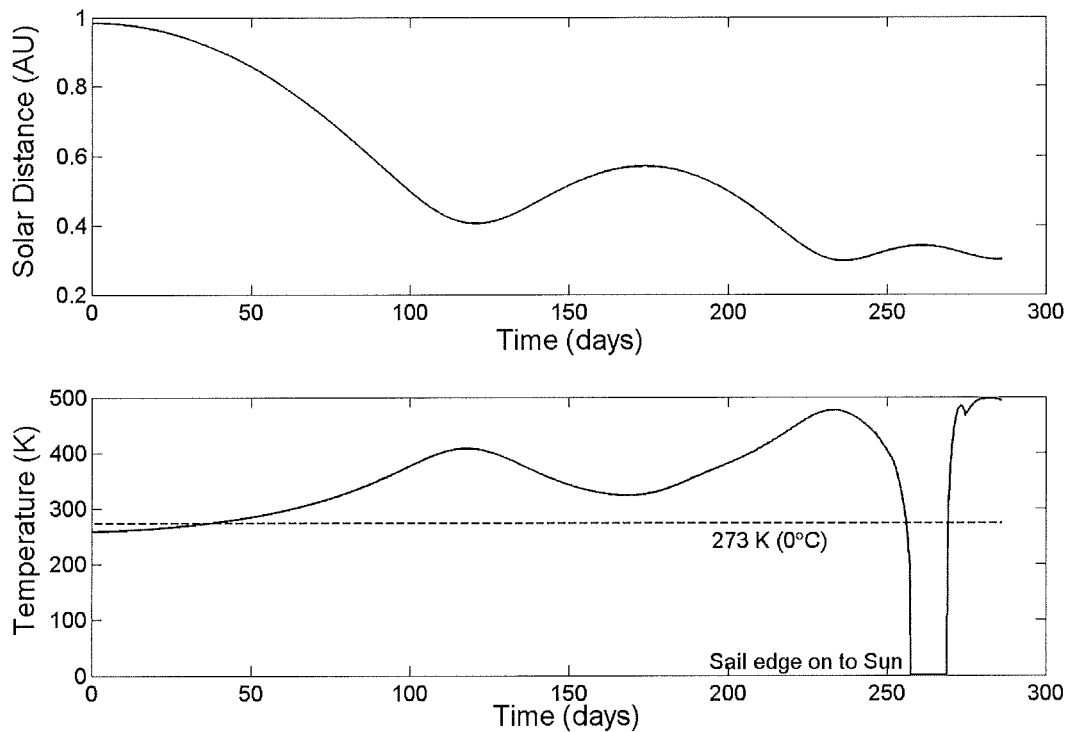


Figure 4.21: Earth-cranking orbit heliocentric distance and sail film temperature

For the second phase, the analytical control law method described in Section 4.2.3 has been employed to crank up the orbital inclination to 50.1° with the ascending node equal to that of 2001 QP153. With a characteristic acceleration of 0.5 mm s^{-2} , this cranking process takes of order 424 days to reach the correct asteroid inclination. The trajectory is shown in Figure 4.22 for $6 \frac{1}{2}$ crank revolutions. Figure 4.23 shows the cone and clock angle (up-down discrete switching) profiles along with the temporal change in inclination.

For the third phase, departure from the inclined cranking orbit occurs on November 24, 2015. The sail spirals out in 442 days to rendezvous with asteroid 2001 QP153 on February 8, 2017. Figure 4.24 shows the trajectory, which executes 2.7 revolutions about the Sun. Figure 4.25 shows the cone angle profile only, since the transfer is entirely in-plane. The inclination and right ascension of ascending node do not change, and Figure 4.26 shows the in-plane temporal orbital element evolution. The variation of solar distance and equilibrium sail film temperature are shown in Figure 4.27.

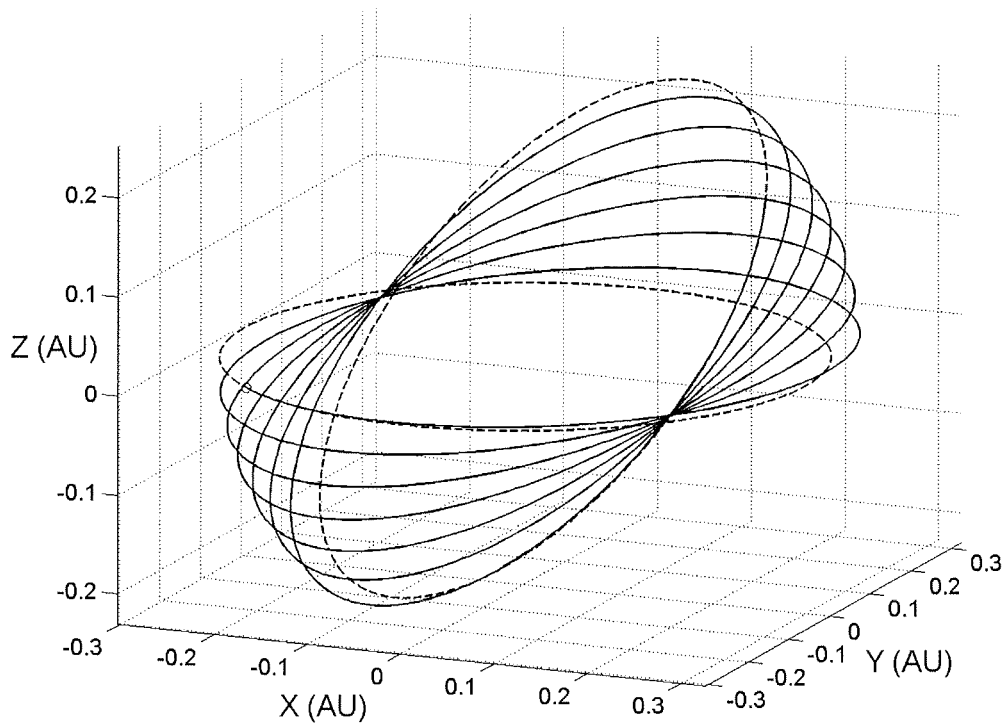


Figure 4.22: 0.5 mm s^{-2} inclination crank-up trajectory

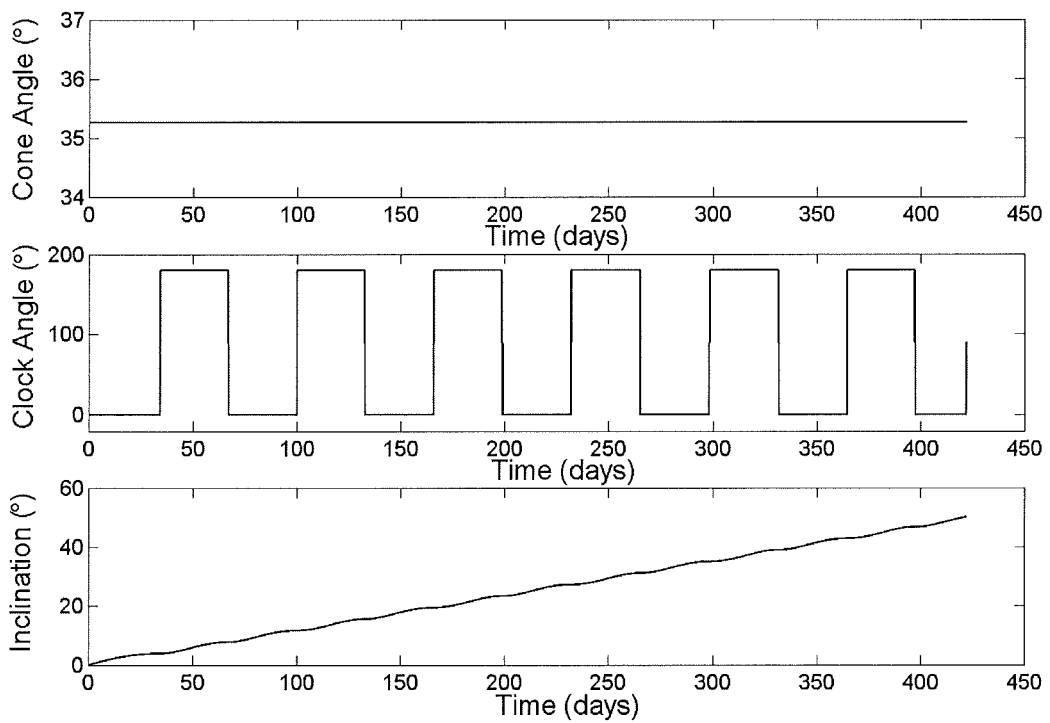


Figure 4.23: Crank-up control angle profiles and inclination change

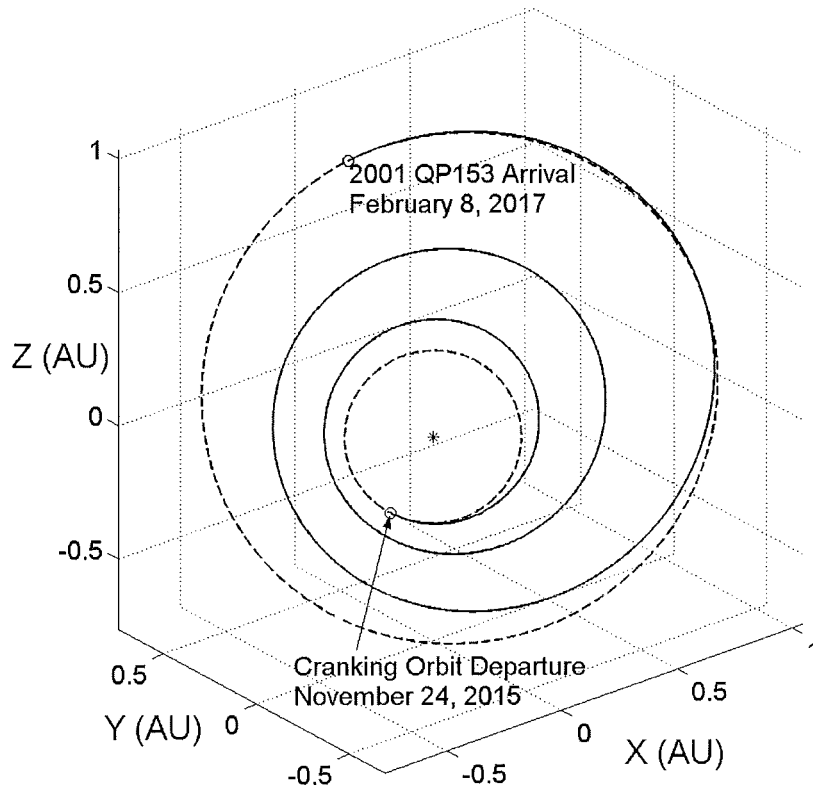


Figure 4.24: 0.5 mm s^{-2} cranking orbit-asteroid rendezvous

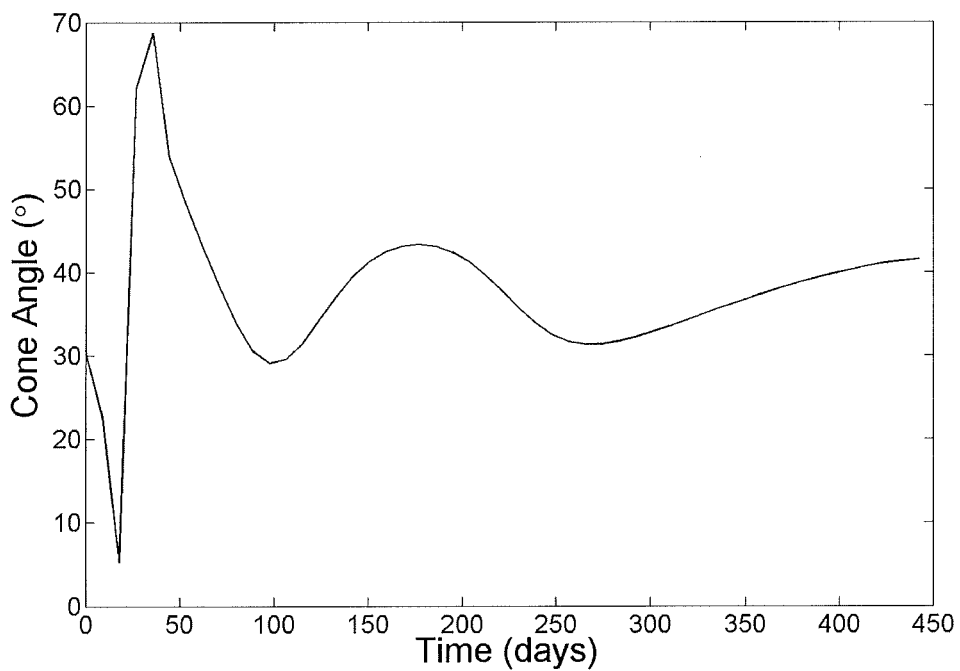


Figure 4.25: Cranking orbit-asteroid rendezvous cone angle profile

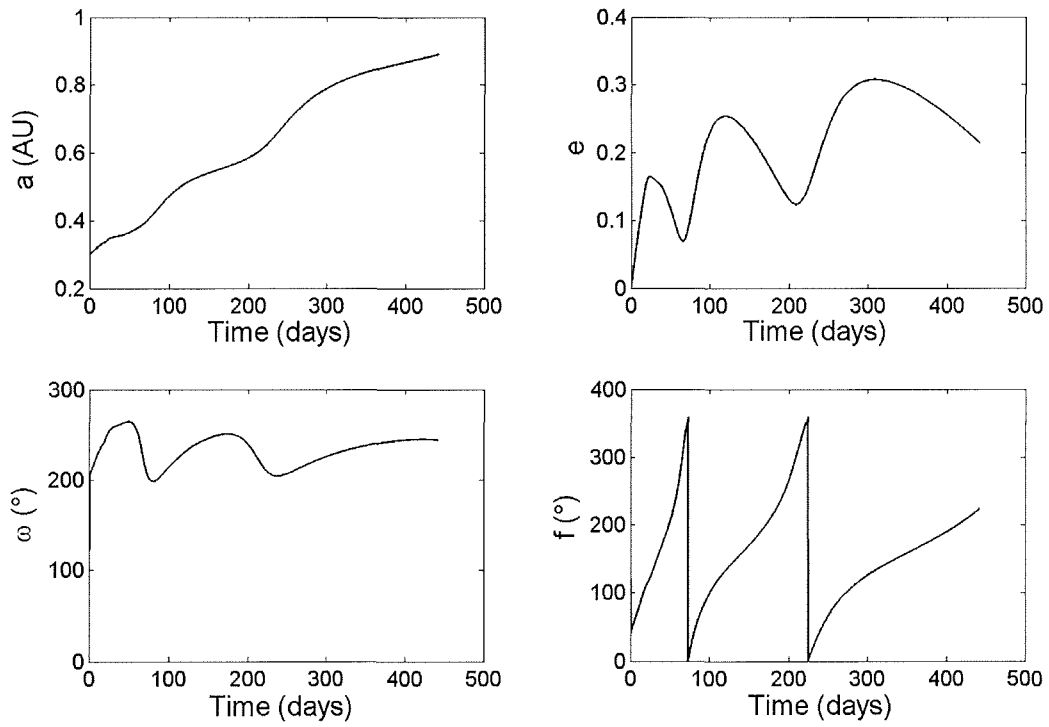


Figure 4.26: Cranking orbit-asteroid rendezvous orbital element evolution

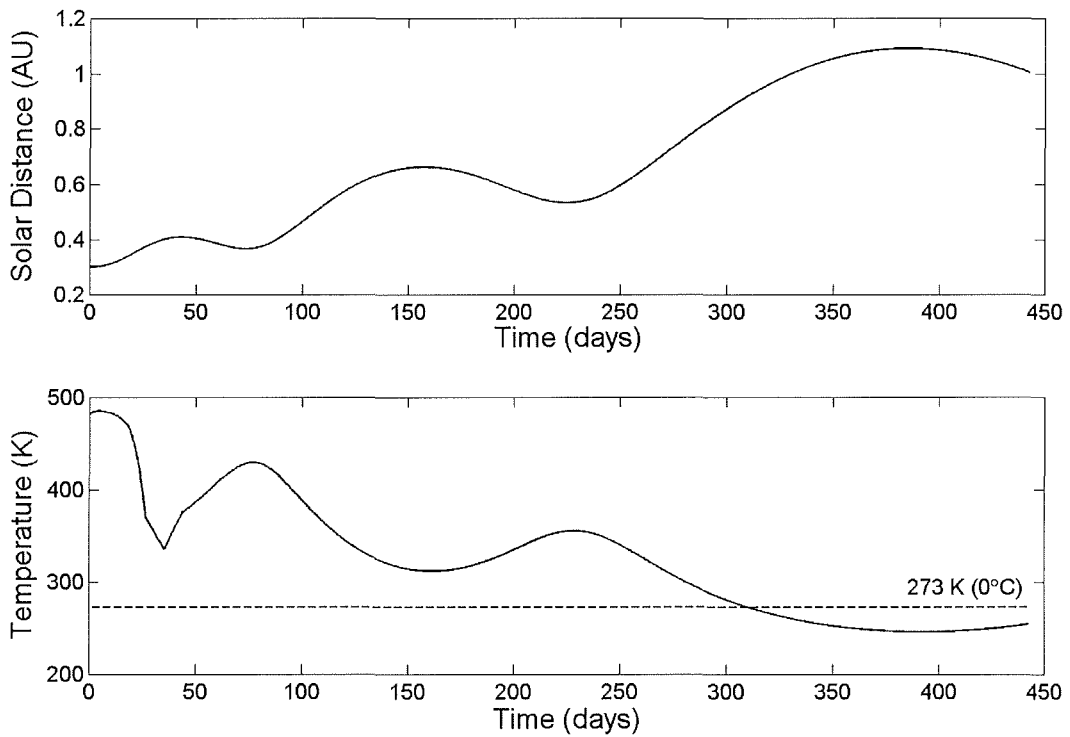


Figure 4.27: Cranking orbit-asteroid heliocentric distance and sail film temperature

4.2.6 Asteroid – Earth Phases

After sample acquisition and asteroid escape, the heliocentric return phase is initiated on August 22, 2017 (two weeks after the close approach of the asteroid to Earth) at a true anomaly of 132.2° . The solar sail then performs a minimum-time spiral down to the 0.3 AU inclined cranking orbit in 351 days, as shown in Figure 4.28. Arrival at 0.3 AU occurs on August 9, 2018 after almost 2 revolutions. Figure 4.29 shows the cone angle profile for the coplanar transfer. The temporal evolution of the planar orbital elements is shown in Figure 4.30. Figure 4.31 shows the heliocentric distance and sail film temperature variation.

After reaching the inclined orbit at 0.3 AU, the sail then executes the crank-down manoeuvre, which takes 340 days to reach zero inclination after almost 5 revolutions. The trajectory is shown in Figure 4.32 and the control profiles are shown in Figure 4.33, along with the reduction in orbit inclination.

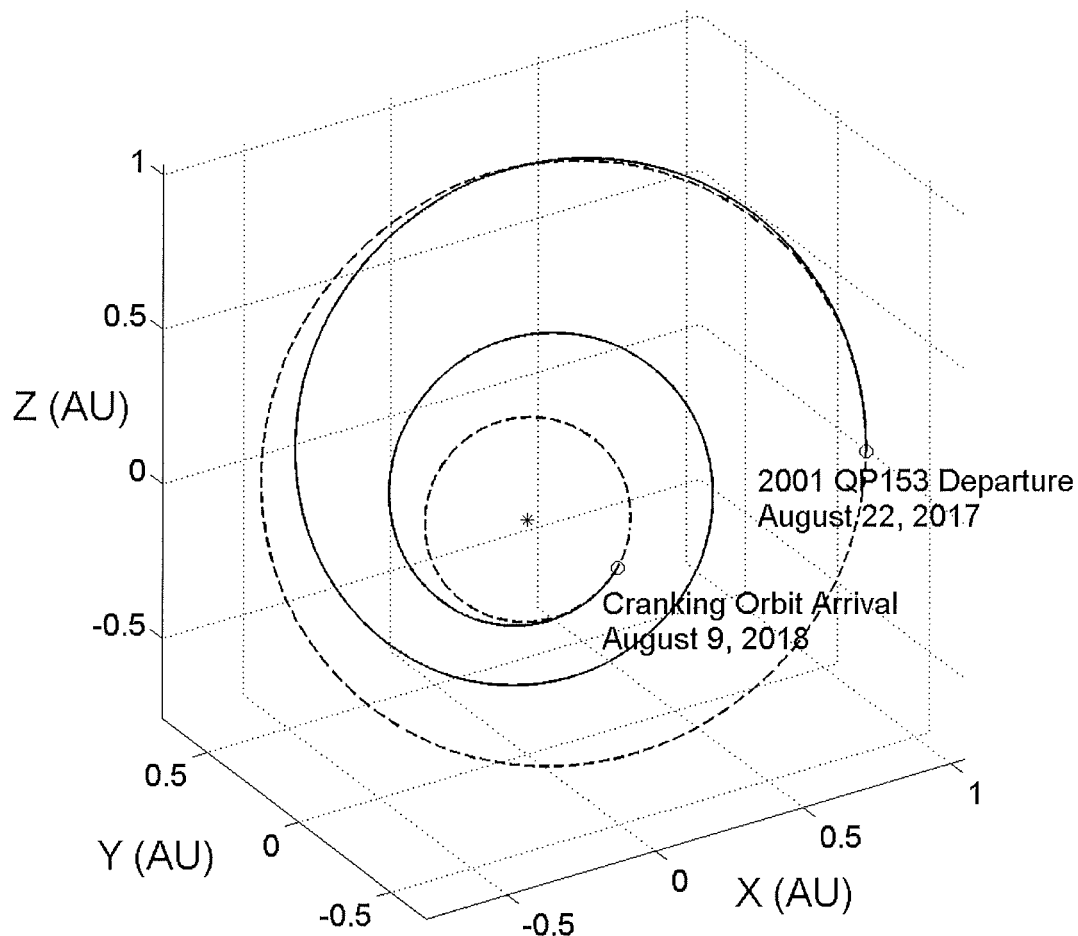


Figure 4.28: 0.64 mm s^{-2} asteroid-cranking orbit transfer

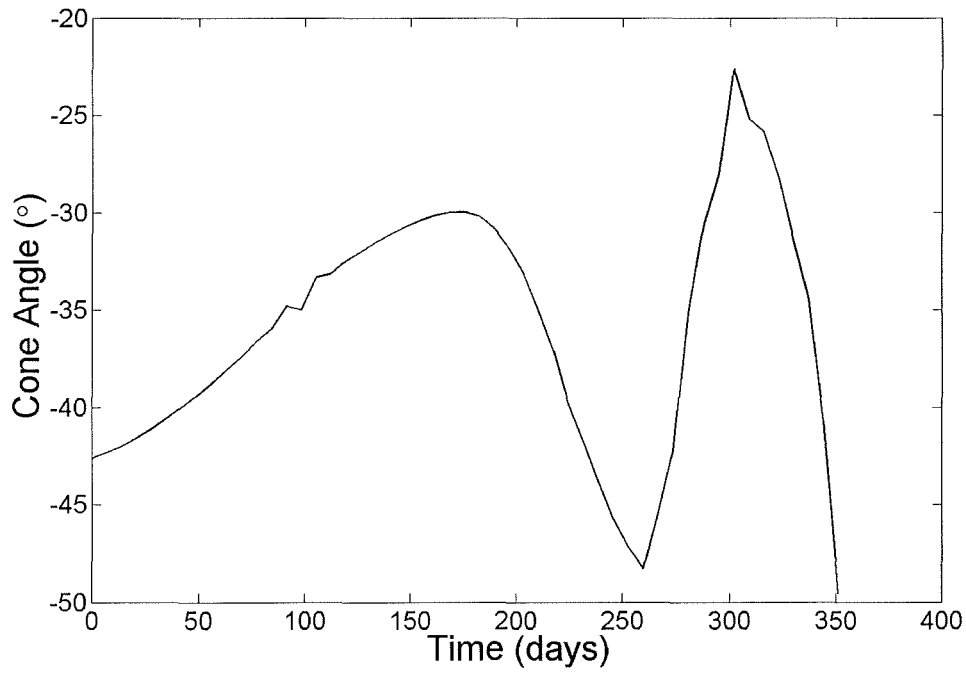


Figure 4.29: Asteroid-cranking orbit transfer cone angle profile

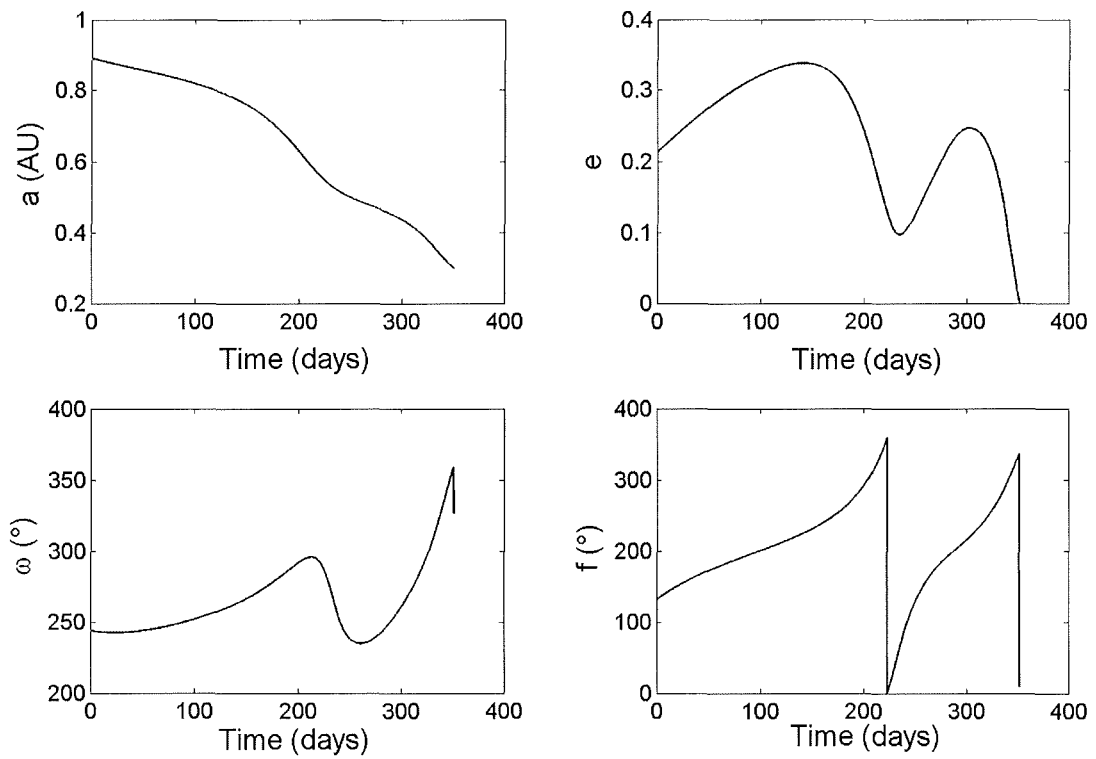


Figure 4.30: Asteroid-cranking orbit transfer orbital element evolution

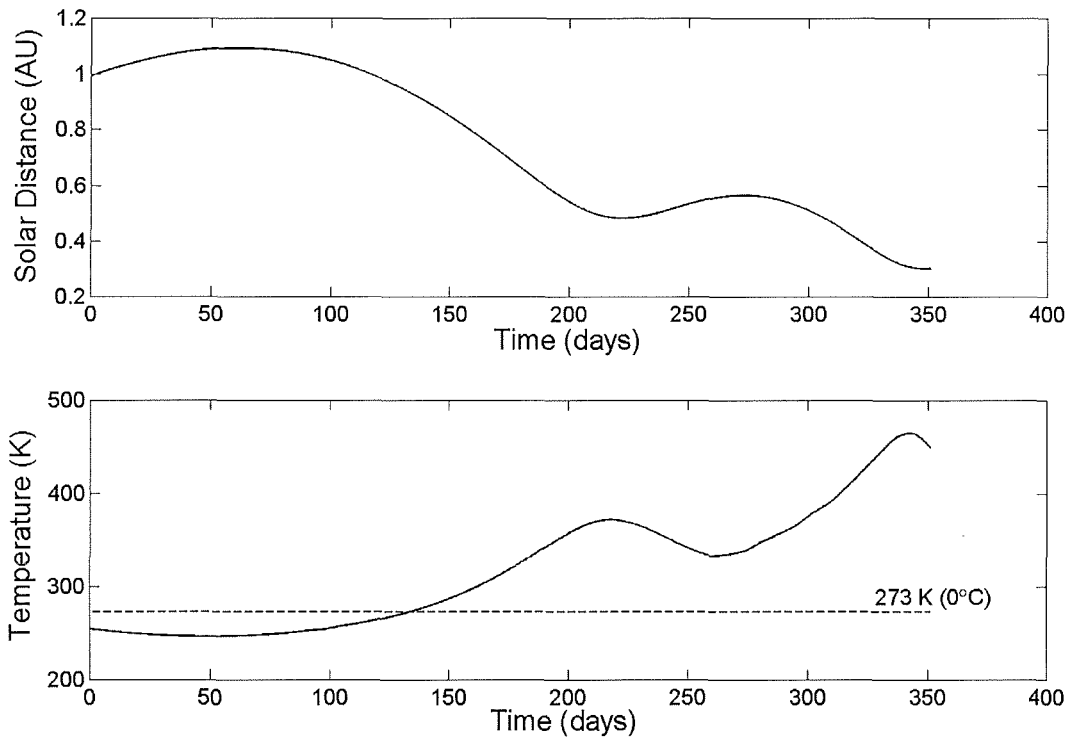


Figure 4.31: Asteroid-cranking orbit transfer heliocentric distance and sail film temperature

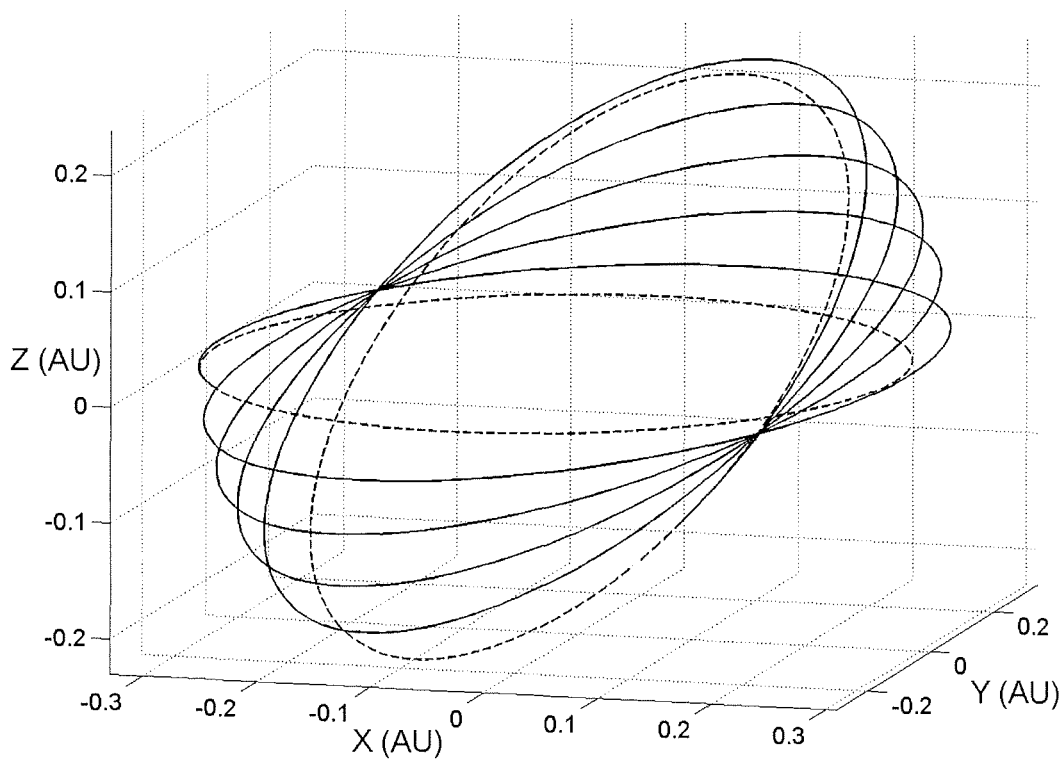


Figure 4.32: 0.64 mm s^{-2} inclination crank-down trajectory

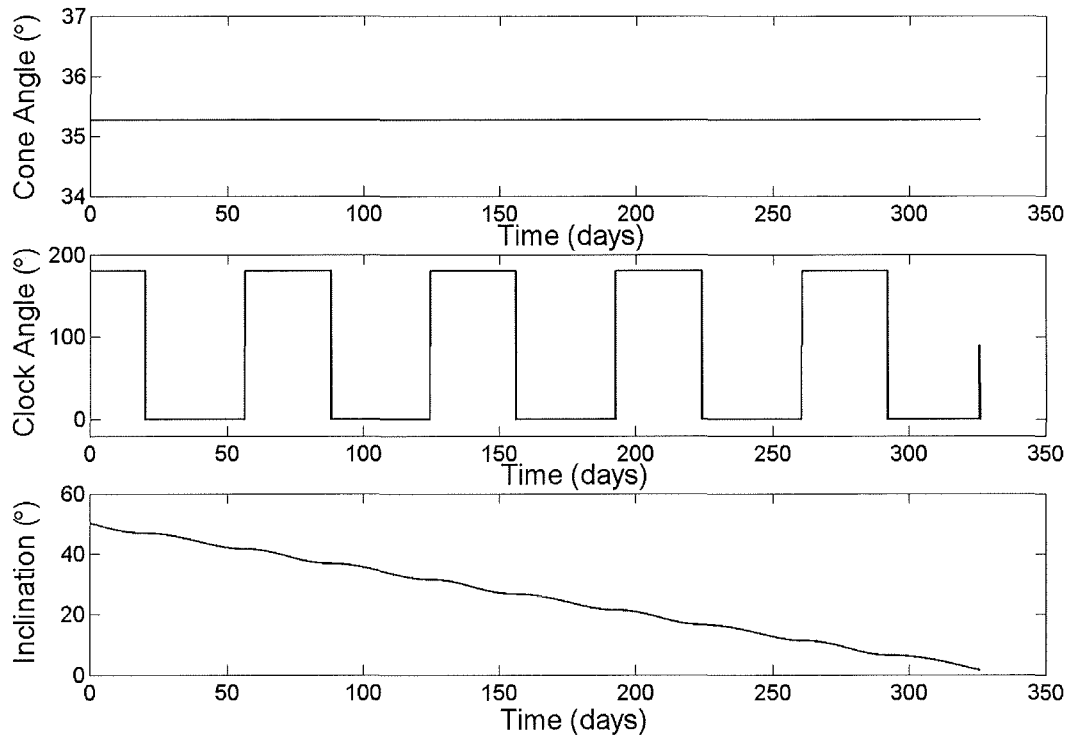


Figure 4.33: Crank-down control angles profiles and inclination change

For the final phase, the departure from the final 0.3 AU cranking orbit in the ecliptic plane occurs on July 15, 2019. From here, the solar sail then returns the sample back to the Earth in 438 days, in under $2\frac{1}{2}$ revolutions with zero hyperbolic excess velocity ($C_3=0$), on September 25, 2020, as shown in Figure 4.34. The control angle profiles are shown in Figure 4.35, with a *very* small out-of-plane component due to the final cranking orbit not quite reaching the ecliptic plane. Figure 4.36 shows the temporal evolution of the orbital elements, with the heliocentric distance and sail film temperature shown in Figure 4.37.

To summarise, there are six heliocentric phases to the trajectory, with the asteroid centred characterisation and sample acquisition phase in the middle [McInnes *et al*, 2003d]. The spacecraft is launched on a Soyuz ST-Fregat ($C_3 = 37 \text{ km}^2 \text{ s}^{-2}$) on December 14, 2013, and the sample arrives back at the Earth on September 25, 2020. The total mission duration is therefore 6.78 years, a quite impressive trip time considering the complex trajectory, extremely high target orbit inclination and relatively modest sail size. Table 4.11 provides a summary of the mission timeline.

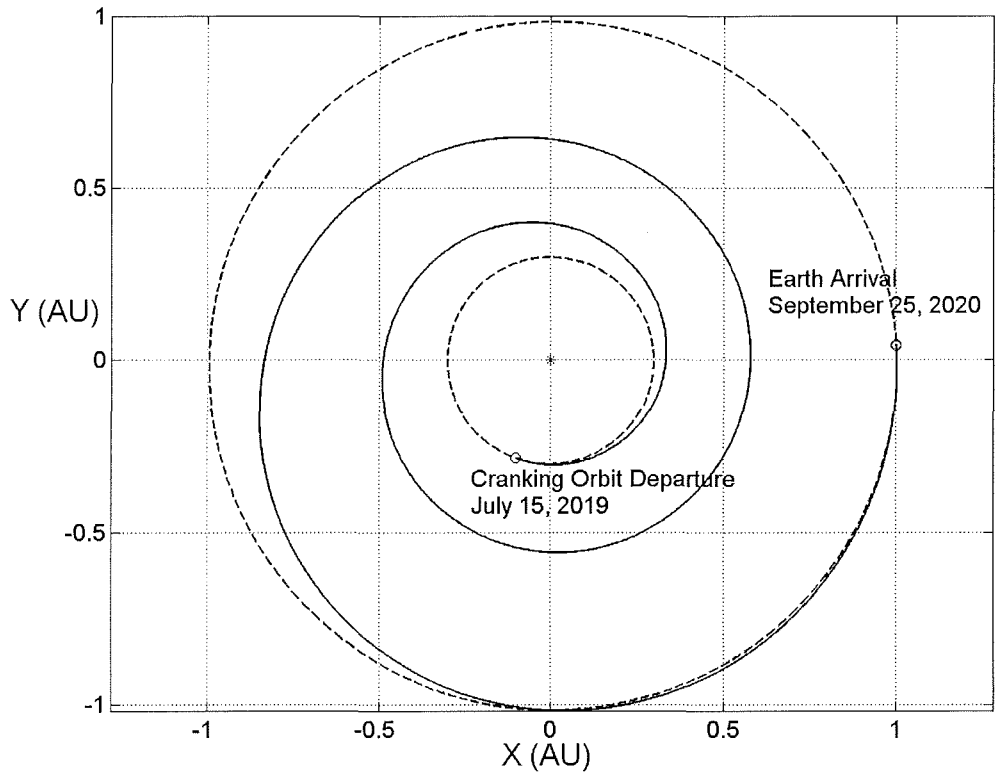


Figure 4.34: 0.64 mm s^{-2} cranking orbit-Earth spiral

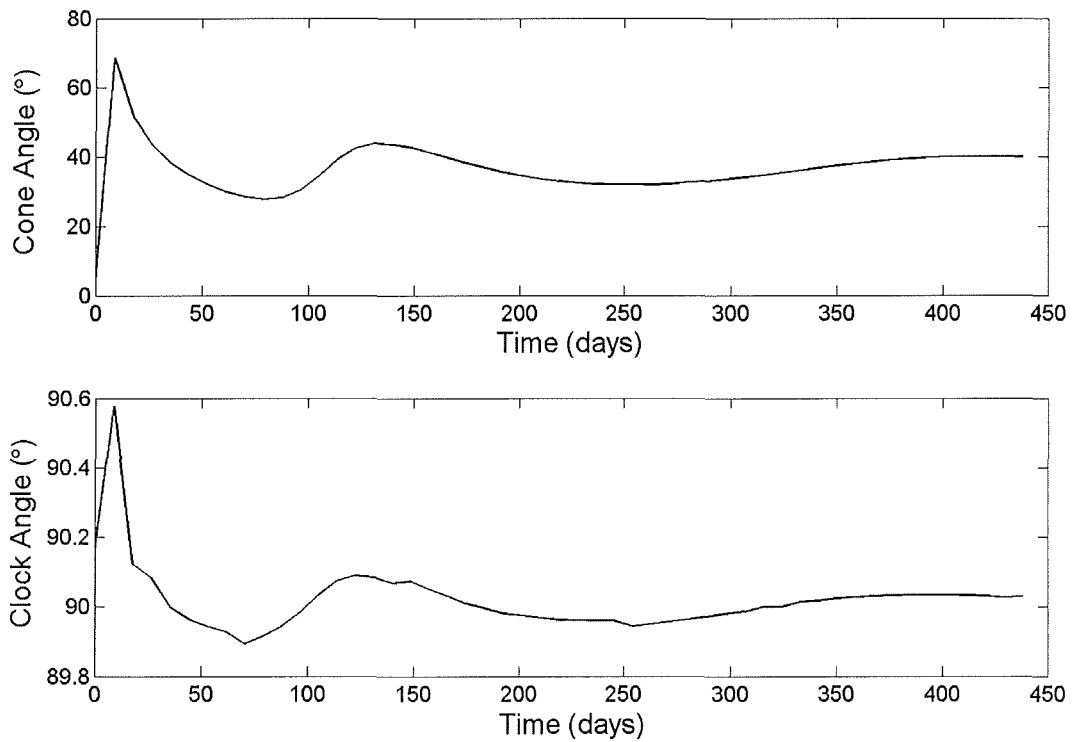


Figure 4.35: Cranking orbit-Earth control angle profiles

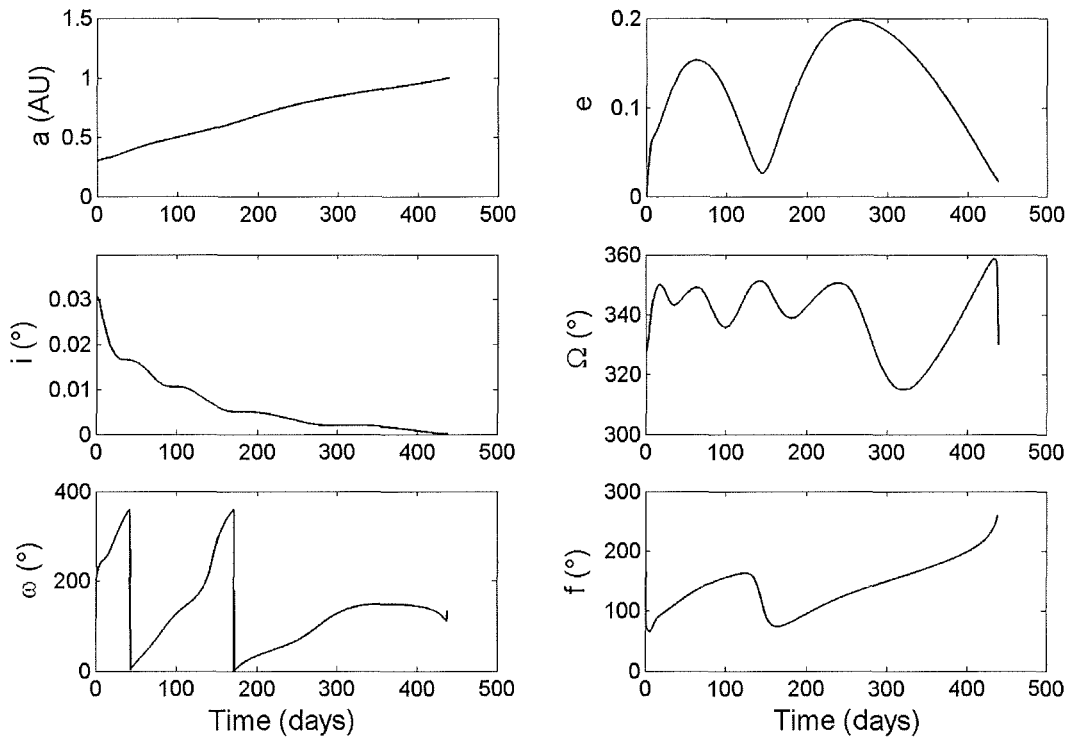


Figure 4.36: Cranking orbit-Earth orbital element evolution

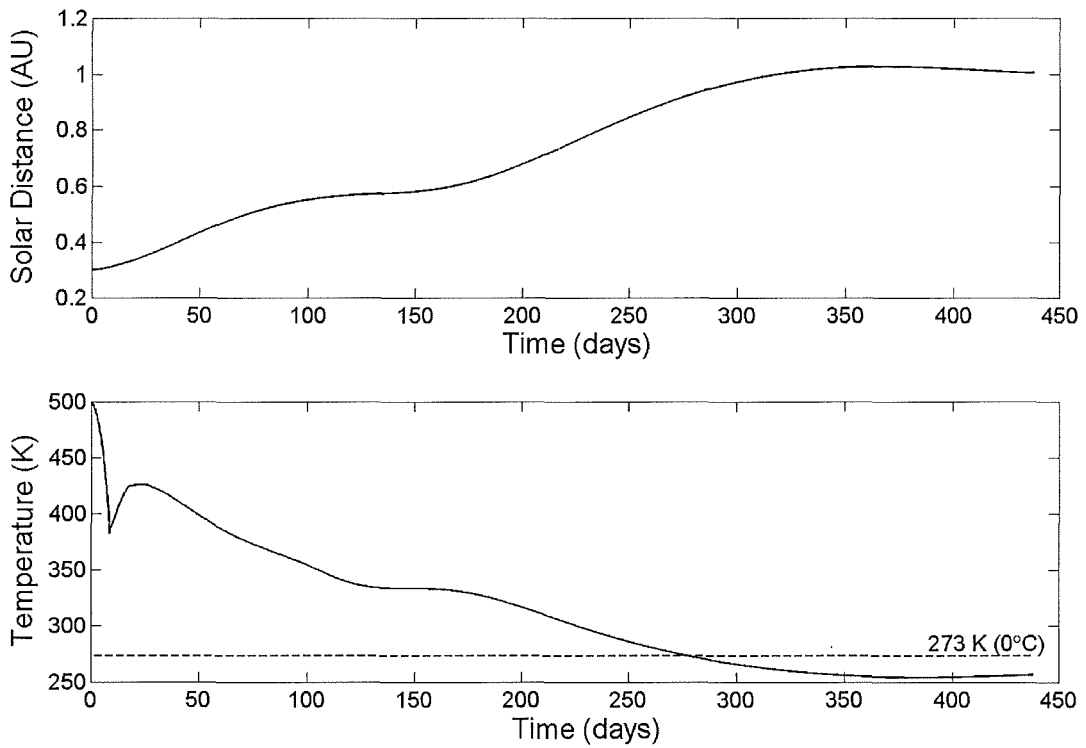


Figure 4.37: Cranking orbit-Earth heliocentric distance and sail film temperature

Event	Date / Duration
Soyuz ST–Fregat Launch ($C_3=37 \text{ km}^2 \text{ s}^{-2}$)	December 14, 2013
Earth – 0.3 AU spiral	0.78 years
Cranking orbit arrival	September 26, 2014
Crank-up manoeuvre	1.16 years
Cranking orbit departure	November 24, 2015
0.3 AU – 2001 QP153 spiral	1.21 years
2001 QP153 Arrival ($C_3 = 0$)	February 8, 2017
Earth close approach	August 8, 2017
2001 QP153 departure ($C_3 = 0$)	August 22, 2017
2001 QP153 – 0.3 AU spiral	0.96 years
Cranking orbit arrival	August 9, 2018
Crank-down manoeuvre	0.93 years
Cranking orbit departure	July 15, 2019
0.3 AU – Earth spiral	1.20 years
Earth arrival ($C_3 = 0$)	September 25, 2020
Total Mission Duration	6.78 years

Table 4.11: Asteroid Sample Return mission timeline

4.3 Summary and Discussion

Trajectories to a variety of small bodies have been generated, to demonstrate the high Δv capability and open-ended nature of solar sailing. Trajectories to the Short Period Comet Wirtanen have been produced, where it was found that a characteristic acceleration of 1.0 mm s^{-2} could enable a 68% reduction in trip-time and a 44% reduction in launch mass, over the original Rosetta mission.

An investigation of flyby missions to newly discovered Long Period Comets has been performed, with previous examples adopted for illustration. Primarily, trajectories to Hale-Bopp and others were produced, with high performance sails to flyby at perihelion, or at an orbit node. A descending node flyby of Hale-Bopp could have been accomplished using a characteristic acceleration of 2.0 mm s^{-2} in 270 days. The sail could then be returned to Earth for target reconfiguration to the next new LPC in 261 days or, alternatively, go on to flyby a second comet. Mission analysis for the Hale-Bopp opportunity revealed that a minimum characteristic acceleration of 0.36 mm s^{-2} would have enabled interception of Hale-Bopp with launch just after first discovery. With a cruise stage mass of 100 kg, the sail required would be $94 \times 94 \text{ m}$, with an assembly loading of 10 g m^{-2} . Although this technology level would not have been available at the time of Hale-Bopp apparition, it is of mid-term performance, and may be feasible in the near-future for future LPC apparitions.

Solar sails have been shown to be highly attractive for Main-belt asteroid rendezvous missions. Although trip-times would be quite long, due to the reduced solar radiation pressure at 2 AU, in principle, many asteroids could be visited. With a 1.0 mm s^{-2} sail, similar trip times to the NASA Dawn mission could be realised for rendezvous with Vesta and Ceres. Using the Dawn cruise stage with a sail assembly loading of 3.56 g m^{-2} , the launch mass could be reduced by 33%. The mission targets could also be extended to two further asteroids, for a rigorous 20 year quadruple asteroid survey.

Extensive analysis of a round-trip, sample return trajectory to a high-energy, high-inclination Near-Earth Asteroid (2001 QP 153) has been conducted to demonstrate the extremely large Δv capability of solar sailing. Parametric analysis of a triple phase trajectory, utilising an inclination cranking manoeuvre, revealed that a sample could be returned in under 7 years from a target inclined at 50° to the ecliptic plane. The use of a positive C_3 of $37 \text{ km}^2 \text{ s}^{-2}$ and spiral down can quickly attain a 0.3 AU cranking orbit. The use of circle-ellipse/ellipse-circle trajectory symmetry has been used to crucial effect in trajectory optimisation. This difficult trajectory problem was selected to show the truly enabling potential of solar sailing for high-energy small body missions.

Chapter 5

Outer Solar System Trajectories

In this Chapter, an investigation of the use of solar sails to reach the outer solar system is conducted, specifically for the planets Jupiter and Pluto. Solar radiation pressure is weak in the outer solar system, but it will be seen that a solar sail can achieve high velocities for flyby missions using a close solar pass.

In the first section, missions to Jupiter will be analysed. Only high performance sails can perform a direct rendezvous, due to the much decreased solar radiation pressure available to circularise the trajectory on approach to Jupiter. The variation of transfer time against characteristic acceleration is assessed for flat sails. Additionally, this is done for the compound sail concept. For lower performance sails, the possibility of using a close solar approach to reach high velocities is investigated, with an assessment of using one or two loops. It is feasible that the solar sail could carry a chemical stage to the Jovian system, for orbital insertion. The propellant required for capture should be minimised by minimisation of the arrival velocity. Therefore, the solar sail flyby concept will be augmented by attempting to minimise the relative flyby velocity at the expense of solar sail trip time. To further minimise the required sail performance, it is also of interest to determine the effect of positive launch C_3 on minimised arrival velocity. This complex problem will involve a trade-off between C_3 , arrival velocity, the number of trajectory loops, and trip time, in order to minimise the required sail characteristic acceleration.

In the second section, Pluto flyby missions are analysed, both for a fast single loop trajectory, and for a slower multiple loop trajectory. No minimisation of the arrival velocity will be attempted, since Pluto orbit insertion will not be considered. For the single loop trajectory, the variation of trip-time against characteristic

acceleration is investigated. It will also be determined if locally optimal control laws, that maximise the rate of change of eccentricity, can be used for multiple loop Pluto flyby trajectories.

5.1 Jupiter Trajectories

From a trajectory design perspective, Jupiter is a difficult target to reach in a reasonable timescale. Jupiter has a low eccentricity of 0.048 and an inclination of just 1.3° , but its semi-major axis is 5.2 AU, where the available solar flux is greatly diminished. Large launch vehicles can provide the necessary hyperbolic excess to reach Jupiter directly, but large chemical insertion burns and complex gravity assists at the Jovian moons are still required for capture. Solar electric propulsion and, particularly, Nuclear Electric Propulsion (NEP), can provide benefits, at the expense of launch mass, due to the large solar arrays or reactor thermal radiators required. It will be shown that high performance solar sails could reach Jupiter directly, or lower performance sails could be used to perform a slow Jupiter flyby, but practically, the arrival velocity can only be reduced to a lower limit.

5.1.1 Earth – Jupiter Circular-Coplanar Transfer

Since the photon pressure at 5.2 AU is weak, it does not appear that solar sailing will be an effective mode of propulsion for Jupiter exploration missions. However, a solar sail can utilise a close solar pass to attain the high velocities necessary to reach the outer solar system (as will be shown in Section 5.1.2), although its ability to circularise a highly eccentric transfer spiral is limited and capture by chemical propulsion may be required. However, a high performance sail can perform a direct spiral transfer, arriving at Jupiter with zero hyperbolic excess energy.

Using the circular-coplanar transfer analysis implemented throughout Chapters 3 and 4, an investigation of the required performance level of the solar sail has been conducted. This analysis was carried out initially for the conventional flat sail (high performance sails dictate a spinning disk), and for the compound sail concept [Malanin and Repyakh, 1974, Forward, 1990, Uphoff, 1994, McInnes, 2000]. Figure 5.1 shows the variation of the (open final azimuth) transfer time from

a 1 AU circular orbit to a 5.2 AU circular orbit. It can be seen that a desirable heliocentric transfer time of less than 6 years (that of the NASA Jupiter Icy Moons Orbiter – JIMO) would require a characteristic acceleration of greater than 2.5 mm s^{-2} for the flat sail, or greater than 1.6 mm s^{-2} for the compound sail. If the compound sail can be fabricated, then it shows significant advantages over the flat sail for Jupiter rendezvous. However, further conceptual design needs to be conducted into the fabrication of a compound sail. To date, no specific hardware concepts exist. The compound sail can reduce the trip time by 2 years for a relatively low acceleration of 1.0 mm s^{-2} , whereas a minimum reduction of 1 year is evident up to an extremely advanced sail of 10.0 mm s^{-2} performance. It is also of interest to note that both trip time curves level off beyond 3.0 mm s^{-2} . This analysis puts a maximum value on the characteristic acceleration and means that extremely high performance sails ($>3.0 \text{ mm s}^{-2}$) are not necessarily required for the maximum allowable heliocentric transfer of order 6 years. Of course, the higher the sail characteristic acceleration available, the more effective the sail would be for Jupiter-centered orbital operations.

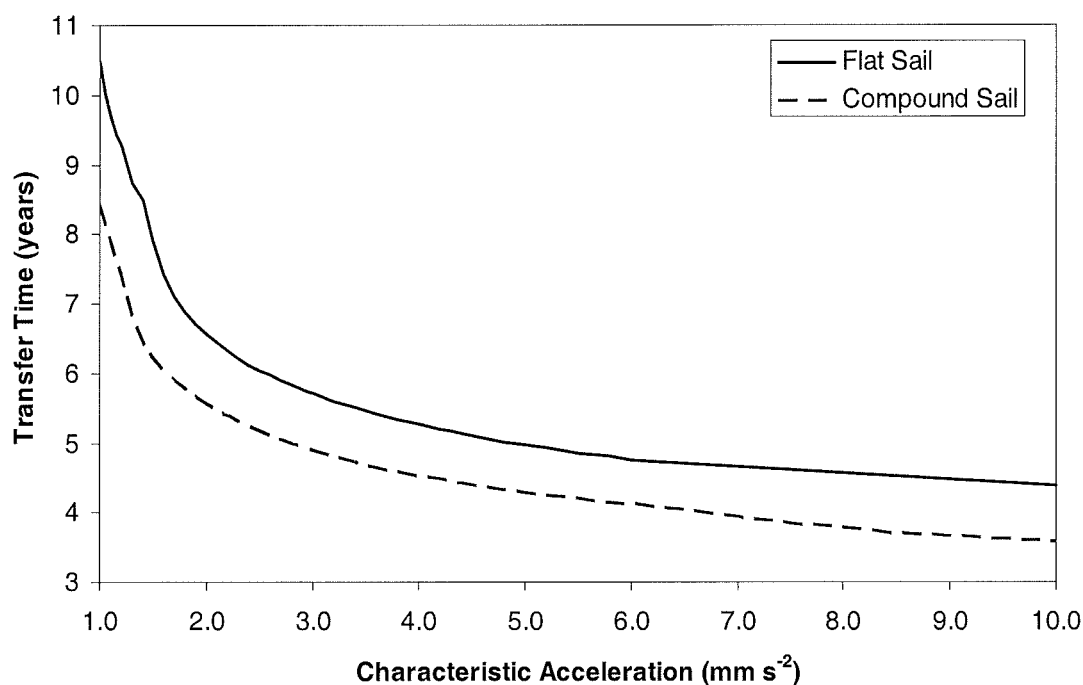


Figure 5.1: Earth – Jupiter circular-coplanar transfer time for flat and compound sails

An upper bound of 6 years was placed on the transfer time so that the resulting mission concept is competitive with the NASA JIMO NEP mission. The flat sail acceleration of 3.0 mm s^{-2} is representative of spinning disk designs such as the JPL Interstellar Probe concepts [Wallace *et al*, 2000] and results in a transfer time of 5.7 years. Figure 5.2 shows the trajectory for such a solar sail, where it is observed that, although the spacecraft rapidly reaches the vicinity of 5.2 AU, there is a long circularisation phase at 5.2 AU where the sail attempts to make optimum use of the weak solar pressure to attain a circular orbit. Again, a characteristic acceleration as high as 3.0 mm s^{-2} is representative of a high performance solar sail that may be fabricated using advances in thin film technology and a spinning sail concept to greatly reduce the sail structural mass fraction. It is concluded that direct rendezvous is not practical with near term square solar sails, but with development, spin stabilised disk solar sails could enable direct rendezvous. As a nearer term concept, it is envisaged that a relatively slow flyby of Jupiter would be accomplished, with a chemical stage used at Jupiter to remove the arrival hyperbolic excess velocity. This concept will be discussed later in Section 5.1.3.

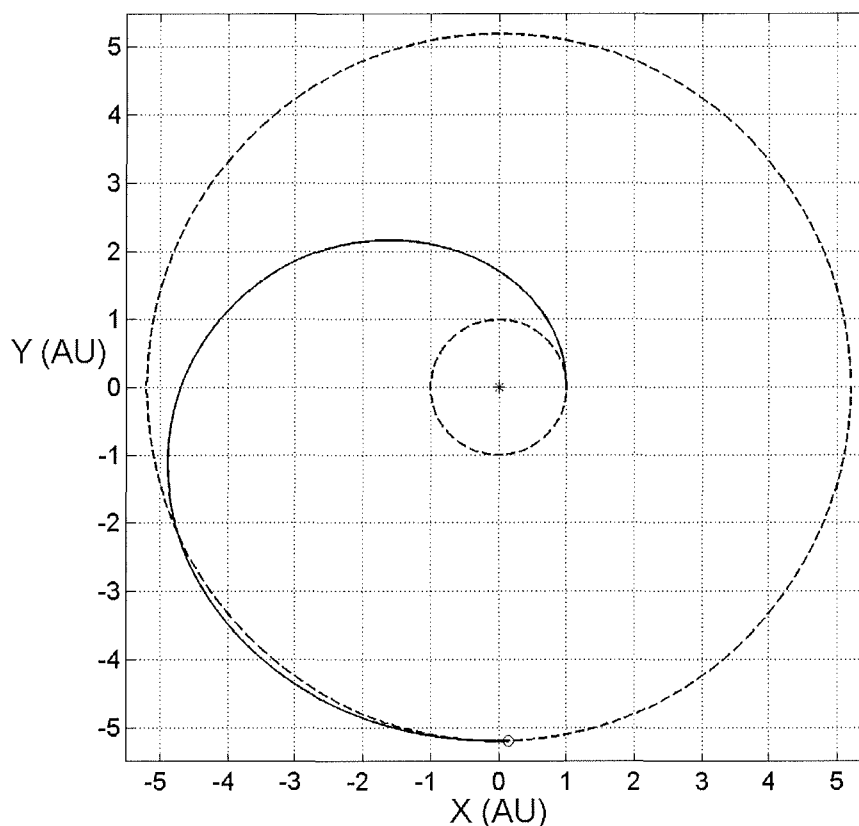


Figure 5.2: 5.7 year Earth – Jupiter transfer (3.0 mm s^{-2})

5.1.2 Jupiter Fast Flyby

If the objective of a mission to Jupiter is a fast flyby, then the solar sail trajectory can be optimised to effect a manoeuvre known as a solar photonic assist, first devised by Carl Sauer at JPL during the 1970s, and described in papers by Sauer [1999]. Leipold [2000] and Leipold and Wagner [1998] have also expanded on this trajectory concept. The basic concept is that, instead of spiraling directly outwards, the sail firstly 'brakes', or increases orbit eccentricity, to spiral inwards towards the Sun where the light pressure is much greater. Once a certain minimum solar distance is reached, governed by thermal limitations or trip-time trade-off, the solar sail thrust vector is then rotated and directed along the local velocity vector to increase the orbital energy at this perihelion distance. Because of the larger photon flux at close solar distances, the thrust produced by even a low performance sail can be significant. For example, a sail with a characteristic acceleration of 1.0 mm s^{-2} can exhibit an actual acceleration of up to 11.1 mm s^{-2} at 0.3 AU, more than a factor of 10 greater. This thrust along the local velocity vector acts to increase the orbit eccentricity and energy such that within a short arc of the orbit the sail has been accelerated onto a trajectory with an aphelion in the outer solar system. For interstellar precursor type missions to 100 AU and beyond, where the aim is to maximise the exit velocity at approximately 5 AU (where the photon pressure is so low that the sail can be jettisoned), it is advantageous to have a larger initial aphelion and smaller initial perihelion to maximise the orbit eccentricity and reach solar system escape, as shown in Figure 5.3, subject to thermal limitations.

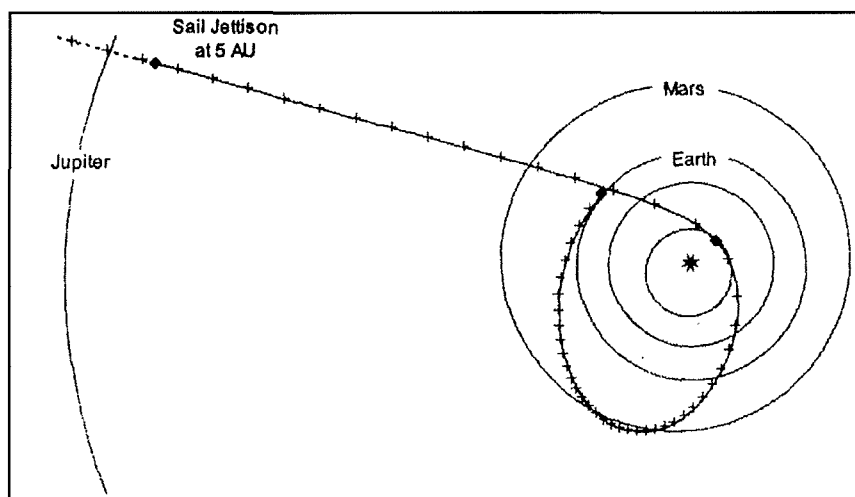


Figure 5.3: Perihelion constrained 10 year trajectory to 100 AU [Sauer, 1999]

For a minimum-time flyby of Jupiter there has to be some trade-off between reducing the perihelion distance and minimising the trip-time, since some time is added by spiraling closer to the Sun, and temporarily moving away from the Sun with a larger initial aphelion. Sauer [1999] does not specifically treat minimum-time trajectories to Jupiter, but the photonic assist concept has been briefly applied to the problem by Leipold [2000].

For the flyby trajectory analysis in this section, the initial guess for the NPSOL optimisation process is generated using simple trial and error, or an analytical control law that maximises the rate of change of the orbit eccentricity. The initial trajectories obtained then form the basis for using incremental feedback to obtain other true minimum-time trajectories. Again, the number of control nodes was 51. Figure 5.4 shows the variation of flyby time with characteristic acceleration for perihelion limits of 0.25 and 0.3 AU. It can be seen that the difference between the two curves only begins to become apparent above 2.5 mm s^{-2} . This is thought to be because the lower accelerations cannot make best use of a lower perihelion limit, since the inwards spiral time is excessively long. High performance sails can however exploit lower perihelia to generate shorter trip times. For example, a sail exhibiting a characteristic acceleration of 3.0 mm s^{-2} can execute a minimum-time solar photonic assist trajectory to Jupiter with a perihelion of 0.264 AU. Since Jupiter flyby is being considered within the context of lower performance sails, then the perihelion limit will remain at 0.3 AU, principally to limit the thermal loads on the solar sail.

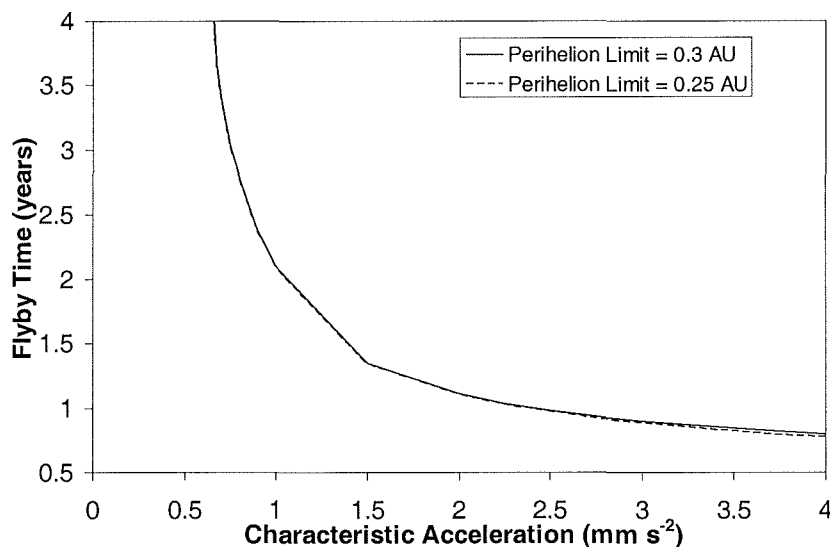


Figure 5.4: Fast Jupiter coplanar flyby times using solar photonic assist

Figure 5.5 shows an example of a solar photonic assist trajectory that would enable flyby of Jupiter with a characteristic acceleration of 1.0 mm s^{-2} in 766 days (2.1 years). However, the relative velocity at flyby is 16.6 km s^{-1} . The ‘thrust reversal’ necessary to execute the photonic assist is depicted in the cone angle profile shown in Figure 5.6. The clock angle is always 90° for a coplanar flyby. In reality, Jupiter has a small inclination of 1.3° , but the clock angle would only need to vary by a small amount. The lowest characteristic acceleration obtained using incremental feedback was 0.65 mm s^{-2} , which reached Jupiter in 4.23 years, with a relative velocity of 6.8 km s^{-1} . This arrival hyperbolic excess is low enough that capture could be achieved using chemical propulsion. For accelerations lower than this, the solar sail needs to execute an extra solar pass – known as the ‘dual photonic assist’ [Leipold, 2000]. The trajectory for 0.65 mm s^{-2} is shown in Figure 5.7, where it can be seen that Jupiter is reached close to the aphelion of the post photonic assist trajectory. It should be noted that, in general, the arrival excess velocity is lower for lower performance sails.

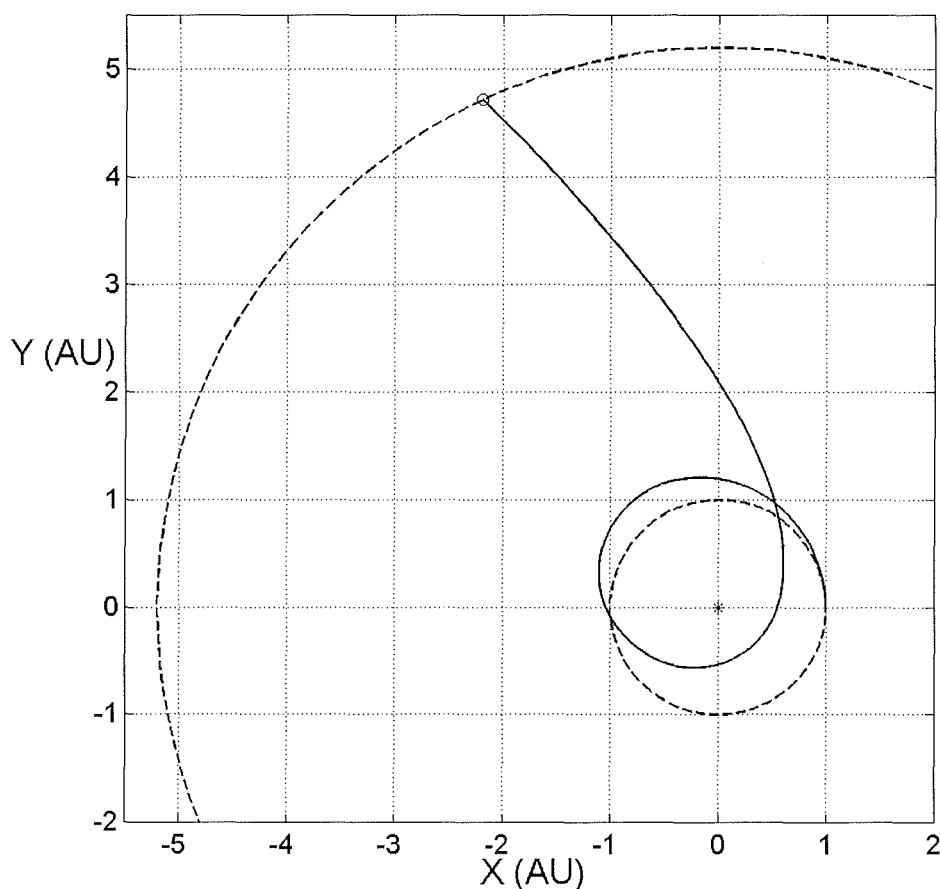


Figure 5.5: 1.0 mm s^{-2} Jupiter fast coplanar flyby (2.1 years)

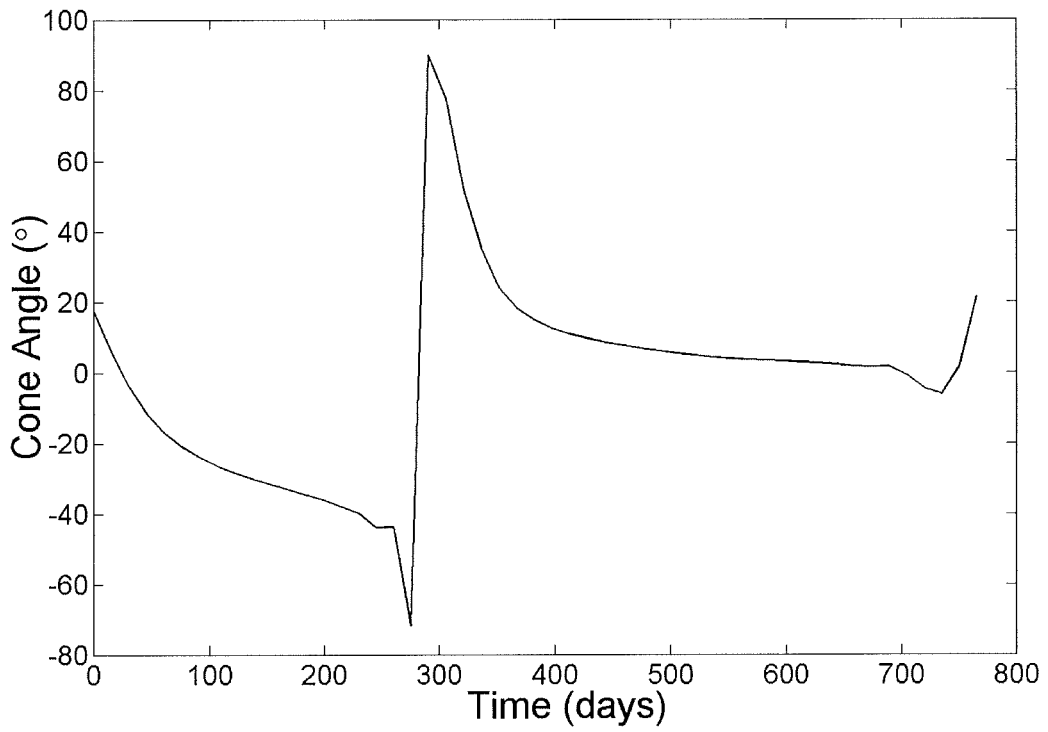


Figure 5.6: 1.0 mm s^{-2} Jupiter fast coplanar flyby control angle profile

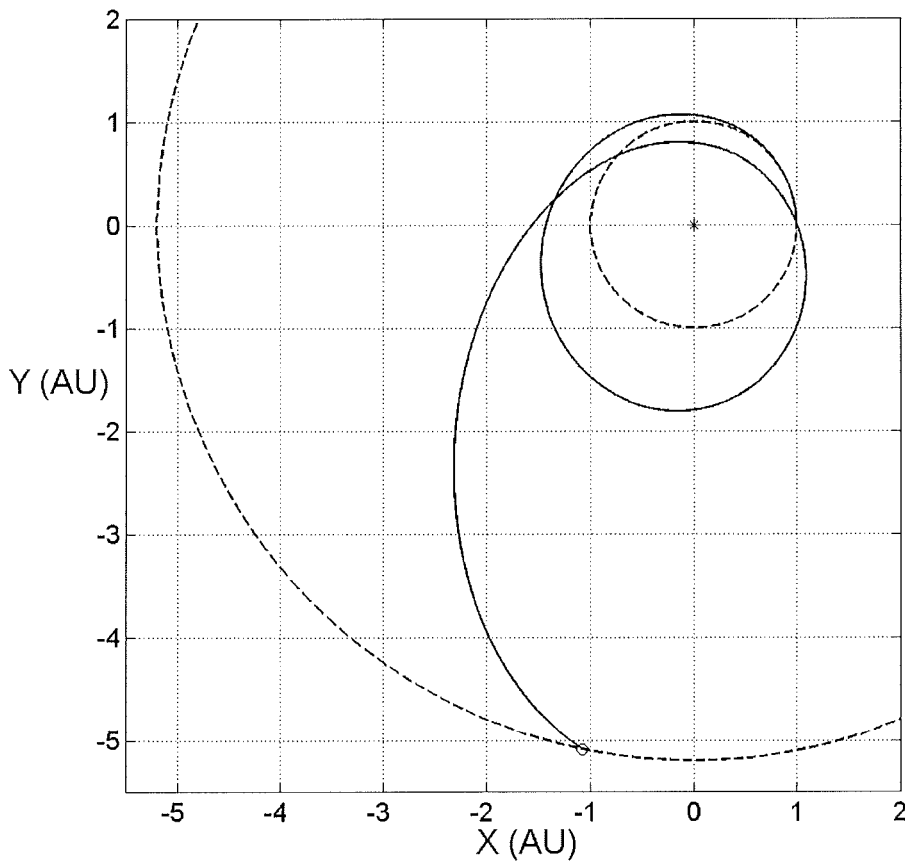


Figure 5.7: 0.65 mm s^{-2} Jupiter fast coplanar flyby

The dual photonic assist is essentially an extension of the single photonic assist concept. The initial guess for the optimiser can be obtained directly using analytical control laws which maximise the rate of change of orbit eccentricity. Low performance sails are not capable of reaching Jupiter after the first photonic assist, since their subsequent aphelion falls short. The sail is therefore directed to fall back inwards to the Sun for a second energy increasing photonic assist to boost the sail orbit energy. The number of control nodes for the dual assist trajectory was increased to 101 to provide adequate control resolution for the extra orbit revolution. Figure 5.8 shows a dual photonic assist trajectory for a characteristic acceleration of 0.5 mm s^{-2} . The optimiser has of course ‘minimised’ the first two aphelia in an attempt to reduce the trip time. The trip time is 4.18 years and the sail arrives with an excess velocity of 9.44 km s^{-1} . This trip time is actually *lower* than that for the single photonic assist using a *higher* acceleration of 0.65 mm s^{-2} , because of the second photonic assist. This seems to be at odds with the second revolution used, but this is explained by noting that the arrival excess velocity is quite high. Figure 5.9 shows the cone angle evolution, where clearly there are now two thrust reversal manoeuvres.

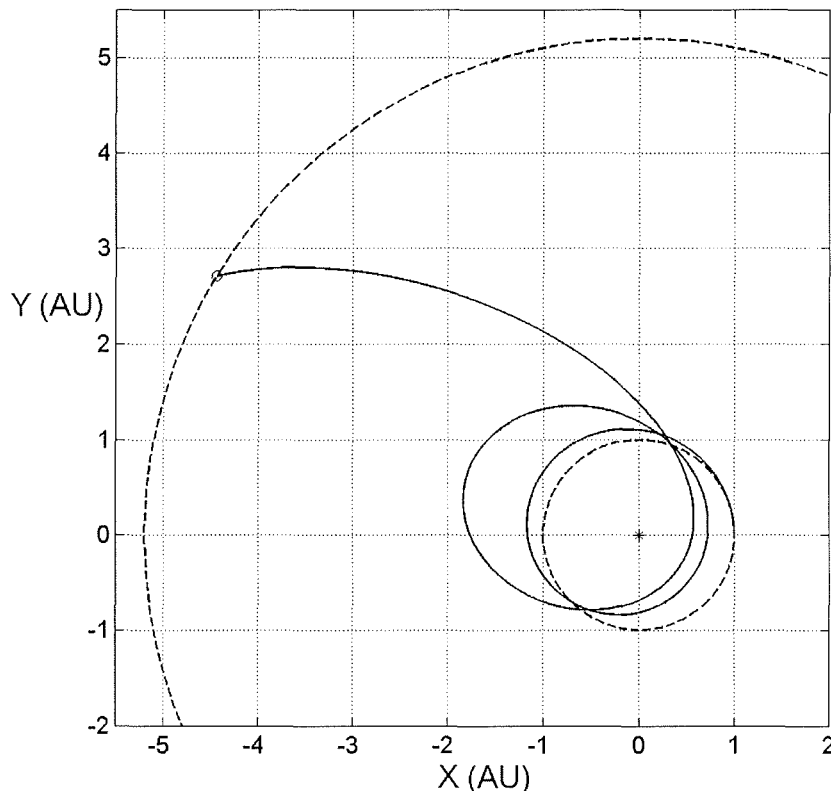


Figure 5.8: 0.5 mm s^{-2} dual photonic assist Jupiter flyby trajectory

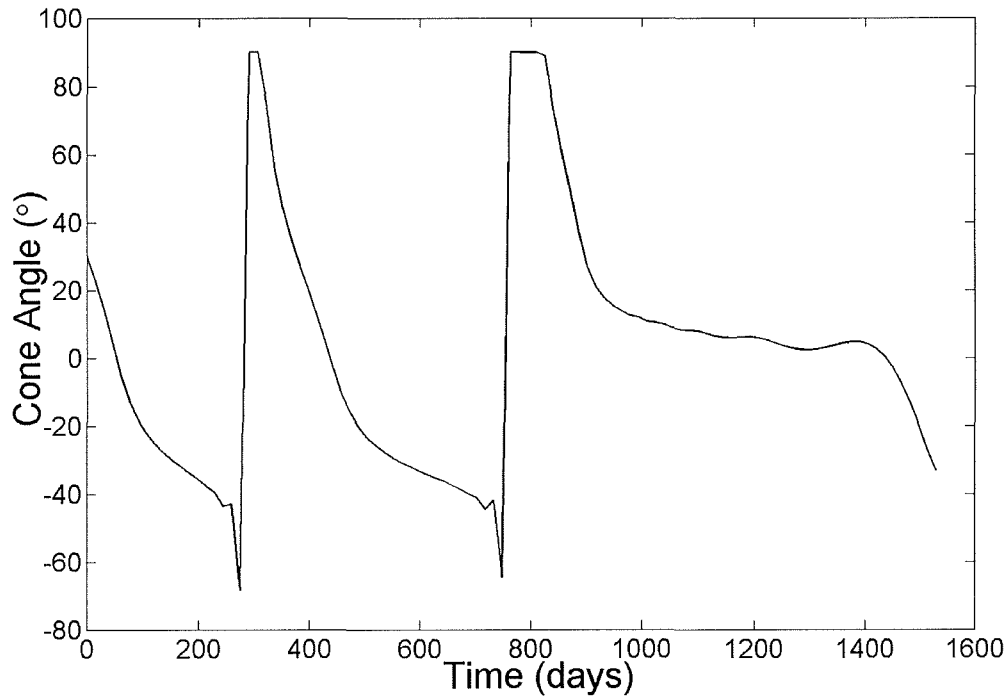


Figure 5.9: 0.5 mm s^{-2} dual photonic assist control profile

5.1.3 Minimised Relative Velocity Flyby

For the minimum-time Jupiter flyby trajectories detailed above, it is evident that the unconstrained flyby velocity is too high to allow for a reasonably sized chemical orbit insertion burn. Therefore the optimisation code was adjusted to minimise the relative velocity at flyby (for a circular-coplanar Jupiter orbit with open azimuth), while the transfer time was fixed and increased by incremental feedback. The initial point used was the minimum-time trajectory described above for the single photonic assist. It was necessary to fix the trip time since NPSOL only allows for one objective function. If the trip time was left as an optimisation variable, then the final trip time was then just that of the upper bound set, so the fixed trip time incremental feedback method was implemented instead. The relative velocity was calculated in polar coordinates by taking the radial velocity of Jupiter to be zero and the tangential velocity to be 13.06 km s^{-1} , the circular orbit velocity at 5.2 AU. The results of increasing trip time in small increments, from the minimum trip time, is shown in Figure 5.10, for characteristic accelerations of 0.65, 0.75, and 1.0 mm s^{-2} , single photonic assist flybys. In Figure 5.10 it can be seen that it is difficult to reduce the relative flyby velocity much below 6 km s^{-1} . This arrival excess can be reduced via a

suitable combination of chemical burns, and gravity assists at the Jovian moons [Oberto *et al.*, 1999]. In principle, the perihelia of the photonic assists can be selected so that essentially any final trajectory asymptote direction can be achieved. This, coupled with the long orbit period of Jupiter (11.86 years) in relation to the orbit period of the Earth, means that the trip time is relatively insensitive to launch date and should repeat itself over 1 year intervals.

Figure 5.11 shows an example 5.4 year dual photonic assist trajectory with a characteristic acceleration of 0.5 mm s^{-2} , where the trajectory approximates a Hohmann-type transfer after the second solar pass. This feature has also been noted by Leipold [2000]. The control angle profile is shown in Figure 5.12, again with two thrust reversal slews at the two perihelia. Other anomalous spikes are an artefact of the numerical optimisation algorithm and do not significantly affect the overall trajectory optimality. These spikes may appear due to the fixed trip time constraint. Figure 5.13 shows the temporal evolution of the orbital elements. The eccentricity curve clearly shows the eccentricity ‘pumping’ taking place at each perihelion pass, along with the semi-major axis boost at the second solar pass. The variation of the equilibrium sail film temperature with sail attitude and heliocentric distance is calculated, as in Chapters 3 and 4, and is shown in Figure 5.14. It can be seen that the maximum sail temperature is 338 K (65°C), and occurs at the minimum solar distance of 0.57 AU, on the second solar photonic assist at about 1070 days. This temperature is well below the predicted upper limit for polyimide films at 520 K. Therefore, thermal issues do not appear to be a driver for the double loop Jupiter trajectory. However, it should be noted that the solar sail will experience two thermal pulses as it passes through perihelion, as can be seen in Figure 5.14. Further investigation may be required to assess the effect of a second thermal pulse on a sail film which has already been thermally aged by an initial thermal pulse, although since the maximum sail temperature remains modest (338 K), this is not anticipated to be problematic.

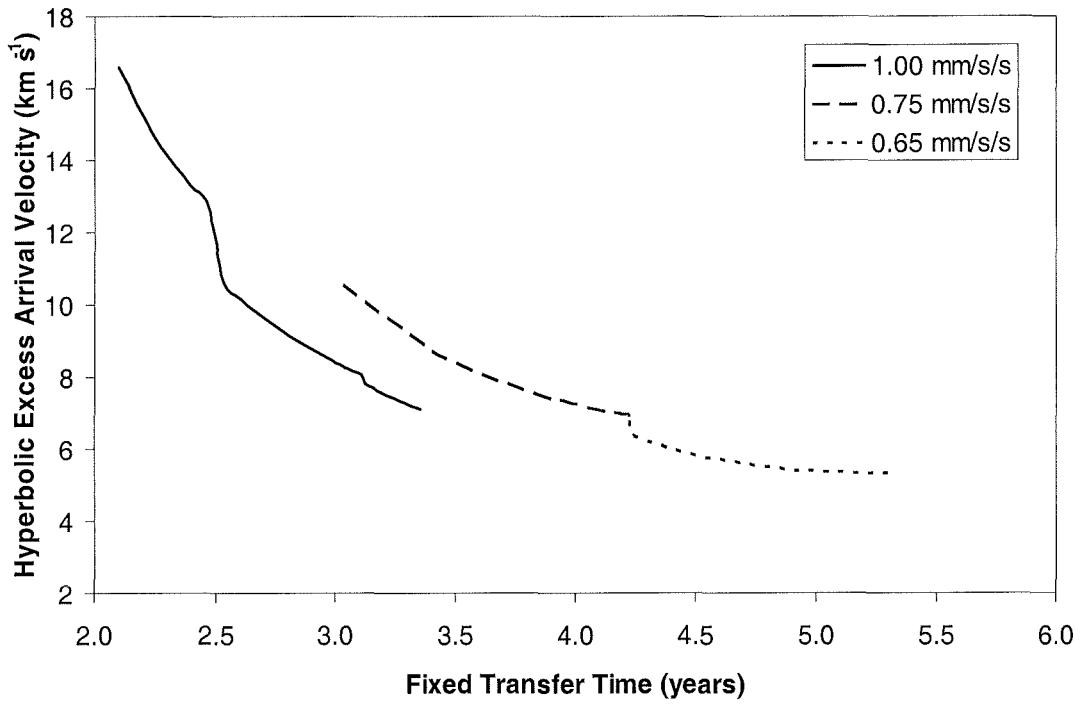


Figure 5.10: Minimised relative velocity, single photonic assist flyby, curves for 0.65, 0.75, and 1.0 mm s^{-2}

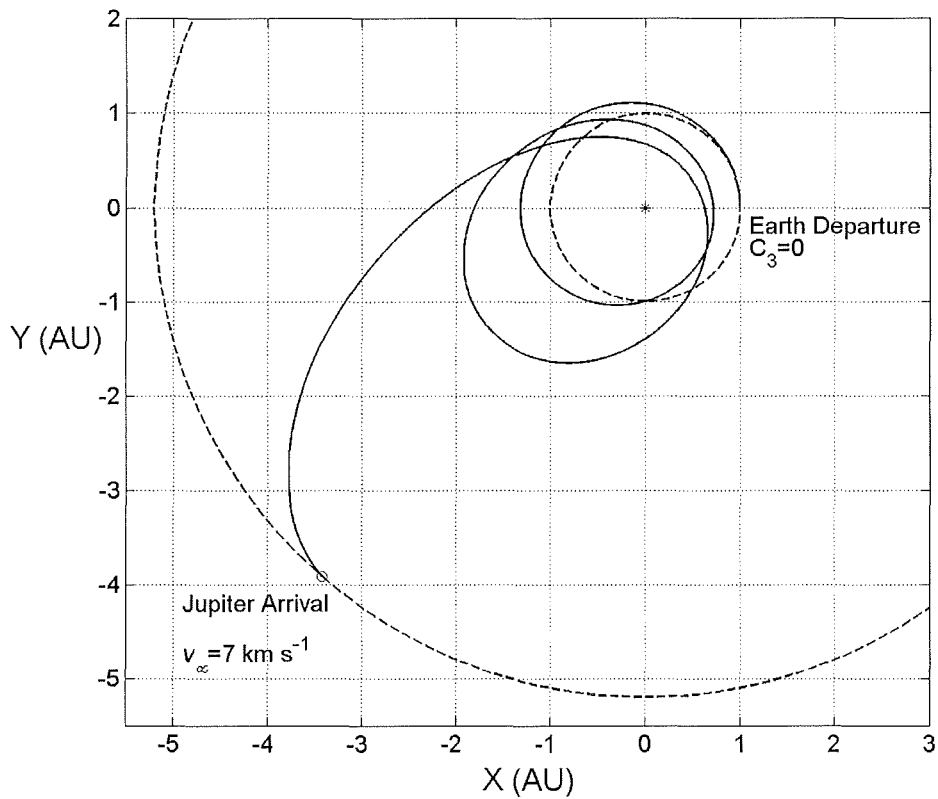


Figure 5.11: 0.5 mm s^{-2} Earth–Jupiter, 5.39 year, dual photonic assist flyby, with minimised arrival excess velocity

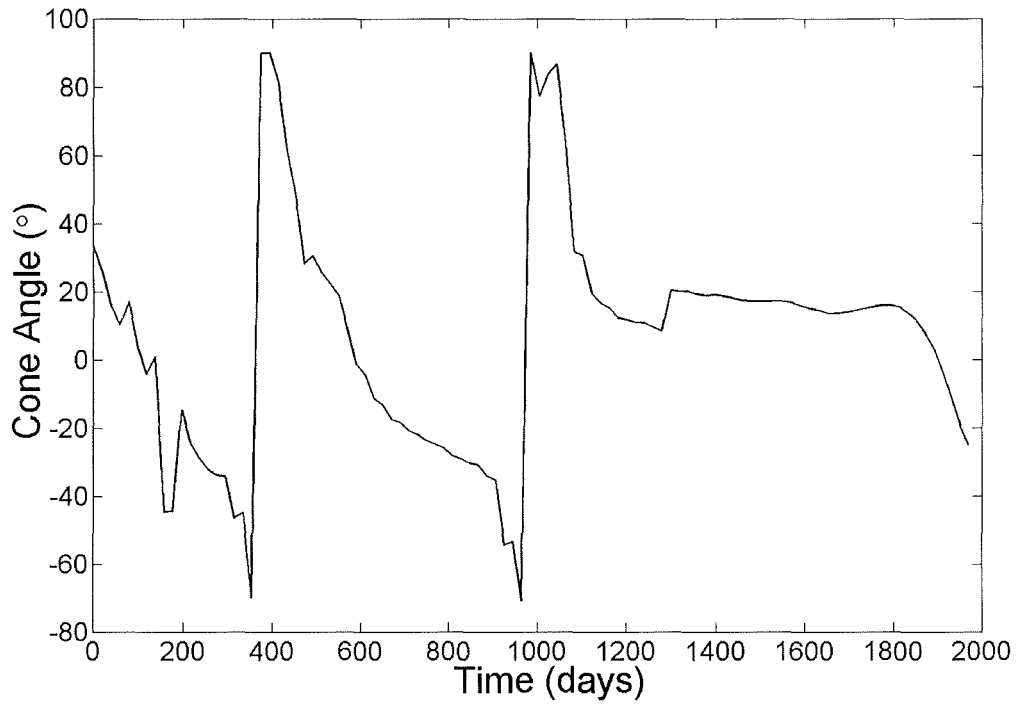


Figure 5.12: 0.5 mm s^{-2} Earth–Jupiter, 5.39 year, dual photonic assist flyby control profile

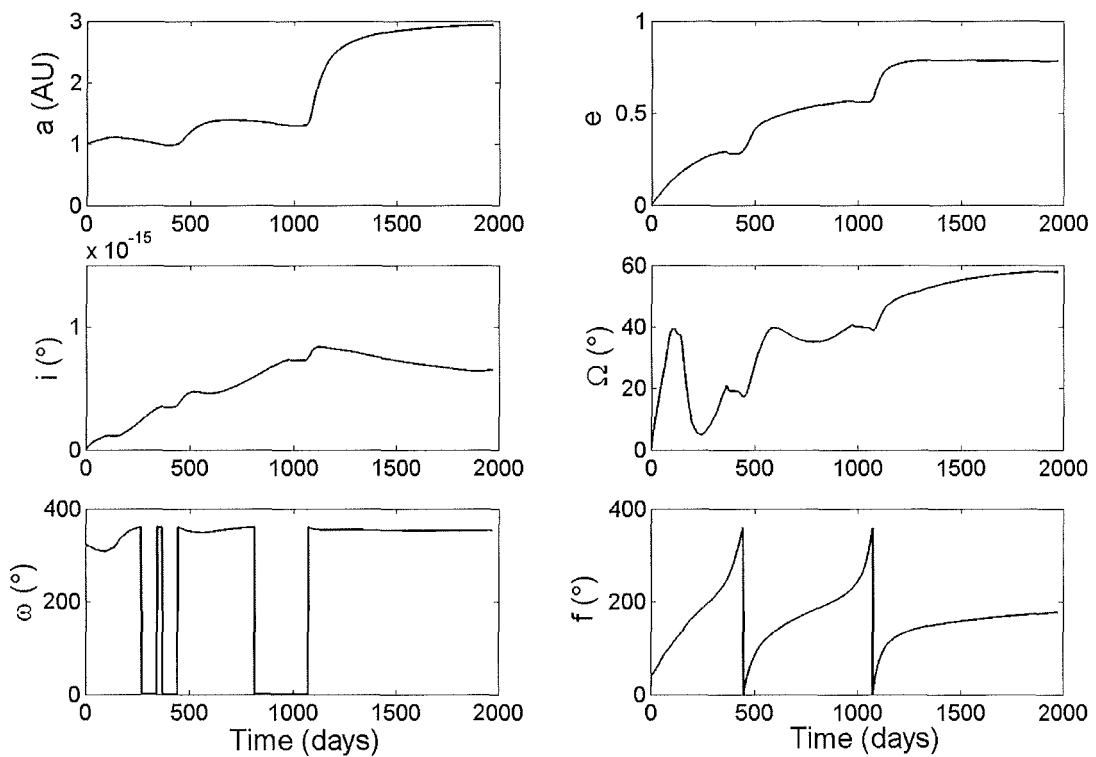


Figure 5.13: 0.5 mm s^{-2} Earth–Jupiter, 5.39 year, orbital element evolution

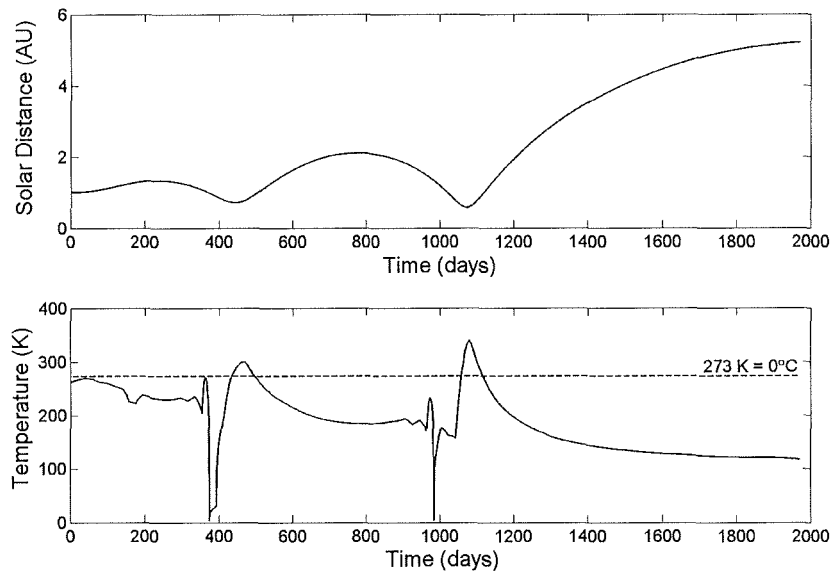


Figure 5.14: 0.5 mm s^{-2} Earth–Jupiter, 5.39 year, distance and sail film temperature

5.1.4 Effect of Positive C_3 on Minimised Arrival Velocity for Lower Characteristic Accelerations

The NLP solver SNOPT offered a more robust approach to the minimisation of the relative velocity on arrival at Jupiter, so this algorithm was adopted over NPSOL for optimisation of low acceleration and positive C_3 transfers. In the first instance, minimum time trajectories were generated for dual assist transfers for a number of characteristic accelerations (lower than those above). Figure 5.15 shows trip times for a range of characteristic accelerations, for dual photonic assist trajectories to Jupiter, with a launch C_3 of zero. Subsequent data points were generated by incremental feedback optimisation, but it was not possible to go below 0.426 mm s^{-2} with a dual assist at $C_3=0$, since the trajectory end-point ‘aphelion’ just misses 5.2 AU. To reach 5.2 AU with lower accelerations would require an extra loop, or triple photonic assist, or the increase of the launch C_3 . The solar distance of the final perihelion is lower for an increased number of loops and, besides increasing the trip time, the more loops and lower perihelion – the higher the relative velocity at Jupiter (even if this is minimised). Therefore, it is considered prudent to limit the number of photonic assist to two loops about the Sun. For the lower end of the curve in Figure 5.15 (0.426 mm s^{-2}), the hyperbolic arrival velocity at Jupiter is approximately 6.6 km s^{-1} , and increases to 12.4 km s^{-1} at the higher (0.6 mm s^{-2}) end of the curve. In general, the higher the characteristic acceleration, the higher the arrival velocity.

Next, minimised arrival velocity trajectories were generated for a range of trip times and several different characteristic accelerations. For minimised arrival velocity trajectories, a closer distance of the final perihelion is not desirable, since the eccentricity increases markedly and the arrival velocity is too high. It is more important to increase the radius of aphelion, for successive perihelion passes that do not approach much closer than 1 AU. The arrival-velocity/trip-time curves were generated for several values of positive launch C_3 . Because a low perihelion is undesirable, the positive excess C_3 was applied in the same direction as the velocity of the Earth so as to rapidly increase the aphelion radius. The effect of this is to give the solar sail a large initial aphelion, so that a single heliocentric loop may be removed in reaching Jupiter. For example, a low acceleration dual photonic assist trajectory might be reduced to a single loop transfer. Similarly, a lower acceleration sail normally ($C_3=0$) requiring 3 loops to reach Jupiter (prohibited due to larger arrival velocity), could be achieved using 2 loops. The transition from 2 loops down to 1 loop is demonstrated in Figure 5.16, for a characteristic acceleration of 0.5 mm s^{-2} in a 1900 day trajectory (for example). It can be seen that the $C_3=0$ trajectory must use a dual photonic assist, and hence a relatively low final perihelion, to reach 5.2 AU. The $C_3=10 \text{ km}^2 \text{ s}^{-2}$ trajectory already has an appreciable initial aphelion radius and so the final perihelion does not need to be as low. The resulting single photonic assist gives a much slower arrival velocity. The final perihelion for the single assist is unusually large at about 1.1 AU. It is not thought that the sail could attain a lower perihelion on first pass if forced to, since the initial aphelion is applied by the positive C_3 .

Figures 5.17, 5.18, 5.19, and 5.20 show the minimised arrival velocity C_3 curves as a function of trip time for 0.50, 0.45, 0.43, and 0.40 mm s^{-2} , respectively. For each C_3 and characteristic acceleration, the optimisation-fixed trip time was varied while the arrival velocity was minimised. The optimisation was 2D coplanar, with a minimum perihelion inequality constraint of 0.3 AU, and a final solar distance equality constraint of 5.2 AU. In general, it is seen that as the transfer time is reduced (down to the minimum time limit for the prescribed number of loops), the arrival excess velocity increases. So if the (fixed) trip time is extended much beyond 6 years, then the arrival velocity tends towards lower values, reducing the size of the insertion burn.

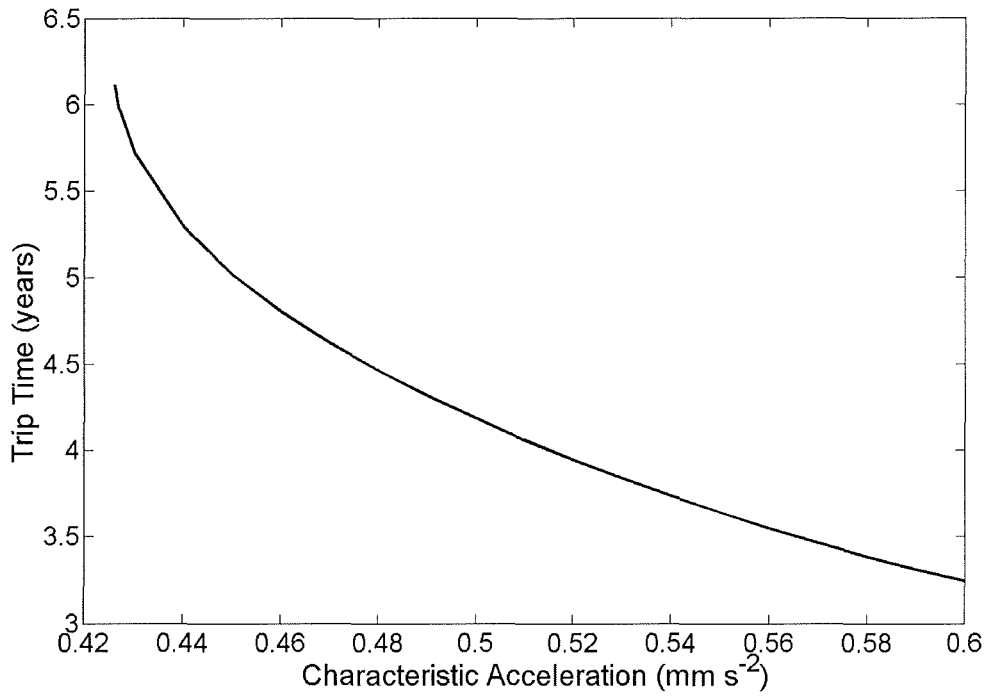


Figure 5.15: Minimum trip time against characteristic acceleration for a dual photonic assist Earth-Jupiter transfer ($C_3=0$)

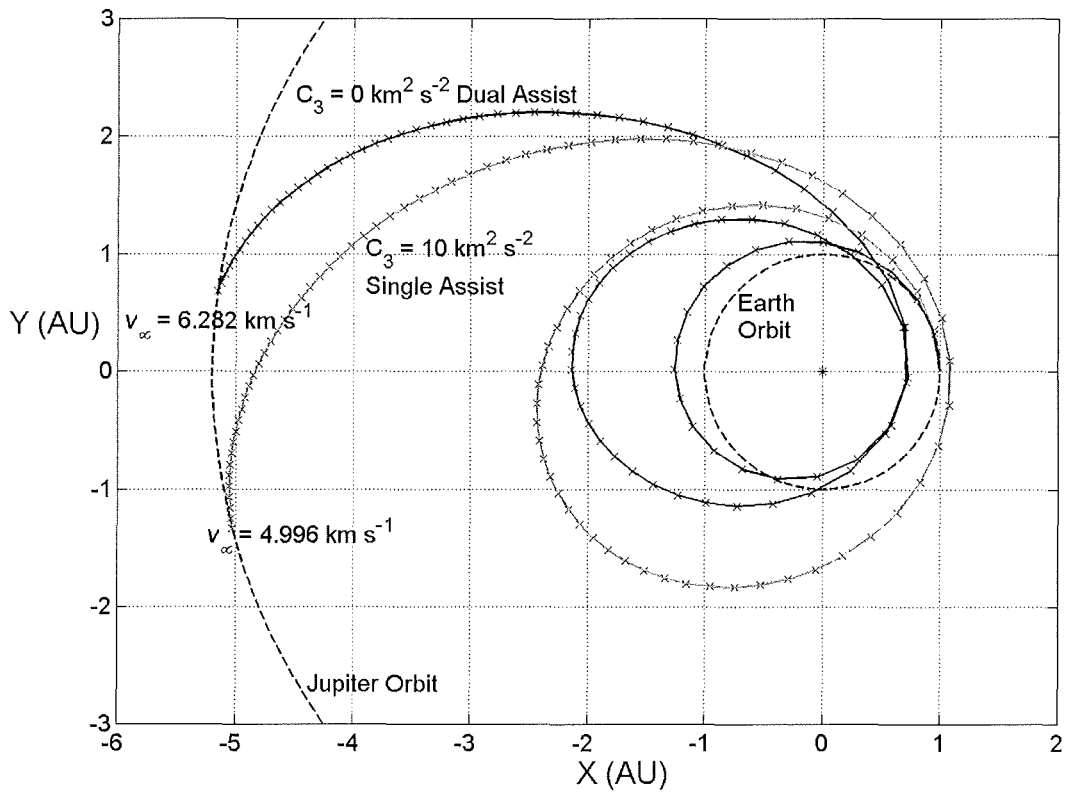


Figure 5.16: 0.5 mm s^{-2} Earth-Jupiter trajectory: effect of increasing C_3 to reduce number of heliocentric revolutions, thereby reducing arrival velocity

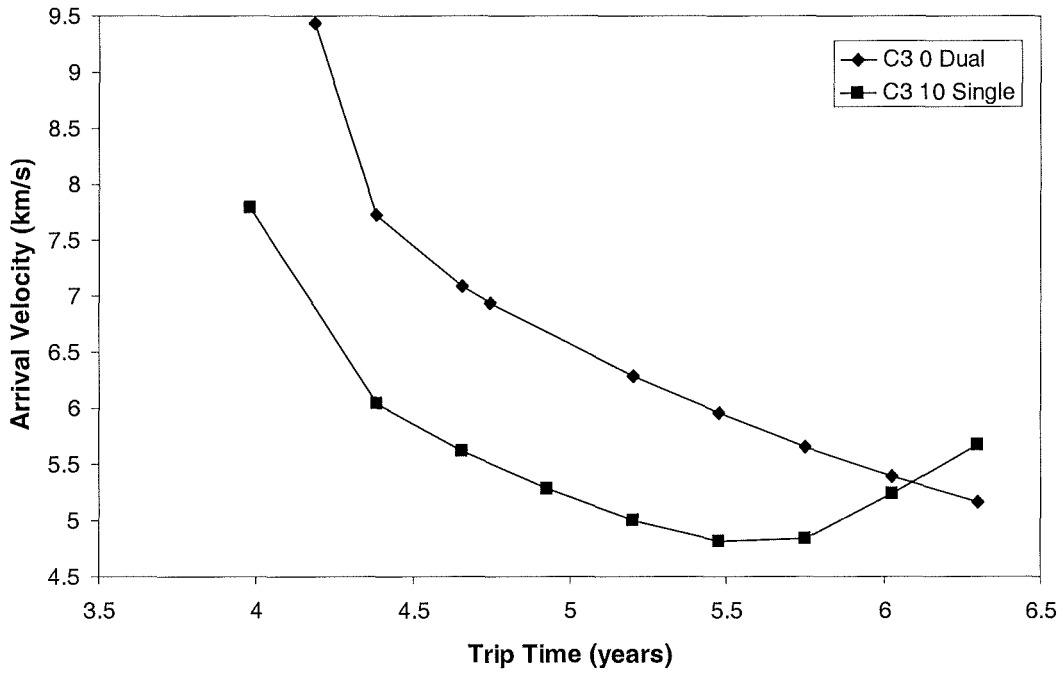


Figure 5.17: Minimised arrival velocity against trip time for 0.50 mm s^{-2} (C_3 in units of $\text{km}^2 \text{ s}^{-2}$)

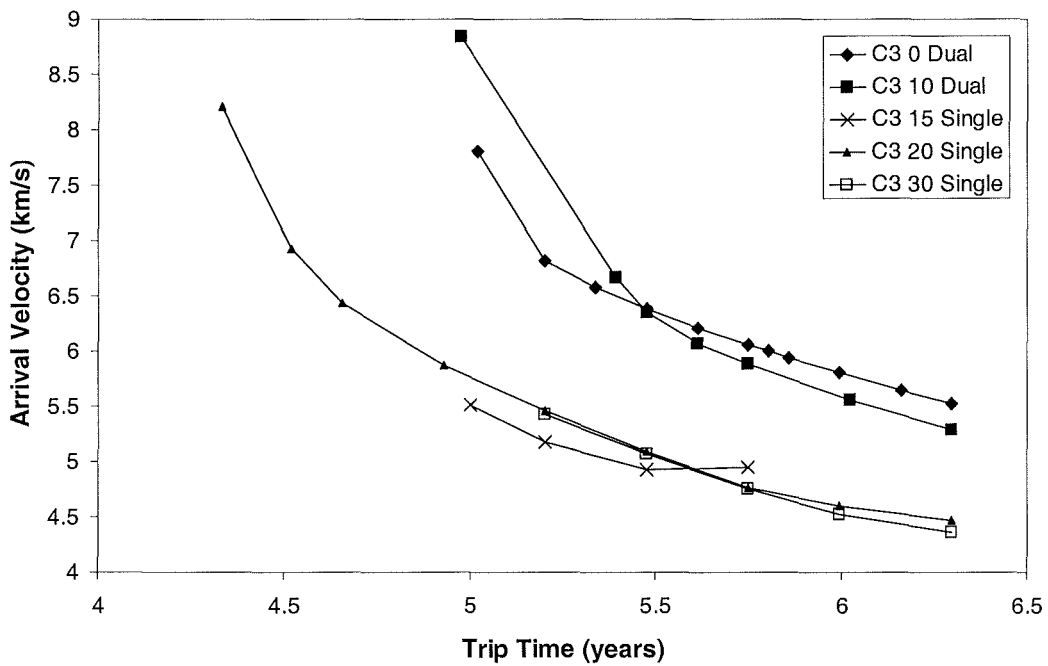


Figure 5.18: Minimised arrival velocity against trip time for 0.45 mm s^{-2} (C_3 in units of $\text{km}^2 \text{ s}^{-2}$)

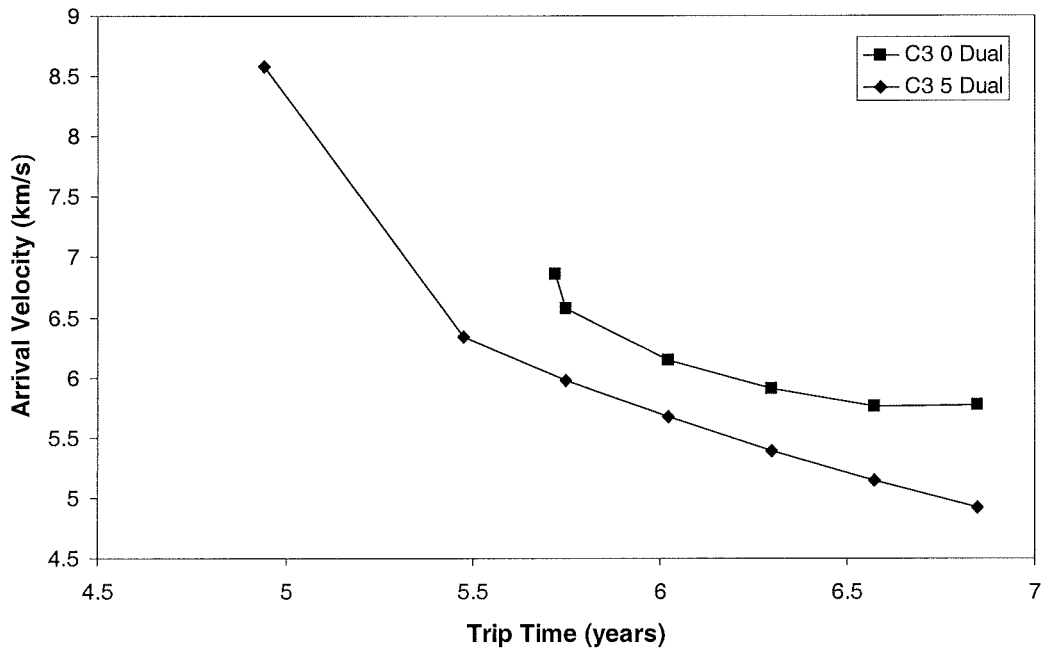


Figure 5.19: Minimised arrival velocity against trip time for 0.43 mm s^{-2} (C_3 in units of $\text{km}^2 \text{ s}^{-2}$)

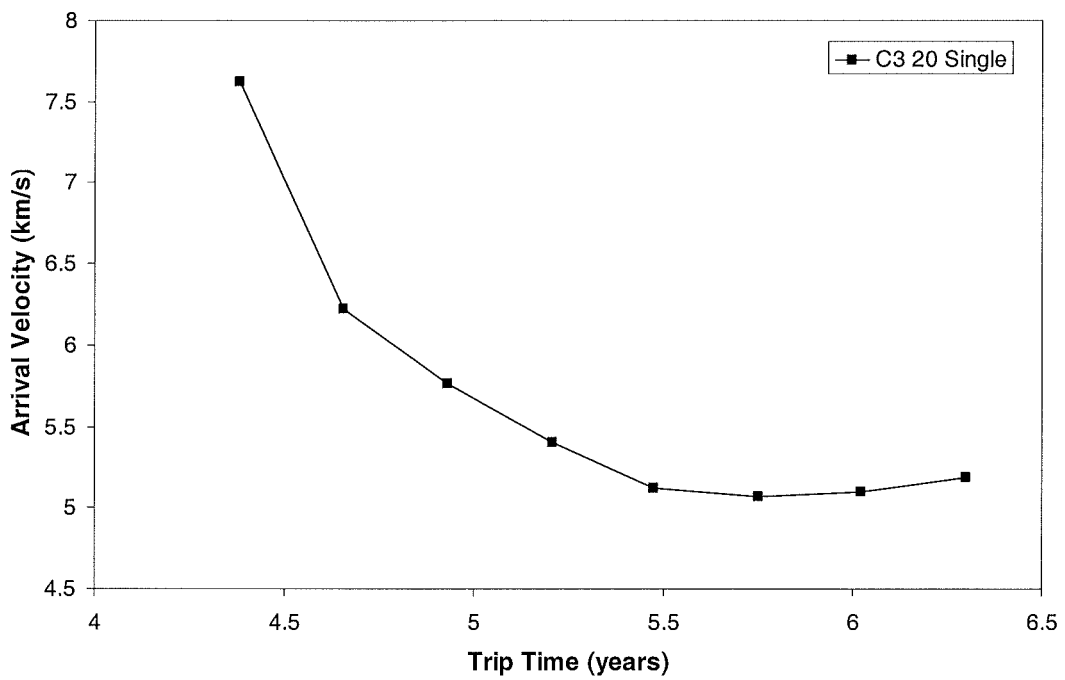


Figure 5.20: Minimised arrival velocity against trip time for 0.40 mm s^{-2} (C_3 in units of $\text{km}^2 \text{ s}^{-2}$)

It is important to stress here that, although the trajectory analysis was quite thorough, a continuous surface of increasing C_3 for each acceleration considered was not possible. This is partly due to the difficulty in obtaining initial guesses for optimisation (use was made of a maximum-eccentricity analytical control law, in addition to trial-and-error techniques), and partly due to the trajectory discontinuity between 1, 2 and 3 loops. As a compromise, the curves produced are at acceptable values of C_3 , but with enough of a range to be fairly complete, in the region of interest. In these curves, for these characteristic accelerations, it is clear that arrival velocities less than approximately 4300 m s^{-1} are not possible without resorting to trip times much greater than 6 years. There may be a lower limit to the arrival velocity, constrained by the velocity of Jupiter. To go much lower than 4000 m s^{-1} would no doubt require a direct spiral to Jupiter, effectively a rendezvous, with considerably higher performance solar sails. There are some anomalies in the C_3 curves for 0.5 mm s^{-2} (Figure 5.17) and for 0.45 mm s^{-2} (Figure 5.18). At larger trip times, some of the higher positive C_3 curves tend to increase again, and even produce *higher* arrival velocities than for lower C_3 curves. This is quite counter-intuitive, but it is probably due to the C_3 and initial aphelion being too high, the trip time being too high, and the outward thrust constraint on the solar sail attitude combining such that the sail thrust cannot adequately shape the trajectory for the fixed trip time. The effect of this is illustrated in Figure 5.21, which shows a 0.5 mm s^{-2} , single photonic assist, minimised arrival velocity trajectory, for a C_3 of $10 \text{ km}^2 \text{ s}^{-2}$. The transfer time is arbitrarily fixed at 2300 days (6.3 years), and it is seen that the solar sail passes through 5.2 AU 483 days before the trajectory end-point, and then arrives at the end of sail control at Jupiter with minimum arrival velocity. Analysis of the control angle profile for this trajectory has revealed that the portion outside of 5.2 AU, from aphelion to the end-point, has 90° pitch, so that the sail is coasting for 184 days. This is probably an effect of the outwards hemisphere constraint on the sail thrust vector, and the extended trip time. It seems that some C_3 curves appear to have an 'optimal' trip time, with respect to minimum arrival velocity. In addition to these C_3 curves, numerous other point-trajectories have been generated within and below the previously discussed range of 0.5 down to 0.4 mm s^{-2} , and down to as low as 0.35 mm s^{-2} .

An example trajectory with a low performance sail exhibiting a characteristic acceleration of 0.37 mm s^{-2} was produced. A program was coded based on SNOPT that minimised arrival relative velocity at Jupiter, using the ephemeris of Earth and Jupiter. The preceding 2D coplanar trajectory was used as the cone angle initial guess and the clock angle profile was initially zero. The trip time was fixed at 6 years, and a minimum distance constraint of 0.3 AU was imposed, but never reached. The initial trajectory was rotated to obtain the approximate launch date where the trajectory end-point was in the vicinity of Jupiter. 200 control segments (201 nodes) were used to obtain adequate resolution, with a constraint tolerance of 10,000 km. Figure 5.22 shows the trajectory, launched on December 1, 2012 with a C_3 of $5 \text{ km}^2 \text{ s}^{-2}$, and arriving on December 1, 2018, with an arrival hyperbolic excess velocity of 6.567 km s^{-1} . Figure 5.23 shows the control angle profiles, and Figure 5.24 shows the orbital element evolution. Figure 5.25 shows that the radial velocity tends towards zero at Jupiter arrival, and the maximum temperature does not exceed 315 K, a few days after the minimum solar approach of 0.68 AU. This final perihelion does not go too low, such that the arrival velocity would be increased.

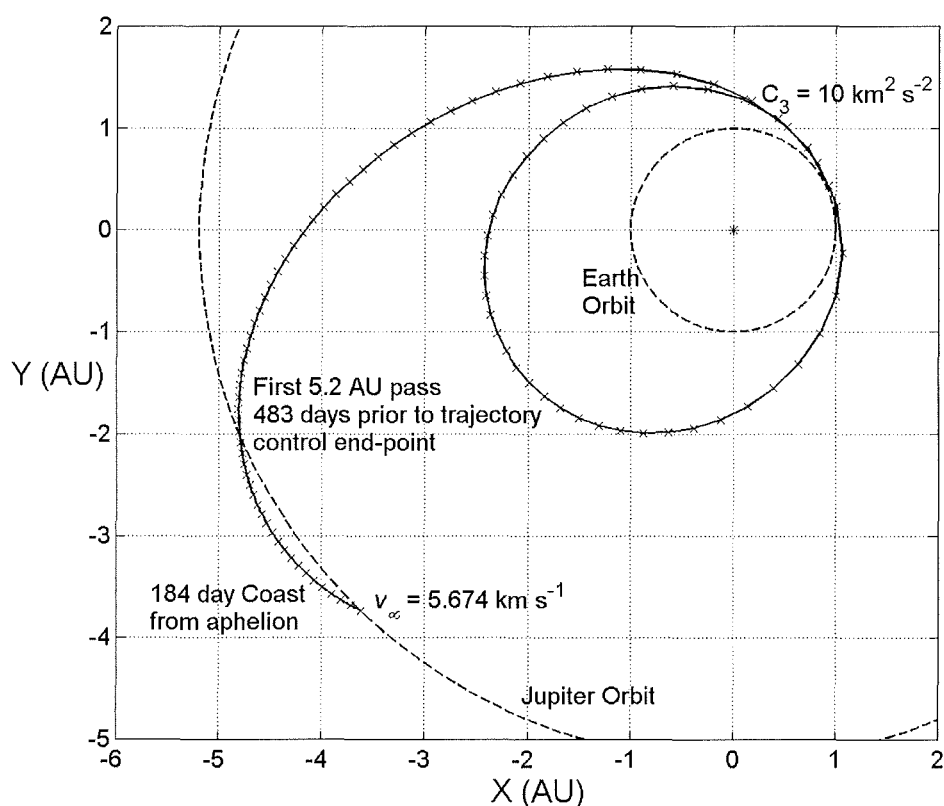


Figure 5.21: 0.5 mm s^{-2} , $C_3=10 \text{ km}^2 \text{ s}^{-2}$ single loop, Earth-Jupiter trajectory, with 'overshoot' and coast segment outside of 5.2 AU (2300 days)

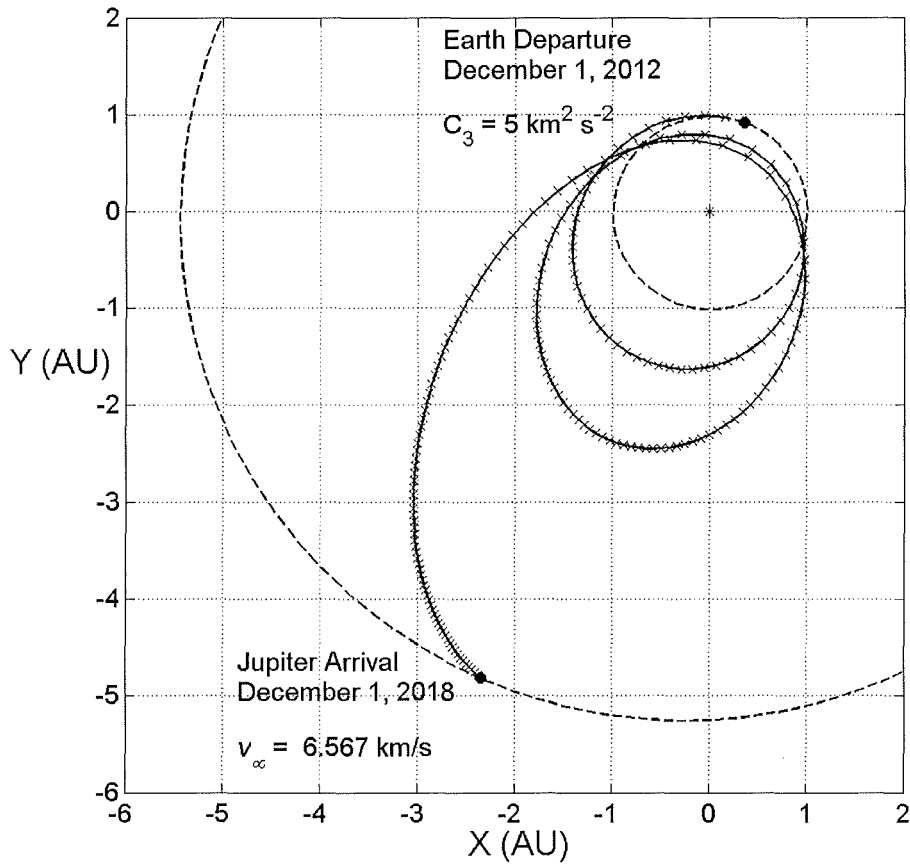


Figure 5.22: Earth-Jupiter, 6 year, 0.37 mm s^{-2} trajectory with minimised arrival velocity

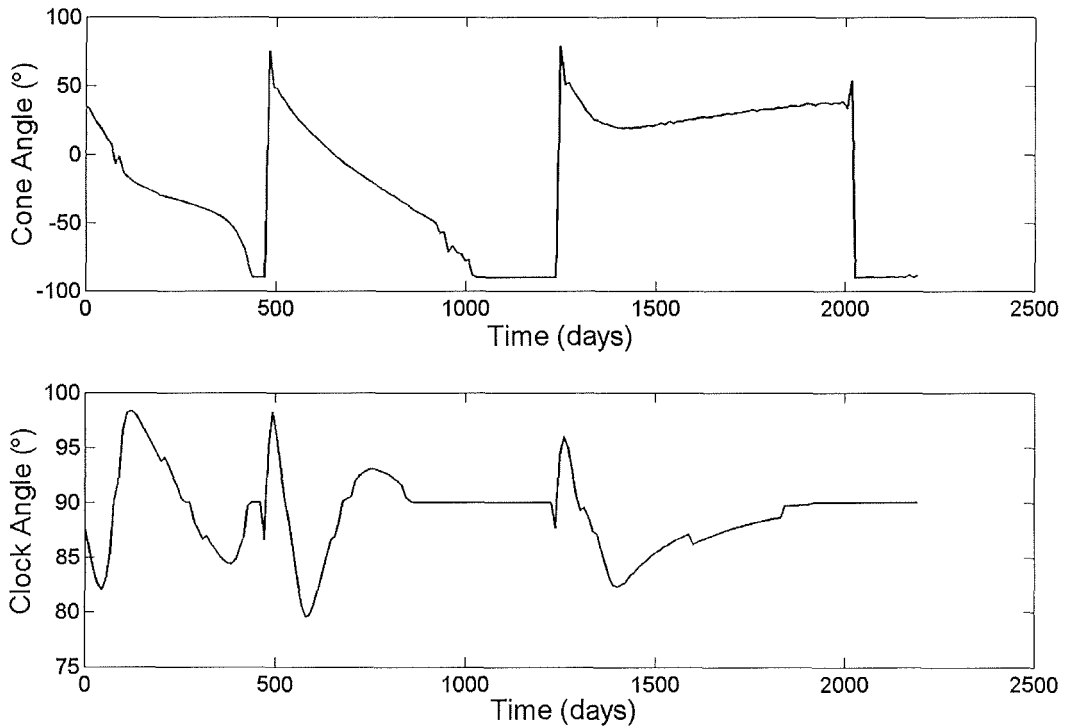


Figure 5.23: 0.37 mm s^{-2} trajectory control angle profile

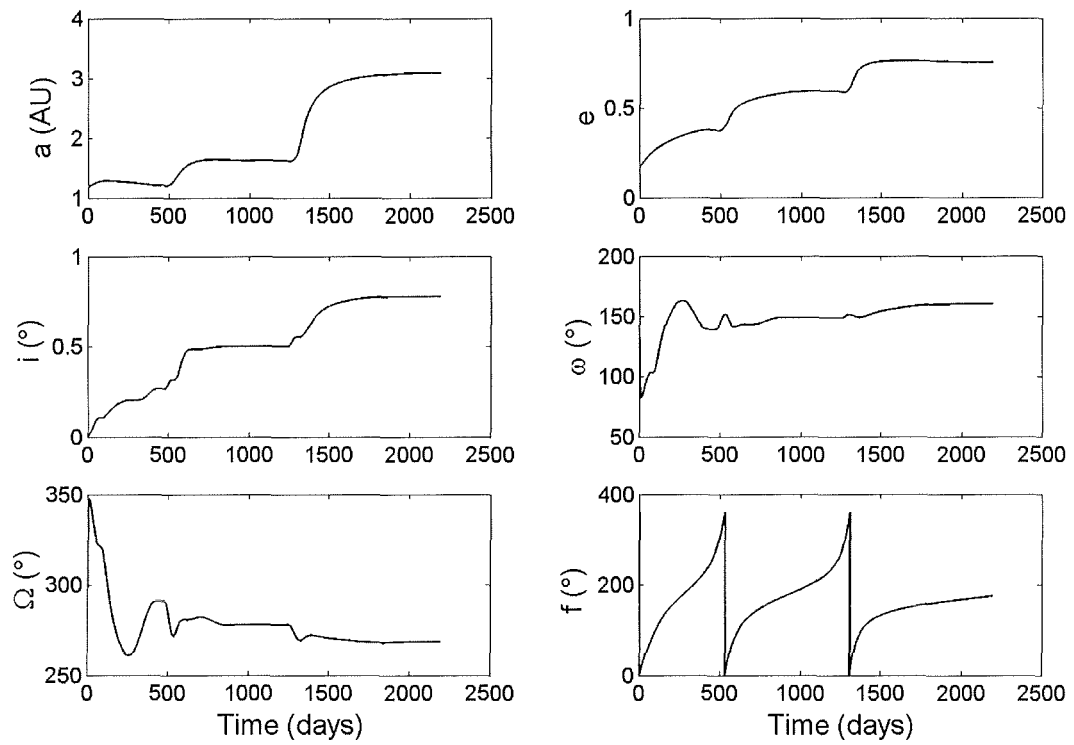


Figure 5.24: 0.37 mm s^{-2} trajectory orbital element evolution

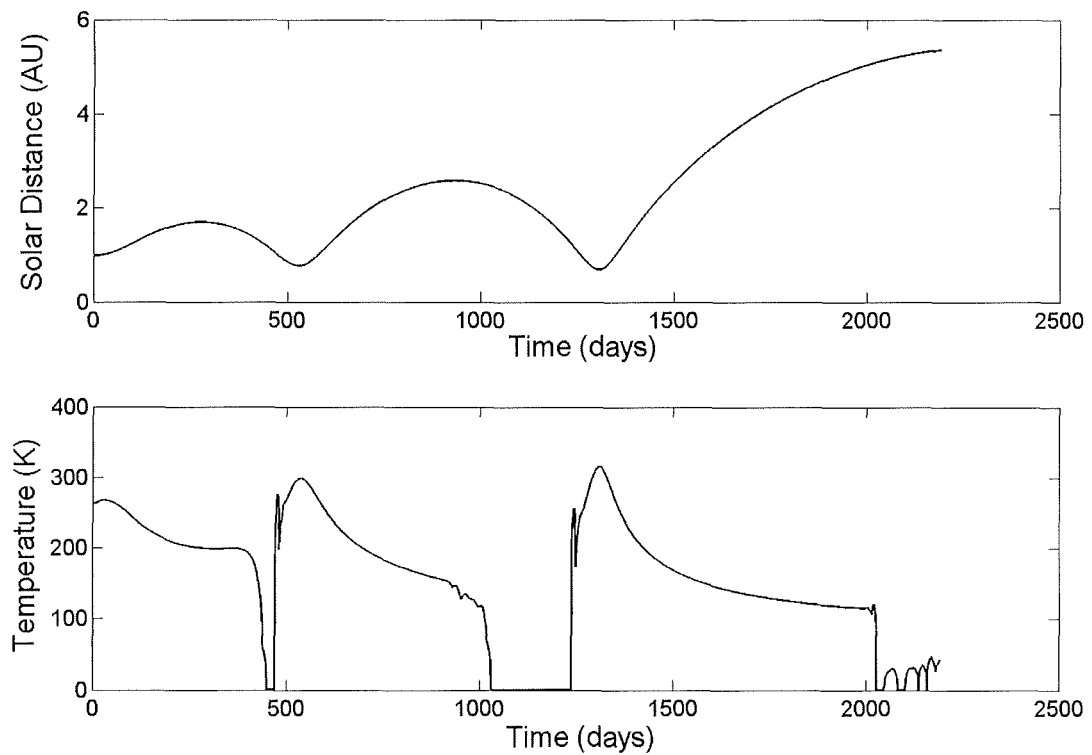


Figure 5.25: 0.37 mm s^{-2} trajectory heliocentric distance and sail film temperature

5.2 Pluto Trajectories

Missions to the outer solar system, beyond Jupiter and Saturn and towards Pluto and the Kuiper Belt, inherently require a long duration cruise. In addition, a Jupiter gravity assist is commonly employed to reduce the launch energy required. Reaching Jupiter in itself is a difficult task, as has been found, and usually requires gravity assists at the inner planets for chemical propulsion. Pluto is believed to belong to the Kuiper Belt, which begins at approximately 30 AU, possibly extending to as far as 100 AU. The Δv requirements are large for ballistic transfers. A direct, minimum-energy Hohmann transfer to Pluto requires a C_3 of $135 \text{ km}^2 \text{ s}^{-2}$, an orbit insertion burn of 6.3 km s^{-1} , and takes 45 years, whereas a direct 7 year flyby trajectory would require a C_3 of order $280 \text{ km}^2 \text{ s}^{-2}$. This fast flyby launch energy can be substantially reduced using a Jupiter gravity assist, but still requires over $100 \text{ km}^2 \text{ s}^{-2}$ at launch [Minovitch, 1994]. The launch energy can be reduced through inner planet gravity assists, but at the expense of increased trip time and diminished launch opportunities. The NASA New Frontiers mission to Pluto and the Kuiper Belt is scheduled for a direct launch to Jupiter, where a gravity assist is used to reach Pluto. The launch is expected to occur in January 2006 aboard an Atlas V 551, with Star 48B upper stage. The energy supplied by the launcher is $149\text{-}157 \text{ km}^2 \text{ s}^{-2}$, arriving at Jupiter in March/April 2007, and arriving at Pluto-Charon 10 years later in 2016 [Guo and Farquhar, 2002]. It is therefore clear that the launch energy required to reach Pluto is considerable for conventional mission concepts.

Solar sail trajectories to Pluto and the Kuiper Belt have been investigated in recent years [Sauer, 1999] based on the high cruise speeds enabled by using inner loops about the Sun, as was used to reach Jupiter in Section 5.1. Yen has obtained trajectories to Pluto using both solar electric propulsion and solar sails [Yen, 2001]. Yen shows that a typical SEP mission launched in 2010 would require 22.7 years to reach Pluto, whereas a solar sail with a characteristic acceleration of 0.55 mm s^{-2} would require just 10.8 years [C. Yen, 2003, personal email communication]. Leipold has also produced trajectories to Pluto, a single "photonic assist" trajectory for 1.0 mm s^{-2} in 13.2 years and a dual assist trajectory for 0.7 mm s^{-2} in 10.5 years [Leipold, 2000]. The effect of the number of initial close approaches to the Sun (to drive up the orbit eccentricity) in attaining the solar system escape velocities necessary to reach the edge of the Kuiper Belt at 30 AU, is shown in Figure 5.26

[Sweetser and Sauer, 2001]. These trajectories are the minimum trip times to a heliocentric distance of 30 AU, with zero inclination changes, and as such are somewhat less than the time required to reach Pluto, which has a relatively high inclination. The dashed curves correspond to a perihelion limit constrained to the labelled closest approach, whereas the solid line has no constraint imposed. A direct spiral transfer corresponds to 0.5 revolutions, a single solar fly-by is the 1.5 revolution curve, 2.5 revolutions is the two fly-by case, with the three fly-by case denoted by 3.5 revolutions. It can be seen that in every case the greater the number of close solar approaches, as the number of revolutions is increased by an integer number each time, the trip times are always reduced. However, the degradation of the sail film caused by repeated close solar passes could be high. Therefore, a trade-off should ultimately be conducted between trip time and the number of assists, to minimise degradation of the sail film.

Trajectory optimisation using the NPSOL/SNOPT parameter optimisation method described in Chapter 2 was found to be problematic. Linear interpolation was again used between discrete control nodes. The resolution of these nodes has to be extremely high for multiple “photonic assist” trajectories. This is because during the photonic assist the cone angle rotates through up to 180° . At approximately 0.25 AU from the Sun the solar radiation pressure force is *significantly* larger than at 1 AU. In addition, if the true continuous control angle profile (as used by Yen [2001] and Sauer [1999] in the calculus of variations method) executes a thrust reversal at perihelion through a cone angle range $\pm 90^\circ$, then a parameterised, erroneous peak cone angle of, for example $\pm 80^\circ$, will produce a significantly greater thrust, altering the resulting trajectory. The total number of control nodes can be increased up to 1000 nodes for a triple photonic assist, at the limit of computational ability and posing extreme demands on the ability of the optimisation algorithm NPSOL to handle that number of parameters. However, because these control nodes are equally spaced in time over 10-15 years to get to Pluto, the distance between nodes at the final perihelion that targets the asymptote is around a few days, covering a considerable distance about perihelion. Therefore, the resolution of the trajectory cannot be achieved with sufficient accuracy. It is also possible to optimise the trajectory past the final photonic assist to about 5 AU (where the solar radiation pressure force diminishes rapidly) and then propagate with the sail attitude fixed face

on to the Sun at zero pitch. This enables the use of a manageable number of parameters, with the distance between the nodes being smaller, thereby increasing the nodal resolution. Unfortunately, it was found that the number of control nodes was not high enough even for a 1700 day period of optimisation. If any more than 1000 control nodes is used then the optimisation algorithm becomes unstable.

The method which was ultimately adopted was to use an analytical control law that maximises the rate of change of orbit eccentricity until just prior to the final photonic assist, and then optimise with 50 control nodes for the remainder of the journey to Pluto. Macdonald [2005], has recently had greater success with blended analytical control laws for Pluto, and Heliopause trajectories. For high performance sails with just one assist, the trajectories were fully optimised, but the lower performance sails had to be optimised using the eccentricity control law for the initial eccentricity pumping loops.

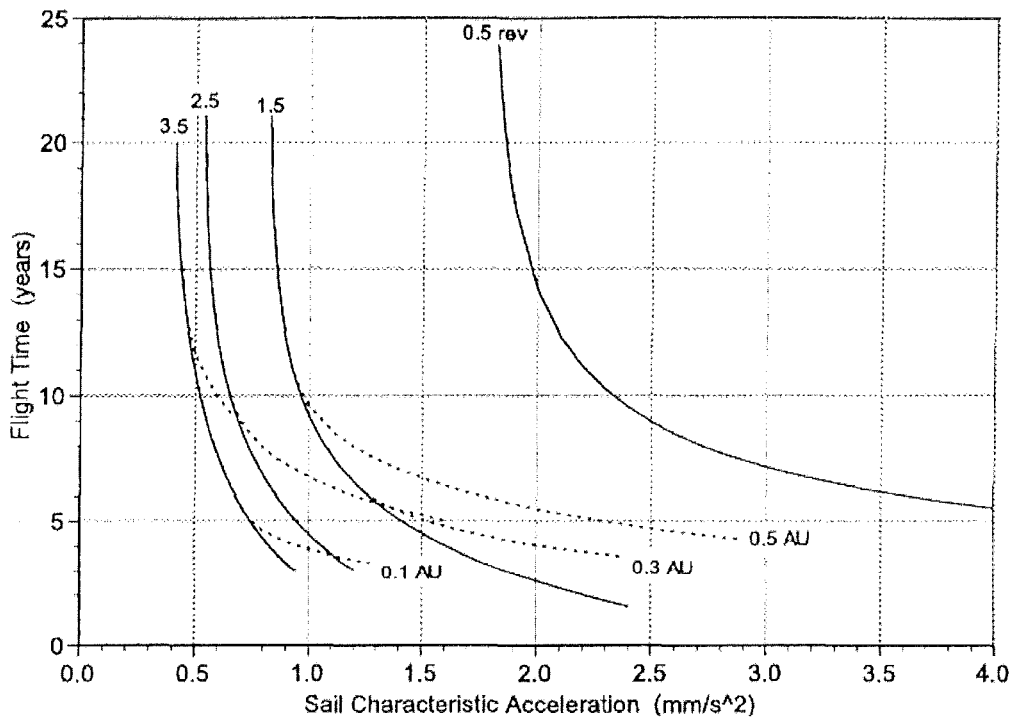


Figure 5.26: Trip times to 30 AU against characteristic acceleration [Sweetser and Sauer, 2001]

5.2.1 Single Photonic Assist Fast Flyby

A high-performance spinning disk sail could be used to reach Pluto after just one solar photonic assist. It can be seen from Figure 5.26 that there is a negligible penalty in choosing just a single assist against the dual assist, once the characteristic acceleration is increased above 1.5 mm s^{-2} , since the curves level off and the trip times to 30 AU are relatively low. The fast Pluto flyby trajectories were fully optimised with 201 control nodes (200 equally spaced linear interpolation segments), giving a manageable 403 optimisation parameters for the NPSOL optimiser. Figure 5.27 shows the effect on trip time to Pluto for the single photonic assist trajectory with characteristic accelerations from 1.0 to 3.0 mm s^{-2} . An inequality constraint was placed on the minimum solar approach distance of 0.25 AU so that a conventional polyimide sail with aluminium and chromium coatings can be considered. In fact, this thermal limit was only reached for accelerations approaching 3.0 mm s^{-2} . As in Figure 5.26, the curves appear to level off at above 2.0 mm s^{-2} . The hyperbolic excess velocity at Pluto flyby is shown in Figure 5.28, where it is observed that the velocity is a reciprocal of the trip time, as expected.

The effect of varying the launch date on the trip time was investigated for a characteristic acceleration of 1.0 mm s^{-2} . A scan from 2003 to 2015 is shown in Figure 5.29. It is observed that as Pluto moves away from its 1989 perihelion, due to a later launch date, this has the effect of increasing the transfer time as the final heliocentric distance is increasing. As Pluto moves away, it is also moving closer to its 2018 descending node passage. However, this has little effect on the trip time, since the solar photonic assist can be used to effect an inclination change close to the Sun. The hyperbolic excess velocity in Figure 5.29 can be seen to fluctuate by only a small amount, since as Pluto moves away in its orbit, both the spacecraft velocity and the planet velocity are decreased, leaving the relative velocity almost unchanged. The variation of the trip time over one Earth year is of order 6 months, but this has negligible impact on trip time since the photonic assist can be used to effectively select any departure asymptote. Therefore, it is concluded that in the timeframe considered, a solar sail mission to Pluto would not be constrained by launch date. A low launch energy ballistic mission, however, is severely constrained to the launch windows of the Jupiter gravity assist and any prior inner planet assists.

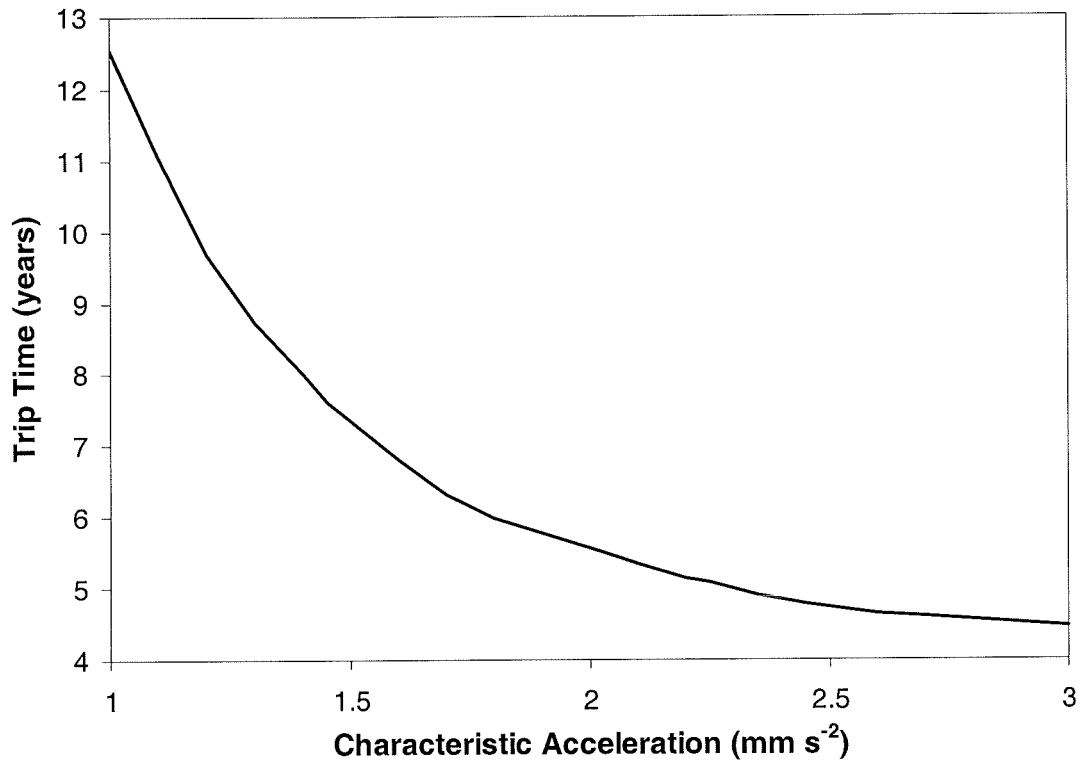


Figure 5.27: Pluto flyby single photonic assist trip times (departure Feb. 5, 2014)

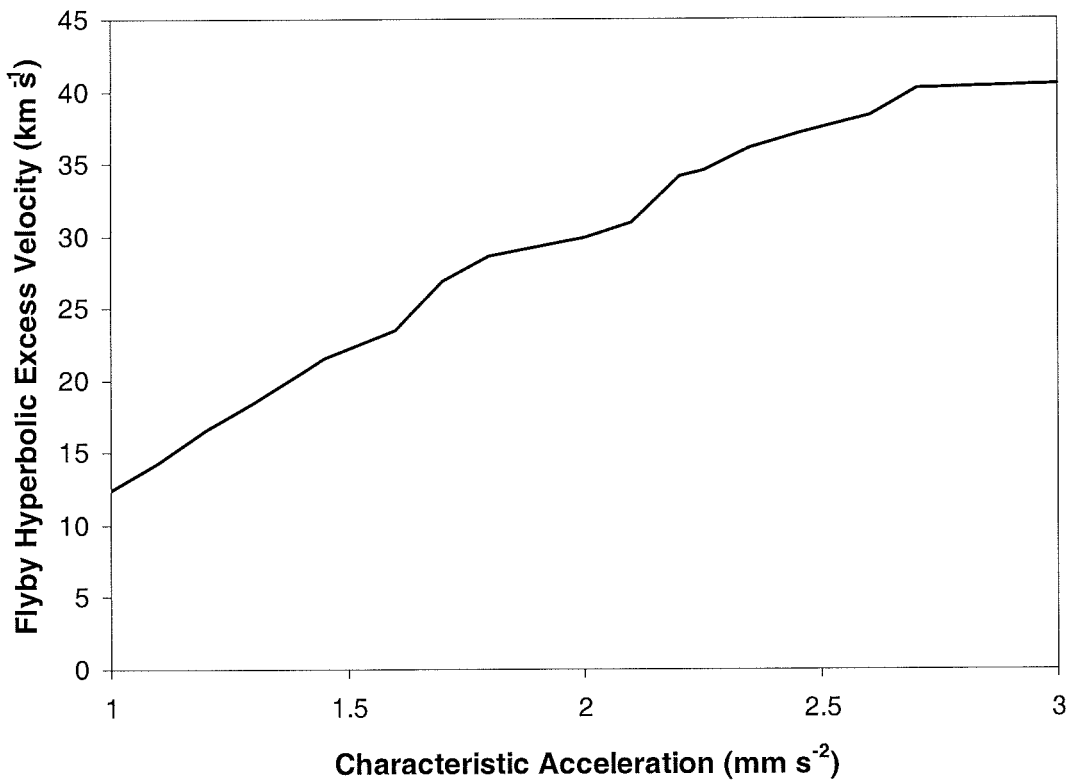


Figure 5.28: Pluto single photonic assist flyby velocity (departure Feb. 5, 2014)

For a high performance spinning disk sail with a characteristic acceleration of 3.0 mm s^{-2} , a fast flyby of Pluto can be achieved in just 4.46 years. The fully optimised single photonic assist trajectory is shown in Figure 5.30. Earth departure is on February 5, 2014 with zero hyperbolic excess velocity. A C_3 of zero is in marked contrast to the $C_3 \sim 100 \text{ km}^2 \text{ s}^{-2}$ launch excess required for ballistic missions. In Figure 5.30 the ticks on the trajectory correspond to the 201 control nodes, spaced 8.15 days apart. Pluto flyby occurs on July 23, 2018, which is before 2020, when the atmosphere is expected to freeze back onto the surface. The flyby relative velocity is high at 40.45 km s^{-1} , and it is unclear what effect such a fast encounter would have on the science returns from the mission.

Figure 5.31 shows a magnified 4 x 4 AU image of the initial photonic assist. The closest solar approach is at the enforced limit of 0.25 AU. Figure 5.32 shows the control angle profile. The cone angle thrust reversal manoeuvre can be seen in the initial portion. The irregularity in the remainder of the trajectory is due to the insensitivity of the trajectory to thrust orientation at large distances from the Sun, and is an artefact of the numerical algorithm only. The NPSOL optimisation algorithm can essentially choose the control angles to be any value beyond say 5 AU, since the photon pressure on the sail is so weak that the solar sail thrust has negligible effect on the trajectory shape. A large number of control nodes causes some instability of NPSOL. This cone angle fluctuation is observed to be time-averaged about zero. The eccentricity boost close to the Sun can clearly be seen in Figure 5.33, which shows the temporal evolution of the orbital elements. Figure 5.34 shows the heliocentric distance and sail film temperature against time. The maximum temperature reached at 0.25 AU is 440 K, below the polyimide substrate limit of $\sim 520 \text{ K}$, assuming an aluminium front coating and high emissivity chromium rear coating.

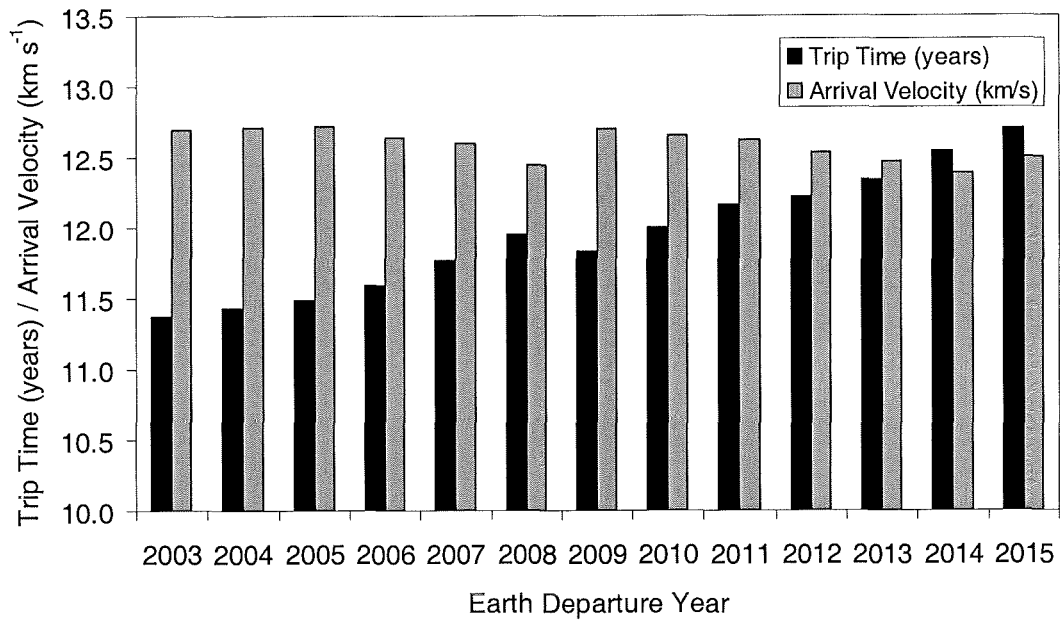


Figure 5.29: Launch date scan for 1.0 mm s⁻²

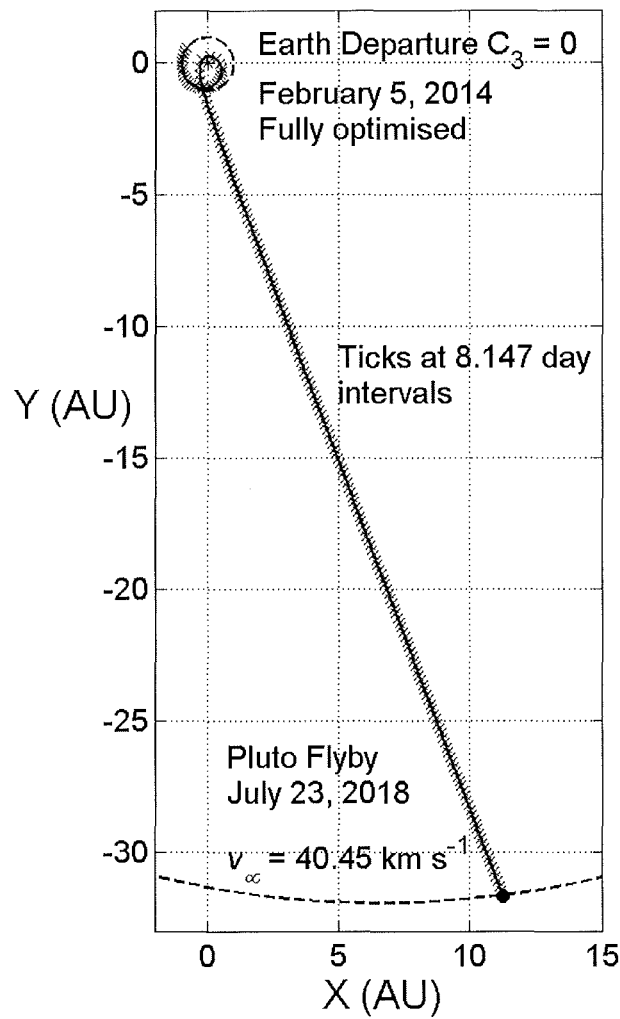


Figure 5.30: 3.0 mm s⁻² fully optimised single photonic assist Pluto flyby

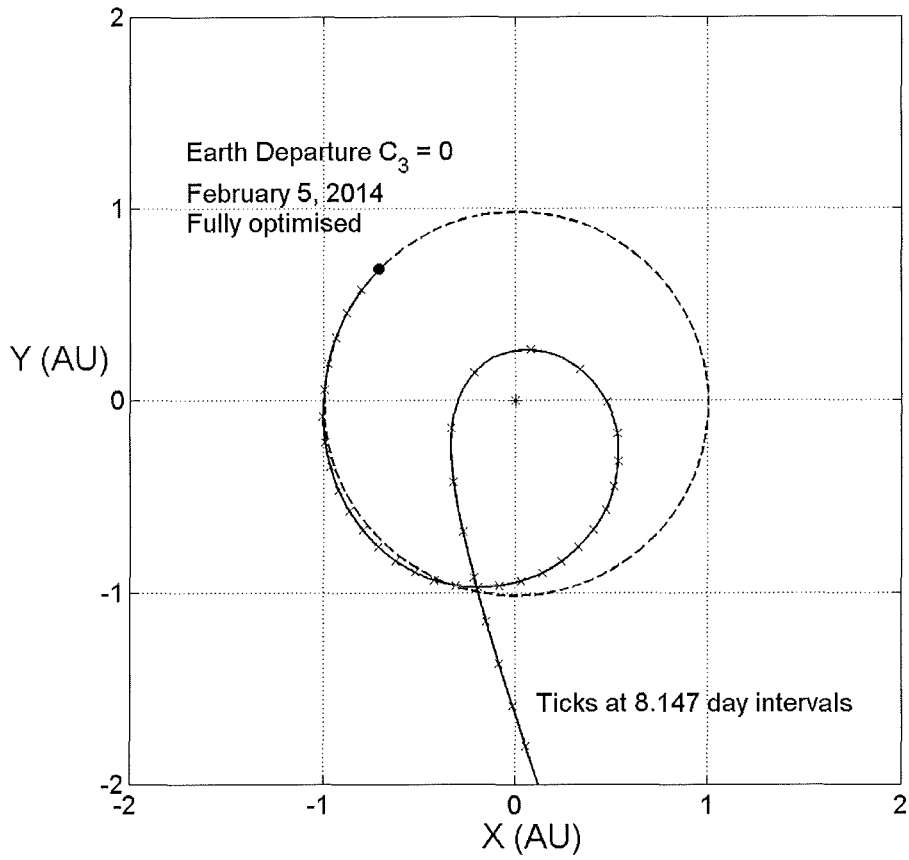


Figure 5.31: Magnified image of initial 3.0 mm s^{-2} single photonic assist

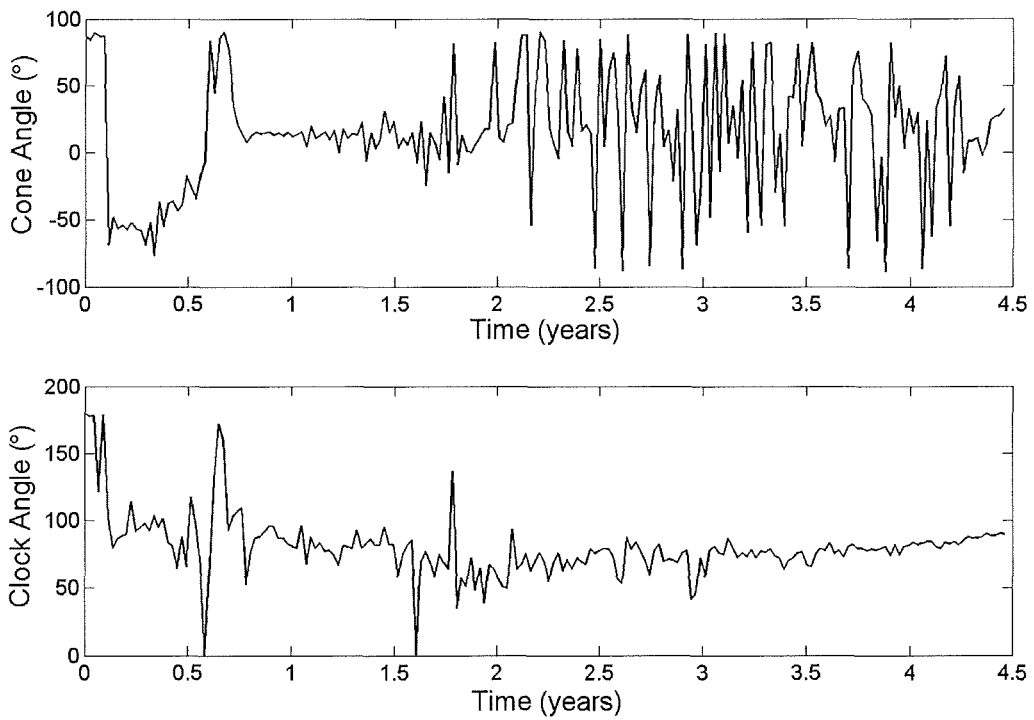


Figure 5.32: 3.0 mm s^{-2} single photonic assist Pluto flyby cone and clock angle profile

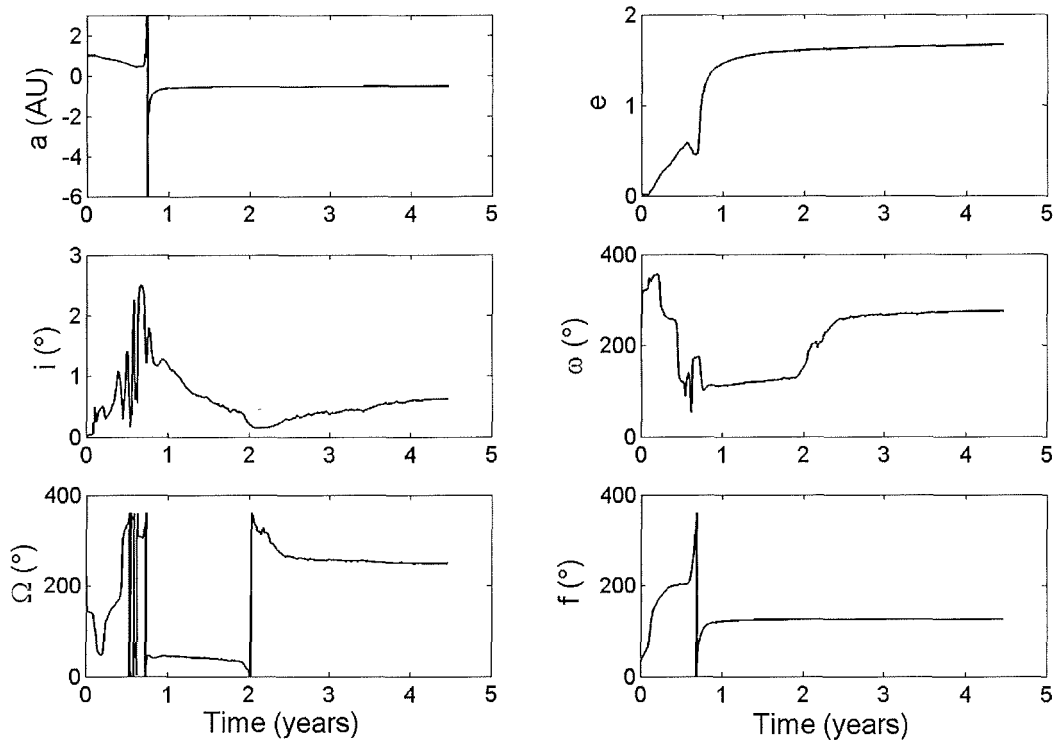


Figure 5.33: 3.0 mm s^{-2} single photonic assist Pluto flyby orbital elements

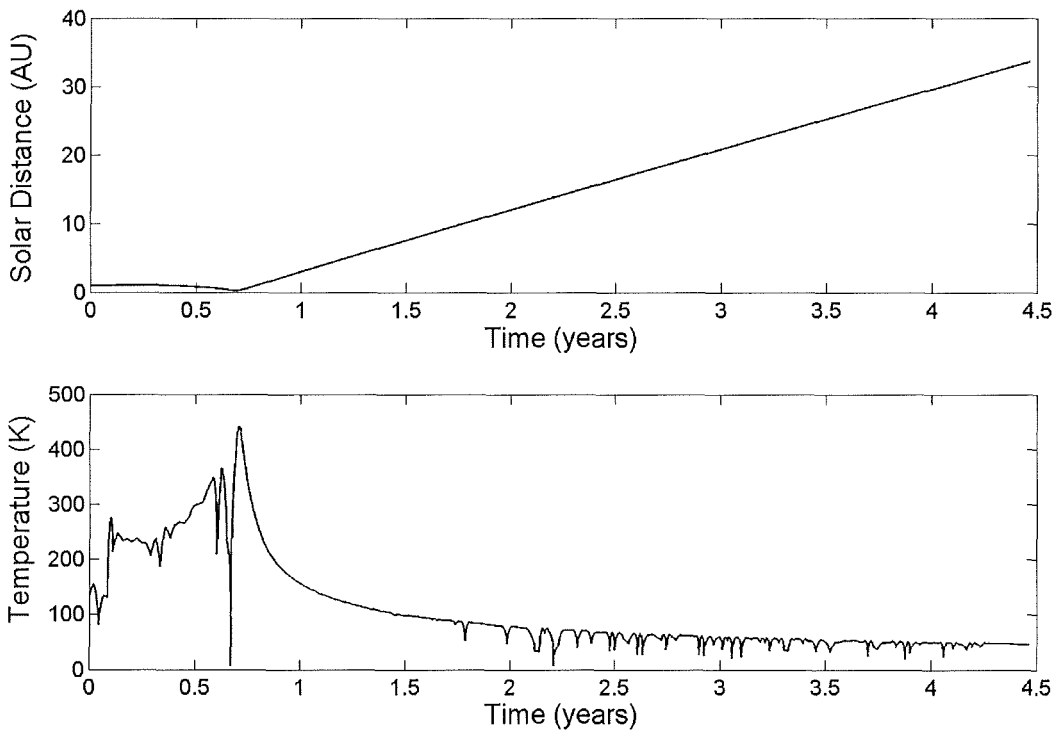


Figure 5.34: 3.0 mm s^{-2} single photonic assist Pluto flyby heliocentric distance and sail film temperature

5.2.2 Triple Photonic Assist – Slow Flyby

A slow flyby of Pluto can be achieved using a square solar sail with a characteristic acceleration of 0.5 mm s^{-2} . An analytical control law is used to maximise the rate of change of orbit eccentricity, producing a triple photonic assist trajectory with 3 eccentricity pumping loops about the Sun. The control law is used for 4.7 years until *just prior* to the third perihelion. Then, NPSOL is used to optimise the remaining trajectory to Pluto with 51 control nodes, or 50 equal linear interpolation segments. In this regard, the optimisation of the final perihelion pass can target the hyperbolic asymptote and obtain the correct inclination to flyby Pluto. Earth departure is on May 3, 2010 with $C_3=0$, arriving at Pluto 14.13 years later on June 17, 2024. The trajectory is shown in Figure 5.35 with ticks corresponding to the control nodes at 68.9 day intervals. The closest solar approach is at 0.32 AU, greater than the constraint of 0.25 AU imposed, to trade-off spiral-down time against total trip time. The flyby velocity at Pluto is a slower 14.53 km s^{-1} , more akin to the NASA New Frontiers mission 12 km s^{-1} fly-by speed. Yen [2001, 2003, personal email communication] has generated a trajectory to Pluto using an ideal sail characteristic acceleration of 0.5545 mm s^{-2} with the true optimal, Calculus of Variations method, that underpins the NASA/JPL VARITOP trajectory tool.

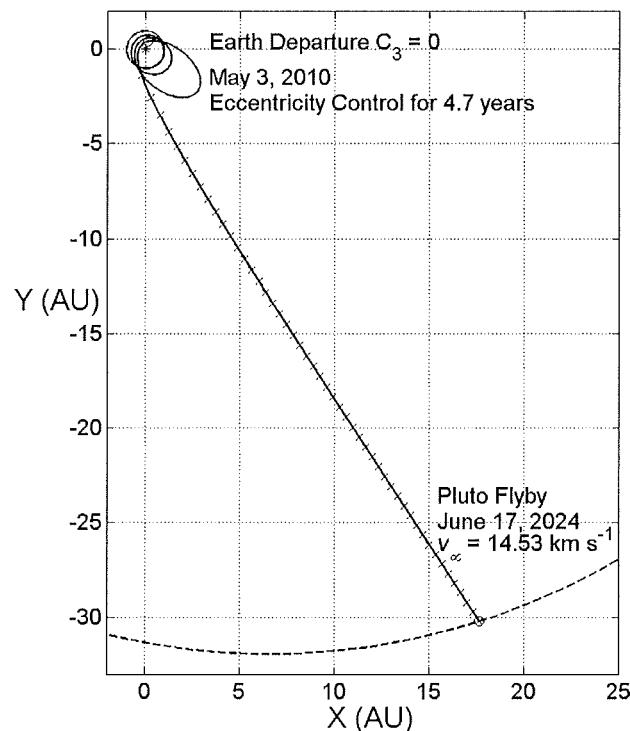


Figure 5.35: 0.5 mm s^{-2} triple photonic assist Pluto flyby

The trip time for Yen's triple assist trajectory is 10.8 years because of the somewhat higher acceleration. If the characteristic acceleration were reduced to 0.5 mm s^{-2} , then extrapolation from Figure 5.26 yields a true optimal Pluto flyby time of order 13 years. This means that the trajectory from the hybrid eccentricity control law and NPSOL optimiser is close to the true optimal trip time. Figure 5.36 shows the initial three photonic assists in magnified detail, with the transition point from closed loop eccentricity control to open loop optimisation at 4.7 years labelled. The cone and clock angle control profiles are shown in Figure 5.37. The clock angle is fixed at 90° for in-plane thrust during the eccentricity control. The 3 thrust reversal manoeuvres at each perihelion can be seen and then the discontinuity when transition to optimised control takes place. The low number of nodes during the optimised phase means that the NPSOL optimiser can produce a smooth profile here. The temporal evolution of the orbital elements seen in Figure 5.38 shows the eccentricity pumping and the inclination boost on the final perihelion, as optimised control takes over. The heliocentric distance and sail film temperature are shown in Figure 5.39. The gap in the temperature is due to control transition, where there is a discontinuity in the cone angle. The maximum temperature occurs on the third close solar pass at 458 K, again below the expected 520 K polyimide film limit.

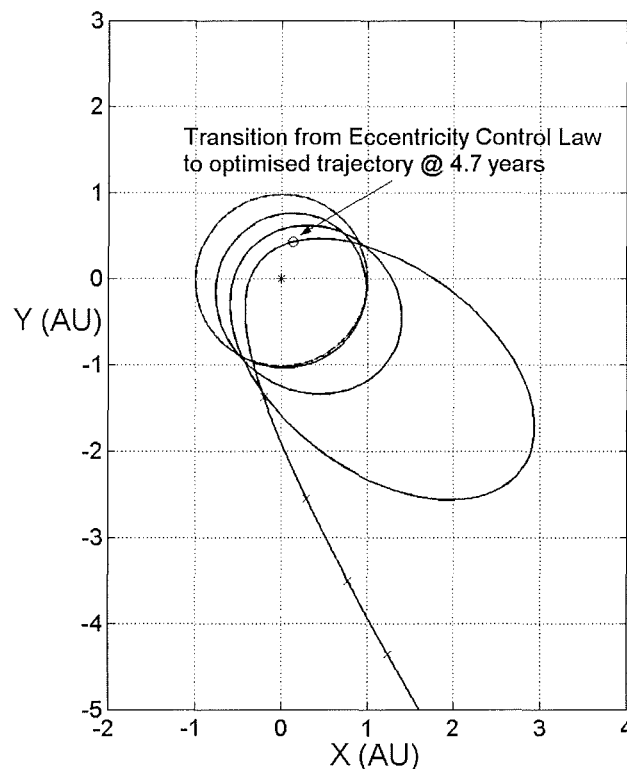


Figure 5.36: Magnified image of initial 0.5 mm s^{-2} Pluto flyby

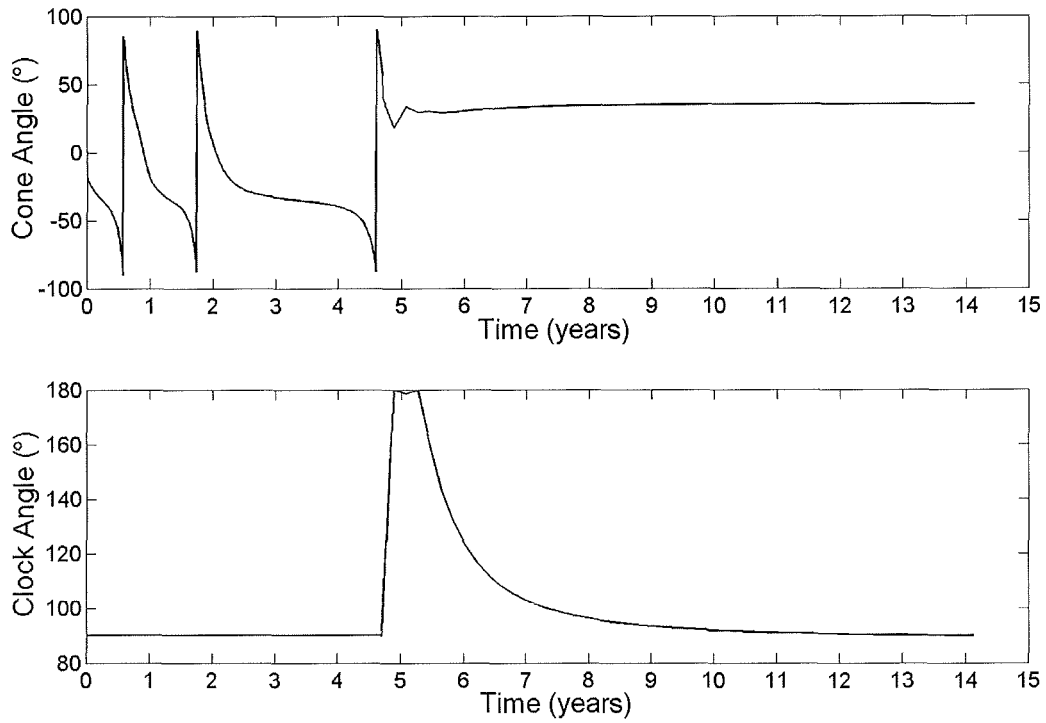


Figure 5.37: 0.5 mm s^{-2} triple photonic assist Pluto flyby control angle profile

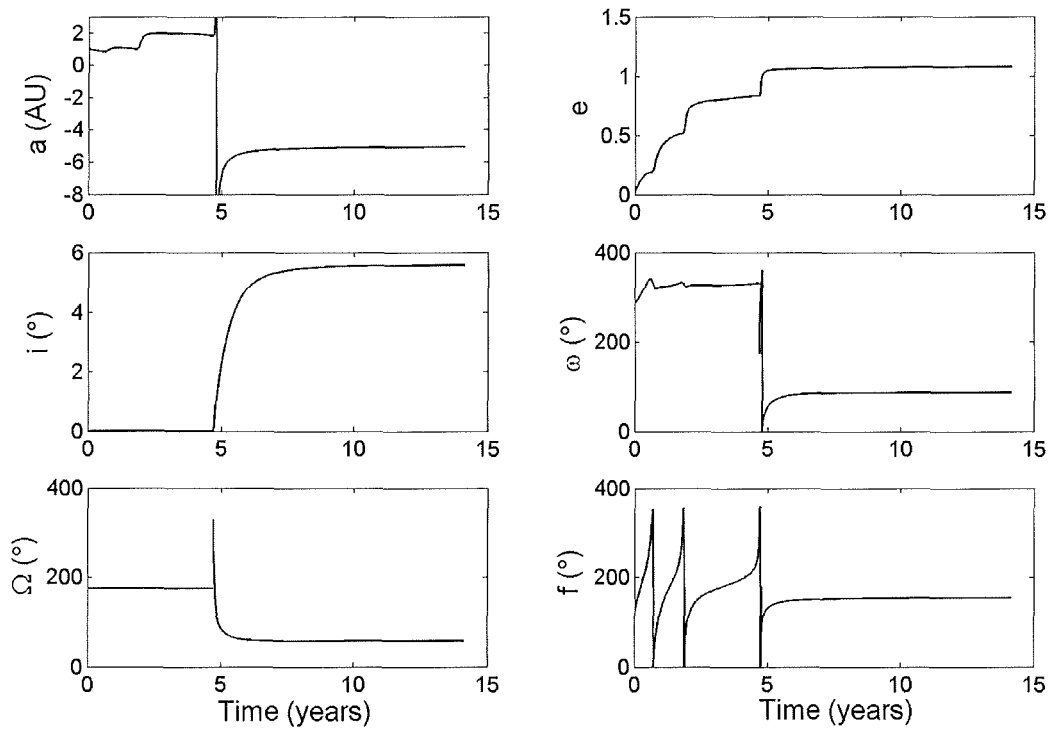


Figure 5.38: 0.5 mm s^{-2} triple photonic assist Pluto flyby orbital elements

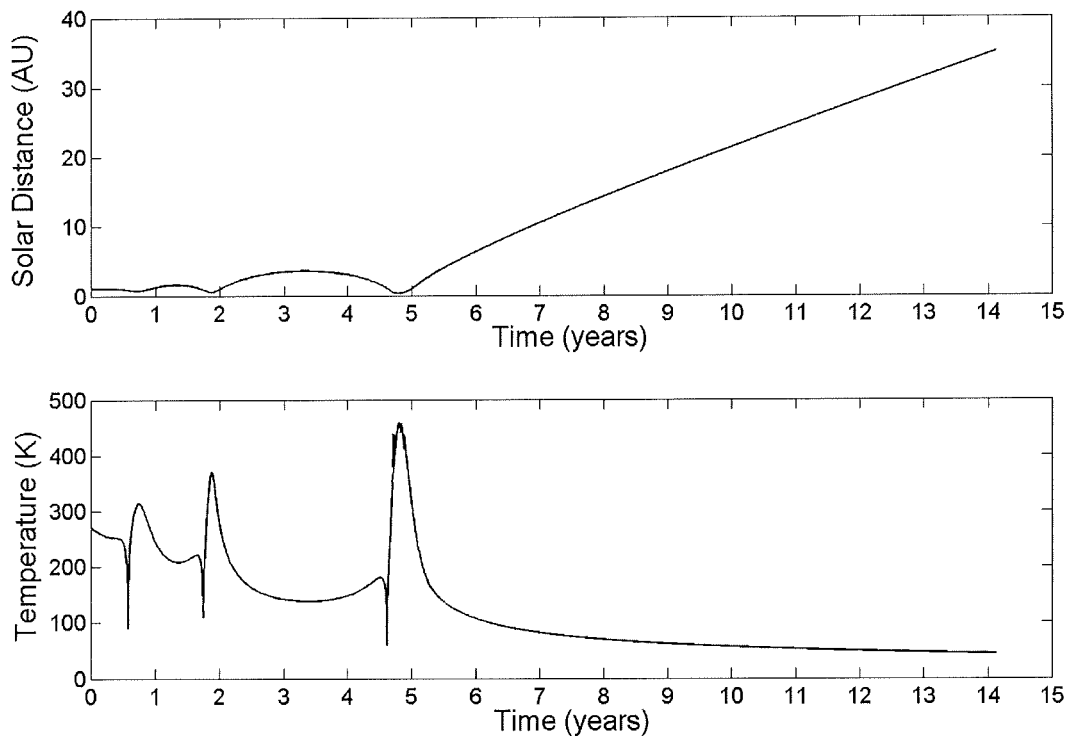


Figure 5.39: 0.5 mm s^{-2} triple photonic assist Pluto flyby heliocentric distance and sail film temperature

5.3 Summary and Discussion

Solar sail trajectories to Jupiter and Pluto have been generated in this Chapter. Analysis of trip-time against characteristic acceleration revealed that a high performance sail (3.0 mm s^{-2}) could be used to perform a direct rendezvous with Jupiter ($C_3=0$) in 5.7 years. Flyby trajectories have also been analysed, making use of the solar photonic assist concept. A single-loop, minimum time flyby of Jupiter could be achieved using a characteristic acceleration of 0.65 mm s^{-2} in 4.2 years. In an attempt to reduce the arrival hyperbolic excess velocity, in the context of Jovian orbit insertion, the remaining bulk of the Jupiter work concentrated on minimisation of the arrival velocity, for multiple loop flyby trajectories. A parametric analysis was conducted by minimising the arrival velocity for single-loop trajectories, while incrementing the trip time. It was discovered that it was problematic to reduce arrival velocity much below 6 km s^{-1} . Subsequently, deeper analysis was conducted for dual-loop minimised arrival velocity trajectories. Lower characteristic

accelerations were used in combination with positive launch excess energy in a trade-off with trip time and the number of close solar loops. It was found that the positive C_3 can be used to reduce the number of loops by creating an initial larger aphelion. The reduced number of loops results in a higher final perihelion radius, which means that the arrival velocity is lower. For a 6 to 7 year limit on trip time, the minimum arrival velocity obtained was of order 4300 m s^{-1} . This analysis could not produce continuous surface plots, but a number of intriguing features were evident. An example trajectory was shown, to represent the trade-off required between the trajectory parameters. Both characteristic acceleration and arrival velocity (which reflects the size of the chemical orbit insertion burn needed) affect total launch mass, although the characteristic acceleration is probably the more important factor, since sail size depends on both the acceleration required and the mass of the chemical propellant within the cruise stage. A six year trajectory was shown, with a characteristic acceleration of 0.37 mm s^{-2} , departing the Earth on December 1, 2012 with a launch C_3 of $5 \text{ km}^2 \text{ s}^{-2}$, arriving at Jupiter with an arrival excess velocity of 6.57 km s^{-1} . Further work is required into the relationship between all of the trajectory parameters for reaching Jupiter.

After initial parametric analysis of the relationship between characteristic acceleration and Pluto arrival velocity for single-loop flyby, two Pluto flyby scenarios were generated. Firstly, a high performance sail could be used with a fully optimised single photonic assist, to reach Pluto in under 4.5 years, with a characteristic acceleration of 3.0 mm s^{-2} ($C_3=0$). Departure on February 5, 2014 would enable Pluto flyby on July 23, 2018. This arrival date is critically important from a scientific viewpoint, since the atmosphere of Pluto is expected to freeze back onto the surface in 2020, as Pluto moves away from the Sun in its orbit [Guo and Farquhar, 2002]. Finally, a slower Pluto flyby would be enabled using a characteristic acceleration of 0.5 mm s^{-2} , in a triple photonic assist manoeuvre generated using a combination of a locally optimal eccentricity control law and the NPSOL optimisation method. The trip time in this case is 14.1 years with a C_3 of zero. Both these trajectories are in marked contrast to chemical propulsion, which would require a C_3 of order $100 \text{ km}^2 \text{ s}^{-2}$, even when using a Jupiter gravity assist. The work presented in this Chapter serves as a precursor for Chapter 6, which will show a detailed investigation of trajectories to the Heliopause at 200 AU.

Chapter 6

Interstellar Heliopause Probe Trajectories

In this Chapter, extensive parametric analysis of trajectories to the Heliopause is conducted. The work builds on the solar photonic assist concept, which was used for Jupiter and Pluto missions in Chapter 5. The necessarily high solar system escape velocities require the use of multiple loops for lower performance sails, and thus very low perihelion radii. This has direct implications for the thermal loading on the sail film and structure. Therefore, to complement the trajectory analysis, an investigation of the effect of minimum solar distance, front-surface reflectivity, and back-surface emissivity on sail film temperature must be performed. For a fast mission to the Heliopause, the variation of trip-time and sail jettison velocity (at 5 AU) against characteristic acceleration and final perihelion radius will be investigated, and an example trajectory presented. For a slower Heliopause mission, using lower performance solar sails, the analysis will focus on the use of multiple loops, with dual and triple photonic assists. The variation of escape velocity, and thus trip-time, will be investigated as a function of final perihelion radius and characteristic acceleration. The question of whether a Jupiter gravity assist can be used on the exit asymptote will be investigated, and it will be seen if any useful reduction in trip-time is possible. Finally, following on from the analysis in Chapter 5, the effect of positive launch excess energy at launch will be investigated, to see if there is any appreciable benefit for Heliopause trajectories. The parametric analysis will be complemented by numerous example trajectories.

The trajectory requirements for the ESA/ESTEC Interstellar Heliopause Probe (IHP) concept are to reach a heliocentric distance of 200 AU in less than 25 years, delivered using a Soyuz-Fregat launch vehicle [Lyngvi *et al*, 2003]. This requires a minimum solar system escape velocity of order 8-10 AU per year. In addition, the escape asymptote of the trajectory should be directed towards the nose

of the Heliopause. This is the shortest distance to the Heliopause, where the bow shock occurs as the Sun moves through the interstellar medium. The ecliptic coordinates of the nose of the Heliopause are at a longitude/azimuth of 254.5° and a latitude/elevation of 7.5° .

A roadmap of propulsion options for interstellar travel has been produced by Wallace [1999]. The NASA Interstellar Probe (ISP) mission centres on the use of a very high performance spin-stabilised disk sail, exhibiting a characteristic acceleration of 3.04 mm s^{-2} , that will reach 200 AU in 15 years with a thermally limited, close solar approach of 0.25 AU [Wallace *et al*, 2000, Garner *et al*, 2000]. The single solar photonic assist trajectories used for the NASA ISP study were generated by Carl Sauer at JPL, and are detailed in an extensive parametric study [Sauer, 1999]. The NASA ISP baseline trajectory is shown in Figure 6.1. Parametric studies of multiple photonic assists have been conducted at NASA/JPL for missions to Pluto and the Kuiper belt that could be extended to the Heliopause [Sweetser and Sauer, 2001]. C. Yen at JPL has generated a dual assist trajectory that reaches 200 AU in 29 years, with a characteristic acceleration of 1.0 mm s^{-2} , and with a perihelion thermally constrained at 0.3 AU [Yen, 2001]. A number of novel fast Heliopause trajectories have also been discovered by G. Vulpetti, using a strategy of orbital angular momentum reversal, but this is not considered necessary for IHP missions [Vulpetti, 1997]. Recently, trajectory analysis has been conducted by Leipold *et al* [2003]. Leipold has focused on using lower performance sails than NASA, that are enabled using a conventional 3-axis stabilised square sail with DLR derived composite booms. In particular, a 21.2 year 0.75 mm s^{-2} trajectory has been presented, that spirals down to 0.37 AU and then executes a dual photonic assist (see Figure 6.2). However, the closest solar approach was just 0.1 AU, placing severe thermal loads on the spacecraft and sail assembly. Conventional polyimide sail substrates (thermal limit $\sim 520 \text{ K}$) with conventional aluminium and chromium coatings will not be able to survive to less than 0.25 AU, and only then for short durations. The temperature effects on the bonding of the sail film segments and boom temperature is thought to be even more critical than the maximum temperature of the sail film itself [M. Leipold, 2004, personal email communication].

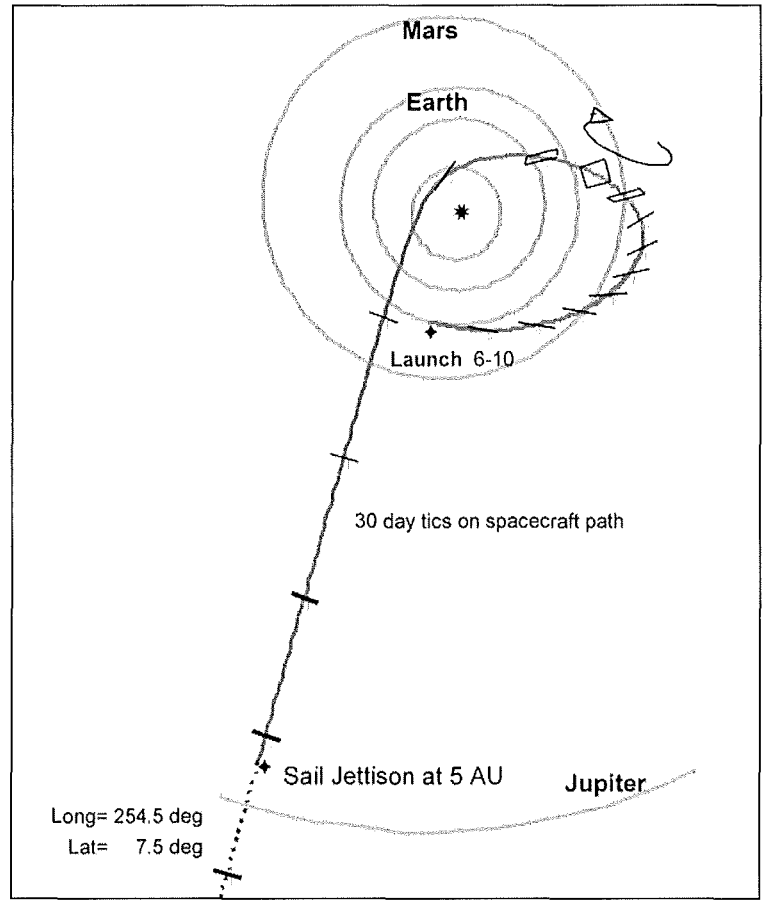


Figure 6.1: NASA Interstellar Probe, 0.25 AU solar pass [Wallace *et al*, 2000]

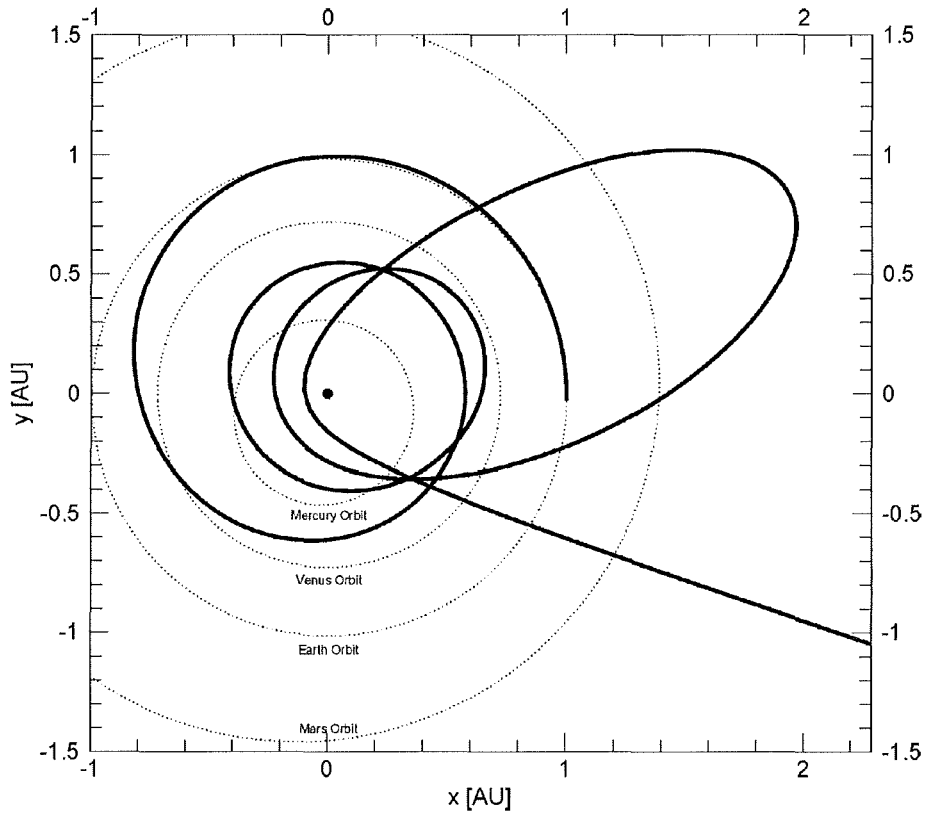


Figure 6.2: 0.75 mm s^{-2} , 21 year trajectory, 0.1 AU solar pass [Leipold *et al*, 2003]

Multiple solar passes will also amplify the degradation of the sail, so it is prudent to minimise the duration and number of close solar passes, thus minimising the number of photonic assists. In the subsequent analysis the preference will therefore be for a single assist trajectory with a perihelion no lower than 0.25 AU, if possible. This drives the sail configuration towards a disk sail due to the larger characteristic acceleration required to reach 200 AU in 25 years [McInnes *et al*, 2004a].

6.1 Fast IHP Mission (single loop)

A parametric analysis was conducted into high performance single photonic assist trajectories. A parameter optimisation method was again used as described in Chapter 2. An improved sequential quadratic programming algorithm was used as the core optimiser. NPOPT 6.2 is a dense non-linear programming algorithm contained within the SNOPT package developed at Stanford University. This optimiser was found to be somewhat more robust for IHP trajectories than the previously utilised NPSOL software. For a preliminary investigation to obtain approximate trip times to 200 AU, the optimisation approach adopted was to maximise the velocity at the point of sail jettison (5 AU) and then optimise the cone angle (2D coplanar) and transfer time until sail jettison. The post-jettison time to 200 AU can then be determined by analytical propagation of the hyperbolic ballistic trajectory. The results for single photonic assist trajectories using high performance characteristic accelerations from 1.5 mm s^{-2} to 3.0 mm s^{-2} are shown in Figure 6.3. The corresponding 200 AU total trip times are shown in Figure 6.4. The contours are for when thermal limits are placed on the closest solar approach. The solid curve, for unconstrained solar approach, could perhaps be improved towards the lower end of the curve by increasing the initial aphelion, but this must be traded off against the overall trip time. For example, the unconstrained 1.5 mm s^{-2} trajectory to 250 AU obtained by Sauer [1999] passes within just 0.1 AU of the Sun through forcing a large aphelion at almost the orbit of Jupiter, before spiralling back in towards the Sun (see Figure 6.5). The optimisation approach in this thesis does not easily lend itself to these kind of unconstrained manoeuvres. The most important issue to note is that photonic assist trajectories are highly sensitive to the minimum perihelion distance.

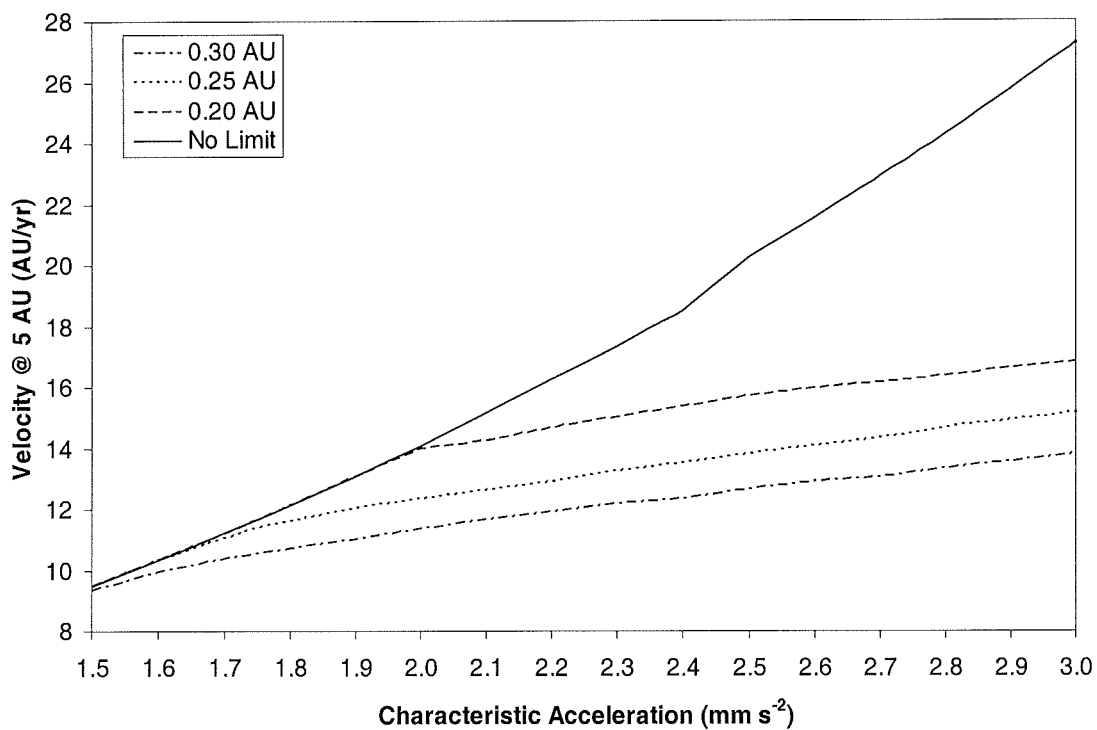


Figure 6.3: Constrained perihelion contours of velocity at 5 AU

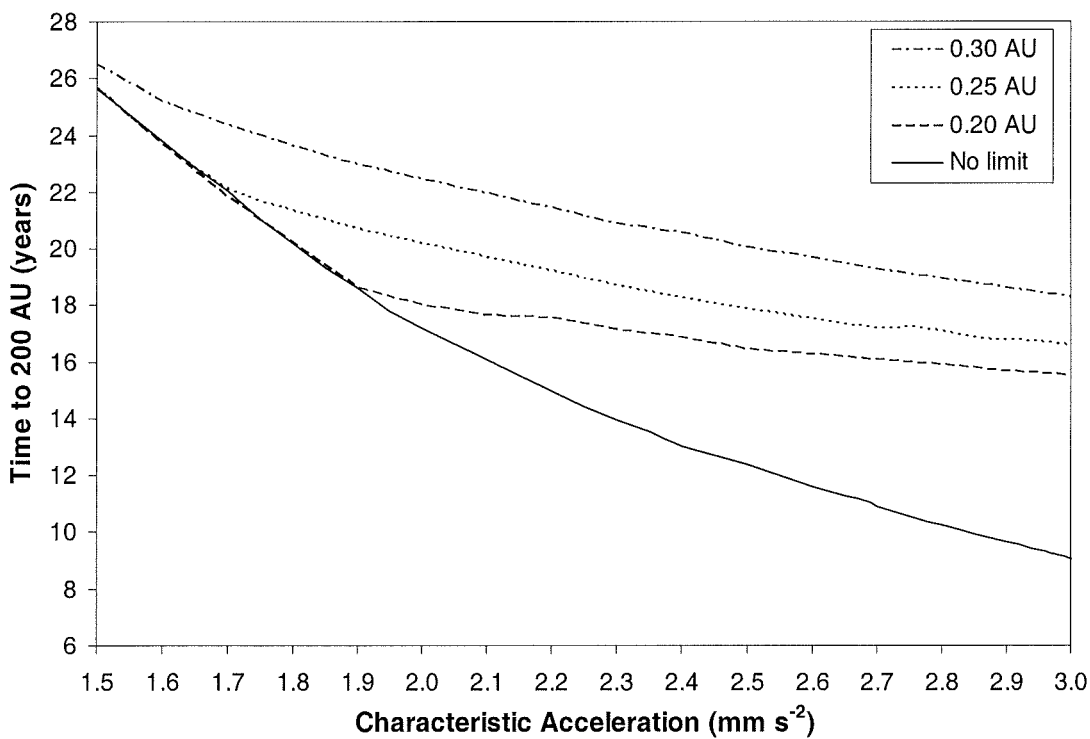


Figure 6.4: Constrained perihelion contours of trip time to 200 AU

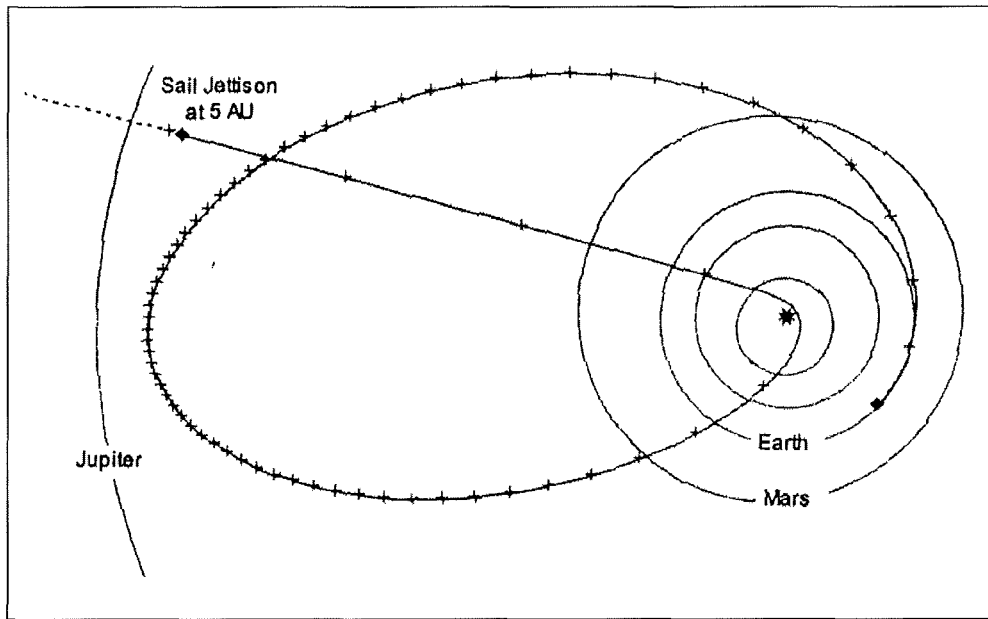


Figure 6.5: Unconstrained 20 year trajectory to 250 AU (0.1 AU solar approach)
[Sauer, 1999]

Figure 6.6 shows an example of a 2D single photonic assist trajectory for a characteristic acceleration of 3.0 mm s^{-2} , starting from a 1 AU circular orbit with a perihelion limit of 0.25 AU. The trip time is of order 15 years to a distance of 200 AU from the Sun. The shape of the trajectory is quite similar to the JPL trajectory in Figure 6.1, but with the initial aphelion being a little larger. The parameter optimisation method uses linear interpolation between discrete nodes for the cone angle (clock angle is fixed within the ecliptic for this initial analysis). 51 nodes (50 equal segments in time) were adopted for the single photonic assist trajectories. Figure 6.7 shows the trajectory for a lower acceleration of 1.5 mm s^{-2} , with the maximum desired trip time of order 25 years. It should be noted that a 25 year mission with lower accelerations could only be accomplished if the thermal limit is relaxed to allow a solar pass closer than 0.25 AU. The effect of close approaches on trip time will be investigated in more detail in Section 6.2, but it is unlikely that a conventional sail could survive to less than 0.25 AU, and even then only for short durations [M. Leipold, 2004, personal email communication], unless advanced coatings are considered.

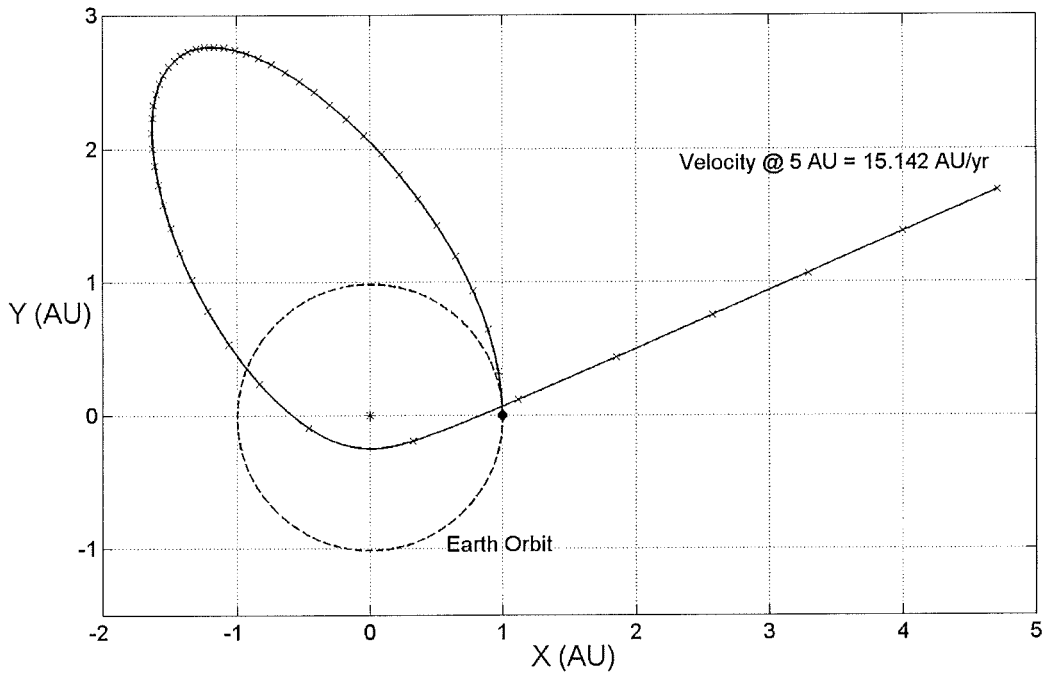


Figure 6.6: 15 year 3.0 mm s^{-2} single photonic assist IHP trajectory ($r_p = 0.25 \text{ AU}$)

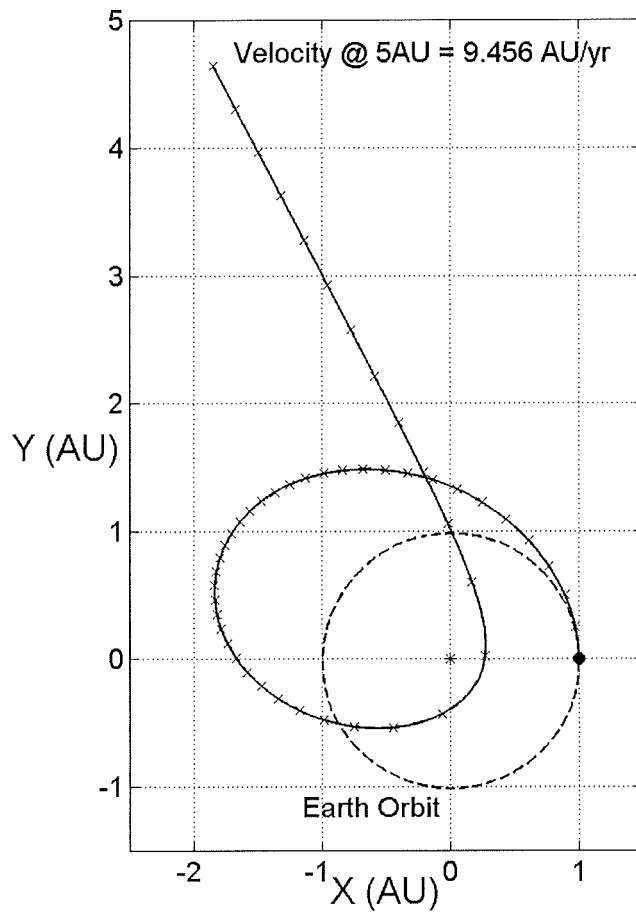


Figure 6.7: 25 year 1.5 mm s^{-2} single photonic assist IHP trajectory ($r_p = 0.25 \text{ AU}$)

As a specific example of a fast mission to the Heliopause, akin to the NASA/JPL ISP mission, a launch date specific trajectory with an acceleration of 3.0 mm s^{-2} is presented. A launch opportunity has been identified, departing the Earth on May 5, 2010, with $C_3=0$. Figure 6.8 shows a short departure date scan two months about this date. Again, because of the 0.25 AU perihelion constraint, the sail cannot pass closer to the Sun to reach the correct escape asymptote for different launch dates; it has to modify the initial loop, with a detrimental effect on trip time. This launch opportunity will again repeat annually, in phase with the orbit period of the Earth, since the Heliopause nose direction is fixed. Figure 6.9 shows the launch date optimal trajectory, with the X-Z axes projection shown in Figure 6.10, showing the out-of-plane motion to reach an elevation of 7.5° . The trip time to 200 AU is 15.7 years. Figure 6.11 shows the control profile with the thrust reversal manoeuvre clear in the cone angle history. The irregularities are due to the relative insensitivity of the trajectory to small fluctuations in the control angles, and are an artefact of the numerical optimisation algorithm. In Figure 6.12, the trajectory becomes hyperbolic after 740 days. Figure 6.13 shows that the maximum sail film temperature reaches 516 K, probably at the limit for conventional polyimide films.

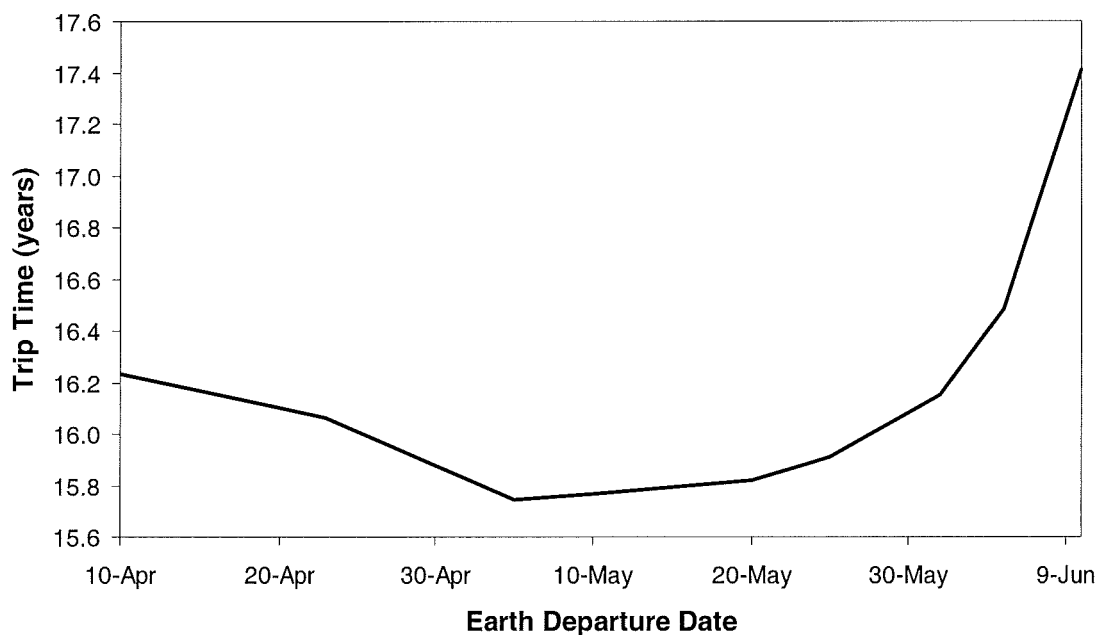


Figure 6.8: Variation of trip time about optimal launch date to Heliopause nose for 3.0 mm s^{-2}

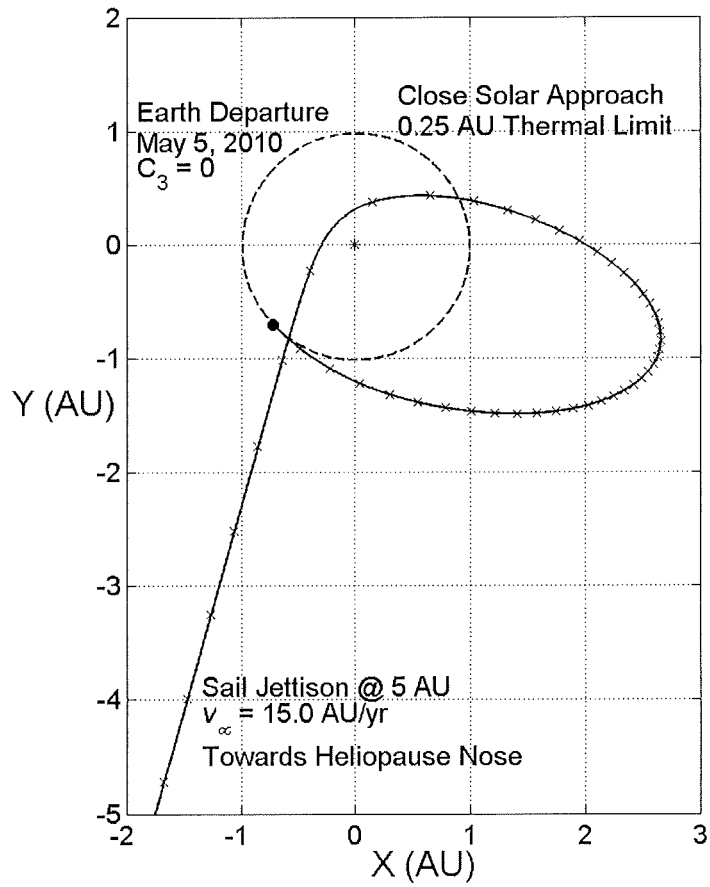


Figure 6.9: 15 year 3.0 mm s^{-2} trajectory to Heliosphere nose at 200 AU

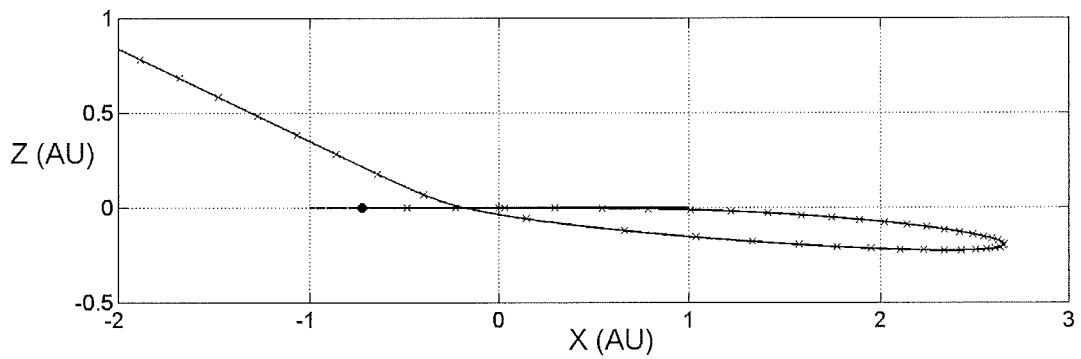


Figure 6.10: 15 year mission X-Z out-of-ecliptic projection (escape asymptote is not in X-Z plane – final elevation 7.5°)

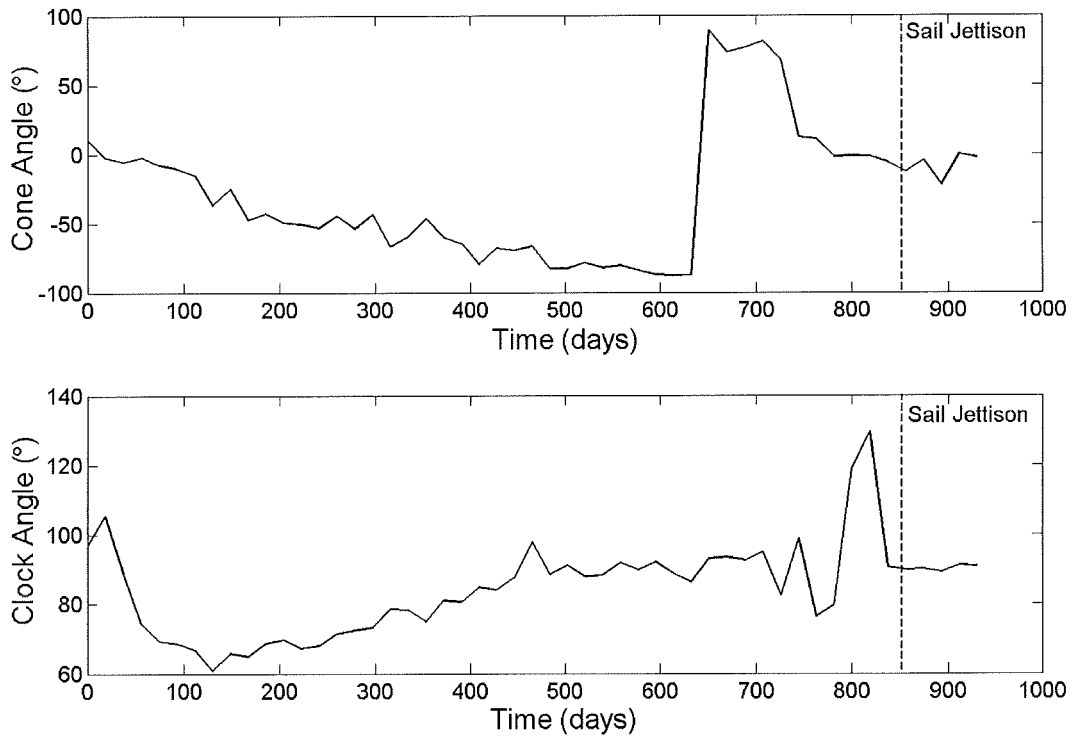


Figure 6.11: 15 year mission control angle profile

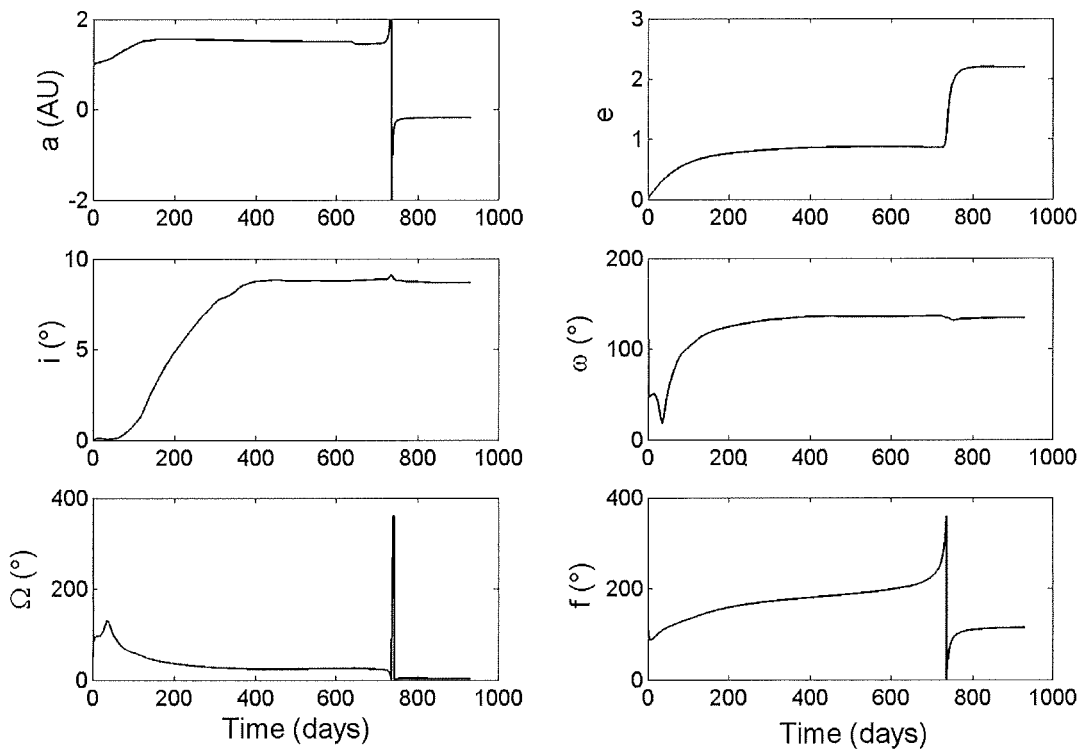


Figure 6.12: 15 year mission orbital element temporal evolution

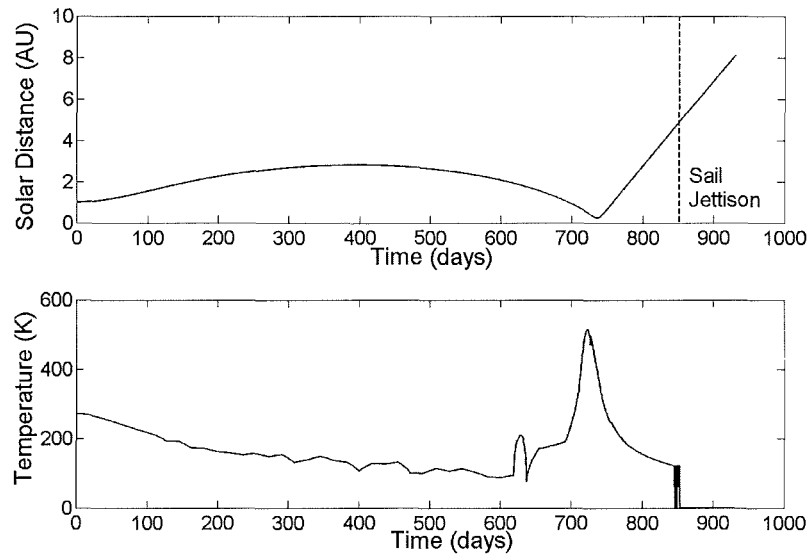


Figure 6.13: 15 year mission heliocentric radius and sail film temperature

6.2 Slow IHP Mission (multiple loops)

For lower performance solar sails two, or even three close solar passes are necessary in order to achieve hyperbolic solar system escape velocity. As used in Chapter 5, an analytical control law that maximised the rate of change of orbit eccentricity was used to find an initial guess for the NPOPT optimiser that maximises the velocity at sail jettison. For these multiple loop trajectories 201 control nodes were used. Again, for preliminary analysis, the trajectory is simulated in two dimensions with an open final escape asymptote direction. For a low characteristic acceleration of 0.5 mm s^{-2} , a triple solar photonic assist can be executed in order to reach 0.27 AU, by pumping-up the orbit eccentricity. Figure 6.14 shows the trajectory, which takes approximately 46 years to reach 200 AU. Figure 6.15 shows a 36 year dual assist trajectory for a higher acceleration of 0.75 mm s^{-2} . The closest solar approach is 0.26 AU, where the sail temperature is close to the conventional thermal limit. It is possible to realise trip times less than 25 years with this acceleration by using an exotic navigation strategy as shown in Figure 6.2, but again it is emphasised that sail (and spacecraft bus) survival to 0.1 AU appears extremely difficult. A 26 year trajectory to 200 AU is shown in Figure 6.16. The characteristic acceleration of 0.85 mm s^{-2} can enable a close solar pass of 0.16 AU to be reached with two loops. This solar distance is again thermally demanding, but it is again noted that, providing a heat tolerant sail and payload can be fabricated (having a detrimental impact on sail assembly loading), lower accelerations could be used to reach 200 AU in 25 years.

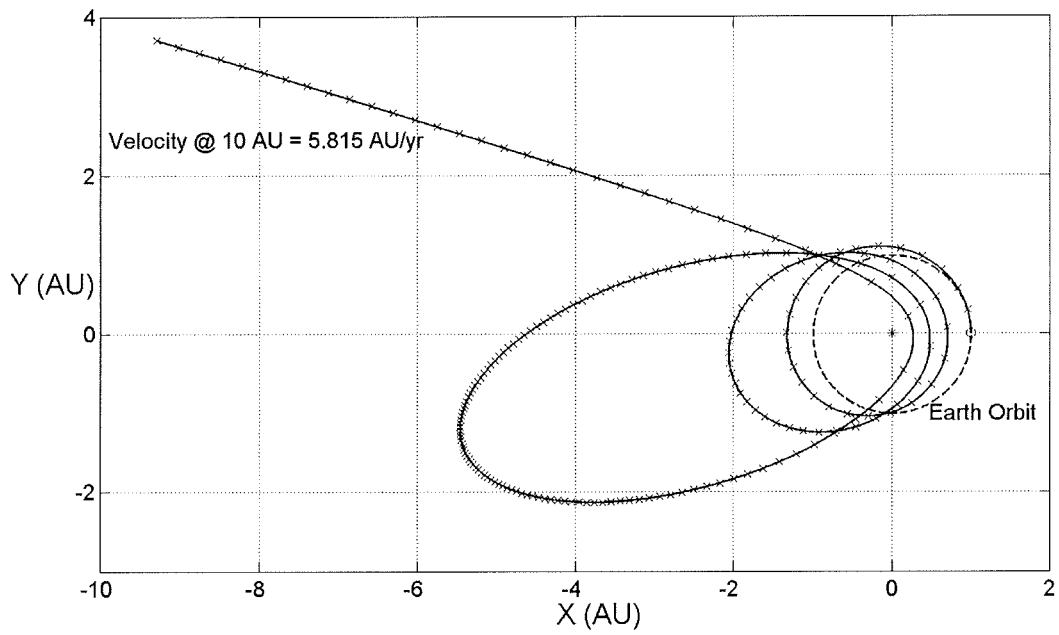


Figure 6.14: 46 year 0.5 mm s^{-2} triple photonic assist IHP trajectory ($r_p = 0.27 \text{ AU}$)

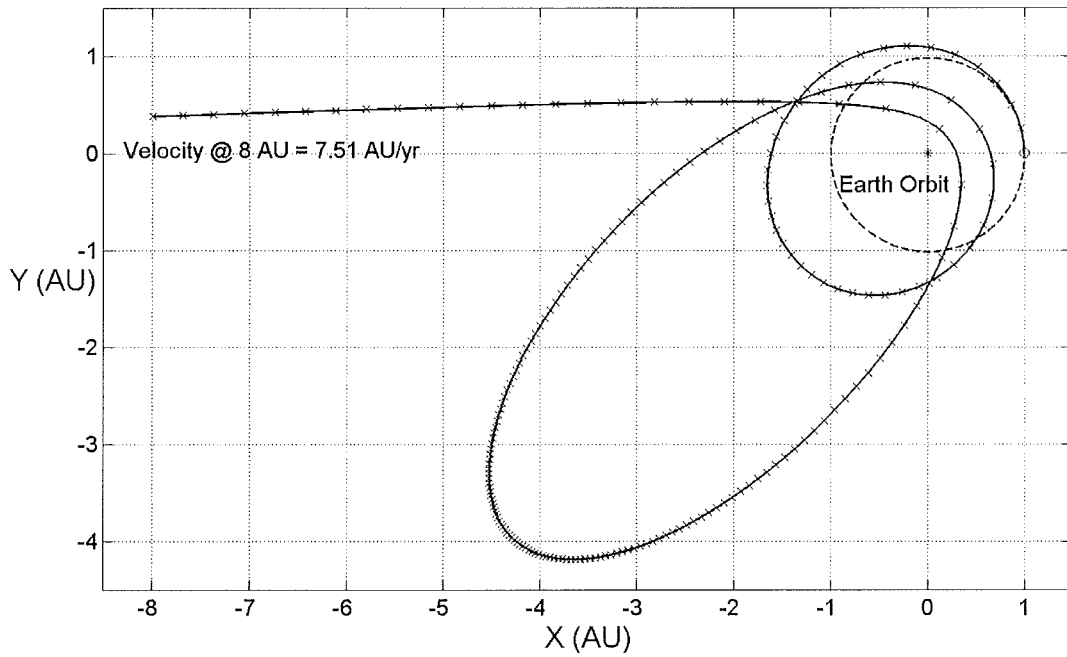


Figure 6.15: 36 year 0.75 mm s^{-2} dual photonic assist IHP trajectory ($r_p = 0.26 \text{ AU}$)

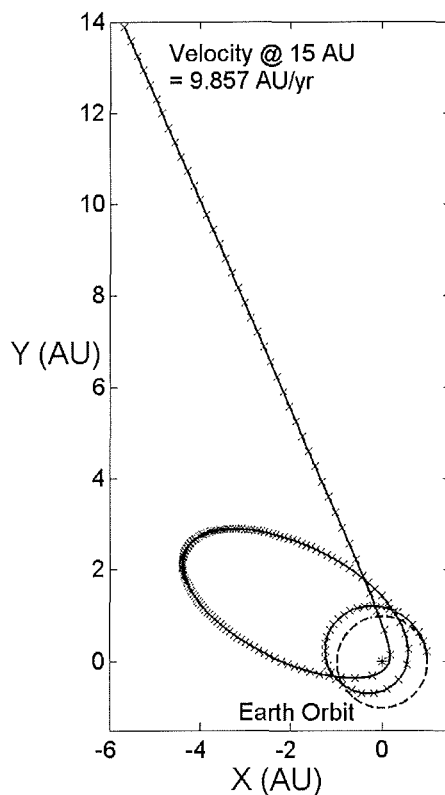


Figure 6.16: 26 year 0.85 mm s^{-2} dual photonic assist IHP trajectory ($r_p = 0.16 \text{ AU}$)

Preliminary analysis carried out has demonstrated that the trip time to 200 AU is probably more sensitive to the perihelion on the last solar pass than to the sail characteristic acceleration used. The initial sail spiralling is probably just a means of reaching the final perihelion distance, whether it be 1, 2 or 3 loops, or with an excess launch C_3 . A parametric analysis will now be carried out using an approach of optimising ‘half-arcs’ from the final perihelion to 5 AU (maximising the velocity). In this way, the effect of final close approach with low characteristic accelerations, on trip time can be rapidly ascertained. This approach is sub-optimal, but can provide a good initial estimation of trip-times.

As a preliminary step for the half-arc optimisations from final perihelion, the effect of aphelion radius on perihelion velocity, for final perihelia between 0.05 and 0.40 AU, was investigated, for closed orbits only. It can be seen in Figure 6.17 that the perihelion velocity is relatively insensitive to the aphelion radius, for aphelia between 1 and 5 AU. Perihelion velocity only varies by $\pm 6\%$. Therefore, in the approximate analysis to follow, the final aphelion distance will be assumed to be 2 AU. The corresponding perihelion velocities for perihelia between 0.05 and 0.25 AU will be used to form the initial conditions for optimisation. Maximum velocities

at 5 AU (sail jettison) were then obtained by optimising with 51 control nodes in two-dimensional motion. The trip time from the final perihelion to 200 AU can then be obtained from the optimised half-arc time and the final maximised velocity. The initial spiralling to reach the final close approach is longer for the lower accelerations, but this can perhaps be negated by using excess launch capacity to reduce the number of loops required. In this approximate analysis, it will be assumed that the initial spiralling to reach the closest approach is short in relation to the post perihelion time to 200 AU. For a 25 year trip time to 200 AU, the escape velocity at 5 AU must be greater than 8-10 AU per year (depending on the duration of the initial spiralling to perihelion). The results for the half-arc optimisations are shown in Figure 6.18. In Figure 6.18, the escape velocities are slightly less than the true fully optimised trajectories, but are a reasonably good approximation. The 0.75 mm s⁻² case with a 0.1 AU final perihelion, in Figure 6.18, gives a comparable trip time (~23 years) to the trajectory [Leipold *et al*, 2003] in Figure 6.2 (21.2 years). The velocities for 0.5 mm s⁻² at 0.25 AU, 0.75 mm s⁻² at 0.25 AU, 0.85 mm s⁻² at 0.15 AU and 1.5 mm s⁻² at 0.25 AU are all slightly lower than the fully optimised trajectories shown in Figures 6.14 ($r_p = 0.27$ AU), 6.15 ($r_p = 0.26$ AU), 6.16 ($r_p = 0.16$ AU) and 6.7 ($r_p = 0.25$ AU), respectively, but are good approximations. Figure 6.18 clearly shows the marked sensitivity of the escape velocity (and trip time) to the minimum perihelion of the final photonic assist. This is particularly noticeable for perihelia below 0.15 AU. Clearly, if these extremely close solar distances could be survived, then low acceleration sails could in principle reach the Heliopause within 25 years. The conclusions to be reached from Figure 6.18 are, that a 25 year mission to 200 AU is possible for:

- Perihelion limit of 0.25 AU – Minimum acceleration ~1.5 mm s⁻²
- Perihelion limit of 0.20 AU – Minimum acceleration ~1.2 mm s⁻²
- Perihelion limit of 0.15 AU – Minimum acceleration ~0.9 mm s⁻²
- Perihelion limit of 0.10 AU – Minimum acceleration ~0.6 mm s⁻²

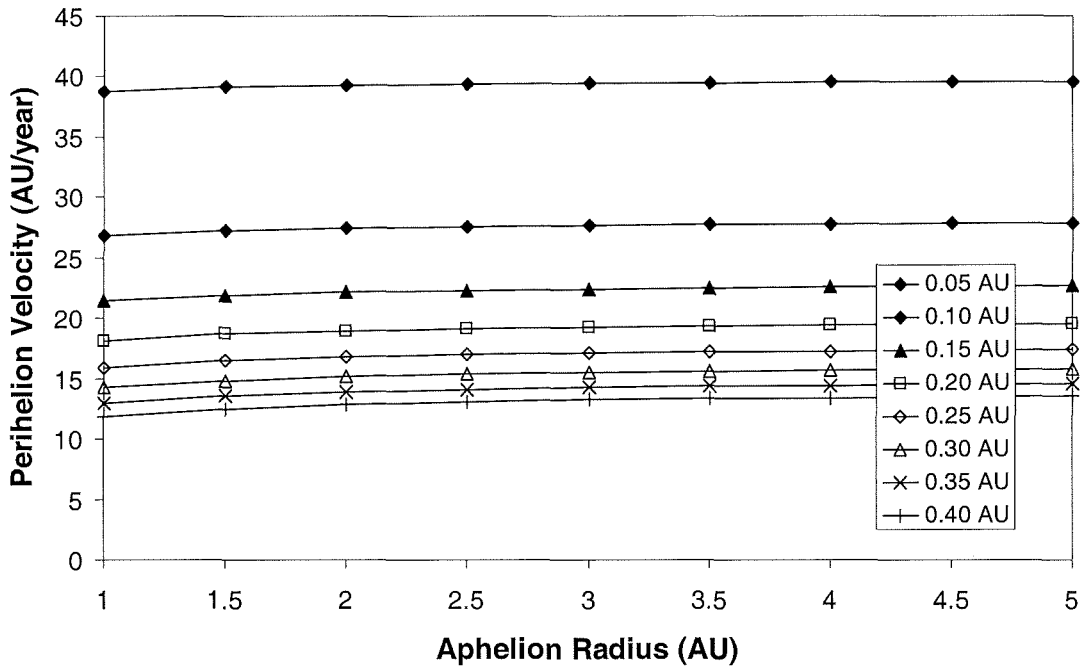


Figure 6.17: Perihelion radius contours showing sensitivity of perihelion velocity to aphelion radius for closed orbits

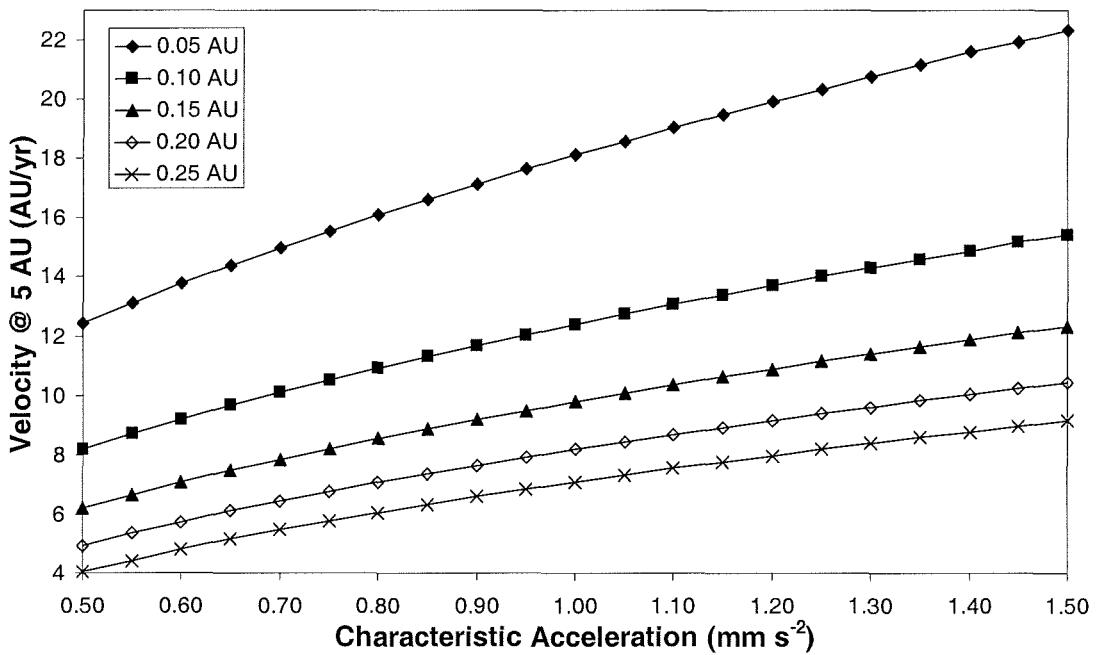


Figure 6.18: Half-arc trajectory velocity at 5 AU with closest approach contours

Therefore, for a single photonic assist with a perihelion limit of 0.25 AU, a characteristic acceleration of order 1.5 mm s^{-2} appears necessary. To further demonstrate why it is deemed necessary to impose a 0.25 AU limit on the Heliopause trajectories, contours of closest approach distance against sail back surface emissivity for different values of the sail front reflectivity were obtained. This was performed for maximum sail film temperatures of 520 K [Wright, 1992] in Figure 6.19, 623 K [Leipold *et al*, 2003] in Figure 6.20, and, hypothetically, 800 K in Figure 6.21, and 1000 K in Figure 6.22. The closest solar approach allowed was calculated using a black-body approximation as was performed in previous chapters (see Chapter 3, for example). In this case the sail is assumed to be facing the Sun with a pitch angle of 0° and a front coating emissivity close to zero. If it is assumed that a conventional sail film has an aluminium front coating with a reflectivity of 0.85, and the back of the sail is coated with chromium of emissivity 0.64, then it can be seen that the closest approach allowed with a thermal limit of 520 K is 0.28 AU. However, this decreases to 0.25 AU when the sail is pitched at 35° to the Sun-line. For a thermal limit of 623 K, the sail can approach only as close as 0.2 AU, which brings the required characteristic acceleration down to $\sim 1.2 \text{ mm s}^{-2}$. It should also be noted that the melting point of the aluminium front coating is 933 K, but the maximum allowed substrate temperature is expected to be well below this. It might reasonably be assumed that advances in high reflectivity and high emissivity coatings will occur more rapidly than the development of high performance sails. Therefore, if a lower performance sail could be manufactured with advanced high reflectivity and high emissivity coatings to enable solar passes closer than 0.25 AU, while remaining below the $\sim 520 \text{ K}$ limit for Polyimide films, then 25 year trip times for moderate square sails would be possible. Looking once more at Figure 6.18, it is seen that a 25 year trip time would be possible for a low performance sail of 0.85 mm s^{-2} , but only if the solar approach was as close as $\sim 0.15 \text{ AU}$.

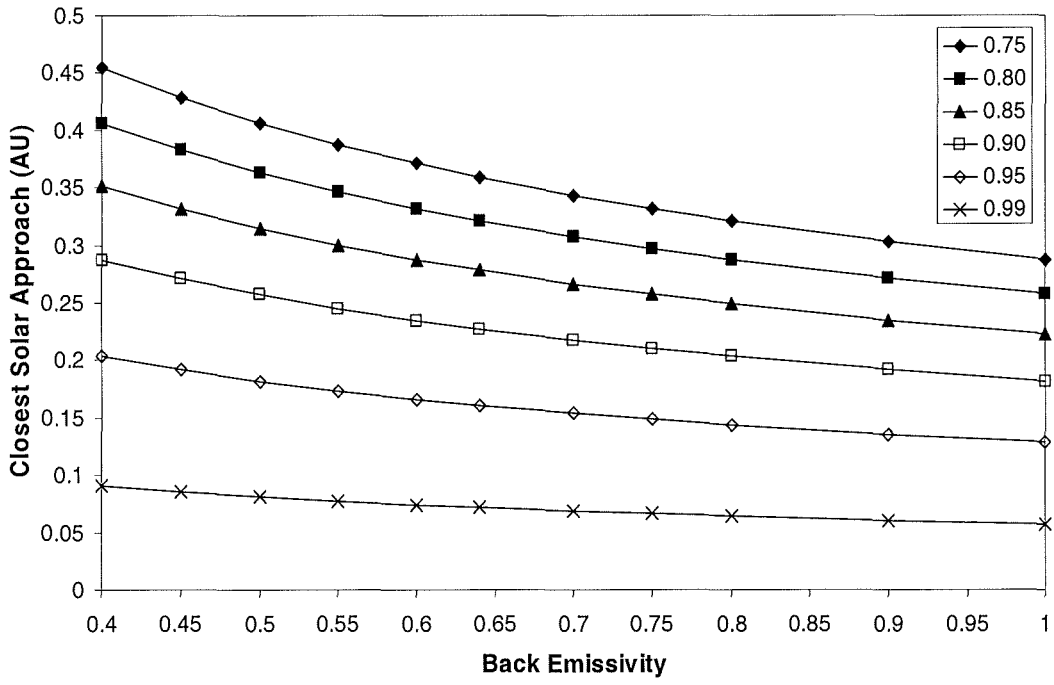


Figure 6.19: Reflectivity contours for closest approach with 520 K thermal limit

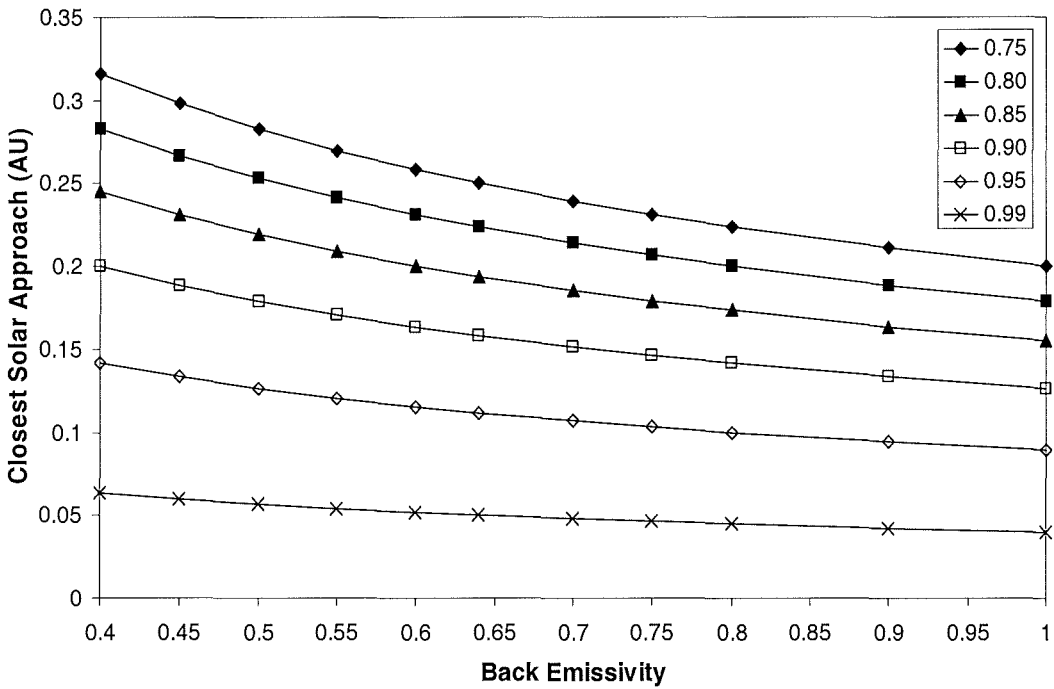


Figure 6.20: Reflectivity contours for closest approach with 623 K thermal limit

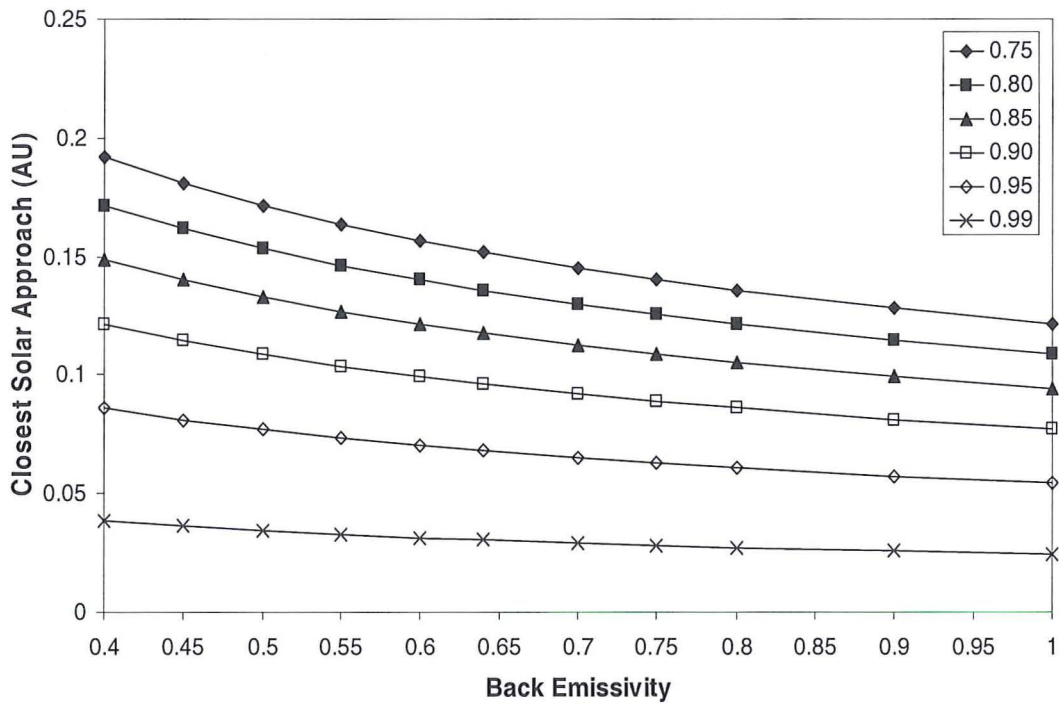


Figure 6.21: Reflectivity contours for closest approach with 800 K thermal limit

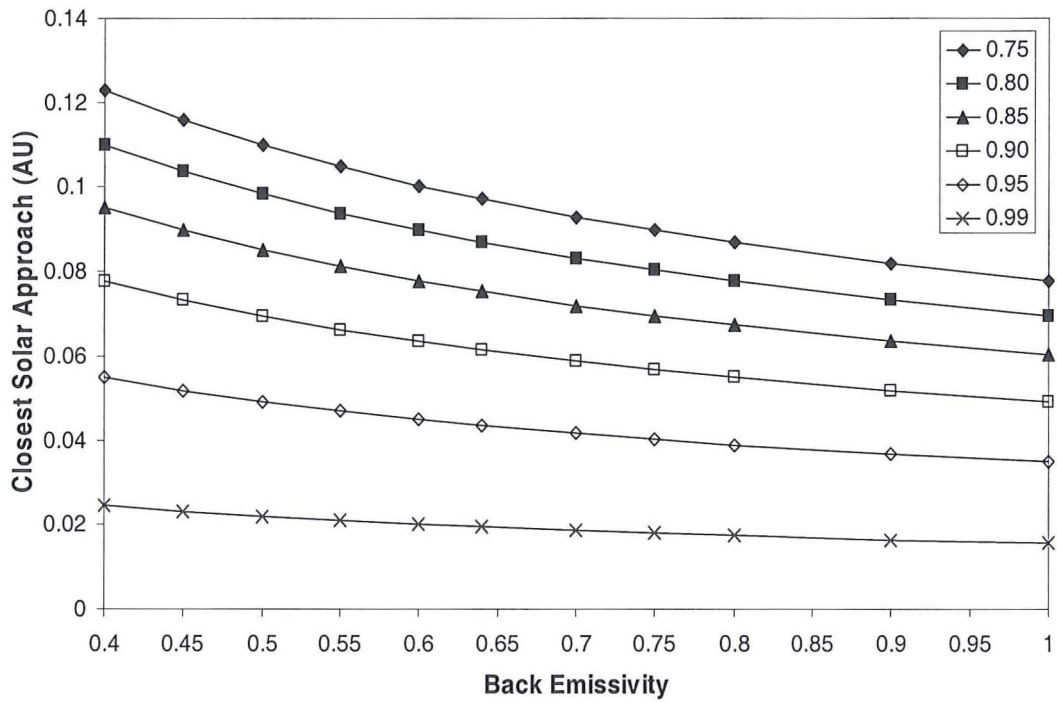


Figure 6.22: Reflectivity contours for closest approach with 1000 K thermal limit

It is now assumed that the sail has a front-side emissivity of 0.05. The reflectivity could be increased to 0.94, or greater, by using layered combinations of silver and aluminium, utilising a constructive interference phenomenon by adding thin-film layers over the base reflector [Wright, 1992]. For the sail to remain below 520 K with zero pitch, the backside emissivity must be greater than 0.83. At 35° pitch the requirements are for a reflectivity of 0.93 and an emissivity of 0.8. High reflectivity coatings are currently being developed with up to 90% emissivity, and high initial reflectivities may indeed be possible, but sail degradation after multiple loops may reduce the thermal properties of the sail. Accelerations of 0.75 mm s⁻² and below may require an excessively close approach (<0.1 AU) and thus extremely advanced coatings. In addition, it should be noted that a high emissivity sail will reject much of the transmitted heat, which will place thermal loads on the payload.

Using the thermal considerations above it was noted that a conventional sail film would only be able to reach as close as 0.25 AU, and only then when pitched slightly away from the Sun. Even this closest approach is likely to cause some degradation of the sail film, so the duration must be minimised, as it would be for a rapid solar pass. In addition, repeated solar passes are likely to have a detrimental effect on the sail: the reflectivity could be reduced to the extent that the thrust at the final photonic assist is not sufficient to meet mission goals. The minimum acceleration for the 0.25 AU thermal limit that enables a 25 year trip time to 200 AU is selected to be 1.5 mm s⁻². A launch opportunity has been identified departing the Earth on February 1, 2010, with C₃=0. The trip time to 200 AU is 24 years. Figure 6.23 shows a short departure date scan two months about this date. Because of the 0.25 AU perihelion constraint, the sail cannot approach closer to the Sun to reach the correct escape asymptote for different launch dates; it has to modify the initial loop, with a detrimental effect on trip time. This launch opportunity will repeat annually, in phase with the orbit period of the Earth, since the Heliopause nose direction is essentially fixed. Figure 6.24 shows the launch date optimal trajectory, with the X-Z axes projection shown in Figure 6.25, showing the out-of-plane motion to reach an elevation of 7.5°. Figure 6.26 shows the control profile, with the thrust reversal manoeuvre clear in the cone angle history. In Figure 6.27, the trajectory becomes hyperbolic after 560 days, reaching a final inclination of 7.5°. Figure 6.28 shows that the maximum film temperature reaches 523 K, at the limit for conventional films.

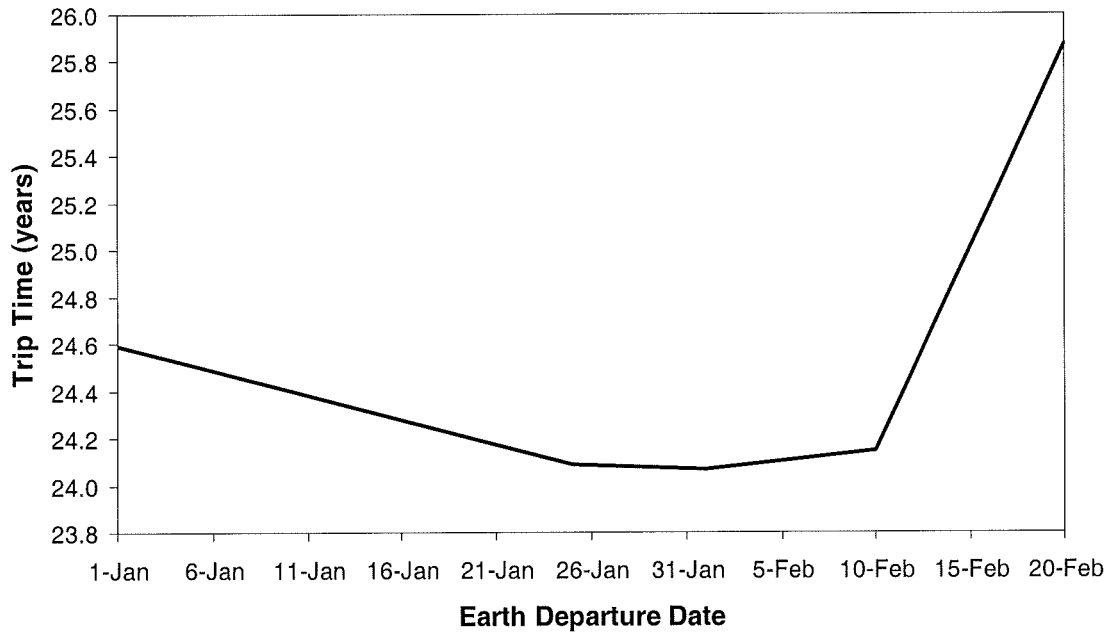


Figure 6.23: Variation of trip time about optimal launch date to Heliopause nose for 1.5 mm s^{-2}

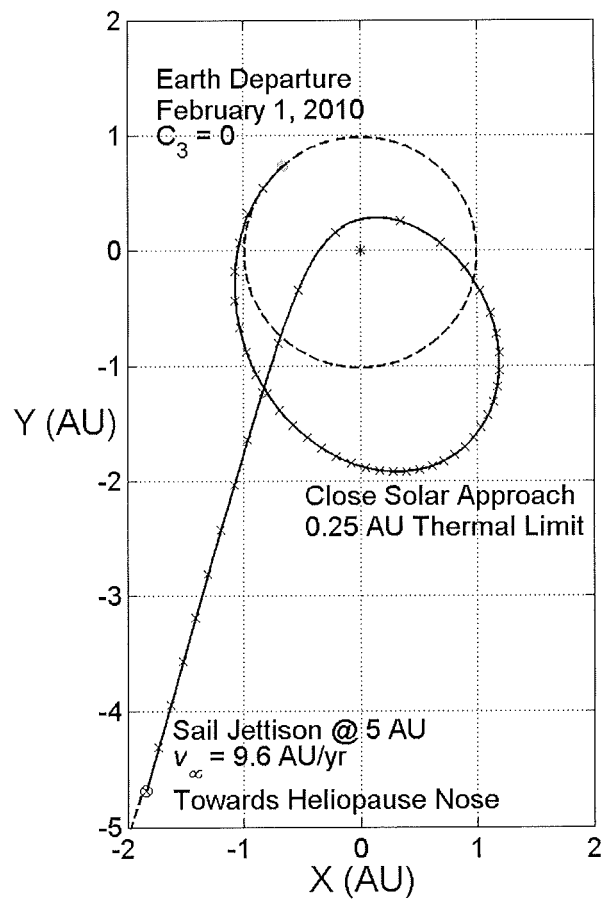


Figure 6.24: 24 year 1.5 mm s^{-2} trajectory to Heliosphere nose at 200 AU

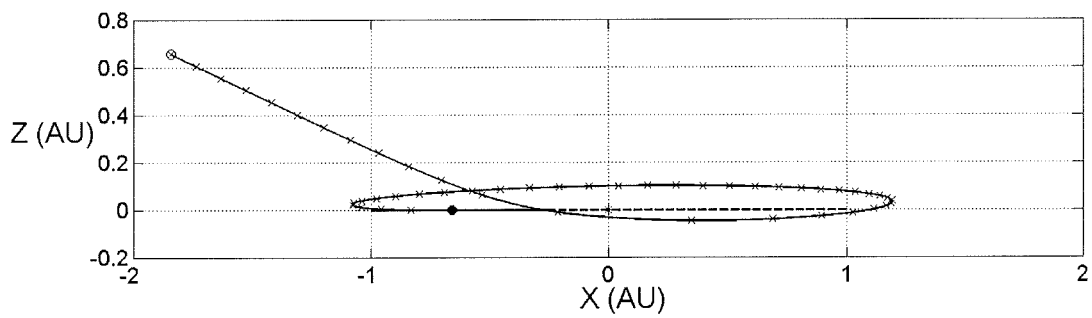


Figure 6.25: 24 year mission X-Z out-of-ecliptic projection (escape asymptote is not in X-Z plane – final elevation 7.5°)

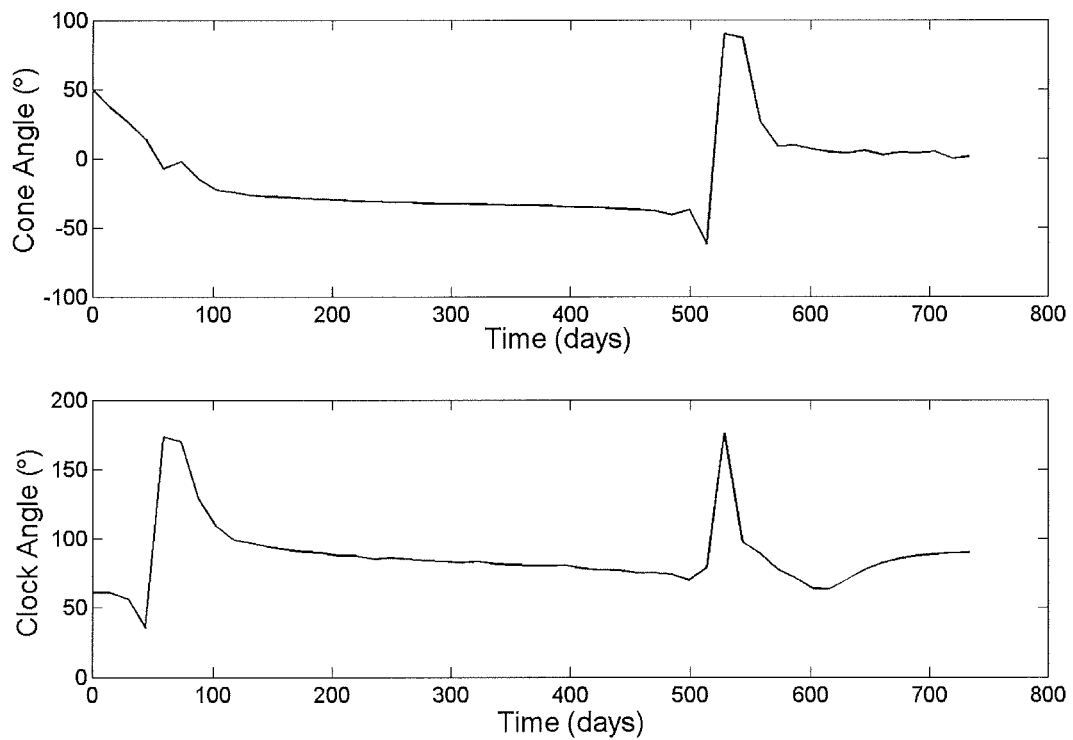


Figure 6.26: 24 year mission control angle profile

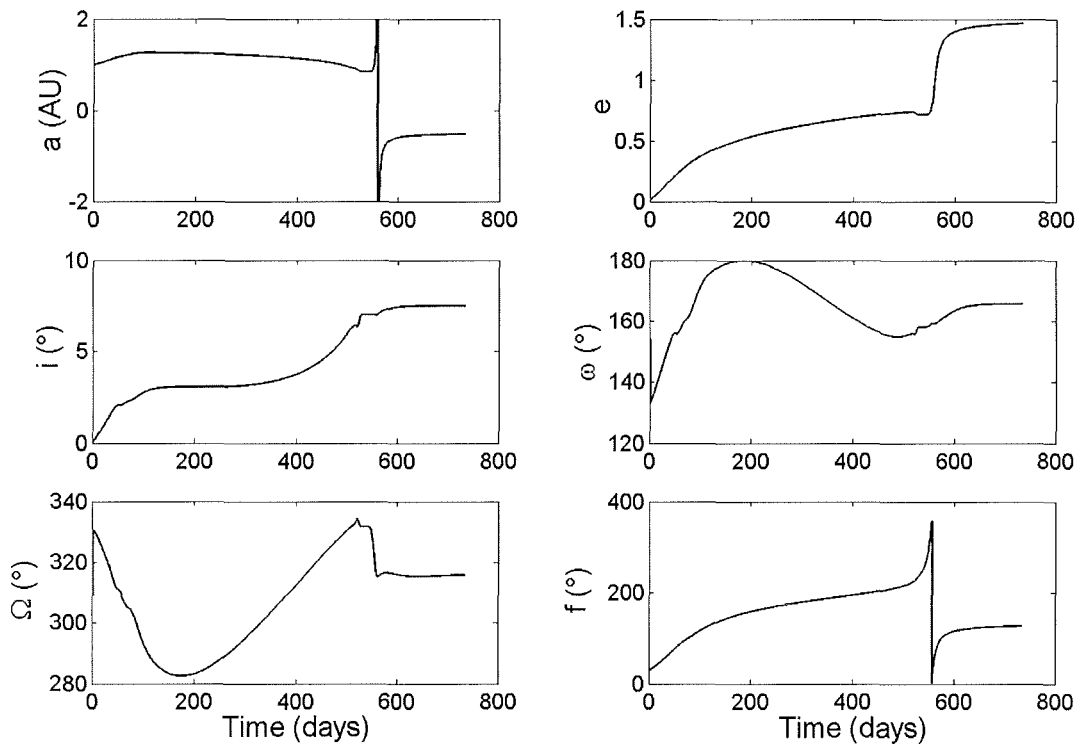


Figure 6.27: 24 year mission orbital element temporal evolution

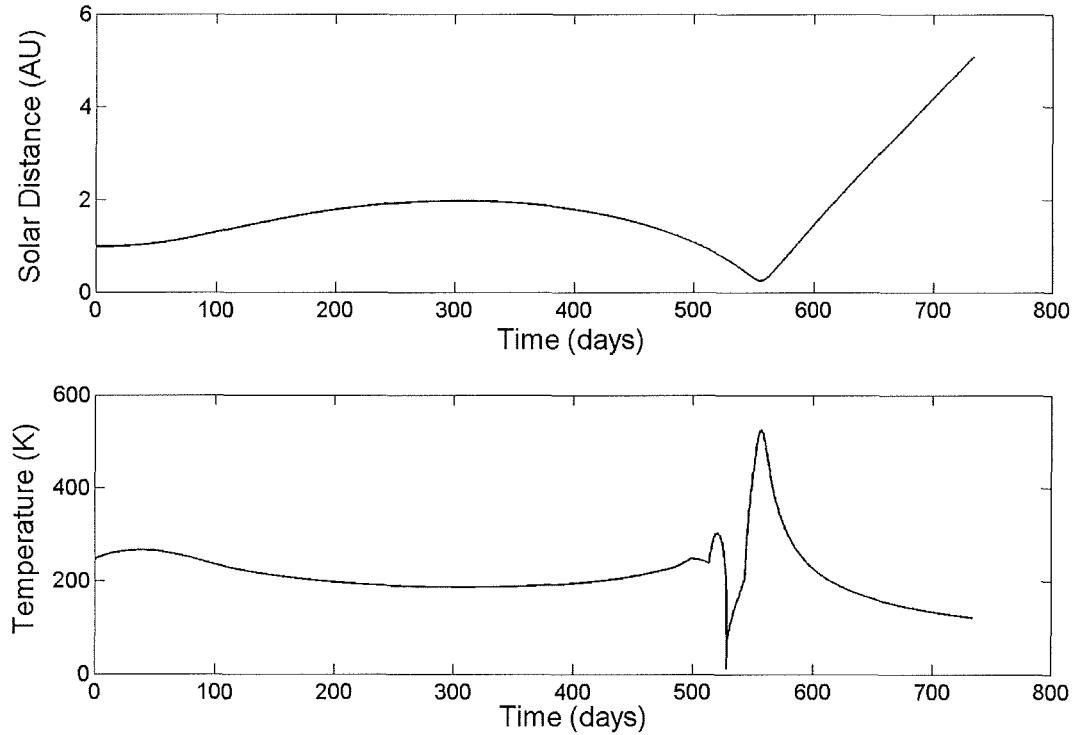


Figure 6.28: 24 year mission heliocentric radius and sail film temperature

To obtain a good range of IHP trajectories, it was considered prudent to analyse trajectories using a characteristic acceleration slightly below the previous example. A characteristic acceleration of 1.0 mm s^{-2} was selected to illustrate the case. The eccentricity control law that was employed in generating the initial guess for some other multiple loop trajectories had to be modified somewhat, since it just produced a single photonic assist for this acceleration value, with a perihelion of only 0.5 AU. The modification was to ‘force’ a 90° pitch angle near the first photonic assist if the eccentricity exceeded ~ 0.7 . This ensured that the spacecraft did not reach escape velocity on the first pass but, on resumption of eccentricity control, executed a second photonic assist. This dual photonic assist enables a close solar approach of 0.20-0.25 AU to be reached. This initial guess was transcribed to 201 control nodes over 3.2 years. Some manual modification of the nodes through and after the final assist was necessary to obtain an initial guess that produced the maximum velocity in the first instance. Since this turned out to be a difficult problem, the variables and two constraints (minimum perihelion radius and final radius at 200 AU), were scaled. The total trip time to 200 AU was minimised in 2D simulations, ignoring the position of the Heliosphere nose.

For a minimum perihelion radius constraint of 0.25 AU the trip time to 200 AU was 29.0 years. This trajectory is shown in Figure 6.29, where the escape velocity after the optimal control phase is 8.7 AU/yr (at 3.5 AU). When this constraint was reduced to 0.20 AU (severely increasing thermal loads), the total trip time was 26.5 years, marginally higher than the 25 year limit. The trajectory in this case is shown in Figure 6.30, where the escape velocity is 9.3 AU/yr (at 4.1 AU). It is noted that Yen [2001], shows that a 1.0 mm s^{-2} dual assist trajectory with a 0.3 AU perihelion constraint could reach 200 AU in 29 years. Two trajectories are shown in that Yen’s paper, a 0.5 mm s^{-2} triple assist, reaching 200 AU in 44 years, and the 1.0 mm s^{-2} trajectory. During the Pluto work, detailed in Chapter 5, personal email communication with Dr. Chen-Wan Yen (NASA/JPL), revealed that the 0.5 mm s^{-2} characteristic acceleration is in fact corrected for non-perfect reflectivity, and that the ideal sail acceleration is $0.55453 \text{ mm s}^{-2}$. Yen’s trajectories are for ideal solar sails, with no centre-line effect. It is therefore reasonable to assume that Yen’s 29 year 1.0 mm s^{-2} dual assist 0.3 AU trajectory has an ideal acceleration of order 10% higher, at $\sim 1.1 \text{ mm s}^{-2}$. This asserts some validity upon the 29 year trip time of the 1.0 mm s^{-2} , 0.25 AU trajectory obtained in Figure 6.29.

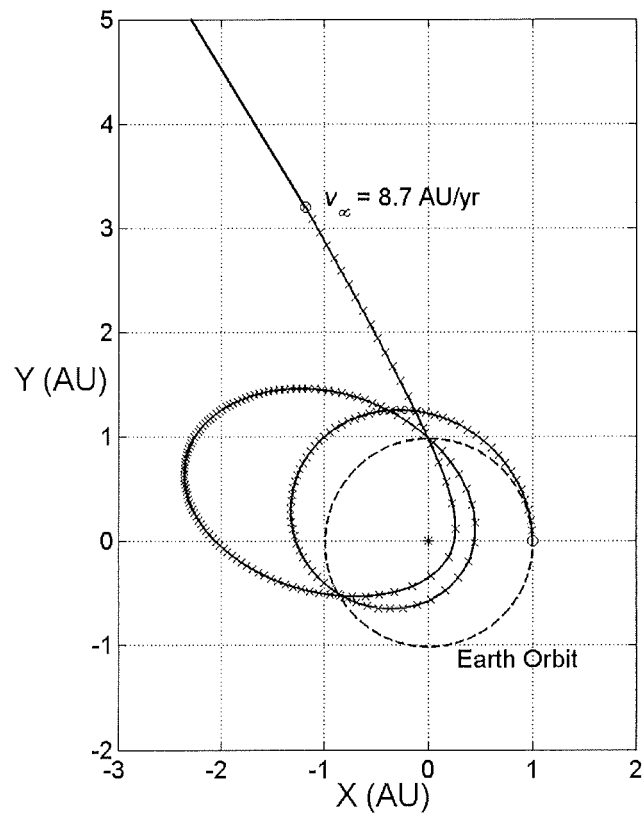


Figure 6.29: 29 year 1.0 mm s^{-2} dual photonic assist IHP trajectory ($r_p = 0.25 \text{ AU}$)

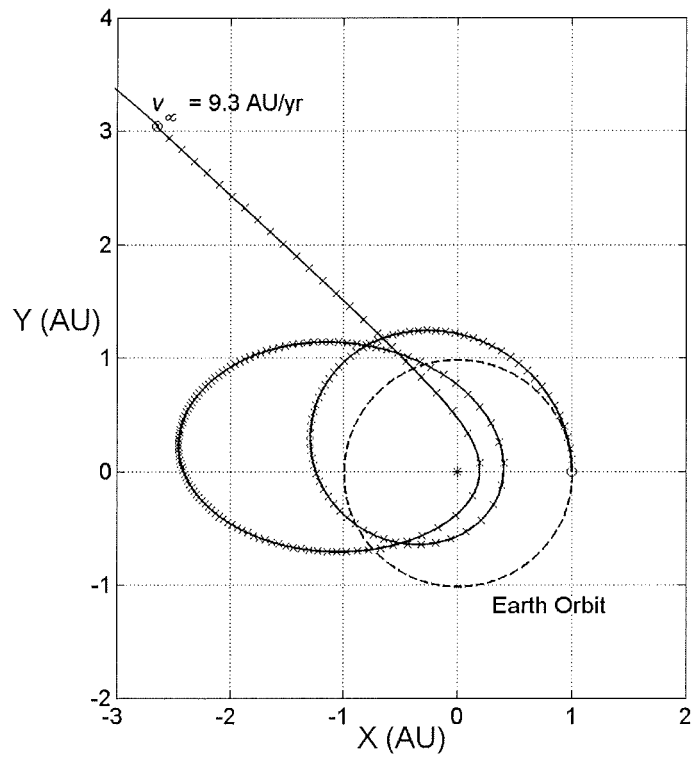


Figure 6.30: 26.5 year 1.0 mm s^{-2} dual photonic assist IHP trajectory ($r_p = 0.20 \text{ AU}$)

6.3 Jupiter Gravity Assist on Escape Trajectory

The effect of using a Jupiter gravity assist (JGA) on the outgoing escape trajectory was investigated. It should be noted at the outset that the optimal opportunity will only present itself once every 11.8 years for a trajectory to the Heliopause nose, equal to the period of Jupiter's orbit. However, Jupiter will be in the correct position in 2017. Since the initial optimised trajectory is towards Jupiter, which has a low inclination, the 7.5° latitude of the Heliopause nose needs to be attained entirely by using the gravity assist. There are of course additional operational risks associated with a close Jupiter swing-by, as well as the radiation issue of passing so close to Jupiter. Radiation exposure should however be minimal since the spacecraft will be travelling at high speed.

In this approximate analysis, the gravity assist was treated as a simple patched-conic, similar to the method used for computing the Venus gravity assist, en-route to Mercury in Chapter 3. The trajectory assumed two-body dynamics with entirely coplanar motion. The orbit of Jupiter was assumed to be circular at 5.2 AU, with a corresponding tangential velocity of 2.755 AU/yr. Essentially, the escape trajectory was assumed to be perpendicular to the orbit of Jupiter. Preliminary values were calculated of the attainable Δv , for pre-JGA velocities of between 5 and 15 AU/yr, and for a range of perijove radii up to 2 million km. This covers the range of the mean distances of the Galilean moons. Callisto is at 1,882,700 km and Io is at 421,800 km. The results of this investigation are shown in the surface plot of Figure 6.31. The contour of 9 AU/yr is marked, which is approximately the velocity necessary for reaching 200 AU in 25 years. For higher initial velocities, corresponding to higher performance sails, it can be seen that the resulting Δv from the JGA is only 7-10% of the initial escape velocity. Therefore, using a JGA for fast Heliopause missions with characteristic accelerations greater than 1.5 mm s^{-2} does not offer any significant reduction in trip time. Low performance sail trajectories, which would ordinarily reach the Heliopause in a little over 25 years, would benefit to some extent from a JGA. For example, if the initial sail velocity was 7 AU/yr, then the Δv obtained from the JGA is of order 2 AU/yr. Referring to Figure 6.18, it can be seen that a 0.75 mm s^{-2} sail could increase the solar approach distance from 0.12 AU to 0.17 AU using a JGA, for example. The perijove radius required would be 150,000 km (Jupiter radius is 71,000 km), however this will change if targeting of

the Heliopause nose is taken into account. It is important to note that the resulting escape velocity will no doubt need to be higher than 9 AU/yr for lower accelerations, since extensive spiralling is necessary to reach the close solar approach. In this case the initial spiralling phase may be reduced by using the excess C_3 capacity of the launcher, which will be discussed in Section 6.4.

It is therefore concluded that a Jupiter gravity assist is of negligible benefit for fast IHP missions, and only a modest benefit to slower IHP missions. The benefits obtained are probably outweighed by the launch window constraints and additional operational complexity of the JGA. For example, the sail will be jettisoned prior to JGA and so the IHP spacecraft must be sized for sufficient Δv to accurately target the JGA.

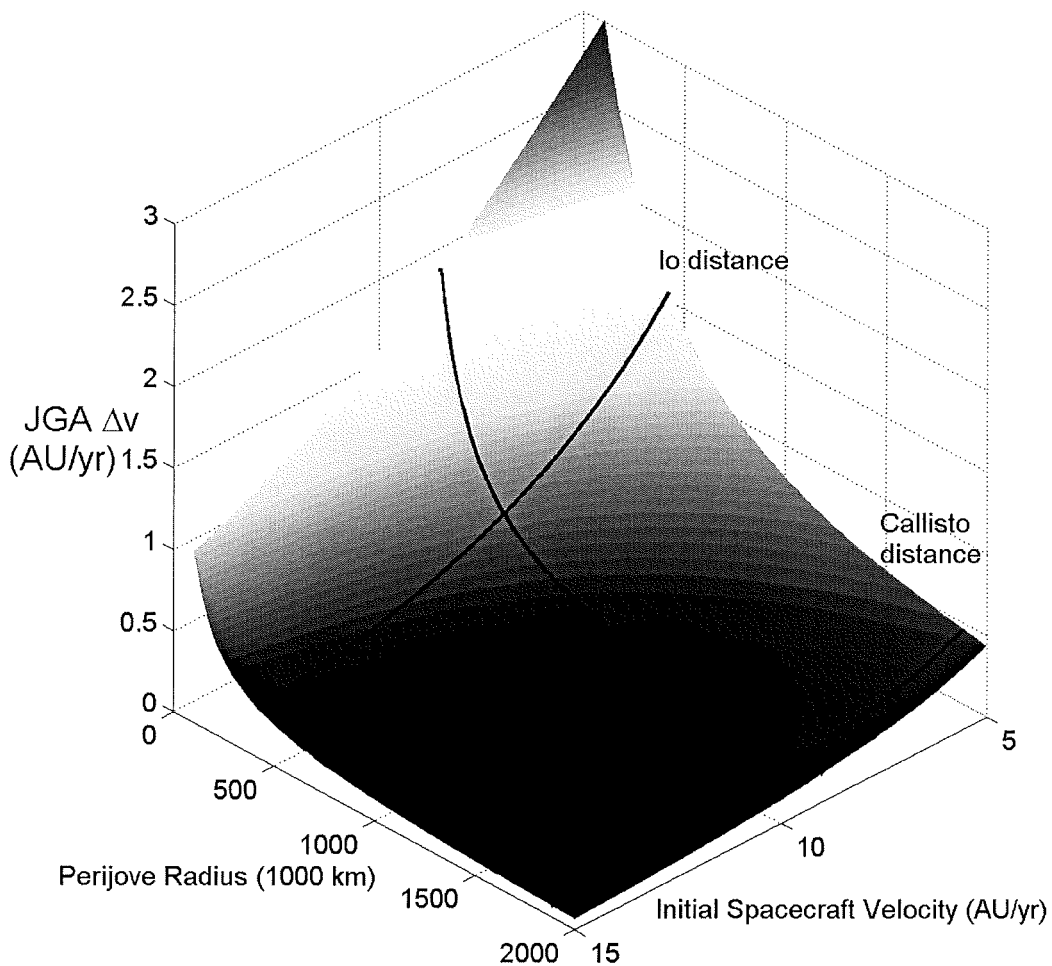


Figure 6.31: Approximate Jupiter gravity assist Δv

An example of a 25 year mission to the Heliopause using a low characteristic acceleration of 0.85 mm s^{-2} and highly reflective and emissive coatings is shown in Figure 6.32. The representative effect of a patched-conic Jupiter gravity assist at Io distance is included. The trajectory in this case is coplanar and the ephemeris of the Earth and Jupiter, and the direction of the Heliopause nose are ignored. The total trip time to 200 AU with a JGA is 25.0 years. The JGA is applied at 6 years, after thrust vector optimisation ends, increasing the spacecraft velocity by 0.59 AU/yr to 10.87 AU/yr . Figure 6.33 shows the control profile with the two thrust reversal manoeuvres clear. In Figure 6.34, the trajectory becomes hyperbolic after 5.6 years. Figure 6.35 shows that the maximum sail film temperature reaches 501 K at 0.16 AU , but only if it is assumed that the back emissivity is 0.9 , the front emissivity is 0.05 , and a front reflectivity of 0.92 can be obtained. The trip times for other perijove radii, for this trajectory, are listed in Table 6.1.

Perijove Radius ($\times 1000 \text{ km}$)	ΔV (AU/yr)	Post Jupiter Velocity (AU/yr)	Total Trip-Time (yrs)
100	1.74	12.02	23.0
200	1.09	11.37	24.3
300	0.79	11.07	24.6
400	0.62	10.90	24.9
421.8 (Io distance)	0.59	10.87	25.0
No JGA	0	10.28	26.1

Table 6.1: Representative effect of JGA on 200 AU trip time (0.85 mm s^{-2})

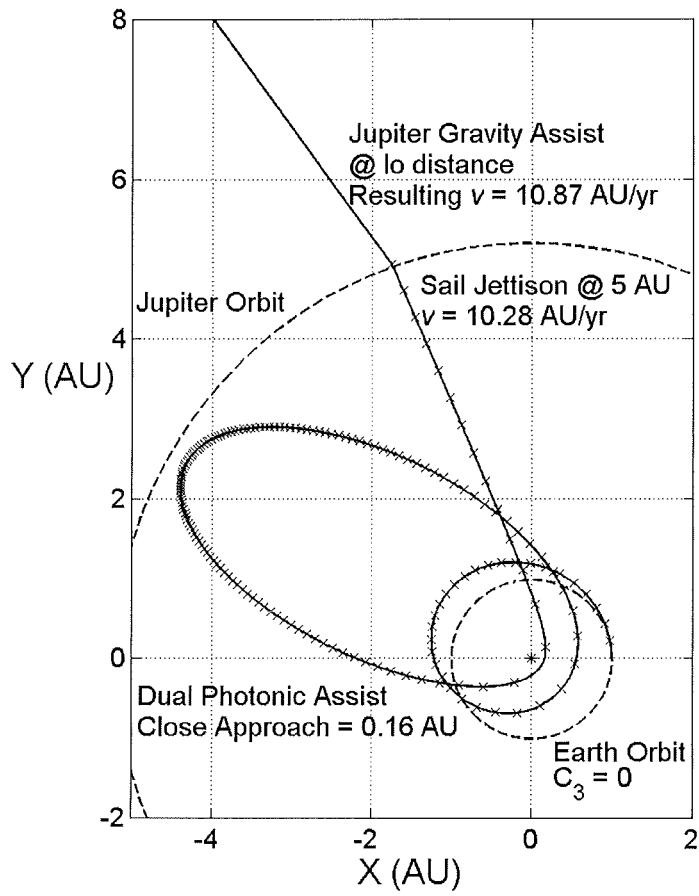


Figure 6.32: 25 year 0.85 mm s^{-2} trajectory with Jupiter gravity assist

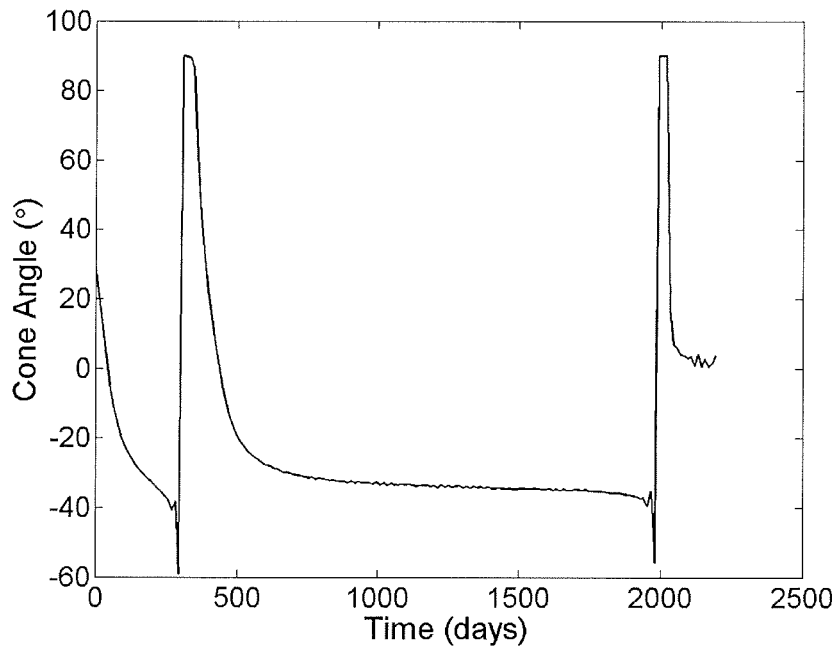


Figure 6.33: 25 year 0.85 mm s^{-2} , pre-JGA control angle profile

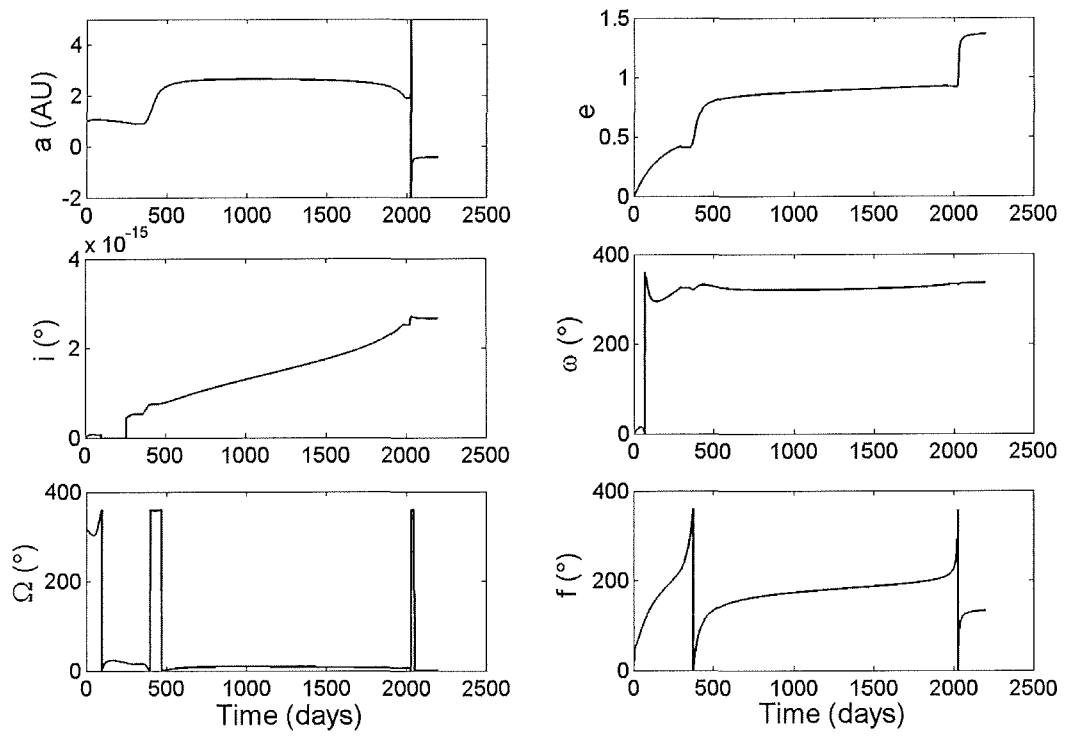


Figure 6.34: 25 year 0.85 mm s^{-2} , pre-JGA orbital element temporal evolution

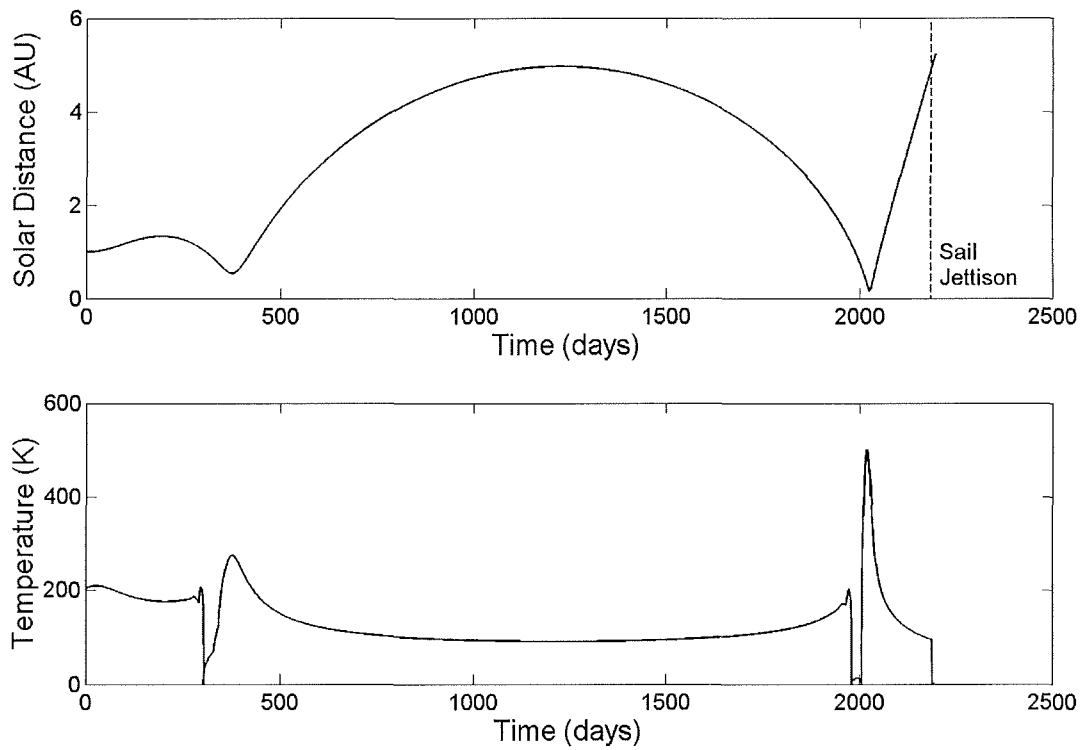


Figure 6.35: 25 year 0.85 mm s^{-2} , pre-JGA heliocentric radius and sail film temperature

6.4 Effect of Excess C_3 at Launch

An investigation of the effect of using the considerable excess C_3 capacity available on a Soyuz-Fregat launcher for an IHP mission was conducted [McInnes *et al*, 2004a]. At the outset, it was considered that an excess C_3 would offer only a small benefit to IHP missions, since the key parameter in determining the trip time to 200 AU is the perihelion distance of the final photonic assist. The excess C_3 could be used to attain a low perihelion more quickly, however this ‘spiral-down’ time is small in comparison to the perihelion-to-200-AU cruise time. For low acceleration sails, where multiple spirals are needed to reach the extremely close approaches necessary, then the excess C_3 can perhaps be used to reach the close solar approach in a shorter time. Therefore, fewer loops are required and there may therefore be less sail degradation.

As a brief demonstration of the effect of excess C_3 on Heliopause trajectories, Figure 6.36 shows two 0.85 mm s^{-2} IHP trajectories, generated using a locally optimal analytical control law that maximises the rate of change of orbit eccentricity. The leftmost spiral shows the effect of using a positive C_3 in the same direction as the velocity of the Earth. It is seen that this is a single photonic assist trajectory, with one less loop than the $C_3=0$ trajectory (as was noticed in Chapter 5). The excess C_3 is used to increase the initial aphelion prior to a close perihelion. However, the sail must still be used to reduce the perihelion, only being effective when below ~ 2 AU. Therefore, the sail does not have enough time to reduce the perihelion to a low enough value. The rightmost curve shows the more useful approach, when the excess C_3 is applied in opposition to the velocity of the Earth, so that a close approach can be reached in reduced time. It is seen that only a single aphelion is required with 1.5 revolutions occurring, thereby reducing the original ($C_3=0$) 2.5 revolution dual assist spiral to a single assist trajectory. This saves a small amount of trip time in order to reach hyperbolic escape conditions, but more importantly reduces the accumulated thermal loads on the sail, through a reduced number of close solar approaches.

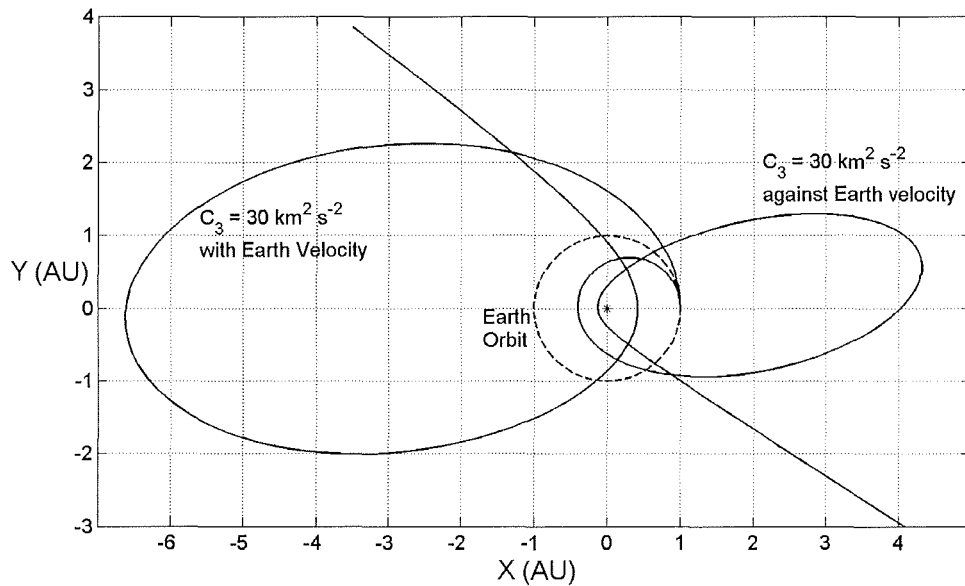


Figure 6.36: Effect of positive C_3 with and against Earth velocity for 0.85 mm s^{-2}

For high performance sails, a single assist is almost always obtained, and a close perihelion can be reached quickly using the sail thrust alone. Therefore, positive C_3 for high performance sails is unlikely to offer any significant trip time saving. Figure 6.37 shows a fast 3.0 mm s^{-2} IHP trajectory with an initial launch excess energy of $20 \text{ km}^2 \text{ s}^{-2}$ (within Soyuz-Fregat capacity for the IHP spacecraft considered [McInnes *et al*, 2004a]). Some trip time is saved in reaching the 0.25 AU perihelion. However, the elimination of the initial aphelion means that the resulting escape velocity at 5 AU is only 13.78 AU/yr. This is less than the C_3 zero velocity of 15.29 AU/yr, meaning that the total trip time to 200 AU is 15.0 years, with only a small saving of order 313 days. It is clear that, even though the perihelion velocity of an elliptical orbit is insensitive to the aphelion radius, the time allowed for sail-shaping of the trajectory does have some effect on the resulting perihelion velocity and escape speed. Further work is required on this aspect, but the assumptions used for Figure 6.18 are probably still valid for approximate preliminary analysis.

Figure 6.38 shows a slower 1.5 mm s^{-2} IHP trajectory with a launch excess of $20 \text{ km}^2 \text{ s}^{-2}$. The lower limit on the perihelion is constrained to be 0.25 AU, however the optimisation algorithm selected a perihelion of 0.29 AU in order to maximise the velocity at 5 AU. Again, the initial spiral down time has been reduced, but the escape velocity at 5 AU is only 6.79 AU/yr. The total trip time is then considerably longer than for C_3 zero (~ 25 years), at around 34 years. It seems that for single photonic assist trajectories, the initial aphelion (for $C_3 = 0$) is needed in order to

increase the perihelion speed, since the sail has adequate time to shape the trajectory prior to perihelion. The application of positive C_3 takes the spacecraft to the perihelion in a short time. It is possible that excess C_3 may be of benefit for dual assist trajectories with high performance sails, but only if the perihelion limit was much lower than 0.25 AU.

For the case of low performance excess C_3 IHP trajectories, Figure 6.39 shows a 0.85 mm s^{-2} trajectory with an excess C_3 of $20 \text{ km}^2 \text{ s}^{-2}$. The final perihelion is the same as for the C_3 zero trajectory at 0.16 AU. Some time is saved by the elimination of the first aphelion of the C_3 zero trajectory. The escape velocity at 5 AU is slightly less, at 9.52 AU/yr. The total trip time saving is then of order 0.6 years, with a total trip time to 200 AU of 25.5 years. Therefore, the considerable excess capacity on the Soyuz-Fregat launcher does not seem to offer an appreciable benefit for low performance IHP missions either. As an aside, Figure 6.40 shows an example of the use of an excess C_3 of $30 \text{ km}^2 \text{ s}^{-2}$ to reduce the sail requirements to 0.75 mm s^{-2} , while maintaining a thermal limit of 0.20 AU. The trip time to 200 AU is 29.1 years and, even though the first of the two loops is removed, it is not much less than the C_3 zero trip time. It is clear from this analysis that excess C_3 offers little benefit for IHP trajectories, but further work should be conducted in future, even if this is a computationally complex optimisation task.

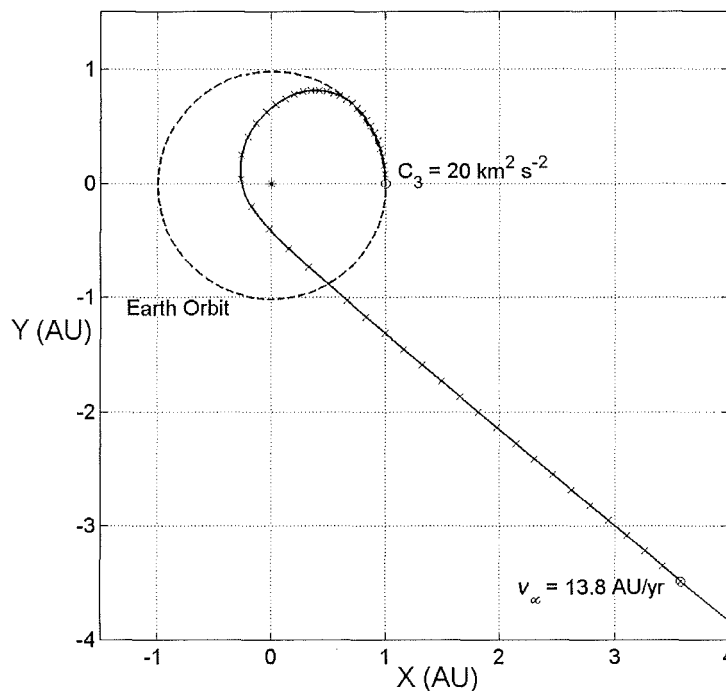


Figure 6.37: $C_3 = 20 \text{ km}^2 \text{ s}^{-2}$ 3.0 mm s^{-2} IHP trajectory

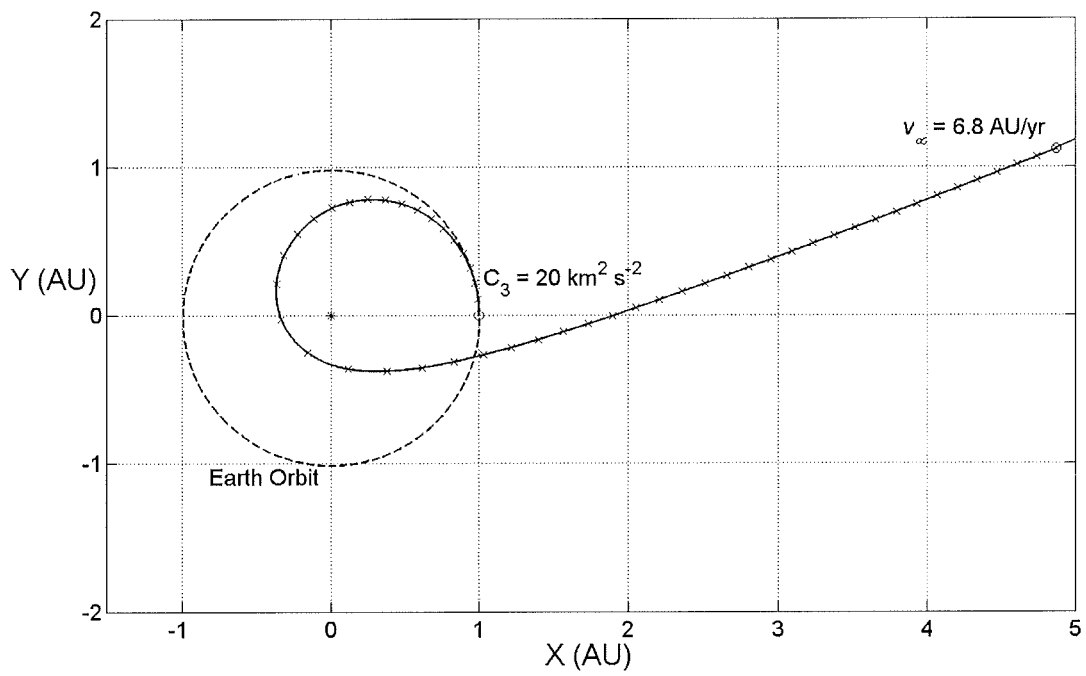


Figure 6.38: $C_3 = 20 \text{ km}^2 \text{ s}^{-2}$ 1.5 mm s^{-2} IHP trajectory

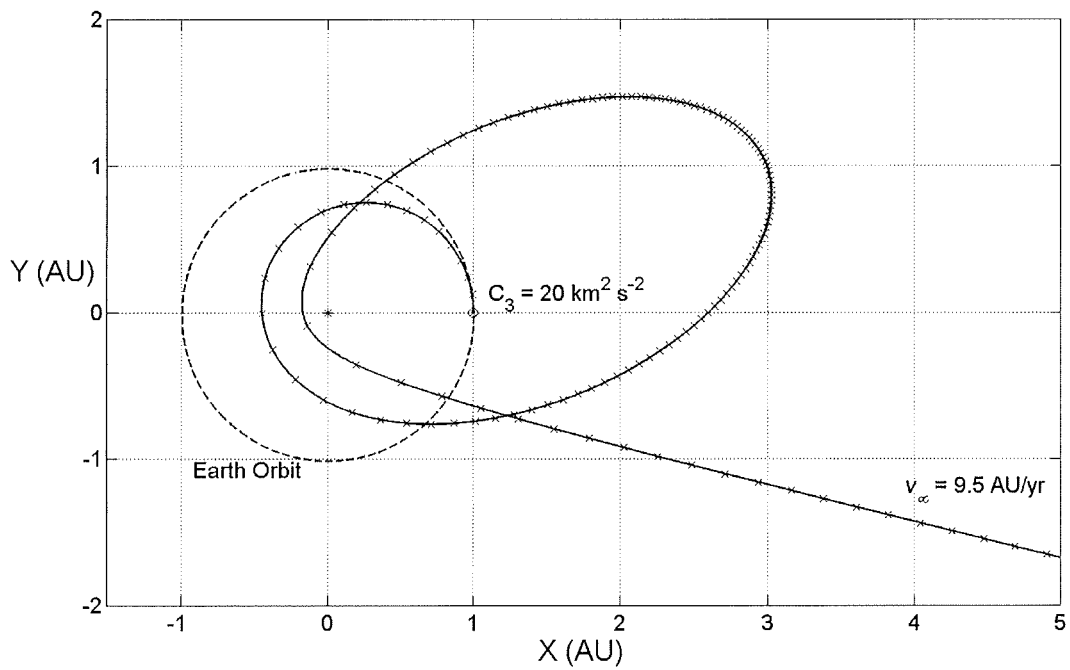


Figure 6.39: $C_3 = 20 \text{ km}^2 \text{ s}^{-2}$ 0.85 mm s^{-2} IHP trajectory ($r_p = 0.16 \text{ AU}$)

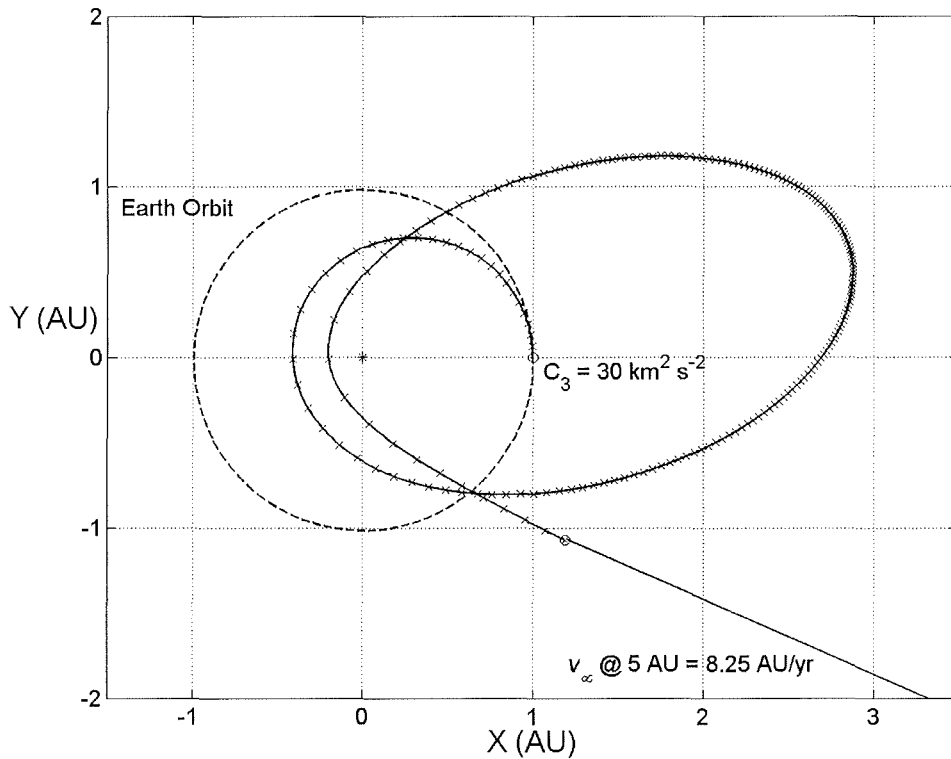


Figure 6.40: 29 year $C_3 = 30 \text{ km}^2 \text{ s}^{-2}$ 0.75 mm s^{-2} IHP trajectory ($r_p = 0.20 \text{ AU}$)

6.5 Summary and Discussion

A detailed investigation into trajectories to the Heliopause has been conducted, following on from the Outer Solar System work in Chapter 5. The well-known solar photonic assist concept has been utilised for fast single-loop trajectories (~ 15 years), slow single loop trajectories, and slow multiple-loop trajectories (~ 25 years). For fast trajectories, a parametric study was conducted with the optimisation approach to maximise the velocity at 5 AU. The 5 AU velocity and 200 AU trip-time was found as a function of characteristic acceleration, for numerous constraints on minimum solar approach distance. The selected example trajectory was similar to the NASA ISP mission, with a 3.0 mm s^{-2} solar sail used to reach the Heliopause at 200 AU, in a time-minimised 15.7 years, with a minimum solar distance constraint of 0.25 AU. A launch opportunity was identified on May 5, 2010 ($C_3=0$), which included a brief launch date scan about the optimal departure date.

Numerous trajectories to the Heliopause have been optimised that make use of multiple solar photonic assists for slow missions (of order 25 years). Initially, a novel parametric analysis of optimising trajectory half-arcs was conducted. This was

a sub-optimal approach, which made use of the assumption that the final perihelion velocity was relatively insensitive to aphelion radius. This then removed the complex initial spiralling optimisation problem, so that a characteristic acceleration and final perihelion radius could be selected, to reach the Heliopause in 25 years. The minimum final perihelion radius was constrained by thermal loading of the sail film. Parametric analysis of the minimum possible solar approach was conducted for a number of theoretical maximum temperature values. For conventional aluminium/chromium coated, polyimide film substrates, the minimum possible solar radius was found to be 0.25 AU, as expected. Ultimately, to minimise thermal loading, a single-loop trajectory was chosen for an example. A 1.5 mm s^{-2} solar sail was used to reach the Heliopause at 200 AU, in 24 years, with a minimum solar distance constraint of 0.25 AU. A launch opportunity was identified on February 1, 2010 ($C_3=0$). Again, the example trajectory was complemented by a brief launch date scan. Other dual photonic assist trajectories were also generated for 1.0 mm s^{-2} , a 29 year trajectory with final perihelion of 0.25 AU, and a 27 year trajectory at 0.20 AU. The latter would require high heat tolerant sail materials.

Next, an investigation of the possibility of using a Jupiter gravity assist to reduce the required escape velocity, and thus required performance, was conducted. It was found that a Jupiter gravity assist was of negligible use for very fast trajectories, since the Δv imparted was a small fraction of the initial velocity. For a low performance, 0.85 mm s^{-2} dual photonic assist trajectory ($C_3=0$), with highly reflective/emissive coatings allowing a 0.16 AU solar approach, a Jupiter gravity assist at Io distance was shown to impart a Δv of only 0.6 AU/yr, enabling a reduction in trip-time of only 1 year to 25.0 years. A Jupiter gravity assist is of little use for a Heliopause mission, although future work should investigate if there are any benefits for outer planet missions.

In an investigation of the effect of excess launcher C_3 , it was found that the best approach here was to apply C_3 against the initial velocity vector, so as to reach low perihelia more quickly. Although this has the effect of reducing the initial spiralling time and/or eliminating one or more loops, this trip-time saving is minimal compared to the large cruise time. Positive C_3 was found to be of little use for Heliopause trajectories, but this requires further work for confirmation.

Chapter 7

Solar Polar Orbiter Trajectories

In this Chapter, extensive parametric analysis of transfers to a true, Earth-resonant, solar polar orbit will be conducted. This mission is unique to solar sailing and the analysis will be performed in more detail than previous studies. The analysis will centre on the cranking orbit concept, used in Chapter 4 for a high-inclination asteroid. The transfer will involve an optimised spiral down to a low solar distance, crank-up to polar orbit, and then, if necessary, an optimised spiral out to resonant solar polar orbit. Nominally, the optimised phases will be in one plane, but an investigation of spiralling to small inclinations will be conducted, in addition to the effect of positive excess launch energy. An example trajectory will be defined, which is launch date specific, with the propagation of the final solar polar orbit also shown.

For a true Solar Polar Orbiter mission [McInnes *et al*, 2004b, Macdonald *et al*, 2005] the desired solar polar orbit is defined by the direction of the solar poles. The solar equator is inclined at 7.25° to the ecliptic plane, with a Right Ascension of Ascending Node angle of $75.76^\circ + 1.397^\circ$ per century (from J2000). This means that the desired polar orbit that must pass over the North Solar Pole is inclined at $i_{SPO} = 82.75^\circ$ with a Right Ascension of Ascending Node of $\Omega_{SPO} = 75.76^\circ + 180^\circ + 0.01397 \text{ yr}^{-1}$. The Right Ascension of the North Solar Pole is thus 90° more than this angle, at 345.76° in J2000. In the last twenty years, research has revealed that the direction of the solar poles is less well defined than thought [Balthasar *et al*, 1987], but the above values will be used. It is desirable that the polar orbit be correctly phased with the Earth to aid mission science returns and avoid solar conjunctions. As described in McInnes *et al* [2004b], the polar orbit should be resonant with the Earth, for visibility and communications reasons, with a circular orbit radius of $N^{-2/3}$ AU, where N is the integer resonant number of orbits per year, $N=1$ (1 AU),

$N=2$ (0.63 AU), $N=3$ (0.48 AU), $N=4$ (0.40 AU), and so on. For example, if the initial position on the polar orbit is correctly phased with the azimuth of the Earth, then the Earth-Sun-spacecraft angle is $90^\circ \pm 60^\circ$ for the $N=3$ resonance. This phasing means that when the spacecraft crosses the ecliptic plane it is separated from the Earth by 90° in longitude, which allows for viewing of the solar corona along the Earth-Sun line, by keeping the spacecraft close to the plane of the solar limbs as seen from the Earth [Neugebauer *et al*, 1998]. The $N=3$ resonant polar orbit at 0.48 AU has been selected as the base-line orbit in McInnes *et al* [2004b], to provide frequent polar observations without imposing high thermal loads, but $N=2$ and $N=4$ orbits will also be considered in the trajectory analyses.

7.1 Solar Polar Orbit Transfer

Transfers to solar polar orbits have been analysed in parametric studies at JPL [Sauer, 1999], and briefly by Leipold [2000]. The trajectories generated by Sauer were an improved approach on the crude analysis adopted for the transfers in previous work by NASA/JPL [Neugebauer *et al*, 1998]. The trajectory approach centres on the ‘cranking orbit’ concept to rapidly increase orbit inclination, which was made use of in Chapter 4 for reaching a high-inclination asteroid. This approach will again be briefly described here.

After an optimised spiral in to a zero or low inclination circular orbit at the cranking orbit radius, an analytical control law that maximises the rate of change of inclination, by switching the clock angle by 180° every half orbit, is used. The cone angle is fixed at an optimum angle of 35.26° , to provide maximum out-of-plane thrust, although this of course also results in a radial force component. However, the final cranked orbit has a shape fairly close to the initial orbit. The control laws are again shown in Eq. 7.1 and 7.2. In Eq. 7.2, *sign* is defined as plus or minus one, depending on the sign of the cosine term. Following Sauer [1999], we have adopted a two or three phase approach to the trajectory structure. Closer cranking orbit radii enable more rapid acquisition of polar inclinations, and a third outward spiral phase may be necessary to reach the first few resonant orbits (e.g. $N = 1, 2, 3$).

$$\text{Cone Angle: } \alpha = \tan^{-1}\left(\frac{1}{\sqrt{2}}\right) \quad [7.1]$$

$$\text{Clock Angle: } \delta = \frac{\pi}{2} \{1 - \text{sign}[\cos(\omega + f)]\} \quad [7.2]$$

Approximate trip times can thus be obtained by adding the trip times for each of the phases, but this neglects the phasing of the orbits, the Earth ephemeris, and the orientation of the line of nodes of the polar orbit. The position of the line of nodes acts to constrain the optimal launch window to every 6 months. In general the actual trip-time will be slightly longer than these approximate times.

7.2 Approximate Trip-Times

The analytical control law discussed above was used to obtain cranking times, in conjunction with a 4th order Runge-Kutta integrator, terminated when the inclination was satisfied to a tolerance of 10^{-3} radians. Figure 7.1 shows the variation of cranking time against characteristic acceleration and the cranking orbit radius. It is seen that the cranking time is very sensitive to the cranking orbit radius, whereas the curve levels off at higher accelerations. In general, the closer the orbit to the Sun, the faster the inclination change. However, a trade-off is necessary to determine the optimum cranking radius when the time taken to reach and, if necessary, spiral back out from cranking orbit is taken into account. The rate of change of inclination is independent of solar distance, but closer orbits have shorter periods, and so the inclination change is effected more rapidly. It will be seen below that the cranking time dominates the total trip time, and so the closer the cranking orbit the more rapidly the solar polar orbit can be attained, subject to thermal constraints. For zero launch C_3 (positive C_3 will be investigated later), inward spiral trip-times were produced by optimising circular-coplanar transfers from 1 AU to the polar/cranking orbit radius using NPSOL. These spiral times were added to the cranking times at the resonant orbit radii and the total 2-phase trip times are shown in Figure 7.2. This is for the first six resonant orbits: it is clear that cranking at 1 AU or 0.63 AU is extremely time consuming, so a 3-phase approach must be adopted to reach these orbits. A 3-phase approach is also beneficial for the higher resonance numbers, if the close solar orbit thermal loads can be withstood.

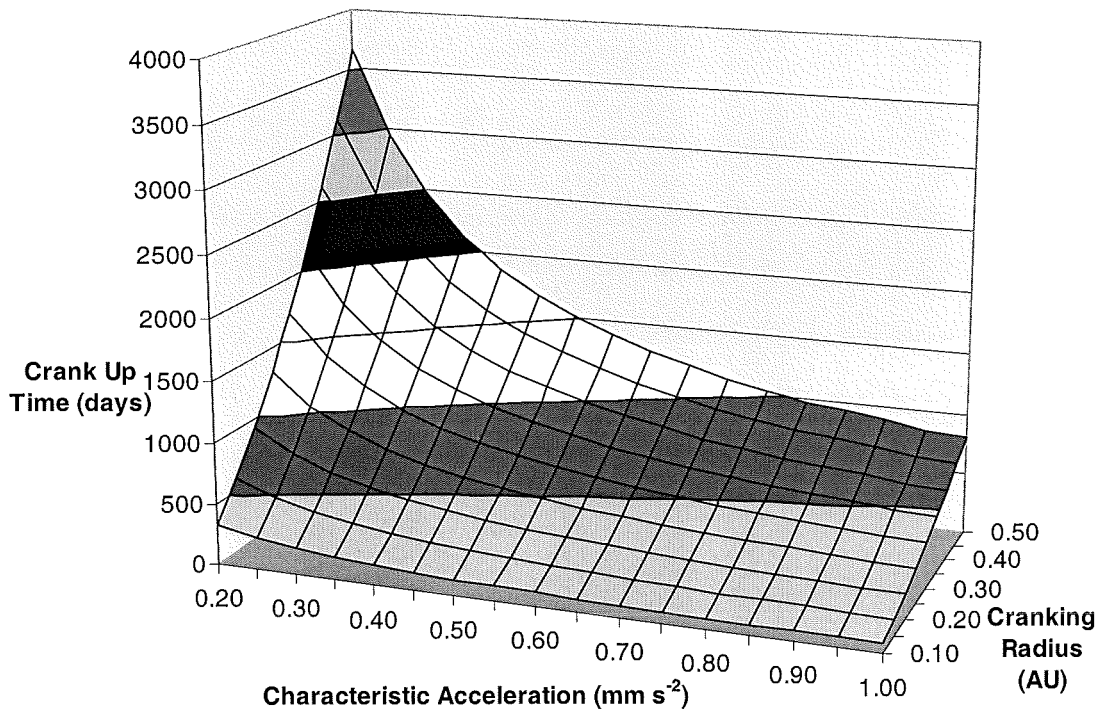


Figure 7.1: Cranking times from zero to 82.75° , against cranking orbit radius and solar sail characteristic acceleration

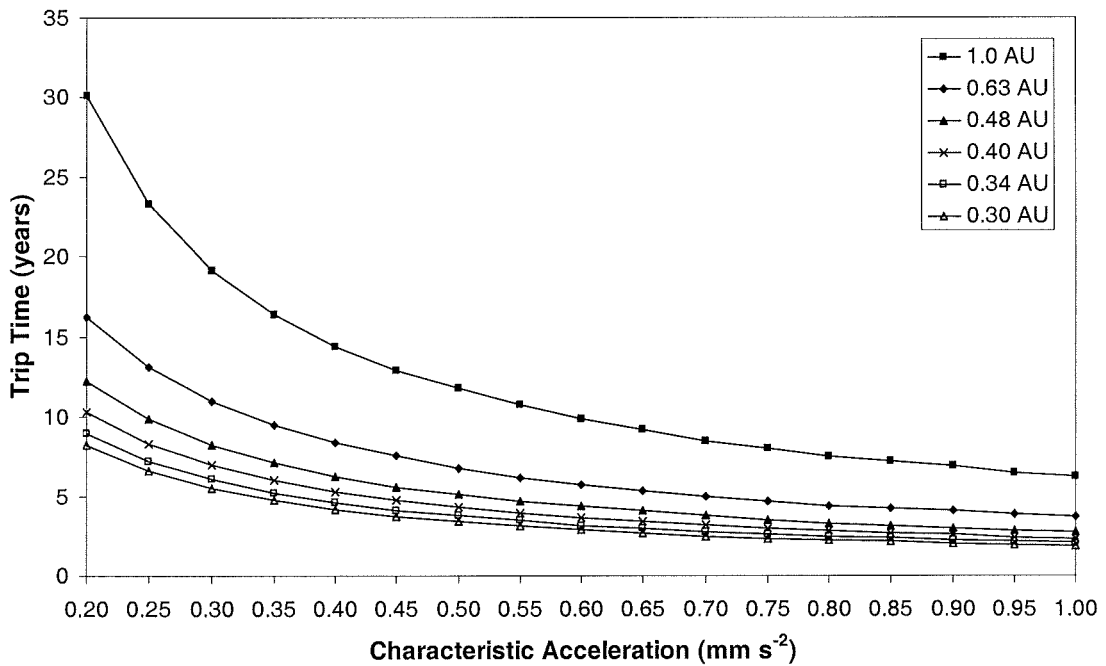


Figure 7.2: Two-phase trip times to polar orbit, by cranking at resonances

Circle-to-circle, coplanar trip times were obtained for the third phase of transfers from a range of cranking orbit radii to the first 3 resonant orbits. These times were then added to the inward spiral and cranking times at each cranking orbit radius and over a range of characteristic accelerations. Figure 7.3 shows the total trip time as a function of characteristic acceleration and cranking orbit radius for reaching the first resonance orbit, a 1 AU solar polar orbit. A moderate characteristic acceleration of 0.5 mm s^{-2} would require a fairly close cranking orbit of 0.3 AU for a mission duration below 5 years. This requirement could be alleviated by using the positive C_3 , as will be discussed later. Figure 7.4 shows the equivalent surface plot of results for reaching the second resonance, at 0.63 AU. Figure 7.5 shows the 3-phase total trip times for reaching the 0.48 AU, third resonant orbit. Figure 7.5 and Figure 7.2 validates the 0.5 mm s^{-2} , two-phase to 0.48 AU trajectory that was discovered by NASA/JPL to be of order 5 years [Sauer, 1999]. It should be noted here that work conducted at JPL does not include positive C_3 or take into account Earth ephemeris, orbital orientation and phasing, which will be investigated later in this Chapter.

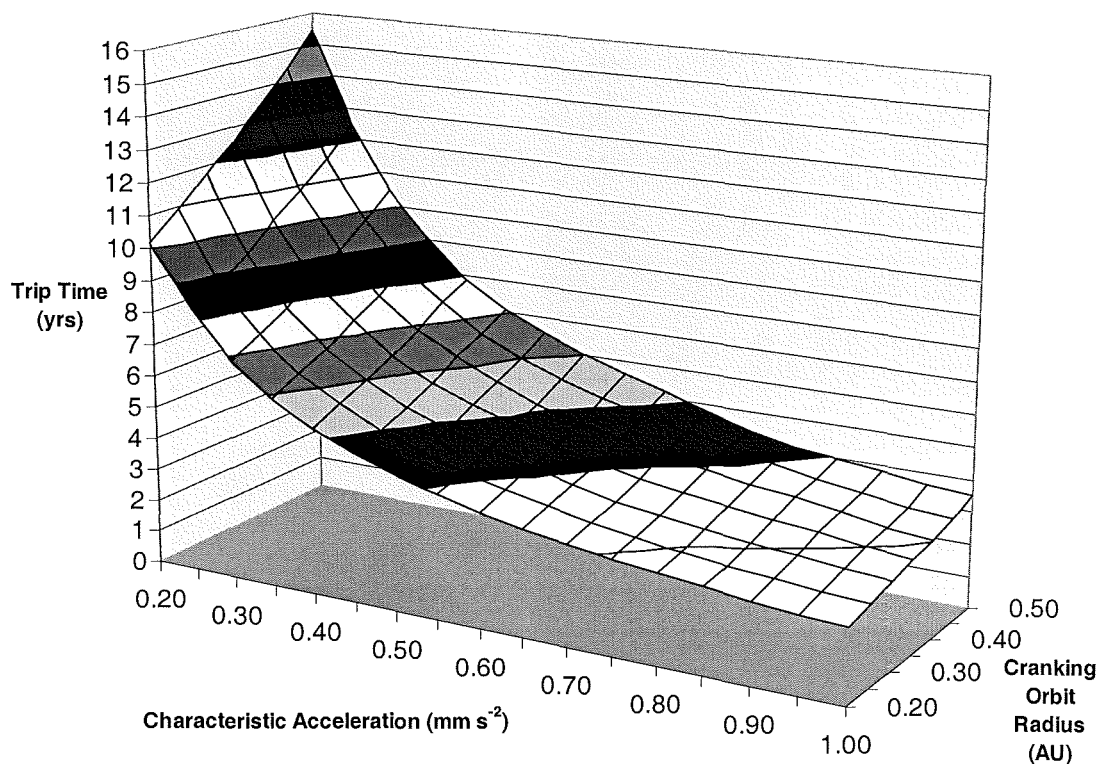


Figure 7.3: Three-phase, total trip times to 1 AU ($N=1$) solar polar orbit

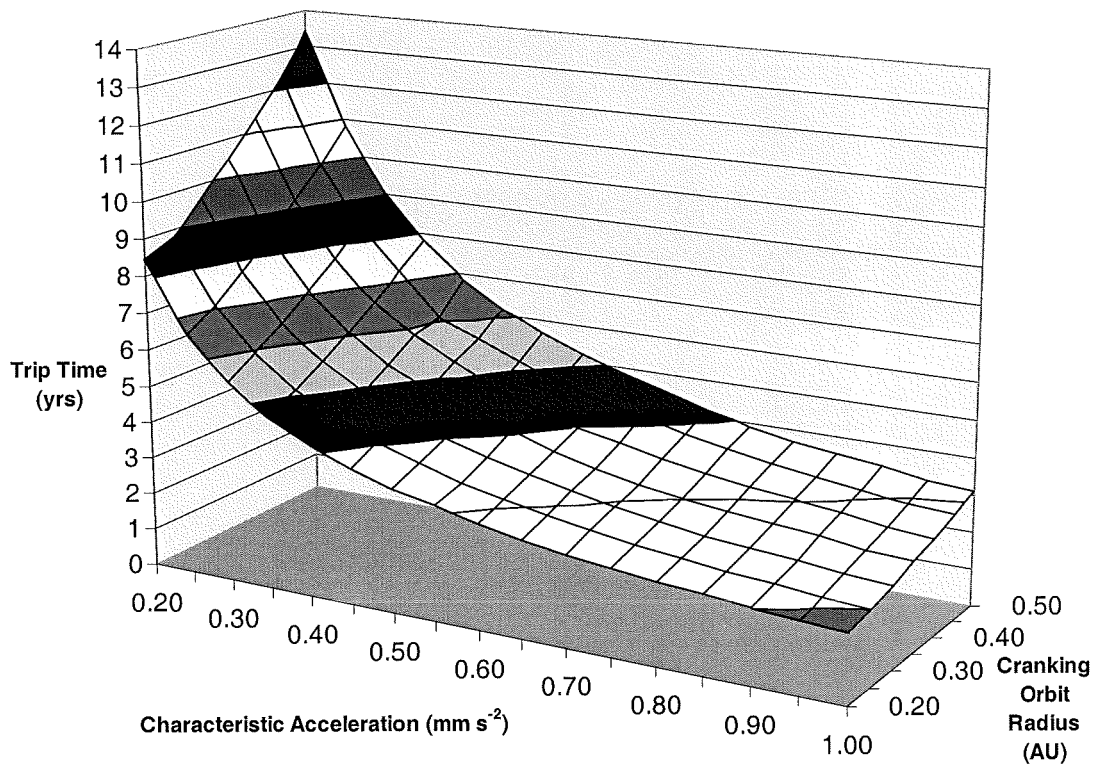


Figure 7.4: Three-phase total trip times to 0.63 AU ($N=2$) solar polar orbit

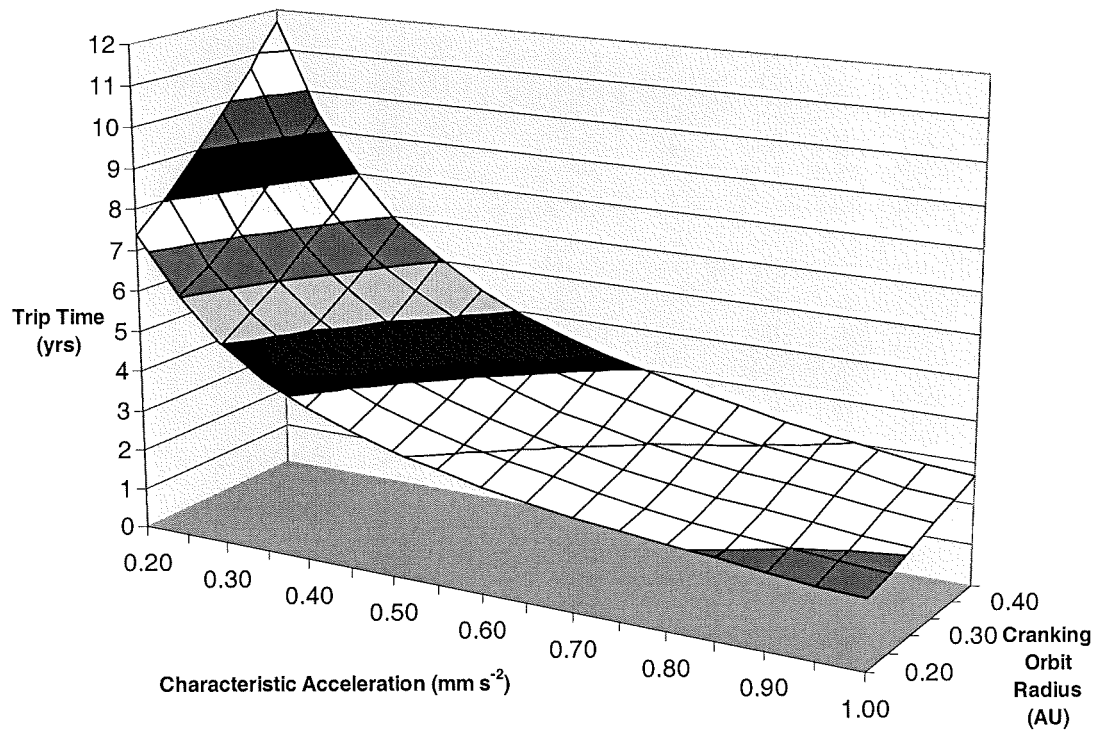


Figure 7.5: Three-phase total trip times to 0.48 AU ($N=3$) solar polar orbit

It has been established above that a base-line mission to a 0.48 AU solar polar orbit, with a thermal sub-system sized for cranking at 0.48 AU, would require a characteristic acceleration of order 0.5 mm s^{-2} for a 5 year mission [McInnes *et al*, 2004b]. It was then necessary to tune the trajectory (for a range of characteristic accelerations in a parametric study) to see if any reduction in sail performance, and hence sail size, could be achieved by spiralling in to a higher inclination before cranking, and to attempt to reduce trip-time by using the considerable payload capacity of the Soyuz Fregat launch vehicle to increase the launch C_3 .

7.3 Inward Spirals to Low Inclinations at 0.48 AU

In Sauer's parametric study [1999], he optimises inward spirals to a 15° inclination before starting the cranking manoeuvre. If a third outward spiral phase is desired then the final 15° to reach polar orbit was also optimised. Sauer makes use of the *locally optimal* cranking control law and does not supply a fully optimised trajectory to polar orbit. It was also noted that the total transfer time is relatively insensitive to initial cranking orbit inclinations above 10° [Sauer, 1999]. This section will concentrate on the two-phase transfer to a 0.48 AU polar orbit. The effect of optimising a circle-to-circle inward spiral from 1 AU to 0.48 AU was investigated, for a number of different initial cranking orbit inclinations. The optimised inward spiral times were then added to the remaining cranking time necessary to make-up the inclination to polar orbit. The NPSOL optimisation matched the semi-major axis, eccentricity and inclination as constraints. Figure 7.6 shows the total trip time saving, as a function of characteristic acceleration, for initial cranking orbit inclinations of 5° , 10° , 15° and 20° . It can be seen that, although the overall saving is less than 6 months, optimising to 10 - 20° is significantly better than for 5° . In general, 15° seems the optimum value, as was arbitrarily chosen by Sauer [1999]. As the initial cranking orbit inclination is increased beyond these values, many more revolutions are needed and so the optimiser requires more control nodes – placing greater demands on the optimisation software. The fluctuation in the curves in Figure 7.6 is thought to be related to the number of orbital revolutions. The small trip-time saving when cranking at 0.30 AU is also shown.

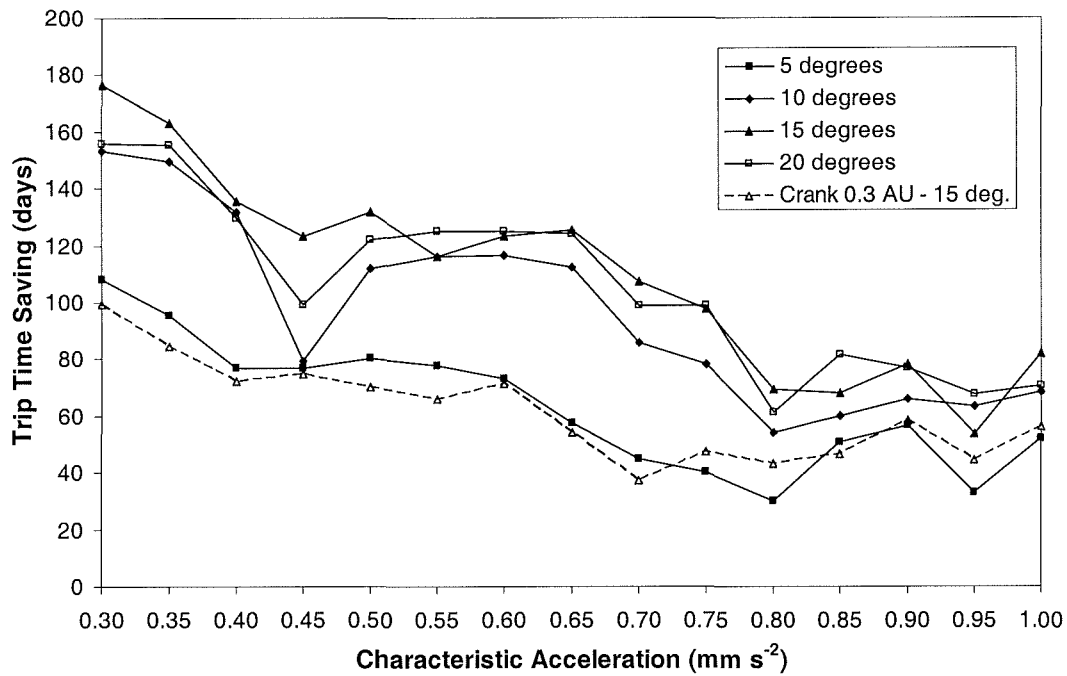


Figure 7.6: Effect of optimised spiral to low inclinations on total trip time to 0.48 AU polar orbit

7.4 Excess Launch Energy ($C_3 > 0$)

Circular-coplanar optimisations of the inward spiral phase were conducted while increasing the launch C_3 to $40 \text{ km}^2 \text{ s}^{-2}$, in opposition to the velocity of the Earth. 51 control nodes were used, and no constraint was placed on the minimum solar distance. In the final example reference trajectory, a minimum constraint will be necessary, since a loop slightly inside the cranking orbit radius will violate the thermal sub-system sizing and cranking orbit selection [McInnes *et al*, 2004b]. The unconstrained trajectories here usually passed inside the cranking orbit radius due to the perihelion of the initial Earth escape trajectory being too low at high values of C_3 . Figure 7.7 shows the effect of using positive C_3 on the spiral-down time to different cranking orbit radii at characteristic accelerations of 0.5 mm s^{-2} and below. For higher accelerations and higher cranking orbit radii, the curve levels off sooner than for low accelerations and low cranking orbits. Therefore, there is more benefit of using the excess C_3 capability to reach lower cranking orbit radii with low performance sails. It should be noted that for higher characteristic accelerations, the sail size and hence launch mass is higher, and for lower cranking orbit radii, the

increased mass of the thermal sub-system will increase launch mass. These considerations mean that the actual excess C_3 available on the Soyuz-Fregat launcher would be reduced, due to the higher launch mass [McInnes *et al*, 2004b].

A characteristic acceleration of 0.5 mm s^{-2} was selected, from the approximate analysis earlier, to reach a 0.48 AU polar orbit cranking at 0.48 AU, with a total transfer time of order 5 years. An attempt was made to reduce the sail performance requirements by using the excess C_3 available, with optimised spiral-in to $15\text{-}20^\circ$ inclination. In an attempt to achieve further savings, the effect of using a non-zero launch declination, to attain an initial inclined orbit at launch, was investigated. It was found that small increases in launch declination had the effect of significantly reducing the in-plane excess velocity to the detriment of trip time. Non-zero launch declination was therefore not considered further. In order to produce an approximate solar polar orbit transfer with a trip time of order 5 years, it was found that the characteristic acceleration needed was of order 0.42 mm s^{-2} for a C_3 of $40 \text{ km}^2 \text{ s}^{-2}$. The payload performance curve for the Soyuz-Fregat terminates at $38.84 \text{ km}^2 \text{ s}^{-2}$ (negligible trip time penalty), suggesting that some extra ballast mass will need to be placed in the launch fairing [McInnes *et al*, 2004b].

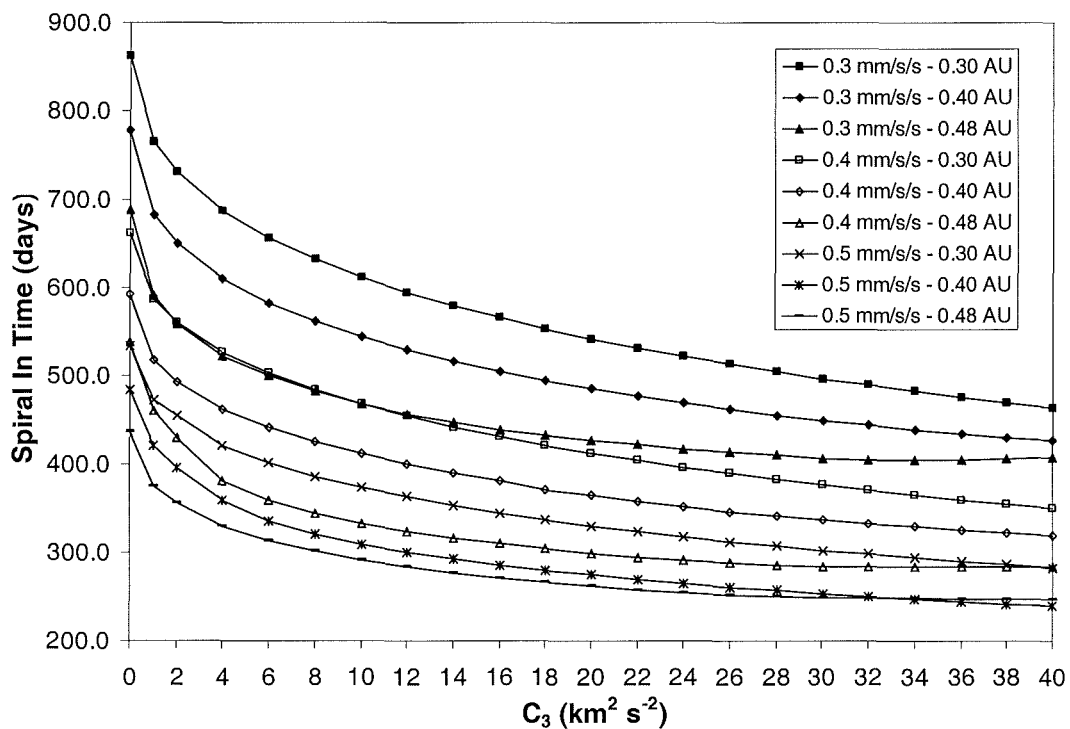


Figure 7.7: Spiral-in time to cranking orbit radii of 0.30, 0.40 and 0.48 AU for characteristic accelerations of 0.3, 0.4 and 0.5 mm s^{-2} , against launch C_3 .

7.5 Reference Trajectory

The problem of obtaining the correct phasing at arrival on the solar polar orbit was deemed to be best tackled by arbitrarily selecting an arrival date and position on the solar polar orbit that is correctly phased with the Earth. Then, the analytical cranking control law was used in a reverse integration down to a low inclination. The resulting orbital elements were then used as the initial conditions for a reverse optimisation ‘back’ to the Earth. The solar polar orbit arrival position was defined to be at the North Solar Pole, with the Earth-Sun-sail angle at 90° . That is, with the Earth azimuth angle aligned with the descending node of the polar orbit. The Earth was found to be at this azimuth angle on June 7.23, 2015, which was thus defined to be the Solar Polar Orbit arrival date. This allows for an approximate Earth departure date in the year 2010. The orbital elements on arrival at the Solar Polar Orbit (SPO) are a semi-major axis, $a_{SPO} = 0.48$, eccentricity, $e_{SPO} = 0$, inclination, $i_{SPO} = 82.75^\circ$, argument of perihelion, $\omega_{SPO} = 0$ (open), right ascension of ascending node, $\Omega_{SPO} = 255.9756^\circ$ (at arrival), and true anomaly, $f_{SPO} = 90^\circ$.

The inclination control law was used with a negative time step and the crank time was found for cranking in reverse to approximately 15° inclination. The instantaneous orbital elements and date were then extracted and used as the initial conditions for optimisations in reverse using both NPSOL and SNOPT. The software code for the control segment loop was adjusted to account for stepping the linear interpolation of control nodes in reverse. Extensive trial-and-error and incremental feedback were used to obtain a solution for the reference trajectory, which was verified by plotting the trajectory via forwards integration. For a characteristic acceleration of 0.42 mm s^{-2} , the spacecraft is launched on May 16, 2010, with a positive launch excess energy of $C_3 = 38.84 \text{ km}^2 \text{ s}^{-2}$. A constraint was placed on the minimum solar distance of 0.48 AU, and the sail then performs an optimised spiral down to the cranking orbit inclined at 14.42° in 457.5 days. This intermediate orbit has a semi-major axis of 0.4828 AU and an eccentricity of 0.0762 AU, obtained from the initial reverse integration, to account for the osculating nature of the cranking phase. The analytical control, cranking manoeuvre then takes place on August 17, 2011, to raise the inclination to 82.75° for a circular 0.48 AU solar polar orbit in 1390 days. The complete trajectory is shown in Figure 7.8, where the total mission duration is 5.06 years.

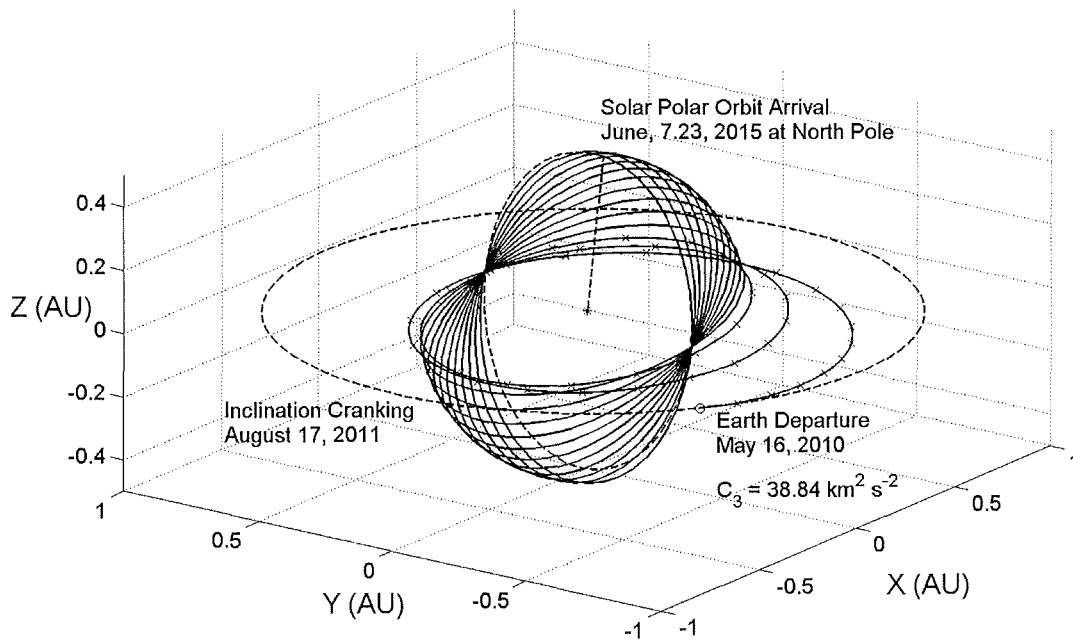


Figure 7.8: 0.42 mm s^{-2} Solar Polar Orbit transfer trajectory

Figure 7.9 shows the X-Z axes projection, which demonstrates the inclination change effected by the optimised phase. The ecliptic projection of the optimised phase is shown in Figure 7.10. The spacecraft does not approach closer than 0.48 AU from the Sun, with the solar sail being used to circularise and incline the orbit after positive C_3 injection. Figure 7.11 shows the optimised phase control angle profiles. These not particularly smooth, but that is probably because of the trajectory constraints imposed by the ephemeris of the Earth and the minimum solar distance. In general, the cone angle stays within $60\text{-}70^\circ$ of the Sun-line, except at the end of this phase. Figure 7.12 shows the temporal evolution of the orbital elements during the optimised phase, where the final inclination reaches 14.42° . The minimum solar distance of 0.48 AU is represented in Figure 7.13, with the sail film temperature reaching a maximum value of 394.3 K. The sail film was modelled with a reflectivity of 0.85, zero front surface emissivity, and a rear emissivity of 0.64, for aluminium and chromium, respectively.

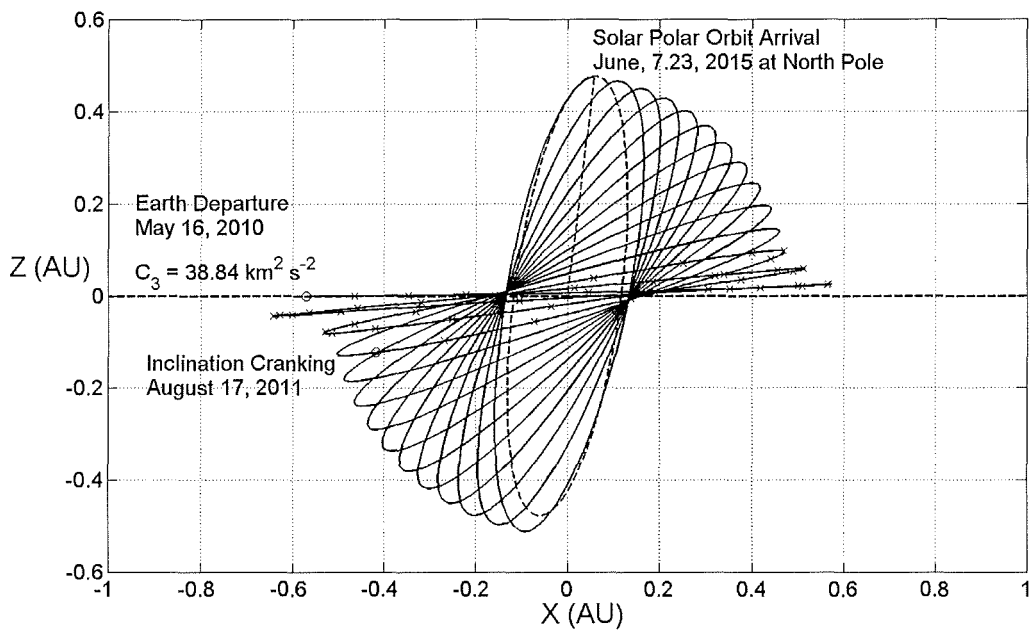


Figure 7.9: 0.42 mm s^{-2} Solar Polar Orbiter mission X-Z projection

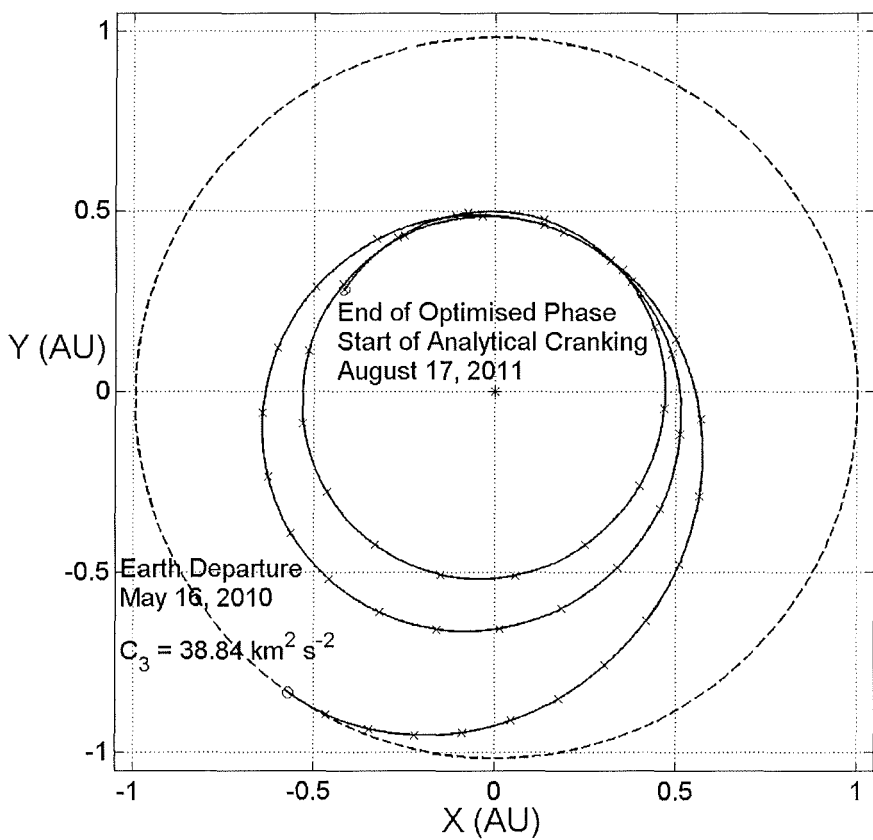


Figure 7.10: 0.42 mm s^{-2} Solar Polar Orbiter mission optimised phase

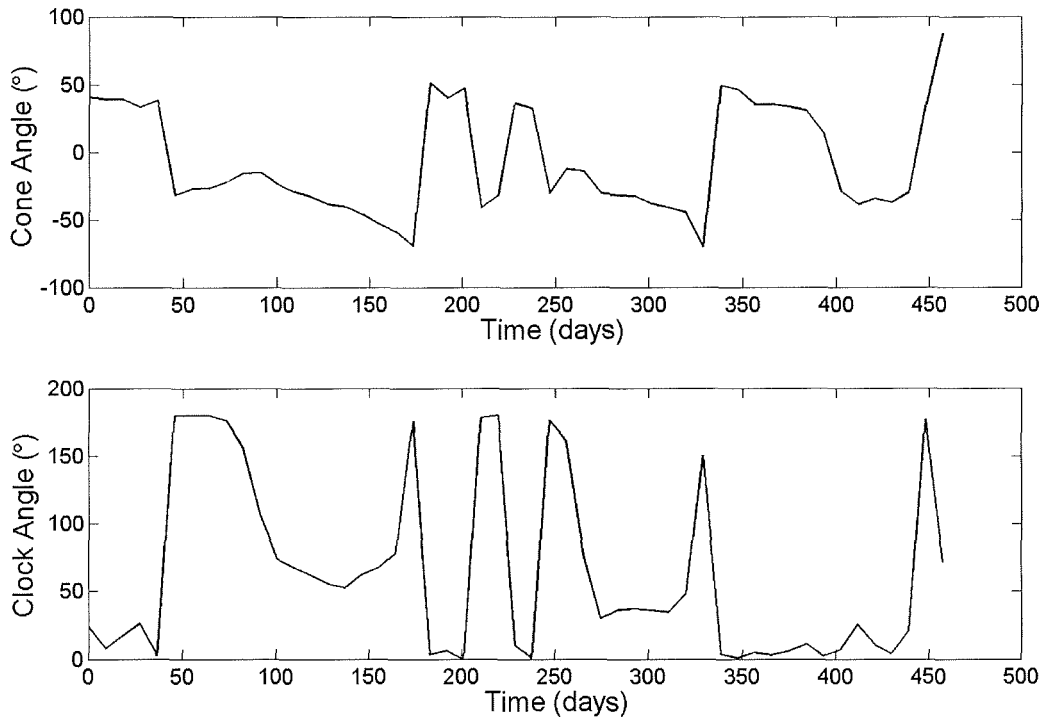


Figure 7.11: 0.42 mm s^{-2} trajectory optimised phase control angle profile

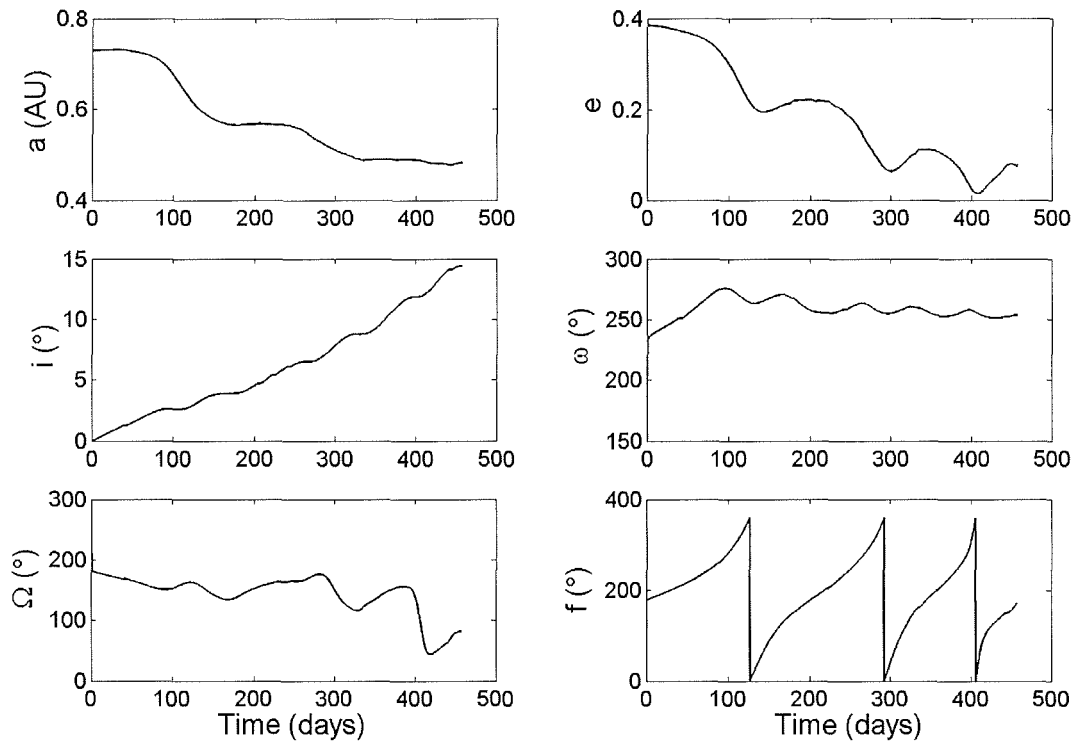


Figure 7.12: 0.42 mm s^{-2} trajectory optimised phase orbital elements

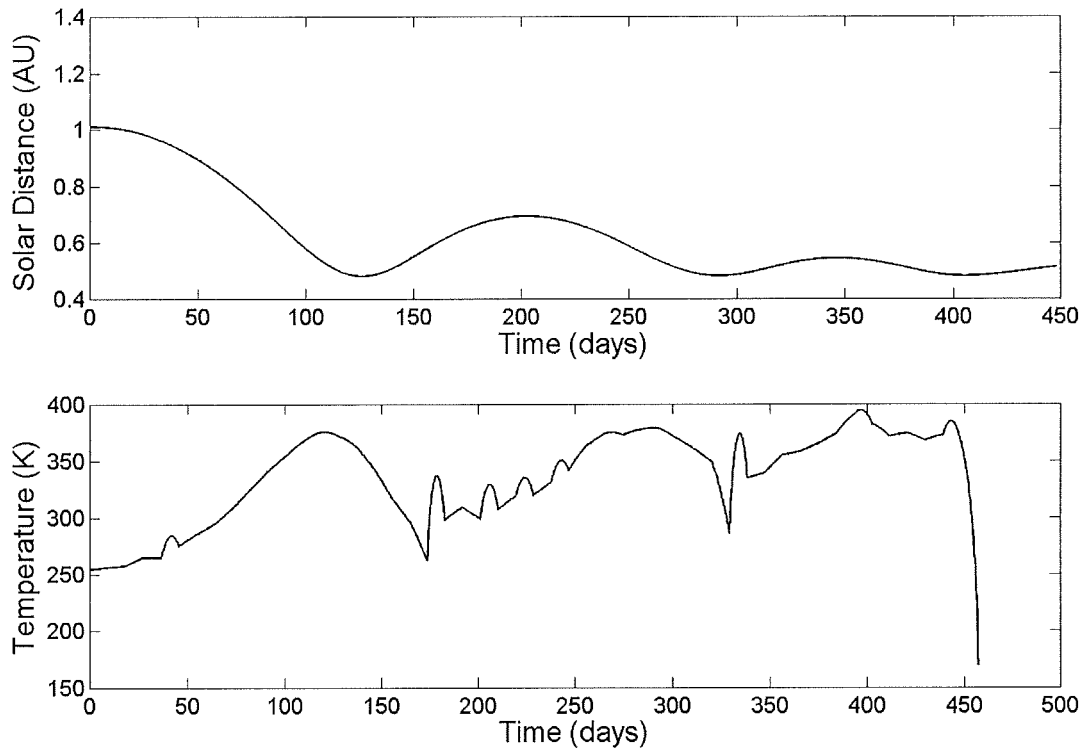


Figure 7.13: Optimised phase heliocentric distance and sail film temperature

A specific view of the cranking orbit is shown in Figure 7.14, with the control profiles produced by the control law shown in Figure 7.15. The oscillatory nature of the orbital elements is shown in Figure 7.16 with the heliocentric distance and sail film temperature depicted in Figure 7.17. The semi-major axis, eccentricity and distance remain unchanged for every complete orbit revolution.

With the solar sail jettisoned, the spacecraft orbit was propagated over 1000 days along the solar polar orbit. As expected, there were no solar conjunctions, and the correct 3:1 resonance with the Earth was evident. Figure 7.18 shows the Earth-Sun-Sail, Sun-Sail-Earth and Sun-Earth-Sail angles, where the orbit period of the 0.48 AU polar orbit is 121.465 days. It is noted that the Earth-Sun-Sail (although sail has been jettisoned) angle oscillates about 90° by 60° , and the very slight deviation from this is due to the non-zero eccentricity of the Earth's orbit. This angle profile is also equivalent to the profile shown in Neugebauer *et al* [1998], except that the polar orbit in that case is retrograde at 90° , hence it is the mirror image (about y-axis) of Figure 7.18. The Earth-spacecraft distance is shown in Figure 7.19, reaching a maximum distance of order 1.45 AU.

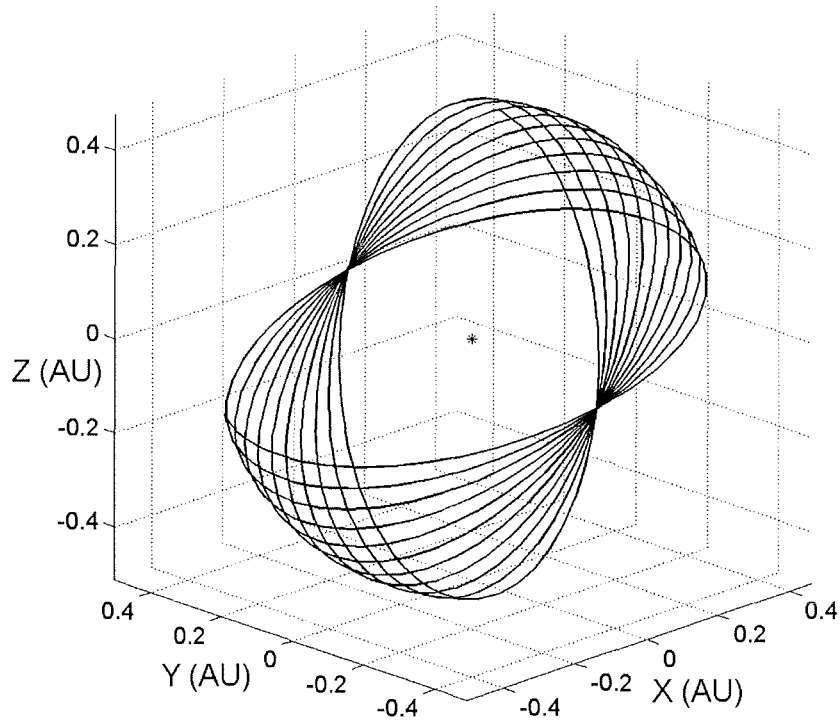


Figure 7.14: 0.42 mm s^{-2} cranking phase trajectory

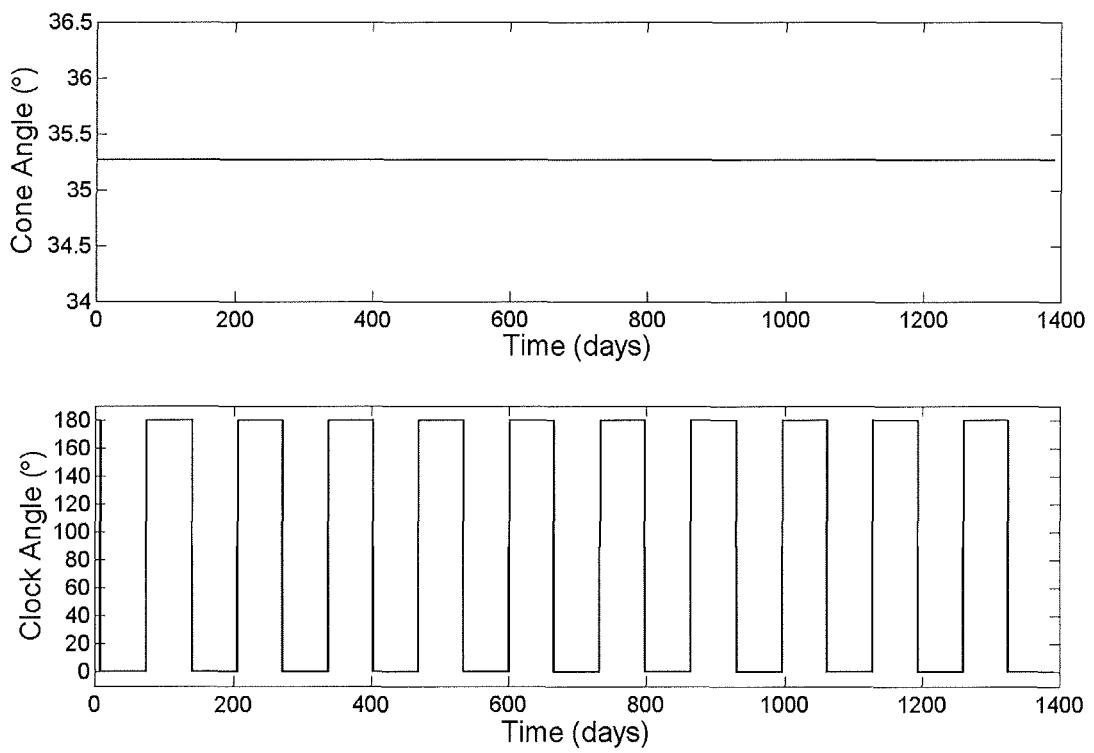


Figure 7.15: 0.42 mm s^{-2} cranking phase control profile

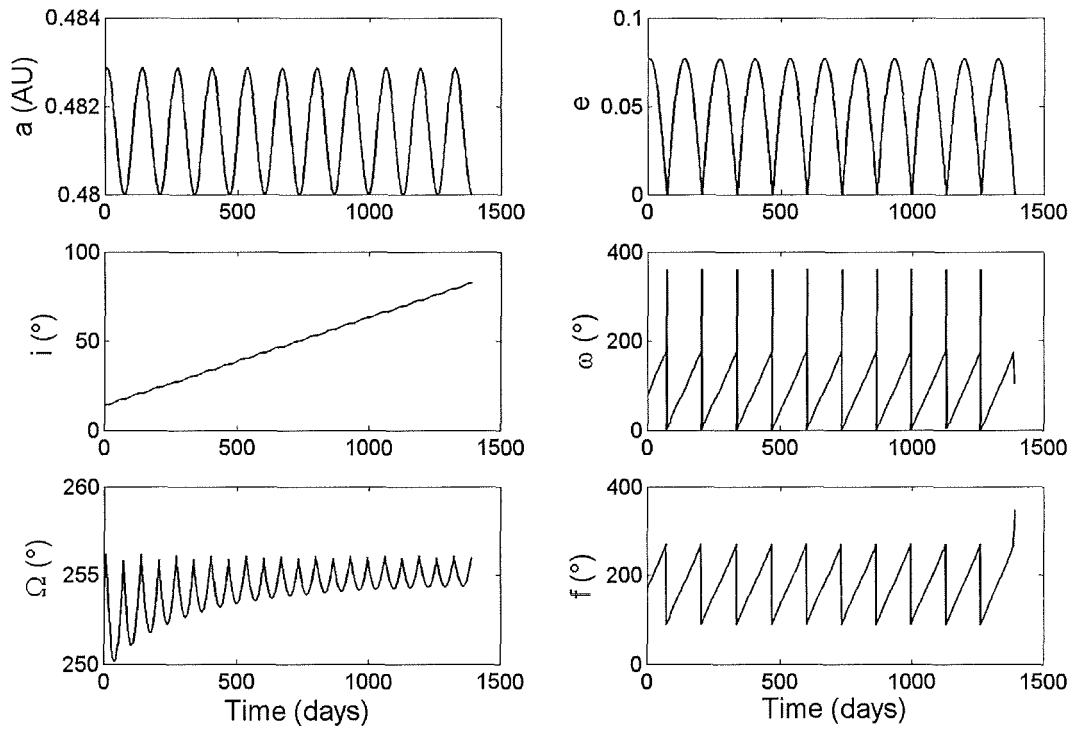


Figure 7.16: 0.42 mm s^{-2} cranking phase orbital elements

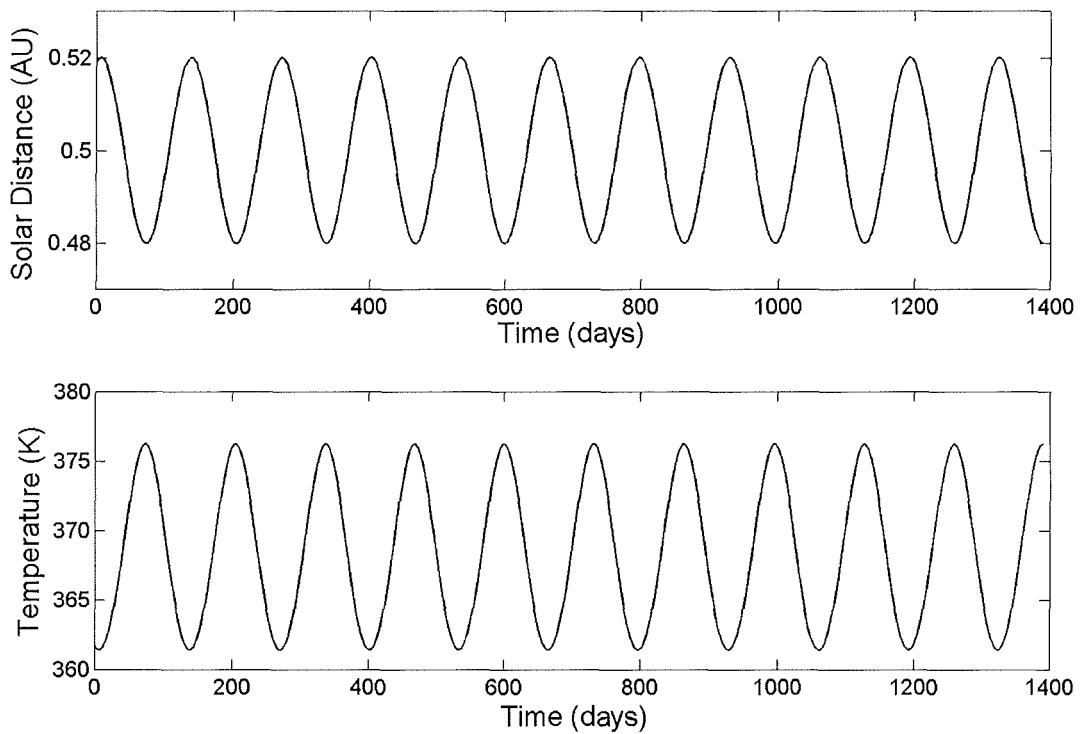


Figure 7.17: 0.42 mm s^{-2} cranking phase heliocentric distance and sail film temperature

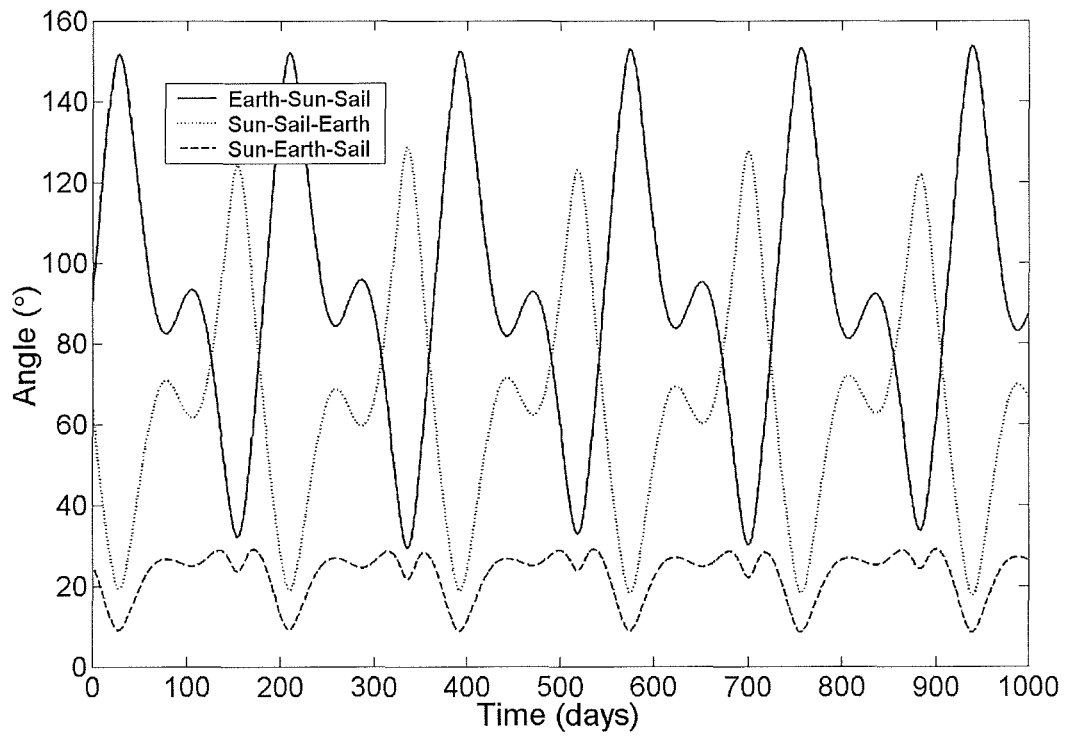


Figure 7.18: Solar polar orbit propagation telecommunications angles

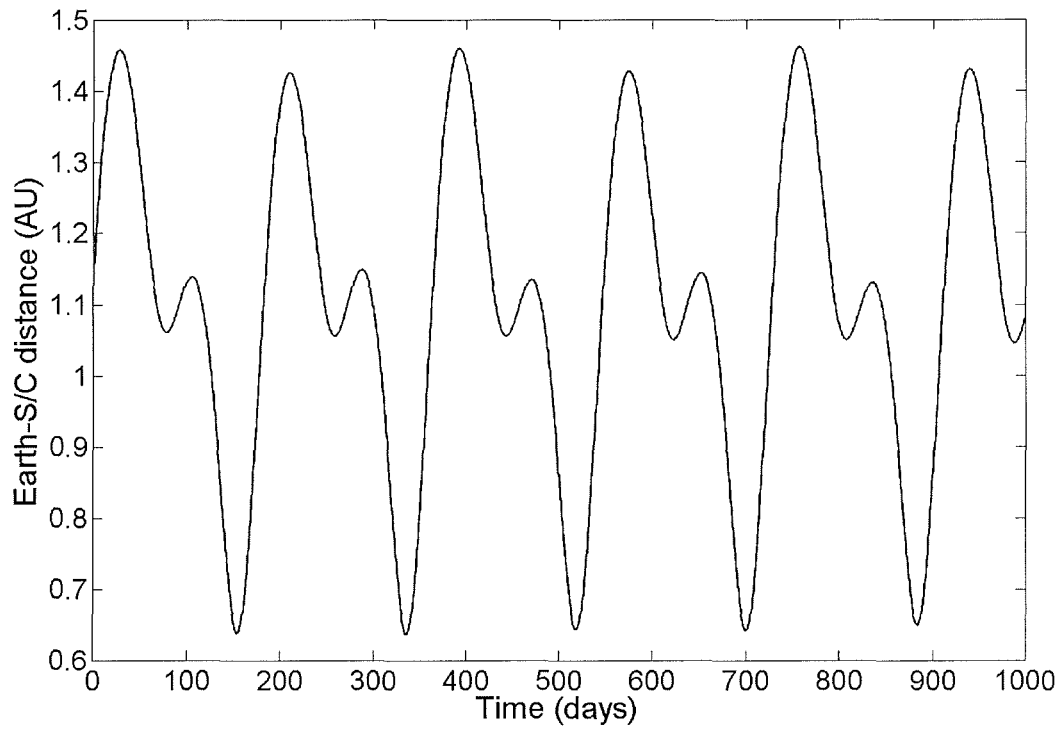


Figure 7.19: Solar polar orbit propagation Earth-spacecraft distance

7.6 Fast Mission to 0.48 AU Polar Orbit

As an example of how a faster mission to solar polar orbit could be accomplished, the cranking orbit was reduced to 0.30 AU, with the minimum solar distance also constrained at this distance. The characteristic acceleration was set a little higher at 0.5 mm s^{-2} . At this sail performance the sail side length is of order 200 m, and the closer cranking radius causes an increase in the mass of the thermal sub-system [McInnes *et al*, 2004b]. This increased launch mass results in a maximum C_3 of $27.9 \text{ km}^2 \text{ s}^{-2}$. Ignoring the ephemeris of the Earth and the final phasing, the optimised, positive C_3 inward spiral time (coplanar) was found to be 320.3 days. For visualisation purposes, the initial Earth azimuth angle was set to be 138.4° to allow for the correct line of nodes to be attained. The resulting orbital elements were then passed to the analytical cranking algorithm, which cranked the orbit up to $\sim 82.75^\circ$ in 705.9 days. 90° was added to the initial Ascending Node angle and 90° was subtracted from the true anomaly to ensure the control law produced the correct line of nodes in polar orbit. A third phase was then optimised to spiral out from the cranking orbit to the final orbit radius of 0.48 AU. Four constraints were matched: the semi-major axis, eccentricity, inclination and ascending node angle, and 3:1 resonance polar orbit (not-phased) was achieved in 110.3 days. The total trip time to polar orbit was thus 3.11 years, for this fast-mission option. Figure 7.20 shows the entire three phases of the trajectory.

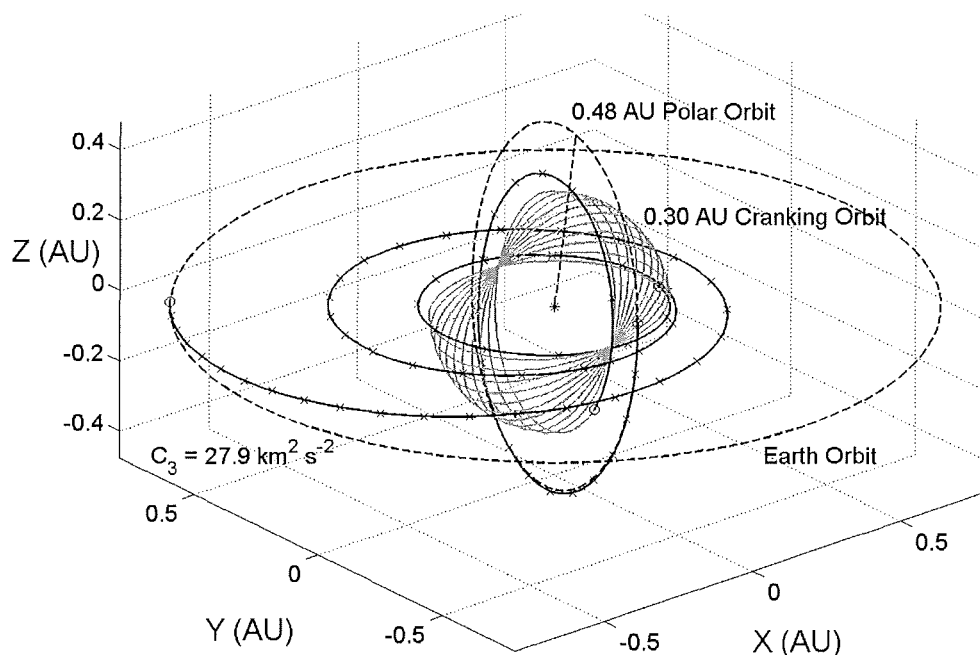


Figure 7.20: 0.5 mm s^{-2} , Fast 3.1 year trajectory to 0.48 AU polar orbit

7.7 Summary and Discussion

Trajectory analysis for a solar sail mission to orbit directly over the solar poles has been carried out. Optimisation of transfer trajectories was investigated, using an inclination cranking manoeuvre, to spiral to a polar orbit, resonant with the Earth. Approximate trip-times were generated in a parametric analysis, using a two or three-phase trajectory. These consisted of a circle-to-circle inward spiral, locally optimal cranking manoeuvre to 82.75° and, if necessary, a spiral back out from close solar distance to the operational orbit. The two-phase total trip-times for all resonant solar polar orbit radii were presented, as well as three-phase times to the first three resonances. It was found that a 0.48 AU polar orbit could be reached in 5 years, by cranking at 0.48 AU, which was also discovered previously by Sauer [1999].

An investigation of inward spirals to initial cranking orbit radii of 0.48 AU, inclined at up to 20° was conducted, to reduce the time spent using the cranking control law. Similar to Sauer [1999], it was found that the overall trip time saving was insensitive to initial cranking orbit inclinations above 15° , but the parametric analysis was shown in greater detail here. In addition, the effect of spiralling in to 15° inclination at 0.30 AU was shown to have minimal effect on overall trip-time. The effect of positive launch C_3 on inward spirals was included, for reaching a range of cranking orbit radii, not previously documented in the literature.

With the trajectory fine-tuning mentioned above, a minimal characteristic acceleration of 0.42 mm s^{-2} was shown to deliver the sail to the 0.48 AU solar polar orbit at the north pole in just over 5 years (two-phase). Optimisation and integration was performed in reverse to ensure correct resonant orbit phasing with the Earth, departing on May 16, 2010, with a C_3 of $39 \text{ km}^2 \text{ s}^{-2}$. The final orbit resonance with the Earth was confirmed by forward propagation. One further example of a faster, 3.1 year, transfer was presented using a characteristic acceleration of 0.5 mm s^{-2} . Here, Earth ephemeris and final orbit phasing was not addressed. The three-phase trajectory was shown to spiral down to 0.30 AU from a C_3 of $28 \text{ km}^2 \text{ s}^{-2}$, crank up to 82.75° , then spiral back out to 0.48 AU solar polar orbit. From a detailed parametric analysis, this Chapter has presented positive C_3 , launch date specific results, with correctly phased final resonant polar orbits, which is not previously documented in the literature.

Chapter 8

Non-Keplerian Orbit Transfers

In this Chapter, new transfers to exotic Non-Keplerian Orbits (NKO) are produced, for two-body displaced orbits, using high performance sails, and for three-body, artificial equilibria, using lower performance sails. The dynamics of these families of orbits have been described by McInnes [1999]. In this thesis a parametric study of transfers to displaced two-body NKOs is conducted. In addition, transfers to two interesting applications of artificial Lagrange points will be shown. These are the Geostorm orbit, displaced Sunward of the Earth-Sun L_1 point, and the Polar Observer orbit, displaced above the poles of the Earth. Transfers to such NKOs have not previously been documented in the literature.

8.1 Two-Body Non-Keplerian Orbits

Solar sails do not require propellant mass, and so exhibit an effectively infinite specific impulse over long mission durations. The continuous thrust produced enables quite exotic, displaced Non-Keplerian Orbits (NKO). High performance sails could use these NKOs as unique vantage points for Infra-Red telescopes, displaced above the ecliptic plane, where there is much less resolution-limiting dust. NKOs could also be used for permanently viewing the solar poles, or as levitators [Forward, 1991]. One example of a family of NKOs will be described here, based on a more detailed investigation by McInnes [1999, Chapter 5].

The constant solar radiation pressure force can be used in two (and three) body systems to displace a circular orbit (or, in principal, an eccentric orbit as well) above or below the ecliptic plane, and artificially maintain a desired orbit period. The dimensions and period of this Displaced NKO are defined by the sail lightness number (or characteristic acceleration) and cone angle (the clock angle in this case is

zero, for no transverse component of thrust). Figure 8.1 shows how this displaced NKO can be produced through balancing solar gravity with the centripetal and solar radiation pressure force, where ω is the orbital angular momentum vector in this section. In the rotating frame of reference, the equation of motion, is given by Eq. 8.1. The left hand side of the equation contains the kinematic, coriolis and centripetal acceleration terms, and the right hand side contains the solar sail acceleration and gravitational acceleration, defined by Eq. 8.2 and the gravitational potential in Eq. 8.3.

$$\frac{d^2\mathbf{r}}{dt^2} + 2\boldsymbol{\omega} \times \frac{d\mathbf{r}}{dt} + \boldsymbol{\omega} \times (\boldsymbol{\omega} \times \mathbf{r}) = \mathbf{a} - \nabla V \quad [8.1]$$

$$\mathbf{a} = \beta \frac{\mu}{r^2} (\hat{\mathbf{r}} \cdot \mathbf{n})^2 \mathbf{n} \quad [8.2]$$

$$V = -\frac{\mu}{r} \quad [8.3]$$

A modified potential can be defined, $U=V+\Phi$, by noting that the centripetal acceleration term is conservative, such that it is defined by a scalar potential in Eq. 8.4, and therefore the centripetal acceleration term becomes Eq. 8.5. The equation of motion in the rotating frame now becomes the reduced form as Eq. 8.6 [McInnes, 1999].

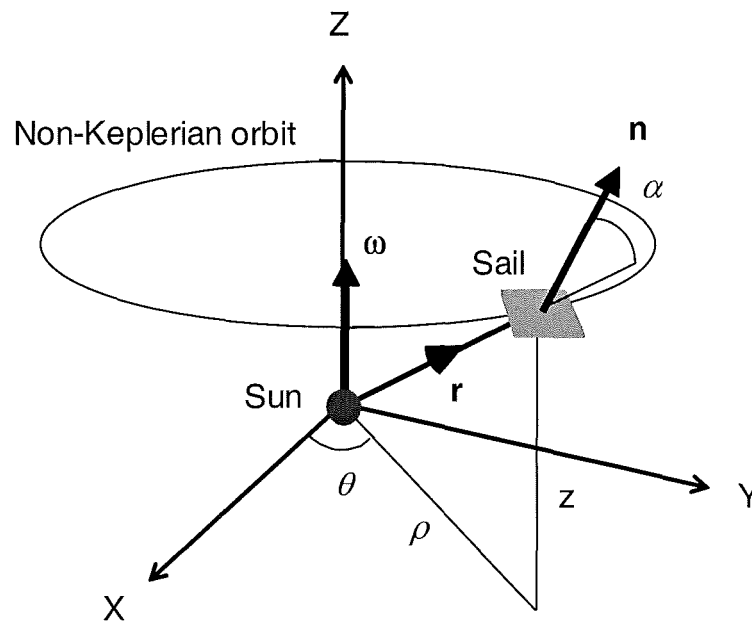


Figure 8.1: Sun-centred Non-Keplerian Orbit (inertial frame) [adapted from McInnes, 1999]

$$\Phi = -\frac{1}{2}|\boldsymbol{\omega} \times \mathbf{r}|^2 \quad [8.4]$$

$$\nabla\Phi = \boldsymbol{\omega} \times (\boldsymbol{\omega} \times \mathbf{r}) \quad [8.5]$$

$$\frac{d^2\mathbf{r}}{dt^2} + 2\boldsymbol{\omega} \times \frac{d\mathbf{r}}{dt} + \nabla U = \beta \frac{\mu}{r^2} (\hat{\mathbf{r}} \cdot \mathbf{n})^2 \mathbf{n} \quad [8.6]$$

For an equilibrium solution to this equation in the rotating frame the first two terms must be zero, and the vector product of Eq. 8.6 is taken with \mathbf{n} , to obtain Eq. 8.7, where ε is an arbitrary scalar multiplier. Since \mathbf{n} is a unit vector of magnitude unity then Eq. 8.7 results in a definition of \mathbf{n} for equilibrium in Eq. 8.8.

$$\nabla U \times \mathbf{n} = 0 \quad \Rightarrow \quad \mathbf{n} = \varepsilon \nabla U \quad [8.7]$$

$$\mathbf{n} = \frac{\nabla U}{|\nabla U|} \quad [8.8]$$

For a circular displaced NKO, only uniform azimuthal motion is required, such that there is no component of \mathbf{n} in the azimuthal direction (clock angle $\delta = 0$). Therefore, \mathbf{n} is only in the plane defined by $\hat{\mathbf{r}}$ and $\boldsymbol{\omega}$, so the vector and scalar products of Eq. 8.8 with $\hat{\mathbf{r}}$ is taken, to obtain the required sail cone angle in Eq. 8.9. The scalar product of Eq. 8.6 with \mathbf{n} can also be performed to obtain the required sail lightness number in Eq. 8.10.

$$\tan \alpha = \frac{|\hat{\mathbf{r}} \times \nabla U|}{\hat{\mathbf{r}} \cdot \nabla U} \quad [8.9]$$

$$\beta = \frac{r^2 \nabla U \cdot \mathbf{n}}{\mu (\hat{\mathbf{r}} \cdot \mathbf{n})^2} \quad [8.10]$$

In the cylindrical coordinate system of Figure 8.1, the modified potential is given by Eq. 8.11. Then, evaluating the potential gradient and using Eqs. 8.9 and 8.10, Eq. 8.12 and 8.13 are obtained in the cylindrical coordinate system, where ω is the required orbital angular velocity of the displaced NKO, and $\tilde{\omega}$ is the angular velocity of a circular orbit of radius r .

$$U = -\left[\frac{1}{2} \rho^2 \omega^2 + \frac{\mu}{r} \right] \quad [8.11]$$

$$\tan \alpha = \frac{(z/\rho)(\omega/\tilde{\omega})^2}{(z/\rho)^2 + [1 - (\omega/\tilde{\omega})^2]} \quad , \quad \tilde{\omega}^2 = \frac{\mu}{r^3} \quad [8.12]$$

$$\beta = \frac{\left[1 + \left(\frac{z}{\rho}\right)^2\right]^{1/2} \left[\left(\frac{z}{\rho}\right)^2 + \left(1 - \left(\frac{\omega}{\tilde{\omega}}\right)^2\right)^2 \right]^{3/2}}{\left[\left(\frac{z}{\rho}\right)^2 + \left(1 - \left(\frac{\omega}{\tilde{\omega}}\right)^2\right)^2 \right]^2} \quad [8.13]$$

These equations can then be used to determine the required sail cone angle and lightness number for a given NKO of dimension z by ρ , and period $2\pi/\omega$. Nested cylinders and tori of sail lightness number are generated by Eq. 8.13, shown in Figure 8.2, for one-year NKOs, which shows contours of equal required lightness number against NKO dimension. It should be noted that NKOs can be produced with any orientation, not necessarily orbiting about the ecliptic pole. Figure 8.2 also shows the transition from torus to cylinder, when the sail lightness number is unity. The asymptotes where the required lightness number tends towards infinity is shown. A complete treatment of these families of NKOs is given in McInnes [1999], along with an investigation of their stability and control properties. For a circular NKO, of dimension 0.5×0.5 AU, the required sail lightness number is 0.88 (5.22 mm s^{-2}). This is a very high performance sail, but may be feasible using a spin-stabilised disk and a highly miniaturised payload.

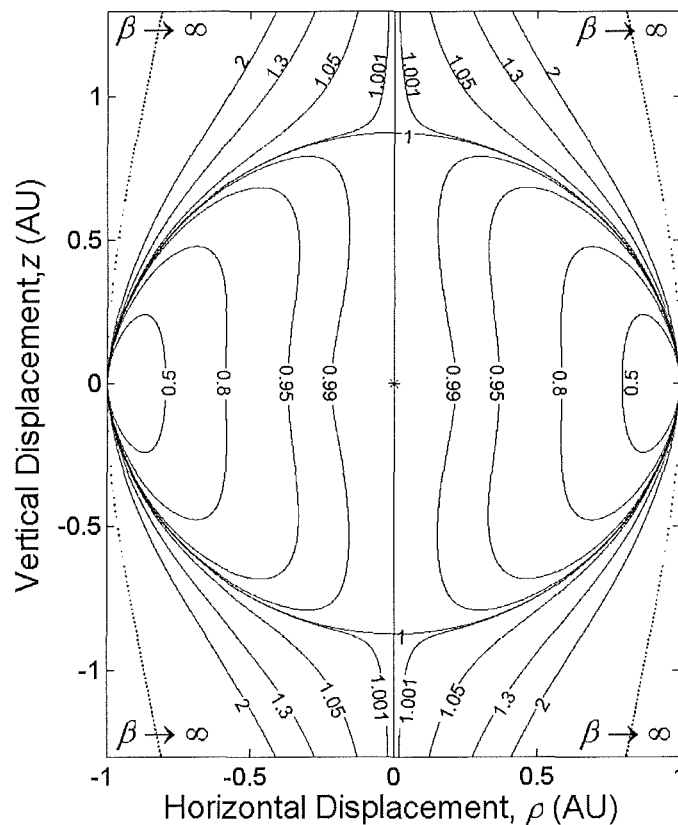


Figure 8.2: Contours of lightness number against displaced NKO dimension

Using the optimisation method of Chapter 2, new transfers to these displaced NKO have been generated from Earth orbit [Hughes and McInnes, 2002b]. Naturally, the same sail performance was used for the transfers as was required for the operational displaced orbit. Figure 8.3 shows the results for a range of final vertical displacements and horizontal distances within the ecliptic plane, which is equivalent for the other 3 quadrants. It is observed that all the trip times are naturally quite short, due to the very high performance sails used, even when spiralling to almost 1 AU above the ecliptic plane. The most difficult NKO to reach is horizontally close to the Sun with a large vertical displacement. However, the required sail lightness number for that NKO is much higher than the closer NKOs to 1 AU orbit, and so the trip time is increased by no more than 200 days. It is also noted that it appears to be easier to reach larger vertical displacements, than to approach close to the Sun. The transfer time results in Figure 8.3 correlate with the sail performances in Figure 8.2, naturally.

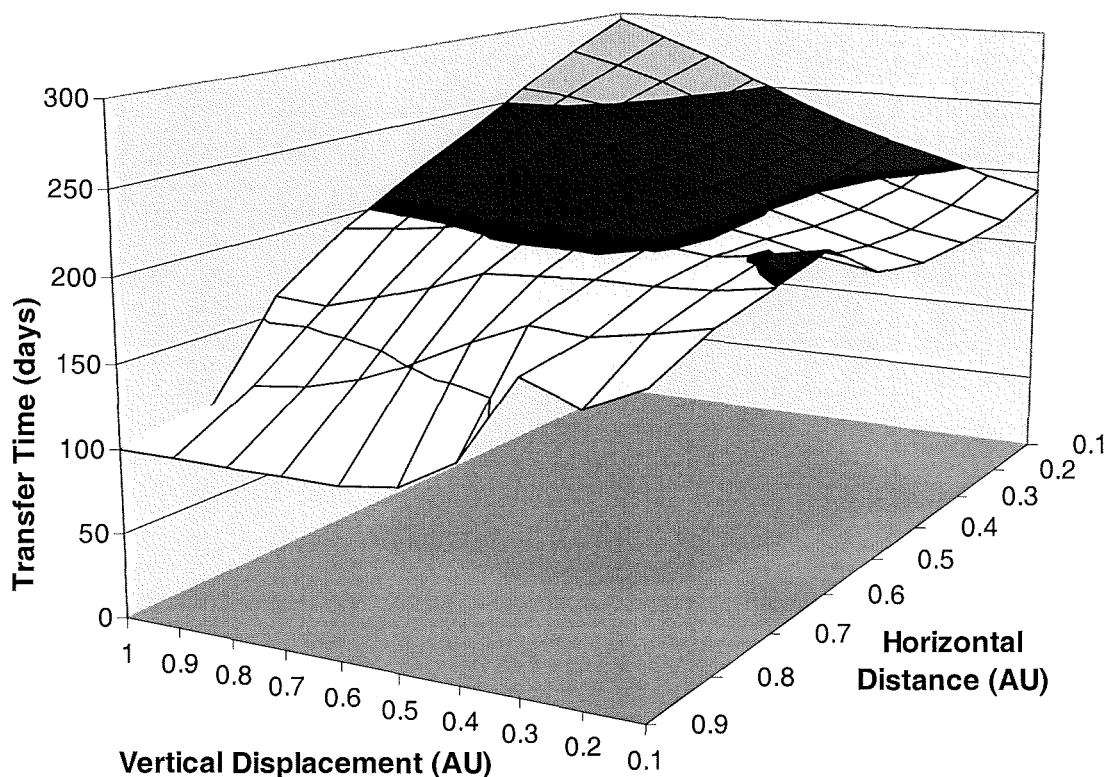


Figure 8.3: Transfer times to 1 year displaced Non-Keplerian Orbits

An example of a transfer to a displaced NKO will now be presented. For any future transfer to a displaced NKO, it would perhaps be desirable to arrive on the final orbit phased such that the spacecraft orbits synchronously with the Earth. Since the NKO defined has a 1 year period, then if the arrival phasing was correct, the solar sail would orbit in phase with the Earth, above the Sun-Earth line (it is noted that this is still a two-body orbit). This constraint was incorporated into the optimiser and a transfer to an Earth-Synchronous Non-Keplerian Orbit was generated. The trajectory to a 0.5 x 0.5 AU 1 year NKO is shown in Figure 8.4, with a lightness number of 0.88 (5.22 mm s^{-2}). The transfer time in this case is 211 days. It should also be noted that this trip time is the same for any Earth departure date, and will only vary by a small amount due to the Earth's eccentricity. The optimal control angle profile has been generated using a low number of fixed segments, shown in Figure 8.5. The initial guess has been generated using a Genetic Algorithm, since the control angle profile for these new transfers is non-intuitive [Hughes and McInnes, 2001, 2002b]. Figure 8.6 shows another example of transfers from a 1 AU circular orbit to a three different NKOs of 0.9 x 0.2 AU (lightness number of 0.43), 0.5 x 0.5 AU (lightness number of 0.88) and 0.3 x 0.7 AU (lightness number of 0.97). The trajectories are optimised using 10 fixed control angle segments (see Chapter 2 for a discussion of control representation). A transfer to 0.9 x 0.2 AU takes 159 days and to 0.5 x 0.5 AU takes 203 days (a little faster than for the Earth-synchronous case), whereas to 0.3 x 0.7 AU NKO takes 224 days.

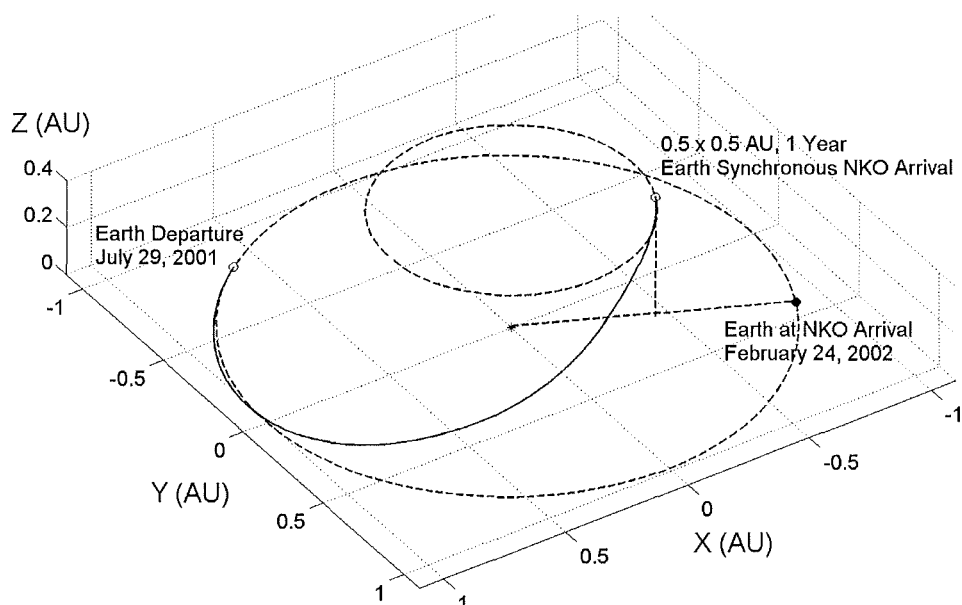


Figure 8.4: Minimum-time transfer to Earth synchronous 0.5 x 0.5 AU, 1 year NKO

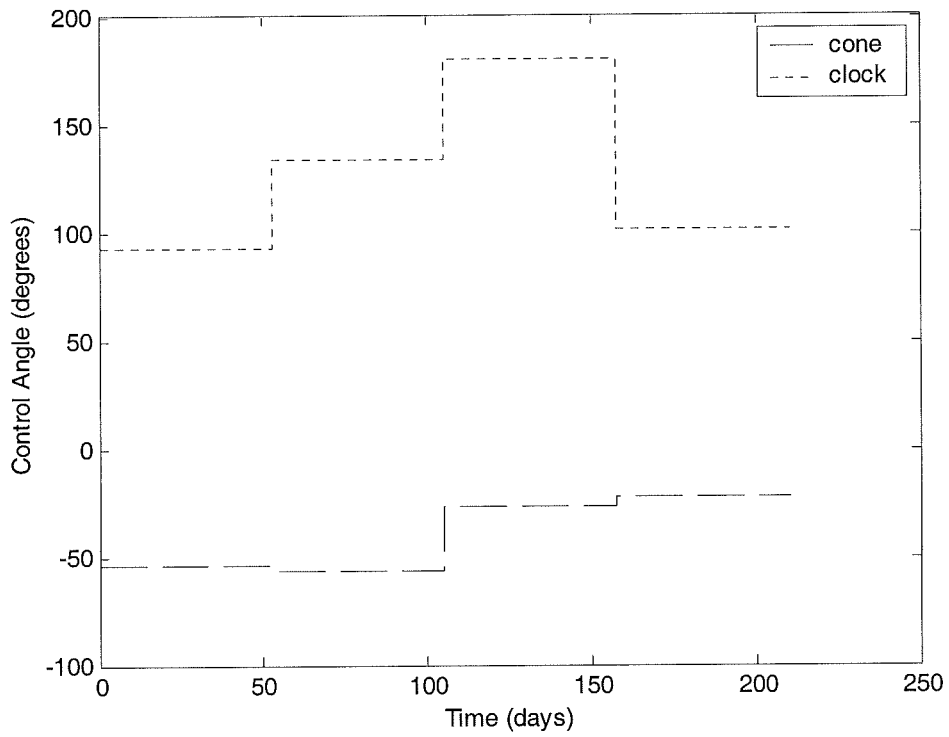


Figure 8.5: Control profile for transfer to Earth synchronous 0.5×0.5 AU NKO

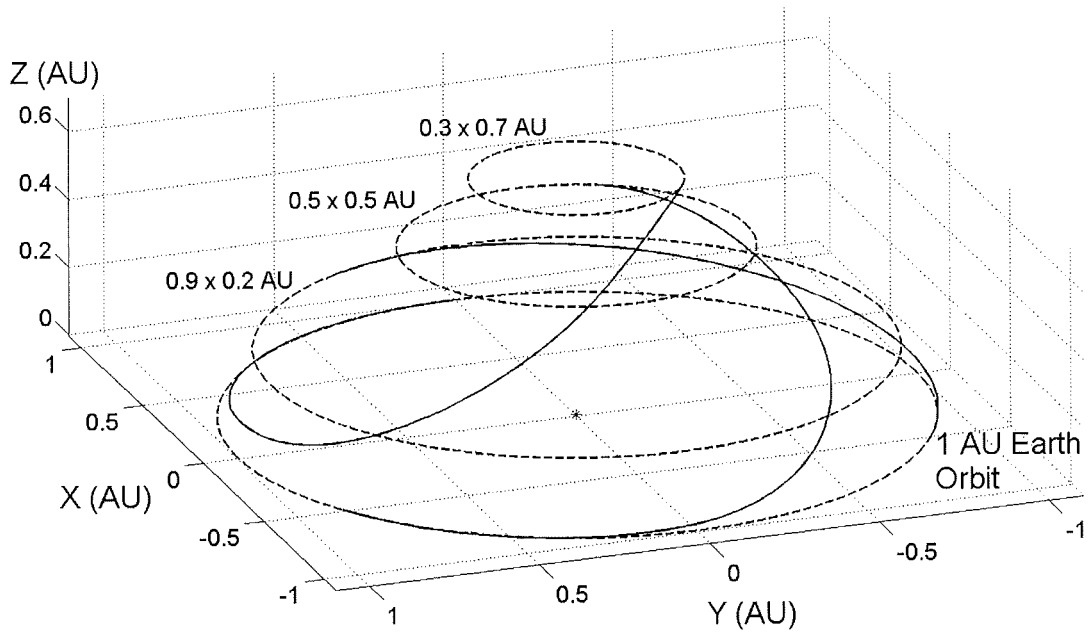


Figure 8.6: Minimum-time transfer to three different NKOs

8.2 Three-Body Non-Keplerian Orbits

The Lagrange points are a well known consequence of the restricted three-body problem. However, the addition of the solar sail enables a large family of Artificial Lagrange point equilibria, similar to the displaced NKO's described earlier, but with much lower sail performance requirements [McInnes, 1999, Chapter 5]. The two-body NKO's above require very high lightness numbers, but these three-body NKO's would only require near to mid-term performance sails. The orbit geometry is depicted in Figure 8.7, and again, a detailed analysis of these three-body NKO's is provided in McInnes [1999]. Similar equations for the required sail lightness number and cone angle can be derived, with a clock angle of zero. For ideal sails, contours of sail loading have been generated by McInnes and are shown in Figure 8.8, for families of artificial Lagrange points in the Earth-Sun-Sail system. The contours correspond to sail loadings of 5 (contour 4) to 30 g m^{-2} (contour 1). It is recalled from Chapter 1, that sail loading is the total mass of the solar sail spacecraft, divided by the total sail area. Therefore, a sail loading of 5 g m^{-2} corresponds to a characteristic acceleration of 1.82 mm s^{-2} , or a sail lightness number of 0.31. These sail performances are much lower than those required in section 8.1.

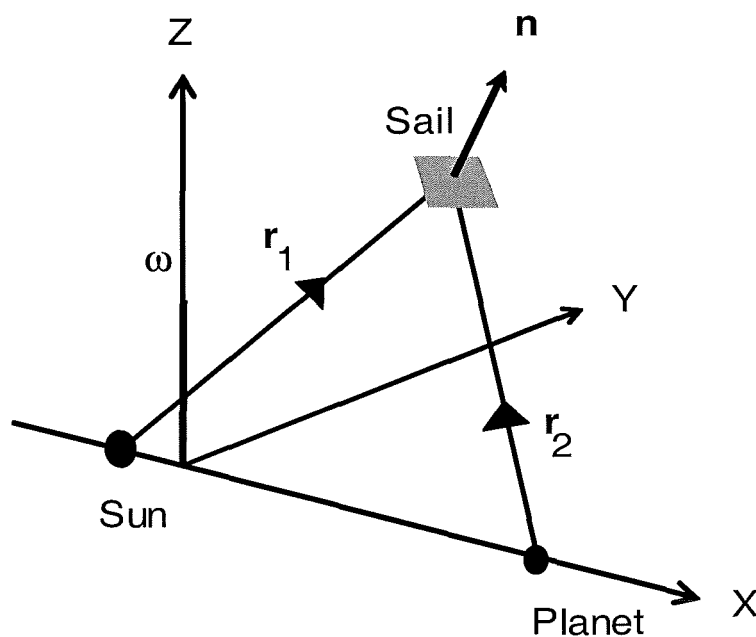


Figure 8.7: Solar sail in a restricted three-body system

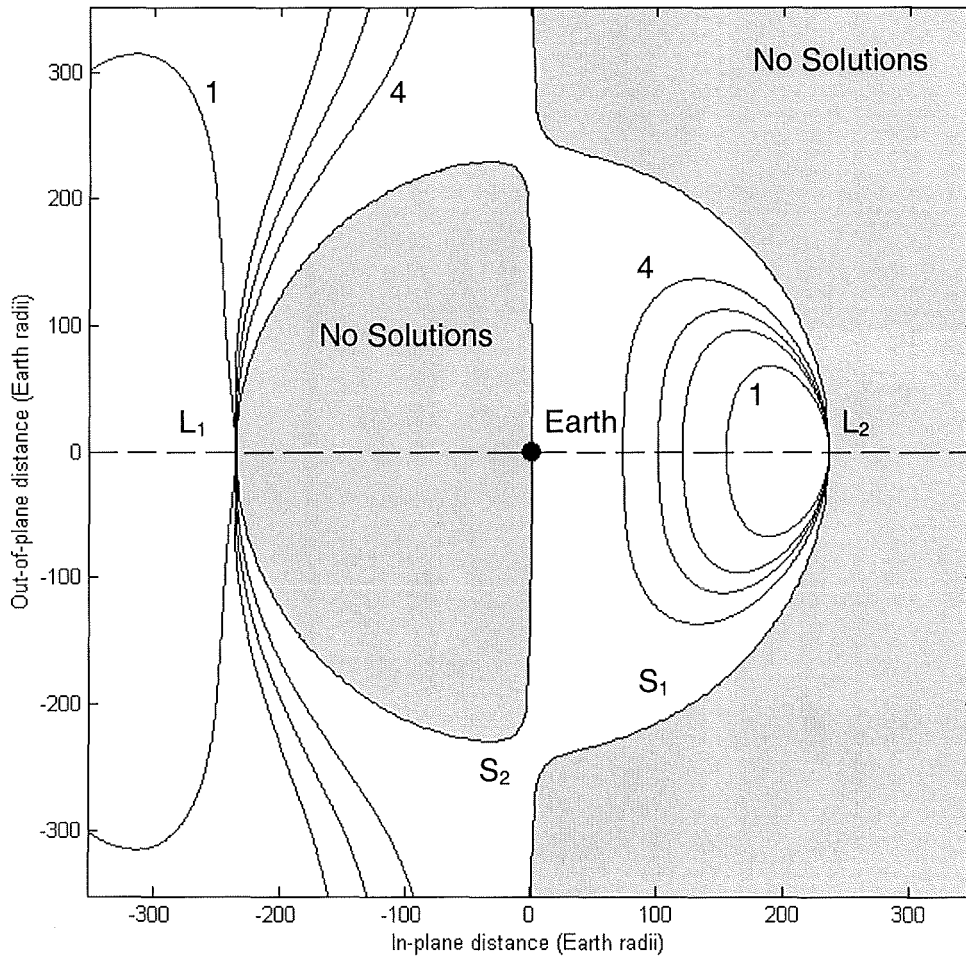


Figure 8.8: Contours of (ideal) sail loading for families of artificial equilibria [C. R. McInnes]

Near-term applications of 3-body NKO are envisaged in the Geostorm and Polar Observer missions [McInnes, 2000b]. Geostorm was a mission concept studied by NASA/JPL, in which a modest solar sail spacecraft is placed Sunward of the classical Earth-Sun L_1 point. The use of a magnetometer to detect solar wind polarity would enable a twofold increase in the solar storm warning time of conventional L_1 Halo orbiters such as SOHO. The Polar Observer mission would use an artificial Lagrange point displaced above the ecliptic plane, high above one of the Earth's poles. This would provide real-time views of the polar latitudes for studying climate change, or could provide line-of-sight telecommunications for high-latitude ground-stations and users. The trajectory analysis presented here was conducted as part of a commercial mission concept study, with an industry specified payload and sail concept.

The problem of solar sail heliocentric transfer to artificial Lagrange points in the Earth-Sun-Spacecraft 3-body system is one that has not been addressed in the literature. The approach to obtaining the optimal control profiles for minimum-time transfer from Earth escape conditions described here is similar to section 8.1, but with the added complication of the Earth's perturbing force. Because of the lack of previous data to refer to, the control parameters are not obvious or intuitive.

The definition of the perturbation due to the Earth is adapted from a description provided by Corneliese [1978]. The perturbing acceleration in the Inertial ECI frame, \mathbf{a}_{Earth} due to the Earth is defined in Eq. 8.14, where μ_{Earth} is the gravitational parameter of the Earth (3.036×10^{-6} in canonical units, where $\mu_{Sun} = 1$), and \mathbf{r}_{Earth} is the position vector of the Earth, and \mathbf{r}_{Sail} is the position vector of the solar sail spacecraft.

$$\mathbf{a}_{Earth} = \mu_{Earth} \left(\frac{\mathbf{r}_{Earth} - \mathbf{r}_{Sail}}{|\mathbf{r}_{Earth} - \mathbf{r}_{Sail}|^3} - \frac{\mathbf{r}_{Earth}}{|\mathbf{r}_{Earth}|^3} \right) \quad [8.14]$$

When the perturbations due to the Earth and sail thrust are added into the variational equations of motion, this takes place in the RTN coordinate frame of the spacecraft. Therefore, the perturbing acceleration of the Earth must be transformed to RTN axes by the standard rotation matrix in Eq. 8.15, where the true longitude, $u = \omega + f$ (ω is again the argument of perihelion).

$$\mathbf{R} = \begin{bmatrix} \cos u \cos \Omega - \sin u \cos i \sin \Omega & \cos u \sin \Omega + \sin u \cos i \cos \Omega & \sin u \sin i \\ -\sin u \cos \Omega - \cos u \cos i \sin \Omega & -\sin u \sin \Omega + \cos u \cos i \cos \Omega & \cos u \sin i \\ \sin i \sin \Omega & -\sin i \cos \Omega & \cos i \end{bmatrix} \quad [8.15]$$

The radial, transverse and normal (RTN) perturbations experienced by the spacecraft are thus the sum of the light pressure ($R_{Sail}, T_{Sail},$ and N_{Sail}) and Earth gravity acceleration components ($R_{Earth}, T_{Earth},$ and N_{Earth}), as in Eq. 8.16.

$$\begin{aligned} R &= R_{Sail} + R_{Earth} \\ T &= T_{Sail} + T_{Earth} \\ N &= N_{Sail} + N_{Earth} \end{aligned} \quad [8.16]$$

The eccentricity of the Earth has been taken into account, but it has been found that this makes only a 1-2 day penalty in transfer time for artificial Lagrange point transfers.

8.2.1 Transfer to Geostorm Orbit

The two-point boundary value problem is specified by the initial conditions at the transition from Earth-centred to Sun-centred control at Earth escape, and the final cartesian coordinates of the sub- L_1 artificial Lagrange point. The initial conditions for heliocentric optimisation, after Earth escape, are shown in Table 8.1. The Earth escape conditions were generated by M. Macdonald at the University of Glasgow using blended analytical control laws [Macdonald, 2005]. The Earth escape start date of heliocentric control is on November 22, 2006. On this date the distance from the solar sail to the Earth is 296 Earth radii. In this case, Earth escape occurs when the sail is on the anti-Sunward side of the Earth, because planet centred escape has been found to be possible only when the sail is travelling away from the Sun [Macdonald, 2005]. This will prolong the heliocentric transfer since the sail will have to move *around* the Earth's sphere of influence to reach the sub- L_1 point on the Sunward side.

The Geostorm orbit is Earth synchronous, so the cartesian coordinates of the final boundary conditions must be obtained from the sub- L_1 radial fraction of the instantaneous Earth-Sun distance – this fraction is 0.9793. To avoid interference from the solar radio disk, the sail is pitched to maintain an artificial Lagrange point lagging 0.0018 AU behind the Sun-Earth line.

Orbital Element	Initial Value	Unit
Semi-major axis, a	1.03606724	AU
Eccentricity, e	0.03826949	-
Inclination, i	0.00524375	radians
Argument of Perihelion, ω	5.96790237	radians
Right Ascension of Ascending Node, Ω	0.98102761	radians
True Anomaly, f	0.38771775	radians
Start Date	2454062.11172382	Julian days

Table 8.1: Geostorm transfer initial conditions at Earth escape

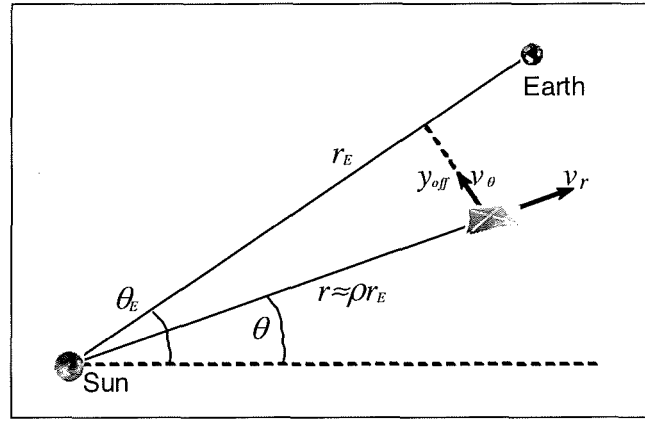


Figure 8.9: Geostorm Sub- L_1 point orbit geometry in ecliptic plane (not to scale)

In the inertial frame, the Earth's orbit and Geostorm 'orbit' are eccentric. Firstly, the instantaneous orbital elements of the Earth are converted to spherical polar coordinates at the final end-time. Then, the spherical polar coordinates of the sub- L_1 point are obtained from the fraction of the Earth-Sun radial distance, and Earth-Sun line offset. The sub- L_1 point geometry is shown in Figure 8.9, and lies entirely within the ecliptic plane, where, ρ is the in-plane distance from the Sun, as a fraction of r_E , and y_{off} is the Sun-Earth line offset, which lags behind the Earth. Also, r_E is the instantaneous Earth-Sun distance. The six element, spherical polar state vector of the sub- L_1 point is then defined by assuming that the rate of change of azimuth angle is the same for the Earth and the sub- L_1 point at each instant in time (although $\dot{\theta}$ is not constant along an eccentric orbit). The sub- L_1 point, polar state-vector is given by Eq. 8.17 – 8.20, with $\phi = 0$ and $v_\phi = 0$, where the Earth is denoted by a subscript E.

$$r = \rho r_E \quad [8.17]$$

$$\theta = \theta_E + \frac{y_{off}}{\rho r_E} \quad [8.18]$$

$$v_r = \rho v_{r_E} \quad [8.19]$$

$$v_\theta = \rho v_{\theta_E} \quad [8.20]$$

The polar state vector is then converted to cartesian coordinates for constraint evaluation. The vertical component of position and velocity is zero as expected, since the Earth's orbit has negligible out-of-plane motion relative to the ecliptic plane. The NPSOL optimiser was used to generate a Geostorm transfer trajectory,

with the Genetic Algorithm utilised to generate the initial control estimate. The control profile was characterised by fixed cone and clock angles across each control segment to make attitude control simpler. The prescribed sail characteristic acceleration was assigned a mid-term level of 0.323 mm s^{-2} , which enables a sub- L_1 point 0.9793 times the instantaneous Earth-Sun distance, offset 0.0018 AU from the Sun-Earth line. The total sail areal density was assigned to be 26.1 g m^{-2} , based on $0.9 \mu\text{m}$ Mylar film and inflatable booms. With a sail reflective efficiency of 85% , the actual sail lightness number is then 0.0586 . Figure 8.10 shows the optimised trajectory, with arrival at the sub- L_1 point 365 days (1 year) later. This transfer has unfavourable initial conditions on the anti-Sunward side of the Earth, and so time is lost by the necessity to pass *around* the Earth to reach the Sunward side. Optimisation starting from sub-escape points on the Sunward side of the Earth have proved unsuccessful and so further work would be necessary to determine a more optimal solution. A magnified view of the final sub- L_1 point arrival is shown in Figure 8.11. The optimisation tolerances selected meant that the final difference in the Earth-Sail distance was within 293 km . Figure 8.12 shows the trajectory relative to the Earth with the positive x -axis along the Sun-Earth line. The large loop away from the Earth, up to 5000 Earth radii behind the Earth-Sun line, is explained by noting that the sail begins the transfer at greater than 1 AU , so initially has a longer orbit period than the Earth. This causes the sail to drift behind the Earth, and only catch up again when inside of 1 AU .

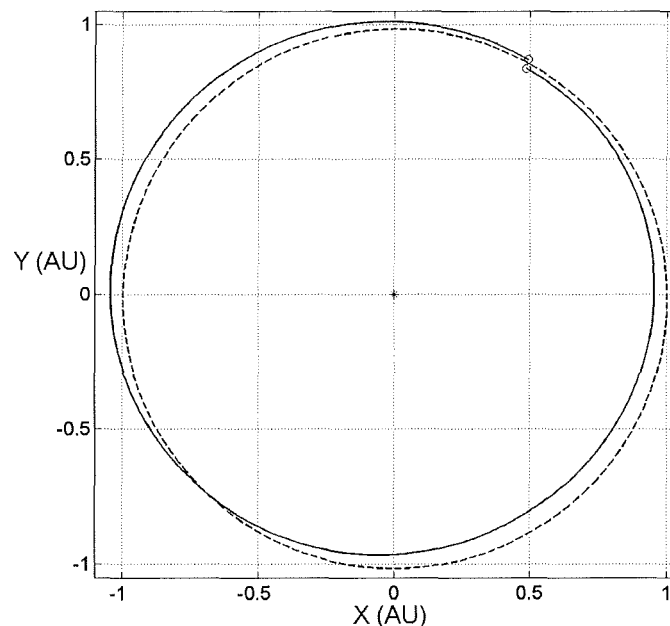


Figure 8.10: Optimal 0.3223 mm s^{-2} transfer, from Earth escape to Geostorm orbit

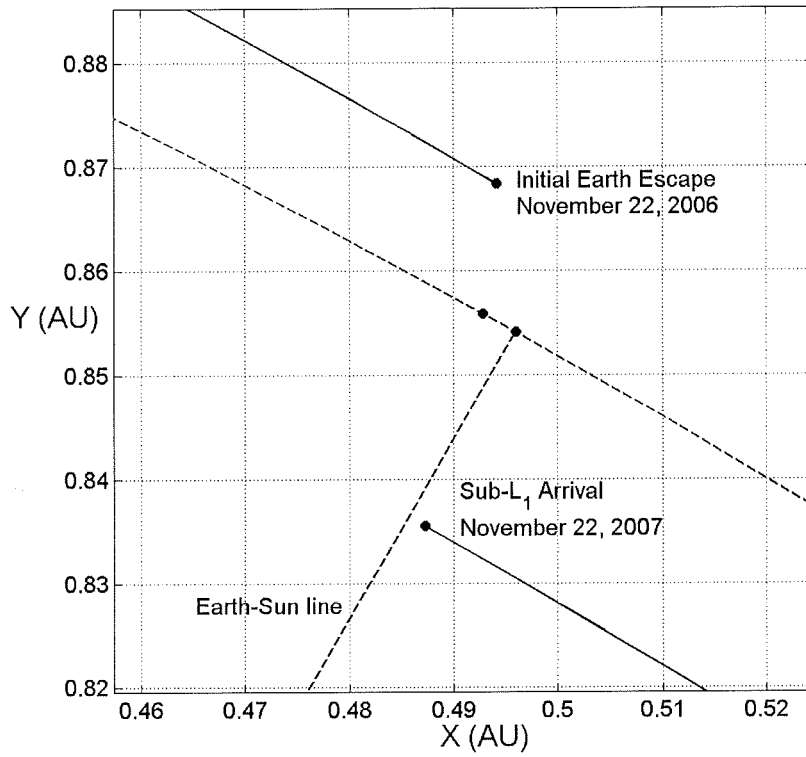


Figure 8.11: Magnified image of final Geostorm Sub-L₁ point approach

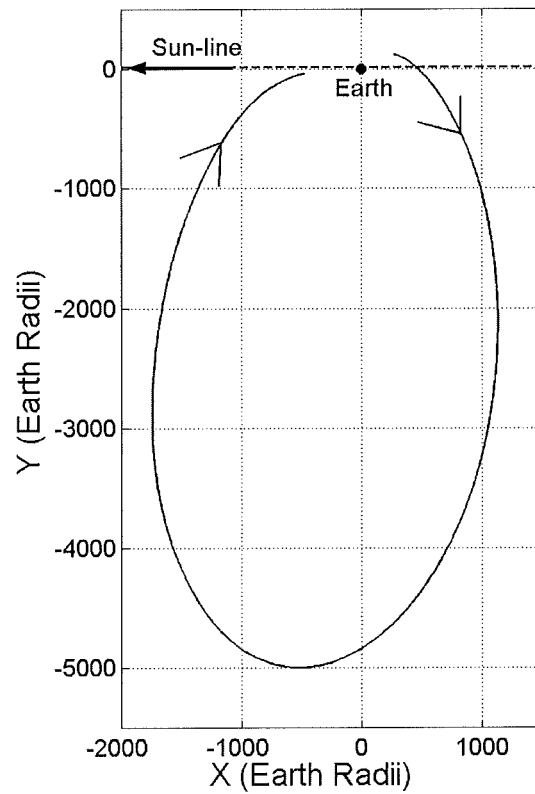


Figure 8.12: Geostorm transfer Earth-relative trajectory (Sun-Earth along positive x-axis)

8.2.2 Transfers to Polar Observer Orbit

The optimisation approach used here was again a hybrid method of the Genetic Algorithm and the NPSOL optimiser. It was found that for the departure conditions set out below, the Genetic Algorithm produced good optimal trajectories by itself, but some reduction in transfer time and fine tuning of the final hover-point errors could be achieved when passing this solution to NPSOL. The average fitness value produced by the Genetic Algorithm was consistently of order 10^5 , satisfying the constraints to within 0.005 AU. This was sufficient to allow NPSOL to converge on a globally optimal solution. The initial conditions for heliocentric optimisation, after kick motor firing and Earth centred manoeuvring, are shown in Table 8.2. Again, the Earth escape conditions were generated by blended analytical control laws [Macdonald, 2005]. The sail has been deployed for 5 days at zero pitch angle for subsystem checkouts and sail integrity assessments. The start date of heliocentric control is on November 24.5, 2005. On this date the distance to the Earth is 103 Earth radii.

The polar observer orbit is Earth synchronous, so the cartesian coordinates of the final boundary conditions must be obtained from the hover point offset distance above and Sunward of the instantaneous state vector of the Earth.

Orbital Element	Initial Value	Unit
Semi-major axis, a	1.00840115	AU
Eccentricity, e	0.04596391	-
Inclination, i	0.00743413	radians
Argument of Perihelion, ω	1.15510229	radians
Right Ascension of Ascending Node, Ω	0.96221207	radians
True Anomaly, f	5.24906598	radians
Start Date	2453698.74826235	Julian days

Table 8.2: Polar Observer hover-point transfer initial heliocentric conditions

Firstly, the instantaneous orbital elements of the Earth are converted to spherical polar coordinates at the final end-time. Then, the spherical polar coordinates of the hover point are obtained by adding-in the offset of E_{ALT} , the distance of the hover point from the centre of mass of the Earth, and γ , the tilt angle from the ecliptic pole. A tilt angle of 45° at 400 Earth radii should satisfy observational requirements of polar regions. The hover-point geometry is shown in Figure 8.13, and has the same azimuth as the Earth. The in-plane distance from the Sun, ρ and the out-of-plane distance above the ecliptic, z are calculated from the offset and tilt angle, by $\rho = r_E - E_{ALT} \sin \gamma$ and $z = E_{ALT} \cos \gamma$, where r_E is the instantaneous Earth-Sun distance. The six element, spherical polar state vector of the hover point is then defined by assuming that the rate of change of azimuth angle is the same for the Earth and the hover point at each instant (again $\dot{\theta}$ is not constant along an eccentric orbit). The hover-point, polar state-vector is given by Eq. 8.21 – 8.26, where the Earth is denoted by a subscript E.

$$r = \sqrt{\rho^2 + z^2} \quad [8.21]$$

$$\theta = \theta_E \quad [8.22]$$

$$\phi = \tan^{-1}\left(\frac{z}{\rho}\right) \quad [8.23]$$

$$v_r = v_{r_E} \cos \phi \quad [8.24]$$

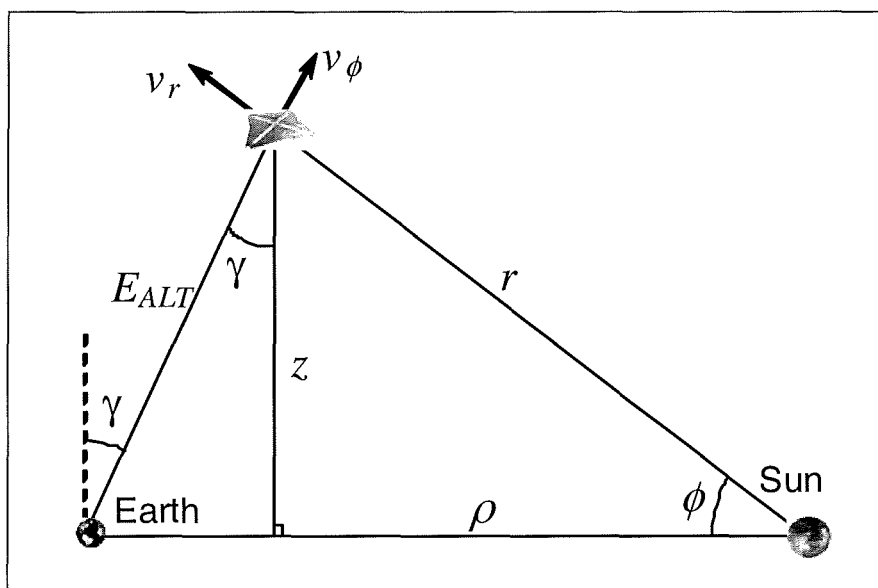


Figure 8.13: Polar Observer hover-point geometry in vertical plane (not to scale)

$$v_\theta = \rho \frac{v_{\theta_E}}{r_E} \quad [8.25]$$

$$v_\phi = -v_{r_E} \sin \phi \quad [8.26]$$

The polar state vector is then converted to cartesian coordinates for constraint evaluation. The vertical component of position is constant, and velocity is near zero as expected, since the Earth's orbit has negligible out-of-plane motion.

The NPSOL optimiser was used to generate an Earth escape to hover-point transfer trajectory, with the Genetic Algorithm utilised where necessary. For a hover point directly over the polar axis of the Earth ($\gamma=23.5^\circ$), the minimum characteristic acceleration required is 0.5464 mm s^{-2} , although the characteristic acceleration selected was somewhat less due to the lower elevation requirement of 45° defined. Transfer trajectories were optimised for a range of accelerations up to 0.7 mm s^{-2} . Figure 8.14 shows the variation of the transfer time with characteristic acceleration. The gradient of the curve seems to level off beyond 0.58 mm s^{-2} . The gradient also tends to decrease slightly at low accelerations ($<0.55 \text{ mm s}^{-2}$) suggesting that the eccentricity, and so solar distance variance, is having a small effect.

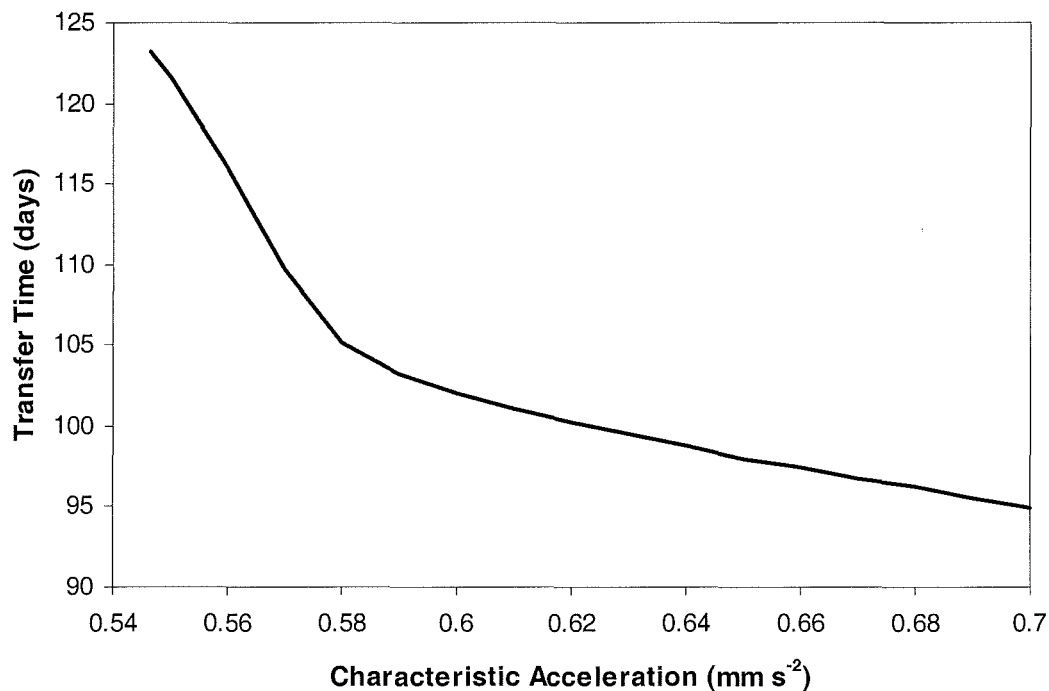


Figure 8.14: Transfer time to Polar Observer hover-point, dependence on characteristic acceleration

The NPSOL optimiser was used to generate a hover-point transfer trajectory from the initial conditions prescribed in Table 8.2, with the Genetic Algorithm utilised to generate the initial control estimate. The control profile was again characterised by fixed cone and clock angles across control segment to make attitude control simpler. For a hover point with an elevation of 45° at 400 Earth radii, the total sail areal density was assigned to be 26.3 g m^{-2} , corresponding to a minimum ideal characteristic acceleration of 0.323 mm s^{-2} . With a sail reflective efficiency of 85%, the real sail lightness number is then 0.0585. Figure 8.15 shows the trajectory, with arrival at the hover point 120.7 days later. The optimisation tolerances selected meant that the final distance of the spacecraft from the desired hover position was within 383 km. Figure 8.16 shows the optimal cone and clock angle control profile. The control profiles are simple and regular, with the cone (pitch) angles never straying more than 51° from the Sun-line. The cone angle is also fairly constant at approximately 45° for the first half of the trajectory, which suggests that a reduced number of segments and a simpler control method could be adopted in future work. Figure 8.17 shows the trajectory relative to the Earth with the positive x-axis along the Sun-Earth line. An approximate sphere of influence of 144.2 Earth radii is also shown for comparison [Leipold, 2000]. Here the Sun-centred trajectory takes over from Earth centred control 40 Earth radii inside the sphere of influence, from where it rises up and towards the Sun in a slight helical motion. The variation of the Earth-Sail distance can be seen in further detail in Figure 8.18.

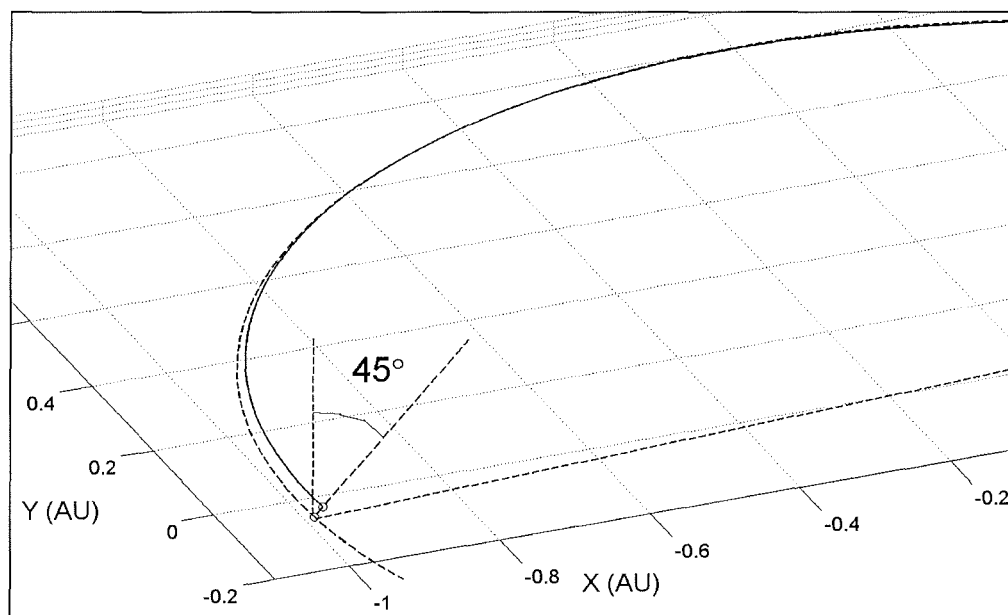


Figure 8.15: Optimal 0.3227 mm s^{-2} transfer to 45° 400 Earth radii hover-point

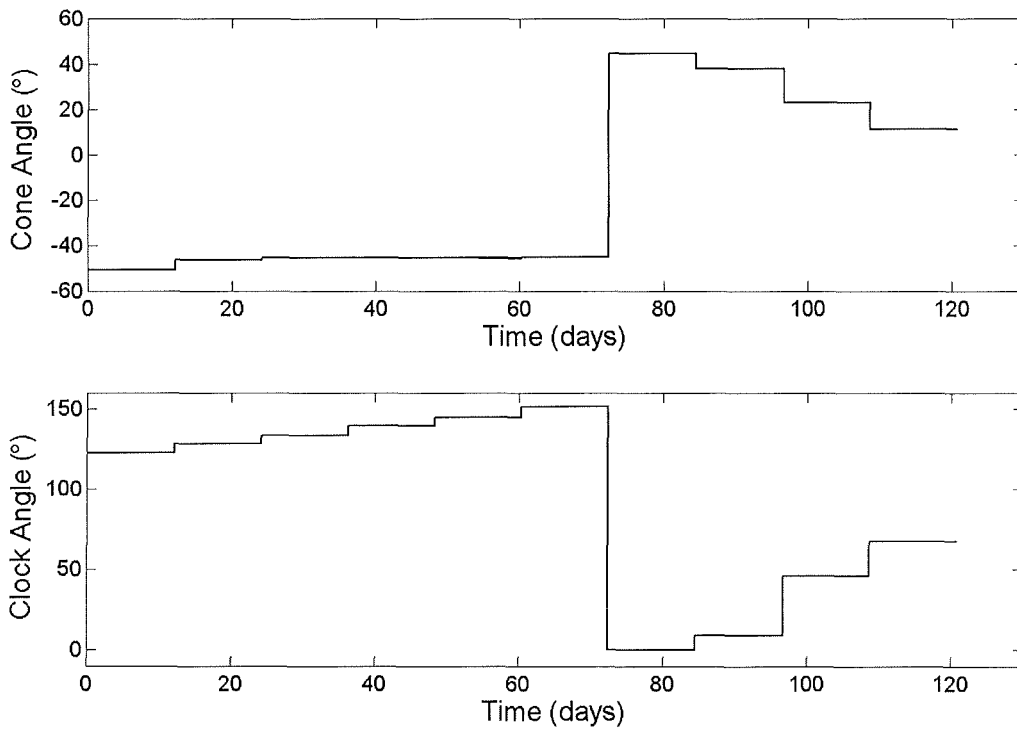


Figure 8.16: Polar observer transfer control profile

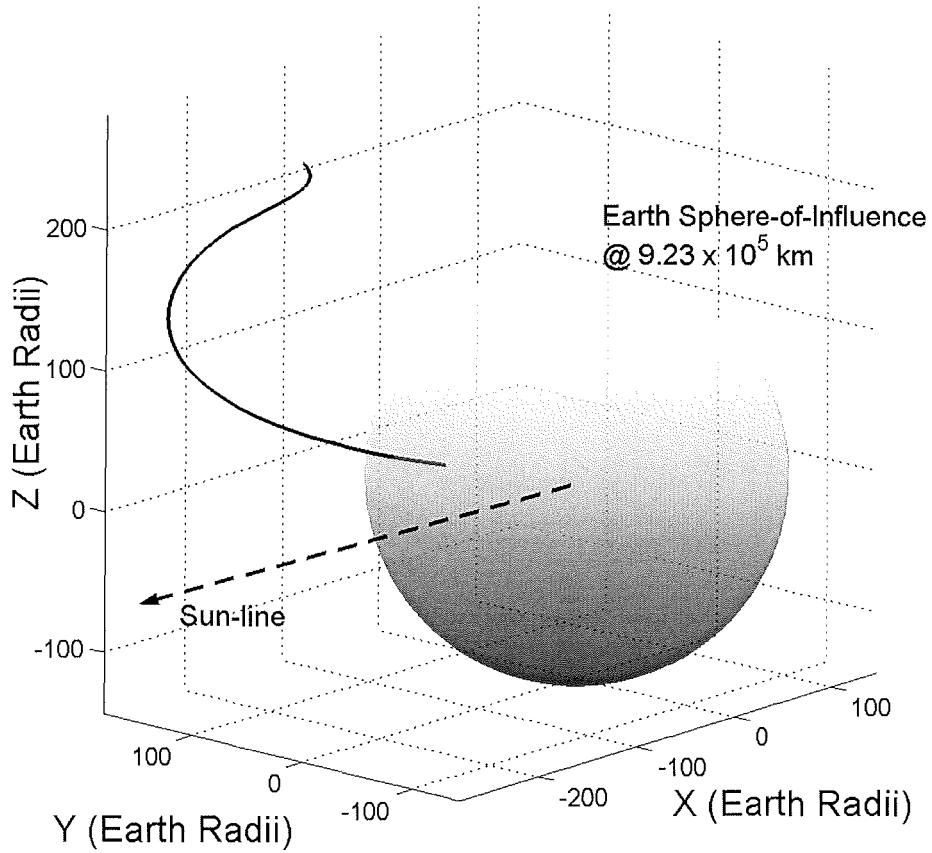


Figure 8.17: Polar observer transfer Earth-relative trajectory (with sphere of influence depicted)

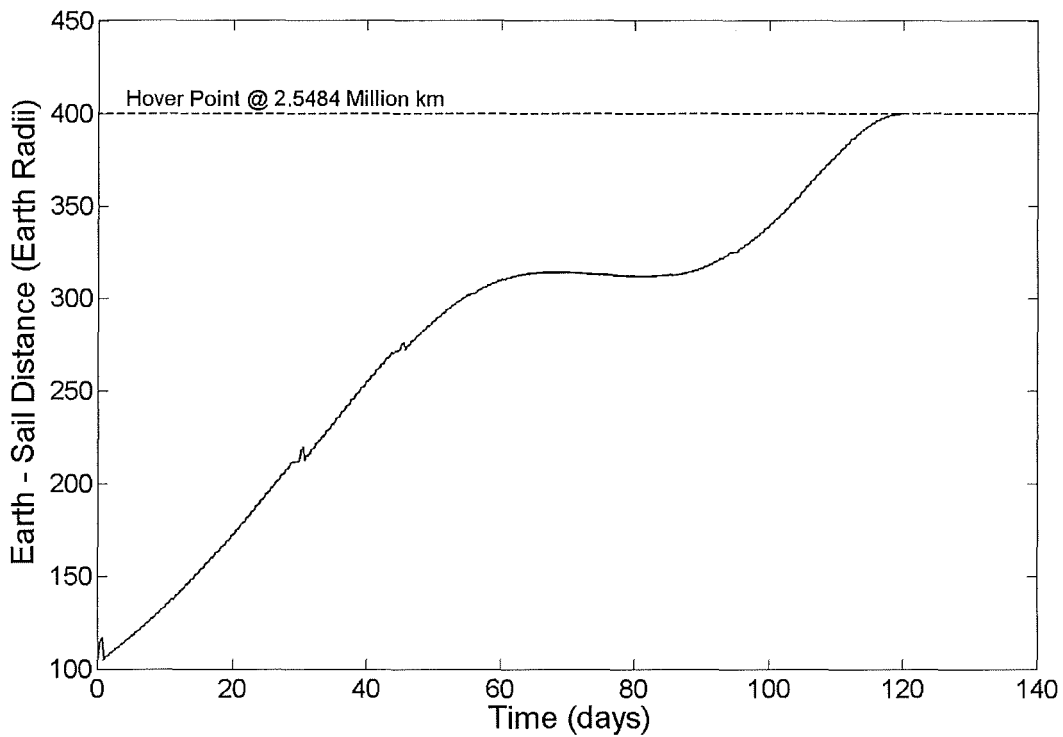


Figure 8.18: Polar observer transfer Earth – Sail distance along trajectory

Using the characteristic acceleration of 0.323 mm s^{-2} , the effect of uncertainties in sail attitude control was investigated for open loop transfers. A positive bias was added to each control angle in the profiles. For the trajectory of 120.7 days, the transfer time was kept fixed, but a differing bias was added. Figure 8.19 shows the trajectory dispersion for different positive control angle bias, for ecliptic and X-Z axes projection in the Earth-centred Sun-line relative rotating frame. Figure 8.20 shows a 3D view of the trajectory dispersion. It can be seen that the dispersion is much greater in the X-Y plane than in the X-Z plane. It can be seen that a control angle bias of 1° would result in a final displacement error of order 60 Earth radii. A larger bias is likely to compromise mission objectives. The effect of errors in control angles should be investigated in more depth for all solar sail trajectories in future work.

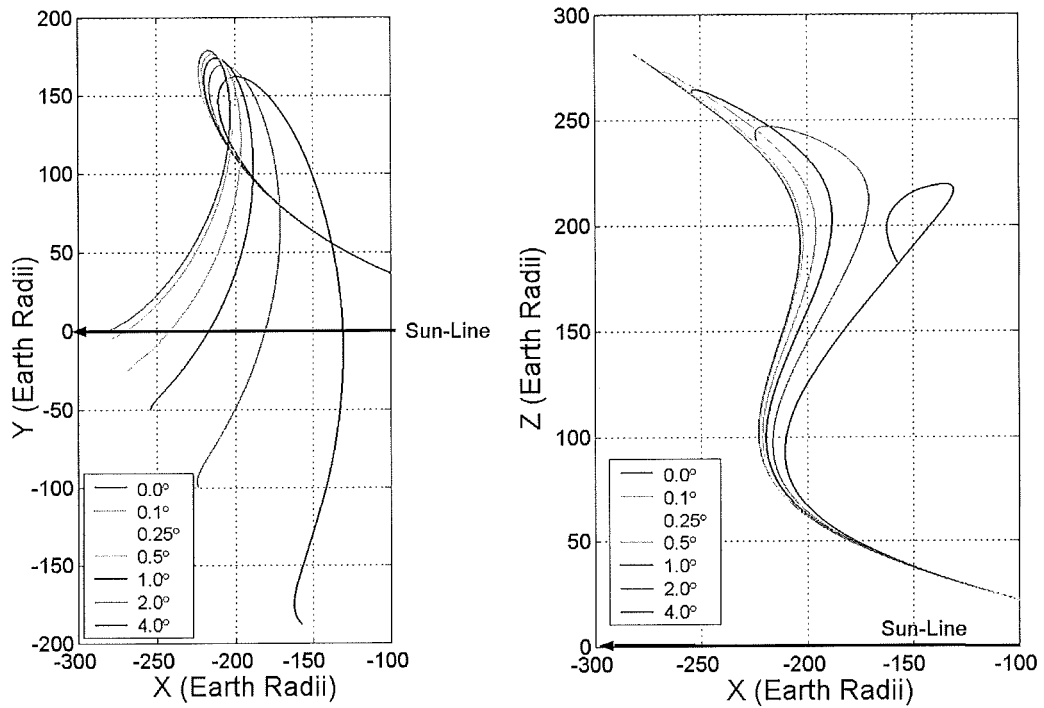


Figure 8.19: Ecliptic projection and X-Z projection of positive control angle bias trajectory dispersion (Earth-centred Sun-line relative axes)

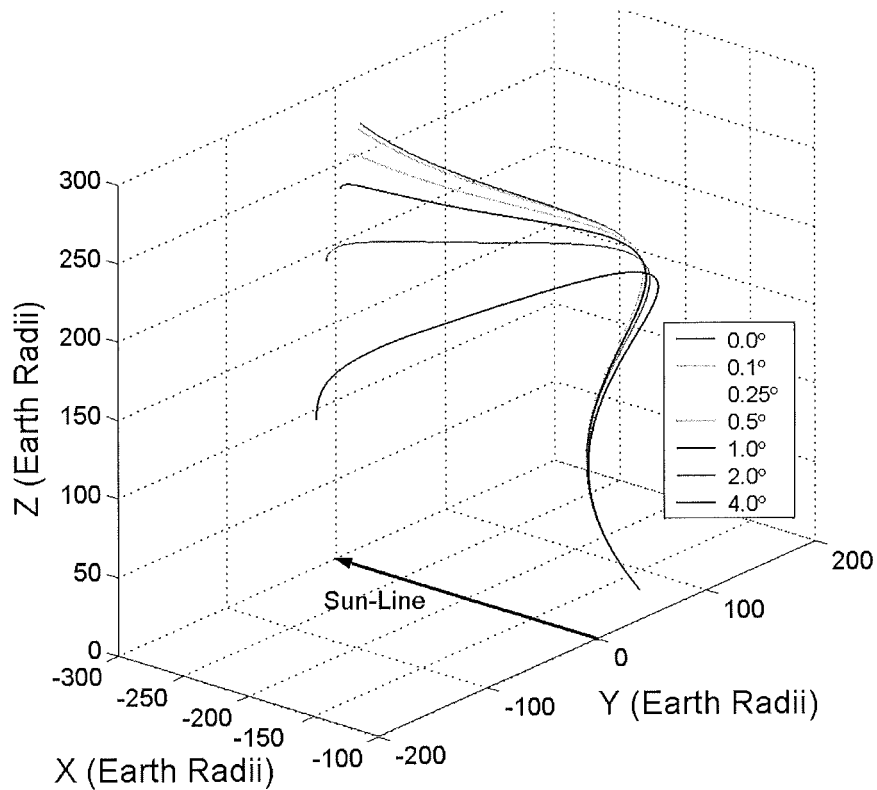


Figure 8.20: Positive control angle bias trajectory dispersion (Earth centred Sun-line relative axes)

8.3 Summary and Discussion

To summarise, the problem of transfer to two-body displaced Non-Keplerian Orbits and three-body artificial equilibria has been addressed. These novel orbits are unique to solar sailing and optimised transfers have not been presented elsewhere in the literature. For two-body displaced NKO, a range of optimised transfers revealed that the trip-times only varied from 100 to 300 days, since the required sail performance is directly related to the final NKO dimensions. It also appeared to be easier to reach large vertical displacements than for closer distances to the Sun. A number of example trajectories were presented. A 1 year Earth-synchronous NKO of dimension 0.5 x 0.5 AU could be reached in 211 days, using a sail lightness number of 0.88, with only 4 control segments. A 1 year NKO of dimension 0.3 x 0.7 AU could be reached in 224 days, using a sail lightness number of 0.97, with 10 control segments.

A brief introduction to three-body artificial equilibria was provided, along with a description of the Geostorm and Polar Observer mission concepts. These orbits are relatively close to the Earth and so it is likely that a real mission would use a ballistic transfer. However, these near-term missions could be used to further demonstrate solar sailing, by using the solar sail to perform the transfer manoeuvre. To this end, optimal trajectories were generated to the nominal Geostorm orbit and to a Polar Observer orbit. After a description of the problem geometry and constraint formulation, it was shown that the Geostorm orbit could be reached from Earth escape in 365 days, with a minimum required characteristic acceleration of 0.323 mm s^{-2} . For the Polar Observer mission, an investigation of the effect of characteristic acceleration on minimised transfer-time to a hover-point directly over a pole was conducted, although the minimum characteristic acceleration is dependent on desired hover-point position. To satisfy observational requirements, an example hover-point, at 45° above the ecliptic, 400 Earth radii above the Earth, could be reached in 121 days, with a minimum characteristic acceleration of 0.323 mm s^{-2} . For the Polar Observer transfer, an investigation of errors in the optimal control angle profile revealed that a control angle error of greater than $\sim 1^\circ$ would mean the spacecraft would be a considerable final displacement from the desired hover-point.

Chapter 9

Conclusions and Discussion

In this Thesis, a broad and extensive range of heliocentric solar sail trajectories have been optimised using a Non-Linear Programming method, based on Sequential Quadratic Programming. This method was often hybridised with a Genetic Algorithm or locally-optimal analytical control laws, to generate an initial guess. The optimisation was carried out in Fortran77. An overview of the available numerical optimisation methods was provided and a description of the selected method was given. This method appears to be robust and flexible, but some optimisation problems with rapid control slews were difficult to solve, due to limitations on parameterisation resolution.

9.1 Inner Solar System trajectories

Extensive departure date scans were carried out for solar sail transfers to Mars, Venus and Mercury in the context of sample return missions. From the trajectory analysis alone, it was found that minimum time launch windows do indeed exist for solar sail interplanetary transfers. In addition, minimum total mission duration launch windows were identified. Even though propellant minimisation is not relevant for solar sails, it is clearly of benefit to depart on an optimal date that results in overall minimum trip time, not least to reduce ground segment costs. These launch windows were identified in the 2010-2020 timeframe, where it was found that the minimum time departure opportunities are spaced according to the synodic period of the planets involved. These minima occur just before trip-time maxima, separated by a discontinuity, due to just missing the target planet, and so requiring an extra revolution. Analysis of using positive launch excess energy was also provided. The trajectory analysis shown here was included in a wider study of overall sample

return mission design which included subsystems design, spacecraft and sail sizing, launch vehicle selection, and cost analysis [McInnes *et al*, 2003a, 2003b, 2003c]. This trajectory analysis naturally influenced the conclusions of the sample return mission studies [Hughes *et al*, 2005]. Solar sailing is not attractive for Mars sample return due to a threefold increase in mission duration over conventional propulsion. Solar sail Venus sample return is also too long, at 5 years (although it just about breaks even with a ballistic outbound transfer and a smaller solar sail for return only [Hughes *et al*, 2005]). Solar sailing can provide significant benefits for Mercury sample return through reducing mission duration to well under 5 years. The large reduction in trip-time over conventional concepts is through the use of a direct transfer without resorting to gravity assists. A brief analysis showed that the use of a Venus gravity assist could, in principle, reduce trip time a little.

9.2 Small-Body Trajectories

Short Period Comet rendezvous missions have been shown to be an attractive application of solar sail propulsion due to their high energy requirements. The original Rosetta mission to Wirtanen could perhaps have been accomplished using solar sailing, with a 68 % reduction in trip time, and a 44 % reduction in launch mass, reducing the mission cost. To show how a solar sail could rapidly intercept a newly discovered Long Period Comet, novel trajectories to examples such as Hale-Bopp and others have been analysed. The option of Earth return or dual comet flyby was analysed to show what the turnaround time would be for the next new LPC interception. Solar sails could open up vast opportunities for multiple asteroid survey missions, given enough time. Replacing the solar electric propulsion component of the Dawn mission with a solar sail, that can obtain equivalent trip-times, could result in a 33 % reduction in launch mass. It was shown that a unique advantage of using a solar sail would be to extend the mission objectives to orbit two further asteroids. The trajectory analysis of a sample return mission to a high-energy, high-inclination Near-Earth Asteroid was shown, as part of a wider sample return mission study [McInnes *et al*, 2003d]. The trajectory aspects were shown to be a 3-phase manoeuvre, using a cranking orbit to increase inclination. The novel concept of symmetry between outbound and return spirals between circular and

elliptical orbits was successfully utilised for generating initial guesses. Due to the high Δv required, solar sailing is truly enabling for this class of target.

9.3 Outer Solar System Trajectories

Solar sail missions to the Outer Solar System have been analysed for a range of Jupiter missions and to Pluto. Again, the trajectory analysis was a contribution to a full mission study [McInnes *et al*, 2003e, 2003f, 2004c]. Trajectories were optimised with low performance square sails and with high performance disc sails. The use of multiple photonic assists and positive launch excess was also investigated. Jupiter flyby missions would perhaps be feasible using modest sized sails, because the arrival velocity is not important. Only large, high performance spinning sails can be used for Jovian orbit rendezvous and capture, due to the weak solar radiation at Jupiter. Lower performance sails would require large chemical insertion burns for orbit capture. The large mass of propellant involved would greatly increase sail size and launch mass, and so the trajectory approach was to minimise arrival velocity subject to a maximum trip time. This trade-off was conducted by varying the number of loops around the Sun and the launch excess velocity. Ultimately, it was found that it was impossible to reduce the arrival velocity below a certain level. The propellant mass required for capture would still be too large to enable a low sail size. Jupiter is, therefore, not an attractive target for solar sailing. Pluto is six times further away from the Sun than Jupiter and only flyby is possible with all methods of propulsion. Trajectory analysis showed that a fast 4.5 year mission could be realised, whereas a slower 14 year trajectory is also possible.

9.4 Interstellar Heliopause Probe Trajectories

Trajectory analysis for a mission to the Heliopause was conducted as part of a wider study into a solar sail Interstellar Heliopause Probe mission [McInnes *et al*, 2004a]. Fast, single-loop trajectories were analysed along with slower, multiple-loop trajectories, with a 25 year time constraint to reach 200 AU. The concept of using maximised-velocity half-arc trajectories was used, optimised from the final

perihelion of the photonic assist, to simplify the optimisation problem. While this approach was not-optimal, it provided initial parametric data so that the lowest characteristic acceleration could be selected for further analysis. The maximum sail film temperature was used to limit the closest solar approach, and this had a direct effect on the maximum escape velocity at 5 AU, where the sail was to be jettisoned. Two slow trajectories using a single loop and multiple loops were baselined, for higher and lower performance sails, respectively. In addition a high performance fast trajectory was also investigated. The use of a simple Jupiter gravity assist was analysed, but did not reap any considerable benefit, since the spacecraft is already moving quite fast. For a conventional aluminium/chromium sail at 0.25 AU, the conclusions were that a fast 3.0 mm s^{-2} sail (large disk) could reach 200 AU in 15 years, and a slower 1.5 mm s^{-2} sail (small disk) would take 25 years. If high performance sail coatings allowed solar approach as close as 0.16 AU, which is also highly unlikely from a thermal systems viewpoint, then a 0.85 mm s^{-2} sail (medium square) would take 25 years using a Jupiter gravity assist. Perhaps the best solution would be to use a large square sail of 1.0 mm s^{-2} , to reach 200 AU in 26 years, however, this would still require high performance coatings to reach within 0.20 AU of the Sun. Finally, an investigation of using positive launch C_3 was conducted, but it was found that there was only any benefit for reaching the final perihelion faster, reducing some of the initial spiralling, and consequently the overall trip time saving was quite small.

9.5 Solar Polar Orbiter Trajectories

Trajectory analysis of a solar sail mission to transfer to an orbit directly over the poles of the Sun was conducted as part of a Solar Polar Orbiter mission study [McInnes *et al*, 2004b]. A detailed parametric analysis was carried out using a two or three-phase manoeuvre, based around the cranking orbit concept. Variations on the nominal trajectory concept investigated include optimised spirals to a low inclination and using positive launch excess, before cranking up the orbit. For a 5 year two-phase trajectory to a 0.48 AU resonant polar orbit, the minimum characteristic acceleration was found to be 0.42 mm s^{-2} . In addition, it was found that a faster, 3.1 year, three-phase trajectory to 0.48 AU polar orbit was possible by

cranking at 0.30 AU, with a characteristic acceleration of 0.5 mm s^{-2} . This trajectory analysis was conducted in greater detail than any previous solar sail polar orbiter study.

9.6 Non-Keplerian Orbit Transfers

The final chapter provided a brief introduction to the unique, displaced Non-Keplerian Orbits which are enabled by solar sailing. Original high performance sail transfers to displaced, two-body NKO's have been generated for a range of final NKO dimensions. Although the required sail performance is very high and dependent on NKO dimension, transfer to essentially any geometry above the ecliptic plane can be accomplished in less than 300 days. The first transfers to mid-performance three-body NKO's were optimised, for the Geostorm and Polar Observer missions, along with some brief control angle sensitivity analysis. These transfers to displaced NKO's have not been analysed before in the literature.

9.7 Further Work

Further work would be to incorporate imperfect reflectivity, billowing and other non-ideal sail effects into the dynamical model, and to re-optimize most of the trajectories and make comparisons with the ideal cases in this thesis. Detailed optical and parametric force models should also be available in the next few years due to current hardware development programmes. Inclusion of the finite solar disc model and perturbations from the other planets should be included in future work. Progression of the Venus gravity assist for Mercury into a full three-dimensional optimisation should be conducted, taking into account the ephemeris and optimising flyby altitude and orientation. This could be part of a wider volume of work to develop a full solar sail multiple gravity assist optimisation tool, although the objective would be to minimise trip time and not propellant mass. Of course, the problem of generating initial guesses would be more complex and this would probably require much user intervention. Further work on the optimisation algorithm would be to increase the robustness of the optimisation method by further hybridising global search algorithms with the local optimiser, to hopefully obviate the need for time-

consuming initial guess searches. It may also prove fruitful to investigate other local search methods such as collocation in greater detail. However, the objective of this thesis was to generate realistic families of trajectories, not to develop better optimisation algorithms.

Lastly, due to the nature of optimisation, it is inevitable that the search space of all the problems is plagued by local minima. Most of the results discovered in this thesis are original and so there are no previous trajectories in the literature with which to validate them against. Besides, there are many parameters affecting the optimal solution, so it is unlikely that two authors will produce exactly the same trajectory with different optimisation methods. The best method used to validate the global optimality of the trajectories was to independently visualise the optimal solution using trajectory integration. Some engineering judgement was used to assess optimality by seeing how ‘smooth’ the control profile was, and if the trajectory itself had any unnecessary features. It often sufficed to manually smooth and re-optimize solutions with irregular control profiles. Of course, it could prove inefficient to keep searching for the true global optima in future work. The author is confident that the majority of results in this thesis are close enough to the global optima to reduce the need for re-optimisation in future work, with only a few exceptions.

9.8 Key Thesis Contributions

This thesis is a broad and extensive heliocentric trajectory database that future researchers can refer to. This can help with validation of new solar sail optimisation algorithms and software, and provide input for preliminary mission assessment studies. The detailed parametric analyses have been constrained by realistic limitations on mission duration, sail characteristic acceleration, and sail film thermal loading. In addition, the targets and mission objectives for which solar sailing is not attractive are identified, which will help researchers to concentrate their efforts on missions where solar sailing is truly enabling, or significantly reduces launch mass. The key contributions to the field of solar sail heliocentric trajectory optimisation, provided by this thesis, are outlined below.

- Sample return missions to Mars and Venus are not attractive for solar sailing due to long trip times, with realistic sail performances. However, a Mercury sample return mission is a highly attractive application of solar sailing due to significant reductions in mission duration and launch mass.
- Minimum time launch windows exist for solar sail missions to the terrestrial planets. Sequences of trip-time minima and maxima have been found, separated by discontinuities and spaced according to the planetary synodic period. In addition, similar launch windows exist for the total mission duration of sample return missions.
- Positive launch hyperbolic excess energy is of little benefit, and even detrimental, for trajectories to Mars. However, positive C_3 can significantly reduce trip-time for missions to Mercury.
- Solar sails can enable a significant reduction in launch mass for Short Period Comet and Main-Belt asteroid rendezvous. Long Period Comet flyby soon after first discovery is also feasible. Solar sailing appears to be truly enabling for high-energy Near-Earth Asteroid sample return missions.
- Rapid flyby missions to the outer planets are possible with solar sails, but Jupiter orbit insertion appears unattractive due to the weak solar radiation pressure at Jupiter distance from the Sun.
- Solar sailing can be used to reach the Heliopause in 25 years or less, subject to thermal limitations on closest solar approach. Positive launch C_3 is of negligible benefit for solar sail Heliopause missions.
- Extensive parametric analysis of transfers to a true solar polar orbit has revealed that a near-term solar sail of characteristic acceleration 0.42 mm s^{-2} would enable a 5 year transfer duration.
- New transfers to displaced Non-Keplerian Orbits and artificial Lagrange points have been produced, which have not previously been documented in the literature.

References

- [1] Anselmi, A., and Scoon, G. E. N., 2001, "BepiColombo, ESA's Mercury Cornerstone Mission," *Planetary and Space Science*, Vol. 49, pp. 1409-1420.
- [2] Bacon, R. H., 1957, "Logarithmic Spiral: An Ideal Trajectory for the Interplanetary Vehicle with Engines of Low Sustained Thrust," *American Journal of Physics*, Vol. 27, No. 3, pp. 164-165.
- [3] Bader, J. L., 2002, "Optimal Low-Thrust Out-of-Ecliptic Trajectories," MAE 502 Final Project Report, Dept. of Mechanical and Aerospace Engineering, Princeton University, January.
- [4] Balthasar, H., Stark, D., and Wöhl, 1987, "The Solar Rotation Elements i and Ω Derived from Recurrent Single Sunspots," *Astronomy and Astrophysics*, Vol. 174, pp. 359-360.
- [5] Bartholomew-Biggs, M. C., Dixon, L. C. W., Hersom, S. E., Maany, Z. A., Flury, W., and Hechler, M., 1987, "From High Thrust to Low Thrust: Application of Advanced Optimisation Methods to Mission Analysis," *ESA Journal*, Vol. 11, pp. 61-73.
- [6] Bauer, T. P., Wood, L. J., and Caughey, T. K., 1982, "Low-Thrust Perturbation Guidance," AIAA-82-1430, AIAA/AAS Astrodynamics Conference, San Diego, California, August 9-11.
- [7] Bauer, T. P., Wood, L. J., and Caughey, T. K., 1983, "Gain Indexing Schemes for Low-Thrust Perturbation Guidance," *Journal of Guidance*, Vol. 6, No. 6, Nov.-Dec., pp. 518-525.
- [8] Betts, J. T., 1994, "Optimal Interplanetary Orbit Transfers by Direct Transcription," Technical Report, Mathematics and Engineering Analysis, Research and Technology Division, Boeing Computer Services, Seattle.

- [9] Betts, J. T., 1998, "Survey of Numerical Methods for Trajectory Optimization," *Journal of Guidance, Control, and Dynamics*, Vol. 21, No. 2, March-April, pp. 193-207.
- [10] Breakwell, J. V., and Rauch, H. E., 1966, "Optimum Guidance for a Low Thrust Interplanetary Vehicle," *AIAA Journal*, Vol. 4, No. 4, April, pp. 693-704.
- [11] Bruschi, R. G., and Vincent, T. L., 1971, "Low-Thrust, Minimum-Fuel, Orbital Transfers," *Astronautica Acta*, Vol. 16, No. 2, pp. 65-74.
- [12] Bryson, A.E., Jr. and Ho, Y.C., 1975, *Applied Optimal Control*, Hemisphere, New York, 1975, pp. 42-69.
- [13] Cichan, T., and Melton, R. G., 2001, "Optimal Trajectories for Non-Ideal Solar Sails," AAS/AIAA Astrodynamics Specialists Conference, Quebec City, Canada, July 30 – August 2.
- [14] Cochran, J. E., Jr., and Lee, S., 1991, "Optimal Low-Thrust Trajectories Using Equinoctial Elements," IAF-91-348, 42nd Congress of the International Astronautical Federation, Montreal, Canada, October 5-11.
- [15] Cohen, D., Gloyer, P., and Rogan, J., 2002, "Preliminary Design of a High Performance Solar Sailing Mission," SSC02-II-5, 16th Annual AIAA/USU Conference on Small Satellites, Utah State University, Utah, August.
- [16] Colasurdo, G., and Casalino, L., 2001, "Optimal Control Law for Interplanetary Trajectories with Solar Sail," AAS 01-469, AAS/AIAA Astrodynamics Specialists Conference, Quebec City, Canada, July 30-August 2.
- [17] Colasurdo, G., and Casalino, L., 2002, "Missions to Asteroids Using Solar Electric Propulsion," *Acta Astronautica*, Vol. 50, No. 11, pp. 705-711.
- [18] Conway, B. A., 1995, "Optimization of Spacecraft Trajectories Using Nonlinear Programming," *From Newton to Chaos*, Edited by A. E. Roy and B. A. Steves, Plenum Press, New York, pp. 287-296.
- [19] Conway, B. A., 1997, "Optimal Low-Thrust Interception of Earth-Crossing Asteroids," *Journal of Guidance, Control, and Dynamics*, Vol. 20, No. 5, September-October, pp. 995-1002.

- [20] Cornelise, J. W., 1978, *Rocket Propulsion and Spaceflight Dynamics*, Pittman, London.
- [21] Coverstone-Carroll, V. L., 1996, "Near-Optimal Low-Thrust Trajectories via Micro-Genetic Algorithms," *Journal of Guidance, Control and Dynamics*, Vol. 20, No. 1, pp. 196-198.
- [22] Coverstone-Carroll, V., and Williams, S. N., 1994, "Optimal Low Thrust Trajectories Using Differential Inclusion Concepts," *The Journal of the Astronautical Sciences*, Vol. 42, No. 4, October-December, pp. 379-393.
- [23] Coverstone-Carroll, V., Hartmann, J. W., and Mason, W. J., 2000, "Optimal Multi-Objective Low-Thrust Spacecraft Trajectories," *Computer Methods in Applied Mechanics and Engineering*, Vol. 186, pp. 387-402.
- [24] Crain, T., Bishop, R. H., Fowler, W., and Rock, K., 1999, "Optimal Interplanetary Trajectory Design via Hybrid Genetic Algorithm/Recursive Quadratic Program Search," AAS 99-133, AAS/AIAA Spaceflight Mechanics Meeting, Breckenridge, Colorado, February 7-10.
- [25] Dachwald, B., and Seboldt, W., 2002, "Optimization of Interplanetary Rendezvous Trajectories for Solar Sailcraft Using a Neurocontroller," AIAA/AAS Astrodynamics Specialist Conference and Exhibit, Monterey, California, August 5-8.
- [26] Desai, R., and Patil, R., 1996, "Salo: Combining Simulated Annealing and Local Optimization for Efficient Global Optimization," *Proceedings of the 9th Florida AI Research Symposium (FLAIRS-'96)*, Key West, Florida, pp. 233-237, June.
- [27] Eagle, C. D., 1999, *Orbital Mechanics Toolbox (in Fortran and Matlab)*, Science Software.
- [28] Eagle, C. D., 2000, "Aerospace Trajectory Optimization Using Direct Transcription and Collocation," <http://cdeagle.cnhost.com/dto.pdf>, May 9.
- [29] Enright, P. J., and Conway, B. A., 1991, "Optimal Finite-Thrust Spacecraft Trajectories Using Collocation and Nonlinear Programming," *Journal of Guidance*, Vol. 4, No. 5, September-October, pp. 981-985.

- [30] Enright, P. J., and Conway, B. A., 1992, "Discrete Approximations to Optimal Trajectories Using Direct Transcription and Nonlinear Programming," *Journal of Guidance, Control, and Dynamics*, Vol. 15, No. 4, July-August, pp. 994-1002.
- [31] Forward, R. L., 1990, "Solar Photon Thruster," *Journal of Spacecraft*, Vol. 27, No. 4, July-August.
- [32] Forward, R. L., 1991, "Statite: A Spacecraft That Does Not orbit," *Journal of Spacecraft and Rockets*, Vol. 28, No. 5, pp. 606-611.
- [33] Fowler, W. T., Crain, T., and Eisenreich, J., 1999, "The Influence of Coordinate System Selection on Genetic Algorithm Optimization of Low-Thrust Spacecraft Trajectories," Paper 99-130, AAS/AIAA Spaceflight Mechanics Meeting, Breckenridge, Colorado, February 7-10.
- [34] French, J. R., and Wright, J., 1986, "Solar Sail Missions to Mercury," *Journal of the British Interplanetary Society*, Vol. 40, pp. 543-550.
- [35] Frisbee, R. H., 2001, "Solar and Electromagnetic Sails for the Mars Cargo Mission," NASA JPL/MSFC/UAH 12th Annual Advanced Space Propulsion Workshop, University of Alabama in Huntsville, Huntsville, Alabama, April 3-5.
- [36] Frisbee, R. H., and Brophy, J. R., 1997, "Inflatable Solar Sails for Low-Cost Robotic Mars Missions," 33rd AIAA/ASME/SAE/ASEE Joint Propulsion Conference and Exhibit, Seattle, WA, July 6-9.
- [37] Garner, C. E., Layman, W., Gavit, S. A., and Knowles, T., 2000, "A Solar Sail Design For A Mission To The Near-Interstellar Medium," STAIF 2000, Albuquerque, New Mexico, January 30 – February 3.
- [38] Garwin, R. L., 1958, "Solar Sailing – A Practical Method of Propulsion Within the Solar System," *Jet Propulsion*, Vol. 28, pp. 188-190.
- [39] Gill, P. E., Murray, W., Saunders, M. A., Wright, M. H., 1998, "User's Guide for NPSOL 5.0: A Fortran Package for Nonlinear Programming," Technical Report SOL 86-1, Revised July 30.

- [40] Goffe, W. L., Ferrier, G. D., and Rogers, J., 1994, "Global Optimization of Statistical Functions with Simulated Annealing," *Journal of Econometrics*, Vol. 60, No. 1/2, Jan-Feb, pp. 65-100.
- [41] Goldberg, D. E., 1989, *Genetic Algorithms in Search, Optimization, and Machine Learning*, Addison-Wesley Publishing Company, Inc., Reading, Massachusetts.
- [42] Guo, Y., and Farquhar, R. W., 2002, "New Horizons Mission Design for the Pluto-Kuiper Belt Mission," AIAA 2002-4722, AIAA/AAS Astrodynamics Specialist Conference and Exhibit, Monterey California, August 5-8.
- [43] Hargraves, C. R., and Paris, S. W., 1987, "Direct Trajectory Optimization Using Nonlinear Programming and Collocation," *Journal of Guidance*, Vol. 10, No. 4, July-August, pp. 338-342.
- [44] Hartmann, J. W., 1999, "Low-Thrust Trajectory Optimisation Using Stochastic Optimization Methods," M.S. Thesis, University of Illinois at Urbana-Champaign, Illinois, January.
- [45] Hartmann, J. W., Coverstone-Carroll, V. L., and Williams, S. N., 1998, "Optimal Interplanetary Spacecraft Trajectories via a Pareto Genetic Algorithm," *The Journal of the Astronautical Sciences*, Vol. 46, No. 3, July-September, pp. 267-282.
- [46] Hughes G. W., Macdonald, M., McInnes C. R., Atzei, A., and Falkner, P., 2005, "Sample Return from Mercury and other Terrestrial Planets Using Solar Sail Propulsion," submitted to *Journal of Spacecraft and Rockets*, February.
- [47] Hughes, G. W., and McInnes, C. R., 2001, "Solar Sail Hybrid Trajectory Optimization," AAS/AIAA Astrodynamics Specialists Conference, Quebec City, Canada, July 30 – August 2.
- [48] Hughes, G. W., and McInnes, C. R., 2002a, "Mercury Sample Return Missions Using Solar Sail Propulsion," IAC-02-W-2.08, 53rd International Astronautical Congress, Houston, TX, October 10-19.
- [49] Hughes, G. W., and McInnes, C. R., 2002b, "Solar Sail Hybrid Trajectory Optimization for Non-Keplerian Orbit Transfers," *Journal of Guidance, Control and Dynamics*, Vol. 25, No. 3, May-June, pp. 602-604.

- [50] Hughes, G. W., and McInnes, C. R., 2004, "Small-Body Encounters Using Solar Sail Propulsion," *Journal of Spacecraft and Rockets*, Vol. 41, No.1, January-February, pp. 140-150.
- [51] Hughes, G. W., Macdonald, M., McInnes, C. R., Atzei, A., and Falkner, P., 2003, "Terrestrial Planet Sample Return Missions Using Solar Sail Propulsion," 5th IAA International Conference on Low-Cost Planetary Missions, ESA/ESTEC, The Netherlands, September 24-26.
- [52] Huyer, W., and Neumaier, A., 1999, "Global Optimization by Multilevel Coordinate Search," *Journal of Global Optimization*, Vol. 14, pp. 331-355.
- [53] Jayaraman, T. S., 1980, "Time-Optimal Orbit Transfer Trajectory for Solar Sail Spacecraft," *Journal of Guidance and Control*, Vol. 3. No. 6, Nov.-Dec., pp. 536-542.
- [54] Kemble, S., 2001, "Optimised Transfers from Earth to Mercury," IAF-01-A.5.03, 52nd International Astronautical Congress, Toulouse, France, October 1-5.
- [55] Kemble, S., 2002, "Comparison of Optimal Low Thrust Ascent and Descent Trajectories for Upper Stages and Planetary Landers," IAC-02-A.6.06, 53rd International Astronautical Congress, Houston, Texas, October 10-19.
- [56] Kluever, C. A., 1997, "Optimal Low Thrust Interplanetary Trajectories by Direct Method Techniques," *The Journal of the Astronautical Sciences*, Vol. 45, No. 3, July-September, pp. 247-262.
- [57] Kluever, C. A., 1998, "Simple Guidance Scheme for Low-Thrust Orbit Transfers," *Journal of Guidance, Control, and Dynamics*, Vol. 21, No. 6, pp. 1015-1017.
- [58] Kluever, C. A., 2000, "Comet Rendezvous Mission Design Using Solar Electric Propulsion Spacecraft," *Journal of Spacecraft and Rockets*, Vol. 37, No. 5, Sept.-Oct., pp. 698-700.
- [59] Kluever, C. A., and Abu-Saymeh, M., 1998, "Mercury Mission Design Using Solar Electric Propulsion Spacecraft," *Journal of Spacecraft and Rockets*, Vol. 35, No. 3, pp. 411-413.

- [60] Koblik, V., 2003, "Solar Sail Motion in Near-Sun Regions," University of Turku, Finland, ISBN 951-29-2375-0.
- [61] Królikowska, M., 2001, "A study of the original orbits of "hyperbolic" comets," *Astronomy & Astrophysics*, Vol. 376, pp. 316-324.
- [62] Leipold M., and Wagner, O., 1998, "'Solar Photonic Assist' Trajectory Design for Solar Sail Missions to the Outer Solar System and Beyond," AAS 98-386, AAS/GSFC International Symposium on Space Flight Dynamics, Greenbelt, Maryland, May 11-15.
- [63] Leipold, M., 2000, "Solar Sail Mission Design," Doctoral Thesis, Technische Universität München, DLR-Forschungsbericht, February.
- [64] Leipold, M., Borg, E., Lingner, S., Pabsch, A., Sachs, R., and Seboldt, W., 1995, "Mercury Orbiter with a Solar Sail Spacecraft," *Acta Astronautica*, Vol. 35, Suppl., pp. 635-644.
- [65] Leipold, M., Fichtner, H., Heber, B., Groepper, P., Lascar, S., Burger, F., Eiden, M., Niederstadt, T., Sickinger, C., Herbeck, L., Dachwald, B., Seboldt, W., 2003, "Heliopause Explorer – A Sailcraft Mission to the Outer Boundaries of the Solar System," 5th IAA International Conference on Low-Cost Planetary Missions, ESTEC, Noordwijk, The Netherlands, September 24-26.
- [66] London, H. S., 1960, "Some Exact Solutions of the Equations of Motion of a Solar Sail With Constant Sail Setting," *American Rocket Society Journal*, Vol. 30, pp. 198-200.
- [67] Lyngvi, A., Falkner, P., Peacock, A., 2003, "The Interstellar Heliopause Probe", Tools and Technologies for Future Planetary Exploration, 37th ESLAB Symposium, ESTEC.
- [68] Macdonald, M., 2005, Doctoral Thesis, University of Glasgow.
- [69] Macdonald, M., and McInnes, C.R., 2001, "Analytic Control Laws for Near-Optimal Geocentric Solar Sail Transfers", AAS 01-472, AAS/AAIA Astrodynamics Specialist Conference, Québec City, Québec, Canada.
- [70] Macdonald, M., Hughes, G. W., McInnes, C. R., Lyngvi, A., and Falkner, P., 2005, "Solar Polar Orbiter Mission," submitted to *Journal of Spacecraft and Rockets*, February.

- [71] MacNeal, R. H., 1967, "The Heliogyro, an Interplanetary Flying Machine," NASA CR-84460, Astro Research Corporation, June.
- [72] Malanin, V. V., and Repyakh, A. V., 1974, "On the Motion of a Craft with Two Solar Sails," *Problemy Mekhaniki Upravlyayemogo Dvizheniya*, No. 5, pp. 99-108.
- [73] McInnes, C. R., 1999, *Solar Sailing: Technology, Dynamics and Mission Applications*, Springer-Verlag, Chichester, ISBN 1-85233-102-X.
- [74] McInnes, C. R., 2000a, "Payload Mass Fractions for Minimum-Time Trajectories of Flat and Compound Solar Sails," *Journal of Guidance, Control, and Dynamics*, Vol. 23, No. 6, November, pp. 1076-1078.
- [75] McInnes, C. R., 2000b, "Near-Term, Low Cost Missions for Solar Sails," *Journal of the British Interplanetary Society*, Vol. 53, pp. 48-61.
- [76] McInnes, C. R., Hughes, G. W., and Macdonald, M., 2003 "Low-Cost Mercury Orbiter and Sample Return Missions Using Solar Sail Propulsion," *The Aeronautical Journal*, No. 2790, August, pp. 469-478.
- [77] McInnes, C. R., Hughes, G. W., and Macdonald, M., 2003a, Technical Note 1 – Mars Sample Return, ESTEC 16534/02/NL/NR, ESA/ESTEC Contract Report, University of Glasgow.
- [78] McInnes, C. R., Hughes, G. W., and Macdonald, M., 2003b, Technical Note 2 – Venus Sample Return, ESTEC 16534/02/NL/NR, ESA/ESTEC Contract Report, University of Glasgow.
- [79] McInnes, C. R., Hughes, G. W., and Macdonald, M., 2003c, Technical Note 3 – Mercury Sample Return, ESTEC 16534/02/NL/NR, ESA/ESTEC Contract Report, University of Glasgow.
- [80] McInnes, C. R., Hughes, G. W., and Macdonald, M., 2003d, Technical Note 4 – Small-Body Sample Return, ESTEC 16534/02/NL/NR, ESA/ESTEC Contract Report, University of Glasgow.
- [81] McInnes, C. R., Hughes, G. W., and Macdonald, M., 2003e, Technical Note 6 – Jupiter Exploration Mission, ESTEC 16534/02/NL/NR, ESA/ESTEC Contract Report, University of Glasgow.

- [82] McInnes, C. R., Hughes, G. W., and Macdonald, M., 2003f, Technical Note 8 – Pluto-Kuiper Belt and Oort Cloud Exploration Missions, ESTEC 16534/02/NL/NR, ESA/ESTEC Contract Report, University of Glasgow.
- [83] McInnes, C. R., Hughes, G. W., and Macdonald, M., 2004a, Technical Note 9 – Interstellar Heliopause Probe, ESTEC 16534/02/NL/NR, ESA/ESTEC Contract Report, University of Glasgow.
- [84] McInnes, C. R., Hughes, G. W., and Macdonald, M., 2004b, Technical Note 10 – Solar Polar Orbiter, ESTEC 16534/02/NL/NR, ESA/ESTEC Contract Report, University of Glasgow.
- [85] McInnes, C. R., Hughes, G. W., and Macdonald, M., 2004c, Technical Note 11 – Jupiter Microsat Explorer, ESTEC 16534/02/NL/NR, ESA/ESTEC Contract Report, University of Glasgow.
- [86] Melbourne, W. G., and Sauer, C. G. Jr., 1961, “Optimum Thrust Programs for Power-Limited Propulsion Systems,” *Astronautica Acta*, Vol. 8, Fasc. 4, pp. 205-227.
- [87] Melbourne, W. G., and Sauer, C. G. Jr., 1963, “Optimal Interplanetary Rendezvous With Power-Limited Vehicles,” *AIAA Journal*, Vol. 1, No. 1, January, pp. 54-60.
- [88] Minovitch, M. A., 1994, “Fast Missions to Pluto Using Jupiter Gravity-Assist and Small Launch Vehicles,” *Journal of Spacecraft and Rockets*, Vol. 31, No. 6, pp. 1029-1037.
- [89] Morrow, E., 2002, “Solar Sail Orbit Operations,” Doctoral Thesis, University of California, San Diego.
- [90] Morrow, E., Scheeres, D. J., and Lubin, D., 2001, “Solar Sail Orbit Operations at Asteroids,” *Journal of Spacecraft and Rockets*, Vol. 38, No. 2, Mar.-Apr., pp. 279-286.
- [91] Murphy, D. M., Murphey, T. W., and Gierow, P. A., 2002, “Scalable Solar Sail Subsystem Design Considerations,” AIAA 2002-1703, 43rd Structures, Structural Dynamics, and Materials Conference, Denver, Colorado, April 22-25.

- [92] Neugebauer, M., *et al*, 1998, "A Solar Polar Sail Mission," University of California, San Diego, NASA/JPL and NASA/GSFC report, February 2, 1998. <http://spacephysics.jpl.nasa.gov/spacephysics/SolarPolarSail/>
- [93] Oberto, B., *et al*, 1999, "Europa Lander 4-99 SSE Roadmap Review" NASA/JPL Advanced Projects Design Team Final Report, April.
- [94] Otten, M., and McInnes, C. R., 1999, "Optimising Interplanetary Solar Sail Trajectories," Department of Aerospace Engineering Final Year Project Report, University of Glasgow, November.
- [95] Perozzi, E., and Fabiani, V., 1998, "On Targeting Long-Period and New Comets for Small Satellite Missions," Proceedings of the Workshop on Space Exploration and Resources Exploitation, ESA Publication ESA-WPP-151, pre-print.
- [96] Perozzi, E., Rondinelli, G., Di Genova, G., Pittich, E. M., and Valsecchi, G. B., 1996, "Small Satellite Missions to Long-Period Comets : The Hale-Bopp Opportunity," *Acta Astronautica*, Vol. 39, No. 1-4, pp. 45-50.
- [97] Powers, R. B., Coverstone-Carroll, V. L., and Prussing, J. E., 1999, "Solar Sail Optimal Orbit Transfers to Synchronous Orbits," AAS 99-034 AAS/AIAA Astrodynamics Conference, Girdwood, Alaska, August 16-19.
- [98] Rauwolf, G. A., and Coverstone-Carroll, V. L., 1996, "Near Optimal Low-Thrust Orbit Transfers Generated by a Genetic Algorithm," *Journal of Spacecraft and Rockets*, Vol. 33, No. 6, November-December, pp. 859-862.
- [99] Rauwolf, G. A., and Friedlander, A., 1999, "Near-Optimal Solar Sail Trajectories Generated by a Genetic Algorithm," Paper 99-332, AAS/AIAA Astrodynamics Specialists Conference, Girdwood, Alaska, August 15-19.
- [100] Russell, C. T., Coradini, A., Feldman, W. C., Jaumann, R., Konopliv, A. S., McCord, T. B., McFadden, L. A., McSween, H. Y., Motolla, S., Neukum, G., Pieters, C. M., Raymond, C. A., Smith, D. E., Sykes, M. V., Williams, B. G., and Zuber, M. T., 2002, "Dawn: A Journey to the Beginning of the Solar System," Paper 02-020 Asteroids, Comets, Meteors Conference, Berlin, Germany, Jul.-Aug.

- [101] Salama, M., White, C., Leland, R., 2003, "Ground Demonstration of a Spinning Solar Sail Deployment Concept," *Journal of Spacecraft and Rockets*, Vol. 40, No.1, January-February, pp. 9-14.
- [102] Santo, A. G., *et al*, 2001, "The MESSENGER mission to Mercury: spacecraft and mission design," *Planetary and Space Science*, Vol. 49, pp. 1481-1500.
- [103] Sauer, C. G., 1999, "Solar Sail Trajectories for Solar-Polar and Interstellar Probe Missions," AAS 99-336, AAS/AIAA Astrodynamics Specialists Conference, Girdwood, Alaska, August 15-19.
- [104] Sauer, C. G., Jr., 1976, "Optimum Solar-Sail Interplanetary Trajectories," AAS/AIAA Astrodynamics Conference, San Diego, California, August 18-20.
- [105] Scheel, W. A., and Conway, B. A., 1994, "Optimization of Very-Low-Thrust, Many-Revolution Spacecraft Trajectories," *Journal of Guidance, Control, and Dynamics*, Vol. 17, No. 6, November-December, pp. 1185-1192.
- [106] Schlinghoff, H., 1987, "Control Laws for Optimal Spacecraft Navigation," *Journal of Spacecraft*, Vol. 24, No. 1, Jan.-Feb., pp. 48-51.
- [107] Scoon, G., Lebreton, J-P., Coradini, M., *et al*, 1999, "Mercury Sample Return", Assessment Study Report, ESA Publication SCI(99)1.
- [108] Seywald, H., and Kumar, R. R., 1995, "Genetic Algorithm Approach for Optimal Control Problems with Linearly Appearing Controls," *Journal of Guidance, Control and Dynamics*, Vol. 18, No. 1, Jan-Feb, pp. 177-182.
- [109] Simon, K., and Zakharov, Y., 1995, "Optimization of Interplanetary Trajectories with Solar Sail," IAF-95-A.2.08 46th International Astronautical Congress, Oslo, Norway, October 2-6.
- [110] Sims, J. A., 2000, "Trajectories to Comets Using Solar Electric Propulsion," AAS 00-134, AAS/AIAA Spaceflight Mechanics Meeting, Clearwater, Florida, January.
- [111] Sweetser, T. H., and Sauer, C. G., 2001, "Advanced Propulsion Options for Missions to the Kuiper Belt," AAS/AIAA Astrodynamics Specialists Conference, Quebec City, Canada, July 30-August 2.

- [112] Tahan, D., and Guelman, M., 2000, "Earth to Mercury Sub-Optimal Trajectories with Solar Electric Propulsion and Venus Gravity Assist," 40th Israel Annual Conference on Aerospace Sciences, Haifa, Israel, February 23-24.
- [113] Tang, S., and Conway, B. A., 1995, "Optimization of Low-Thrust Interplanetary Trajectories Using Collocation and Nonlinear Programming," *Journal of Guidance, Control, and Dynamics*, Vol. 18, No. 3, May-June, pp. 599-604.
- [114] Teofilato, P., and De Pasquale, E., 1998, "A Fast Guidance Algorithm of Autonomous Navigation System," *Planetary and Space Science*, Vol. 46, No. 11/12, pp. 1627-1632.
- [115] Thorne, J. D., and Hall, C. D., 1996, "Approximate Initial Lagrange Costates for Continuous-Thrust Spacecraft," *Journal of Guidance, Control, and Dynamics*, Vol. 19, No. 2, March-April, pp. 283-288.
- [116] Trottemant, E. J., and Biesbroeck, R. G. J., 2000, "Genetic Gradient Method: A Hybrid Method for Trajectory Optimisation," 51st International Astronautical Congress, Rio de Janeiro, Brazil, 2-6 October.
- [117] Tsu, T. C., 1959, "Interplanetary Travel by Solar Sail," *American Rocket Society Journal*, Vol. 29, pp. 422-427.
- [118] Uphoff, C., 1994, "Very Fast Solar Sails," International Conference on Space Missions and Astrodynamics III, Politecnico di Torino, Torino, Italy, June.
- [119] Vasile, M., and Bernelli-Zazzera, F., 2001, "Combining Low-Thrust and Gravity Assist Manoeuvres to Reach Planet Mercury," AAS/AIAA Astrodynamics Specialist Conference, Quebec City, Quebec, Canada, July 30 – August 2.
- [120] Vulpetti, G., 1997, "Sailcraft at High Speed by Orbital Angular Momentum Reversal," *Acta Astronautica*, Vol. 40, No. 10, pp. 733-758.
- [121] Walker, M. J. H., Ireland, B., and Owens, J., 1985, "A Set of Modified Equinoctial Orbit Elements," *Celestial Mechanics*, Vol. 36, pp. 409-419.
- [122] Wallace, R. A., 1999, "Precursor Missions to Interstellar Exploration," Paper 114, IEEE Aerospace Conference, Big Sky, Montana, March.

- [123] Wallace, R. A., Ayon, J. A., and Sprague, G. A., 2000, "Interstellar Probe, Mission/System Concept," Paper No. 53, 2000 IEEE Aerospace Conference, Big Sky, Montana, March, in *Aerospace Conference Proceedings*, Vol. 7, Ed. Schncier N, *et al.*, IEEE, Danvers, Massachusetts, pp. 385-396.
- [124] Wie, B., 2001, "Dynamic Modelling and Attitude/Orbit Control System Design for Solar Sail Spacecraft," NASA Solar Sail Working Group, JPL Contract No. 1228156, Draft Interim Report, July 10.
- [125] Wood, L. J., 1982, "Comment on "Time-Optimal Orbit Transfer for Solar Sail Spacecraft," *Journal of Guidance and Control*, Vol. 5, No. 2, March-April, pp. 221-224.
- [126] Wright, J. L., 1992, *Space Sailing*, Gordon and Breach Science Publishers, Amsterdam, ISBN 2-88124-842-X.
- [127] Yen, C. L., 1985, "Ballistic Mercury Orbiter Mission via Venus and Mercury Gravity Assists," AAS 85-346, AAS/AIAA Astrodynamics Specialists Conference, Vail, Colorado, August 12-15.
- [128] Yen, C. L., 2001, "Comparing Solar Sail and Solar Electric Propulsions for Propulsive Effectiveness in Deep Space Missions," AAS/AIAA Spaceflight Mechanics Meeting, Santa Barbara, California, February 11-15.
- [129] Zhukov, A. N., and Lebedev, V. N., 1964, "Variational Problem of Transfer Between Circular Orbits by Means of a Solar Sail," UDC 629.195, *Cosmic Research*, Vol. 2, No. 1, pp. 41-44.

